Transactions of the ASME® Journal of Fluids Engineering

Published Bimonthly by The American Society of Mechanical Engineers

VOLUME 125 • NUMBER 6 • NOVEMBER 2003

FLUIDS ENGINEERING DIVISION
Editor
JOSEPH KATZ (2005)
Assistant to the Editor
LAUREL MURPHY (2005)

Associate Editors
MALCOLM J. ANDREWS (2006)
S. BALACHANDAR (2005)
STEVEN L. CECCIO (2004)
ISMAIL CELIK (2003)
WILLIAM W. COPENHAVER (2004)
THOMAS B. GATSKI (2003)
FERNANDO F. GRINSTEIN (2005)
HAMID JOHARI (2006)
JINKOOK LEE (2006)
JEFFREY S. MARSHALL (2003)
M. VOLKAN ÖTÜGEN (2004)
MICHAEL W. PLESNIAK (2004)
AJAY K. PRASAD (2003)
DENNIS SIGINER (2005)
KYLE D. SQUIRES (2005)
YOSHINOBU TSUJIMOTO (2005)

BOARD ON COMMUNICATIONS
Chair and Vice-President
OZDEN OCHOA

OFFICERS OF THE ASME
President, **REGINALD VACHON**
Exec. Director
V. R. CARTER
Treasurer
R. E. NICKELL

PUBLISHING STAFF
Managing Director, Engineering
THOMAS G. LOUGHLIN
Director, Technical Publishing
PHILIP DI VIETRO
Managing Editor, Technical Publishing
CYNTHIA B. CLARK
Manager, Journals
JOAN MERANZE
Production Coordinator
JUDITH SIERANT
Production Assistant
MARISOL ANDINO

Transactions of the ASME, Journal of Fluids Engineering (ISSN 0098-2202) is published bimonthly (Jan., Mar., May, July, Sept., Nov.) by The American Society of Mechanical Engineers, Three Park Avenue, New York, NY 10016. Periodicals postage paid at New York, NY and additional mailing offices.
POSTMASTER: Send address changes to Transactions of the ASME, Journal of Fluids Engineering, c/o THE AMERICAN SOCIETY OF MECHANICAL ENGINEERS, 22 Law Drive, Box 2300, Fairfield, NJ 07007-2300.
CHANGES OF ADDRESS must be received at Society headquarters seven weeks before they are to be effective. Please send old label and new address.

STATEMENT from By-Laws. The Society shall not be responsible for statements or opinions advanced in papers or ... printed in its publications (B7.1, Par. 3).
COPYRIGHT © 2003 by the American Society of Mechanical Engineers. Authorization to photocopy material for internal or personal use under those circumstances not falling within the fair use provisions of the Copyright Act, contact the Copyright Clearance Center (CCC), 222 Rosewood Drive, Danvers, MA 01923, tel: 978-750-8400, www.copyright.com. Request for special permission or bulk copying should be addressed to Reprints/Permission Department.

INDEXED by Applied Mechanics Reviews and Engineering Information, Inc. Canadian Goods & Services Tax Registration #126148048.

TECHNICAL PAPERS

TECHNICAL BRIEFS

(Contents continued on inside back cover)

This journal is printed on acid-free paper, which exceeds the ANSI Z39.48-1992 specification for permanence of paper and library materials. ∞™
♲ 85% recycled content, including 10% post-consumer fibers.

Downloaded 03 Jun 2010 to 171.66.16.159. Redistribution subject to ASME license or copyright; see http://www.asme.org/terms/Terms_Use.cfm

(Contents continued)

Journal of Fluids Engineering Volume 125, Number 6 NOVEMBER 2003

ANNOUNCEMENTS

A. Lozano
LITEC/CSIC,
Maria de Luna, 10,
50018-Zaragoza, Spain
e-mail: alozano@litec.csic.es

H. Amaveda
Centro Politécnico Superior de Ingenieros,
Area de Mecánica de Fluidos,
Universidad de Zaragoza,
Maria de Luna, 3,
50015-Zaragoza, Spain

F. Barreras
LITEC/CSIC,
Maria de Luna, 10,
50018-Zaragoza, Spain

X. Jordà

M. Lozano

Centre Nacional de Microelectrònica
(CNM-CSIC),
Campus UAB, 08193 Bellaterra,
Cerdanyola del Vallès, Spain

High-Frequency Ultrasonic Atomization With Pulsed Excitation

Ultrasonic atomization is a very convenient method to produce sprays of very small droplets. Resulting droplet size distributions are very narrow and the mean diameter is essentially only controlled by the excitation frequency. Generation of droplets in the micron range requires MHz waves, with voltages around 30 V, which translates into power requirements on the order of 10 W. Tunable wave generators with these characteristics are somewhat uncommon. To explore the capabilities of ultrasonic atomization for inhalation therapies, an excitation source, described in this paper, has been designed. The characteristics of the sprays obtained when driving with it a piezoceramic disk are analyzed. [DOI: 10.1115/1.1603301]

Introduction

Ultrasonic atomization has some specific characteristics that make it advantageous over other traditional mechanical methods, like pressure or gas-assisted systems, to generate sprays of very small droplets. In particular, the resulting droplet size distributions are very narrow, and the droplet diameter is essentially controlled only by the ultrasonic frequency, [1]. For these reasons, the use of ultrasonic atomizing devices is becoming increasingly popular for a number of applications, for example in domestic humidifiers, or medical nebulizers. This last use has boosted the interest in ultrasonic based systems because they are being considered a potential substitute for the disposable pressurized metered dose inhalers (PMDI) based on liquefied fluorocarbon gases that are massively consumed all over the world for asthma treatments and that might be banned in a near future because of the severe restrictions in the use of halogenated organic compounds.

Although the first application of ultrasonic waves to generate sprays was proposed by Wood and Loomis in the beginning of the XX century, [2], there remain many aspects not completely understood about the physics controlling this process. In particular, the interaction between two intervening mechanisms, surface capillary waves, [3–5], and hydrodynamic cavitation is still debated, [6,7].

Due to technical limitations a majority of the experimental studies on ultrasonic atomization has been performed in large systems with low forcing frequencies, usually below 400 kHz. To generate droplets adequate to be inhaled in medical applications (typically around 5 μm) frequencies in the MHz range are required. Although some references describe circuits for ultrasonic excitation, [8], versatile tunable wave generators capable of supplying voltages up to 50–60 V and powers of tens of Watts are very uncommon. For this reason, a wave generator has been specifically designed to excite ultrasonic transducers, and this paper describes it along with its performance tested in a series of experiments.

Excitation System

The development of piezoelectric ceramics in the last decades, has situated them as the preferred material for ultrasonic transducers, because of their excellent electromechanical properties and their low cost. The family of PZT ceramics (lead, zirconium, and titanium compounds) are the base for most piezoelectric transducers due to their high polarizing parameters. Geometrically, these transducers are usually manufactured as disks made of the sinterized material with a terminal on each side. Their electrical behavior near the resonance frequency is described by the impedance plot of Fig. 1, obtained with a HP4195A Spectrum Analyzer for an American Piezo Ceramics, [9], PZT disk and the R-L-C equivalent circuit of Fig. 2(*a*). The capacitor C_O takes into account the effect of contact metallization on each side of the ceramic. However, for higher frequencies, further impedance changes, of smaller amplitudes, can also be detected, corresponding to higher eigenmodes of the disk. Consequently, the transducer behavior would be more accurately described by a set of R-L-C branches, in parallel with the C_O capacitance, as depicted in Fig. 2(*b*). For the disk vibration to achieve amplitudes high enough to produce atomization, it has to be excited at the resonance frequency. At this point the resistance is only of a few ohms, and the power consumption is appreciable. Unfortunately, only a fraction of the power consumption contributes to the mechanical vibration, while a large part is dissipated as heat. For these reasons, it is essential to use tunable generators, capable of supplying alternate voltages with required powers, up to 50 W. However, heating the ceramic above its Curie temperature causes its depolarization leaving it

---

Contributed by the Fluids Engineering Division for publication in the JOURNAL OF FLUIDS ENGINEERING. Manuscript received by the Fluids Engineering Division Apr. 30, 2002; revised manuscript received Apr. 30, 2003. Associate Editor: A. K. Prasad.

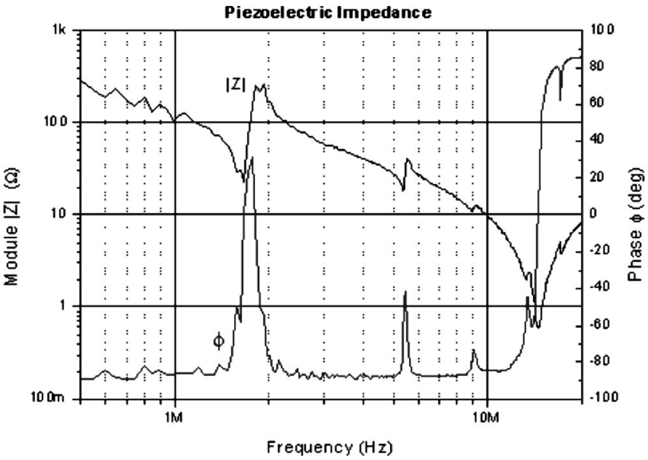

Fig. 1 Impedance plot of a typical piezoelectric transducer

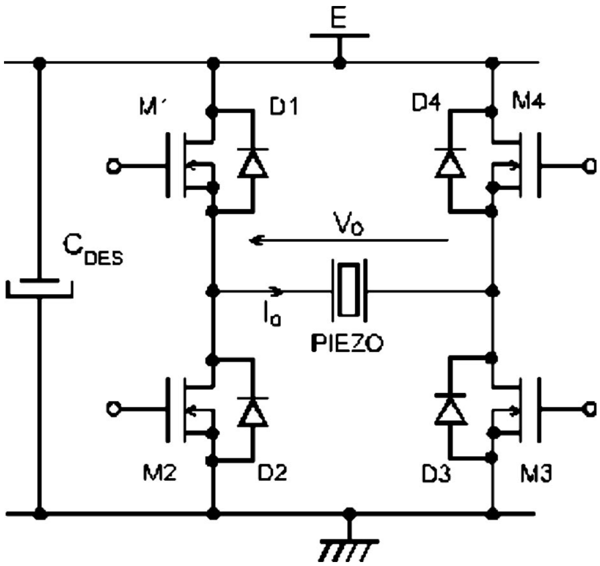

Fig. 3 H-bridge topology of the DC-AC power converter operated in ZVS conditions

unusable for atomization purposes. For this reason, a pulsed excitation system where bursts are produced with a controlled timing prevents undesired overheating.

The whole system comprises a power stage directly connected to the transducer, a DC power supply connected to the power stage, and the control unit. Considering the electrical behavior of the piezoelectric transducer described by a series R-L-C circuit, the H-bridge topology shown in Fig. 3 can apply an alternate square wave voltage from a DC main voltage supply, obtaining quasi-sinusoidal current waveforms, [10]. The MOSFET transistors represented in Fig. 3 are controlled following a ''diagonal'' pattern; i.e., M1 and M3 are controlled by the same control signal, as is the case for M2 and M4. If these gate control signals show a frequency slightly higher than the resonance one, a ZVS (zero voltage switching) condition is obtained and when the transistors are turned ON their drain-to-source voltage is almost zero. This switching strategy decreases switching losses in the power devices, a very relevant subject in high-frequency converter applications. Another interesting issue of the H-bridge topology is that using a DC link voltage E, the peak-to-peak output voltage of the converter is $2E$. The selection of power MOSFETs, gate drive integrated circuits and optocouplers have required a particular attention to ensure their correct operation at high frequencies. VDMOS (vertical double-diffused MOS) have been selected because of their high commutation speed. Furthermore, this transistor structure includes an inner antiparallel diode that can be used as freewheel, [11]. Antiparallel freewheel diodes are used to always maintain a current in the inductive loads, avoiding interruptions that would cause elevated current peaks. The specific transistor employed has been an IRFU110, [12], which limits the maximum voltage deliverable to 100 V. The converter layout has also followed an accurate design process to avoid the influence of parasitic inductance.

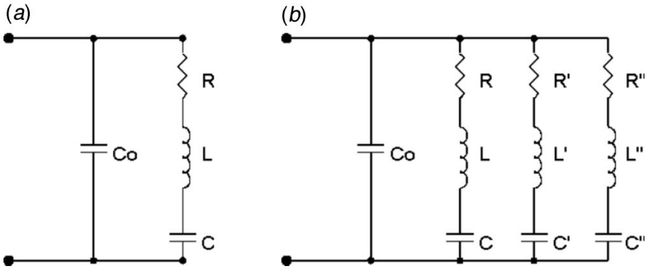

Fig. 2 Electrical circuits equivalent to a ceramic disk: (*a*) simple R-L-C circuit; (*b*) set of R-L-C branches, in parallel with the C_O capacitance

Concerning the control stage, it has been based on CMOS logic components. Generation of the various impulses that originate the control signals in the power stage has been achieved by means of the CMOS version of the well known ''555'' timer. One main design criterion has been to use standard circuits in order to obtain a low cost, robust and easy-to-maintain system. The final performance given by the control stage can be summarized as follows:

- oscillation frequency of the pulse train making up each burst (switching frequency of the MOSFET transistors), between 500 kHz and 2 MHz,
- single burst or repetitive burst mode,
- burst repetition rate between 1 Hz and 1 kHz, and
- number of pulses in each burst, from 1 to 99,999.

Experimental Results

The system has been functionally tested in order to validate its main characteristics. During this phase, an R-L-C circuit using discrete components was connected to the DC-AC converter and almost ideal waveforms and ZVS switching conditions were observed. Nevertheless, when a piezoelectric transducer was connected to the DC-AC converter, the current and voltage waveforms of Fig. 4 were observed, showing high-frequency superposed ripple. After an accurate analysis including circuit simulation (SPICE), this phenomenon has been explained by sudden voltage variations at the output of the converter exciting higher normal-mode frequencies of the piezoelectric ceramic. The experimental output current can be accurately described by the superposition of, at least, three harmonic components. Hence, when dealing with the power converter, the accepted equivalent circuit of the ultrasonic transducer must be modified to include two additional R-L-C branches in parallel with the main one.

To observe the performance of the complete system, different measurements have been performed using a PZT ceramic disc of 1.668 MHz resonance frequency and atomizing small amounts of water. The transducer, shown in Fig. 5 in the atomization process, had a diameter of 20 mm and a thickness of 1.3 mm. The liquid volume (typically 0.5 ml) was deposited over the disk surface, and its level was maintained approximately constant during the atomization process while the measurements were obtained. The maximum voltage that can be delivered to the ceramic without damag-

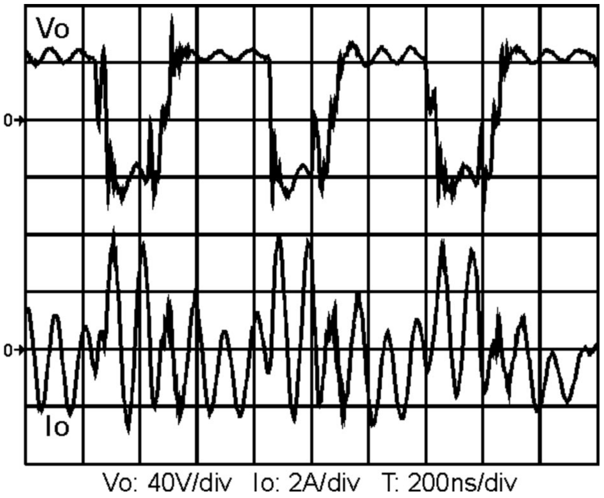

Fig. 4 Current and voltage waveforms of the transducer during the atomization process at 1,668 MHz

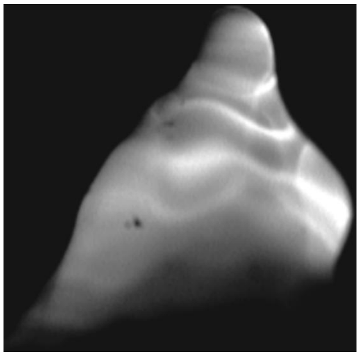

Fig. 6 Cone formation on the liquid surface when rising the voltage to 10 V

ing is 50 V. For voltages below 10 V no atomization was observed. Excitation bursts of 80,000 pulses at a repetition rate of 1 kHz. were applied to the transducers. It was noticed that bursts formed by less than 10,000 pulses were not capable of initiating the atomization.

To measure droplet size distributions a Malvern Mastersizer S laser difractometer, [13], equipped with a 300 mm focal length lens, has been used. According to the manufacturer specifications, this lens is suitable to cover a droplet diameter range from 0.5 μm to 900 μm. The laser beam was crossing the spray cloud 5 mm above the transducer surface. For each measurement, 500 readings of the detector units (''sweeps'') were averaged. Such process was completed in one second, approximately corresponding to 20 forcing bursts. The maximum obscuration in the Malvern measurements was lower than 25 percent, with a minimum of 3.6 percent for the lowest voltage (10 V) due to the reduced flow rate. The room was darkened to maximize the measurements contrast for low obscuration values.

To calculate the droplet size distribution, the polydisperse model of the Malvern software was selected, as recommended by the manufacturer when the distribution shape is not known a priori. From the distributions, mean diameters and other statistical indicators have been calculated. Those parameters considered to be relevant to the nebulization of medical drugs and inhalation of the resulting aerosol have been selected: D_{10} and D_{30} diameters, 10 percent and 50 percent volume percentiles $D_{v0.1}$ and $D_{v0.5}$, and cumulated volume fraction below 5 μm. This last parameter is especially significant because customarily pressurized metered dose inhalers for respiratory track diseases such as asthma are required to deliver at least 30 percent of the nebulized droplets with diameters smaller than 5 μm.

The ultrasonic atomization process can be summarized as follows. When excited with the periodic 1.668 MHz signal, the disk starts vibrating. For voltages below 10 V no atomization is produced, although a pattern of surface waves forms on the liquid surface. As the voltage is increased, the liquid assumes a conical shape (Fig. 6), irrespective of the surface waves. At a determinate voltage, superimposed both to the whole mass displacement that produces the conical shape and the interfacial waves, a fine mist of small droplets is generated.

Droplet size distributions for different forcing voltages are presented in Fig. 7. In agreement with previous studies that relate droplet diameter only to the ultrasonic frequency, [1], it is observed that the distributions are essentially independent of the wave amplitude. Several features can be outlined. There are two main peaks around 3.5 μm and 5.5 μm, respectively. A lower peak located at 1.5 μm can also be discerned for most of the voltages applied. The peak at 50–60 μm, of variable height is

Fig. 5 Image of the piezoceramic disk used in the present experiments, during the atomization process

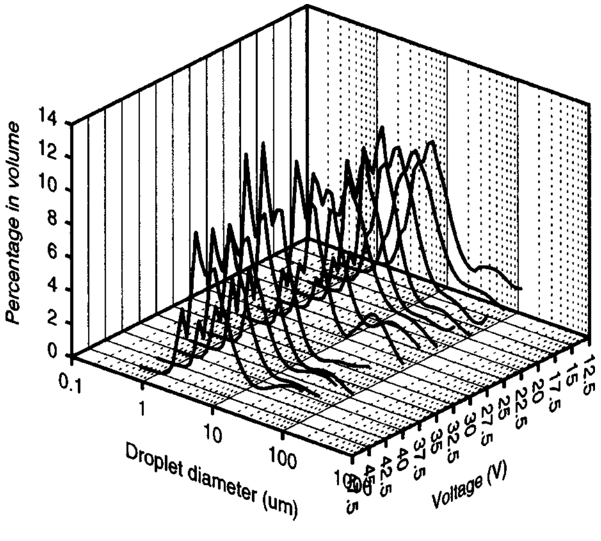

Fig. 7 Variation of the droplet size distribution with voltage

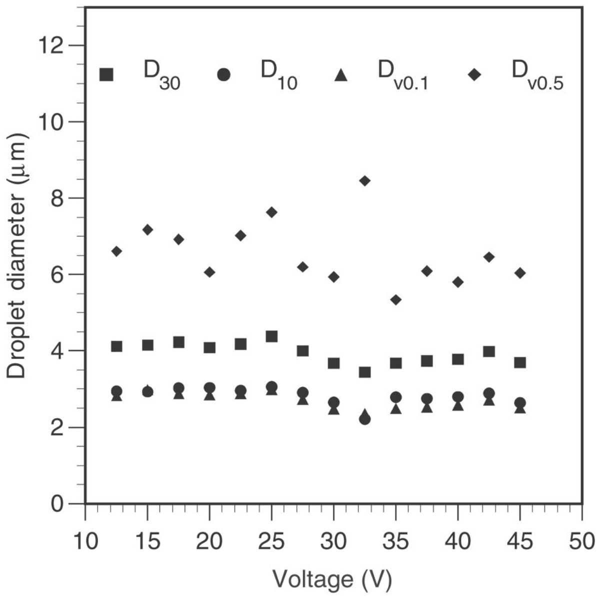

Fig. 8 Mean diameter, D_{10}, mass mean diameter, D_{30}, 10 percent and 50 percent volume percentiles, $D_{v0.1}$ and $D_{v0.5}$ as a function of the forcing voltage. All these parameters have been derived from the distributions in Fig. 7.

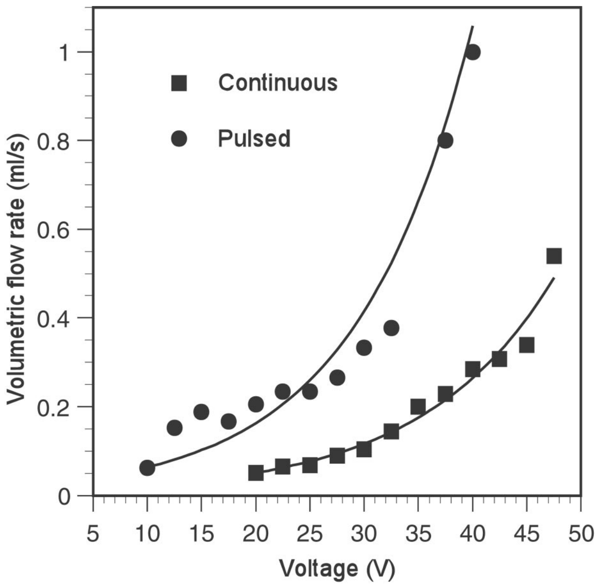

Fig. 10 Atomization rate as a function of voltage

most likely due to droplets that detach from the liquid surface due to the bulk motion of the liquid cone, and is probably independent of the disk resonance frequency.

It is important to note that the distribution functions displayed actually represent histograms with bins of a width that is not constant. On the contrary, it increases exponentially with the diameter. For this reason, plotting the histogram in logarithmic coordinates gives a direct indication of the liquid volume percentage in each bin as if they were equal.

Starting from the size distribution functions, the statistical parameters described above have been calculated. All of them are plotted in Fig. 8. As expected, they are insensitive to voltage variations, confirming other reported observations. Mean diameters are situated below 5 μm, and only the 50 percent volume percentile $D_{v0,5}$ exceeds this value, due to the stronger influence of large droplets that comprise a sensible volume fraction of the total atomized water. Similarly, the volume percentage below 5 μm (Fig. 9) shows an excellent behavior with most values over 40 percent, and reaching a maximum that exceeds 55 percent.

It is important to observe that although the droplet diameter is independent of the excitation amplitude, the atomization rate increases with voltage. This dependence can be observed in Fig. 10. Two curves are compared. The continuous one corresponds to excitation with a sinusoidal generator of fixed frequency and $(0, +V)$ amplitude for a given voltage V, while the pulsed has been obtained forcing the ceramic disk with the driver developed for the present research. It is evidenced that the optimized energy

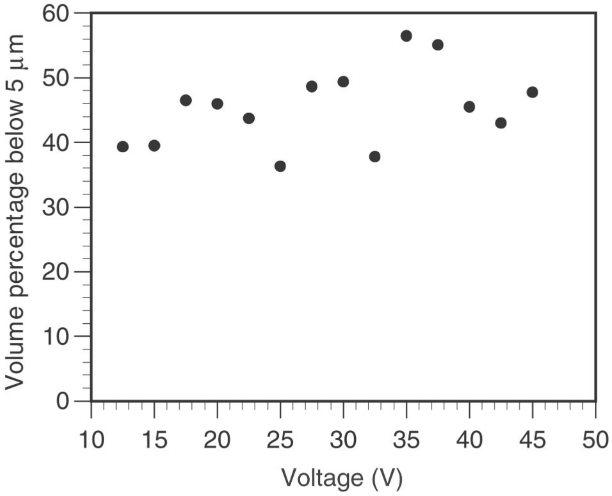

Fig. 9 Volume fraction of droplets with diameter below 5 μm as a function of the excitation voltage

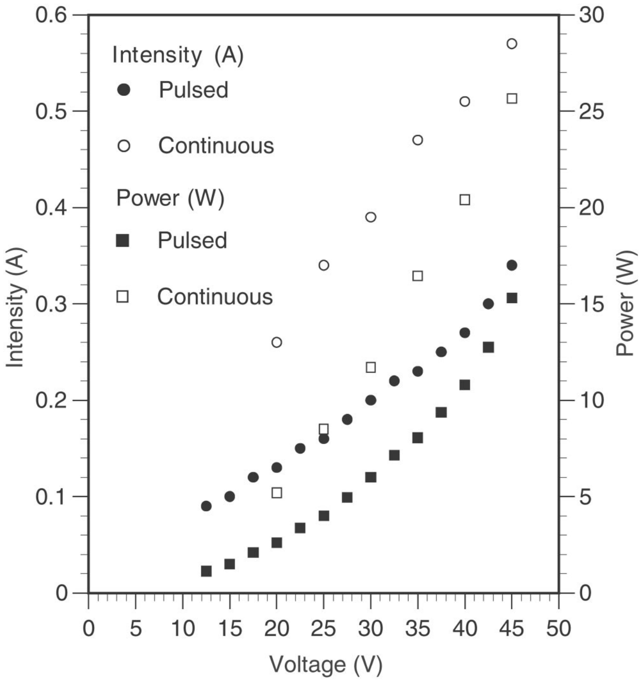

Fig. 11 Intensity and power required for the atomization when forcing at increasing voltages

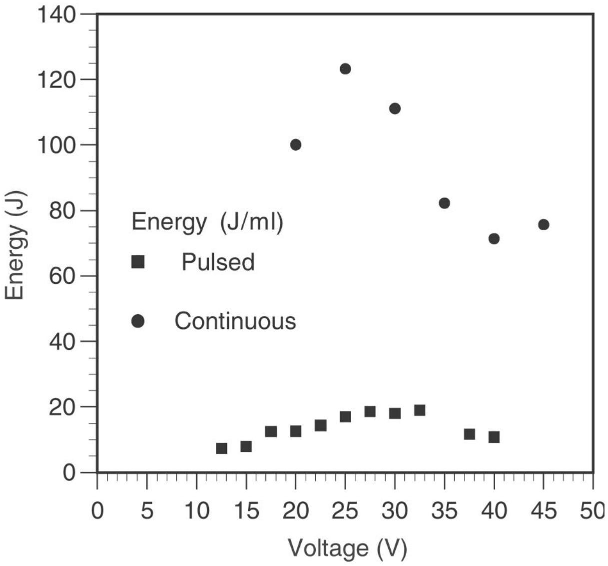

Fig. 12 Energy required to atomize 1 ml of water as a function of voltage

delivery contributes both to increase the atomization flow rate and to decrease the minimum voltage with which atomization is initiated.

Increasing the voltage results also in an increased current consumption. Figure 11 shows the simultaneous behavior of current and power while voltage is raised up for both excitation sources. Again it is observed that the one here developed results to be more efficient. Power requirements around 15 W are needed for a forcing voltage of 45 V. These results might suggest the convenience of atomizing at the lowest possible voltages. However, this reasoning has to be combined with the flow rate values. The total energy required to atomize 1 ml of water is displayed in Fig. 12. It suggests the use of either low or high voltages. The lower end is limited by the minimum forcing voltage needed to achieve atomization, and, for some applications by a minimum flow rate required or a maximum atomization time allowed (for example for single-shot inhalations). The higher limit will be limited by the maximum instant power deliverable from the source and by disk overheating leading the ceramic to exceed its Curie point.

In any case, it might be illustrative to estimate the minimum power and energy requirements for the atomization process. The surface energy of a number N of droplets with diameter D is

$$E = N\sigma\pi D^2$$

where σ is the surface tension coefficient. Assuming a total volume of water V to be atomized of 1 ml, and an excitation voltage of 30 V, the mean diameter will be ~ 3 μm, and $E = 0.144$ J. According to Fig. 11, the required power is ~6 W. The low droplet ejection velocity of 10–20 cm/s (see Barreras et al. [14]) makes the kinetic energy contribution negligible. Consequently, for this particular case, only about 0.8 percent of the supplied power is effectively used in nebulizing the liquid.

Conclusions

An electronic system specifically designed to excite piezoceramic disks for ultrasonic atomization has been designed. It is based on a DC-AC converter with H-bridge topology switching ZVS mode optimized for R-L-C type loads. The equivalent circuit of a piezoelectric resonator approximately corresponds to this type, hence the design seems to be advantageous. However, the abrupt voltage variations at the output cause the excitation not only of the fundamental resonance frequency of the disk but also of higher order harmonics slightly deteriorating the performance. The system has been designed to operate in burst mode, sending a predetermined number of pulses, thus limiting ceramic overheating. It is capable of supplying up to 100 V, in a tunable frequency range from 500 kHz to 2 MHz. With this system, a series of measurements have been obtained exciting a disk with a 1.688 MHz resonance frequency and atomizing water. When voltage exceeds a threshold voltage of 10 V a fine moist is produced. The resulting droplet size distribution presents two main peaks at 3.5 μm and 5.5 μm, and is insensitive to voltage variations in good agreement with previously reported experiments. The spray characteristics are excellent with mean diameters D_{10} and D_{30} below 5 μm. Power consumption is about 10 W. The driving system here presented results to be more efficient than other simple oscillator circuits, because it requires less power and energy to atomize a same amount of water.

References

[1] Lang, R. J., 1962, ''Ultrasonic Atomization of Liquids,'' J. Acoust. Soc. Am., **34**(1), pp. 6–8.

[2] Wood, W. R., and Loomis, A. L., 1927, ''The Physical and Biological Effects of High Frequency Sound-Waves of Great Intensity,'' Philos. Mag., **4**(22), pp. 417–437.

[3] Sorokin, V. I., 1957, ''The Effect of Fountain Formation at the Surface of a Vertically Oscillating Liquid,'' Sov. Phys. Acoust., **3**, pp. 281–291.

[4] Eisenmenger, W., 1959, ''Dynamic Properties of Surface Tension of Water and Aqueous Solutions of Surface Active Agents With Standing Capillary Waves in the Frequency Range From 10 kHz to 1.5 MHz,'' Acoustica, **9**, pp. 327–340.

[5] Sindayihebura, D., and Bolle, L., 1998, ''Ultrasonic Atomization of Liquid: Stability Analysis of the Viscous Liquid Film Free Surface,'' Atomization Sprays, **8**, pp. 217–233.

[6] Söllner, K., 1936, ''Experiments to Demonstrate Cavitation Caused by Ultrasonic Waves,'' Trans. Faraday Soc., **32**, pp. 1537–1538.

[7] Eknadiosyants, O. K., 1968, ''Role of Cavitation in the Process of Liquid Atomization in an Ultrasonic Fountain,'' Sov. Phys. Acoust., **14**(1), pp. 80–84.

[8] Zaitsu, T., Shigehisa, T., Shoyama, M., and Ninomiya, T., 1996, ''Piezoelectric Transformer Converter With PWM Control,'' *IEEE APEC Conference*, pp. 279–283.

[9] American Piezo Ceramics, Inc., Mackeyville, PA.

[10] Mohan, N., Undeland, T. M., and Robbins, W. P., 1989, *Power Electronics: Converters, Applications and Design*, John Wiley and Sons, New York.

[11] Grant, D. A., and Gowar, J., 1989, *Power MOSFETS, Theory and Applications*, John Wiley and Sons, New York.

[12] International Rectifier, El Segundo, CA.

[13] Malvern Instruments Ltd., Malvern, U.K.

[14] Barreras, F., Amaveda, H., and Lozano, A., 2002, ''Transient High-Frequency Ultrasonic Water Atomization,'' Exp. Fluids, **33**(3), pp. 405–413.

The Stretching of a Viscoplastic Thread of Liquid

M. A. M. Al Khatib
HBCC,
King Fahd University of Petroleum & Minerals,
P.O. Box 5087,
Dhahran, Saudi Arabia
e-mail: alkhatibm@yahoo.com

The problem of stretching a viscoplastic (yield-stress) thread of a liquid hanging vertically is considered. The length of the thread at later times and the time at which it ruptures is determined. A Lagrangian coordinate system is used to analyze the extension of the thread as it sags under its own weight, with negligible inertial effects. The biviscosity model has been used to characterize viscoplastic fluids; the Newtonian and Bingham models can be recovered as limiting cases. The Bingham limit is of special interest.

[DOI: 10.1115/1.1624427]

1 Introduction

We consider a short thread of incompressible liquid hanging as in Fig. 1. This thread then stretches under its own weight to become thinner and thinner. The purpose of this paper is to determine the length of the thread, of a liquid of viscoplastic type (that is, exhibiting a yield stress), at later times and the time at which it ruptures. If it is initially uniform, the thinner part of the thread is of course close to the point of attachment. And so the point of rupture is close to the point of attachment. The theory used will of course fail near this point but the work here will not be significantly affected because the failure of the theory will occur in a small part of the thread while most of the thread will not be affected.

Many authors have studied the stretching and breakup of a thread of fluid. Matta and Tytus [1] studied liquid stretching experimentally by using a falling cylinder for Newtonian and viscoelastic fluids. The elongational viscosity is determined from the stress/deformation rate ratio. They noticed that the results for Newtonian liquids are consistent with Trouton expression while the elongational viscosity of viscoelastic liquids increases with time. Sridhar et al. [2] studied stretching Newtonian and viscoelastic liquids to measure the extensional viscosity by using an extra weight in addition to the weight of the liquid. Markovich and Renardy [3] studied stretching and breakup of Newtonian and viscoelastic filaments pulled by a constant weight numerically by a finite difference method. They used the Oldroyd fluid ‘‘B’’ model to represent viscoelastic fluids. Markovich and Renardy noticed that Newtonian filaments show a rapid increase in elongation at one particular point while the addition of a viscoelastic polymer prevents, or at least delays, the breakup, even if it makes only a small difference to shear viscosity. Renardy [4] used numerical and asymptotic methods to study the surface tension driven instability of Newtonian and viscoelastic jets. The Giesekus and the upper convected Maxwell models are used to represent the viscoelastic fluid. For the Newtonian case, he established a relationship between the initial shape of the jet and the asymptotic approach to breakup. For the Oldroyd fluid ‘‘B,’’ no breakup occurs, and he studied the evolution of the jet for large time.

This type of motion which is classified as an extensional flow is of great interest because it fits the motion in many applications such as spinning and drawing of polymer or glass fibers for use in textiles, glass reinforced plastics, or optical fibers (Denn [5], De Wynne et al. [6] and Doyle [7]), light bulbs, and glass tubing (Doyle [7]); rheological measurement by fiber extension and fiber spinning for polymers and glasses (Doyle [7] and Rekhson and Day [8]); and in geophysics examples in the areas of oil recovery (Gaudet et al. [9]) and analyzing the stability of a very viscous fluid layer overlying a less dense (Canright and Morris [10], and Houseman and Molnar [11]).

The problem here in this paper is quite similar to the problem discussed by Stokes et al. [12]. Stokes et al. used the finite element method to study the extensional fall of a very viscous fluid drop and used the slender-drop theory which is the same theory of Wilson [13]. As noted before, the slender-drop theory used will of course fail near the point of rupture. Stokes et al. developed a method for correcting the slender-drop theory where the part which includes the point of rupture can be predicted accurately. This is done by assuming that the part of the thread of fluid close to the boundary is within a region separated by two parallel disks moving relative to one another in the direction normal to their surface. Of course this is possible in their case because they deal with a Newtonian fluid and an exact solution can be found. It is not possible to use the same method because there is no corresponding exact solution for non-Newtonian fluids.

We shall use the uniaxial elongational approach to analyze the extension of a viscous thread as it stretches under its own weight. The forces involved in the process are viscous and gravitational forces. Inertia and surface tension are neglected because of the typically large viscosity of the viscoplastic liquids.

2 Formulation

We shall start discussing the problem of stretching a thread of fluid at constant force in a general way in order to facilitate our real problem. Let $Ox_1x_2x_3$ be Cartesian axes with Ox_3 directed along the axis of a cylinder of a fluid. By applying a force to the end of the cylinder, it stretches in the direction of its axis with velocity field u_1, u_2, and u_3. Assuming that the cross-section of the cylinder remains uniform, we get

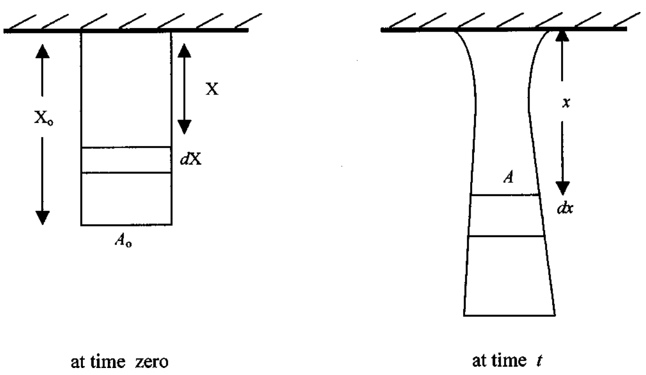

at time zero

at time t

Fig. 1 A diagram of a thread hanging vertically at time zero and at time *t*

Contributed by the Fluids Engineering Division for publication in the JOURNAL OF FLUIDS ENGINEERING. Manuscript received by the Fluids Engineering Division November 20, 2002, revised manuscript received June 4, 2003. Associate Editor: D. Siginer.

$$u_1 = b(t)x_1, \quad u_2 = b(t)x_2 \quad \text{and} \quad u_3 = a(t)x_3. \tag{1}$$

Now by using (1) and the continuity equation we get

$$2b + a = 0.$$

So the strain rate tensor may be written as

$$e_{ij} = \begin{pmatrix} -\frac{1}{2} & 0 & 0 \\ 0 & -\frac{1}{2} & 0 \\ 0 & 0 & 1 \end{pmatrix} a(t)$$

where $a(t) = \dot{L}/L = -\dot{A}/A$, and $L(t)$ and $A(t)$ are the length and cross-section area of the cylinder, respectively.

Next we want to find an expression for the total stress tensor, σ_{ij}. We know that

$$\sigma_{ij} = -p\,\delta_{ij} + \tau_{ij} \tag{2}$$

where p is the pressure.

From the assumption in (1) we get

$$\tau_{11} = \tau_{22}$$

which implies

$$\sigma_{11} = \sigma_{22}.$$

As inertial effects are neglected $(\partial\sigma_{ij}/\partial x_j = 0)$, the total stresses σ_{11} and σ_{22} are independent of x_1 and x_2, and they are independent of x_3 by assumption. At the free surface, by disregarding the atmospheric pressure, we have

$$\sigma_{11} = \sigma_{22} = 0.$$

This implies that

$$\sigma_{11} = \sigma_{22} = 0 \tag{3}$$

anywhere in the cylinder. Equations (2) and (3) imply that

$$\sigma_{33} = \tau_{33} - \tau_{11}. \tag{4}$$

Stretching at constant stress would require $\sigma_{33} = \text{constant}$; we consider here the more practical case of stretching at constant force, when we have

$$\sigma_{33}A = F = \text{constant}.$$

Now we deal with our problem by analyzing the motion from the instant when a uniform thread of fluid of length X_o and cross-section area A_o is suspended vertically from its upper end (see Fig. 1).

Let P be an element of the thread of length dX, and at a distance X from the point of attachment at a time $t=0$ (see Fig. 1). The thread then starts stretching downward under its own weight. At a later time, t, we describe the length of the element P by dx where $x(X,t)$ is the distance between the element P and the point of attachment, and we describe the cross-section area of the thread by $A(X,t)$ (see Fig. 1). The equation of conservation of volume for the element P reads

$$A_o \; dX = A \; dx,$$

i.e.,

$$\frac{\partial x}{\partial X} = \frac{A_o}{A}. \tag{5}$$

Next we consider the force balance on the fluid between X and $X + dX$, denoting longitudinal stress, σ_{33}, by $S(X,t)$. (The sign convention here is that positive S corresponds to tension). As the only forces involved in the process are viscous forces, $(SA)_X$ and $-(SA)_{X+dX}$, and gravitational forces, $-\rho g A \; dx$, the force balance equation is given by

$$(SA)_X - (SA)_{X+dX} - \rho g A \;\; dx = 0. \tag{6}$$

Thus

$$\frac{\partial}{\partial X}(SA) = -\rho g A \frac{\partial x}{\partial X} = -\rho g A_o, \tag{7}$$

which can be integrated to give

$$SA = \rho g A_o (X_o - X) \tag{8}$$

because $S = 0$ at $X = X_o$. Of course this equation has a simple interpretation that the longitudinal force at P equals the weight of all the fluid below. As this force is constant for each particle, we can use the general theory explained above, denoting x_3 by X.

Now we select the biviscosity model to characterize viscoplastic fluids. This model assumes that the material behaves as a Newtonian fluid with very large viscosity until the critical "yield stress" is exceeded. Above the yield stress, the material has a rapidly decreasing viscosity. (see, for example Beverly and Tanner [14] and Wilson [15]). Thus,

$$\tau_{ij} = 2\,\eta_1 e_{ij}; \quad \frac{1}{2}\tau_{ij}\tau_{ij} < \tau_1^2$$

$$\tau_{ij} = 2\,\eta_2 e_{ij} + \frac{\tau_o}{(2e_{ij}e_{ij})^{1/2}} e_{ij}; \quad \frac{1}{2}\tau_{ij}\tau_{ij} > \tau_1^2 \tag{9}$$

where τ_{ij} is the deviatoric stress tensor, e_{ij} strain rate tensor, τ_o and τ_1 are two distinguished stresses. The stresses are related by

$$\tau_o = \tau_1(1 - \epsilon) \tag{10}$$

where ϵ is the dimensionless ratio η_2/η_1 and the Bingham model is approached in the limit $\epsilon \to 0$ ($\epsilon = 1$ gives the Newtonian case). Barnes and Walters [16], by using an accurate rheometer, give experimental evidence that shows some flow of viscoplastic liquids can occur at stresses less than the yield stress, and they found that these liquids demonstrate (approximately) Newtonian behavior in this region, with a very large viscosity. These results motivate the use of biviscosity model to characterize viscoplastic fluids.

By scaling A with A_o, X with X_o, t with $(\eta_2/\rho g X_o)$, τ_{ij} with $\rho g X_o$ and e_{ij} with $\rho g X_o/\eta_2$ the dimensionless form of (8) and (9) will be given by

$$SA = (1 - X) \tag{11}$$

$$\tau_{ij} = \frac{2}{\epsilon} e_{ij}; \quad \frac{1}{2}\tau_{ij}\tau_{ij} < k^2$$

$$\tau_{ij} = 2e_{ij} + \frac{k(1-\epsilon)}{(2e_{ij}e_{ij})^{1/2}} e_{ij}; \quad \frac{1}{2}\tau_{ij}\tau_{ij} > k^2 \tag{12}$$

where $k = \tau_1/\rho g X_o$.

We continue the theory for the biviscosity model. The longitudinal stress is given by

$$S = \frac{3}{\epsilon} a; \quad \frac{1}{2}\tau_{ij}\tau_{ij} < k^2$$

$$S = \left(1 + \frac{k(1-\epsilon)}{\sqrt{3}a}\right) 3a; \quad \frac{1}{2}\tau_{ij}\tau_{ij} > k^2 \tag{13}$$

where $a = -\dot{A}/A$.

Now we want to answer the question; whether at the initial time the whole thread of the fluid is unyielded, or contains a yielded part. To answer this question we have to see whether the yield criterion is satisfied at the initial time or not.

From the yield criterion, $\frac{1}{2}\tau_{ij}\tau_{ij} = k^2$, together with (12) we get

$$\frac{\sqrt{3}}{\epsilon} a = k \tag{14}$$

for the fluid particle at the yield point. In terms of S, the same condition (by (13)) is

$$S=\sqrt{3}k. \tag{15}$$

At $t=0$ Eq. (11) becomes

$$S=(1-X). \tag{16}$$

As the stretch in any fluid element of the thread depends on the weight of liquid below it, so the closer to the point of attachment the more stretch occurs. In other words, the maximum stress will be at $X=0$. Thus the thread starts yielding at a fluid particle at or close to the point of attachment. And so, from Eqs. (15) and (16) we can see that the thread will contain a yielded part at the initial time if

$$k<\frac{1}{\sqrt{3}} \tag{17}$$

that is, the ratio of the viscous forces to gravitational forces is less than $1/\sqrt{3}$.

3 Solution

The solution of the problem will be given for the case $\epsilon=0$ where it reduces to a Bingham fluid (that is, the fluid is absolutely rigid until the critical yield stress, τ_o, is exceeded). And this is because ϵ is very small for most of viscoplastic fluids. However, results for any ϵ are given in the Appendix.

When $k>1/\sqrt{3}$, the whole thread of the fluid will be unyielded at the initial time. That is the whole thread will be absolutely rigid, and so its cross-section area and length, at any time, are given by

$$A=1 \tag{18}$$

$$x=1. \tag{19}$$

In this case, the thread will never rupture.

When $k<1/\sqrt{3}$, the thread contains a yielded part at the initial time, adjacent to the point of attachment. That is the thread will be yielded for $0<X<X_y$ and unyielded for $X_y<X<1$ where X_y is the location of the yield surface (X_y will be determined later in this section).

The future work for the case $k<1/\sqrt{3}$ will be carried out as follows: First, we find the cross-section area, A, of the yielded part of thread for all $0<X<X_y$. Second, we find the location of the yield surface, X_y. Third, we find the total length of the thread. Last we find the time of rupture of the thread, t_r.

The cross-section area of the yielded part of the thread at anytime, t, for all $X<X_y$ is obtained by combining Eqs. (11) and (13) as follows:

$$\left(1+\frac{k}{\sqrt{3}a}\right)3aA=(1-X). \tag{20}$$

By substituting $a=-\dot{A}/A$ in (20) we get

$$\dot{A}-\frac{k}{\sqrt{3}}A=\frac{1}{3}(X-1). \tag{21}$$

By integrating (21) with the initial condition

$$A=A_o \quad \text{at} \quad t=0$$

which is given in dimensionless form by

$$A=1 \quad \text{at} \quad t=0, \tag{22}$$

we get the cross-section area, A, of the yielded part of the thread at anytime

$$A=\left[1-\frac{1}{\sqrt{3}k}(1-X)\right]\exp\left(\frac{kt}{\sqrt{3}}\right)+\frac{1}{\sqrt{3}k}(1-X). \tag{23}$$

In Eq. (23) A must be decreasing, and as the exponent is positive, this makes sense only if

$$1-\frac{1}{\sqrt{3}k}(1-X)<0 \tag{24}$$

(otherwise the cross-section area, A, will be increasing by the time as (23) shows, and this is not possible because A is decreasing with time). Equation (24) is true and it can be proved by using (11) to (13) along with the yield criterion, $\frac{1}{2}\tau_{ij}\tau_{ij}=k^2$, as follows:

$$1-\frac{1}{\sqrt{3}k}(1-X)=\left(1-\frac{1}{1-\epsilon}\right)=\left(\frac{-\epsilon}{1-\epsilon}\right)<0.$$

The cross-section area of the unyielded part of the thread at anytime, t, for all $X_y<X<1$ will be the same as Eq. (18).

By equating the cross-section areas of the unyielded and yielded parts in (18) and (23) we get the location of the yield surface, X_y, which is given by

$$X_y=-\sqrt{3}k+1. \tag{25}$$

Next we want to find the total length of the thread, $x(X,t)$. For this purpose we need the dimensionless form of (5), which may be written as

$$\frac{\partial x}{\partial X}=\frac{1}{A}. \tag{26}$$

The length of the yielded part is obtained by integrating (26) on the interval $0<X<X_y$ with A given in (23) and with the boundary condition

$$x=0 \quad \text{when} \quad X=0 \tag{27}$$

which is given by

$$x=\frac{1}{m}\ln\left|\frac{m+\exp\left(\frac{kt}{\sqrt{3}}\right)}{m(1-X)+\exp\left(\frac{kt}{\sqrt{3}}\right)}\right| \tag{28}$$

where $m=(1/\sqrt{3}k)\,[1-\exp(kt/\sqrt{3})]$.

The length of the unyielded part $(X_y<X<1)$ is given by

$$x=\sqrt{3}k. \tag{29}$$

The total length of the Bingham thread is obtained from (28) and (29) with $X=1$ which is given by

$$x=\frac{1}{m}\ln\left|\frac{1}{\sqrt{3}k}\left[\exp\left(\frac{-kt}{\sqrt{3}}\right)-1\right]+1\right|+\sqrt{3}k. \tag{30}$$

The graph of (30) is given in Fig. 5 with $\epsilon=0$.

The time of rupture of the thread, t_r, is obtained by setting the cross-section area, A, in Eq. (23) to zero with $X=0$ which gives

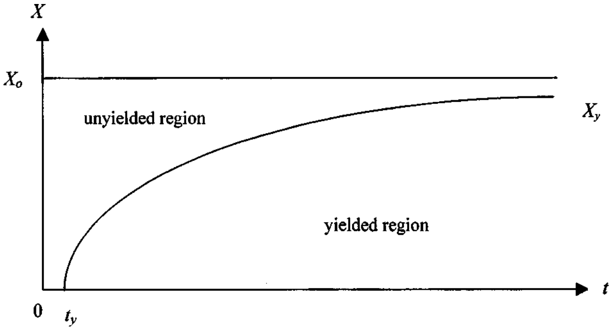

Fig. 2 A diagram for case $k>1/\sqrt{3}$

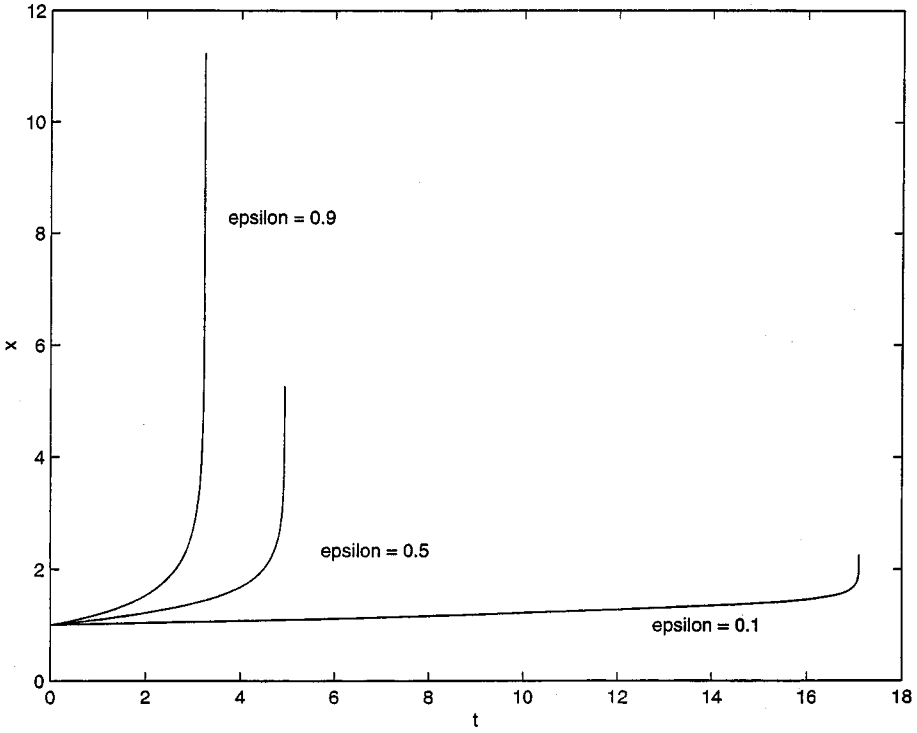

Fig. 3 The length, x, of a viscoplastic thread against the time, t, in the case $k>1/\sqrt{3}$

$$t_r = \frac{\sqrt{3}}{k}\ln\left(\frac{1}{1-\sqrt{3}k}\right). \tag{31}$$

Note that Eq. (23) has been chosen to find the time of rupture because (23) represents the cross-section area of the yielded part of the thread which is close to the point of attachment and the rupture will take place at a fluid particle close to that point.

4 Concluding Remarks

The problem of stretching a thread of viscoplastic fluids has been investigated. We focused on the case $\epsilon=0$ where it reduces to a Bingham fluid. We noticed that when $k>1/\sqrt{3}$, the whole thread of the fluid will be unyielded at initial time. That is the whole thread will be absolutely rigid. In this case, the thread will never rupture, and the length of the thread, at any time, is $x=1$. When $k<1/\sqrt{3}$, the thread contains a yielded part at the initial time, adjacent to the point of attachment. In this case, the length of the thread and the time of rupture are given by (30) and (31), respectively.

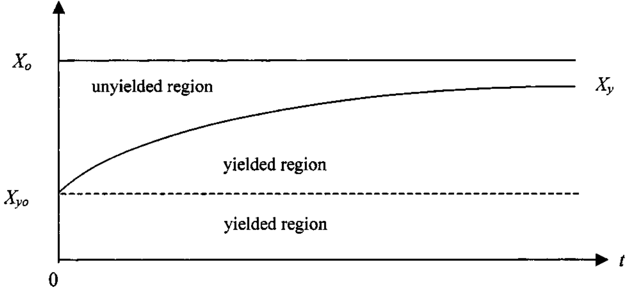

Fig. 4 A diagram for the case $k<1/\sqrt{3}$

Acknowledgment

The author is grateful to HBCC and King Fahd University of Petroleum & Minerals for their continuous help and support.

Appendix

Here we give the results of this problem for any viscoplastic fluid, that is for any ϵ, for both cases $k>1/\sqrt{3}$ and $k<1/\sqrt{3}$.

$k>1/\sqrt{3}$. When $k>1/\sqrt{3}$, the whole thread of the fluid will be unyielded at the initial time. Figure 2 shows a clear description for the problem in the case $k>1/\sqrt{3}$. As we notice from Fig. 2, the thread will be unyielded for the time, $t<t_y$, and the yield criterion will be satisfied sooner or later on any fluid particle because A decreases and so S increases (from (11)).

From (11) and the first equation of (13), we get

$$\dot{A} = \frac{\epsilon}{3}(X-1). \tag{32}$$

Integrating (32) with the initial condition given in (22) we get the cross-section area, A, of the thread at any time, $t<t_y$

$$A = \frac{\epsilon}{3}(X-1)t+1. \tag{33}$$

From (14), (32), and (33) the time, t_y, can be written as

$$t_y = \frac{3}{\epsilon}\left(1-\frac{1}{\sqrt{3}k}\right). \tag{34}$$

As mentioned before, the thread will start yielding on a fluid particle close to the point of attachment (i.e., at $X=0$). When $t>t_y$ then thread will contain yielded and unyielded parts, and the yield surface which separates these two parts will not be always on the same fluid element. The figure indicates that at times $t>t_y$ the yield surface is on the fluid particle $X=X_y$. The corresponding cross-section area of the thread, for a fixed fluid particle, X, is obtained from (11) and (15) which can be written as

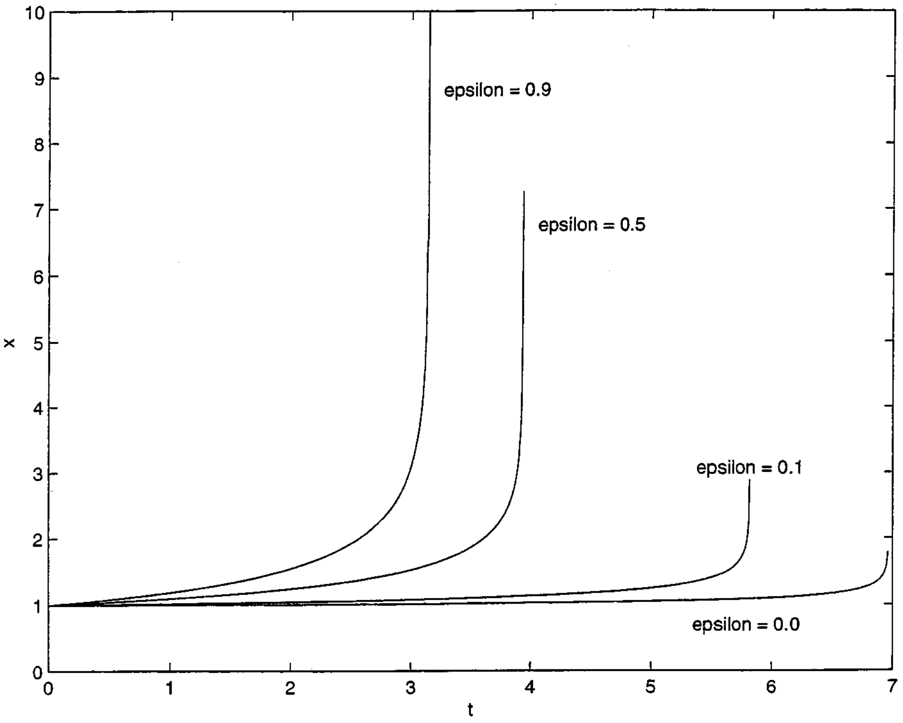

Fig. 5 The length, *x*, of a viscoplastic thread against the time, *t*, in the case $k<1/\sqrt{3}$

$$A_y=\frac{1}{\sqrt{3}k}(1-X). \tag{35}$$

By combining Eqs. (33) and (35) we get the locus $X_y(t)$ which can be written as

$$X_y=\frac{-3}{\dfrac{\sqrt{3}}{k}+\epsilon t}+1. \tag{36}$$

The cross-section area of the yielded part of the thread is obtained by following the same procedures used in obtaining (33), and it can be written as

$$A=\frac{\epsilon}{\sqrt{3}k(1-\epsilon)}(X-1)\exp\left(\frac{(1-\epsilon)\sqrt{3}k}{\epsilon}\left[\frac{1}{X-1}+\frac{1}{\sqrt{3}k}+\frac{\epsilon}{3}t\right]\right)+\frac{(1-X)}{\sqrt{3}(1-\epsilon)k}. \tag{37}$$

Before the thread of the fluid starts yielding (i.e., for $t<t_y$) its length can be obtained by integrating (26) with A given in (33) and with the boundary condition in (27) which is given by

$$x=\frac{3}{\epsilon t}\ln\left|\frac{\dfrac{\epsilon}{3}t(X-1)+1}{1-\dfrac{\epsilon}{3}t}\right|$$

and so the total length is given by its total length can be written as

$$x=\frac{3}{\epsilon t}\ln\left|\frac{1}{1-\dfrac{\epsilon}{3}t}\right|. \tag{38}$$

After the thread starts yielding (i.e., for $t>t_y$), the length of the thread is obtained by adding the length of the yielded and unyielded parts. Here the length of the yielded and unyielded parts is obtained numerically. Figure 3 shows the graph of the length of the thread, x, for different values of ϵ.

The time of rupture of the thread, t_r, in this case is given by

$$t_r=\frac{3}{\epsilon}\left[\frac{\epsilon}{\sqrt{3}k(1-\epsilon)}\ln\left(\frac{1}{\epsilon}\right)-\frac{1}{\sqrt{3}k}+1\right] \tag{39}$$

$k<1/\sqrt{3}$. When $k<1/\sqrt{3}$, the thread contains a yielded part at the initial time, adjacent to the point of attachment.

Figure 4 shows a clear description for the problem in the case $k<1/\sqrt{3}$. As we notice from Fig. 4, at the initial time the thread will be yielded for $0<X<X_{yo}$, and unyielded for $X_{yo}<X<1$, and the location of the yield surface is given by $X_{yo}=-\sqrt{3}k+1$. Figure 4 also shows that any unyielded fluid particle, X, will yield at time, $t=(-3/\epsilon)\,[1/(X-1)+1/\sqrt{3}k]$ and then the yielded and unyielded parts will be separated by a yield surface which is not always at the same fluid element. So for a fixed fluid particle, X, the corresponding cross-section area of the thread when it yields, A_y, and the value of the fluid particle, X_y, when it coincides with the yield surface are given by

$$A_y=\frac{1}{\sqrt{3}k}(1-X) \tag{40}$$

$$X_y=-\frac{1}{\left[\dfrac{1}{\sqrt{3}k}+\dfrac{\epsilon}{3}t\right]}+1. \tag{41}$$

For $0<X<X_{yo}$, the length of the thread is given by

$$x=\frac{-\sqrt{3}(1-\epsilon)}{kl}\ln\left|\frac{\dfrac{kl}{\sqrt{3}(1-\epsilon)}(1-X)+\exp\left(\dfrac{(1-\epsilon)t}{\sqrt{3}k}\right)}{\dfrac{kl}{\sqrt{3}(1-\epsilon)}+\exp\left(\dfrac{(1-\epsilon)t}{\sqrt{3}k}\right)}\right| \tag{42}$$

where $l=[1-\exp((1-\epsilon)t/\sqrt{3}k)]$.

For $X>X_{yo}$, the length of the thread is obtained numerically. Figure 5 shows the graph of the length of the thread for different values of ϵ.

The time of rupture of the thread, t_r, in this case is given by

$$t_r=\frac{\sqrt{3}}{k(1-\epsilon)}\ln\left(\frac{1}{1-\sqrt{3}k(1-\epsilon)}\right). \tag{43}$$

References

[1] Matta, J. E., and Titus, R. P., 1990, ''Liquid Stretching Using a Falling Cylinder,'' J. Non-Newtonian Fluid Mech., **35**, pp. 215–229.

[2] Sridhar, T., Tirtaatmadja, V., Nguyen, D. A., and Gupta, R. K., 1991, ''Measurement of Extensional Viscosity of Polymer Solutions,'' J. Non-Newtonian Fluid Mech., **40**, pp. 271–280.

[3] Markovich, P., and Renardy, M. A., 1985, ''Finite Difference Study of the Stretching and Breakup of Filament of Polymer Solutions,'' J. Non-Newtonian Fluid Mech., **17**, pp. 13–22.

[4] Renardy, M. A., 1995, ''A Numerical Study of the Asymptotic Evolution and Breakup of Newtonian and Viscoelastic Jets,'' J. Non-Newtonian Fluid Mech., **59**, pp. 267–282.

[5] Denn, M. M., 1980, ''Continuous Drawing of Liquids to Form Fibers,'' Annu. Rev. Fluid Mech., **12**, pp. 365–387.

[6] De Wynne, J., Ockendon, J. R., and Wilmott, P., 1989, ''On a Mathematical Model for Fiber Tapering,'' SIAM (Soc. Ind. Appl. Math.) J. Appl. Math., **49**, pp. 983–990.

[7] Doyle, P. J., 1994, *Glass Making Today*, R. A. N. Publishers, OH.

[8] Rekhson, S., Lu, Z., and Day, C., 1991, ''Computer Modelling of Glass Processing,'' *Coll. papers from the 52nd conf. on glass problems*, pp. 65–77.

[9] Gaudet, S., Mckinley, G. H., and Stone, H. A., 1996, ''Extensional Deformation of Newtonian Liquid Bridges,'' Phys. Fluids, **8**, pp. 2568–2579.

[10] Canright, D., and Morris, S., 1993, ''Bouyant Instability of a Viscous Film Over a Passive Fluid,'' J. Fluid Mech., **255**, pp. 349–372.

[11] Houseman, G. A., and Molnar, P., 1997, ''Gravitational (Rayleigh-Taylor) Instability of a Layer With Non-Linear Viscosity and Connective Thinning of Continental Lithosphere,'' Geophys. J. Int., **128**, pp. 125–150.

[12] Stokes, Y. M., Tuck, E. O., and Schwartz, L. W., 2000, ''Extensional Fall of a Very Viscous Fluid Drop,'' Q. J. Mech. Appl. Math., **53**, pp. 565–582.

[13] Wilson, S. D. R., 1988, ''The Slow Dripping of a Viscous Fluid,'' J. Fluid Mech., **190**, pp. 561–570.

[14] Beverly, C. R., and Tanner, R. I., 1992, ''Numerical Analysis of Three Dimensional Bingham Plastic Flow,'' J. Non-Newtonian Fluid Mech., **42**, pp. 85–115.

[15] Wilson, S. D. R., 1993, ''Squeezing Flow of a Bingham Material,'' J. Fluid Mech., **47**, pp. 211–219.

[16] Barnes, H. A., and Walters, K., 1985, ''The Yield Stress Myth?'' Rheol. Acta, **24**(4), pp. 323–326.

C. Midya

G. C. Layek

Department of Mathematics,
The University of Burdwan,
Burdwan, WB, India

A. S. Gupta

Department of Mathematics,
Indian Institute of Technology,
Kharagpur, India

T. Ray Mahapatra

Department of Mathematics,
R. B. C. College,
Naihati,
24-parganas(N), WB, India

Magnetohydrodynamic Viscous Flow Separation in a Channel With Constrictions

An analysis is made of the flow of an electrically conducting fluid in a channel with constrictions in the presence of a uniform transverse magnetic field. A solution technique for governing magnetohydrodynamic (MHD) equations in primitive variable formulation is developed. A coordinate stretching is used to map the long irregular geometry into a finite computational domain. The governing equations are discretized using finite difference approximations and the well-known staggered grid of Harlow and Welch is used. Pressure Poisson equation and pressure-velocity correction formulas are derived and solved numerically. It is found that the flow separates downstream of the constriction. With increase in the magnetic field, the flow separation zone diminishes in size and for large magnetic field, the separation zone disappears completely. Wall shear stress increases with increase in the magnetic field strength. It is also found that for symmetrically situated constrictions on the channel walls, the critical Reynolds number for the flow bifurcation (i.e., flow asymmetry) increases with increase in the magnetic field.

[DOI: 10.1115/1.1627834]

1 Introduction

The study of laminar flow in tubes or channels with constriction has received considerable attention in recent years in view of its engineering as well as physiological applications. Such flows occur in many fluidic devices, e.g., in orifices, valves as well as arteriosclerotic blood vessels. Lee and Fung [1] obtained numerical solution for flow in a tube with constriction at low Reynolds number. It was found that at a certain critical value of the Reynolds number, separation occurs resulting in the formation of an eddy downstream of the constriction. Lee [2] investigated steady laminar flow through a variable constriction in a vascular tube. Cheng [3] investigated steady viscous flow through a channel with symmetric cosinusoidal constrictions on both the walls at same location assuming flow symmetry about the channel centerline. Vradis, Zalak, and Bentson [4] studied the steady incompressible viscous flow in a channel with a local constriction having the shape of a Gaussian distribution. Assuming symmetry of the flow about the channel centerline, they found that the flow separates downstream of the constriction.

Solutions for steady viscous flow in fixed-wall vessels were obtained numerically for a variety of nonuniformities on the channel wall by Shyy and Sun [5], and Huang and Seymour [6]. It is well known that the flow through a plane symmetric sudden expansion becomes asymmetric about the central plane as the Reynolds number increases. This was experimentally demonstrated by Durst, Melling, and Whitelaw [7], Cherdron, Durst, and Whitelaw [8], and Sobey [9]. In fact in a channel when one wall provides a channel expansion then if the flow rate is high enough, separation can occur in the lee of the expansion. If flow occurs through a sudden symmetric expansion as in the experiments of Durst, Pereira, and Tropea [10], then separated regions can form either side of the main flow. What is observed is that the two symmetric separated regions may not remain the same size and the flow seems to attach to one or the other wall and this phenomenon is referred to in the literature as the Coanda effect (see [11]). In sudden expansion problem, the point of bifurcation (where the flow becomes asymmetric) lies near the Reynolds number of 125 (see [10]). The asymmetry of the flow comes through a symmetry-breaking bifurcation and in smooth transition. The separation zone grows linearly with increasing Reynolds number. Above a certain Reynolds number, however, one recirculation zone increases in length in comparison with the other recirculation zone and causes flow asymmetry.

Despite the ubiquity of boundary layer separation and the importance of its consequences on the flow as a whole, a proper understanding of the phenomenon and its analytical description have not yet been achieved. However, separation is undoubtedly associated with the fact that a steady state of the boundary layer adjoining a solid boundary is impossible with an appreciable fall in velocity of the external stream. On the other hand, control of boundary layer separation is of practical significance in aerodynamics and in physiological flows. Several methods have been developed for the purpose of artificially controlling the behavior of the boundary layer. The purpose of these methods is to affect the whole flow in a desired direction by influencing the structure of the boundary layer. For instance, in the case of flow past a circular cylinder with suction applied on one side of it through a small slit, the flow on the suction side adheres to the cylinder over a considerably larger portion of its surface and separation is avoided; the drag is reduced considerably, and simultaneously a large lift force is induced owing to the lack of symmetry of in the flow pattern (see [12]). Fluid flow separation and various boundary layer control techniques were elaborately described in Gad-el-Hak and Bushnell [13]. The application of magnetohydrodynamic (MHD) principles is yet another method for affecting the flow field in a desired direction by altering the structure of the boundary layer. In fact the application of MHD to biology and medicine is receiving considerable attention of physiologists, medical practitioners, and fluid dynamicists (Barnothy [14]), owing to their importance in biomedical engineering in general and in the treatment of various pathological states in particular. Since blood is electrically conducting, its flow in a cardiovascular system is likely to be affected by the application of an external magnetic field. In fact the Lorentz force arising out of the flow across magnetic lines of force acts on the constituent particles of blood and changes the hemodynamic indicators of blood flow. The potential use of MHD principles in prevention and rational therapy of arterial hypertension was explored by Vardanyan [15], who found that for steady flow of blood in an artery of circular cross section, a

---

Contributed by the Fluids Engineering Division for publication in the JOURNAL OF FLUIDS ENGINEERING. Manuscript received by the Fluids Engineering Division September 4, 2002; revised manuscript received June 24, 2003. Associate Editor: M. V. Ötügen.

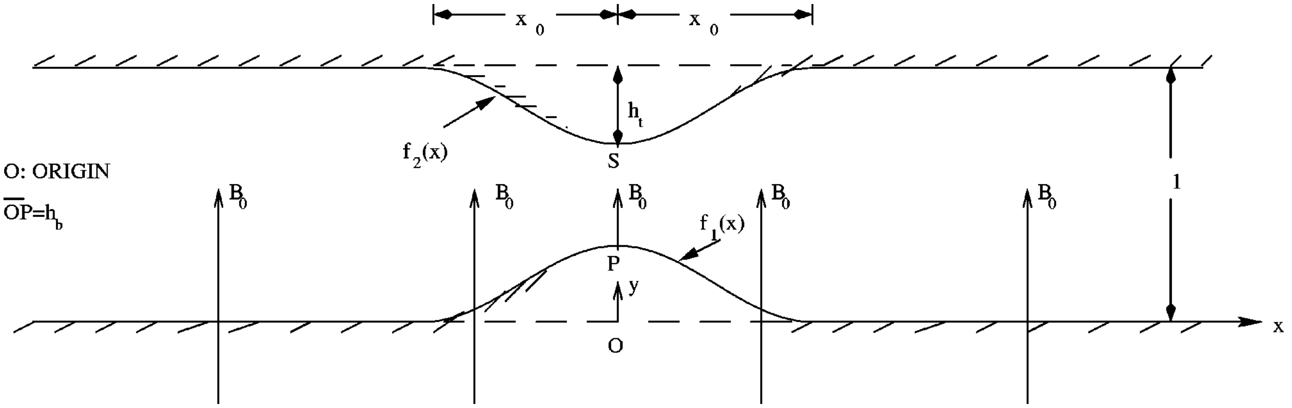

Fig. 1 A sketch of the physical problem

uniform transverse magnetic field alters the flow rate of blood. Pal, Misra, and Gupta [16] investigated the steady MHD flow of an electrically conducting viscous fluid in a slowly varying channel in the presence of a uniform transverse magnetic field. MHD flow of a non-Newtonian fluid in a channel of slowly varying cross section in the presence of a uniform transverse magnetic field was studied by Misra, Pal, and Gupta [17]. In both these problems, [16,17], flow symmetry about the channel axis was assumed.

In this paper viscous flow of an electrically conducting fluid in a channel with symmetric and asymmetric constrictions is studied numerically without assuming flow symmetry about the centerline of the channel. The flow is permeated by a uniform magnetic field applied normal to the plane of the channel wall. Finite-difference staggered grid is employed to solve the governing equations of the fluid flow. A coordinate transformation is used to map a long irregular geometry into a finite regular computational domain. Flow separation zones are compared with the corresponding zones for flow of an electrically nonconducting fluid. It is shown that the separation zone decreases in size due to the application of the magnetic field. It is also found that the flow asymmetry at high Reynolds number is delayed in the presence of the magnetic field.

2 The Governing Equations

Consider the two-dimensional flow of an incompressible viscous electrically conducting fluid (with electrical conductivity σ) of density ρ, in a long parallel-plate channel having locally symmetric and asymmetric constrictions on both the plates at the same location. Let (x^*, y^*, z^*) be the cartesian coordinates of any point in the flow domain, where x^*-axis is along the bottom plate and y^* is the normal to both the plates. Let u^*, v^* be the velocity components along x^* and y^* directions, respectively, p^* the pressure and $U/4$ be the centerline velocity for parallel flow in the channel far upstream of the constrictions. A uniform magnetic field B_0 is imposed along y^*-axis (Fig. 1). The Navier-Stokes equations, by taking into account the Lorentz forces due to magneto-hydrodynamic (MHD) interactions, are written as

$$\frac{\partial u^*}{\partial x^*}+\frac{\partial v^*}{\partial y^*}=0, \tag{1}$$

$$\frac{\partial u^*}{\partial t^*}+u^*\frac{\partial u^*}{\partial x^*}+v^*\frac{\partial u^*}{\partial y^*} = -\frac{1}{\rho}\frac{dp^*}{dx^*}+\nu\left(\frac{\partial^2 u^*}{\partial x^{*2}}+\frac{\partial^2 u^*}{\partial y^{*2}}\right)-\frac{\sigma B_0^2}{\rho}u^*, \tag{2}$$

$$\frac{\partial v^*}{\partial t^*}+u^*\frac{\partial v^*}{\partial x^*}+v^*\frac{\partial v^*}{\partial y^*}=-\frac{1}{\rho}\frac{\partial p^*}{\partial y^*}+\nu\left(\frac{\partial^2 v^*}{\partial x^{*2}}+\frac{\partial^2 v^*}{\partial y^{*2}}\right), \tag{3}$$

where the induced magnetic field is assumed to be negligible in comparison with the external magnetic field which is justified for MHD flow at small magnetic Reynolds number, [18]. In fact such an assumption is valid for flow of liquid metals (e.g., mercury or liquid sodium) or blood flow in arteries. For example, in flow of blood (with electrical conductivity $\sigma=6\times10^{-1}$ mhos m^{-1}) in the left coronary artery (with radius 3.75×10^{-3} m) with velocity 8.8 m/hour, the magnetic Reynolds number is 0.02. Further electrical conductivity σ of the fluid is assumed constant. For mercury, σ is 10^{-5} e.m.u and for liquid sodium $\sigma=10^{-4}$ e.m.u. It is also assumed that the external electric field is zero and the electric field due to polarization of charges is negligible.

Introducing the following dimensionless variables

$$t=t^*U/h,\quad x=x^*/h,\quad y=y^*/h,\quad u=u^*/U,\quad v=v^*/U,$$
$$p=p^*/\rho U^2 \tag{4}$$

the above equations become

$$\frac{\partial u}{\partial x}+\frac{\partial v}{\partial y}=0, \tag{5}$$

$$\frac{\partial u}{\partial t}+\frac{\partial u^2}{\partial x}+\frac{\partial uv}{\partial y}=-\frac{\partial p}{\partial x}+\frac{1}{\mathrm{Re}}\left(\frac{\partial^2 u}{\partial x^2}+\frac{\partial^2 u}{\partial y^2}\right)-\frac{M^2}{\mathrm{Re}}u, \tag{6}$$

$$\frac{\partial v}{\partial t}+\frac{\partial uv}{\partial x}+\frac{\partial v^2}{\partial y}=-\frac{\partial p}{\partial y}+\frac{1}{\mathrm{Re}}\left(\frac{\partial^2 v}{\partial x^2}+\frac{\partial^2 v}{\partial y^2}\right), \tag{7}$$

where $\mathrm{Re}(=Uh/\nu)$ is the Reynolds number, $M(=B_0 h\sqrt{\sigma/\rho\nu})$ is the Hartmann number, and h is the width of the straight part of the channel.

3 Boundary Conditions

The streamwise and transverse velocity components should be zero at the rigid walls (no-slip condition). At the inlet and outlet boundaries, the Hartmann velocity profile, [18], is prescribed. On the upper $(y=f_2(x))$ and lower $(y=f_1(x))$ wall of the channel, the no-slip boundary conditions are

$$u=0,\quad v=0 \text{ at } y=f_2(x),\quad f_1(x). \tag{8}$$

The functions $f_1(x)$ and $f_2(x)$ which represent the lower and upper walls of the channel are given by

$$f_1(x)=\begin{cases}\frac{1}{2}h_b(1+\cos(\pi x/x_0)) & : \quad |x|\leqslant x_0\\ 0 & : \quad |x|\geqslant x_0\end{cases},$$

$$f_2(x)=\begin{cases} 1-\frac{1}{2}h_t(1+\cos(\pi x/x_0)) & : \quad |x|\leqslant x_0 \\ 1 & : \quad |x|\geqslant x_0 \end{cases}. \tag{9}$$

Here h_t and h_b are contraction parameters which are depicted in Fig. 1.

The inlet flow far upstream and the outlet flow far downstream of the constrictions are assumed to be Poiseuille flow in the absence of magnetic field and Hartmann flow, [19], in the presence of magnetic field.

The steady equation of motion in the presence of magnetic field B_0 far upstream (or far downstream) of the constrictions is

$$0=-\frac{\partial p^*}{\partial x^*}+\rho\nu\frac{d^2u^*}{dy^{*2}}-j_zB_0, \tag{10}$$

where $u^*(y^*)$ is the velocity of the unidirectional flow parallel to the channel walls. Electric current flows normal to the plane of flow and Ohm's law gives the current density j_z as

$$j_z=\sigma(E_z+u^*B_0), \tag{11}$$

where the electric field E_z is constant because $\nabla\times\mathbf{E}=0$ in the steady flow. Since the physical variables except pressure are functions of y^* only, it follows from (10) that $\partial p^*/\partial x^*=\text{constant}$, and this external pressure gradient is needed to drive the flow against viscous stress and the (retarding) magnetic force.

Eliminating j_z between (10) and (11) gives on using (4),

$$\frac{d^2u}{dy^2}-M^2u=-\frac{h^2}{\rho\nu U}\left(\frac{\partial p^*}{\partial x^*}+\sigma E_zB_0\right), \tag{12}$$

where $u(y)=u^*(y^*)/U$.

Since $U/4$ is the centerline velocity for this parallel flow, the solution of (12) satisfying the boundary conditions $u=0$ at $y=0$ and $u=0$ at $y=1$ gives the Hartmann velocity distribution

$$u(y)=\frac{\cosh\frac{M}{2}-\cosh\left(M\left(y-\frac{1}{2}\right)\right)}{8\sinh^2\frac{M}{4}}, \tag{13}$$

with

$$\frac{h^2}{\rho\nu U}\left(\frac{\partial p^*}{\partial x^*}+\sigma E_zB_0\right)=\frac{M^2\cosh\frac{M}{2}}{8\sinh^2\frac{M}{4}}. \tag{14}$$

Further the flow rate Q in the channel is assumed constant. Thus

$$Uh\int_0^1 u\,dy=Q=\text{constant}, \tag{15}$$

which gives from (13)

$$\frac{h}{8\sinh^2\frac{M}{4}}\left(\cosh\frac{M}{2}-\frac{2}{M}\sinh\frac{M}{2}\right)=\frac{Q}{U}. \tag{16}$$

Elimination of U from (14) and (16) gives the external pressure gradient $-\partial p^*/\partial x^*$ as

$$-\frac{\partial p^*}{\partial x^*}=\frac{\rho\nu QM^3}{h^3\left(2\tanh\frac{M}{2}-M\right)}+\sigma E_zB_0. \tag{17}$$

Since we are simulating an electrically short-circuited condition $(E_z=0)$, we find from (17) that for maintaining a constant flow rate Q, the external pressure gradient is a function of the Hartmann number M given by

$$-\frac{\partial p^*}{\partial x^*}=\frac{\rho\nu QM^3}{h^3\left(2\tanh\frac{M}{2}-M\right)}. \tag{18}$$

It may further be noted that under an electrically short-circuited condition, there is a nonzero net electric current normal to the plane of the flow since all the current flows in one direction. This can be seen from (11) with $E_z=0$. In fact

$$\int_0^h j_z\,dy^*=\sigma B_0\int_0^h u^*\,dy^*, \tag{19}$$

which gives upon using (15) the net current normal to the plane of flow as σB_0Q.

We thus have the following conditions at the inlet and outlet boundaries. At $x=\pm\infty$,

$$u=y-y^2, \qquad \text{for } M=0$$

$$u=\frac{\cosh\frac{M}{2}-\cosh\left(M\left(y-\frac{1}{2}\right)\right)}{8\sinh^2\frac{M}{4}}, \quad \text{for } M\neq 0. \tag{20}$$

4 Initial Condition

The initial condition is that there is no flow inside the region of the channel with constrictions while, on the other hand, Hartmann velocity profile is prescribed at inlet boundary far upstream of the constrictions. Physically this means that the flow is approaching the constriction gradually.

5 Coordinate Transformation

It is somewhat unsatisfactory to simply impose the far-field boundary conditions at moderately large distances since, with increasing Reynolds number, the disturbances created by the constrictions are sizeable even far downstream. For this reason, a suitable transformation is introduced to map the long region of interest into a finite one. Equations (5)–(7) are transformed by the introduction of the new variables,

$$t=t, \quad \xi=\tanh(kx), \quad \eta=\frac{y-f_1(x)}{f_2(x)-f_1(x)}, \tag{21}$$

where k is a constant which controls the grid distribution in the computational plane. The grids in the physical plane are dense near the origin due to the nature of the function tanh(kx). The value of k is taken as 0.12 for low Reynolds number flows and 0.08 for high Reynolds number flows. The transformation defined in (21) transforms the curved upper boundary $y=f_2(x)$ into a straight line $\eta=1$, the curved lower boundary $y=f_1(x)$ into a straight line $\eta=0$ and the outflow and inflow boundaries into $\xi=\pm 1$. In the new system of coordinates (ξ,η), a uniformly spaced rectangular grid is superimposed on the $[-1,1]\times[0,1]$ domain.

Using the chain rule of differentiation, the continuity Eq. (5) becomes

$$k(1-\xi^2)\frac{\partial u}{\partial\xi}-k(1-\xi^2)G(\xi,\eta)\frac{\partial u}{\partial\eta}+\frac{1}{g_2(\xi)-g_1(\xi)}\frac{\partial v}{\partial\eta}=0, \tag{22}$$

and the momentum equations (Eqs. (6) and (7)) reduce to

$$\frac{\partial u}{\partial t}+k(1-\xi^2)\frac{\partial u^2}{\partial \eta}-k(1-\xi^2)G(\xi,\eta)\frac{\partial u^2}{\partial \eta}+\frac{1}{g_2(\xi)-g_1(\xi)}\frac{\partial uv}{\partial \eta}$$
$$=-k(1-\xi^2)\frac{\partial p}{\partial \xi}+k(1-\xi^2)G(\xi,\eta)\frac{\partial p}{\partial \eta}$$
$$+\frac{1}{\mathrm{Re}}\Bigg[k^2(1-\xi^2)^2\frac{\partial^2 u}{\partial \xi^2}-2k^2\xi(1-\xi^2)\frac{\partial u}{\partial \xi}$$
$$-\{k^2(1-\xi^2)^2\{H(\xi,\eta)-2G(\xi,\eta)L(\xi)\}$$
$$-2k^2\xi(1-\xi^2)G(\xi,\eta)\}\frac{\partial u}{\partial \eta}-2k^2(1-\xi^2)^2G(\xi,\eta)\frac{\partial^2 u}{\partial \xi\partial \eta}$$
$$+\left\{k^2(1-\xi^2)^2G^2(\xi,\eta)+\frac{1}{\{g_2(\xi)-g_1(\xi)\}^2}\right\}\frac{\partial^2 u}{\partial \eta^2}\Bigg]-\frac{M^2}{\mathrm{Re}}u. \tag{23}$$

$$\frac{\partial v}{\partial t}+k(1-\xi^2)\frac{\partial uv}{\partial \xi}-k(1-\xi^2)G(\xi,\eta)\frac{\partial uv}{\partial \eta}+\frac{1}{g_2(\xi)-g_1(\xi)}\frac{\partial v^2}{\partial \eta}$$
$$=-\frac{1}{g_2(\xi)-g_1(\xi)}\frac{\partial p}{\partial \eta}+\frac{1}{\mathrm{Re}}\Bigg[k^2(1-\xi^2)^2\frac{\partial^2 v}{\partial \xi^2}$$
$$-2k^2\xi(1-\xi^2)\frac{\partial v}{\partial \xi}-\{k^2(1-\xi^2)^2\{H(\xi,\eta)-2G(\xi,\eta)L(\xi)\}$$
$$-2k^2\xi(1-\xi^2)G(\xi,\eta)\}\frac{\partial v}{\partial \eta}-2k^2(1-\xi^2)^2G(\xi,\eta)\frac{\partial^2 v}{\partial \xi\partial \eta}$$
$$+\left\{k^2(1-\xi^2)^2G^2(\xi,\eta)+\frac{1}{\{g_2(\xi)-g_1(\xi)\}^2}\right\}\frac{\partial^2 v}{\partial \eta^2}\Bigg], \tag{24}$$

where

$$f_i(x)=g_i(\xi),\quad f_i'(x)=k(1-\xi^2)g_i'(\xi),$$
$$f_i''(x)=k(1-\xi^2)[-2k\xi g_i'(\xi)+k(1-\xi^2)g_i''(\xi)],\quad i=1,2$$
$$G(\xi,\eta)=\frac{\eta g_2'(\xi)+(1-\eta)g_1'(\xi)}{g_2(\xi)-g_1(\xi)},$$
$$H(\xi,\eta)=\frac{\eta g_2''(\xi)+(1-\eta)g_1''(\xi)}{g_2(\xi)-g_1(\xi)},$$
$$L(\xi)=\frac{g_2'(\xi)-g_1'(\xi)}{g_2(\xi)-g_1(\xi)},\quad x=\frac{1}{2k}\ln\left(\frac{1+\xi}{1-\xi}\right),\quad -1<\xi<1, \tag{25}$$

Here a prime denotes derivative with respect to the argument.

The boundary conditions in the transformed coordinate system are

$$u=0,\quad v=0\quad \text{at}\ \ \eta=0,1. \tag{26}$$

The inlet velocity profile at $\xi=-1$ and the outlet velocity profile at $\xi=+1$ are both given by

$$u(\eta)=\eta-\eta^2,\quad M=0$$
$$=\frac{\left(\cosh\left(\frac{M}{2}\right)-\cosh M\left(\eta-\frac{1}{2}\right)\right)}{8\sinh^2\left(\frac{M}{4}\right)},\quad M\neq 0. \tag{27}$$

6 Method of Solution

The above governing equations along with the initial and boundary conditions are solved by the finite difference method. Control volume-based finite-difference discretization of the above equations is carried out in staggered grid, popularly known as MAC (Marker and Cell) proposed by Harlow and Welch [20]. In this type of grid alignment, the velocities and the pressure are evaluated at different locations of the control volume as shown in Fig. 2. The continuity equation for an incompressible flow contains only the velocity components and there is no direct link with the pressure as there is for compressible flow through the density. In conventional (nonstaggered) grid, the primitive variables (u, v, p) for two-dimensional flow are coupled to every alternate node. The use of the staggered grid permits coupling of the u, v, and p solutions at adjacent grid points. This in turn prevents the appearance of oscillatory solutions, particularly for p, that can occur if centred differences are used to discretize all derivatives on a nonstaggered grid.

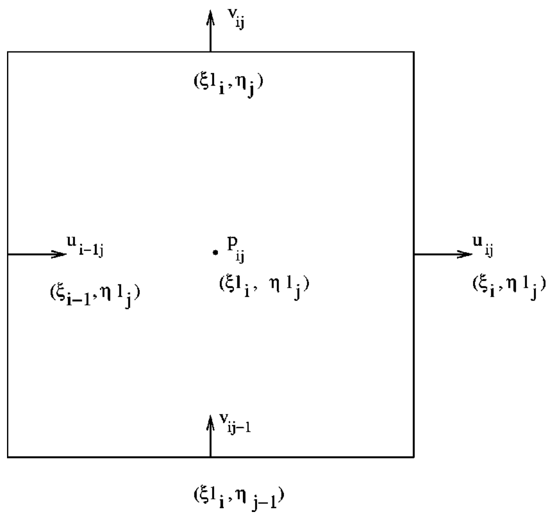

Fig. 2 Arrangement of dependent variables in a typical MAC cell

The time derivative terms are differenced according to the first-order accurate two-level forward time-differencing formula. The convective terms in the momentum equations are differenced with a hybrid formula consisting of central differencing and second-order upwinding. The diffusive terms are differenced by second-order accurate three-point central difference formula. The source terms are centrally differenced keeping the position of the respective fluxes at the centers of the control volumes. Thus in finite-difference form with $t=n\delta t$, $\xi=i\delta\xi$, $\eta=j\delta\eta$, and $p(\xi,\eta,t)=p(i\delta\xi,j\delta\eta,n\delta t)=p_{ij}^n$, superscript n refers to the time direction, δt is the time increment, and $\delta\xi$, $\delta\eta$ are the length and width of the (i,j)th control volume.

The discretized form of the continuity equation at the (i, j) cell takes the form

$$k(1-\xi l_i^2)\frac{u_{ij}^n-u_{i-1j}^n}{\delta\xi}-k(1-\xi l_i^2)G(\xi l_i,\eta l_j)\frac{u_{tc}-u_{bc}}{\delta\eta}$$
$$+\frac{1}{g_2(\xi l_i)-g_1(\xi l_i)}\frac{v_{ij}^n-v_{ij-1}^n}{\delta\eta}=0, \tag{28}$$

where the quantities ξl_i, ηl_j, u_{tc} and u_{bc} are defined as

$$\xi l_i=\xi_i-\frac{\delta\xi}{2},\quad \eta l_j=\eta_j-\frac{\delta\eta}{2},$$
$$u_{tc}=0.25(u_{ij}^n+u_{i-1j}^n+u_{i-1j+1}^n+u_{ij+1}^n),$$
$$u_{bc}=0.25(u_{ij-1}^n+u_{i-1j-1}^n+u_{i-1j}^n+u_{ij}^n). \tag{29}$$

Here $(\xi l_i, \eta l_j)$ and (ξ_i, η_j) are the coordinates of the cell center and the right top corner of the cell, respectively. Further u_{tc} and u_{bc} stand for u-velocities at the top and bottom middle positions of the control volume of the continuity equation. Considering the source, convective and diffusive terms at the nth time level, the momentum equation in the ξ-direction given by Eq. (23) is put in the finite-difference form

$$\frac{u_{ij}^{n+1}-u_{ij}^{n}}{\delta t}=k(1-\xi_i^2)\frac{p_{ij}^n-p_{i+1j}^n}{\delta\xi}+k(1-\xi_i^2)G(\xi_i,\eta l_j)\frac{p_t-p_b}{\delta\eta}+Ucd_{ij}^n. \tag{30}$$

Here p_t, p_b, and Ucd_{ij}^n are defined as follows:

$$p_t=0.25(p_{ij}^n+p_{i+1j}^n+p_{ij+1}^n+p_{i+1j+1}^n), \tag{31}$$

$$p_b=0.25(p_{ij}^n+p_{i+1j}^n+p_{ij-1}^n+p_{i+1j-1}^n), \tag{32}$$

$$Ucd_{ij}^n=\frac{1}{\mathrm{Re}}\,\mathrm{Diff}u_{ij}^n-\mathrm{Con}u_{ij}^n-\frac{M^2}{\mathrm{Re}}u_{ij}^n, \tag{33}$$

where p_t and p_b stand for pressure at the top and bottom middle positions of the u-momentum cell, respectively, and $\mathrm{Diff}u_{ij}^n$ and $\mathrm{Con}u_{ij}^n$ are the diffusive and convective terms of the u-momentum equation at the nth time level at (i, j) cell. The diffusive terms are discretized centrally as

$$\frac{\partial^2 u}{\partial \xi^2}=\frac{u_{i+1j}^n-2u_{ij}^n+u_{i-1j}^n}{(\delta\xi)^2}+O((\delta\xi)^2), \tag{34}$$

$$\frac{\partial^2 u}{\partial \eta^2}=\frac{u_{ij+1}^n-2u_{ij}^n+u_{ij-1}^n}{(\delta\eta)^2}+O((\delta\eta)^2). \tag{35}$$

A central difference formula is used for the mixed derivative $\partial^2 u/\partial\xi\partial\eta$ in uniform grid.

In the present scheme the convective terms are differenced with a combination of central differencing and second-order upwind differencing schemes. The velocities $(u_r, u_l, u_t, u_b, v_t, v_b)$ at the interface of the control volume are calculated by the same interpolation formula for both the schemes. Thus for the u-momentum equation, the different symbols are defined by

$$u_r=(u_{ij}^n+u_{i+1j}^n)/2, \quad u_l=(u_{ij}^n+u_{i-1j}^n)/2, \tag{36}$$

$$u_t=(u_{ij}^n+u_{ij+1}^n)/2, \quad u_b=(u_{ij}^n+u_{ij-1}^n)/2, \tag{37}$$

$$v_t=(v_{ij}^n+v_{i+1j}^n)/2, \quad v_b=(v_{ij-1}^n+v_{i+1j-1}^n)/2 \tag{38}$$

where the suffixes r, l, t, and b correspond to right, left, top, and bottom middle positions of the control volume, respectively. In the second-order upwind scheme the choice of taking the momentum flux ϕ passing through the interface of the control volume depends on the sign of the velocities at that interface (see [21]). Thus the momentum fluxes for u-momentum are given by

$$\text{if} \quad u_r\geqslant 0, \quad \phi_{ur}=u_{ij}^n, \tag{39}$$

$$\text{if} \quad u_r<0, \quad \phi_{ur}=u_{i+1j}^n, \tag{40}$$

$$\text{if} \quad u_l\geqslant 0, \quad \phi_{ul}=u_{i-1j}^n, \tag{41}$$

$$\text{if} \quad u_l<0, \quad \phi_{ul}=u_{ij}^n. \tag{42}$$

Suffix u of ϕ denotes the quantity for u-momentum. In like manner,

$$\text{if} \quad v_t\geqslant 0, \quad \phi_{ut}=u_{ij}^n, \tag{43}$$

$$\text{if} \quad v_t<0, \quad \phi_{ut}=u_{ij+1}^n, \tag{44}$$

$$\text{if} \quad v_b\geqslant 0, \quad \phi_{ub}=u_{ij-1}^n, \tag{45}$$

$$\text{if} \quad v_b<0, \quad \phi_{ub}=u_{ij}^n. \tag{46}$$

Hence the finite-difference form of the different convective terms in the u-momentum equation are given by

$$\frac{\partial u^2}{\partial\xi}=(1-\beta)\frac{u_r^2-u_l^2}{\delta\xi}+\beta\frac{u_r\phi_{ur}-u_l\phi_{ul}}{\delta\xi}, \tag{47}$$

$$\frac{\partial u^2}{\partial\eta}=(1-\beta)\frac{u_t^2-u_b^2}{\delta\eta}+\beta\frac{u_t\phi_{ut}-u_b\phi_{ub}}{\delta\eta}, \tag{48}$$

$$\frac{\partial uv}{\partial\eta}=(1-\beta)\frac{u_tv_t-u_bv_b}{\delta\eta}+\beta\frac{v_t\phi_{ut}-v_b\phi_{ub}}{\delta\eta}, \tag{49}$$

where β is a combination factor which is determined from the numerical stability criteria. With $\beta=0$, the scheme becomes central differencing and when $\beta=1$, it is a second-order upwind differencing scheme.

The finite-difference equation approximating the momentum equation in the η-direction is

$$\frac{v_{ij}^{n+1}-v_{ij}^n}{\delta t}=\frac{1}{g_2(\xi l_i)-g_1(\xi l_i)}\left(\frac{p_{ij}^n-p_{ij+1}^n}{\delta\eta}\right)+Vcd_{ij}^n, \tag{50}$$

where

$$Vcd_{ij}^n=\frac{1}{\mathrm{Re}}\,\mathrm{Diff}v_{ij}^n-\mathrm{Con}v_{ij}^n. \tag{51}$$

Here $\mathrm{Diff}v_{ij}^n$ and $\mathrm{Con}v_{ij}^n$ are the finite-difference representation of diffusive and convective terms of the v-momentum equation for the nth time level at the cell (i, j). The diffusive and convective terms in the v-momentum equation are differenced in the same manner to those in the u-momentum equation. The criterion used in the u-momentum equation for the momentum fluxes is also employed for the v-momentum fluxes.

The Poisson equation for pressure is obtained by combining the discretized form of the momentum and continuity equations. The final form of the Poisson equation for pressure is

$$\begin{aligned}(A+B+C+D)p_{ij}^n-Ap_{i+1j}^n-Bp_{i-1j}^n+(F-E-D)p_{ij-1}^n\\ +(E-F-C)p_{ij+1}^n+E(p_{i+1j+1}^n-p_{i+1j-1}^n)\\ +F(p_{i-1j-1}^n-p_{i-1j+1}^n)\\ =-\left[\frac{\mathrm{Div}_{ij}^n}{\delta t}+k(1-\xi l_i^2)\frac{Ucd_{ij}^n-Ucd_{i-1j}^n}{\delta\xi}\right.\\ \left.+\frac{Vcd_{ij}^n-Vcd_{ij-1}^n}{(g_2(\xi l_i)-g_1(\xi l_i))\delta\eta}\right].\end{aligned} \tag{52}$$

Here Div_{ij}^n is the finite-difference representation of the divergence of the velocity field at cell (i, j). The expressions for A, B, C, D, E, F are presented below.

$$A=\frac{k^2(1-\xi_i^2)(1-\xi l_i^2)}{(\delta\xi)^2},$$

$$B=\frac{k^2(1-\xi_{i-1}^2)(1-\xi l_i^2)}{(\delta\xi)^2},$$

$$C=\frac{1}{(g_2(\xi l_i)-g_1(\xi l_i))^2(\delta\eta)^2}=D,$$

$$E=G(\xi_i,\eta l_j)\frac{k^2(1-\xi_i^2)(1-\xi l_i^2)}{4\delta\xi\delta\eta}$$

$$F=G(\xi_{i-1},\eta l_j)\frac{k^2(1-\xi_{i-1}^2)(1-\xi l_i^2)}{4\delta\xi\delta\eta}.$$

The advantage in using MAC cell is that the pressure boundary condition is not needed at the boundaries where velocity vector is specified, because the domain boundaries are chosen to fall on velocity nodes. For the cells adjacent to the upper wall $(\eta=1)$, we get from v-momentum equation

$$p_{ij+1}^n=p_{ij}^n+\{g_2(\xi l_i)-g_1(\xi l_i)\}\delta\eta Vcd_{ij}^n. \tag{53}$$

Thus the Poisson equation for pressure for the cells adjacent to the upper wall $(\eta=1)$ is

$$\begin{aligned}(A+B+D+E-F)p^n_{ij}&+(E-A)p^n_{i+1j}-(B+F)p^n_{i-1j}\\&+(F-E-D)p^n_{ij-1}+Fp^n_{i-1j-1}\\&+[g_2(\xi l_i)-g_1(\xi l_i)]\delta\eta(E-F)Vcd^n_{ij}-Ep^n_{i+1j-1}\\&+[g_2(\xi l_{i+1})-g_1(\xi l_{i+1})]\delta\eta EVcd^n_{i+1j}\\&-[g_2(\xi l_{i-1})-g_1(\xi l_{i-1})]\delta\eta FVcd^n_{i-1j}\\&=-\left[\frac{\mathrm{Div}^n_{ij}}{\delta t}+k(1-\xi l_i^2)\frac{Ucd^n_{ij}-Ucd^n_{i-1j}}{\delta\xi}\right.\\&\qquad\left.-\frac{Vcd^n_{ij-1}}{\delta\eta(g_2(\xi l_i)-g_1(\xi l_i))}\right],\end{aligned}\tag{54}$$

where p^n_{ij} is the pressure located at the cell center inside the flow domain.

The Poisson equation for pressure for the cells adjacent to the inlet boundary at $\xi=-1$ can be expressed as

$$\begin{aligned}(A+C+D)p^n_{ij}&-Ap^n_{i+1j}-Dp^n_{ij-1}-Cp^n_{ij+1}\\&=-\left[\frac{\mathrm{Div}^n_{ij}}{\delta t}+k(1-\xi l_i^2)\frac{Ucd^n_{ij}}{\delta\xi}+\frac{Vcd^n_{ij}-Vcd^n_{ij-1}}{\delta\eta(g_2(\xi l_i)-g_1(\xi l_i))}\right],\end{aligned}\tag{55}$$

where p^n_{ij} is the pressure at the cell center inside the flow domain. Similarly, the Poisson equations for pressure for the cells adjacent to the lower wall ($\eta=0$) and outlet boundary ($\xi=1$) are obtained. The Poisson equation for pressure (Eq. (52)) is solved iteratively by successive over-relaxation (SOR) method. The value of the over-relaxation parameter is taken here as 1.2.

7 Pressure and Velocity Corrections

In most of the codes based on staggered grid formulations, the local dilatation term at the $(n+1)$th time level, Dil^{n+1}_{ij}, is set equal to zero. Here we replace the term:

$$\mathrm{Dil}^{n+1}_{ij}=\left[k(1-\xi l_i^2)\frac{u^{n+1}_{ij}-u^{n+1}_{i-1j}}{\delta\xi}+\frac{1}{g_2(\xi l_i)-g_1(\xi l_i)}\frac{v^{n+1}_{ij}-v^{n+1}_{ij-1}}{\delta\eta}\right]$$

by

$$\left[G(\xi l_i,\eta l_j)k(1-\xi l_i^2)\frac{u_{tc}-u_{bc}}{\delta\eta}\right],$$

where u_{tc} and u_{bc} are at the nth time level, in order to obtain the exact form of the transformed continuity equation in the Poisson equation for pressure, so that the decoupled tendency (checkerboard effect) of pressure field gets eliminated. With this incorporation, the pressure equation becomes independent of $(n+1)$th time level velocity field. For a large number of grid points, a very large number of iteration steps are needed for satisfactory level of convergence (here the convergence criterion for SOR iterative scheme is that the pressure difference between two successive iterations is less than 0.5×10^{-5}). To reduce the computation time for each cycle, the number of iterations in the SOR iteration scheme is kept limited (here the number of iterations is 10). But convergence of the pressure solutions cannot be expected with such a small number of iterations. So the velocity field obtained after solving the momentum equations using an already known inaccurate pressure field may not satisfy the continuity equation. This necessitates a corrector stage. In this stage pressure and subsequently velocities are corrected to get a more accurate velocity field in the sense that it will satisfy the continuity equation more accurately. This second stage starts with computing the divergence of velocity field for each cell. If it is found to be greater than 0.5×10^{-6} at any cell in absolute sense, pressure is corrected for each cell in the flow field. The velocity components at the sides of the cell are then adjusted. The pressure correction formula is

$$p^n_{ij}=p^*_{ij}+\omega_2\delta p_{ij},\tag{56}$$

where p^*_{ij} is obtained after solving the Poisson equation, ω_2 ($\leqslant 0.5$) is an under-relaxation parameter and

$$\delta p_{ij}=-\frac{\mathrm{Div}^*_{ij}}{\delta t(A+B+C+D)},\tag{57}$$

where Div^*_{ij} is the value of the divergence of velocity field at the cell (i, j) obtained after solving the Poisson equation for pressure. The velocity correction formulas are

$$u^{n+1}_{ij}=u^*_{ij}+\frac{k(1-\xi_i^2)\,\delta t\,\delta p_{ij}}{\delta\xi}\tag{58}$$

$$u^{n+1}_{i-1j}=u^*_{i-1j}-\frac{k(1-\xi_{i-1}^2)\,\delta t\,\delta p_{ij}}{\delta\xi},\tag{59}$$

$$v^{n+1}_{ij}=v^*_{ij}+\frac{\delta t\,\delta p_{ij}}{(g_2(\xi l_i)-g_1(\xi l_i))\,\delta\eta},\tag{60}$$

$$v^{n+1}_{ij-1}=v^*_{ij-1}-\frac{\delta t\,\delta p_{ij}}{(g_2(\xi l_i)-g_1(\xi l_i))\,\delta\eta},\tag{61}$$

where u^*_{ij}, u^*_{i-1j}, v^*_{ij}, v^*_{ij-1} represent the updated velocity field obtained after solving the Poisson equation for pressure.

8 Stability Restriction of the Numerical Scheme

To make the finite-difference scheme numerically stable, certain restrictions are imposed on the mesh sizes $\delta\xi$, $\delta\eta$ and also on δt. The time step is governed by two restrictions. The first restriction is related to the convection of the fluid, requiring that the fluid can not move through more than one cell in one time step. So the time step must satisfy the inequality

$$\delta t\leqslant \mathrm{Min}\left[\frac{\delta\xi}{|u|},\frac{\delta\eta}{|v|}\right]_{ij},\tag{62}$$

where minimum is in the global sense. Secondly, momentum must not diffuse more than one cell in one time step. This condition, which is related to the viscous effects, according to Hirt's [22] stability analysis implies

$$\delta t\leqslant \mathrm{Min}\left[\frac{\mathrm{Re}}{2}\frac{\delta\xi^2\delta\eta^2}{(\delta\xi^2+\delta\eta^2)}\right]_{ij}.\tag{63}$$

Denoting the right-hand side of (62) and (63) by δt_1 and δt_2, respectively, we find that both these inequalities are satisfied if the time step δt satisfies

$$\delta t\leqslant \mathrm{Min}[\delta t_1,\delta t_2].$$

Hence in our computations we take

$$\delta t=c\,\mathrm{Min}[\delta t_1,\delta t_2],$$

where c is a constant lying between 0.05 and 0.25.

The present numerical scheme is semi-implicit and the present code is employed for the prediction of flow variables for moderate Reynolds number flows. A typical value of the time step δt (i.e., typical CFL number) is obtained as 0.002 with the grid size $\delta\xi=\delta\eta=0.01$ for Re$=$1000. For high Reynolds number flows, time step (consistent with the above two inequalities) has to be reduced accordingly.

Moreover, the combination factor β is selected according to the inequality

$$1\geqslant\beta\geqslant \mathrm{Max}\left[\left|\frac{u\,\delta t}{\delta\xi}\right|,\left|\frac{v\,\delta t}{\delta\eta}\right|\right]_{ij}.$$

Table 1 Results of different grid sizes for a long straight channel at $\mathrm{Re}=600$, $M=0$

Grid	Property	$y\to 0$	0.1	0.3	0.5	0.7	0.9	1
100×50	u	0	0.089947	0.209878	0.249854	0.209878	0.089947	0
200×100	u	0	0.089996	0.209965	0.249958	0.209965	0.089996	0
Exact	$u=y-y^2$	0	0.09	0.21	0.25	0.21	0.09	0

This inequality yields a very small value of the parameter β. As a safety measure the value is multiplied by a factor 1.2, in practice.

9 Numerical Algorithm

One complete calculation cycle comprises of the following steps:

Stage 1

a. Velocities u_{ij}^n and v_{ij}^n are initialized at each cell (i, j). This is done either from the result of previous cycle or from the prescribed initial conditions.

b. Time step (δt) is calculated from stability criteria.

c. The Poisson equation for pressure is solved to get the intermediate pressure field (p_{ij}^*) using velocities u_{ij}^n and v_{ij}^n of the nth time step.

d. The momentum equations are solved to get intermediate velocities u_{ij}^* and v_{ij}^* in an explicit manner using the velocities u_{ij}^n, v_{ij}^n and pressure (p_{ij}^*) as found from solution of Poisson equation for pressure.

Stage 2

(e) The maximum cell divergence of velocity field is calculated and is checked for its limit. If satisfied, steady-state convergence or limiting nondimensional time criterion is checked for whether to stop calculation. If maximum divergence is not satisfactorily low, it becomes necessary to go to step (f).

(f) The pressure at each cell of the flow domain is corrected and subsequently the velocities of that and left and bottom neighboring cells are adjusted to get u_{ij}^{n+1}, v_{ij}^{n+1}, and p_{ij}^n. Then step (e) is again performed.

This completes the necessary calculations for advancing the flow field through one cycle in time. The process is to be repeated until steady-state convergence or limiting nondimensional time is achieved.

In what follows u-velocity, v-velocity and shear stress are computed when the steady state is reached.

10 Results and Discussion

The governing equations of motion are solved numerically using pressure-based finite difference approximation. The grid-independent study is made for the verification of the present numerical scheme. The values of u-velocity at different ordinates in a straight channel are compared with the exact solution at $\mathrm{Re}=600$ as shown in Table 1. This shows good agreement between exact values of u-velocity and the computational values of u-velocity obtained from different grid sizes for a long straight channel.

Results obtained from this scheme for a locally constricted channel for different grid sizes are computed at $\mathrm{Re}=600$ and are presented in Table 2.

Table 2 shows that u and v velocities are in good agreement in different grid sizes. The actual computations are carried out on 200×100 and 200×50 uniform grids for high and moderate Reynolds number flows, respectively.

For the verification of our numerical scheme, the shear stress on the upper wall in the absence of magnetic field $(M=0)$ are compared with those obtained by Vradis, Zalak, and Bentson [4] in the case when the shape of the constriction was taken in the form of a Gaussian profile and flow symmetry was assumed about the centerline of the channel at $\mathrm{Re}=50$ (see Fig. 3). This is justified since at low Reynolds number, flow in a channel with geometric symmetry $(h_t=h_b)$ will also be symmetric about the channel centerline. Subsequent computations of flow characteristics will vindicate this assertion. It is clear from this figure that at a given location, the shear stress at the upper wall denoted by τ_w increases with increase in the magnetic parameter M. The physical explanation for this is as follows. As the magnetic field increases, the Hartmann layer (where the voticity is confined) which is formed near the walls becomes thinner resulting in increase in the velocity gradient at the walls. Thus the shear stress increases with increase in M. It can be further seen from the figure that for a given value of M, the flow separates at a point downstream of the constriction (where $\tau_w=0$) and then reattaches at a point further downstream where τ_w again vanishes. It is interesting to note that the length of the separation zone (i.e., the distance between the point of separation and the point of reattachment) decreases with increase in M and the separation zone disappears altogether at $M=4$. We thus arrive at the novel result that the magnetic field tends to delay separation and by applying a strong magnetic field, the flow separation can be completely prevented. In this connection it is important to mention that since the flow rate is assumed constant, the external pressure gradient is a function of Hartmann number M as shown in Eq. (18). Thus it is not the case that simply applying a strong magnetic field eliminates separation—in a practical situation, the externally applied pressure gradient will need to be adjusted appropriately. Certainly in blood flow through arteries, pressure and its gradient are likely to be crucial items in determining whether such a method is suitable for medical application. This result admits of the following physical interpretation. Near the channel axis of the constricted region, where effects of viscosity are not pronounced, the Lorentz force arising out of the flow of electric current in the presence of magnetic field (given by the last term in Eq. (2)) has a retarding influence on the flow. Since in the steady state, the flux of fluid flowing across any cross-section of the channel is constant, it follows that the axial velocity near the channel wall at the same cross-section increases with increase in

Table 2 Results of different grid sizes for a locally constricted channel at $\mathrm{Re}=600$, $M=0$ with $x_o=2$, $h_b=0.3$, $h_t=0.3$ at $x=0$

Grid	Property	$y\to 0.3$	0.34	0.42	0.50	0.58	0.66	0.7
100×50	u	0	0.270166	0.520523	0.562355	0.518616	0.268363	0
200×100	u	0	0.269179	0.519295	0.561244	0.518496	0.268444	0
100×50	v	0	0.004011	0.007834	−0.000530	−0.008728	−0.004349	0
200×100	v	0	0.003916	0.008059	−0.000199	−0.008392	−0.004045	0

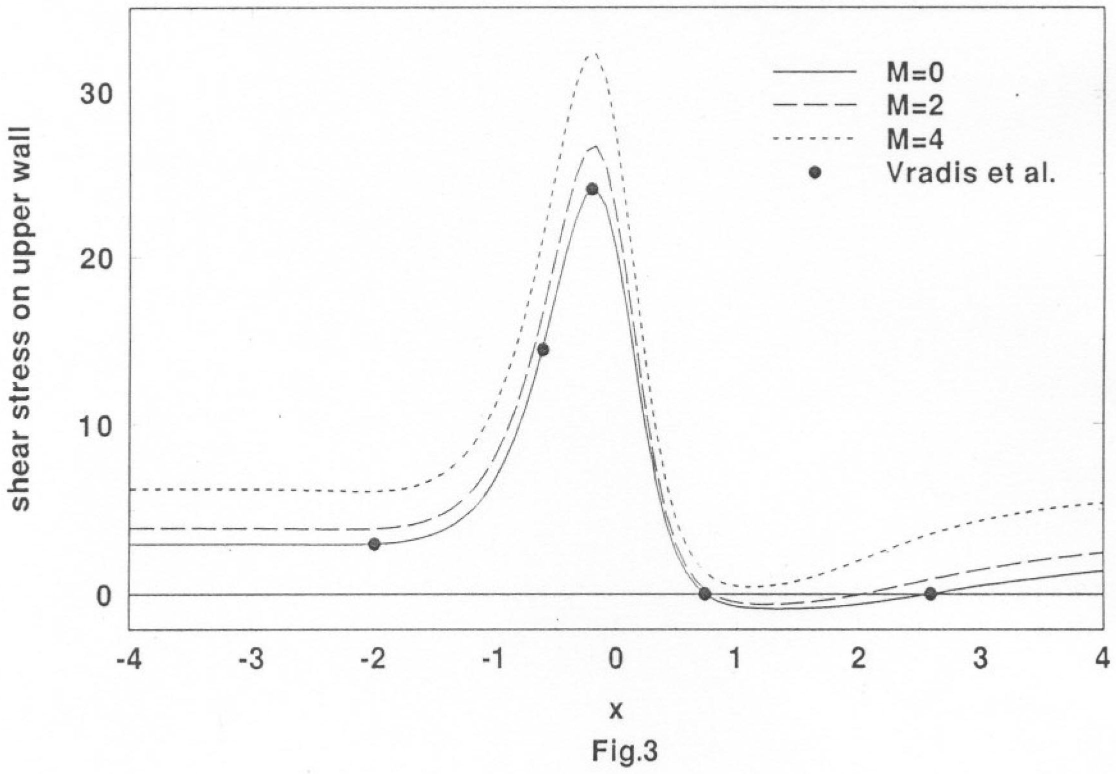

Fig. 3 Distribution of shear stress on upper wall for different values of M at Re=50, $x_0=1$, $h_t=0.5$.

M. This increase in fluid velocity near the walls with increasing M enables the fluid to overcome the influence of any adverse pressure gradient (downstream of the constriction) and thereby enhances the ability of the fluid to withstand flow separation near the wall. This result seems to be of great physiological interest and likely to have important medical applications. One limitation of our analysis on prevention of flow separation with regard to medical application may be noted. In the present study, electrically short-circuited condition is simulated. However, for flow in blood vessels, the situation is more likely to correspond to the open-circuit condition (zero net current). Zamir and Roach [23] suggested that intimal cushions may occur due to flow separation whereby the flow of blood in a cardiovascular system can reverse its direction. Further the suppression of flow separation has enormous applications in engineering design and chemical systems involving problems associated with heat and mass transfer.

In the present study, we investigate flow separation in the constricted channel with the shape of the constriction given by Eq. (9) in the presence of magnetic field. Numerical computations are carried out for differents values of M, Re, h_t, h_b, and x_0, where h_t and h_b are the heights of the top and bottom constriction and x_0 is the width of the constriction. Figure 4(a) shows the u-velocity profile at the location $x=1.507$ for various values of M with Re $=1000$, $h_t=h_b=0.3$, and $x_0=2$. It can be seen that inspite of the geometric symmetry ($h_t=h_b$), the velocity profile for $M=0$ is not symmetric about the channel centerline and shows different separated zones in the upper and lower walls of the channel. We thus conclude that in the absence of magnetic field, flow in a channel with geometric symmetry becomes asymmetric followed by separation at high Reynolds number.

Although the flows separate at high Reynolds number, these flows are steady because the Reynolds number is not high enough to cause turbulence and further the magnetic field also stabilizes the flow (see [24]). These steady flows are invariably asymmetrically separated flows since as the Reynolds number increases, the bifurcation of flow (i.e., development of flow asymmetry) occurs before flow separation takes place.

A further point may be noted. We have assumed that the two vertical sides of the channel (i.e., the channel walls parallel to xy-plane in Fig. 1) are at a very large distance D apart such that depth of the channel $h \ll D$. This ensures that the flow in the channel is effectively two-dimensional so that the flow variables are functions of x and y and no secondary flows are considered. Thus any three-dimensional effect due to the dependence of the physical variables on the transverse coordinate z can be neglected. Hence it is expected that the neglect of three-dimensional effects will not affect the development of flow bifurcations.

It is seen, however, that as M increases, the velocity profile gradually becomes symmetric and separation also gradually diminishes. Separation disappears completely for $M=10$ and the velocity profile has a symmetric shape as shown in Fig. 4(a). In Fig. 4(b), velocity profiles are displayed at several locations in the channel for $M=0$, 3, 5, and 7 with Re=1000, $h_t=h_b=0.3$ and $x_0=2$. It can be clearly seen that at $M=0$, the flow shows tendency to separate downstream of the constriction and this tendency gradually disappears with increase in M.

Figures 5(a) and 5(b) show the distribution of shear stress (dimensionless) τ_w on the upper and lower walls in the case of asymmetric constriction geometry ($h_t=0.5, h_b=0$) for several values of M with Re=350 and $x_0=1$. Here also the separation zone decreases with increase in M and separation completely disappears for $M=8$. Figure 6(c) gives the pressure distribution on the upper wall for several values of M in the case of asymmetric constriction geometry ($h_t=0.5, h_b=0$) for Re=350 and $x_0=1$.

Let us try to have an estimate of the value of the magnetic field strength B_o in different regions of the human cardiovascular sys-

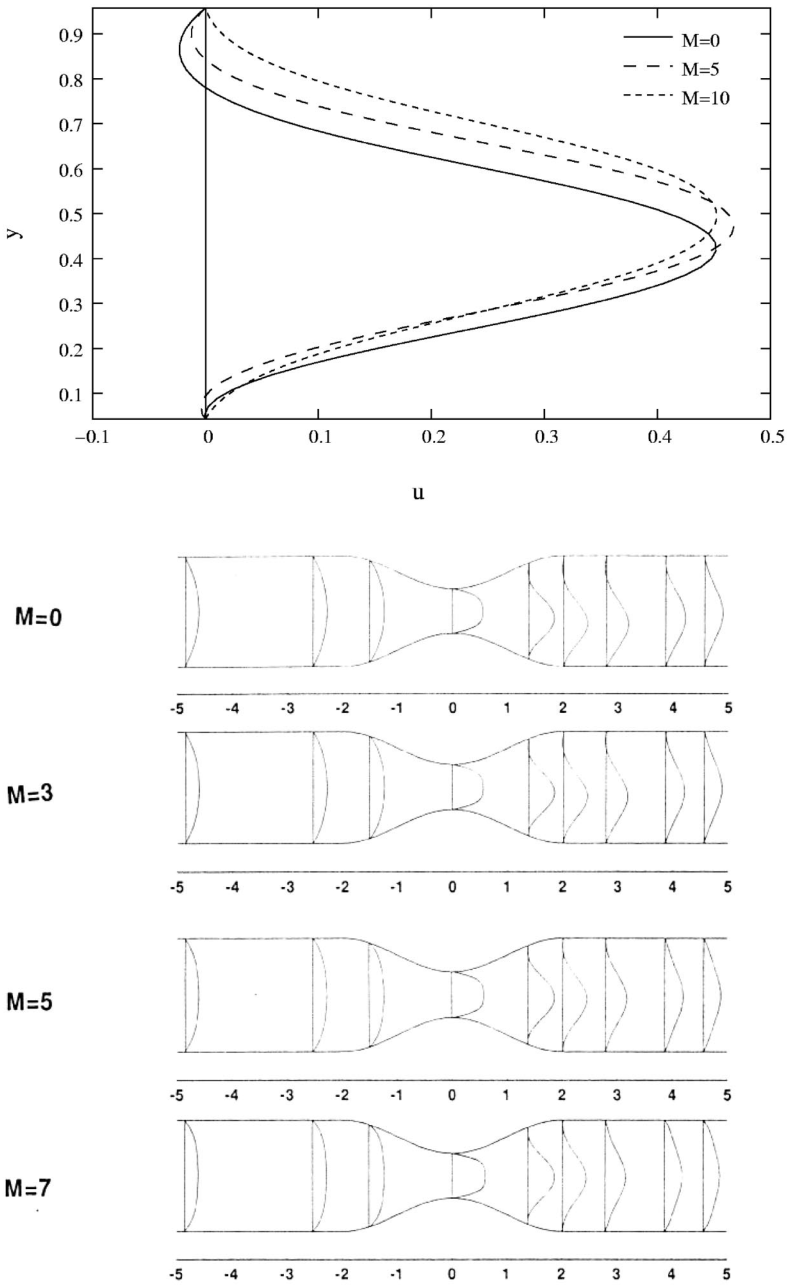

Fig. 4 (***a***) **Velocity profiles for different values of *M* at $x=1.507$ for Re=1000, $h_t=0.3$, $h_b=0.3$, $x_0=2$. (*b*) Velocity profiles for $M=0$, 3, 5, and 7 at $x=-4.855$, -2.534, -1.507, 0, 1.38, 2.017, 2.79, 3.868, and 4.568 for Re=1000, $h_t=0.3$, $h_b=0.3$, $x_0=2$.**

tem for the Hartmann numbers 8 and 17. We find $B_o=92.38$ Gauss, $B_o=196.299$ Gauss for $M=8$ and 17, respectively by taking the viscosity of blood to be 4.5×10^{-3} kg sec^{-1} m^{-1} and electrical conductivity $\sigma=6\times10^{-1}$ mhos m^{-1} (see [15]) for the main left coronary artery (with the radius 3.75×10^{-3} m). For the femoral artery (with the radius 2.25×10^{-3} m), the values of the magnetic field strength are $B_o=153.96$ Gauss and 327.165 Gauss for the Hartmann numbers 8 and 17, respectively. The above values of the radii of different arteries are taken from McDonald [25].

The distributions of τ_w for various values of M are shown in Figs. 6(*a*) and 6(*b*) at a high Reynolds number (Re=2000) with $h_t=h_b=0.3$ and $x_0=2$. For $M=0$, a large separation bubble is formed downstream of the constriction, which decreases in size as M increases. The separation completely disappears for $M=17$.

It is found from our computations that in the nonmagnetic case ($M=0$) for a symmetric configuration ($h_t=h_b=0.3$ and $x_0=2.$), the flow becomes asymmetric before it separates at the upper wall and the lower wall at different Reynolds numbers. It so happens that as the Reynolds number increases, the flow first separates on the upper wall when Re=350. However, when Re=400, flow separates at both walls. Thus even for a symmetric configuration, the occurrence of separation either at the upper wall or the lower wall is not random. The fact that separation first occurs at the upper wall is attributed to the bifurcation of the flow (i.e., the flow no longer remains symmetric about the central axis of the chan-

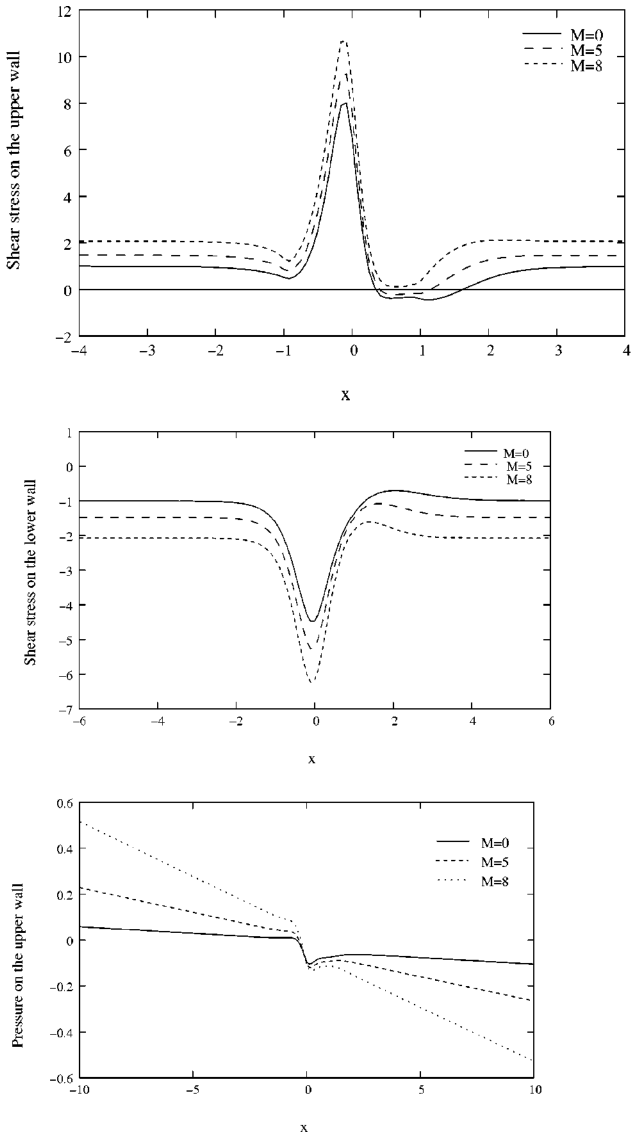

Fig. 5 (***a***) **Distribution of shear stress on upper wall for different values of *M* at Re=350, x_0=1, h_t=0.5, h_b=0.** (***b***) **Distribution of shear stress on lower wall for different values of *M* at Re=350, x_0=1, h_t=0.5, h_b=0.** (***c***) **Distribution of pressure on the upper wall for the constriction geometry x_0=1, h_t=0.5, h_b=0, Re=350 for different values of *M*.**

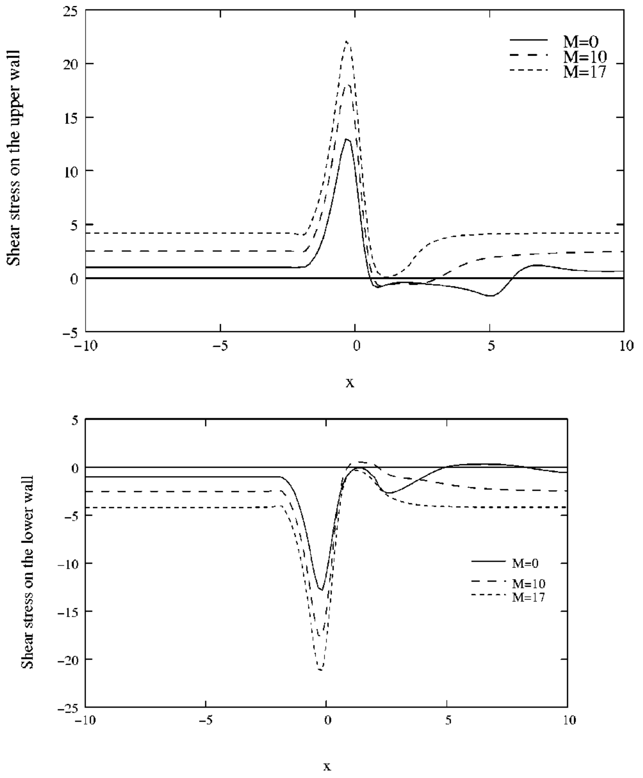

Fig. 6 (***a***) **Distribution of shear stress on upper wall for different values of *M* at Re=2000, x_0=2, h_t=0.3, h_b=0.3.** (***b***) **Distribution of shear stress on lower wall for different values of *M* at Re=2000, x_0=2, h_t=0.3, h_b=0.3.**

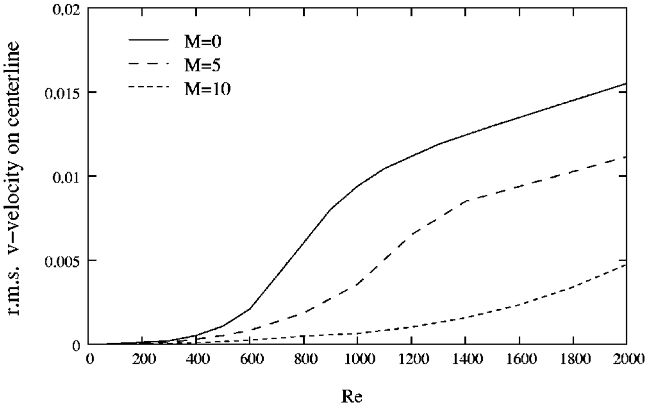

Fig. 7 Distribution of r.m.s. *v*-velocity on the channel centerline against Re for different values of *M* with x_0=2, h_t=0.3, h_b=0.3

nel) at a certain critical value of Reynolds number Re_c (which is 300 for $h_t=h_b=0.3$ and $x_0=2$). before flow separation takes place. In the presence of magnetic field ($M\neq 0$) bifurcation of flow (development of flow asymmetry) occurs at Re_c=370 for $M=5$ and the flow separates on the upper wall at Re=620 and the flow separates on both the walls at Re=665. What exactly happens to bring about the asymmetry or what triggers it, is not clear at this juncture. It could be due to the following two reasons:

i. When the Reynolds number increases above a particular critical value, there could be a small pressure differential occurring between the two sides (just downstream of the constriction) which pulls the flow to one of the sides, i.e., triggers the asymmetry.
ii. The growth of the shear layers originating at the two lips near the exits of the constriction and their subsequent interaction might be responsible for the asymmetry.

We now focus our attention on the asymmetric flow. A measure of asymmetry of the flow is v_{mc} which is the root-mean-square (r.m.s.) v-velocity on the centerline of the channel, the flow being symmetric when $v_{mc}=0$. Figure 7 shows the variation of v_{mc} with Re for various values of M when $h_t=h_b=0.3$ and $x_0=2$. It is clearly seen that for low Reynolds number, the flow is symmetric. The transition of v_{mc} from a value zero to a nonzero value is, however, smooth and not abrupt as observed by Fearn et al. [11]. The Reynolds number at which the flow becomes asymmetric ($v_{mc}\neq 0$) is the critical Reynolds number Re_c. It is very difficult to fix Re_c numerically. It is observed from Fig. 7 that for $M=0$, there is symmetry breaking when Re_c=300 and the flow becomes asymmetric when Re exceeds 300. This graph further reveals that

$\mathrm{Re}_c \simeq 370$ for $M=5$ and $\mathrm{Re}_c \simeq 510$ for $M=10$. Thus one can infer that increase in the magnetic field tends to make the flow more symmetric and for high enough values of M, the flow not only becomes symmetric but separation is also completely prevented.

Acknowledgment

One of the authors (C. M.) acknowledges financial support from the Council of Scientific and Industrial Research (CSIR), New Delhi, India for pursuing this work. Another author (A. S. G.) acknowledges the financial assistance of the Indian National Science Academy (INSA) for carrying out this work.

The authors thank the referees for their comments which enabled improved presentation of this paper.

References

[1] Lee, J. S., and Fung, Y. C., 1970, ''Flow in Locally Constricted Tubes at Low Reynolds Number,'' ASME J. Appl. Mech., **37**, pp. 9–16.
[2] Lee, T. S., 1994, ''Steady Laminar Fluid Flow Through a Variable Constrictions in Vascular Tube,'' ASME J. Fluids Eng., **116**, pp. 66–71.
[3] Cheng, R. T., 1972, ''Numerical Solution of the Navier-Stokes Equations by the Finite-Element Method,'' Phys. Fluids, **15**, pp. 2098–2105.
[4] Vradis, G., Zalak, V., and Bentson, J., 1992, ''Simultaneous Variable Solutions of the Incompressible Steady Navier-Stokes Equations in Curvilinear Coordinate Systems,'' ASME J. Fluids Eng., **114**, pp. 299–305.
[5] Shyy, W., and Sun, C. S., 1993, ''Development of a Pressure-Correction/Staggered-Grid Based Multigrid Solver for Incompressible Recirculating Flows,'' Comput. Fluids, **22**, pp. 51–76.
[6] Huang, H., and Seymour, B. R., 1995, ''A Finite Difference Method for Flow in a Constricted Channel,'' Comput. Fluids, **24**(2), pp. 153–160.
[7] Durst, F., Melling, A., and Whitelaw, J. H., 1974, ''Low Reynolds Number Flow Over a Plane Symmetrical Sudden Expansion,'' J. Fluid Mech., **64**, pp. 111–128.
[8] Cherdron, W., Durst, F., and Whitelaw, J. H., 1978, ''Asymmetric Flows and Instabilities in Symmetric Ducts With Sudden-Expansion,'' J. Fluid Mech., **84**, pp. 13–31.
[9] Sobey, I. J., 1985, ''Observation of Waves During Oscillatory Channel Flow,'' J. Fluid Mech., **151**, pp. 395–406.
[10] Durst, F., Pereira, J. C., and Tropea, C., 1993, ''The Plane Symmetric Sudden-Expansion Flow at Low Reynolds Numbers,'' J. Fluid Mech., **248**, pp. 567–581.
[11] Fearn, R. M., Mullin, T., and Cliffe, K. A., 1990, ''Nonlinear Flow Phenomena in a Symmetric Sudden Expansion,'' J. Fluid Mech., **211**, pp. 595–608.
[12] Schlichting, H., 1968, *Boundary Layer Theory*, 6th Ed., translated by J. Kestin, McGraw-Hill, New York.
[13] Gad-el-Hak, M., and Bushnell, D. M., 1991, ''Separation Control: Review,'' ASME J. Fluids Eng., **113**, pp. 5–30.
[14] Barnothy, M. F., ed., 1964, *Biological Effects of Magnetic Fields*, Vol. 1, Plenum Press, New York.
[15] Vardanyan, V. A., 1973, ''Effect of Magnetic Field on Blood Flow,'' Biofizika, **18**, pp. 491–496.
[16] Pal, B., Misra, J. C., and Gupta, A. S., 1996, ''Steady Hydromagnetic Flow in a Slowly Varying Channel,'' Proc. Natl. Inst. Sci. India, Part A, **66**(A), III, pp. 247–262.
[17] Misra, J. C., Pal, B., and Gupta, A. S., 1998, ''Hydromagnetic Flow of a Second-Grade Fluid in a Channel—Some Applications to Physiological Systems,'' Math. Mod. Meth. Appl. Sci., **8**(8), pp. 1323–1342.
[18] Shercliff, J. A., 1965, *A Textbook of Magnetohydrodynamics*, Pergamon Press, New York.
[19] Sutton, G. W., and Sherman, A. 1965, *Engineering Magnetohydrodynamics*, McGraw-Hill, New York.
[20] Harlow, F. H., and Welch, J. E., 1965, ''Numerical Calculation of Time-Dependent Viscous Incompressible Flow of Fluid With Free Surface,'' Phys. Fluids, **8**, pp. 2182–2189.
[21] Roache, P. J., 1985, *Computational Fluid Dynamics*, Hermosa Publishers, NM.
[22] Hirt, C. W., 1968, ''Heuristic Stability Theory for Finite-Difference Equations,'' J. Comput. Phys., **2**, pp. 339–355.
[23] Zamir, M., and Roach, M. R., 1973, ''Blood Flow Downstream of a Two-Dimensional Bifurcation,'' J. Theor. Biol., **42**, pp. 33–41.
[24] Cowling, T. G., 1957, *Magnetohydrodynamics*, John Wiley and Sons, New York.
[25] McDonald, D. A., 1974, *Blood Flow in Arteries*, Edward Arnold Press, London.

Weixing Yuan
Assistant Research Officer,
Aerodynamics Laboratory,
Institute for Aerospace Research,
National Research Council of Canada,
Ottawa, ON K1A OR6, Canada
e-mail: weixing.yuan@nrc-cnrc.gc.ca

Günter H. Schnerr[1]
Professor,
Fachgebiet Gasdynamik,
Lehrstuhl für Fluidmechanik,
Technische Universität München,
D-85747 Garching, Germany
e-mail: schnerr@flm.mw.tu-muenchen.de

Numerical Simulation of Two-Phase Flow in Injection Nozzles: Interaction of Cavitation and External Jet Formation

The present investigation demonstrates the strong interaction of cavitating nozzle flow with the outside jet formation. Due to the strong sensitivity of cavitation on the imposed boundary conditions, simulations with restriction on the internal problem are qualitatively and quantitatively incorrect, so that phenomena like hydraulic flip and supercavitation cannot be revealed. Our results indicate the potential of cavitation for enhancement of atomization and spray quality. [DOI: 10.1115/1.1625687]

1 Introduction

It is well known that cavitation in injection nozzles has a strong impact on spray formation and atomization, which are directly correlated to the efficiency of the combustion process. Wu et al. [1] found that the spray cone angles for cavitation-free nozzles are systematically smaller than those for nozzles likely to cavitate. Chaves et al. [2] verified that supercavitation and turbulence will cause finite disturbances of the jet which, immediately at the nozzle exit, initiate atomization. Due to the small scale of 100 μm–1 mm and the high speed of several hundred meters per second, experiments on this subject are very rare and, if existing, very limited concerning detailed quantitative data. Quantitatively correct experiments, by applying more appropriate larger scale models, are not possible because of the necessity to preserve the exact time scale of the internal cavitation dynamics, which is of the order of 1–10 μs. Depending on the nature of the combustion process, the injection pressure reaches 1000–2000 bar in Diesel engines and is around 100 bar in the new technique of direct injection in Otto engines. In addition, the pressures upstream and behind the nozzle fluctuate with high frequencies in the range of 1–100 kHz.

Therefore, it is obvious that numerical simulations are most important and very promising to improve understanding and for optimization of this complex unsteady turbulent two-phase micro fluid dynamic problem. Our previous work, [3], has focused on attempts in the numerical simulation of the two-phase flow of injection nozzles including external jet flow. The work assumed that the material derivatives of liquid and vapor are equal and opposite in sign. This is true for partially cavitating flow. However, it is invalid if another component (e.g., here air) is involved in the cavitation region, i.e., when the vapor and the gas (air) from the downstream chamber behind the injection nozzle contact each other. Following the idea of this previous work, we removed the non-necessary assumption and recalculated the cases.

Our physical modeling follows the homogeneous two-phase approach and resolves the dispersed bubbly cavitation structure by applying a bubble growth model. The numerical method is a combination of the volume-of-fluid technique with extension for simulation of flows with phase transition for tracking the local vapor production and the collapse of bubbles, respectively. The turbulence model used is the k-ω model of Wilcox [4], at present the original single-phase version and therefore, with the tendency to overestimate viscous effects in two-phase regimes. Consequently, empirical corrections will be implemented which account for the lower eddy viscosity of mixtures with higher gas/vapor contents.

Because of the nearly incompressible main liquid flow and the high sensitivity of cavitation dynamics with respect to pressure boundary conditions, quantitative accurate simulations cannot be restricted to the nozzle flow itself, but require simultaneous treatment of the cavitating flow inside the nozzle, together with the external jet, especially in case of high frequency excitations of the injection pressure. Therefore, our extended model includes simulation of the interaction of the external fluid at the nozzle exit (gas or air) with the liquid and vapor flowing through the nozzle. The external fluid can instantaneously flow into the nozzle and penetrate the cavitation regime as well as pressure waves can leave the nozzle, and directly interact with the jet.

2 Mathematical and Numerical Descriptions

2.1 Governing Equations. The continuity equations for each phase/component of a two-phase cavitating flow consisting of liquid, vapor and gas are

$$\frac{\partial(\alpha_v\rho_v)}{\partial t}+\nabla\cdot(\alpha_v\rho_v\boldsymbol{c}_v)=\dot{m}_v\,, \tag{1}$$

$$\frac{\partial(\alpha_l\rho_l)}{\partial t}+\nabla\cdot(\alpha_l\rho_l\boldsymbol{c}_l)=-\dot{m}_v\,, \tag{2}$$

$$\frac{\partial(\alpha_g\rho_g)}{\partial t}+\nabla\cdot(\alpha_g\rho_g\boldsymbol{c}_g)=0, \tag{3}$$

where t stands for time, $\boldsymbol{c}$ for the velocity, $\dot{m}_v$ for mass exchange rate between the liquid and the vapor. The subscripts l, v, and g stand for the values of pure liquid, pure vapor and pure gas (air). α_i indicates the volume fraction of the fluid component "i" with the compatibility condition

$$\alpha_l+\alpha_v+\alpha_g=1. \tag{4}$$

Note that physically $\boldsymbol{c}_v\neq\boldsymbol{c}_l\neq\boldsymbol{c}_g$. Equations (1)–(3) can be used together with their own corresponding momentum equations for each phase/component to solve two-phase flows. This means three sets of the equation systems are needed to be solved if the external flow of the injection nozzle is considered. It is a natural extension of the two-fluid model and the computations will be extremely costly. To reduce the computational time, the two-phase flow is treated as a homogeneous vapor-liquid-gas mixture. We assume

---

[1] To whom correspondence should be addressed.

Contributed by the Fluids Engineering Division for publication in the JOURNAL OF FLUIDS ENGINEERING. Manuscript received by the Fluids Engineering Division March 11, 2002; revised manuscript received May 14, 2003. Associate Editor: S. L. Ceccio.

that $\boldsymbol{c}_v = \boldsymbol{c}_l = \boldsymbol{c}_g = \boldsymbol{c}$, hence only one set of equations is used for description. The continuity equation, together with the momentum equations for the mixture quantities are

$$\frac{\partial \rho}{\partial t} + \mathrm{div}(\rho \boldsymbol{c}) = 0, \tag{5}$$

$$\frac{\partial(\rho \boldsymbol{c})}{\partial t} + \mathrm{div}\left[\rho \boldsymbol{c}\boldsymbol{c} + \left(p + \frac{2}{3}\mu\, \mathrm{div}\, \boldsymbol{c}\right)\boldsymbol{I}\right] = 2\mu\, \mathrm{div}\, \boldsymbol{D}, \tag{6}$$

where p is the static pressure, $\boldsymbol{I}$ is the unit tensor, and $\boldsymbol{D}$ is the rate of strain (deformation) tensor. The equations of motion are closed with the constitutive relations for the density ρ and the dynamic viscosity μ:

$$\rho = \alpha_l \rho_l + \alpha_v \rho_v + \alpha_g \rho_g, \tag{7}$$

$$\mu = \alpha_l \mu_l + \alpha_v \mu_v + \alpha_g \mu_g. \tag{8}$$

The properties ρ and μ of pure liquid, pure vapor, and pure gas are assumed to be constant. To overcome numerical difficulties due to the strong variation of the density between the liquid and vapor phases, as proposed by Sauer et al. [5], Schnerr et al. [6], and Spalding [7], we use the so-called nonconservative form of the continuity equation (Eq. (5)) with the advantage of continuous volume fluxes at the cell interfaces:

$$\nabla \cdot \boldsymbol{c} = \frac{-1}{\rho}\left(\frac{\partial \rho}{\partial t} + \boldsymbol{c} \cdot \nabla \rho\right) = \frac{-1}{\rho}\frac{d\rho}{dt}. \tag{9}$$

Due to Eqs. (3), (4), (7), and (9), we obtain

$$\frac{d\alpha_g}{dt} = -\alpha_g \nabla \cdot \boldsymbol{c}, \tag{10}$$

$$\frac{d\alpha_l}{dt} = -\frac{d\alpha_v}{dt} - \frac{d\alpha_g}{dt} = -\frac{d\alpha_v}{dt} + \alpha_g \nabla \cdot \boldsymbol{c}, \tag{11}$$

$$\nabla \cdot \boldsymbol{c} = \frac{\rho_l - \rho_v}{\rho + \alpha_g(\rho_l - \rho_g)}\frac{d\alpha_v}{dt}. \tag{12}$$

The nonconservative continuity equation (Eq. (12)) is solved together with the momentum equation (Eq. (6)) by a pressure correction method, here a modified SIMPLE algorithm. The additional term of $d\alpha_v/dt$ is zero for flows without mass transfer between the phases.

Since

$$\frac{\partial \alpha_v}{\partial t} + \nabla \cdot (\alpha_v \boldsymbol{c}) = \frac{d\alpha_v}{dt} + \alpha_v \nabla \cdot \boldsymbol{c}, \tag{13}$$

$$\frac{\partial \alpha_l}{\partial t} + \nabla \cdot (\alpha_l \boldsymbol{c}) = \frac{d\alpha_l}{dt} + \alpha_l \nabla \cdot \boldsymbol{c}, \tag{14}$$

we can derive the following transport equations for the volume fractions α_i:

$$\frac{\partial \alpha_v}{\partial t} + \nabla \cdot (\alpha_v \boldsymbol{c}) = \frac{\rho_l}{\rho + \alpha_g(\rho_l - \rho_g)}\frac{d\alpha_v}{dt}, \tag{15}$$

$$\frac{\partial \alpha_l}{\partial t} + \nabla \cdot (\alpha_l \boldsymbol{c}) = \frac{\rho_v}{\rho + \alpha_g(\rho_l - \rho_g)}\frac{d\alpha_v}{dt}, \tag{16}$$

$$\frac{\partial \alpha_g}{\partial t} + \nabla \cdot (\alpha_g \boldsymbol{c}) = 0. \tag{17}$$

Note that we did not use the relation $d\alpha_v/dt = -d\alpha_l/dt$ which is non-necessarily imposed in the previous work, [3]. The relation is true for partial cavitation but invalid for multicomponent flow. Therefore, the new source terms of the transport equations for the volume fractions α_i (Eqs. (15)–(17)) are slightly different from the previous work. The newly derived equations should theoretically improve the calculation accuracy in the region where all three components (liquid, vapor and gas) are involved.

2.2 Cavitation Model—Bubble Dynamics. The closure of the system of equations requires an appropriate cavitation model. Cavitation may consist of small bubbles only, or may contain larger pockets of vapor. Here the vapor is assumed to consist of mini spherical bubbles, which grow and collapse accordingly to the pressure dynamics. Thus, the vapor fraction can be calculated as

$$\alpha_v = \alpha_l \cdot n_0 \frac{4}{3}\pi R^3, \tag{18}$$

where R is the bubble radius and n_0 is defined as nuclei concentration per unit volume of pure liquid. Due to Eqs. (11), (12), and (18), we can derive the vapor product rate as

$$\frac{d\alpha_v}{dt} = \alpha_l \frac{d\left(n_0 \frac{4}{3}\pi R^3\right)}{dt} + n_0 \frac{4}{3}\pi R^3 \frac{d\alpha_l}{dt}, \tag{19}$$

i.e.,

$$\frac{d\alpha_v}{dt} = \frac{\alpha_l n_0}{1 + \dfrac{\rho + \alpha_g(\rho_v - \rho_g)}{\rho + \alpha_g(\rho_l - \rho_g)} \cdot n_0 \dfrac{4}{3}\pi R^3} \frac{d\left(\frac{4}{3}\pi R^3\right)}{dt}. \tag{20}$$

Again, this equation is different from the previous work, [3], since the non-necessary assumption for the material derivatives of liquid and vapor is removed.

Bubble growth rates have been investigated since the beginning of the last century, [8,9]. The simplest but very effective description for the bubble growth is the Rayleigh relation:

$$\dot{R} = \frac{dR}{dt} = \sqrt{\frac{2}{3}\frac{p(R) - p_\infty}{\rho_l}}, \tag{21}$$

where $p(R)$ is the pressure in the liquid at the bubble boundary and p_∞ is the pressure at a large distance from the bubble. This relation is applicable in the range of moderately low pressures. In order to model both the bubble growth and collapse processes, the following formulation is implemented in the code:

$$\dot{R} = \frac{p(R) - p_\infty}{|p(R) - p_\infty|}\sqrt{\frac{2}{3}\frac{|p(R) - p_\infty|}{\rho_l}}. \tag{22}$$

In this study, $p(R)$ is set equal to the equilibrium vapor pressure p_{vap} and p_∞ to the ambient cell pressure. The bubble growth rate may be zero: $\dot{R} = 0$ when $p(R) = p_\infty$.

The use of the relations of Eqs. (18) and (20) requires knowledge of the nuclei concentration n_0. Unfortunately, this parameter is not easily measured. Fujimoto et al. [10] estimated that the values of n_0 lie near 10^{12} nuclei/m^3 for internal flows of small scale. However, as pointed out by Chen and Heister [11], experimental observations cannot detect bubbles at the submicrometer scale, so many additional nuclei of this size may be present. In addition, the growth of the smallest bubbles will be affected by surface tension forces which are not considered in this model. Furthermore, both nucleation and bubble coalescence may occur. Therefore, it is difficult to prescribe this parameter for injection nozzles. Indeed, one can use a transport equation to calculate the number n of the nuclei and/or bubbles, which is time-consuming and is going to be carried out in the near future. Alternatively, as Chen and Heister [11] indicated, in theory, one could arrive at an optimum nuclei density to match experimental observations for a given cavitation condition and this value would then be used to predict cavitation behavior at all other conditions. Following this idea, we account n_0 as an empirical parameter which will be determined via a numerical way.

2.3 Solution Procedure and Boundary Conditions. Due to Eq. (4), only two of Eqs. (15)–(17) need to be solved. Here, we select Eqs. (16) and (17). These transport equations are explicitly discretized. The solution procedure is similar to the CICSAM (compressive interface capturing scheme for arbitrary meshes) method, [12]. However, because we treat the fluids as a homogeneous mixture in the cavitation domain and do not capture sharp interfaces, the convective terms of Eqs. (16) and (17) for the cavitation domain are approximated using a hybrid method that combines central differencing and upwind differencing algorithms:

$$\alpha_{\text{cellface}} = \beta \alpha_{\text{upwind}} + (1-\beta)\alpha_{\text{downwind}}, \tag{23}$$

where the weighting factor β is set to 0.75 in this study, instead of the CICSAM factor of Ubbink.

The formulation of the numerical solution procedure is based on a cell-centered finite volume method for the variables, e.g., u, v, p, k, ω. The calculations are performed by first computing the volume fraction transportation (Eqs. (16), (17) for the new time-step, and then using the new volume fractions, i.e., the new mixture density, to solve the momentum equation. The momentum equation (Eq. (6)) is implicitly discretized and coupled with the continuity equation (Eq. (12)) via the SIMPLE algorithm, similar to the solution procedure proposed by Ferziger and Perić [13].

To model turbulence, μ_{eff} is used instead of the molecular viscosity μ:

$$\mu_{\text{eff}} = \mu + \mu_t, \tag{24}$$

where μ_t represents the turbulent viscosity which is modeled using the Wilcox $k-\omega$ model, [4]. For details of the turbulence modeling, we refer to the work of Yuan et al. [14].

Solution of the Navier-Stokes equations requires appropriate initial and boundary conditions to make the resulting system of algebraic equations solvable and the results unique. Since the effects of initial and boundary conditions may be remembered by the flow for a considerable time, they can have a significant influence on the results. Therefore, the initial and boundary conditions should be provided as realistic as possible. In this study, stationary liquid in the nozzle and a sharp liquid interface with the air at the nozzle exit are assumed as initial conditions. Both inflow and outflow boundaries are modeled as constant-pressure surfaces. At the inlet, the turbulent kinetic energy k is set to be equal to $6 \times 10^{-4} u_{in}^2$. The value of the specific dissipation rate ω is selected using the length scale equation, see [13,14]. On the wall, the boundary conditions are the impermeability and no-slip for the velocity, and the normal gradient of pressure is assumed to be zero. Wall functions based on the law of the wall are used as boundary conditions for the turbulence modeling, [14].

3 Results

As in our previous work, [14], the two-dimensional plane experimental test cases of Roosen et al. [15] have been re-calculated to validate our numerical scheme and to study the physical effects concerning the interaction between the cavitating flow and the external jet of the injection nozzle. The fluid used in the experiments was tap water. The "bore hole" of the nozzle consists of a rectangular-shaped channel of 0.2 mm×0.28 mm×1 mm (width ×height×length). Differently from the previous work, the present flow regime includes simultaneous treatment of internal and external flow. Figure 1 shows the nozzle geometry and boundary conditions. To reduce the computational time, we assume a two-dimensional flow and symmetry with respect to the nozzle axis. A computational mesh of 95×13 nodes for the nozzle block and 79×49 for the outflow block is used for the spatial discretization of the lower half geometry.

Inception of cavitation in a liquid requires the presence of nuclei. As discussed in Section 2.2, we account n_0 as an empirical parameter and determine it in a numerical way to match experimental observations for given cavitation conditions. This value will then be used to predict cavitation behavior at all other conditions. Our previous work for injection nozzle internal flows, [14], has shown that the numerical solutions using the nuclei concentration of the order of $n_0 = 1 \times 10^{14}$ nuclei/m^3×meter agree very well with experimental observations and the nuclei radius $R_0 = 0.3\,\mu$m is in the insensitive range. In this study, these values will be used, which correspond to an initial vapor fraction of $\alpha_{v0} = 0.0011\%$.

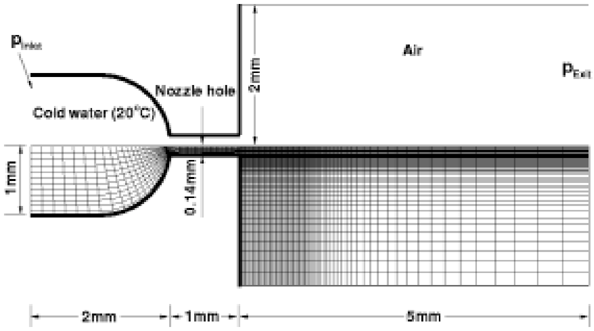

Fig. 1 Computational mesh and boundary conditions of the two-dimensional plane model injection nozzle

3.1 Steady Flow. The calculations are first carried out for the case with $p_{\text{Injection}} = 80$ bar and $p_{\text{Exit}} = 21$ bar. For the sake of simplicity, the inlet pressure p_{Inlet} for the computational domain (Fig. 1) is set as $p_{\text{Injection}}$ in the calculations. The computed result yields a length of the cavitation region approaching 200 μm, which agrees well with the experimental observations of Roosen et al. [15], see Figs. 2 and 3. Chaves et al. [2] have observed that, after a small increase of the injection pressure above the pressure at which cavitation first appears at the nozzle lip, the cavitation regime reaches the nozzle exit. To confirm their observations, another test case with $p_{\text{Injection}} = 80$ bar and $p_{\text{Exit}} = 11$ bar is considered, which demonstrates that under these conditions, the cavitation reaches the nozzle exit, see Figs. 4 and 5. The calculated results confirm that the flow is already supercavitating, although the cavitating region outside the nozzle exit cannot be very obviously recognized in the figure due to the restriction of the color map. The vapor content α_v just behind the nozzle exit reaches 9%. Because some cavitation bubbles collapse outside the nozzle in the supercavitating situation, it is necessary to include the outflow in the calculation.

Reboud et al. [16] and Delannoy et al. [17] found re-entrant jets and cloud shedding processes in divergent tunnels. However, neither re-entrant jets nor disintegrations of the cavity are found in

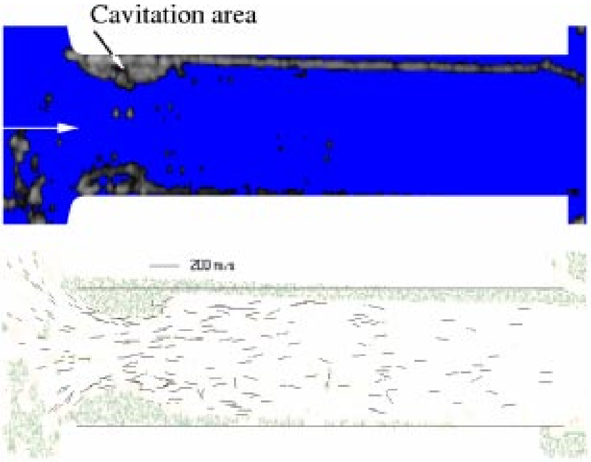

Fig. 2 Experimental density gradient and velocity distribution in the nozzle hole for $p_{\text{Injection}} = 80$ bar and $p_{\text{Exit}} = 21$ bar, flow from left to right, from Roosen et al. [15]

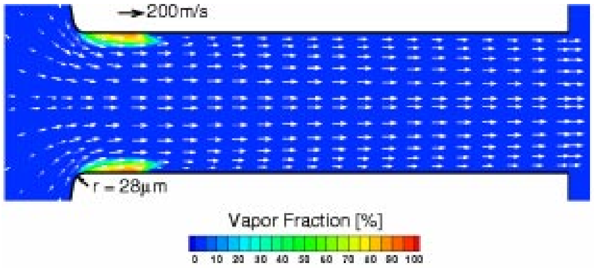

Fig. 3 Computed steady vapor fraction distribution in the nozzle hole. $p_{\mathrm{Inlet}}=80$ **bar,** $p_{\mathrm{Exit}}=21$ **bar=const.,** $\mathrm{Re}=\bar{u}_{\mathrm{Inlet}}\cdot H/\nu \approx 2.78\times 10^4$**.**

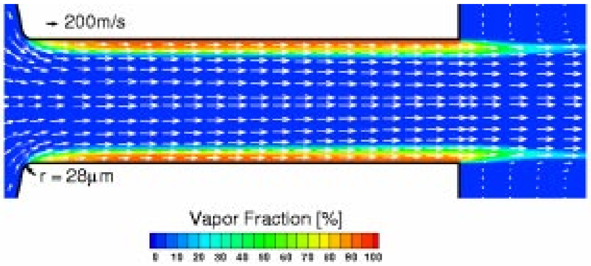

Fig. 6 Computed steady vapor fraction distribution. $p_{\mathrm{Inlet}}=800$ **bar,** $p_{\mathrm{Exit}}=11$ **bar=const.,** $\mathrm{Re}=\bar{u}_{\mathrm{Inlet}}\cdot H/\nu \approx 8.82\times 10^4$**.**

this study. This mechanism was not reported by Roosen et al. [15] either, whose experimental investigations are referenced in this study. This might be attributed to the high speed of the internal flow and the small scale of the nozzle. In the submerged cavitating cases with low speed flow, the cavities have sufficient time to condense and collapse inside the tunnels. On the other hand, the authors believe that the formation of re-entrant jets may be caused by the interaction of the cavitation and the flow separation in the divergent tunnels.

In addition, due to the restriction of the employed turbulence modeling, the sublayer of the boundary layer is not resolved. Some mechanism in the boundary layer cannot be revealed precisely. Chaves et al. [2] found that there is a layer of liquid between the vapor cavity and the nozzle wall. The numerical simulations in this study could not identify whether the white sheets on the wall of the experiments (Figs. 2 and 4) are liquid layers or they are experimental effects due to the wall surface roughness.

Cavitation has its own length scale which is not possible to be scaled up, [2,18]. This length scale is determined by the characteristic collapse time of a given cavity and the flow velocity. If the collapse of a bubble or cavity occurs downstream of the nozzle exit, i.e., in the external jet, this is called supercavitation. Supercavitation occurs if the collapse time of the vapor cavities is longer than the transit time of the fluid through the nozzle. It can be expected that higher pressure differences between the nozzle inlet and exit cause stronger supercavitation. For demonstration of strong supercavitation, an example with a realistic pressure of $p_{\mathrm{Inlet}}=800$ bar and $p_{\mathrm{Exit}}=11$ bar is calculated. Figure 6 shows the computed vapor distribution.

3.2 Periodic Unsteady Flow. Chaves et al. [2] have claimed that supercavitation is an inherent unsteady process that can only occur at high flow velocities. So far, this unsteadiness has not yet been captured because of the constant outflow boundary conditions and the single-phase turbulence model. The collapse process is strongly influenced by the boundary conditions,

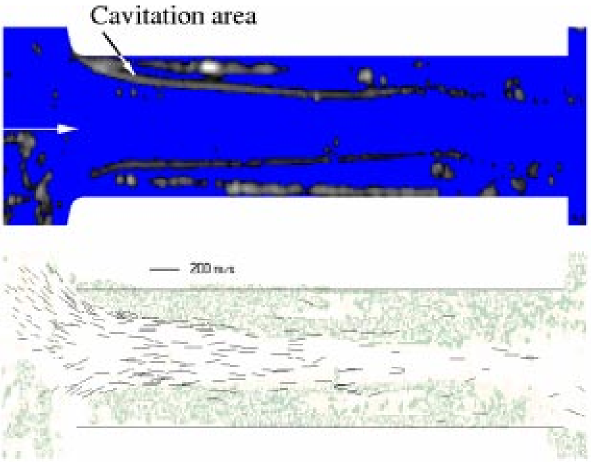

Fig. 4 Experimental density gradient and velocity distribution in the nozzle hole for $p_{\mathrm{Injection}}=80$ **bar and** $p_{\mathrm{Exit}}=11$ **bar, flow from left to right, from Roosen et al. [15]**

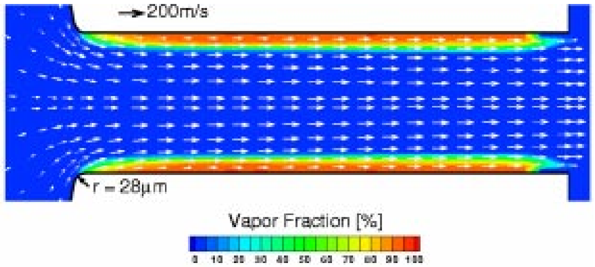

Fig. 5 Computed steady vapor fraction distribution in the nozzle hole. $p_{\mathrm{Inlet}}=80$ **bar,** $p_{\mathrm{Exit}}=11$ **bar=const.,** $\mathrm{Re}=\bar{u}_{\mathrm{Inlet}}\cdot H/\nu \approx 2.78\times 10^4$**.**

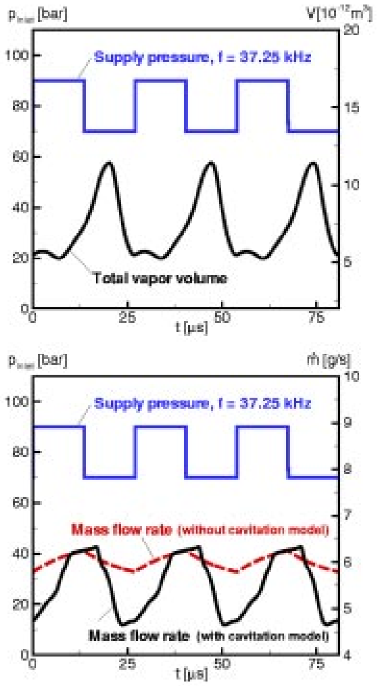

Fig. 7 Integrated total vapor volume within and outside the nozzle (top) and mass flow rate at the nozzle exit (bottom) depending on the rectangular inlet pressure pulse. Downstream chamber pressure $p_{\mathrm{Exit}}=11$ **bar=const.,** $\mathrm{Re}=\bar{u}_{\mathrm{Inlet}}\cdot H/\nu \approx 2.78\times 10^4$**.**

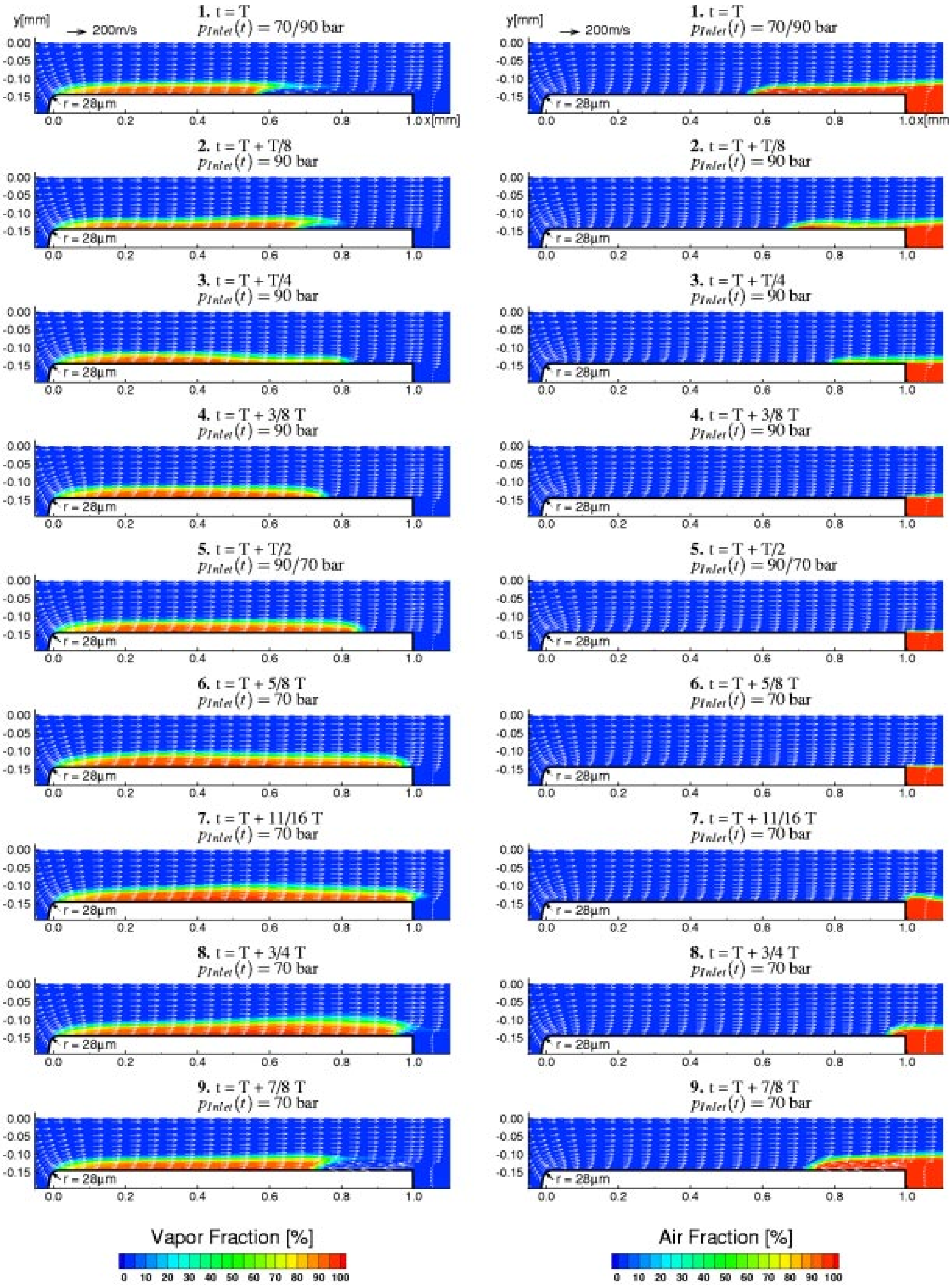

Fig. 8 Unsteady supercavitation of one cycle. Periodic unsteady inlet pressure $p_{\text{Inlet}}=80\pm10$ bar, $f=37.25$ kHz, downstream chamber pressure $p_{\text{Exit}}=11$ bar=const., Re=$\bar{u}_{\text{Inlet}}\cdot H/\nu\approx2.78\times10^{4}$. Left: vapor fraction distribution; right: air fraction distribution.

the nozzle geometry, and the main axial flow. The single-phase turbulence model overestimates the viscous effects in two-phase regions.

In real cases, the pressures upstream and downstream the nozzle fluctuate with high frequencies. The reason for the upstream pressure fluctuation is the well-known ‘‘water hammer’’ effect in the needle chamber. In order to understand the effects caused by the fluctuation of the upstream pressure further, calcu-

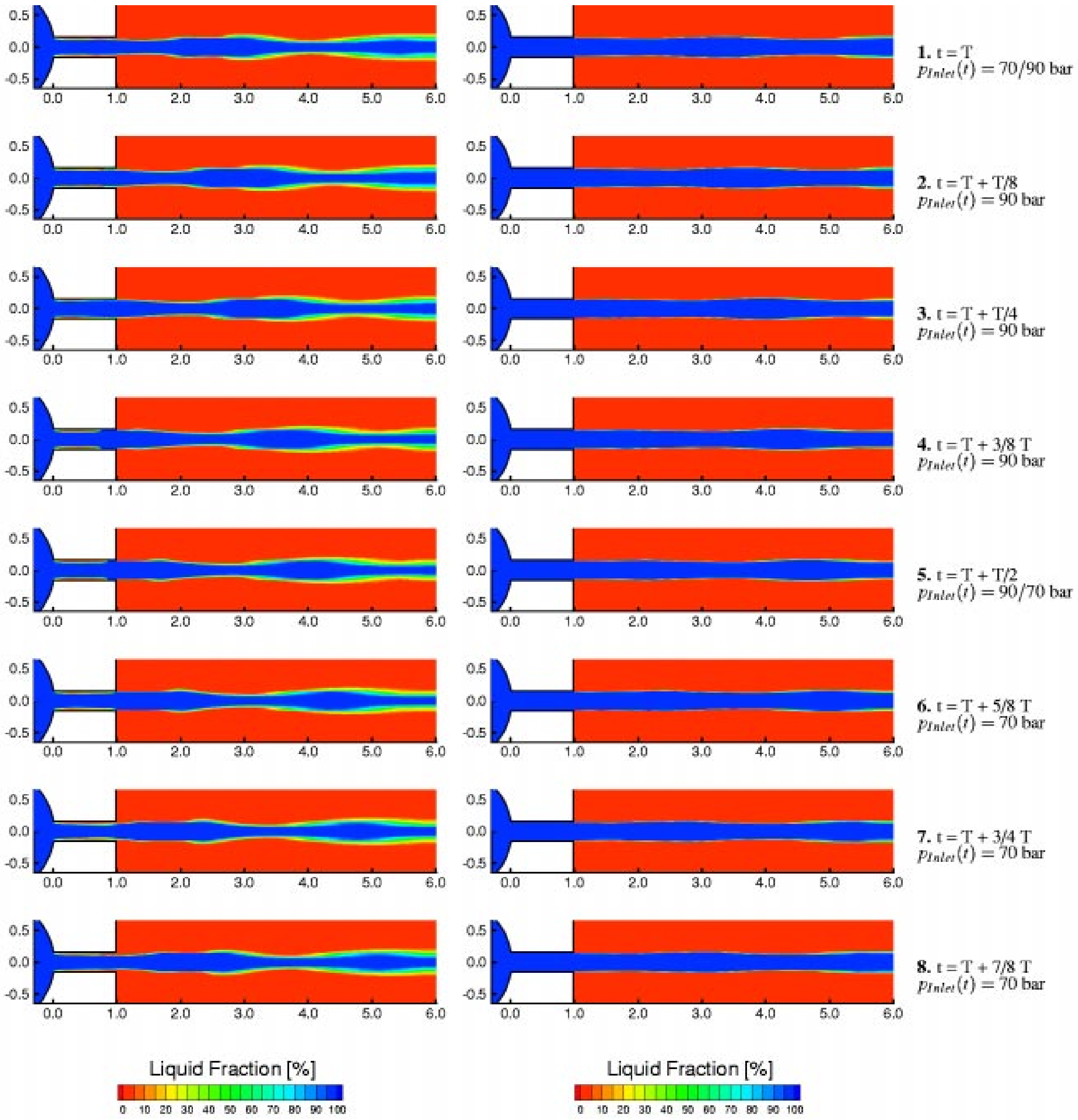

Fig. 9 Unsteady jet flow nearby the nozzle exit. Periodic unsteady inlet pressure $p_{\text{Inlet}}=80\pm10$ bar, $f=37.25$ kHz, downstream chamber pressure $p_{\text{Exit}}=11$ bar. Left: computed with cavitation model, $\text{Re}=\bar{u}_{\text{Inlet}}\cdot H/\nu\approx2.78\times10^4$; right: computed without cavitation model, $\text{Re}=\bar{u}_{\text{Inlet}}\cdot H/\nu\approx3.0\times10^4$.

lations for the case with a rectangular inlet pressure pulse are performed. The pressure pulse and the calculated results are shown in Figs. 7–9.

The integrated total vapor volume within and outside the nozzle shown in Fig. 7 indicates that the cavitation process in the injection nozzle is very complex. As a difference from the unsteady partial cavitation, where only one vapor volume peak is reached, [18], the total vapor volume reveals a secondary peak during one inlet pressure period for this supercavitating flow. The physical reason is the interaction of the cavitation with the air from the nozzle outlet. Figure 8 shows the details of the calculated flow field in the lower half of the nozzle. The time interval is one-eighth of the period. However, a plot at the time $t=T+11/16T$ (Fig. 8.7) is inserted in order to demonstrate the instantaneous supercavitation. The velocity field also shows that the cavitating flow separates temporarily in the nozzle, see plots 8, 9 and 1 in the left column of Fig. 8. In these situations, the gas (air) from the downstream chamber is drawn up the sides of the nozzle into the region of cavitation. This phenomenon, called hydraulic flip, was first observed by Bergwerk [19] and further investigated by Chaves et al. [2] and Soteriou et al. [20,21]. Since both inflow and outflow are modeled as constant-pressure surfaces, the gas (air) is allowed to enter the computational domain in the downstream chamber.

The calculated mass flow rates shown in Fig. 7 demonstrate that the discharge of the nozzle strongly depends on the cavitation intensity. The deviation of the computed mass flow rates, with and without the cavitation model, is on the order of 10% of the averaged mass flow rate, i.e., cavitation chokes the liquid flow and reduces the discharge significantly. In addition, it is recognized from Fig. 7 that the cavitation process enhances the mass flow rate fluctuation, which intensifies the unsteadiness of the jet and jet atomization.

Wu et al. [1] found that the spray cone angles for cavitation-free nozzles are systematically smaller than those for nozzles likely to cavitate. Chaves et al. [2] found that, when cavitation reaches the nozzle exit, the spray angle levels off at a value that is almost independent of the injection pressure. Furthermore, Chaves et al. identified the isolated effect of cavitation: For lower injection pressure, the jet is smooth where cavitation does not reach the nozzle exit. The jet has a rough surface where cavitation has reached the exit. This causes finite disturbances that immediately initiate atomization.

To demonstrate the sole effect of cavitation on the jet, a comparison of the computed liquid fractions with and without the cavitation model is made. The results are depicted in Fig. 9. The dark color indicates the pure liquid. Since the supercavitation predicted using the cavitation model extends only to the near-exit region of the nozzle in this test case, see Fig. 8.7, the liquid-air mixture predominates in the most part of the downstream chamber. It is easily recognized that the integral dark area using the cavitation model is smaller than that without the cavitation model. This confirms that cavitation reduces the discharge as shown in Fig. 7. However, the band of the liquid-gas mixture using the cavitation model is about 25% broader than that without the cavitation model. This means that the liquid has been intensified to spread around. Therefore, it can be thought of that cavitation may have positive influence on the atomization process, even though the disturbance is finite. This agrees qualitatively with the findings of Chaves et al. [2] and Wu et al. [1].

4 Conclusions

A new model concerning the interaction between internal cavitating flow and external jet flow of injection nozzles has been proposed in this paper. The volume-of-fluid (VOF) method has been extended to calculate the volume fractions of liquid, vapor and gas (air). This new model has been successfully used to simulate supercavitation and hydraulic flip in cavitating flow through a model injection nozzle. Further quantitative improvements are to be expected by introducing empirical corrections in the single-phase $k-\omega$ turbulence model.

Acknowledgment

The authors gratefully acknowledge the support from the Deutsche Forschungsgemeinschaft under grant Schn-352/16-2 during performing this work. Sincere thanks are given to Dr.-Ing. P. Roosen and Dipl.-Phys. O. Genge of the Institute for Technical Thermodynamics of the RWTH Aachen (Germany) for providing the experimental data. Thanks are also due to Dr. M. Khalid at the Institute for Aerospace Research, National Research Council of Canada, for meaningful suggestions to this paper.

Nomenclature

$\mathbf{c}$ = velocity vector
H = full height of the nozzle inflow sac
k = kinetic energy of turbulent fluctuations per unit mass
$\dot{m}$ = mass flow rate
$\dot{m}_v$ = mass exchange rate
n_0 = nuclei concentration per unit volume of liquid
p = pressure
R = bubble radius
t = time
T = time of period
u, v = Cartesian components of velocity
V = control volume
x, y = Cartesian coordinates
α = fluid volume fraction per unit volume of mixture
μ = dynamic viscosity
ρ = density
ω = specific dissipation rate

Indices

v, l, g = vapor, liquid, gas
$0, \infty$ = initial, farfield

References

[1] Wu, K.-J., Su, C.-C., Steinberger, R. L., Santavicca, D. A., and Bracco, F. V., 1983, ‘‘Measurements of the Spray Angle of Atomizing Jets,’’ ASME J. Fluids Eng., **105**, pp. 406–413.
[2] Chaves, H., Knapp, M., Kubitzek, A., Obermeier, F., and Schneider, T., 1995, ‘‘Experimental Study of Cavitation in the Nozzle Hole of Diesel Injectors Using Transparent Nozzles,’’ SAE Paper 950290.
[3] Yuan, W., and Schnerr, G. H., 2002, ‘‘Optimization of Two-Phase Flow in Injection Nozzles—Interaction of Cavitation and External Jet Formation,’’ *Proc. 2002 ASME Fluids Engineering Division Summer Meeting*, Montreal, Canada, July 14–18.
[4] Wilcox, D. C., 1998, *Turbulence Modeling for CFD*, DCW Industries, La Cañada, CA.
[5] Sauer, J., and Schnerr, G. H., 2000, ‘‘Unsteady Cavitating Flow—A New Cavitation Model Based on a Modified Front Capturing Method and Bubble Dynamics,’’ *Proceedings of 2000 ASME Fluid Engineering Summer Conference*, Boston, MA, June 11–15.
[6] Schnerr, G. H., and Sauer, J., 2001, ‘‘Physical and Numerical Modeling of Unsteady Cavitation Dynamics,’’ *Proceedings of 4th International Conference on Multiphase Flow*, New Orleans, LA.
[7] Spalding, D. B., 1974, ‘‘A Method for Computing Steady and Unsteady Flows Possessing Discontinuities of Density,’’ CHAM Report 910/2.
[8] Rayleigh, L., 1917, ‘‘On the Pressure Developed During the Collapse of a Spherical Cavity,’’ Philos. Mag., **34** (200), p. 94.
[9] Plesset, M. S., 1969, ‘‘Cavitating Flows,’’ Report No. 85-46, Division of Engineering and Applied Science, California Institute of Technology, Pasadena, CA.
[10] Fujimoto, H., Mishikori, T., Tsukamoto, T., and Senda, J., 1994, ‘‘Modeling of Atomization and Vaporization Process in Flash Boiling Spray,’’ ICLASS-94, Paper VI-13.
[11] Chen, Y., and Heister, S. D., 1996, ‘‘Modeling Cavitating Flows in Diesel Injectors,’’ Atomization Sprays, **6**, pp. 709–726.
[12] Ubbink, O., 1997, ‘‘Numerical Prediction of Two Fluid Systems With Sharp Interfaces,’’ Ph.D. thesis, University of London.
[13] Ferziger, J. H., and Perić, M., 1996, *Computational Methods for Fluid Dynamics*, Springer-Verlag, Berlin.
[14] Yuan, W., Sauer, J., and Schnerr, G. H., 2001, ‘‘Modeling and Computation of Unsteady Cavitation Flows in Injection Nozzles,’’ Mécanique & Industries, **2**, pp. 383–394.
[15] Roosen, P., Unruh, O., and Behmann, M., 1996, ‘‘Untersuchung und Modellierung des transienten Verhaltens von Kavitationserscheinungen bei ein- und mehrkomponentigen Kraftstoffen in schnell durchströmten Düsen,’’ Report of the Institute for Technical Thermodynamics, RWTH Aachen, Germany.
[16] Reboud, J.-L., Stutz, B., and Coutier, O., 1998, ‘‘Two-Phase Flow Structure of Cavitation: Experiment and Modeling of Unsteady Effects,’’ 3rd International Symposium on Cavitation, Grenoble, France.
[17] Delannoy, Y., and Kueny, J. L., 1990, ‘‘Two Phase Flow Approach in Unsteady Cavitation Modelling,’’ ASME Cavitation and Multiphase Flow Forum, New York, NY.
[18] Yuan, W., and Schnerr, G. H., ‘‘Cavitation in Injection Nozzles—Effect of Injection Pressure Fluctuations,’’ *Proceedings 4th International Symposium on Cavitation*, California Institute of Technology, Pasadena, CA.
[19] Bergwerk, W., 1959, ‘‘Flow Pattern in Diesel Nozzle Spray Holes,’’ Proc. Inst. Mech. Eng., **173**(25), pp. 655–660.
[20] Soteriou, C. C. E., Smith, M., and Andrews, R. J., 1993, ‘‘Cavitation Hydraulic Flip and Atomization in Direct Injection Diesel Sprays,’’ IMechE Paper C465/051/93, pp. 45–65.
[21] Soteriou, C., Andrews, R., and Smith, M., 1995, ‘‘Direct Injection Diesel Sprays and the Effect of Cavitation and Hydraulic Flip on Atomization,’’ SAE Paper No. 950080, pp. 27–51.

O. Coutier-Delgosha[1]
R. Fortes-Patella
J. L. Reboud[2]

Laboratoire des Ecoulements,
Géophysiques et Industriels,
B. P. 53,
Grenoble, 38041, France

M. Hofmann
B. Stoffel

Laboratory for Turbomachinery and Fluid Power,
Darmstadt University of Technology,
Darmstadt D-64289, Germany

Experimental and Numerical Studies in a Centrifugal Pump With Two-Dimensional Curved Blades in Cavitating Condition

In the presented study a special test pump with two-dimensional curvature blade geometry was investigated in cavitating and noncavitating conditions using different experimental techniques and a three-dimensional numerical model implemented to study cavitating flows. Experimental and numerical results concerning pump characteristics and performance breakdown were compared at different flow conditions. Appearing types of cavitation and the spatial distribution of vapor structures within the impeller were also analyzed. These results show the ability of the model to simulate the complex three-dimensional development of cavitation in a rotating machinery, and the associated effects on the performance. [DOI: 10.1115/1.1596238]

1 Introduction

The work presented in this paper was carried out in the scope of the European Research Program PROCOPE, between researchers of the TUD (Darmstadt University of Technology, Laboratory for Turbomachinery and Fluid Power) and of the LEGI (Laboratoire des Ecoulements Géophysiques et Industriels de Grenoble). The aim of this European program was to improve the understanding of the unsteady behavior of cavitating flows and the related erosive aggressiveness by experimental analyses and development of numerical models.

In this context, some research works were developed by both laboratories to analyze and to characterized erosion phenomenon, [1,2], as well as to study and to model unsteady cavitating flows around a two-dimensional hydrofoil, [3], and in a cascade of three hydrofoils, [4].

In order to extend those previous analyses, the present study consists of investigations by experimental means and numerical simulation of a special centrifugal test pump in cavitating and noncavitating conditions. Experiments were carried out at the TUD using different experimental techniques. The measurement of classical pump characteristics and performance breakdown at different flow conditions were associated with flow visualisations. Appearing types of cavitation and the spatial distribution of vapor structures within the impeller were analyzed.

Three-dimensional Navier-Stokes codes taking into account the cavitation process have been developed during the last years, [5–8], based on different multiphase flow approaches, [9,10]. Industrial CFD codes are now starting to take into account cavitation models, allowing first applications to pump geometries, [11,12]. In this context, a numerical model for three-dimensional cavitating flows is developed at LEGI, based on the three-dimensional code FINE/TURBO™, developed by NUMECA International. This work is performed in cooperation with the Rocket Engine Division of SNECMA Moteurs and the French Space Agency CNES, with the final objective to provide accurate simulations of unsteady cavitating flows in the inducers of rocket engine turbopumps, [13,14]. The application to the centrifugal pump represents a first step of validation of the model on steady-state cavitating flow in turbomachinery.

2 Geometry

A special impeller geometry has been chosen to easily adapt existing measuring techniques for a single hydrofoil in a test section, [3,15], to a pump test rig. Optical access in two planes was made possible to enable a view perpendicular to the blade surface on both suction and pressure side by Plexiglas windows in the housing and a Plexiglas shroud. The impeller has five single-curved blades with two different radii at inlet and outlet. The part of the blade with the larger radius (the second part in flow direction) was also made of Plexiglas to obtain optical access to the pressure side of the following blade and the entire channel, respectively.

Figure 1(*a*) shows the intersection of the two blade radii. Another characteristic is the parallel hub and shroud to get an almost two-dimensional blade-to-blade channel with constant width. An axial-symmetric housing (Fig. 1(*b*)) is used to obtain almost constant conditions at the impeller outlet (if we neglect gravitational forces that are small compared to the performance of the impeller). With these preconditions we obtain comparable cavitation conditions in each channel without the influence of a volute casing.

Nominal conditions are at a rotational speed of 36 Hz and a flow rate $Q=210\ \mathrm{m}^3/\mathrm{h}$. Specific speed of the impeller is $n_s = nQ^{1/2}/H^{3/4}=20$ (European units: n_s and n in rpm, Q in m^3/s and H in m), the outer impeller diameter equals 278 mm. Cavitation conditions are defined by NPSH value based on the upstream total pressure, water vapor pressure and density at ambient temperature.

3 Visualizations

Besides the measurements of the characteristics of the pump at different flow-rates and cavitation conditions, various visualisation techniques were used. All images shown in this paper were taken at nominal flow rate with various values of NPSH, where both cavitation on suction and pressure side of the blades occurs.

Stroboscopic light was used on one hand for standard imaging and high-speed video with the light-sheet illumination (Fig. 2) was applied to observe self-oscillating states of the cavitation on the blade pressure side or other unsteady effects, [16].

---

[1] Currently at ENSTA UME/DFA, chemin de la Huniere, 91761 Palaiseau cedex, France.

[2] Currently at LTDS/ENISE, Saint-Etienne, France.

Contributed by the Fluids Engineering Division for publication in the JOURNAL OF FLUIDS ENGINEERING. Manuscript received by the Fluids Engineering Division June 26, 2002; revised manuscript received October 24, 2002. Associate Editors: Y. Tsujimoto.

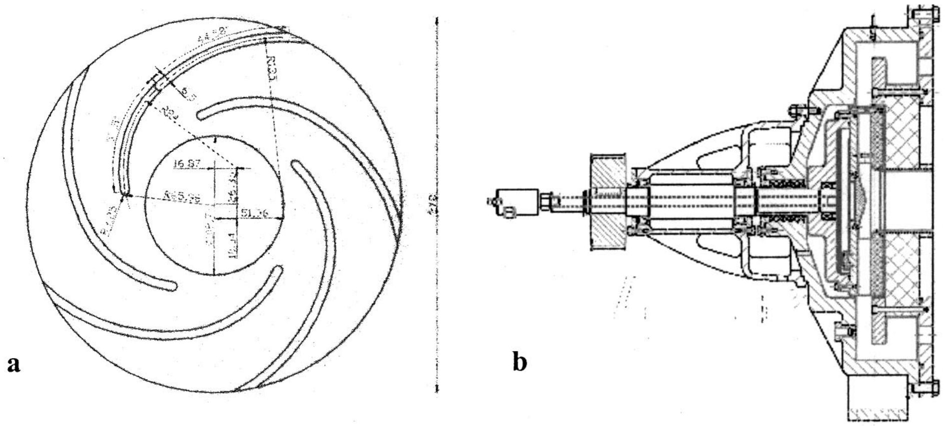

Fig. 1 (*a*) Impeller geometry, (*b*) housing

The investigated flow conditions during the experiments show always unsteady behavior of the leading-edge cavitation, not only concerning the unsteadiness of the closure region of the attached cavitation but also the shedding of vapor structures in the channel. Besides the well-known attached cavitation on pressure and suction side, another type of cavitation occurs at the inlet of the impeller caused by the strong curvature of the streamlines along the front shroud. It is visible either as attached cavitation caused by the depression at the radius (regions B and C in Fig. 3), or as shear cavitation because the flow was separating at the inlet radius of the front shroud at lower values of NPSH (region B in Fig. 4). Dependent on the length of the attached part of the cavitation (region A in all figures) the extent of this shear layer cavitation spreads into the channel as it is shown in Fig. 4 at two different stages of a cavitation cycle. In Fig. 4(*a*) the larger extent of the shear cavitation (region B) on top of the attached part (see region A, the illuminated interface of the cavitation sheet on the pressure side) is visible. In Fig. 4(*b*) (with a smaller cavitation sheet) no shear cavitation can be seen. The contour of the interface of the attached part of the cavitation (region A) already indicates a different state of the typical self-oscillating cloud cavitation condition.

With the aid of laser light-sheet illumination of the vapor-fluid interface, an analysis of the unsteadiness of the attached part of the cavitation in the impeller could be done at half-width of the channel. The images were taken at a rate of 2 Hz but triggered by an angular encoder and a special signal conditioning that allowed to take the image at every phase angle compared to a reference angle with a step size of 1 deg. Hence, the illuminated blade had 18 revolutions between every image.

Based on 500 images, each of them illuminated during 50 μs, a mean gray value distribution was calculated to identify the statistical mean cavity on the leading edge of the blade.

The standard deviation of the gray values or its variance can serve as a quantity to determine the unsteadiness of the cavitation. In regions of these images with higher values of the variance (to be identified as dark regions), the fluctuations of the gray values and, therefore, the fluctuations of the reflecting vapor structures are larger than in regions with a smaller variance. Those regions are constantly filled with either water or vapor. The result of such a treatment is shown in Figs. 5 and 6.

Mean distribution (Figs. 5(*a*) and 6(*a*)): The attached part of the cavitation can only be identified by its two-phase interface, because the light is mainly reflected. But the mean region with a cloud shedding is also indicated by a higher mean gray value just downstream of the closure region of the cavitation sheet. For the comparison with numerical results, we just identify the attached part. As expected, the extent of both regions enlarges with decreasing NPSH value. As already mentioned, the flow has the tendency to separate at the leading edge of the blade, which is enhanced (Fig. 6(*a*)) at lower pressure conditions.

Standard deviation (Figs. 5(*b*) and 6(*b*)): The fluctuation of the shedding becomes larger with decreasing NPSH and its extension fills almost half of the height of the channel. This is a result of the higher production of transient vapor structures from the leading edge cavitation. In contast, the interface of the attached cavitation seems to be rather stable. Probably the flow is clearly separated

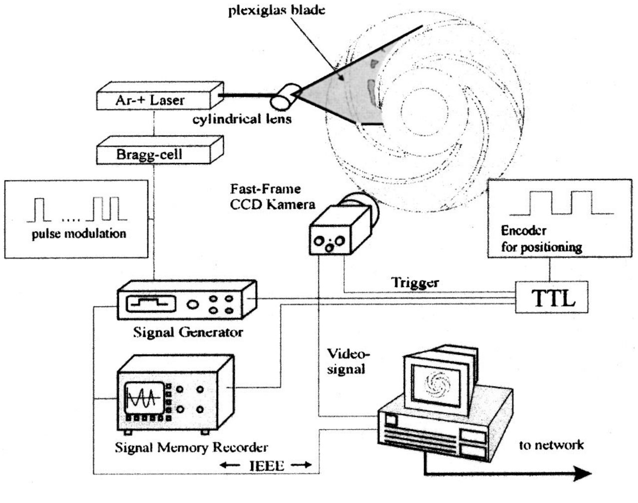

Fig. 2 Visualization setup

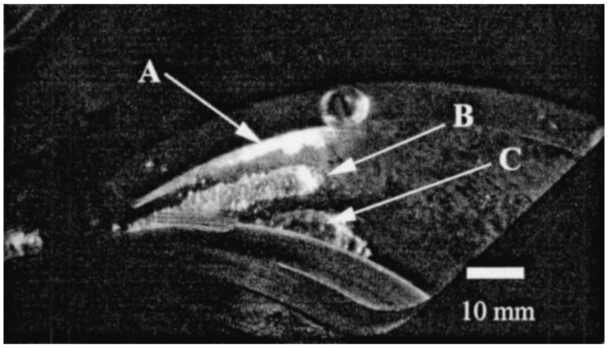

Fig. 3 Unsteady-state of blade cavitation on suction side, NPSH=8 m, stroboscopic light illumination (a scaling bar is added to each image, representing a length of 10 mm)

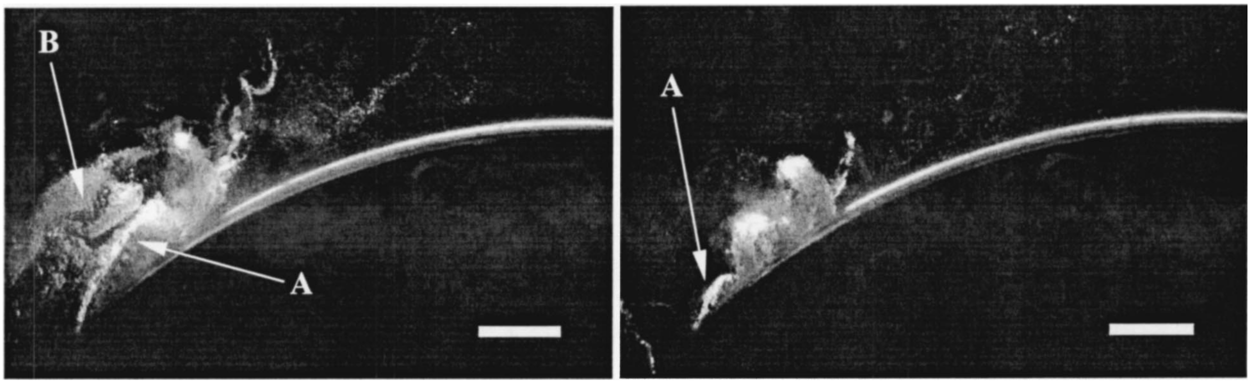

Fig. 4 Unsteady-state of blade cavitation on pressure side at two different time and NPSH=7 m (laser light sheet)

from the leading edge, the separation zone is almost steadily filled with vapor, and only in the closure region vapor is shed into the channel.

4 Physical and Numerical Model

The main features of the physical and numerical models applied to simulate the flow field in the pump are summarized in the present paper. More details are given in [13,14,17].

Cavitating flows are described by a single-fluid model, based on previous numerical and physical work developed at LEGI, [9,18]. This fluid is characterized by a density ρ that varies in the computational domain: when the density in a cell equals that one of the liquid (ρ_1), the whole cell is occupied by liquid, and if it equals that one of the vapor (ρ_v), the cell is full of vapor. Between these two extreme values, a liquid/vapor mixture, still considered as one single fluid, occupies the cell. The void fraction $\alpha=(\rho-\rho_1)/(\rho_v-\rho_1)$ can thus be defined as the local ratio of vapor contained in this homogeneous mixture.

Velocities are assumed to be locally the same for liquid and for vapor. An empirical state law is used to manage the mass fluxes resulting from vaporization and condensation processes. That barotropic law links the density to the local static pressure $\rho(P)$. When the pressure is remarkably higher or lower than vapor pressure, the fluid is supposed to be purely liquid or purely vapor, according to the Tait equation or to the perfect gas law, respectively. The two fluid states are joined smoothly in the vapor-pressure neighborhood. This results in the evolution law presented in Fig. 7, characterized mainly by its maximum slope $1/A_{\min}^2$, where $A_{\min}^2=\partial P/\partial\rho$. $A_{\min}$ can thus be interpreted as the minimum speed of sound in the mixture.

The numerical model of cavitating flows based on that physical description is generated on the basis of the commercial code FINE/TURBO™ developed by NUMECA International. FINE/TURBO™ is a three-dimensional structured mesh code that solves the time dependent Reynolds-averaged Navier-Stokes equations. Time-accurate resolutions of the equations use the dual-time stepping approach. Pseudo-time derivative terms are added to march the solution towards convergence at each physical time-step. The range of application is extended to weakly compressible or incompressible flows by introducing a preconditioning matrix, [19]. The discretization is based on a finite volume approach. Convection terms are treated by a second-order central scheme associated with artificial dissipation terms. The pseudo-time integration is made by a four-step Runge-Kutta procedure. The physical time-derivative terms are discretized with a second-order backward difference scheme. The code resorts to a multigrid strategy to accelerate the convergence, associated with a local time-stepping and an implicit residual smoothing.

The numerical model was adapted to treat the cavitation process, [13,17]. The key point of this adaptation is the modification of the state law of the fluid. Applied barotropic law implies the simultaneous treatment of two different cases: the fluid is highly compressible in the liquid/vapor mixture (the Mach number can be as high as 4 or 5) and is almost incompressible in the pure

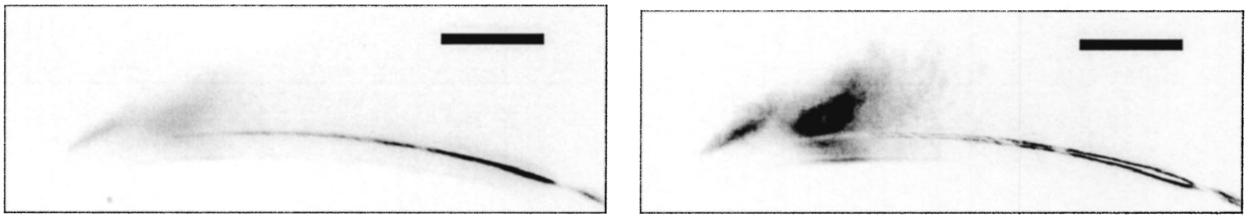

Fig. 5 Mean vapor distribution and standard deviation on pressure side, Qn, NPSH=7 m

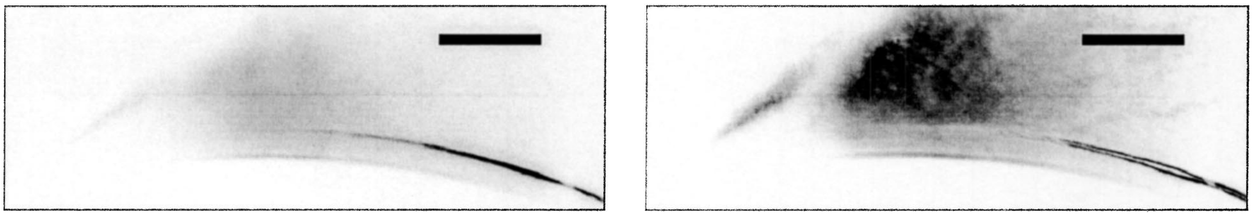

Fig. 6 Mean vapor distribution and standard deviation on pressure side, Qn, NPSH=6 m

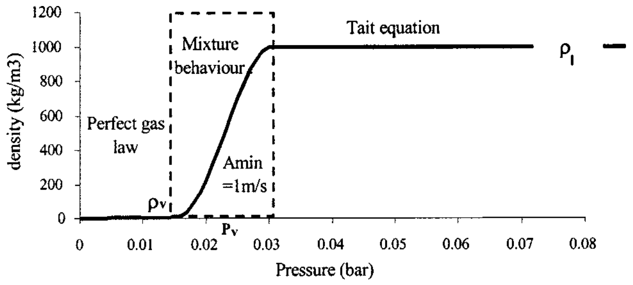

Fig. 7 The barotropic state law $\rho(P)$ for water

vapor or pure liquid areas. So the main difficulty consisted in managing these two different states of the fluid, without creating any spurious discontinuity in the flow field. Besides, cavitation consists in a very sharp and very rapid process. The density variations in time and space are smoothed to avoid numerical instabilities. This under-relaxation of density implies that a minimum number of pseudo time-steps must be imposed within each physical time step to avoid any effect of this parameter on the result.

More details concerning the basic numerical method can be found in [20], and a more precise investigation of the influence of numerical parameters in cavitating conditions (artificial dissipation, turbulence model, physical time step, mesh size . . .) is available in [17].

The model was applied to the presented centrifugal pump geometry. Several meshes were tested, as well H-I typed as H-O typed, including between 300,000 and 700,000 cells. They are composed of two blocks (the impeller and the inlet domain) in the H-I case, and three blocks (the inlet domain, the impeller, and the outlet domain) in the H-O case. Only one blade-to-blade channel is treated, and periodicity conditions are applied to the frontiers with the adjacent channels. This automatically implies that the five channels will behave the same way during the numerical simulation.

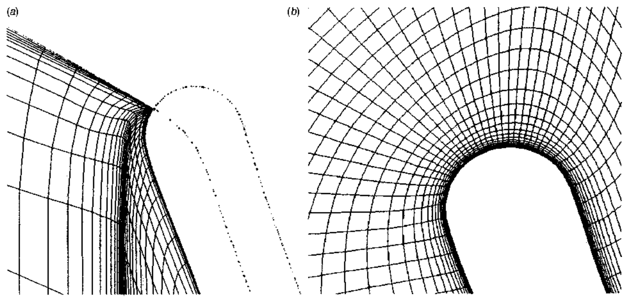

Fig. 8 Mesh of the leading edge with (*a*) a H-I type mesh, (*b*) a H-O type mesh

H-O meshes are particularly well adapted to the present geometry, because of the sharp leading and trailing edges (Fig. 8). H-I meshes induce more important stretchings of the cells in these areas, but they also lead to more reduced mesh sizes.

Noncavitating steady calculations were performed with the different meshes, and the results showed the weak influence of the mesh type on the pump performance and on the pressure field around the leading edge. Consequently, all the simulations presented hereafter were obtained with the H-I 300,000 cells mesh, whose structure is presented in Fig. 9. Special attention was paid to the cavitating areas (suction side of the blade, leading edge . . .): the stability study reported in [17] shows indeed that cells characterized by a high distortion or high aspect ratio strongly penalize the numerical stability in cavitating conditions. Thus, a fine grid is applied in these areas. Figure 9 hereafter shows the radial mesh structure, a three-dimensional view of a complete blade-to-blade channel, and some details of the mesh on the hub surface.

Conditions applied for the simulations are the following:

- Turbulence model: we use for the simulations presented in this paper a Baldwin-Lomax turbulence model. A more detailed study of the influence of the turbulence model on two-dimensional unsteady cavitation simulation is proposed in [21] and [22]. Those works pointed out a major influence of the compressibility effect modeling on the unsteady behavior of cloud cavitation. Other three-dimensional calculations considering different k-ε turbulence models are in progress to improve the physical analyses.
- Boundary conditions (Fig. 10): velocity is imposed at the inlet of the suction pipe. Laws of the wall are imposed along solid boundaries. The relative motion between the inlet pipe walls and the impeller is taken into account. On the other hand, the outlet housing shape is not described and the parallel walls are treated as hub and shroud extensions up to the outlet, at 1.5 times the impeller outer radius, where a uniform static pressure is imposed.
- Initial transient treatment: First of all, a steady step is carried out, with a pseudo vapor pressure low enough to ensure non-cavitating conditions in the whole computational domain. Then, the NPSH is slowly lowered by increasing smoothly the pseudo vapor pressure at each new time-step up to the physical value. Vapor structures spontaneously appear and grow during that process, in the regions of low static pressure. The final NPSH value, depending on the outlet static pressure imposed, is then kept constant throughout the computation.

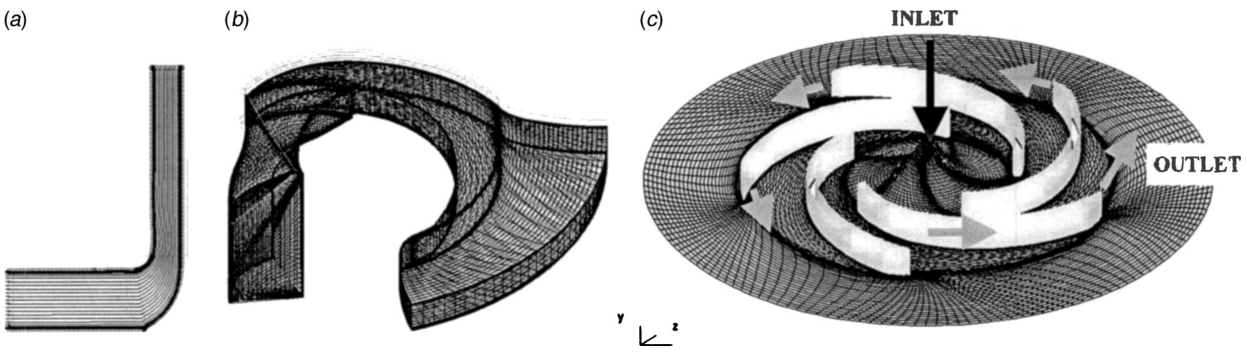

Fig. 9 Mesh applied for the calculations (300,000 cells). (*a*) Meridional view, (*b*) three-dimensional view of a blade-to-blade channel, (*c*) view of the mesh on hub side of the pump. (The entire pump geometry is reconstructed by rotation of the single blade-to-blade channel.)

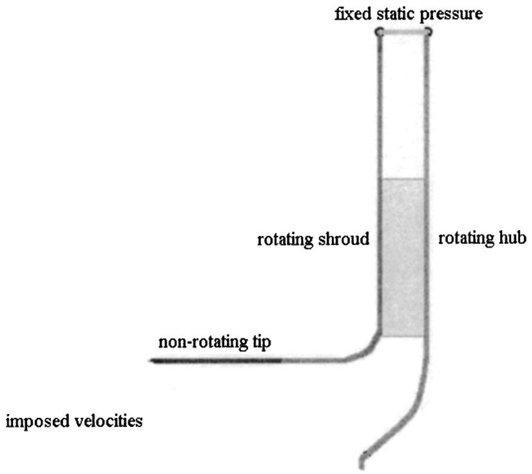

Fig. 10 Boundary conditions

5 Noncavitating Characteristics

Experimental tests and numerical calculations were performed considering a large range of flow-rates, in non-cavitating conditions. Figure 11(*a*) illustrates the computational result at nominal flow rate: the total pressure distribution is represented at half-width of the pump channels. Figure 11(*b*) presents a comparison between the numerical and experimental performance charts. Directly based on the measurements performed, the head of the pump is defined as the difference between downstream static pressure and upstream total pressure.

$$H = \frac{P^{outlet} - P_{tot}^{inlet}}{\rho g}$$

$$\text{where} \quad P_{tot}^{inlet} = P^{inlet} + \frac{\rho V_{inlet}^2}{2}$$

P^{inlet} and P^{outlet} are the static pressures measured, respectively, at the pump inlet and outlet, and V_{inlet} is the mean inlet velocity. The outlet pressure was determined by taking the static wall pressure in the vaneless diffuser at 5 static pressure taps located at a diameter of 500 mm and averaged by connecting all pressure taps to a single pressure transducer.

The total pressure at pump inlet is determined from the wall pressure and the velocity head two diameters upstream of pump inlet where the velocity is calculated from measured flow rate and the area of the measuring cross section. Precise locations of the sensors in the experiments are consistent with the inlet and outlet of the computational domain in the calculation.

We observe a reliable agreement between the pump characteristics given by measurement and computation in the whole range of flow rates investigated experimentally. The model gives a better prediction when the flow rate is over 50 percent of the nominal value ($Qn = 210\ m^3/h$), and the numerical simulation becomes unstable at very low partial flow rate. As a matter of fact, the numerical simulation slightly overestimates the pump head. This is an expected result, since the flow through the side chamber is not taken into account in numerical simulations. This gap flow of the pump impeller has to be added to the flow rate actually passing through the blade-to-blade channels and is therefore slightly higher in the experiments than in the model. At nominal flow rate, the head is overestimated by about 5 percent (40.5 m instead of 38.5 m). The uncertainty of the measured value was estimated to be no more than 0.8 m and corresponds to 2 percent of the value, which also has to be taken into account.

6 Cavitation Behavior

Numerical simulations of the pump are performed in cavitating conditions at several flow rates. First, we present some qualitative results, consisting in a visualisation of the vapor/liquid structures inside the pump at nominal flow rate and for several NPSH values. Then, a quantitative analysis is performed, using the experimental results: head drop charts are studied at three flow rates, and the shape of the cavitating areas at nominal flow rate is compared to visualisations inside a blade-to-blade channel.

6.1 Qualitative Results. The head drop chart H(NPSH) obtained by the calculation at nominal flow rate is drawn in Fig. 12. The green line corresponds to the apparition of vapor in the flow field. The six blue points indicated on the chart are related to the six visualisations of the cavitating flow field presented in Fig. 13 and 14 hereafter. The quantity NPSH has the following definition:

$$NPSH = \frac{P_{tot}^{inlet} - P_{vap}}{\rho g}$$

where the inlet total pressure was defined previously.

The head drop is only partially obtained by the computation: this point will be discussed hereafter.

Figures 13 and 14 show the development of cavitation corresponding to the six operating conditions indicated on the chart. Figure 13 illustrates the apparition and the growing of vapor/

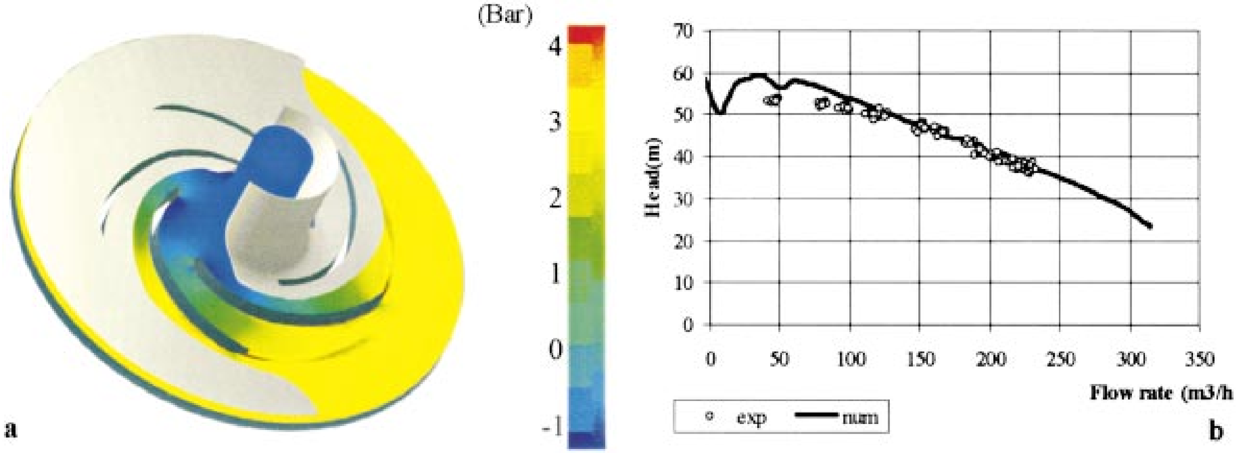

Fig. 11 (*a*) Total pressure elevation in the pump (nominal flow rate), (*b*) characteristics *H*(*Q*) of the pump in noncavitating conditions

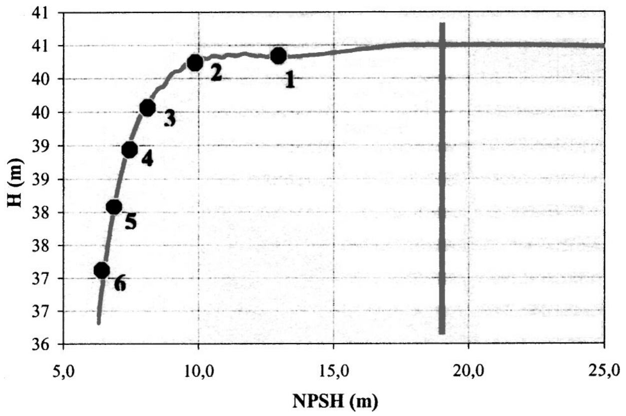

Fig. 12 Head drop chart at nominal flow rate. The points indicate the cavitating conditions visualized on Figs. 13 and 14. The line corresponds to the apparition of vapor.

liquid areas on both faces of the blades, and finally the progressive filling of blade-to-blade channels by the vapor. Blades are colored in gray, the shroud in blue, and the external shape of the two-phase areas (corresponding to a 5 percent void ratio) is colored in yellow.

We observe that cavitation appears first on the suction side (Fig. 13-1), and also quite rapidly on the pressure side (Fig. 13-2). The vapor volume increases mainly on the suction side (Figs. 13-3 and 13-4). A vapor structure also grows on the shroud, in the vicinity of the inlet, caused by the local curvature of the streamlines. It progressively joins the attached cavity on the blade.

The pressure side cavity is almost uniform from hub to shroud, and it grows slowly as the NPSH decreases. On the contrary, the suction side cavitation remains very close to the shroud, where the obstruction is mainly visible (Figs. 13-5 and 13-6).

For a better understanding of the liquid/vapor mixture behavior in the pump, we have presented on Fig. 14 the void ratio distribution on a blade-to-blade surface, close to the shroud. The velocity field is also drawn in each case. It indicates the void ratio variations in the suction side cavity, and in the two-phase areas observed on the shroud.

We observe that the void ratio obtained on the suction side of the blade increases rapidly: it reaches almost 90 percent in the second configuration, in the middle of the attached cavity. On the contrary, the vapor region on the shroud is characterized by a low void ratio, which reaches only 60 percent, and the cavity on the pressure side of the blades is mainly composed of liquid, even when its volume increases. That low void ratio is probably related to fluctuations of the vapor/liquid structures, which are not obtained by the simulation. It is worth noting that we use here a high time-step ($\Delta t = 10^{-4}$ s, i.e. 1/300 of one rotation period), so that the unsteady phenomena are not modelized, and a quasi-static head-drop chart can be obtained. As a consequence, each operating point represented here corresponds to a mean flow field that does not take into account the eventual instabilities generated by cavitation.

6.2 Comparisons With Experiments. Numerical simulation of the cavitation characteristics of the pump was performed at different flow rates. The shape of the cavitating structures is first compared to the experimental visualisations presented above at nominal flow rate. When the NPSH decreases in the calculation, attached cavitation sheets grow both on the suction side and on the pressure side, as observed experimentally. Moreover, vapor structures appear at the inlet radius of the shroud. This cavitation behavior is fully consistent with the observations reported previously. The visualisation obtained in Fig. 3 is compared to the computational results to enhance the reliable agreement. The cavitation number was adjusted to give the same global extent of the cavitation structures as in the experiment: the numerical result then corresponds to a NPSH about 10 percent lower than the experimental one (7 m, instead of 8 m). The three cavitation areas are correctly simulated by the code (Fig. 15): attached cavity on the suction side (A), extent of cavitation on the shroud along the blade (B), and cavitating flow on the inlet radius of the shroud (C). In the computation, attached sheet cavity (A) and extent on the shroud (B) belong to the same vapor structure, while they look like two separated regions in the experiment.

Figure 16 shows the attached cavity on the pressure side of the blade. Its size is compared to the mean distribution obtained from gray level averaging (Fig. 5). Both experimental and numerical NPSH values are equal to 7 m. Here, the calculated cavity appears smaller than the experimental one. Moreover, only the steady attached part of the cavity on the pressure side is obtained by the computation. The transient vapor structures in the unsteady cavity closure region are not found from the simulation. Actually this is still a limitation of the physical and numerical model. The mesh

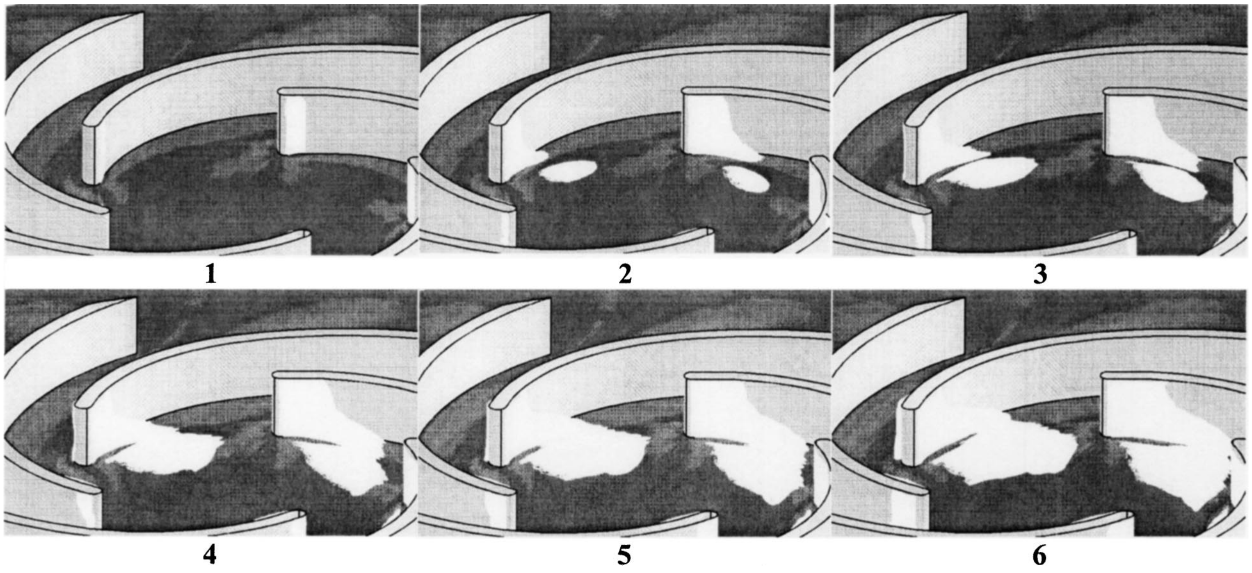

Fig. 13 Development of the two-phase areas as NPSH decreases (corresponding to points on Fig. 12)

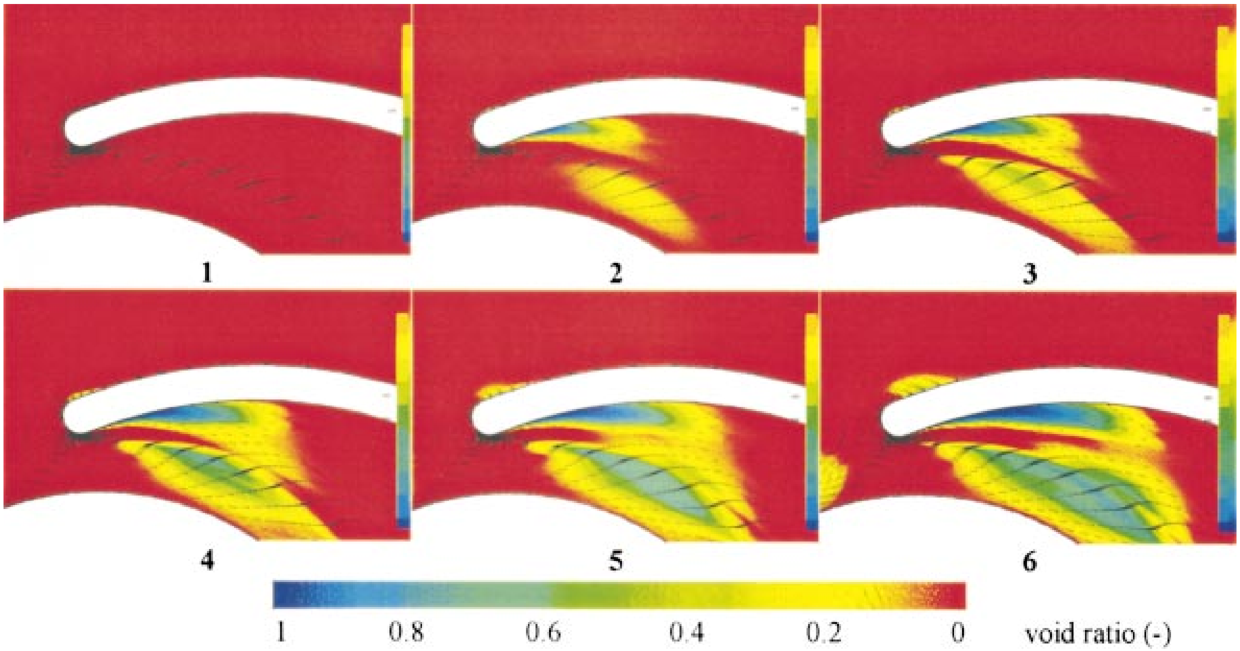

Fig. 14 Void ratio evolution on a blade-to-blade surface close to the shroud, and velocity fields (corresponding to the NPSH decrease represented on Fig. 12)

size and the standard turbulence model used in the calculation do not allow catching the cloud shedding process downstream of the attached cavity. An ongoing work is pursued to improve this aspect.

In Fig. 17, we summarize the whole comparison, by drawing the head drop curves for three different flow rates: namely 0.8Qn, Qn and 1.08Qn. In non-cavitating conditions, we observe again a slight overestimation of the pump head (about 5 percent at nominal flow rate), mainly due to the fact that the gap flow through the side chamber is not considered in the simulation. From the numerical point of view, while decreasing the NPSH, the performance drop appears first as a smooth decrease of the pump head. The final head-drop is only partially simulated because the computation rapidly becomes unstable and stops (this is more particularly the case at 1.08Qn). Our upstream boundary condition consists in imposing in a strict manner the mass flow rate passing the pump. Because the coupling between the pump and the hydraulic loop is not taken into account, the effects of the cavitation blockage on the flow rate are neglected and the head-drop is less progressive than in the experiments. However, all the numerical results represented in Fig. 17 refer to a converged solution at the corresponding physical time-step.

Results obtained from first simulations of the pump cavitation behavior are promising: the head drop is predicted with a good homogeneity with respect to the 3 flow rates. The NPSH values obtained for the 3 percent and 10 percent head drop are globally overestimated in respect to experimental values (of about 1 m for the 10 percent head drop, and 1.5 to 3 m for the 3 percent head drop, see Fig. 18). These results correspond to our first try of predicting the cavitation characteristic of a pump, and a study of the effect of the model parameters (mainly the turbulence model) might probably improve the quantitative agreement.

It can be observed that the head measured in experiments increases a little bit in low conditions before the head drop, for the three flow rates. This effect is not obtained in the calculations. However, it does not exceed 1 to 2 percent of the initial head, whereas the discrepancy between calculations and experiments concerning the pump performance is about 2 to 5 percent. More-

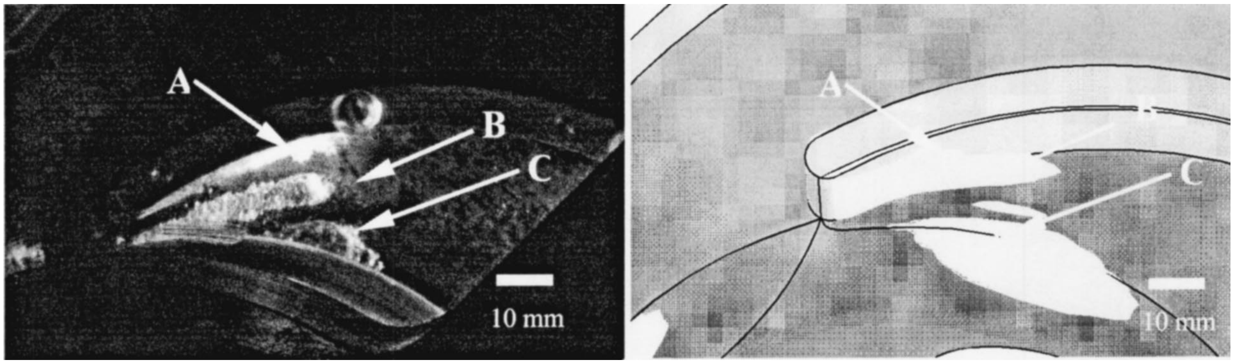

Fig. 15 Vapor structures on suction side (experiment NPSH=8 m, computation NPSH=7 m). Calculation: iso-density contour ($\rho \approx 0.95\rho_1$: void ratio >5 percent) drawn in yellow, shroud in blue, blade in gray.

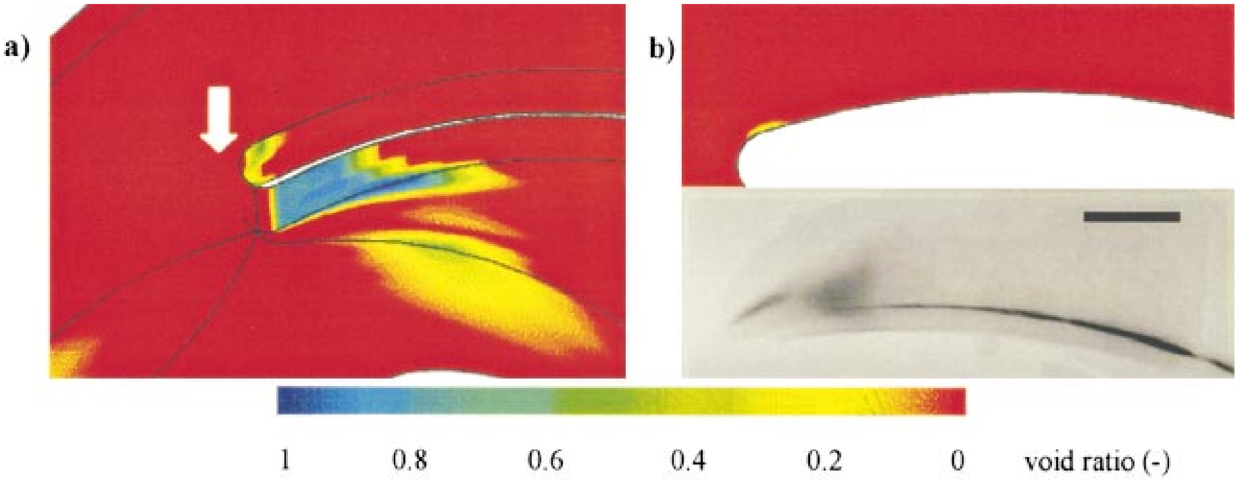

Fig. 16 (*a*) Numerical void ratio distribution, (*b*) pressure side cavity, comparison with experiment (NPSH=7 m)

over this effect, which has been observed also in the case of turbopump inducers [17], is not yet well explained, may be due to a coupling between the pump channels; such a phenomenon can not be predicted here because only one channel is considered. It probably involves slight interactions between the cavities and the boundary layer along the blade sides, which are not simulated with a sufficient accuracy by our simple turbulence model.

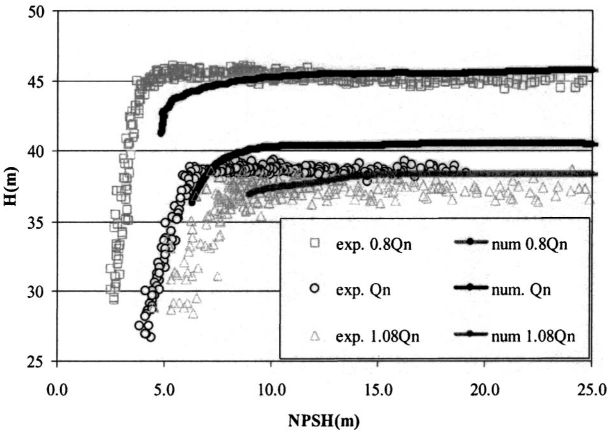

Fig. 17 Head-drop curves in cavitating conditions: comparison at 0.8 Qn, Qn, and 1.08 Qn.

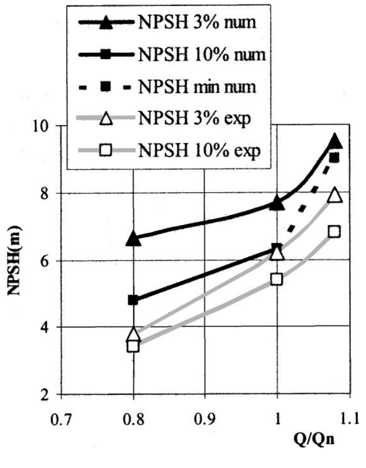

Fig. 18 NPSH values for 3 percent and 10 percent head drop

7 Conclusion

Numerical and experimental results were presented in this study, concerning a test pump having an impeller with 2D curvature blade geometry.

From the experimental point of view, besides the measurements of the cavitation characteristics of the pump in various conditions, a special visualisation set-up was developed to investigate the unsteady behavior of leading edge cavitation. Image processing and statistical treatment of the photographs taken at given impeller position allowed to quantify the attached and cloud cavitation extent.

A numerical model of three-dimensional cavitating flows, based on the three-dimensional code FINE/TURBO™, has been developed to predict the cavitation behavior in turbomachinery, [13,14]. This model was applied to the centrifugal pump geometry. Non-cavitating and cavitating conditions were investigated. Calculations were found to be in good agreement with experimental measurements and visualisations. Experimental and numerical results concerning the pump characteristics and performance breakdown were drawn at different flow conditions and the mean spatial distributions of vapor structures within the impeller were compared: It was found that the main features of the cavitating flow field are correctly simulated by the model. These results show the ability of the model to simulate the complex three-dimensional development of cavitation in rotating machinery, and the associated effects on the performance. This is of first importance for the purpose of pump future design. However, the fluctuating two-phase areas are not simulated yet, and work is in progress to improve the numerical model in that way. This is a necessary further step to predict more efficiently the local void ratio, since its distribution usually slightly evolves when unsteady effects are correctly predicted, [18]. The final objective is to simulate the unsteady effects due to cavitation (cavity self-oscillation, rotating cavitation) in three dimensions, as we already performed in more simple two-dimensional configurations, [4,23].

Acknowledgments

This work is part of a European exchange program PROCOPE with the research teams of Grenoble and Darmstadt as members. The numerical cavitation model implemented in FINE/TURBO™ has been developed with the support of SNECMA Moteurs DMF (Rocket Engine Division), and the French space agency CNES. The experimental work carried out at Darmstadt was part of the research project STO 190/9-2 which was financially supported by the DFG (German Research Foundation).

Nomenclature

$A_{\min}$ = minimum speed of sound in the mixture (m/s)
H = pump head$=(P^{\text{outlet}}-P_{\text{tot}}^{\text{inlet}})/\rho_1 g$ (m)
NPSH = net positive suction head$=(P_{\text{tot}}^{\text{inlet}}-P_{\text{vap}})/(\rho_1 g)$ (m)
P = local static pressure (Pa)
P_{tot} = total pressure$=P+\frac{1}{2}\rho_1 V^2$ (Pa)
P_{vap} = vapor pressure (Pa)
P^{inlet} = static pressure measured in the inlet pipe (Pa)
P^{outlet} = static pressure measured at $r\approx 1.5r^{\text{outlet}}$ (Pa)
Q, Q_n = flow rate, nominal flow rate (m^3/s)
r = local radius (m)
r^{outlet} = radius at the impeller outlet (m)
t, Δt = time, time-step (s)
V = local velocity (m/s)
V_{inlet} = inlet mean velocity (m/s)
α = local void fraction
ρ = local density of the mixture$=\alpha\rho_v+(1-\alpha)\rho_1$ (kg/m^3)
ρ_1 = liquid density (kg/m^3)
ρ_v = vapor density (kg/m^3)

References

[1] Lohrberg, H., Hofmann, M., Ludwig, G., and Stoffel, B., 1999, ''Analysis of Damaged Surfaces. Part II: Pit Counting by 2D Optical Techniques,'' *Proc. of the 3rd ASME/JSME Joints Fluids Engineering Conference*, July, San Francisco, CA, ASME, New York.
[2] Patella, R. Fortes, Reboud, J. L., and Archer, A., 2000, ''Cavitation Mark Measurements by 3D Laser Profilometry,'' Wear, **246**, pp. 59–67.
[3] Hofmann, M., Lohrberg, H., Ludwig, G., Stoffel, B., Reboud, JL., and Fortes-Patella, R., 1999, ''Numerical and Experimental Investigations on the Self-Oscillating Behavior of Cloud Cavitation: Part 1 Visualisation/Part 2 Dynamic Pressures,'' *3rd ASME/JSME Joint Fluids Engineering Conference*, San Francisco, CA, July, ASME, New York.
[4] Lohrberg, H., Stoffel, B., Fortes-Patella, R., Coutier-Delgosha, O., and Reboud, J. L., 2002, ''Numerical and Experimental Investigations on the Cavitating Flow in a Cascade of Hydrofoils,'' Exp. Fluids, accepted for publication.
[5] Takasugi, N., Kato, H., and Yamagushi, H., 1993, ''Study on Cavitating Flow Around a Finite Span Hydrofoil,'' *Cavitation and Multiphase Flow Forum*, ASME, New York, ASME-FED-vol. 153, pp. 177–182.
[6] Alajbevoic, A., Grogger, H., and Philipp, H. 1999, ''Calculation of Transient Cavitation in Nozzle Using the Two-Fluid Model,'' 12th Annual Conf. on Liquid Atomization and Spray Systems, May 16–19, Indianapolis.
[7] Kunz, R., Boger, D., Chyczewski, T., Stinebring, D., and Gibeling, H., 1999, ''Multi-Phase CFD Analysis of Natural and Ventilated Cavitation About Submerged Bodies,'' *3rd ASME/JSME Joint Fluids Engineering Conference*, San Francisco, CA, ASME, New York.
[8] Bunnell, R. A., and Heister, S. D., 2000, ''Three-Dimensional Unsteady Simulation of Cavitating Flows in Injector Passages,'' ASME J. Fluids Eng., **122**, pp. 791–797.
[9] Delannoy, Y., and Kueny, J. L. 1990, ''Two Phase Flow Approach in Unsteady Cavitation Modelling,'' *Cavitation and Multiphase Flow Forum*, ASME, New York, ASME-FED-Vol. 98, pp. 153–158.
[10] Kubota, A., Kato, H., and Yamaguchi, H., 1992, ''A New Modelling of Cavitating Flows: A Numerical Study of Unsteady Cavitation on a Hydrofoil Section,'' J. Fluid Mech., **240**, pp. 59–96.
[11] Combes, J.-F., and Archer, A., 2000, ''Etude de la cavitation dans la pompe SHF,'' *Coll. Machines Hydrauliques: Instationnarités et effets associés*, Société Hydrotechnique de France, Chatou, France.
[12] Medvitz, R. B., Kunz, R. F., Boger, D. A., Lindau, J. W., Yocum, A. M., and Pauley, L. L. 2001, ''Performance Analysis of Cavitating Flow in Centrifugal Pumps Using Multiphase CFD,'' ASME Fluids Engineering Division Summer Meeting, June, New Orleans, LA.
[13] Coutier-Delgosha, O., Fortes-Patella, R., Reboud, J. L., and Hakimi, N., 2001, ''Numerical Simulation of Cavitating Flow in an Inducer Geometry,'' 4th European Conference on Turbomachinery, Mar. 20–23, Firenze, Italy.
[14] Coutier-Delgosha, O., Reboud, J.L., and Fortes-Patella, R., 2001, ''Numerical Study of the Effect of the Leading Edge Shape on Cavitation Around Inducer Blade Sections,'' *Proceedings of the 4th Int. Symp. on Cavitation*, Pasadena, CA, June.
[15] Hofmann, M., 2001, ''Ein Beitrag zur Verminderung des erosiven Potentials kavitierender Strömungen,'' PhD thesis, TU Darmstadt, June.
[16] Hofmann, M., Stoffel, B., Friedrichs, J., and Kosyna, G. 2001, ''Similarities and Geometrical Effects on Rotating Cavitation in 2 Scaled Centrifugal Pumps,'' *Proceedings of the 4th Int. Symp. on Cavitation*, Pasadena, CA, June.
[17] Coutier-Delgosha, O., 2001, ''Modélisation des Ecoulements Cavitants: Etude des comportements instationnaires et application tridimensionnelle aux Turbomachines,'' Ph.D. thesis, INPG, Grenoble, France, Nov.
[18] Reboud, J. L., Stutz, B., and Coutier, O., 1998: ''Two-Phase Flow Structure of Cavitation: Experiment and Modelling of Unsteady Effects,'' *Proceedings of the 3rd Int. Symp. on Cavitation*, Grenoble, France, Apr.
[19] Hakimi, N., 1997: ''Preconditioning Methods for Time Dependent Navier-Stokes Equations,'' Ph.D. thesis, Vrije Univ., Brussels.
[20] Hirsch, C., 1990, *Numerical Computation of Internal and External Flows*, John Wiley and Sons, New York.
[21] Coutier-Delgosha, O., Fortes-Patella, R., and Reboud, J.-L., 2002, ''Evaluation of the Turbulence Model Influence on the Numerical Simulations of Unsteady Cavitation,'' ASME J. Fluids Eng., accepted for publication.
[22] Coutier-Delgosha, O., Fortes-Patella, R., and Reboud, J.-L., 2002, ''Simulation of Unsteady Cavitation With a 2-Equations Turbulence Model Including Compressibility Effects,'' J. of Turbulence, accepted for publication.
[23] Courtot, Y., Coutier-Delgosha, O., and Reboud, J.-L., 2002, ''Numerical Simulation of the Unsteady Cavitation Behavior of an Inducer Blade Cascade,'' AIAA J., proposed for publication.

David A. Johnson
Associate Professor
e-mail: da3johns@uwaterloo.ca

Bryan A. Sperandei
Graduate Student
e-mail: bsperand@uwaterloo.ca

Ross Gilbert
Graduate Student
e-mail: rgilbert@uwaterloo.ca

Department of Mechanical Engineering,
University of Waterloo,
Waterloo, ON N2L 3G1 Canada

Analysis of the Flow Through a Vented Automotive Brake Rotor

Particle image velocimetry (PIV) was used to measure air velocities through a high solidity radial flow fan utilized as an automotive vented brake rotor. A brake rotor is a somewhat unusual fan in that its sole purpose is not to pump air but to dissipate thermal energy, it has no conventional inlet or outlet housing and it has a continuously varying rotational speed. For three typical rotational speeds, the flow characteristics were captured at the inlet and exit of the rotor, as well as internally through the cooling passages. Inlet measurements showed a swirling entry flow condition with significant misalignment of flow onto the vanes. As a result large regions of flow separation were found in the internal vane-to-vane passages on the suction side surfaces, which would lead to poor heat transfer conditions. The main flow exiting the rotor consisted of a series of jets corresponding to the individual rotor passages and were found to be very unstable leading to a rapid decay in velocity. [DOI: 10.1115/1.1624426]

1 Introduction

Automotive brakes are utilized to convert kinetic energy of motion into thermal energy through the friction between stationary brake pads and a rotating surface. Commonly this is done using a cast iron rotating brake rotor with stationary friction surfaces mounted in a caliper. Rotors may be solid disks or two disks separated by a vaned air flow passage (vented rotor). In bringing a vehicle to a stop the brake rotor must be able to store a significant amount of thermal energy since braking occurs in a relatively short period of time. Subsequently, the brake rotor must then dissipate the stored thermal energy quickly in order to be ready for the next application of the brake or friction contact. There are numerous considerations in the design of a vented disk brake rotor and the air flow through the internal passages has previously been of less importance than manufacturing, materials, and structural issues. Improving the rate of heat transfer from a brake rotor will allow for smaller and lighter rotors since the amount of thermal storage required is smaller which will reduce vehicle weight and improve fuel economy. Consequently, vented brake rotors using internal air passages are used in an attempt to increase the level of forced convection and so improve the rate of heat transfer. Early analytical work by Limpert [1] stated that the convective heat transfer coefficient of a vented disk brake rotor is approximately twice that of a solid disk.

Previous work attempting to measure the airflow exiting a brake rotor was completed using pressure based cobra probes, [2–4], to measure the velocity profile in the radial-axial plane at the exit of the rotor but not the radial-angular plane. As well, the inlet and internal passage flow field conditions were not measured. Similar experiments have been carried out on centrifugal fans in water using particle image velocimetry (PIV), [5–8], but the fans tested had volutes, which are never present on an automobile. The purpose of a brake rotor is significantly different due to the thermal energy considerations mentioned above and in that rotors are subject to continuously varying rotational speeds such that the design or operating point can not be defined. Also, the Reynolds numbers examined (ranging from 2.00×10^4 to 1.83×10^5) were lower in those studies than those of the brake rotor in this study (1.82×10^5 to 5.47×10^5). The Reynolds number (Re) is based on the rotor outside diameter and the rotational speed of the rotor,

$$\mathrm{Re}=\frac{\rho\omega D_o^2}{\mu}. \tag{1}$$

All measurements were conducted using standard air at 25°C ($\rho=1.184\ \mathrm{kg/m^3}$, $\mu=1.85\times10^{-5}\ \mathrm{kg/ms}$). Three rotor rotational speeds were used for the measurements: 342, 684, and 1026 rpm, representing typical driving speeds of 50, 100, and 150 km/h, respectively. These three speeds resulted in Reynolds numbers of 1.82×10^5, 3.65×10^5, and 5.47×10^5.

The focus of this study was to determine the characteristics of the airflow for a vented brake rotor using PIV (see Adrian [9] and Grant [10] for a detailed description of the PIV technique). Emphasis was placed on determining the air velocity in as many areas in and around the rotor as possible. With PIV, it was possible to locate the internal areas of separation and recirculation, indicating potential areas of poor heat transfer in the rotor. As well, the recording of many images at each location showed the distinction between turbulence-intensive instantaneous vector maps and smooth, low-turbulence averaged velocity values.

2 Experimental Setup

2.1 Apparatus. The design of the experimental test rig required the fulfilment of several criteria to ensure an optimal environment for PIV. A vertical shaft was mounted to a steel test table using two pillow block bearings to ensure smooth rotation of the rotor with minimal runout. The shaft was chain driven via an adjustable speed DC motor. Rotational speed was determined using a tachometer mounted on the motor which was continuously monitored. The end of the shaft was fitted with a production automotive wheel hub in order to mount the brake rotor. The rotor was mounted with the inlet away from the hub in order to keep that region free of any flow obstruction (see Fig. 1). This is an idealized or optimum arrangement in comparison to an automotive wheel assembly where other components obstruct the incoming flow. Figure 2 shows the rotor as installed on a typical automotive front wheel assembly (excluding the rim and tire). In practice flow entering and leaving the rotor will be hindered by the wheel hub, brake caliper, and dust shield, as well as the rim and tire.

The area surrounding the rotor was then enclosed using acrylic panels in order to contain the seeding particles necessary for PIV measurements while maintaining visual access into the test environment. The dimensions of the enclosure (0.9 m×0.9 m×0.61 m) were chosen large enough so as to eliminate any wall effects in the flow field.

Contributed by the Fluids Engineering Division for publication in the JOURNAL OF FLUIDS ENGINEERING. Manuscript received by the Fluids Engineering Division Oct. 1, 2001; revised manuscript received June 4, 2003. Associate Editor: B. Schiavello.

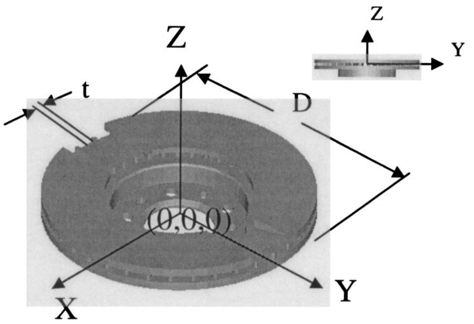

Fig. 1 Vented rotor showing sections removed for internal PIV measurements

2.2 Rotor Geometry. A typical production automotive brake rotor was chosen to represent the radial flow fan used in the PIV experiments. All measurements were performed using this production brake rotor. The cast iron rotor consisted of two flat disks separated by a gap of 8 mm (vane width b) with one disk comprising the hub where the rotor was attached to the rotating shaft. This gap was supported by 37 equally spaced radial vanes. Each disk had an outer diameter (D_o) of 282 mm, and an inner diameter (D_i) of 152 mm. The radial vanes were 54.5 mm in length beginning at a diameter of 168 mm (D_{vi}) and ending at a diameter of 277 mm (D_{vo}) leaving an 8-mm entry distance from the inner radius of the disk to the vane. The purely radial individual vanes were a constant 5.6 mm in thickness (t) from D_{vi} to D_{vo} and were rounded at the entry and exit. This resulted in 37 air flow passages each with a $8.7\,\text{mm}\times 8\,\text{mm}\,(w_1\times b)$ entry and a $17.9\,\text{mm}\times 8\,\text{mm}\,(w_2\times b)$ exit. For all measurements and results shown in this study, the origin of the cartesian coordinate system was located at the center of rotation of the rotor, and at the mid-width of the air passages between the two disks.

In order to visualize the airflow inside the vent passages, optical access was required in the X-Y plane. This was achieved by removing a section of the upper disk, wide enough to expose at least two full vent passages. The missing section was then replaced with an acrylic window with the same thickness and shape in order to replicate the flow through the passages. An identical window was installed 180 deg from the first in order to balance the rotor and limit vibration (see Fig. 1).

Fig. 2 Photograph of a typical front wheel automotive assembly excluding the rim and tire

2.3 Particle Image Velocimetry. Simplistically, PIV operates on the basis of capturing images of a fluid flow and determining how far the fluid has moved from one image to the next. In order to visualize an air flow, seed particles are introduced into the flow and are typically illuminated by a high-power pulsed laser light sheet. To illuminate this particular flow, a dual cavity pulsed (2×120 mJ) Nd-YAG laser was used in order to create a light sheet 2–3 mm in thickness spanning the region of interest. Vaporized mineral oil has been shown to follow airflow quite well, [11], and was used as the seeding medium. The smoke was introduced into the enclosure well upstream of the measurement region around the rotor. As well, the smoke was allowed to stabilize in the enclosure before measurements were obtained. To capture images, a CCD camera (Kodak Megaplus ES 1.0) with 1008×1018 pixel resolution was used. The laser and CCD camera were linked through a Dantec Flowmap PIV 1100 processor. Image processing, cross-correlation of the images, and vector validation was performed using an in-house tailored cross-correlation routine.

To determine the displacement of the particles between successive images an iterative multigrid algorithm was used as described by Gilbert [12], which is an advancement of the work of Scarano and Reithmuller [13]. The iterative multigrid technique uses multiple iterations to determine the velocity field with each successive iteration using smaller interrogation areas that have been offset by an integer amount based on the previous iteration's results. The advancement of the technique by Gilbert [12] was to interpolate between vectors when determining the integer offset for each interrogation area, rather than applying the displacement of the nearest velocity vector.

The advantage of the iterative multigrid technique is the ability to use smaller interrogation areas to reduce the magnitude of the velocity gradients within a single interrogation area as well as increasing the resolution of velocity vectors. Smaller interrogation areas could be used with the standard FFT algorithm, [14], but the time separation between the images would have to be reduced, increasing the relative error of the velocity measurement, [12].

The iterative multigrid algorithm used in these experiments applied an iterative approach to the FFT cross-correlation. An initial estimate of the velocity field was determined using the standard FFT cross-correlation scheme. The next iteration then divided the interrogation area into four smaller, equal areas. The new interrogation areas were then displaced by an integer amount based on a bilinear interpolation of the previous velocity estimate and the FFT cross-correlation was performed to refine the velocity estimate. The process was repeated until the interrogation area was reduced to the desired size. Typically, initial interrogation areas of 64×64 pixels were reduced to 16×16 pixels, using 50% overlap in all cases. This resulted in typical interrogation areas ranging of 4.2 mm×4.2 mm (64×64 pixels) down to 1.05 mm×1.05 mm (16×16 pixels) in size. A signal to noise ratio of 1.4 was used in the cross correlation (i.e., any vectors below this signal to noise ratio were discarded). After the final iteration of processing in each experiment, the vector maps contained 15,252 vectors (123 ×124 vectors).

2.4 Image Orientations. Three distinct flow fields were examined in and around the rotor. In the first setup, the inlet flow entering the air passages along the rotational axis was captured. This was achieved by using a light sheet in the X-Z plane with the region of interest between the center of rotation of the rotor, and inner radius of the upper disk (R_i). The camera was oriented perpendicular to the light sheet and focused on an image area of 85 mm×85 mm, resulting in a resolution of 0.084 mm/pixel. The pulses of the laser were left untriggered so as to obtain an average inlet flow at various angular positions of the rotor. The horizontal (X-Y) plane was also measured in order to determine the levels of

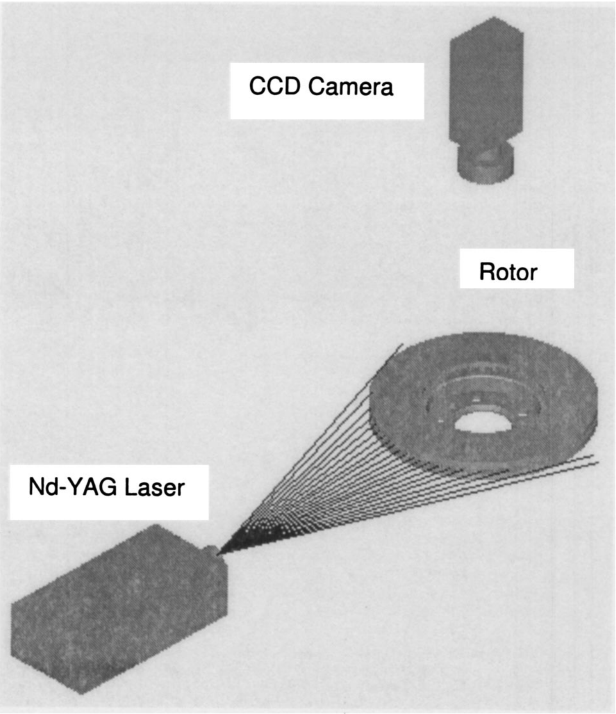

Fig. 3 Orientation of the laser and camera for *X*-*Y* plane PIV measurements

swirl present in the flow before entering the rotor. In this case, the camera was suspended above the rotor while the laser formed a horizontal light sheet from one side of the test enclosure (see Fig. 3).

The second test was arranged in order to visualize the internal airflow through the rotor passages. The laser sheet was oriented in the X-Y plane at the midway point ($Z=0$) of the passages (4 mm from either disk). In this case, the laser was triggered to pulse only when an acrylic section of the disk rotated through the camera's field of view. This was done through the use of a stationary optical switch with a single notch on a rotating wheel that interrupted the light beam and ensured that each image captured the same passages. Thus, the use of the word "triggered" will indicate that all images were captured at the same angular position of the rotor every time (phase resolved). Conversely, "untriggered" will indicate images captured at random time intervals, therefore, at no particular position on the rotor. The straight and radial geometry of the vanes allowed the illumination of two full flow passages in each image. The image area in this test was 65 mm×65 mm, giving a resolution of 0.064 mm/pixel.

In the third and final test, three different laser and camera configurations were used to capture the airflow exiting the passages at the outer diameter of the rotor. In the first two methods, a light sheet in the X-Y plane was placed just beyond the outer diameter of the rotor, still focused on a 65 mm×65 mm area at the middle of the passage width ($Z=0$). The flow was first measured with an untriggered laser pulse for average exit flow conditions, and then repeated with a triggered laser pulse in order to observe the individual jets leaving each flow passage. In the third setup, untriggered images were collected in the X-Z plane so as to view the characteristics of the exiting jets in a vertical plane.

In all cases above, 500 image pairs were collected for each setup and the resultant velocity vectors were ensemble averaged at each position. Each test was repeated for all three rotational speeds. Typical laser pulse separations ranged from 15×10^{-6} to 75×10^{-6} s in order to size the particle displacements appropriately for the interrogation area size.

2.5 Experimental Uncertainty. The rotors used in these studies were actual cast iron production rotors and as a result some geometrical uncertainty existed in the rotor due to its cast manufacturing process. Despite some external machined surfaces, the internal surfaces of the air passages were cast, leaving a comparably rough finish of approximately 0.3 mm. Measurements of the experimental rotor revealed a ±2.3% variation in both the passage height and passage width.

The uncertainty in the machined outer diameter, D_o, of the rotor was determined using manufacturing drawings, while the uncertainty in the rotational speed was determined from tachometer data collected during the measurements. The outer diameter and rotational speeds were found to carry uncertainties of 0.5 mm, and 20 rpm (at all speeds), respectively. This resulted in a Reynolds number uncertainty ranging from 2.3% to 6.2% over the three rotational speeds tested.

For the PIV measurements, the random error due to irregular particles, electronic noise, etc., is shown to be small (<0.07 pixel) by Prasad et al. [15]. For the current measurements, this results in a random error of less than 2% in the determined velocities. The work of Westerweel [16] suggests a typical bias error of 0.05 pixels when using an iterative multigrid algorithm. The resulting bias error in the determined velocities is therefore approximately 1%. Westerweel [17] also suggests a relationship between the particle image diameter and the resulting root-mean-square (RMS) error. Based on the measurements made in this study (average particle image diameters of 2.5 pixels) the expected RMS error is 0.035 pixels, resulting in an additional 0.7% error in the calculated velocities. A detailed analysis of the random, bias, and RMS error associated with PIV is given by Gilbert [12]. Based on the total quoted uncertainty in the calculated velocities (3.7%), the kinetic energy values would have an uncertainty in the range of 5% to 6%.

3 Results and Discussion

3.1 Mean Velocity. Results presented here are all for Re $=3.65\times10^5$ and $N=684$ rpm as all three rotational speeds gave similar results. For all presented data the axes were made dimensionless by the outer radius of the rotor (i.e., $X^*=X/R_o$, etc.),

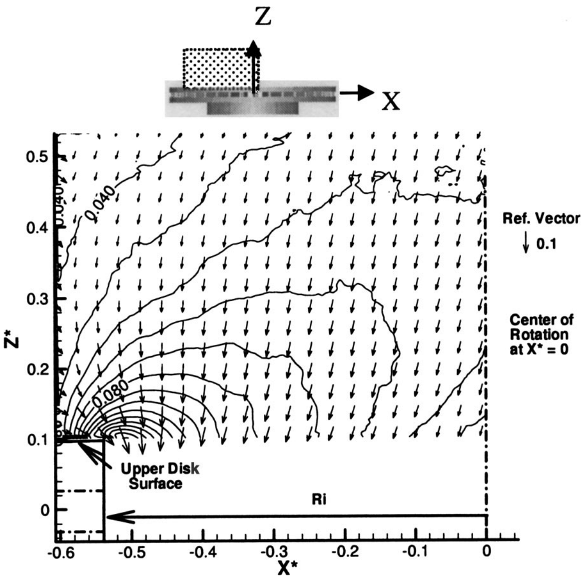

Fig. 4 Absolute mean velocity plot of the inlet flow (*X*-*Z* plane at $Y^*=0$), $N=684$ rpm, dimensionless velocity vector=0.1, contours of isovelocity 0.008 dimensionless velocity units, direction of rotation is out of the page

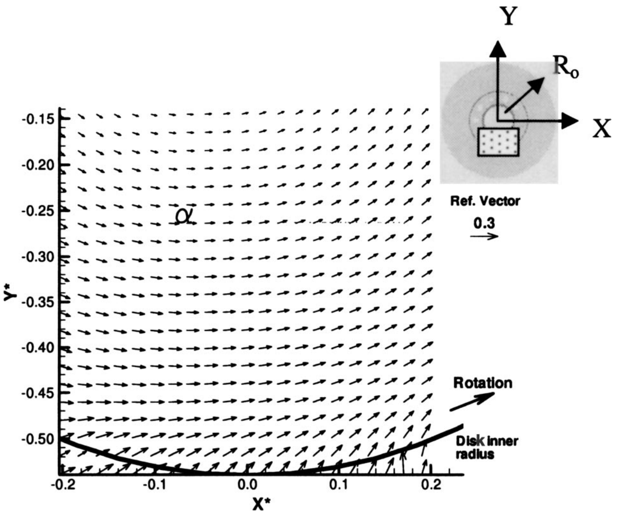

Fig. 5 Absolute mean velocity plot of the inlet flow (X-Y plane at $Z^*=0.1$), $N=684$ rpm, dimensionless velocity vector=0.3

while the mean velocities were normalized by the tangential speed of the rotor at its outer radius, or rotor peripheral speed ($U_o=\omega D_o/2$).

Inlet Flow. Figure 4 shows the mean velocity plot obtained with a vertical light sheet (X-Z plane) at the inlet of the rotor at Re$=3.65\times10^5$. The vertical line at $X^*=0$ represents the axis of rotation of the rotor, and the area of visualization extended just beyond the inner radius of the disk (R_i) where the air passage entrances were located. The velocity contour lines in Fig. 4 are separated by increments of 0.008 dimensionless velocity units. Typical radial fan behavior was observed here as the flow was drawn downwards into the center of the rotor before turning 90° in order to enter the air passages. The largest velocity gradient, as shown by the contour lines, occurred near the inner radius of the rotor disk R_i ($X^*\approx-0.54$). Here the flow was drawn in towards the center of the rotor and forced to accelerate around the edge of the disk and into the air passages.

The results obtained in the X-Y plane at $Z^*=0.1$ (1 mm above the upper disk surface) are shown in Fig. 5 and demonstrate the effect of the rotor rotation on the incoming flow.

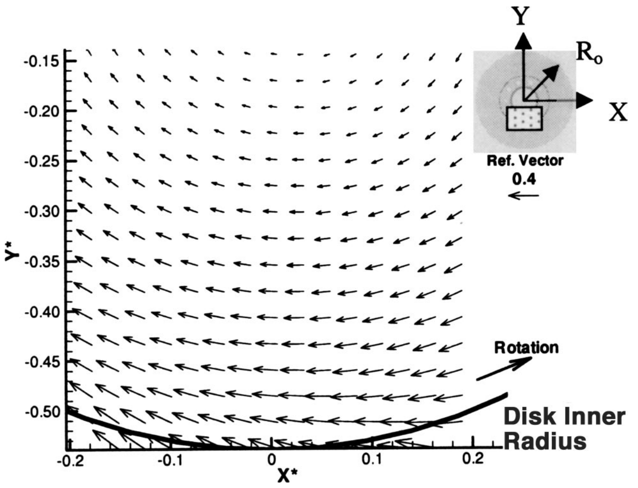

Fig. 6 Relative mean velocity plot of the inlet flow (X-Y plane at $Z^*=0.1$), $N=684$ rpm, dimensionless velocity vector=0.4

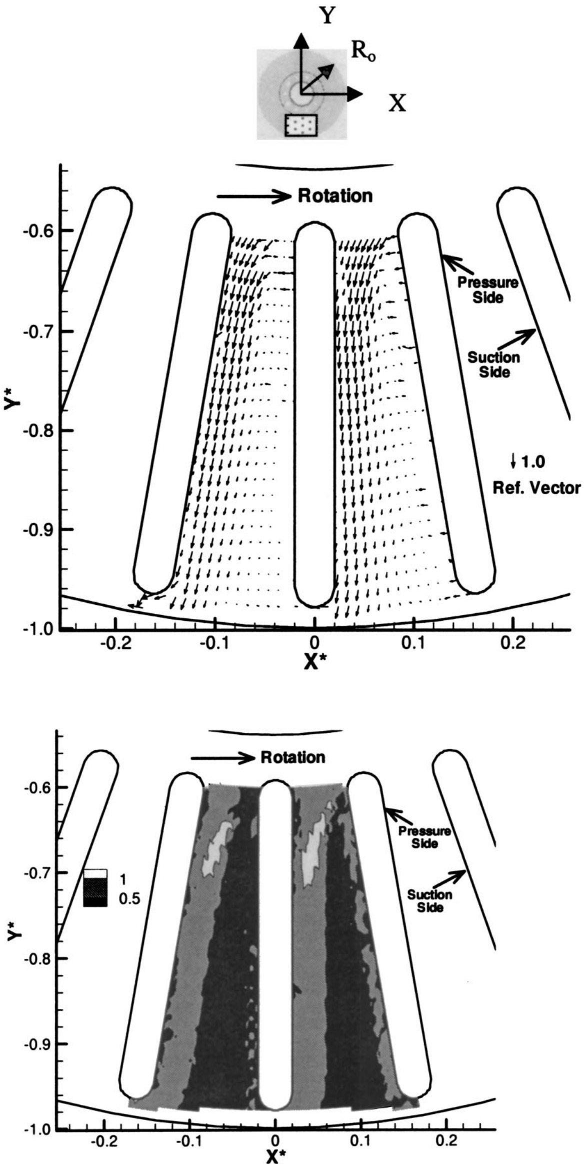

Fig. 7 (*a*) (Top) relative mean velocity vector plot of the internal flow (X-Y plane at $Z^*=0$), $N=684$ rpm, dimensionless velocity vector=1.0. (*b*) (Bottom) relative mean velocity contour plot of the internal flow (X-Y plane at $Z^*=0$), $N=684$ rpm.

The shear forces exerted by the counterclockwise rotating upper disk surface imposed a counterclockwise pre-swirl on the inlet flow. In Fig. 6, the local tangential speed (ωr) has been subtracted from the absolute fluid velocities ($\mathbf{V}$) in Fig. 5 in order to view the velocities relative to the rotor surface ($\mathbf{W}$). All pre-swirl that does not provide zero incidence onto the vane passages is detrimental. This measured pre-swirl is detrimental as it causes the inlet flow to be further misaligned with the air passages in conjunction with the other vector directions and hence increases shock losses at the vane inlet and reduces or restricts the amount of flow entering the rotor.

Internal Flow (X-Y Plane). The velocity vector plot in Fig. 7(a) and velocity contours in Fig. 7(b) show the relative ($\mathbf{W}$) mean velocities at the midplane through the air passages. At Re$=3.65\times10^5$, the fluid reached maximum internal velocities equal to the rotor peripheral speed (U_o) near the inlet ($-0.64<Y^*<-0.70$) and along the pressure side decreasing toward the outlet. With counterclockwise rotation, the pressure and suction sides

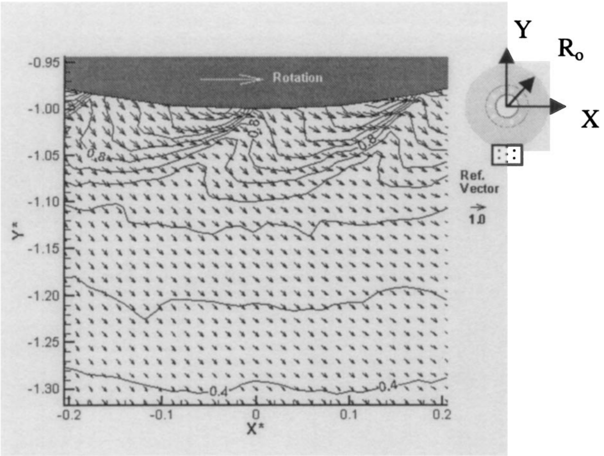

Fig. 8 Absolute mean velocity plot of the exit flow (X-Y plane at $Z^*=0$, triggered), $N=684$ rpm, dimensionless velocity vector $=1.0$. Contours of isovelocity 0.08 dimensionless velocity units.

were easily identified on the left and right sides of the air passages, respectively. There is significant separation and recirculation on the suction side which will be discussed in a subsequent section. The contour plot shows the correspondence between the measured velocities in the two adjacent passages.

Exit Flow—Horizontal Light Sheet (X-Y Plane). Figures 8 and 9 show the distinction between triggered and untriggered PIV data when measuring the flow exiting the rotor air passages. In both cases, the center of rotation was located at ($X^*=0$, $Y^*=0$) and the rotor vanes imposed both a radial and tangential velocity component on the exiting flow. Both figures show the average of 500 image pairs. The images used for Fig. 8 were all taken at the same rotational position as that in Figs. 7(*a*), 7(*b*) (one vane aligned vertically with the line $X^*=0$). In contrast, the 500 images used for Fig. 9 were taken at random rotational positions. In the triggered case (Fig. 8), the contour lines show the effects of the individual rotor vanes, as the exit velocities fluctuate in magnitude and direction depending on their location within the region $-1.05<Y^*<-1.00$ (velocity contour lines in both Figs. 8 and 9 are separated by increments of 0.08). These effects were removed by averaging with the untriggered measurements, as the contour lines of Fig. 9 show little variation in velocity along lines of constant radius. The triggered measurements effectively showed a phase averaged picture of the flow at one rotor location, with peak fluid absolute velocities exceeding $1.1\cdot U_o$. When untriggered, an average of many random instantaneous pictures was observed, and the peak velocities measured were therefore lower at $0.95\cdot U_o$, but were more representative of the overall flow rate achieved through the rotor.

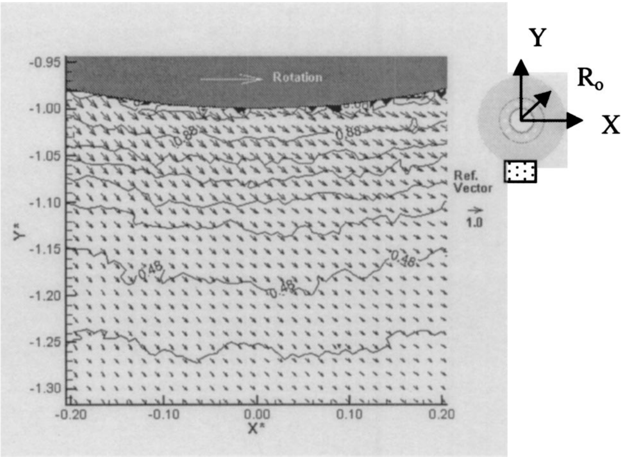

Fig. 9 Absolute mean velocity plot of the exit flow (X-Y plane at $Z^*=0$, untriggered), $N=684$ rpm, dimensionless velocity vector$=1.0$. Contours of isovelocity 0.08 dimensionless velocity units.

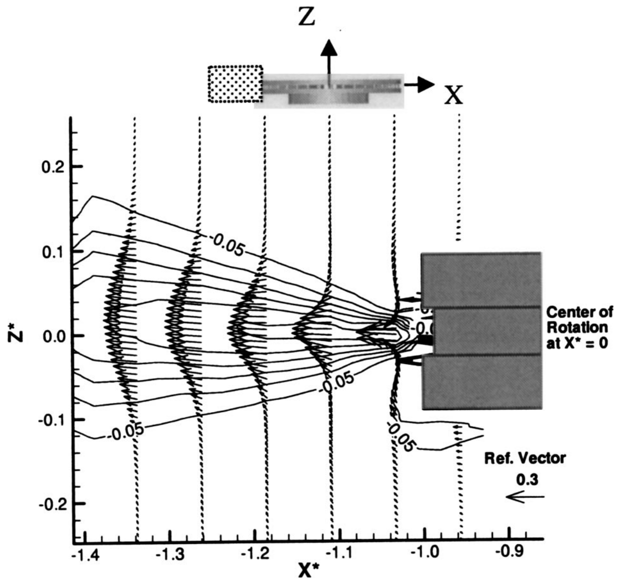

Fig. 10 Absolute mean velocity plot of the exit flow (X-Z plane at $Y^*=0$), $N=684$ rpm, dimensionless velocity vector$=0.3$. Contours of isovelocity 0.05 dimensionless velocity units.

Exit Flow—Vertical Light Sheet (X-Z Plane). The use of a vertically oriented light sheet revealed the behavior of the exit flow as a free jet. Figure 10 shows a side view (X-Z plane) of the rotor at D_o with several exit velocity profiles plotted downstream. Note that the velocity profiles in Fig. 10 represent only the radial component (V_x) of the absolute exit velocity. The velocity contour lines in Fig. 10 are separated by increments of 0.05 dimensionless velocity units. Similar to typical free jet behavior, the profiles steadily decayed with increasing downstream distance (increasing negative X^*). Near the rotor, the profile was narrow and peaked at $0.4\cdot U_o$, while further downstream at $X^*=-1.32$ the profile was much wider and decayed to a peak velocity of $0.25\,U_o$. It is important to note that the velocity profiles in Fig. 10 represent only the radial component (V_x) of the absolute exit velocity, when, in fact, the jets also contain a significant tangential component (V_y), as shown in the X-Y plane (Fig. 9). The direction of the velocity vectors outside of the jet core in Fig. 10 indicated a significant amount of entrainment by the jet. This averaged picture is in contrast to Fig. 11 which shows one of the 500 instantaneous vectors maps used to ensemble average Figure 10. Here, the turbulence and instability in the free jet was apparent. Downstream vortical structures are dimensionally similar to the rotor exit passage dimension.

3.2 Kinetic Energy

Inlet Flow. The turbulent kinetic energy, K_t, was defined using the fluctuating velocity components, u' and v'.

$$K_t=\frac{\overline{u'^2}+\overline{v'^2}}{2} \tag{2}$$

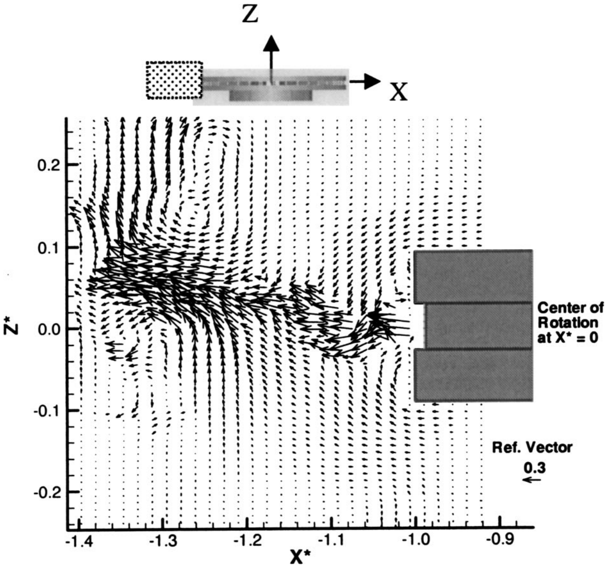

Fig. 11 Absolute mean velocity plot of the exit flow (X-Z plane at $Y^*=0$, single instantaneous vector map), $N=684$ rpm, dimensionless velocity vector=0.3

The values of K_t were then nondimensionalized by U_o^2, the square of the rotor peripheral velocity. Levels of K_t^* were found to fluctuate in a manner similar to the mean velocity plots, with the highest levels occurring in the areas of highest mean velocity gradients. The highest measured values of turbulent kinetic energy occurred at the inlet near the inner diameter of the disk, D_i, where the flow was forced to accelerate around the disk in order to enter the air passages ($X^*\approx-0.55$, $Z^*\approx0.1$ from Fig. 4). In this area, K_t^* values of 0.0056 were observed, compared to an average of 0.0025 throughout the rest of the plotted area in Fig. 4.

Internal Flow. The flow through the air passages displayed the highest turbulent kinetic energy levels in the middle of the passage, along the geometric division line between the pressure and suction side. Here, K_t^* levels peaked at 0.06 and were observed to decrease gradually throughout the passage length to 0.01 at the exit (see Fig. 12).

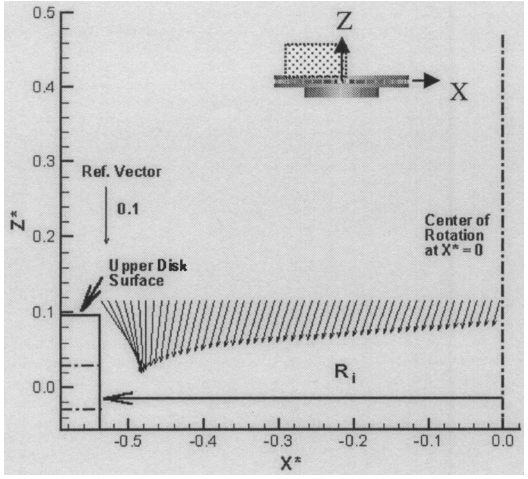

Fig. 13 Inlet velocity profile used to calculate the mass flow entering the rotor, $N=684$ rpm. Rotation out of the page. Dimensionless velocity vector=0.1.

Exit Flow. External to the rotor, the highest levels of turbulent kinetic energy occurred periodically behind each passing vane. For example, the vane oriented with the $X^*=0$ axis in Fig. 8 induced the highest turbulence levels at $X^*\approx-0.045$ and $Y^*\approx-1.03$, an area which trails the tip of the vane as it passes. This area had a turbulent kinetic energy level of 0.046 compared to 0.020 in surrounding areas.

Of all the measured flow areas, turbulent kinetic energy values were highest in the internal passages.

3.3 Flow Balance

Inflow. One method of comparing the experimental results was to compare the volumetric flow rates into and out of the rotor based on the velocity profiles obtained from the PIV measurements. In order to determine the inflow, a representative inlet velocity profile (V_z) was chosen along the upper disk surface ($Z^*\approx0.1$) plane between the center of rotation ($X^*=0$) and the edge of the inner radius ($X^*=0.54$) as close to the upper disk surface

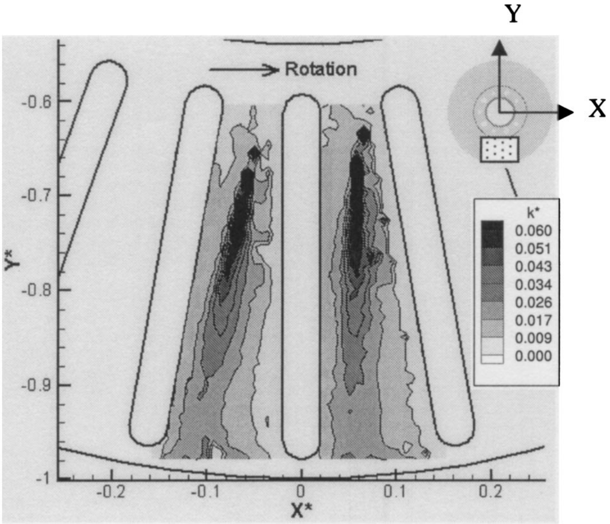

Fig. 12 Nondimensionalized turbulent kinetic energy plot of the internal flow (X-Y plane at $Z^*=0$), $N=684$ rpm

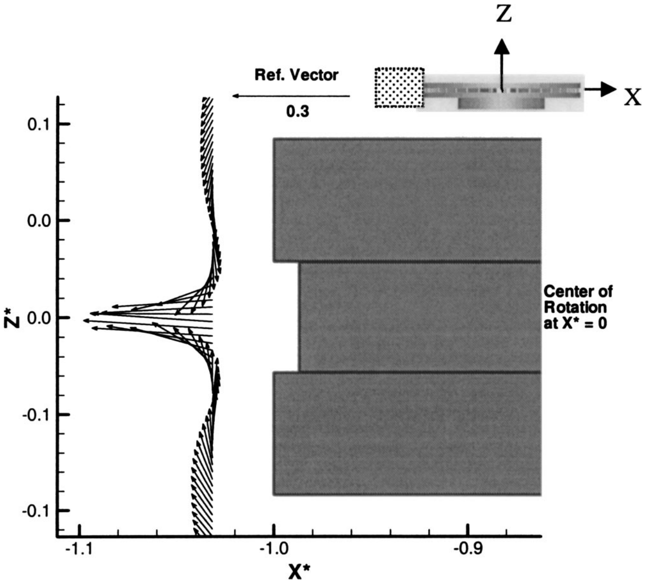

Fig. 14 Exit velocity profile used to calculate the mass flow exiting the rotor, $N=684$ rpm. Dimensionless velocity vector =0.3.

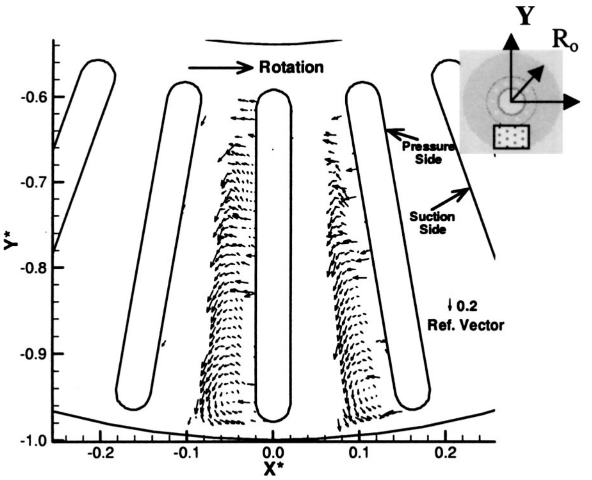

Fig. 15 High resolution vector plot of internal flow (pressure side vectors removed for clarity), $N=684$ rpm. Dimensionless velocity vector=0.2.

as possible. This velocity profile was then revolved 360 deg in order to encompass the entire possible inlet area of the rotor (Fig. 13). The volumetric inflow as represented by the flow number

$$\phi=\frac{Q}{\omega D_o^3}, \tag{2}$$

was thus calculated from the PIV results to be $\phi_{\mathrm{PIV},i}=0.0115$.

Outflow. The velocity profile used in the calculation of the exit flow is shown in Fig. 14. The radial velocities (V_x) in the profile were integrated between $Z^*=\pm 0.028$ and revolved around the outer diameter of the rotor to yield $\phi_{\mathrm{PIV},o}=0.0105$ nondimensional flow units (also determined from the PIV results). This value is comparable to the calculated inflow, although it is lower, leaving a difference of 8.2%. This difference is reasonable given the assumptions made and the integration method utilized to determine the flow rate and it may indicate some mass flow bypassing the inlet and flowing over the upper disk surface due to the position of the inlet flow control volume.

3.4 Separation Points. There are significant regions of flow separation in the internal flow passages of the rotor as shown in the relative velocity vector plots (Figs. 7(*a*) and 7(*b*)). These plots show large areas of little or no flow in the X-Y plane along the entire right (suction) side of the passage. Flow separation began immediately after the passage entrance. The dominant cause of this is the misalignment between the physical radially outward vane angle (90 deg to the tangential direction in the X-Y plane) and the relative velocity approaching the vane as seen in Fig. 6 (dominant tangential velocity direction) and Fig. 4 (minor axial velocity direction). Thus the inlet relative velocity is perpendicular to the physical vane and the incidence angle is very large. Figure 15 re-plots Fig. 7(*a*) with increased vector lengths on the suction side of the passage. Out of plane effects not measured by the planar PIV system are likely significant in this region due to the reverse flow measured near the vane, close to the leading edge (entrance) as well as a recirculation zone centered near the vane trailing edge.

The flow through the radial vanes of the rotor may also be treated as a flow through a rotating diffuser. The study by Rothe and Johnston [18] provide relationships between the Reynold's number Re_Q, rotation number, Ro, and the area ratio between the outlet and inlet area of a diffuser. Re_Q is the Reynolds number based on the inlet flow area,

$$\mathrm{Re}_Q=\frac{w_1(Q/A)}{\nu} \tag{3}$$

while Ro is defined as,

$$Ro=\frac{\omega\cdot w_1}{(Q/A)} \tag{4}$$

The area ratio, AR, is defined as the flow area at the trailing edge (R_{vo}) over the flow area at the leading edge of the rotor (R_{vi}), and was constant for all vanes at 2.06, and at a Re of 3.65×10^5, Re_Q, was 3300 and the rotation number, Ro, was 0.11. Based on these characteristics, this flow falls within a region of two-dimensional stall in [18]. This is due in part to the included expansion angle (9.65 deg) of each air passage which in itself is not enough to cause the level of separation measured. As well, Rothe and Johnston [18] suggest that the presence of rotation increases the tendency for stall in the air passage by suppressing the turbulent mixing and shear stress of the Coriolis acceleration field.

3.5 Independence of Rotational Speed. Figure 16 plots the maximum resultant exit velocities (V_{res}) of the airflow at the three rotational speeds tested. When the velocities were normalized by the peripheral velocity (U_o) of the rotor, a near constant value of 0.895 was observed, indicating a linear relationship between the rotational speed and the volume of airflow in the rotor over the range of speeds tested.

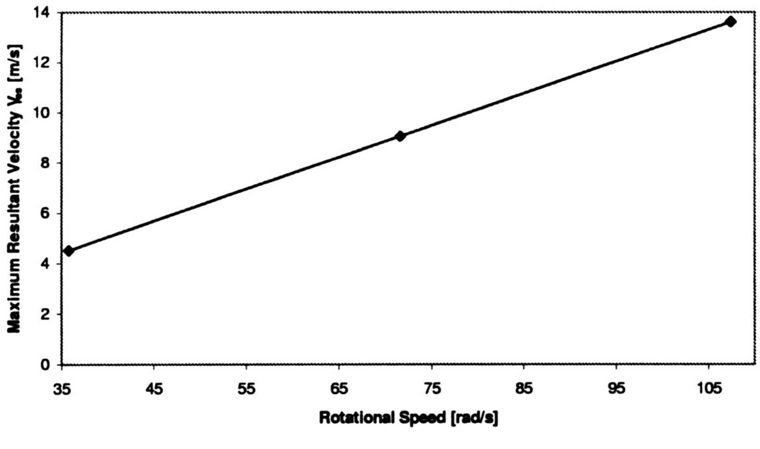

Fig. 16 Relationship between the maximum exit flow velocities and the rotational speed of the rotor

4 Conclusions

PIV measurements of a rotating automotive brake rotor revealed interesting information about the flow structure through the radial vaned air passages. The presence of large separation areas in the air passages indicated poor performance as a radial flow fan. This is caused by the high incidence angle due to misalignment between the relative velocity direction and the physical blade angle. An additional factor was the effect of rotation, where rotation number and diffuser area ratio were used to predict stall. The areas of highest turbulent kinetic energy were found to occur through the middle of the air passages, where large velocity gradients separated the pressure and suction sides. Normalized mean velocity plots showed little variation at the three rotational speeds tested, indicating a linear relationship between the velocities established in the rotor and rotational speed.

These results will serve as useful information towards improving the geometry of the air passages in automotive brake rotors. Improved geometry will result in improved flow through each air passage, making the rotor more efficient in moving air. Further tests are recommended in this aspect in order to verify a relationship between improving the air flow and improving the heat dissipation of the rotor. These rotors operate over a very wide range of rotational speeds and a ‘best design’ for one flow would not characteristically apply to all flow ranges. It is important to note however, that all rotors were tested without any obstructions at the inlet or outlet, and hence, the best possible performance was measured. The inlet and the entire rotor can become severely blocked by other components such as drive shafts and wheel hubs in full automotive wheel assemblies.

Acknowledgments

The authors would like to acknowledge the financial support of the Natural Sciences and Engineering Research Council of Canada (NSERC).

Nomenclature

A = cross-sectional area of rotor air passage inlet (mm^2) ($A = w_1^* b$)
AR = area ratio (w_2/w_1)
b = space between the two brake disks
D_o, D_i = disk outer and inner diameter, respectively (mm)
D_{vo}, D_{vi} = vane outer and inner diameter, respectively (mm)
Q = flow rate (volumetric) (m^3/s)
R_o, R_i = disk outer and inner radius, respectively (mm)
R_{vo}, R_{vi} = vane outer and inner radius, respectively (mm)
Re = rotational Reynolds number
Re$_q$ = Reynolds number based on inlet channel height
Ro = rotation number
V_{res} = absolute resultant air velocity (radial and tangential component) $V_{res} = \sqrt{V_x^2 + V_y^2}$
w_1, w_2 = distance between rotor vanes inlet, outlet, respectively (mm)
X^* = represents radial or tangential direction as indicated in each figure ($X^* = X/R_o$)
Y^* = represents radial or tangential direction as indicated in each figure ($Y^* = Y/R_o$)
Z^* = axial direction ($Z^* = Z/R_o$)

Subscripts

i, o = inlet and outlet, respectively

Greek Symbols

μ = absolute viscosity (kg/ms)
ν = kinematic viscosity (m^2/s)
θ = angular direction
ρ = density (kg/m^3)
ϕ = overall flow number ($Q/\omega D_o^3$)
$\phi_{\mathrm{PIV},i}$ = overall inlet flow number based on PIV results
$\phi_{\mathrm{PIV},o}$ = overall outlet flow number based on PIV results
ω = rotational speed (1/s)

References

[1] Limpert, R., 1975, ‘‘Cooling Analysis of Disc Brake Rotors,’’ SAE Paper No. 751014.

[2] Sisson, A. E., 1978, ‘‘Thermal Analysis of Vented Brake Rotors,’’ SAE Paper No. 780352.

[3] Hudson, M. D., and Ruhl, R. L., 1997, ‘‘Ventilated Brake Rotor Air Flow Investigation,’’ SAE Paper No. 971033.

[4] Jerhamre, A., and Bergstrom, C., 2001, ‘‘Numerical Study of Brake Disc Cooling Accounting for Both Aerodynamic Drag Force and Cooling Efficiency,’’ SAE Paper No. 2001-01-0948.

[5] Paone, N., Riethmuller, M. L., and Van den Braembussche, R. A., 1989, ‘‘Experimental Investigation of the Flow in a Vaneless Diffuser of a Centrifugal Pump by Particle Image Displacement Velocimetry,’’ Exp. Fluids, **7**, pp. 371–378.

[6] Shepherd, I. C., and La Fontaine, R. F., 1993, ‘‘Mapping the Velocity Field in a Centrifugal Fan Using Particle Image Velocimetry,’’ J. Wind. Eng. Ind. Aerodyn., **50**, pp. 373–382.

[7] Shepherd, I. C., La Fontaine, R. F., Welch, L. W., and Downie, R. J., 1994, ‘‘Velocity Measurement in Fan Rotors Using Particle Image Velocimetry,’’ *Laser Anemometry*, ASME, New York, FED-Vol. 191, pp. 179–183.

[8] Akin, O., and Rockwell, D., 1994, ‘‘Flow Structure in a Radial Flow Pumping System Using High Image Density Particle Image Velocimetry,’’ ASME J. Fluids Eng., **116**, pp. 538–544.

[9] Adrian, R. J., 1991, ‘‘Particle-Imaging Techniques for Experimental Fluid Mechanics,’’ Annu. Rev. Fluid Mech., **23**, pp. 261–304.

[10] Grant, I., 1997, ‘‘Particle Image Velocimetry: A Review,’’ Proc. Inst. Mech. Eng., Part C: J. Mech. Eng. Sci., **211**, pp. 55–76.

[11] Melling, A., 1997, ‘‘Tracer Particles and Seeding for Particle Image Velocimetry,’’ Meas. Sci. Technol., **8**, pp. 1406–1416.

[12] Gilbert, R., 2001, ‘‘Evaluation of FFT Based Cross-Correlation Techniques Used in Particle Image Velocimetry,’’ M.A.Sc. thesis, University of Waterloo, Waterloo, Canada.

[13] Scarano, F., and Riethmuller, M. L., 1999, ‘‘Iterative Multigrid Approach in PIV Image Processing With Discrete Window Offset,’’ Exp. Fluids, **26**, pp. 512–523.

[14] Willert, C. E., and Gharib, M., 1991, ‘‘Digital Particle Image Velocimetry,’’ Exp. Fluids, **10**, pp. 181–193.

[15] Prasad, A. K., Adrian, R. J., Landreth, C. C., and Offutt, P. W., 1992, ‘‘Effect of Resolution on the Speed and Accuracy of Particle Image Velocimetry Interrogation,’’ Exp. Fluids, **13**, pp. 105–116.

[16] Westerweel, J., 1997, ‘‘Fundamentals of Digital Particle Image Velocimetry,’’ Meas. Sci. Technol., **8**, pp. 1379–1392.

[17] Westerweel, J., 2000, ‘‘Theoretical Analysis of the Measurement Precision in Particle Image Velocimetry,’’ Exp. Fluids, (Suppl.), pp. S3–S12.

[18] Rothe, P. H., and Johnston, J. P., 1976, ‘‘Effects of System Rotation on the Performance of Two-Dimensional Diffusers,’’ ASME J. Fluids Eng., **9**, pp. 422–430.

Heather L. McClusky
Mary V. Holloway
Timothy A. Conover
Donald E. Beasley
Fellow ASME

Department of Mechanical Engineering,
Clemson University,
106-D Flour Daniel Building,
Clemson, SC 29634

Michael E. Conner
L. David Smith III

Westinghouse Nuclear Fuel,
5801 Bluff Road,
Columbia, SC 29250

Mapping of the Lateral Flow Field in Typical Subchannels of a Support Grid With Vanes

Lateral flow fields in four subchannels of a model rod bundle fuel assembly are experimentally measured using particle image velocimetry. Vanes (split-vane pairs) are located on the downstream edge of the support grids in the rod bundle fuel assembly and generate swirling flow. Measurements are acquired at a nominal Reynolds number of 28,000 and for seven streamwise locations ranging from 1.4 to 17.0 hydraulic diameters downstream of the grid. The streamwise development of the lateral flow field is divided into two regions based on the lateral flow structure. In Region I, multiple vortices are present in the flow field and vortex interactions occur. Either a single circular vortex or a hairpin shaped flow structure is formed in Region II. Lateral kinetic energy, maximum lateral velocity, centroid of vorticity, radial profiles of azimuthal velocity, and angular momentum are employed as measures of the streamwise development of the lateral flow field. The particle image velocimetry measurements of the present study are compared with laser Doppler velocimetry measurements taken for the identical support grids and flow condition. [DOI: 10.1115/1.1625688]

1 Introduction

The flow field in the fuel assembly of a nuclear reactor directly influences the thermal-hydraulic performance of the reactor. Previous research on flow field characteristics in fuel assemblies demonstrates that the flow field is complex and highly three-dimensional. This paper focuses on the development of the lateral flow field in several subchannels downstream of a support grid with vanes in a rod bundle geometry representative of a pressurized water reactor (PWR).

The core of a pressurized water reactor is constructed from multiple fuel assemblies that are housed in a pressure vessel. Each fuel assembly consists of nuclear fuel rods and support tubes that are assembled into a rod bundle. The coolant, pressurized water, is circulated through the core of the reactor and flows parallel to the rods. Support grids are located at regular intervals along the flow direction to support the rods and to maintain the lateral spacing of the rods in the bundle. For normal operating conditions, the elevated pressure of a pressurized water reactor suppresses boiling and the majority of the fuel assembly operates in the single-phase flow regime. A heat exchanger is located downstream of the pressure vessel to transfer the heat produced by the core to a secondary system for power generation.

In the present experimental program, the flow field for a rod bundle geometry corresponding to 17×17 type fuel is examined. A square 5×5 array of rods is employed as the model rod bundle and represents a portion of the actual fuel assembly. The measurements are acquired at atmospheric temperature and pressure for a nominal Reynolds number of 28,000. The support grids for the model rod bundle are constructed from the inner strap of a 17×17 fuel assembly midgrid. The rod pitch, rod diameter, and streamwise spacing of the grids of the model rod bundle are consistent with that of the actual fuel assembly. A generally accepted practice to benchmark new grid designs is to use a 5×5 rod bundle (or similar geometry) for testing to develop local heat transfer correlations and local mass exchange parameters for use in full core models. This testing approach is applicable since the limiting thermal region of the core is in essentially axial flow (Conner et al. [1]). In addition, 5×5 rod bundles are also used in the safety-related departure from nucleate boiling (DNB) testing that sets performance limits on the power of the core, and thus play an important role in the licensing of new fuel designs. Therefore, differences in the lateral flow fields downstream of split-vane pair grid designs in 5×5 rod bundles have implications for both the design and licensing of future rod bundle assemblies. In addition, heat transfer measurements, [2], and CFD predictions, [1], indicate that there is a connection between the lateral flow fields in rod bundle subchannels and local variations in heat transfer coefficients on the rod surfaces. Hot spots on the rod surfaces are potentially detrimental to the overall performance of the rod bundle. Detailed information on the lateral velocity fields in the rod bundle subchannels is needed to support understanding and CFD modeling of local heat transfer characteristics. The ultimate objective is to improve the thermal performance of support grid and vane designs.

To improve the thermal-hydraulic performance of the fuel, support grids are designed with vanes located on the downstream edge of the grid. The vane orientation in a typical support grid with split-vanes pairs is shown in Fig. 1(*a*). Experimental investigations using laser Doppler velocimetry (LDV) for velocity measurements in rod bundles with support grids that have vanes are summarized in Table 1. In these studies, flow field measurements were acquired for streamwise locations beginning at the downstream edge of the grid and extending to streamwise locations up to 53 hydraulic diameters downstream of the grid. Detailed measurements of the development of the flow field adjacent to the vanes (vane region) and downstream of the vanes were included. The typical streamwise distance between grids, or the grid span, was 43 to 53 hydraulic diameters.

Previous experimental and numerical studies have examined time-averaged velocity and turbulence characteristics of the flow fields in model square-arrayed rod bundles. The flow fields were presented as radial profiles of axial and lateral velocity. In addition, the global streamwise development of the velocity field was presented using integral measures such as swirl parameter and cross flow mixing parameter. Previous studies of velocity fields downstream of support grids with split-vanes pairs showed similar qualitative characteristics.

Herr and Pröbstle [3] examined the lateral and axial velocities in the vane region of the support grid. The vanes affect the lateral

---

Contributed by the Fluids Engineering Division for publication in the JOURNAL OF FLUIDS ENGINEERING. Manuscript received by the Fluids Engineering Division Dec. 17, 2002, revised manuscript received June 23, 2003. Associate Editor: A. K. Prasad.

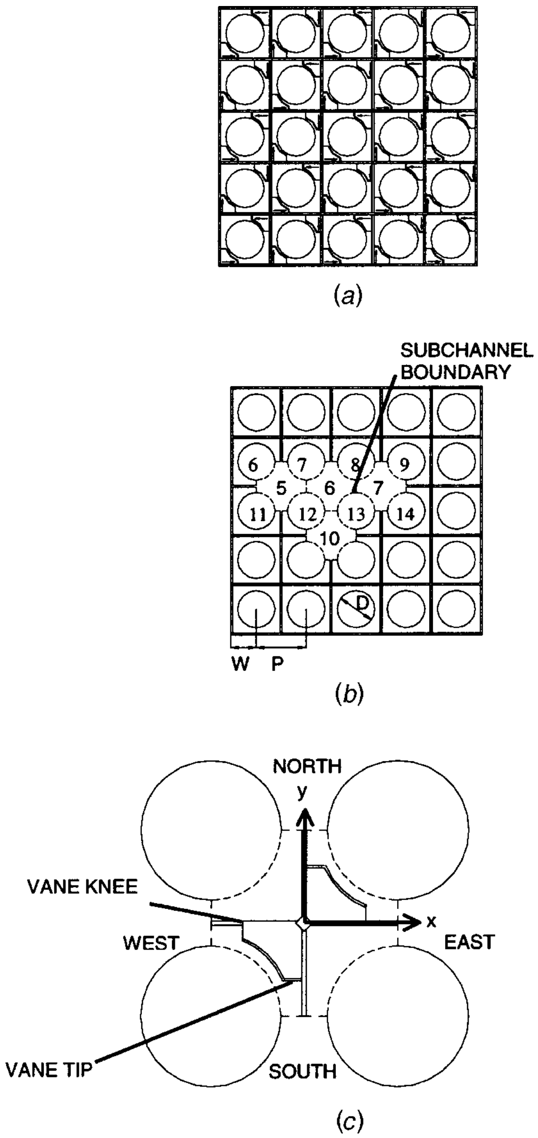

Fig. 1 End view of the support grid (*a*) vane pattern; (*b*) numbering scheme and parameters (D=9.5 mm, P=12.6 mm, W=7.34 mm); (*c*) single subchannel showing the split-vane pair for subchannel 6 with weld nugget (D_h=11.78 mm)

Table 1 LDV investigations in rod bundles

Study	Re	Vane Type	Vane Angle	Test Section	Fluid	z/D_h
[3]	2.0×10^3 to 6.0×10^4	Split-vane	20 deg	2×2 square array	Index of refraction matched	0.3 to 1.5
[7]	1.0×10^5	Mixing vanes	⋯	5×5 square array	Water	−2 to 8
[9]	2.0×10^4	Mixing blade	0 deg, 20 deg, 25 deg, 30 deg, 35 deg	4×4 square array	Water	5 to 45
[4]	8.9×10^4	Split-vane squeezed tube	⋯	5×5 square array	Water	1 to 36
[8]	6.25×10^4	Split-vane	22 deg	5×5 square array	Water	−11 to 53
[23]	2.8×10^4	Split-vane	30 deg	5×5 square array	Water	1.4 to 34.0

flow field by directing high velocity lateral flow into the rod gaps, creating swirling flow in the subchannel, and generating wakes downstream of the vanes in the subchannel. As shown schematically in Fig. 1(*b*), a subchannel is defined as the open flow area between the surrounding rods and/or walls. A single subchannel is shown in Fig. 1(*c*). The azimuthal direction of the swirling flow is determined by the orientation of the vanes. At a streamwise location halfway between the downstream edge of the support grid and the vane tips, Herr and Pröbstle [3] showed that the pressure field in the wake region decreases the magnitude of the swirling flow. At the vane tips, the azimuthal velocity magnitude is on the order of 40% of the average axial velocity (Herr and Pröbstle [3] and Karoutas et al. [4]). As the lateral flow field develops downstream of the vane tips, the magnitude of the lateral velocity decays and is 4% of the average axial velocity by 34 hydraulic diameters downstream, as documented by Karoutas et al. [4]. The shape of the radial profiles of azimuthal velocity is that of a forced-free vortex. Herr and Pröbstle [3] and Karoutas et al. [4] suggest that the qualitative behavior of the radial profile of azimuthal velocity at the vane tips is similar to that of a Lamb-Oseen or Rankine vortex (see Saffman [5]). McClusky et al. [6] measured the lateral velocity field in a single subchannel of a rod bundle fuel assembly using particle image velocimetry. The lateral velocity data were used to obtain azimuthal velocity profiles and the azimuthal velocity profiles were fit to the analytical form of a Lamb-Oseen vortex.

In the vane region, the axial velocity increases near the rod surfaces and decreases near the center of the subchannel (Herr and Pröbstle [3]). At the vane tips, a local minimum in the axial velocity is located at the center of the subchannel and two local maxima are located in the subchannel region (Herr and Pröbstle [3] and Karoutas et al. [4]). Further downstream, the global maximum of axial velocity is located in the subchannel (however, not in the center of the subchannel) and the global minimum of axial velocity is located in the rod gaps (Herer [7], Karoutas et al. [4], and Yang and Chung [8]). Yang and Chung [8] show that for axial locations beyond 15 hydraulic diameters the axial velocity increases with axial direction in the subchannel and decreases with axial direction in the rod gaps. At an axial location of 32 hydraulic diameters, the axial velocity is fully developed as documented by Karoutas et al. [4] and Yang and Chung [8]. At an axial location immediately upstream of a support grid, the maximum velocity is located in the subchannel and is 10–25% higher than the average velocity, and the minimum axial velocity is located in the rod gaps (Herer [7] and Yang and Chung [8]).

In previous studies, measurements of the lateral and axial velocity profiles were acquired in multiple subchannels; however, comparison among the subchannels was not provided even though the data show that the flow fields were asymmetric and were influenced by the housing walls. Differences in the lateral and axial velocity profiles between two subchannels are apparent in the measurements of Karoutas et al. [4]. The magnitude of both the axial and the lateral velocities differs by up to 50% between the two subchannels for streamwise locations near the grid (Karoutas et al. [4]). Yang and Chung [8] showed that the axial velocity profiles near the housing walls are flatter than the axial velocity profile measured near the center of the rod bundle. Shen et al. [9] discussed the effect of the housing walls on the flow field.

Previous research has characterized the turbulent flow structure in rod bundle subchannels using normalized velocity profiles in the near wall region of the housing wall and the rod surfaces, and turbulence measurements in the subchannels and rod gaps. Measured velocity profiles for flow along the surface of the rods for rods located in the central region of the bundle and near the walls of the housing as well as for flow along the surface of the housing agree with the law of the wall (Ouma and Tavoularis [10], Meyer [11], and Krauss and Meyer [12]).

Table 2 CFD investigations in rod bundles

Study	Domain Modeled	Turbulence Model	Re	Vane Type
[4]	Split-vane: 1/2 subchannel squeezed tube: 1/4 subchannel	Standard $k-\varepsilon$	8.9×10^4	Split-vane squeezed tube
[14]	Two subchannel	Standard $k-\varepsilon$	7.7×10^4 to 5.0×10^5	Split-vane
[16]	5×5 and 3×3 support grid	Standard $k-\varepsilon$	2.8×10^4	Split-vane
[15]	Single subchannel	Standard $k-\varepsilon$	6.5×10^4	Split-vane side-supported vane swirl vane twisted vane
[13]	Two subchannel	Standard $k-\varepsilon$, RNG $k-\varepsilon$, nonlinear quadratic $k-\varepsilon$	2.8×10^4	Split-vane

For flow in a rod bundle fuel assembly, the axial and azimuthal turbulence intensities were documented for discrete points within a subchannel and for the streamwise development of the flow. The magnitude of the turbulence intensity upstream of the grid is on the order of 5% and increases to nearly 20% just downstream of the grid (Yang and Chung [8]). At a streamwise location immediately upstream of a grid, the axial turbulence intensity is lower in the subchannel than in the rod gaps. In the region of the flow field downstream of the grid, the axial turbulence intensity is higher in the subchannel than in the rod gaps. In the fully developed region, the axial turbulence intensity is lower in subchannel than in the rod gaps (Herer [7] and Yang and Chung [8]). Yang and Chung [8] showed that the axial turbulence intensity is more isotropic downstream of the grid than upstream of the grid as indicated by the skewness of the measured velocity. The subchannels located further from the housing walls have the largest turbulence intensity (Yang and Chung [8]). Yang and Chung [8] modeled the spatial decay of the turbulence intensity in the rod bundle using the analytical form of the spatial decay rate of turbulence intensity for flow through mesh grids.

Experimental studies have provided insight into the flow fields in rod bundles and have shown that the flow field is complex. Computational fluid dynamics (CFD) has been implemented to provide additional insight into the flow field, to streamline the grid design process, and to perform parametric studies of grid features. Previous numerical simulations of the flow field in rod bundles are summarized in Table 2. The CFD efforts modeled either a portion of a subchannel, a single subchannel, or two subchannels for a single span that commences upstream of the grid. Periodic boundary conditions were implemented at the boundaries of the subchannel. The standard $k-\varepsilon$, RNG $k-\varepsilon$, and nonlinear quadratic $k-\varepsilon$ turbulence models were investigated in the CFD efforts. The importance of benchmarking CFD was discussed in Smith et al. [13]. Karoutas et al. [4] experimentally measured the lateral and axial velocities using LDV, and the LDV data served as benchmark data for CFD. Imaizumi et al. [14] benchmarked CFD results using the circumferential pressure distribution over the surface of the rod. The LDV data of Karoutas et al. [4] and Yang and Chung [8] were used to benchmark the CFD model of In [15].

Ikeda and Hoshi [16] implemented CFD to analyze the flow downstream of both a 5×5 and 3×3 rod bundle with a split-vane pair grid design. A single grid span of each of the rod bundles was modeled computationally. Lateral velocity vectors downstream of the 5×5 rod bundle were presented for a single axial location.

In [15] utilized CFD to compare the flow fields developed from four different vane designs. As presented in Table 2, the four types of vanes are split-vane (with and without a weld nugget cutout), side-supported vane, swirl vane, and twisted vane. Higher values of the swirl parameter and the cross flow mixing parameter were reported for split-vane and twisted vane designs.

The CFD models of both Imaizumi et al. [14] and In [15] examined the flow field downstream of split-vane designs. The dominant flow structures in the lateral flow field are a cross flow (lateral flow) near the rod surfaces and a swirling flow structure. Imaizumi et al. [14] classified the axial development of the lateral flow field into three general regions as: a strong cross flow dominated flow field superimposed with a region of swirling flow, a flow field with cross flow and weakened swirling flow (the center of the swirling flow migrated), and a flow field that has only cross flow. In the region just downstream of a grid with split-vanes, the CFD results of In [15] show a lateral flow field similar to that of Imaizumi et al. [14]. In this region, the lateral flow field has strong cross flow and an elliptical shaped swirling flow region that is oriented along the northwest and southeast axis of the subchannel. Further downstream of the split-vanes, the results of In [15] indicate that the cross flow diminishes and the swirling flow becomes dominant. At the downstream locations, the lateral flow fields predicted by In [15] differ from those predicted by Imaizumi et al. [14] and the differences may be attributed to the differences in the computational domain used to model the rod bundle fuel assembly.

In the present study, particle image velocimetry is employed to obtain full-field lateral velocity measurements in subchannels downstream of a split-vane pair grid design. The streamwise development of the lateral velocity fields in four subchannels is compared in the present study. Figure 1(*c*) shows a two-dimensional projection of the split-vane pair design used in the present study. The angle of each vane relative to the flow direction, or vane angle, is approximately 30 deg for the present study. In addition, there is a weld nugget cutout at the base of the vane pairs. Details of split-vane pairs with and without a weld nugget cutout are discussed in the CFD analysis of In [15]. The blockage ratio (the ratio of the projected area of the grid to the open flow area in the test section) for the support grid design used in the present study is approximately 0.40. Typical, or central, subchannels are selected for analysis in the present study and are designated subchannels 5, 6, 7, and 10 (Fig. 1(*b*)). In previous studies examining the flow fields downstream of split-vane pair grid designs, comparison of velocity fields among different subchannels was minimal and only limited data were presented that addressed the effect of walls on the flow field. The present investigation is an extension of work reported previously by the authors in McClusky et al. [6] that studied the lateral flow fields in a single subchannel downstream of a split-vane pair grid with only one active vane pair. In the present study, measurements are acquired for a fully vaned 5×5 support grid in multiple subchannels to gain insight into differences of the lateral velocity fields among the subchannels.

2 Experimental Facility and Measurements

The experimental facility was designed and constructed to allow full-field measurement of the lateral velocity in multiple subchannels in the rod bundle. The lateral velocity fields are acquired using a particle image velocimetry technique. Details of the experimental facility essential to the particle image velocimetry measurement technique are emphasized below.

2.1 Experimental Facility. A drawing of the experimental facility is shown in Fig. 2. Water is used as the working fluid. The flow loop consists of a constant head tank, heat exchanger, variable speed pump, flow straightener, test section, and flowmeter. The Lexan test section accommodates a square-arrayed 5×5 rod bundle, and the test section height and length are 65 mm and 1.64 m, respectively. The rod bundle is constructed using 9.5 mm

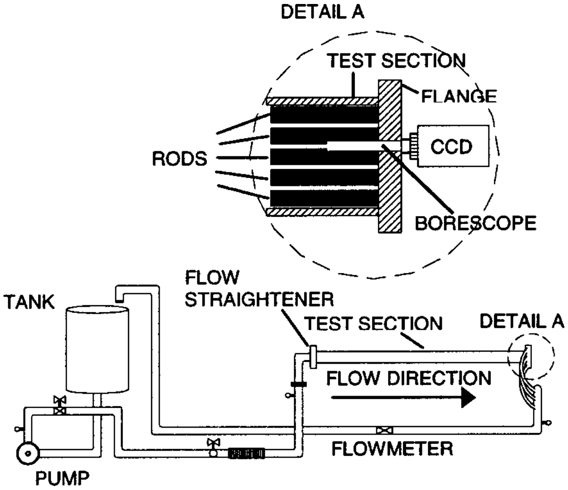

Fig. 2 Drawing of the experimental facility

rods that are supported on a 12.6 mm pitch ($P/D=1.33$, $W/D=0.77$) as shown in Fig. 1(*b*). The hydraulic diameter of a single subchannel is 11.78 mm. Three grids are used to assemble the bundle and are placed on a span of 508 mm. The first grid is located 90 mm downstream of the test section inlet. A hybrid rod construction is employed to allow optical access to the subchannels at axial locations downstream of the third grid. The hybrid rods are constructed from zircaloy and transition to quartz 15 mm upstream of the third grid. The outlet of the test section was designed to accommodate a forward viewing borescope used for PIV measurements. The optical borescope allows measurements of the lateral velocity field in a single subchannel. A cross-sectional view of the test section outlet is provided in Fig. 2.

Lateral velocity data were acquired at an average axial velocity of 2.4 m/s and at a water temperature of 20°C. The Reynolds number based on hydraulic diameter was 28,000. Lateral velocity fields were measured at axial locations of 17 to 200 mm (1.4 to $17.0D_h$) for subchannels 5, 6, 7, and 10.

2.2 Particle Image Velocimetry Measurements. Particle image velocimetry provides opportunity for full-field velocity measurements at a high spatial resolution, which allows detection of spatial structures in the flow. Two-dimensional particle image velocimetry (PIV) is a well-established full-field velocity measurement technique (Raffel et al. [17]). The complex flow field in the rod bundle and the rod bundle geometry place unique demands on the PIV method.

The major components of a PIV system include tracer particles, a light source, and image acquisition equipment. The tracer particles used in the present study are 20–40 μm fluorescent particles (Johns Hopkins University Laboratory for Experimental Fluid Mechanics). To illuminate the tracer particles in the flow, a double-pulsed Nd:YAG laser (Spectra-Physics PIV-400) is used as the light source. The laser light is emitted at a wavelength of 532 nm at a repetition rate of 10 Hz. The pulse duration and pulse energy are 10 ns and 450 mJ, respectively. The laser beam is shaped into a light plane (laser sheet) using an optical slit and cylindrical lens. The resulting laser sheet width is 2.5 mm. Optical access to image the tracer particles in the flow field of the subchannels is achieved using a forward viewing optical borescope (ITI, Inc.) with a viewing angle of 10°, a diameter of 6 mm, and a length of 0.648 m. The particles are imaged onto the CCD array of a Kodak Megaplus 1.0/SC camera that has a resolution of 1108 ×1018 pixels; however, the optical borescope projects a circular image with a diameter of 525 pixels onto the array of the CCD camera. At a working distance of 130 mm, each pixel is 28.16 μm as determined by calibration. The timing of the PIV system is set using a Four-Channel Digital Delay/Pulse Generator (Stanford Research Systems DG 535).

In the present study, high-density PIV using the cross-correlation analysis method is employed (Adrian [18]; Keane and Adrian [19]). In the cross-correlation method, a sequence of image pairs is acquired and results in a sequence of instantaneous velocity fields. In the present study, the instantaneous velocity fields are acquired at a time interval of 0.1 s as determined by the laser repetition rate. The time between the two images in an image pair, or the time delay, was 125 μs. Each image pair is analyzed using an interrogation region size of 32×32 pixels with 50% overlap among neighboring interrogation regions. Thirteen instantaneous velocity fields are acquired in the present study and the time-averaged velocity field is used for discussion and further analysis. At each axial location, the (x,y) origin of the center of the subchannel is located using an in-house image analysis software package.

The uncertainty of the velocity magnitude is estimated based on a formal uncertainty analysis approach and velocity measurements of a fundamental flow field. A formal uncertainty analysis, [20], yields a conservative estimate of the uncertainty and is based on the uncertainty in the particle displacement (resolution is ±1/2 pixel or 14.08 μm) between image pairs and the measured time delay. The uncertainty in the velocity magnitude of each velocity vector based on the formal uncertainty analysis is ±10%. PIV velocity measurements of a fundamental flow field, that of a submerged jet, were within ±3% of the velocity measurements achieved based on a catch and weigh analysis. Based on the result of the formal uncertainty analysis and the uncertainty in the measurements of the fundamental flow field, the uncertainty in the magnitude of each velocity vector in the present study is estimated as ±6%.

3 Results

Particle image velocimetry measurements documented the streamwise development of the lateral velocity fields in four subchannels downstream of a support grid with split-vane pairs. Measurements were acquired for a Reynolds number of 28,000 and for seven axial locations ranging from 1.4 to $17.0D_h$. The results presented represent typical flow patterns identified after investigation of 13 different support grid designs with split-vane pairs. Additional lateral velocity fields obtained by the investigators for flow downstream of different split-vane type support grids can be found in McClusky et al. [6] for a single subchannel and in Armfield [21] and Armfield et al. [22] for multiple subchannels. The Reynolds number investigated in the present study is an order of magnitude lower than that occurring in the core of a nuclear reactor; however, comparisons of the results of the present study with CFD simulations at in-core conditions indicate that the overall flow structures and decay rate of the swirl are similar. Additionally, as stated in Smith et al. [13], a CFD modeling methodology established at low Reynolds numbers can be extended to in-core flow conditions.

The streamwise development of the lateral flow field is characterized into two regions, Region I and II, based on qualitative characteristics of the lateral flow structure. Quantitative measures of the lateral velocity field are presented and the results of the present investigation are compared with McClusky et al. [6]. The measurements of the present study are also compared with laser Doppler velocimetry measurements (Ikeda et al. [23]) for the same rod bundle geometry, support grid design, and flow conditions.

3.1 Lateral Flow Structure. In the present study, the rod bundle is constructed using support grids that are designed with split-vane pairs. The vane geometry and subchannel numbering scheme are presented in Fig. 1. As shown in Fig. 1, the vane pattern in subchannels 5, 7, and 10 is the same and in these subchannels the vanes are oriented in the east and west directions. The vanes in subchannel 6 are oriented in the north and south directions. The bulk flow is in the streamwise direction and large-scale flow structures are generated from the vanes located on the support grid. Figure 3 shows representative lateral velocity fields and axial vorticity fields presented using a normalized Cartesian coordinate system with the origin located at the center of the subchannel. The lateral velocity fields presented in Fig. 3 were selected to illustrate the typical streamwise development of the lateral flow fields as well as the different characteristics identified between subchannels. Additional lateral flow fields are not shown due to space limitations, however, results for all four subchannels are discussed. Two main characteristics of the lateral flow structure are the swirling flow in the central region of the subchannel and the lateral flow within the subchannel near the surfaces of the rods. As previously discussed in this section, the streamwise development of the lateral flow field is characterized as Region I and Region II based on the flow structure observed at the discrete streamwise measurement locations. Region I includes streamwise locations from the vane tips to $4.2D_h$. In Region I, multiple vortices are present in the subchannel. Region II extends from 6.3 to $17.0D_h$, and a single vortex or hairpin shaped flow structure is formed in the subchannel.

The representative flow field presented in Fig. 3(*a*) is in Region I of subchannel 6 at $z/D_h=1.4$. As shown in Fig. 3(*a*), immediately downstream of the vanes four vortices are observed in the subchannel. The term vortex refers to a region of large magnitude vorticity surrounded by an irrotational flow (Saffman [5]). Two vortices are generated from each vane. One vortex is shed from the vane tip (tip vortex) and the second vortex is shed from the knee of the vane (knee vortex). The tip and knee of the vane are indicated in Fig. 1(*c*). The two tip vortices form a corotating vortex pair, with one tip vortex located in the northwest region of the subchannel and the second tip vortex located in the southeast region of the subchannel. The location of the tip vortices is consistent for all subchannels examined in the present study (subchannels 5, 6, 7, and 10). In Fig. 3(*a*), the knee vortices are located in the west and east rod gaps as determined by the vane configuration in subchannel 6. In subchannels 5, 7, and 10, the knee vortices are located in the north and south rod gaps. Strong lateral flows are present along the surfaces of the northeast and southwest rods in subchannels 5, 6, 7, and 10.

As the flow develops in the streamwise direction, the knee vortices have completely dissipated by an axial location of either $2.8D_h$ or $4.2D_h$. Vortex interactions are observed at streamwise locations of $2.8D_h$ and $4.2D_h$. In subchannels 5, 7, and 10 one of the vortices weakens and forms a re-circulation region of primarily axial flow as shown in Fig. 3(*b*). Figure 3(*b*) presents the flow field in subchannel 7 at an axial location of $2.8D_h$ and demonstrates that the tip vortex located in the southeast region is weaker than the tip vortex located in the northwest region of the subchannel. In subchannels 5 and 7, the vortex located in the northwest region of the subchannel is stronger than the vortex located in the southeast region of the subchannel. The southeast vortex is stronger than the northwest vortex in subchannel 10. At an axial location of $4.2D_h$ in subchannels 5, 7, and 10, the weaker tip vortex has dissipated and the formation of a single vortex is initiated. The central vortex is circular in shape. On the contrary, the tip vortices in subchannel 6 are of similar strength at $2.8D_h$ and have merged to form a central vortex by $4.2D_h$. The single vortex is oblong in shape and is oriented along the northwest/southeast direction.

The vortex interactions and merger process observed in the present study is similar to that for corotating paired vortices for the unconfined flows of Devenport et al. [24], Chen et al. [25], and Meunier et al. [26]. The method employed to generate the corotating vortex pair is unique to each investigation. Devenport et al. [24] and Chen et al. [25] experimentally measured the velocity fields downstream of a pair of airfoils and downstream of a flapped airfoil, respectively. In these two studies, an axial velocity component is present. Meunier et al. [26] examined the paired co-rotating vortices created by impulsively starting two flat plates. Each plate was rotated about its vertical axis to create two vortices. The flow field did not have an axial velocity component. The qualitative behavior of the vortex merger is consistent among these three studies. Meunier et al. [26] described the merger process using two stages. In the first stage, the vortices remain at a constant separation distance and rotate around each other. In the second stage, the separation distance between the two vortices rapidly decreases and the vortices merge. In the present study, the merger process of the tip vortices shed from the split-vane pairs has comparable qualitative characteristics.

In the present study, Region I is characterized by multiple vortices in the subchannel that interact, and measurements in this region are from the vane tips to $4.2D_h$. Region II ranges from streamwise measurements locations of 6.3 to $17.0D_h$. In this region, a circular vortex is present in subchannels 5, 6, and 7. A representative flow structure for these subchannels is shown in Fig. 3(*c*) for subchannel 7 at an axial location of $6.3D_h$. The formation of the single vortex in subchannels 5 and 7 results from the dissipation of one of the tip vortices whereas in subchannel 6 the two tip vortices merged to form the single vortex as identified in the lateral flow fields for streamwise locations of 1.4 to $6.3D_h$. As the flow develops in the streamwise direction, the circular vortex migrates within the subchannel for subchannels 5, 6, and 7. The qualitative characteristics of lateral flow field of the present study are similar to the CFD predictions of Imaizumi et al. [14] and In [15]. However, In [15] stated that as the flow develops in the streamwise direction the swirling flow strengthens and the lateral flow weakens whereas the predictions of Imaizumi et al. [14] show that the magnitude of the swirling flow decreases, the vortex migrates in the subchannel, and strong lateral flow is present in the subchannel. The significant differences between the CFD analysis of Imaizumi et al. [14] and In [15] include different computation meshes and domains. The streamwise development of the data of the present study is similar to that of Imaizumi et al. [14].

A hairpin shaped flow structure is present in subchannel 10 in Region II and is shown in Fig. 3(*d*). In subchannel 10, the hairpin shaped flow structure persists for all axial locations in this region. In Ikeda and Hoshi [16], differences in the flow fields between subchannels 7 and 10 were attributed to asymmetries in dimple and spring patterns of the support grid design. The support grid design investigated in Ikeda and Hoshi [16] is similar to the one examined in the present study.

The effect of confinement on the flow field in the 5×5 rod bundle is important as demonstrated by the differences among the flow fields in these four subchannels. The vane pattern, as shown in Fig. 1(*a*), and housing walls create a global flow in the rod bundle that affects the lateral flow in the subchannels. For some distance downstream of the support grid, the development of the lateral flow fields is essentially free of wall effects. However, further downstream the development of the flow is influenced by the walls. For numerous grid designs, a result of the global flow pattern is that the direction of the lateral flow in the rod gaps reverses as the flow develops in the streamwise direction. This characteristic of rod gap flows occurring downstream of support grids with split-vane pairs is discussed in Shen et al. [9]. Shen et al. [9] showed that as the vane angle increased (increased swirl) the streamwise location marking the reversed flow in the rod gaps moved further upstream.

3.2 Integral Analysis.

Integral measures of the streamwise development of the lateral velocity field employed in the present investigation are lateral kinetic energy, maximum lateral velocity, centroid of vorticity, radial profiles of average azimuthal velocity, and average angular momentum.

Lateral kinetic energy is an integral measure of the magnitude of the lateral flow field in the entire subchannel and is independent of the flow structure type. The lateral kinetic energy is based on velocity measurements in the entire subchannel, *S*, and is defined as

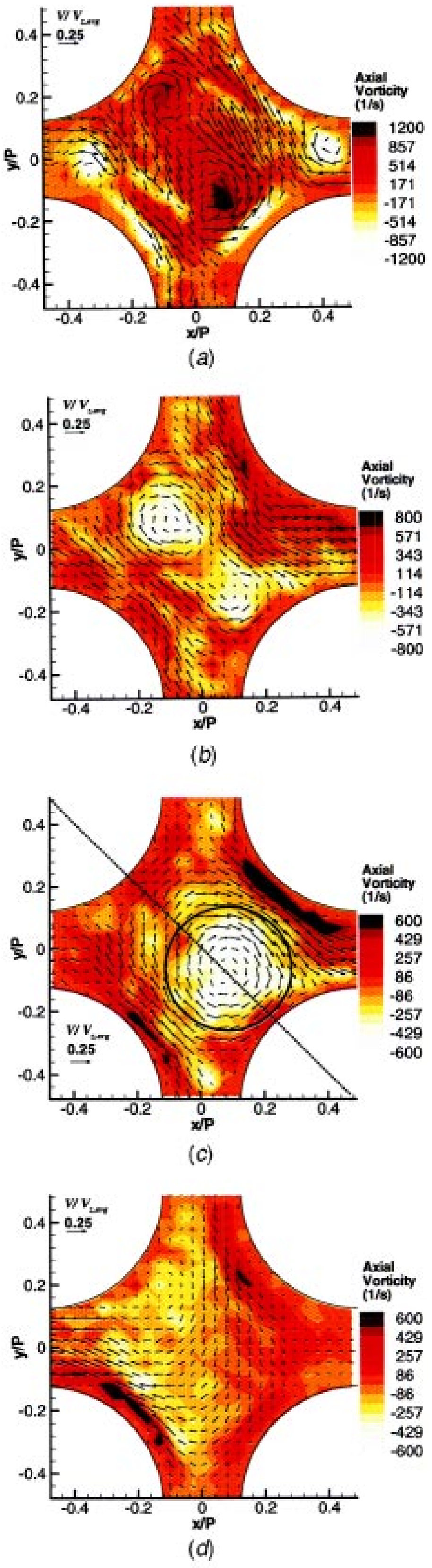

Fig. 3 Lateral velocity and axial vorticity fields for (*a*) Region I: subchannel 6 at 1.4D_h; (*b*) Region I: subchannel 7 at 2.8D_h; (*c*) Region II: subchannel 7 at 6.3D_h; (*d*) Region II: subchannel 10 at 8.5D_h.

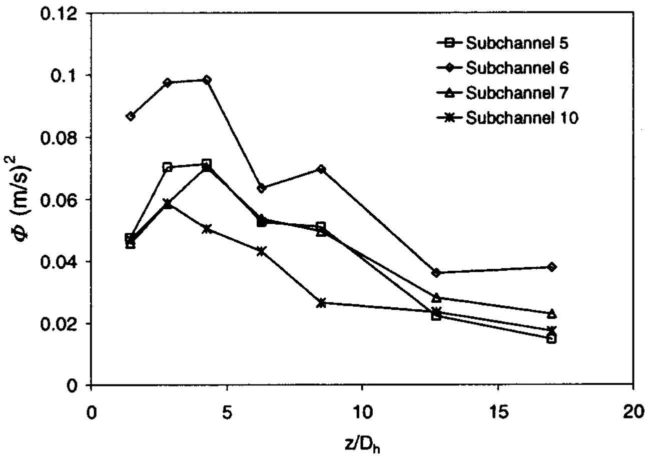

Fig. 4 Streamwise development of lateral kinetic energy

$$\Phi(z)=\frac{1}{2}\frac{\int\int_S(u(x,y,z)^2+v(x,y,z)^2)dxdy}{\int\int_S dxdy}. \qquad (1)$$

The maximum lateral velocity is characterized for two regions within each subchannel: the northeast region and the southwest region as indicated by the dotted diagonal line in Fig. 3(*c*). Within each region, the maximum lateral velocity is determined as the average of the five vectors with the largest velocity magnitude.

The centroid of vorticity, the radial profiles of average azimuthal velocity, and the average angular momentum calculations are performed for lateral velocity fields with a vortical flow structure. The lateral flow structure in subchannels 5, 6, and 7 is characterized by a single vortex whereas a hairpin shaped flow structure is formed in subchannel 10. These measures are not calculated for subchannel 10 data. The center of the swirling flow region is characterized using the centroid of vorticity (Saffman [5]). In the present study, the centroid of vorticity is determined for a circular region located at the visual center of the vortex. For calculating the centroid of vorticity, the radius of the circular region, r_o, is 2.5 mm. The radial profiles of average azimuthal velocity are determined for a circular region located at the centroid of vorticity. An example of the circular region is shown in Fig. 3(*c*). The radius of the circular region used for determining the radial profiles of azimuthal velocity was 3.5 mm for subchannel 6 and was 2.5 mm for subchannels 5 and 7. A fourth-order polynomial curve fit is applied to the data in each region. The output from the curve fitting process represents the average azimuthal velocity. At each axial location, the average angular momentum is calculated for a circular region of 2.5 mm located at the centroid of vorticity. For a detailed discussion of these integral measures see McClusky et al. [6].

3.3 Results of the Integral Measures in Region II.

Figure 4 presents the streamwise development of the lateral kinetic energy for all four subchannels examined in the present study. The maximum lateral kinetic energy is located between 2.8 and 4.2D_h in subchannels 5 and 6. The maximum lateral kinetic energy for subchannel 10 occurs at 2.8D_h and at 4.2D_h for subchannel 7. As the flow develops in the streamwise direction, the lateral kinetic energy decreases. At a streamwise location of 17.0D_h, the lateral kinetic energy is 30 to 50% of the value at 1.4D_h or the lateral kinetic energy is 20 to 40% of the maximum value of lateral kinetic energy. The magnitude of the lateral kinetic energy is larger in subchannel 6 than in the other three subchannels for all streamwise locations.

The maximum lateral velocity in the northeast and southwest regions of subchannels 6, 10, and 5 and 7 are presented in Figs. 5(*a*), (*b*), and (*c*), respectively. Comparison among these figures shows that the magnitude and the spatial decay rate are specific to

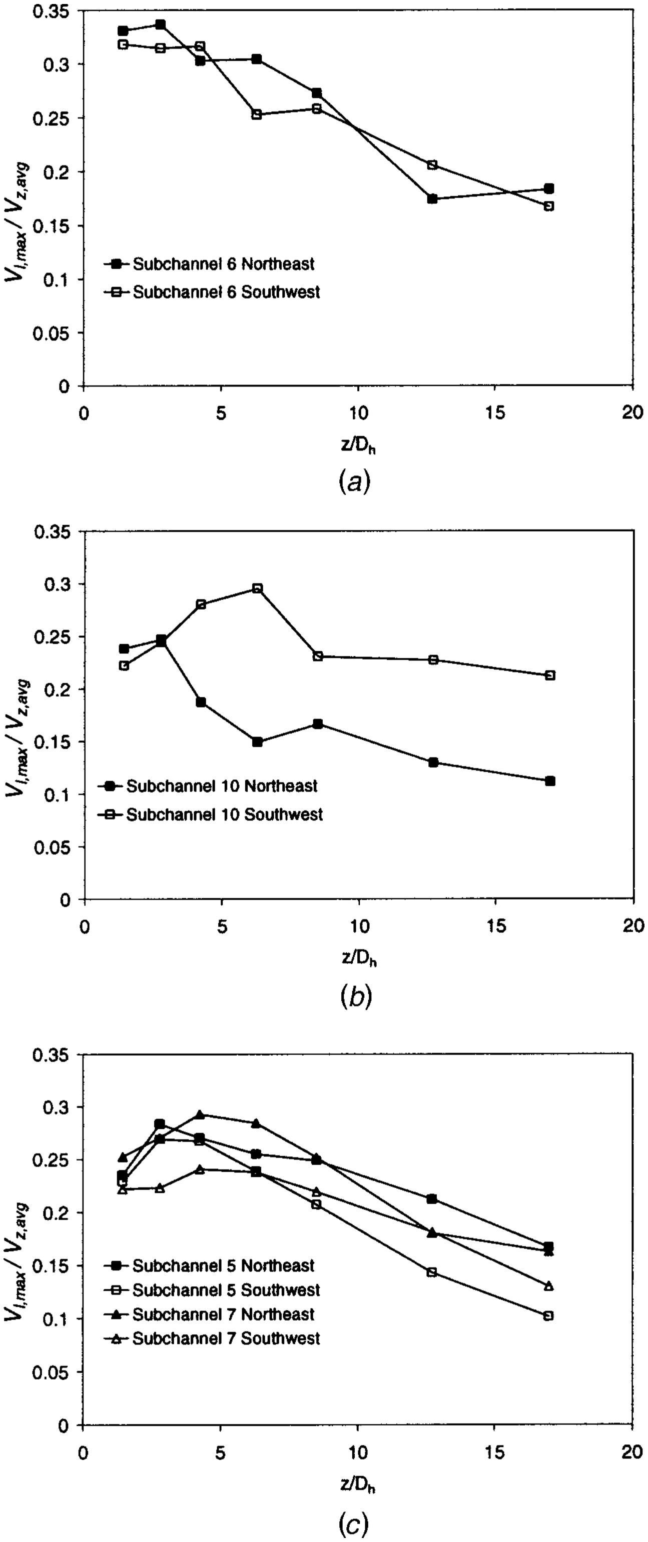

(*a*)

(*b*)

(*c*)

Fig. 5 Maximum lateral velocity for (*a*) subchannel 6; (*b*) subchannel 10; (*c*) subchannels 5 and 7

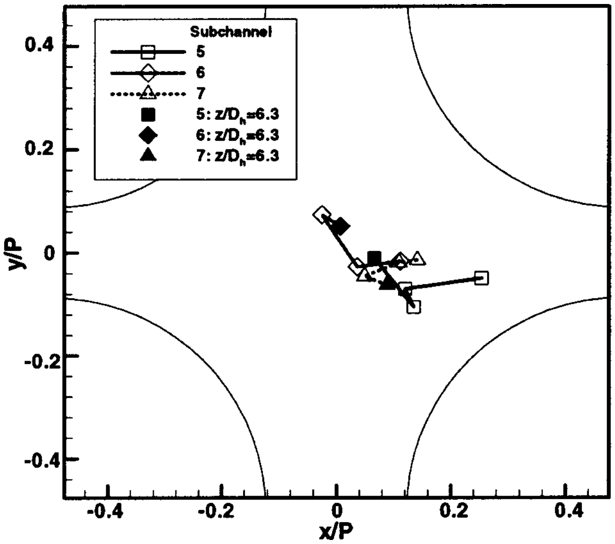

Fig. 6 Location of center of vortex (centroid of vorticity)

a subchannel. In subchannel 6 (Fig. 5(*a*)), the magnitude and the spatial decay rate of the maximum lateral velocity in the northeast region of the subchannel is similar to that in the southwest region. As the flow develops in the streamwise direction in subchannel 10 (Fig. 5(*b*)) the maximum lateral velocity in the northeast region is lower than that in the southwest region. Subchannels 5 and 7 (Fig. 5(*c*)) have similar maximum lateral velocity magnitudes and spatial decay rates. In these subchannels, the maximum lateral velocity is higher in the northeast regions of the subchannels.

The location of maximum lateral velocity within the subchannel varies for a single subchannel in the streamwise direction and among subchannels. Typical locations of the maximum lateral velocity within a subchannel include the flow near the surface of a rod, in a rod gap, or in the approach flow of an impingement point on the surface of a rod. Details of the locations of the maximum lateral velocity are discussed for subchannels 6 and 10. The flow structure in subchannel 6 is characterized by a circular vortex (a representative flow structure is shown in Fig. 3(*c*)). In subchannel 6, for streamwise locations of 6.3 and 8.5D_h the maximum lateral velocity in the northeast region of the subchannel is located near the surface of the northeast rod in the north rod gap. At axial locations of 12.7 and 17.0D_h, the maximum lateral velocity is located along the surface of the southeast rod and is located in flow that impinges on the surface of the northeast rod, respectively. In the southwest region of subchannel 6, the maximum lateral velocity is located along the surface of the southwest rod at streamwise locations of 6.3 and 8.5D_h. At axial locations of 12.7 and 17.0D_h, the maximum lateral velocity impinges on the surface of the southeast rod, and flows out of the south rod gap, respectively. In subchannel 10, a hairpin shaped vortex is formed as shown in Fig. 3(*d*). In the northeast region of the subchannel, the maximum lateral velocity is located along the surface of the northeast rod in the north rod gap at axial locations of 6.3 to 17.0D_h. In this region, flow is entering the subchannel. The maximum lateral velocity in the southwest region of the subchannel is located along the surface of the southwest rod at streamwise locations of 6.3 and 8.5D_h. At an axial location of 12.7D_h, the maximum remains along the surface of the southwest rod, and is located in the west rod gap. The maximum lateral velocity is located in the west rod gap at 17.0D_h.

The flow structure in subchannels 5, 6, and 7 is characterized by a vortex and further analysis of the lateral flow field is performed in these subchannels. The center of the vortex is taken as the centroid of vorticity and is used to show the migration of the vortex within the subchannels. Figure 6 presents the centroid of vorticity in subchannels 5, 6, and 7 for seven streamwise locations ranging from 6.3 to 17.0D_h. For each subchannel, the filled symbol indicates the centroid of vorticity at 6.3D_h. The open symbols indicate the migration of the vortex for the three additional streamwise locations ranging from 8.5 to 17.0D_h. In subchannel 6 at a streamwise location of 6.3D_h, the vortex is located just north of the center of the subchannel whereas the vortex is located to-

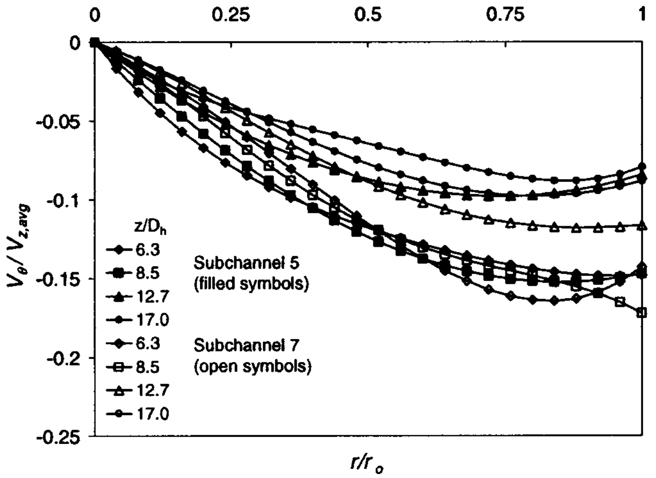

Fig. 7 Radial profiles of azimuthal velocity for subchannels 5 and 7 (r_o=2.5 mm)

ward the surface of the southeast rod in subchannels 5 and 7. As the flow develops in the streamwise direction in all three subchannels, the vortex migrates towards the southeast rod. The rod bundle data of McClusky et al. [6] for a support grid with a single split-vane pair shows that the center of the vortex migrates towards the northwest rod in the subchannel for axial locations of 8.5 to 17.0D_h. The centroid of vorticity is employed as the origin of the coordinate system for calculation of the radial profiles of azimuthal velocity and the streamwise development of the angular momentum.

Radial profiles of azimuthal velocity are shown in Fig. 7 for subchannels 5 and 7 and in Figs. 8 and 9 for subchannel 6. The shape of the radial profile of azimuthal velocity is consistent with a forced-free vortex. The azimuthal velocity follows a forced vortex profile from a radius of zero where the azimuthal velocity is zero to the radial location of the maximum azimuthal velocity. In the region from the location of the maximum azimuthal velocity to the edge of the vortex, the azimuthal velocity profile follows that of a free vortex. This qualitative behavior is similar to a Lamb-Oseen vortex (Chen et al. [25] and McClusky et al. [6]). As the flow develops in the streamwise direction, the azimuthal velocity decreases and the radial location of the maximum azimuthal velocity moves toward the center of the vortex.

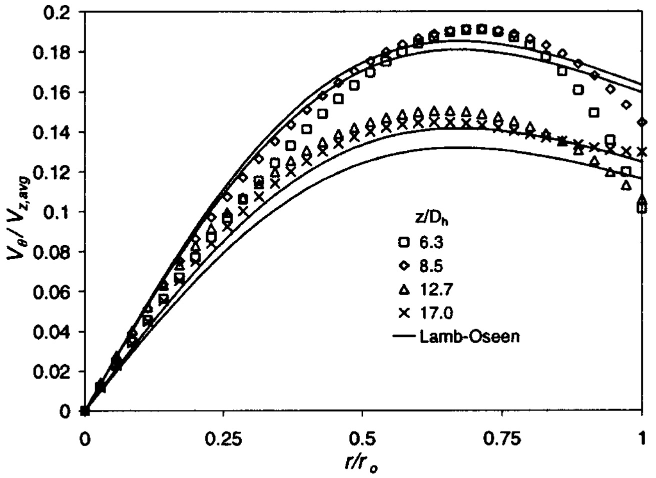

Fig. 8 Radial profiles of azimuthal velocity in subchannel 6 (r_o=3.5) mm)

z/D_h	6.3	8.5	12.7	17.0
$\Gamma(\mathrm{cm}^2/\mathrm{s})$	9.11	10.01	7.13	6.64

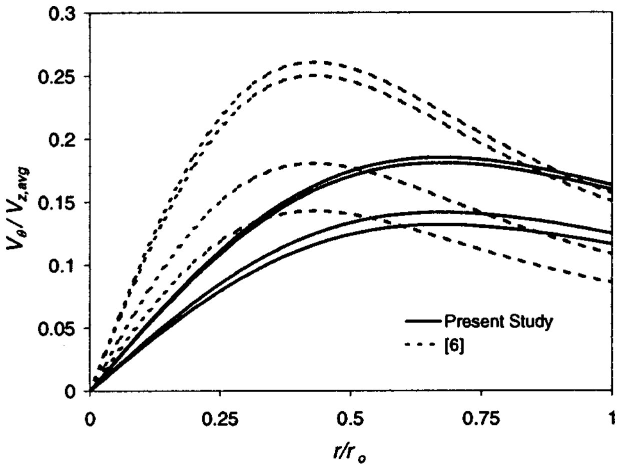

Fig. 9 Comparison of radial profiles of azimuthal velocity for subhcannel 6 of the present study with [6] (r_o=3.5 mm)

Figure 7 presents the radial profiles of azimuthal velocity for subchannels 5 and 7. The swirling flow structures in subchannels 5 and 7 rotate in a clockwise direction as opposed to the counterclockwise rotation of the swirling flow structures in subchannel 6; therefore, the magnitude of the tangential velocity has a negative value. Figure 8 presents the radial profiles of azimuthal velocity for subchannel 6. McClusky et al. [6] used the Lamb-Oseen vortex as an analytical model for the radial profiles of azimuthal velocity. The analytical model for a Lamb-Oseen vortex is

$$V_\theta(r,t)=\frac{\Gamma_0}{2\pi r}(1-e^{-r^2/4\nu t}) \tag{2}$$

where Γ_0 is the asymptotic limit of circulation and is taken as the circulation for a circular region with a 2.5 mm radius located at the centroid of vorticity and following Chen et al. [25] and McClusky et al. [6] $4\nu t$ is taken as a constant. In the rod bundle study of McClusky et al. [6], $4\nu t$ was $1.8\times10^{-6}\,\mathrm{m}^2$ and for subchannel 6 of the present study $4\nu t$ was determined as $4.4\times10^{-6}\,\mathrm{m}^2$. The resulting radial profiles of azimuthal velocity are shown in Fig. 8. The experimental data and the analytical predictions qualitatively agree.

Figure 9 compares the radial profiles of azimuthal velocity developed using the Lamb-Oseen model for the present study with those of McClusky et al. [6]. Both investigations were acquired at the same flow conditions; however, the design of the support grids was different. The support grid employed in McClusky et al. [6] had a single split-vane pair in subchannel 6 and the vanes in all other subchannels were aligned with the bulk flow so that swirling flow was created only in subchannel 6. This flow condition may be thought of as swirling flow in a single subchannel that is surrounded by infinite parallel channels or as swirling flow in a subchannel without wall effects. In the present study, the support grid had split-vane pair located in all subchannels and welds are formed on the grid at the center of the subchannel as shown in Fig. 1(*c*). The azimuthal velocity magnitude is larger for the data of McClusky et al. [6] than the present study. The maximum velocity is located closer to the center of the vortex for the data in McClusky et al. [6] than for the data of the present investigation.

Figure 10 shows the streamwise development of the normalized angular momentum for subchannels 5, 6, and 7 of the present study. The angular momentum was determined for a circular region with a radius of 2.5 mm that is located at the centroid of vorticity. The angular momentum was normalized by the value of angular momentum at 6.3D_h and the values of angular momentum at 6.3D_h are provided in Table 3. At this streamwise location, the largest value of angular momentum results from the flow field in subchannel 6. As the flow develops in the streamwise direction,

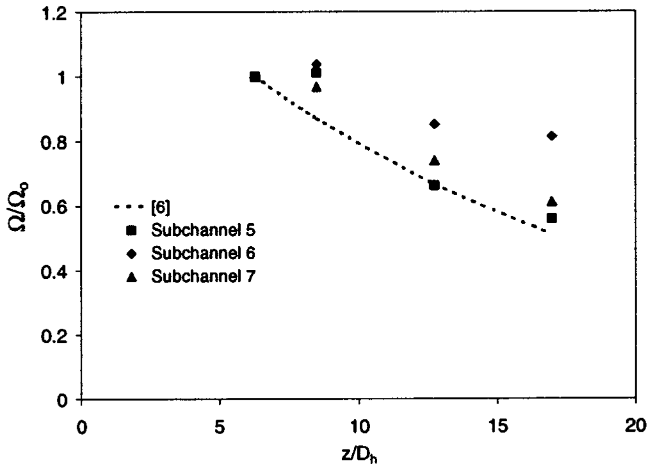

Fig. 10 Streamwise development of angular momentum (see Table 3 for values of angular momentum at 6.3D_h)

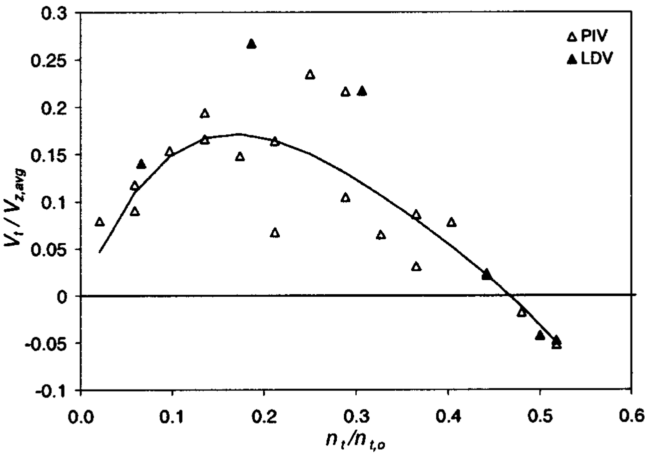

Fig. 11 Comparison of PIV and LDV data for subchannel 7 at 2.8D_h ($n_{t,o}$=8.32 mm)

the angular momentum decreases in the three subchannels. As shown in Fig. 10, the spatial decay of angular momentum is unique to each subchannel. McClusky et al. [6] characterized the spatial decay of angular momentum as

$$\Omega(z/D_h)=C_1e^{-C_2(z/D_h)} \tag{3}$$

Table 3 provides the coefficients C_1 and C_2 for the data of the present study and for McClusky et al. [6]. The coefficient C_2 characterizes the spatial decay of angular momentum, and the smallest value of C_2 is associated with subchannel 6. The lateral flow field in subchannel 6 had the largest value of angular momentum and decays at the slowest rate.

3.4 Comparison of PIV and LDV Measurements. This experimental program to document the velocity field in the rod bundle was conducted in collaboration with Mitsubishi Heavy Industries, Ltd. Mitsubishi Heavy Industries, Ltd independently performed the laser Doppler velocimetry (LDV) measurements in a rod bundle having the same geometry and grid as the present PIV measurements (Ikeda et al. [23]). The LDV data are truly a replication of the present PIV results, as the measurements were acquired in a completely separate flow loop.

Figure 11 provides a comparison between tangential velocity measurements from LDV and PIV in Subchannel 7 at a downstream location of 2.8D_h. The coordinate direction is normal to rod 13, and coincides with the line connecting the centers of rods 13 and 9 (Fig. 1(*b*)). The origin of the coordinate system is located on the surface of rod 13. A coordinate transformation of the PIV and the LDV data was performed to obtain the tangential velocity using this coordinate system. The tangential velocities from the PIV measurement in Fig. 11 were selected from the measured values of PIV that corresponded most closely to the LDV measurement locations. These measurement points are generally within 0.35 mm of the corresponding LDV measurements, with all locations less than 0.5 mm displaced from the LDV measurements. The positive sense of the PIV and LDV tangential velocity component is counterclockwise around rod 13. A curve representing a fourth-order polynomial fit to the PIV data is provided for comparison. Agreement between LDV and PIV measurements is reasonable, and the data show consistent trends with distance from the rod surface. Data were also compared for subchannel 7 at different axial coordinate locations and indicated similar agreement between the independent LDV and PIV measurements. Similar comparisons were made for subchannels 6 and 10 for several axial measurement locations. These comparisons suggest that the location of the flow structures may have been somewhat different in the two facilities, with the flow field in subchannel 10 exhibiting the greatest differences.

Table 3 Angular momentum parameters

Subchannel	Ω (cm^2/s) z/D_h=6.3	C_1 (cm^2/s)	C_2
5	5.59	8.62	0.061
6	6.67	7.96	0.023
7	5.93	8.30	0.049
[6]	⋯	15.5	0.063

As previously mentioned, comparison of the data from these two experiments is a data replication. The combination of the high velocity gradients near the surface of the rods and the uncertainty in the location of the rod surface in the PIV measurements may contribute to the observed differences in the tangential velocity measurements.

4 Summary

The present study documents detailed lateral flow fields for a 5×5 rod bundle assembled using support grids with split vane pairs. Fundamental data from 5×5 (or similar) testing is used to develop local heat transfer and local mass exchange parameters for use in full core thermal design models of a nuclear reactor. This is an accepted and licensed methodology that is also used in safety related DNB testing. Investigation of the detailed lateral flow field downstream of a support grid with vanes provides important information that can be used to benchmark models which can be used to develop improved support grid and vane designs.

Particle image velocimetry was employed to measure the lateral flow field at streamwise locations in four subchannels of a model fuel assembly. The support grids of the model fuel assembly had split-vane pairs located on the downstream edge. Vortical structures are shed from the vanes and persisted in the streamwise direction. The streamwise development of the lateral velocity field was documented using integral measures such as lateral kinetic energy, maximum lateral velocity, centroid of vorticity, radial profiles of azimuthal velocity, and angular momentum. Data were presented for a nominal Reynolds number of 28,000 and for seven streamwise locations ranging from 1.4 to 17.0D_h. The results of the present study were compared with McClusky et al. [6] and with the laser Doppler velocimetry measurements of Mitsubishi Heavy Industries, Ltd (Ikeda et al. [23]). The flow fields in this paper are representative of the flow fields downstream of split vane pairs having a weld nugget cutout in a 5×5 rod bundle. The major flow structures for this type of geometry have been presented and discussed. While the details of the split vane pair grid-design and some data are proprietary, enough information hasbeen provided for general CFD benchmarking.

The streamwise development of the lateral flow field was divided into Region I and II based on the flow structure. Region I begins at the vane tips and extends to $4.2D_h$. In Region I, multiple vortices are present in the subchannel. A corotating vortex pair is shed from the vane tips and the vortex pair persists downstream whereas the knee vortices dissipate. As the flow develops in the streamwise direction, the tip vortices interact. Interactions include dissipation of one vortex or merger of the two tip vortices. At $4.2D_h$ in Region I, a single vortex is present; however, it is not a coherent circular shape. Region II extends from 6.3 to $17.0D_h$, and a single vortex (subchannels 5, 6, and 7) or hairpin shaped flow structure (subchannel 10) forms in the subchannel. In this region, the vortex migrates in the subchannel as the flow develops in the streamwise direction. The flow structure in Region II of the present data agreed well with the flow structure predicted by the CFD results of Imaizumi et al. [14]. Herr and Pröbstle [3] showed that the normalized velocity profiles in the vane region are Reynolds number independent ($2{,}000<\mathrm{Re}<60{,}000$); therefore, the lateral flow structures observed in the present paper ($\mathrm{Re}=28{,}000$) may be qualitatively similar to in-core conditions ($\mathrm{Re}=500{,}000$) of an actual pressurized water reactor.

The integral measures show that the strength of the swirling flow differs among the four subchannels examined in the present study. The lateral velocities in subchannel 6 were larger than in subchannels 5, 7, and 10. In addition, the angular momentum in subchannel 6 had the slowest spatial decay. As the flow developed in the streamwise direction, the vortices in subchannels 5, 6, and 7 migrate toward the southeast rod. The radial profiles of azimuthal velocity in subchannels 5, 6, and 7 were modeled using the analytical form of the azimuthal velocity for a Lamb-Oseen vortex. The measured data were well predicted by the Lamb-Oseen vortex model. Differences in the lateral flow fields have been identified for several subchannels in the 5×5 rod bundle. While these differences are not completely understood, subtle differences in the support grid design, peripheral vane orientation, and the effect of lateral walls are expected to contribute to the differences in these flow fields.

Acknowledgments

This material is based in part upon work supported under a National Science Foundation Fellowship to the second author.

Nomenclature

C_1 = coefficient in angular momentum correlation (cm^2/s)
C_2 = coefficient in angular momentum correlation
D = rod diameter (m)
D_h = hydraulic diameter of the subchannel (m)
P = rod center-to-center pitch (m)
n_t = normal coordinate direction from surface of rod 13 to surface of rod 9 (m)
$n_{t,o}$ = normal coordinate distance from surface of rod 13 to surface of rod 9 (m)
r = radius (m)
r_o = maximum radius of circle used for velocity profiles (m)
Re = Reynolds number based on hydraulic diameter
S = subchannel
t = time (s)
u = x-direction velocity (m/s)
v = y-direction velocity (m/s)
V_l, = lateral velocity, $V_l=\sqrt{u^2+v^2}$, (m/s)
V_t = tangential velocity (m/s)
V_z = axial velocity (m/s)
V_θ = azimuthal velocity (m/s)
W = rod center to housing wall distance (m)
x = lateral PIV coordinate (m)
y = lateral PIV coordinate (m)
z = streamwise coordinate (m)
ν = kinematic viscosity (m^2/s)
Φ = lateral kinetic energy (m^2/s^2)
Γ_0 = circulation (cm^2/s)
Ω = angular momentum (cm^2/s)

References

[1] Conner, M. E., Smith, L. D. III., Paramonov, D. V., Liu, B., and Dzodzo, M., 2003, ''Understanding and Predicting the Flow Field in a Reactor Core,'' *Proceedings of the ENS TopFuel 2003/ANS LWR Fuel Performance Meeting 2003 Topfuel Conference*, Mar. 16–19, Wurzburg, Germany INFORUM GmbH, Bonn, Germany.

[2] Holloway, M. V., Conover, T. A., McClusky, H. L., Beasley, D. E., Conner, M. E., ''The Effect of Support Grid Design on Azimuthal Variation in Heat Transfer Coefficient for Rod Bundles,'' Proceedings of the 2003 ASME International Mechanical Engineering Congress and Exposition, Washington D.C, Nov., IMECE2003-41939.

[3] Herr, W., and Pröbstle, G., 1987, ''Index Matched Flow Measurements in Rod Bundles Near Grid Spacers With Swirl Generators,'' *Second Annual Conference on Laser Anemometry: Advances and Applications*, Sep., Strathclyde, UK, Institution of Mechanical Engineers, London, pp. 117–129.

[4] Karoutas, Z., Gu, C., and Schölin, B., 1995, ''3-D Flow Analysis for Design of Nuclear Fuel Spacer,'' *Proceedings of the Seventh International Meeting on Nuclear Reactor Thermal-Hydraulics*, Sept., Saratoga Springs, NY, American Nuclear Society, La Grange Park, IL, **4**, pp. 3153–3174.

[5] Saffman, P. G., 1992 *Vortex Dynamics*, Cambridge University Press, New York.

[6] McClusky, H. L., Holloway, M. V., Beasley, D. E., and Conner, M. E., 2002, ''Development of Swirling Flow in a Rod Bundle Subchannel,'' ASME J. Fluids Eng., **124**, pp. 747–755.

[7] Herer, C., 1991, ''3-D Flow Measurements in Nuclear Fuel Rod Bundles Using Laser Doppler Velocimetry,'' *Proceedings of the ASME FED Fluid Measurements and Instrumentation Forum*, ASME, New York, **108**, pp. 95–97.

[8] Yang, S. K., and Chung, M. K., 1998, ''Turbulent Flow Through Spacer Grids in Rod Bundles,'' ASME J. Fluids Eng., **120**, pp. 786–791.

[9] Shen, Y. F., Cao, Z. D., and Lu, Q. G., 1991, ''An Investigation of Crossflow Mixing Effect Caused by Grid Spacer With Mixing Blades in a Rod Bundle,'' Nucl. Eng. Des., **125**, pp. 111–119.

[10] Ouma, B. H., and Tavoularis, S., 1991, ''Flow Measurements in Rod Bundle Subchannels With Varying Rod-Wall Proximity,'' Nucl. Eng. Des., **131**, pp. 193–208.

[11] Meyer, L., 1994, ''Measurements of Turbulent Velocity and Temperature in Axial Flow Through a Heated Rod Bundle,'' Nucl. Eng. Des., **146**, pp. 71–82.

[12] Krauss, T., and Meyer, L., 1996, ''Characteristics of Turbulent Velocity and Temperature in a Wall Channel of a Heated Rod Bundle,'' Exp. Therm. Fluid Sci., **12**, pp. 75–86.

[13] Smith III, L. D., Conner, M. E., Liu, B., Dzodzo, M. B., Paramonov, D. V., Beasley, D. E., Langford, H. M., and Holloway, M. V., 2002, ''Benchmarking Computational Fluid Dynamics for Application to PWR Fuel,'' *Proceedings of ICONE 10*, Apr., Arlington, VA, Paper No. ICONE 10-22475.

[14] Imaizumi, M., Ichioka, T., Hoshi, M., Teshima, H., Kobayashi, H., and Yokoyama, T., 1995, ''Development of CFD Method to Evaluate 3-D Flow Characteristics for PWR Fuel Assembly,'' *Transactions of the 13th Annual Conference on Structural Mechanics in Nuclear Technology*, Aug., Porto Alegre, Brazil, IASMIRT, pp. 3–14.

[15] In, W. K., 2001, ''Numerical Study of Coolant Mixing Caused by the Flow Deflectors in a Nuclear Fuel Bundle,'' Nucl. Technol., **134**, pp. 187–195.

[16] Ikeda, K., and Hoshi, M., 2002, ''Development of Mitsubishi High Thermal Performance Grid,'' JSME International Journal Series B, **45**(3), pp. 586–591.

[17] Raffel, M., Willert, C., and Kompenhans, J., 1998, *Particle Image Velocimetry*, Springer, Berlin.

[18] Adrian, R. J., 1991, ''Particle-Imaging Techniques for Experimental Fluid Mechanics,'' Annu. Rev. Fluid Mech., **23**, pp. 261–304.

[19] Keane, R. D., and Adrian, R. J., 1992, ''Theory of Cross-Correlation Analysis of PIV Images,'' Appl. Sci. Res., **49**, pp. 191–215.

[20] PTC 19.1, 1998, Test Uncertainty, *ASME Performance Test Codes*, ASME New York.

[21] Armfield, M. V., 2001, ''Effects of Support Grid Design on Local, Single-Phase Turbulent Heat Transfer in Rod Bundles,'' *Master's thesis*, Clemson University, Clemson, SC.

[22] Armfield, M. V., Langford, H. M., Beasley, D. E., and Conner, M. E., 2001, ''Single-Phase Turbulent Rod Bundle Heat Transfer,'' *Proceedings of 2001 ASME International Mechanical Engineering and Exposition*, ASME, New York, IMECE2001/HTD-24116, pp. 1–8.

[23] Ikeda, K., Makino, Y., and Hoshi, M., 2003, ''Development of CFD Analysis to Estimate Flow Behavior of PWR Grid Spacer,'' *Proceedings of ICONE-11*, Tokyo, Japan, Paper ICONE11-36087.

[24] Devenport, W. J., Vogel, C. M., and Zsoldos, J. S., 1999, ''Flow Structure Produced by the Interaction and Merger of a Pair of Co-rotating Wing-Tip Vortices,'' J. Fluid Mech., **394**, pp. 357–377.

[25] Chen, A. L., Jabob, J. D., and Savas, Ö, 1999, ''Dynamics of Corotating Vortex Pairs in the Wakes of Flapped Airfoils,'' J. Fluid Mech., **382**, pp. 155–193.

[26] Meunier, P., Ehrenstein, U., Leweke, T., and Rossi, M., 2002, ''A Merging Criterion for Two-Dimensional Co-rotating Vortices,'' Phys. Fluids, **14**, pp. 2757–2766.

Lijun Song
Research Assistant

John Abraham
Professor

School of Mechanical Engineering,
Purdue University,
West Lafayette, IN 47907

The Structure of Wall-Impinging Jets: Computed Versus Theoretical and Measured Results

In this work, the structure of computed wall-impinging gas jets is compared with theoretical and experimental results presented in the literature. The computational study employs the k-ε model to represent turbulence. Wall functions are employed to model momentum transfer at the walls. The computed penetration and growth rate of the jet agree with measured and analytical results within 10%. Computed radial velocities in the developed region of the wall jet are self-similar as found in prior experimental and analytical works. The computed radial velocity profile and quantitative values in the outer layer of the jet and the location of the maximum radial velocity agree within 5% with measurements and analytical results. Greater quantitative differences are found in the near-wall region. Mixing characteristics of a wall-impinging jet are compared with those of a round free jet. The wall-impinging jet mixes slower than the round free jet. [DOI: 10.1115/1.1625686]

Introduction

Wall-impinging jets are formed when a free jet impinges on a wall. In our work, we will focus on turbulent round free jets impinging normal to a flat wall. Once the turbulent round free jet impinges on the wall, it spreads radially along the wall and forms a turbulent wall jet. Figure 1 is a schematic representation of the arrangement. The jet shown in Fig. 1 may be divided into three regions: the free jet region, the impingement region and the radial wall jet region, [1]. In this paper, we will use *x* to denote the radial axis and *y* to denote the vertical axis in the jet as indicated on Fig. 1. It is assumed that the wall has no effect on the jet in the free jet region, [2,3].

Wall-impinging jets are encountered in several engineering applications. Such jets are often employed to enhance heat transfer rates, [4,5]. In diesel engines, the impingement of the spray jet on the piston and cylinder walls may lead to flame quenching, a reduction in thermal efficiency and an increase in particulate and unburned hydrocarbon emissions, [6–8]. In fact, our study is motivated by our desire to improve the modeling of these jets within the context of diesel engine applications. In diesel engines operating under warm conditions, i.e., as opposed to cold-start conditions, the liquid fuel itself is unlikely to impinge on the wall as the liquid most likely vaporizes before impingement, [9–12]. Hence, it is the vapor that is likely to impinge on the wall. Thus, our interest is in wall-impinging gas jets.

There have been several prior studies of the structure of the jet in the radial wall jet region shown in Fig. 1. We will subsequently refer to this portion of the jet as the turbulent wall jet. These prior studies will be reviewed below. We will review experimental studies first and then, analytical and computational studies.

One of the earliest experimental studies of the wall jet was that of Bakke [13]. His measurements were obtained by supplying air through a nozzle with an orifice diameter, *D*, of 2.84 cm. The impinging distance, *L*, between the orifice and the wall was 1.5 cm giving an L/D ratio of about 0.53. The jet Reynolds number based on the mean injection velocity, orifice diameter and air diffusivity was about 4.8×10^3. Radial velocity distributions were obtained with a Pitot tube at nondimensional radial distances, x/L, in the range of 9.5 to about 20.2, where *x* is the radial distance from the origin as shown in Fig. 1. In this region, the radial velocity in the wall jet was found to be self-similar when the radial velocity at any radial location was normalized by the maximum radial velocity at that location and the perpendicular distance from the wall was normalized by the half-width of the jet at the radial location. The half-width is defined as the perpendicular distance from the wall to the point between the location of the maximum velocity and the ambient fluid where the velocity is half of the maximum velocity. It was also shown that the rates of decay of the maximum radial velocity and growth of the half-width with respect to the radial distance from the impingement point could be expressed by simple power laws.

Tanaka and Tanaka [14] employed an experimental configuration similar to that of Bakke [13] and considered effects of nozzle orifice diameter and impinging distance. L/D ratios were varied from 0.05 to 0.1. The jet Reynolds number varied from 8.5 $\times10^4$ to 2.3×10^5, i.e., one or two orders of magnitude greater than in the measurements of Bakke [13]. Mean velocities were measured with a hot-wire anemometer at nondimensional radial distances, x/L, of 2 to 100 from the impingement point. The rates of change of the maximum radial velocity and the half-width with the radial distance were found to be close to the results obtained by Bakke [13].

In the two cases above, the measurements were obtained with relatively small L/D ratios such that a free jet region was not present before the impingement. Poreh et al. [15] carried out measurements in wall-impinging jets where L/D ratios were varied from 8.0 to 24.0. The jet Reynolds number varied from 1.2 $\times10^5$ to 3.3×10^5. Mean velocities and turbulence intensities were measured with a constant-temperature hot-wire anemometer at nondimensional radial distances of 0.4 to 2.9. The measured maximum radial velocity and half-width were shown to fit power laws just as in the measurements of Bakke. In addition, they proposed expressions relating the maximum radial velocity and the half-width to the radial distance from the impingement point. Witze and Dwyer [16] employed an experimental configuration similar to that of Poreh et al. [15] and measured the maximum radial velocity and half-width. In their measurements, L/D was 31.7. The jet Reynolds number was about 1.8×10^5. The velocities were measured at nondimensional radial distances of 0 to 1.0. The

---

Contributed by the Fluids Engineering Division for publication in the JOURNAL OF FLUIDS ENGINEERING. Manuscript received by the Fluids Engineering Division February 18, 2002; revised manuscript received July 15, 2002. Associate Editor: A. K. Prasad.

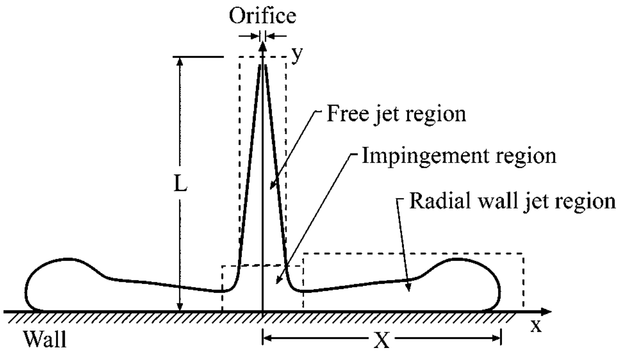

Fig. 1 Structure of an impinging jet

measured constants in the power relationships relating the maximum radial velocity and the half-width to the radial distance were shown to be close to those of Poreh et al. [15]. It is interesting to note that Launder and Rodi [17] in a review of experimental studies of wall jets suggested a linear rather than a power relationship for the growth rate of the half-width with the radial distance, which appears reasonable as the exponent in the power relationship is close to unity.

From a practical point of view, Tomita et al. [18] have reported jet volume measurements in transient-free and wall-impinging jets with the objective of determining entrainment rates in the two jets and comparing them. In their work, air was injected into ambient air where the pressure was 101 kPa and the temperature was 295 K. Three different nondimensional impinging distances, 18.9, 39.6, and 61.0 were considered. The jet Reynolds number was about 1.3×10^4. The jet volume was estimated from particle images which identified the boundary of the jet. It was shown that, for a period time after impingement, the rate of increase of entrained volume for the wall-impinging jet was greater than the rate of increase of entrained volume for the free jet but that the differences reduced with increasing time after impingement, and finally the rate of increase became slower than that of the free jet.

Glauert [19] carried out an analytical study of the turbulent wall jet. The flow at any radial cross section was divided into two regions: an inner region close to the wall and an outer region further away from the wall. The two regions were separated by a middle region where the radial velocity was a maximum. For the inner region, where wall effects are dominant, the velocity was assumed to follow the 1/7th power-law velocity profile of Blasius. In the outer region, where free-shear effects are more dominant, Prandtl's mixing-length hypothesis was employed with the assumption of constant turbulent diffusivity. The two solutions were matched at the point where the radial velocity is a maximum. Shear stresses were assumed to be zero at the point of maximum radial velocity. Glauert obtained a similarity velocity profile which showed agreement with the measured results of Bakke [13] above.

There are also several computational studies reported in the literature that evaluate the capability of turbulence models to predict the flow characteristics of turbulent wall jets. Patankar and Spalding [20] employed the mixing-length hypothesis and showed that satisfactory spreading rate can be achieved if model constants are adjusted. The spreading rate refers to the proportionality constant relating the half-width to the radial distance if a linear relationship exists between them. No conclusions were drawn about velocity profiles in the wall jet. Launder and Rodi [17] stated that for a plane wall jet formed by the impingement of a plane free jet on a wall, the computed spreading rate obtained with the k-ε model may be 30% greater than in experiments. There are no studies employing the k-ε model to study the spreading rate and the velocity profile in radial wall jets which is our interest in this work.

The Contribution of This Work

In this work, a multidimensional model is employed to compute the structure of wall-impinging jets. Our computations are of turbulent round free jets that impinge on walls to form radial wall jets. We investigate the jet from the start of injection. As the jet penetrates into the ambient gas, and after impingement on the wall, the jet may be divided into several sections at any instant in time. Within about 20 orifice diameters from the orifice in the free jet, there is the developing region of the jet where the velocity profile is not self-similar but the structure has reached a steady state. Beyond this point, but several diameters upstream of the impingement point, is the fully developed region of the free jet where the velocity profile is self-similar and the structure is steady. Then there is the impingement region. Beyond the impingement region, but some distance upstream of the tip of the wall jet is the fully developed region of the turbulent wall jet where the velocity profile is self-similar and steady. Then there is the head vortex region which continues to penetrate. In subsequent discussions in this paper, we will investigate the penetration of the tip of the jet with respect to time, i.e., the penetration rate, as well as the structure of the wall jet in the region where self-similarity and steady state have been reached. So, part of our jet is always transient but the other part is at steady state.

In the work presented below, first, the computed rates of jet tip penetration are compared with the measurements of Fujimoto et al. [3]. The measurements of Fujimoto et al. were only of the transient part of the jet and this will be reviewed below. Then, the computed velocity profile, half-width, and maximum radial velocity variations with radial distance and perpendicular-to-wall distance in the wall jet are compared with the measurements of Poreh et al. [15], Witze and Dwyer [16], Bakke [13], and the results from the theoretical analysis of Glauert [19]. Finally, we also compare the mixing characteristics of free and wall-impinging jets and highlight the differences between the two. In the next section, the specific experimental and theoretical results employed for comparisons with our computational results are described. The computational model and conditions are then discussed. Results and discussion follow. The paper ends with summary and conclusions.

Experimental and Theoretical Results

The computed jet tip penetrations in this work will be compared with the measurements of Fujimoto et al. [3]. They presented measurements of jet tip penetrations of transient free and wall-impinging jets as a function of time after start of injection (ASI). The measurements were obtained by injecting acetylene gas, C_2H_2, through a nozzle of 0.16 cm diameter into air where the pressure was 101.3 kPa and the temperature was 293 K. The injection duration was 26 ms with a mean injection pressure of 2.9 kPa. The nozzle orifice was placed at 1.5, 2.0, and 3.0 cm above the wall, i.e., at L/D ratios of 9.4, 15.6, and 18.8. The jet Reynolds number was about 6.0×10^3. Two-dimensional images of both transient-free and impinging gas jets were taken by high-speed photography. Particle image velocimetry was employed to obtain the velocity distribution in the jets. In this paper, the penetration of the transient wall-impinging jet after impingement is defined as the summation of the impinging distance, L, and the radial distance, X, to which the jet has penetrated along the wall, as shown in Fig. 1. In the experiments, the penetrations following impingement, were found to be approximately proportional to the half power of time but smaller than that of the free jet.

In the steady part of the wall jet, the theoretical similarity velocity profile of Glauert [19] and the measured one of Bakke [13] are employed for comparison with the computed results. Furthermore, the maximum radial velocity and half-width will be compared with the measurements of Poreh et al. [15] and Witze and Dwyer [16]. The expressions of Poreh et al. [15] for these variables are

$$\frac{U_m L}{\sqrt{K}} = F_m \left(\frac{x}{L} \right)^m \tag{1}$$

$$\frac{y_{1/2}}{L} = F_n \left(\frac{x}{L} \right)^n \tag{2}$$

where U_m is the maximum radial velocity, $y_{1/2}$ is the jet half-width, x is the radial distance, and m and n are constants. F_m and F_n are generally functions of Reynolds number but were shown to have constant values in the measurements. In their work, Poreh et al. considered L as the distance from the geometrical origin of similarity of the round free jet to the wall. It is approximated as the distance from the orifice to the wall in our work. The values of F_m, F_n, m, and n from Poreh et al. [15] are

$$F_m = 1.32, \quad F_n = 0.098, \quad m = -1.10, \quad n = 0.90. \tag{3}$$

The values from Witze and Dwyer [16] for these constants are

$$F_m = 1.11, \quad F_n = 0.0946, \quad m = -1.12, \quad n = 1.01. \tag{4}$$

The spreading rate cited by Launder and Rodi [17] from their literature review is also employed for comparison. They assumed $n = 1$. Their spreading rate has a value of 0.09.

The Computational Model and Conditions

The multidimensional model employed in this work is an axisymmetric version of a more general model for computing flows, sprays, and combustion in engines, [21–24]. The governing equations that are solved are the general conservation equations with submodels for turbulence and momentum and heat fluxes at the walls. The equations are solved numerically by means of a fully implicit finite volume method, [21]. Turbulence is modeled using either a standard k-ε model [25] or a RNG k-ε model [26].

Wall functions proposed by Launder and Spalding [25] are used to model momentum and heat fluxes at the walls. In this model, source terms are added to the energy and momentum equations to account for fluxes at the walls. The source terms added to the momentum and energy equations have different formulations depending on the distance from the wall of the center, p, of the numerical cell closest to the wall. A nondimensional parameter, Y, is defined as

$$Y = \frac{u^* z_p \rho_g}{\mu_{\text{lam}}} \tag{5}$$

where u^* is the friction velocity, z_p is the distance from the wall to the center of the computational cell, ρ_g is the gas density, and μ_{lam} is the laminar viscosity. The friction velocity is modeled as a function of the turbulent kinetic energy of the near wall cell

$$u^* = C_\mu^{1/4} k_p^{1/2} \tag{6}$$

where C_μ is a model constant and k_p is the turbulent kinetic energy in the near wall cell.

If $Y \leqslant 11.63$, the center of the cell is assumed to be in the laminar sublayer. The flux of momentum is then given by

$$\tau_w = -\frac{\mu_{\text{lam}}}{z_p} u_p . \tag{7}$$

If $Y > 11.63$, the center of the cell is assumed to be in the outer turbulent sublayer where the logarithmic velocity profile is valid. The flux of momentum is then given by

$$\tau_w = -\frac{\rho_g C_\mu^{1/4} k_p^{1/2} u_p}{\frac{1}{\kappa} \ln(EY)} . \tag{8}$$

Heat transfer is modeled in the same way, [21], but it is negligible in this work.

The value of k in the near-wall cell is obtained by solving the k equation. The values of ε_p in the near-wall cell are determined from an equilibrium assumption which states that the dissipation of k, ε, is equal to the production of k in that cell, yielding

$$\varepsilon_p = C_\mu^{3/4} k_p^{3/2} / (\kappa z_p). \tag{9}$$

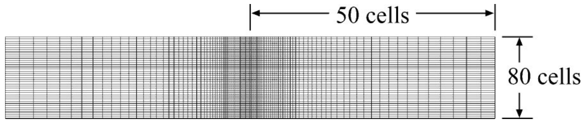

Fig. 2 Cross-section of the constant volume chamber

The model constants for the wall functions are, [27],

$$C_\mu = 0.09, \quad \kappa = 0.4187, \quad E = 9.793.$$

A note about low-Reynolds number models: The standard k-ε model coupled with wall functions has been relatively successful in many cases in predicting the structure of wall bounded flows. In these successful cases, the effects of turbulent diffusion are more dominant than molecular diffusion. For flows at low and transitional Reynolds numbers or close to walls, low-Reynolds number models have been suggested to incorporate effects of molecular viscosity, [28–31]. However, each model has proposed different additional corrections mostly from comparisons with flows in terms of global parameters such as mean velocity, k and ε, [32]. A universally applicable low-Reynolds number model has not yet been proposed. Wilcox [33] pointed out that the major contribution of low-Reynolds number models is to fix the k-ε model's problem in predicting the constant in the law of the wall. For flows in complex geometries such as in Diesel engines, some parameters used for the correction terms of low-Reynolds number models, including the nondimensional distance to the wall, are not well defined. In this work, we will not evaluate all these effects and focus only on the standard and RNG k-ε models.

The computations were carried out in an axisymmetric constant volume chamber shown in Fig. 2. The computational domain is a 1 deg sector with a bore of 10 cm. A stretched grid with a total of 50 cells in the radial direction is employed. The highest resolution in the radial direction is near the axis. A uniform grid size of 0.025 cm is used in the axial direction. Results with higher resolutions, which have a uniform 0.010 cm grid size in the axial direction and a stretched grid with 100 cells in the radial direction, will also be presented to show grid-independence of the lower resolution results. For the free jet computations, the chamber height is 15 cm. The chamber gas is at a pressure of 101 kPa and temperature of 293 K. The injection velocity is deduced from the injection pressure in measurements of Fujimoto et al. [3] as 6000 cm/s.

No-slip wall boundary conditions are employed for the chamber walls. Though the measurements were conducted in open environments, our choice of a closed chamber which will result in an increase in chamber density is not likely to affect the computed jet penetration since the ratio of injected mass to the initial mass in the chamber is about 2.0×10^{-4} at 25 ms ASI for a case where the impinging distance is 2.0 cm. Comparisons between measured and computed results are made before the wall jet reaches the wall.

The jet diffusivity, ν_{jet}, defined as $\nu_{\text{jet}} = C_t K^{0.5}$, [34–36], is 13.7 cm^2/s. K is the injection kinematic momentum. C_t is a constant and we have used a value of 0.0161, [35]. We performed the computation with initial values of k and ε of 14.8 cm^2/s^2 and 1.98×10^3 cm^2/s^3, respectively, in the chamber. As a result, the initial ambient diffusivity has a value of 0.01 cm^2/s. From prior work we know that, as this diffusivity is much smaller than the jet diffusivity, the chamber diffusivity has negligible effect on the mixing characteristics of the jet, [34]. The computed penetration for impinging jets is defined as the impinging distance plus the maximum radial distance where the fuel mass fraction reaches a cutoff value of 0.01. Computed results with a different initial diffusivity and a different cutoff value for fuel mass fraction will also be presented to assess the effect of these variables on the results.

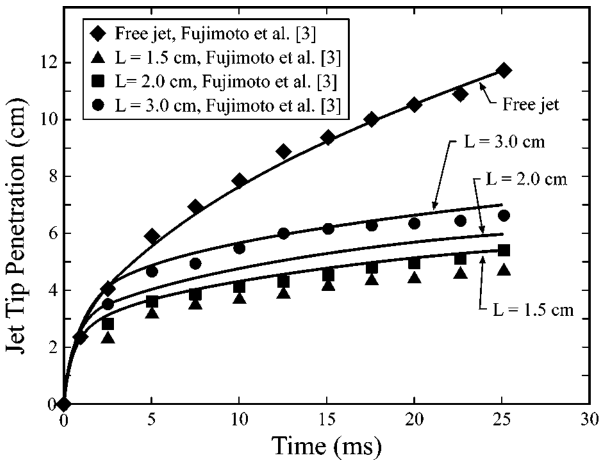

Fig. 3 Measured and computed jet penetrations of free and impinging jets; 0.25 mm (axial)×0.20 mm (radial) minimum grid size

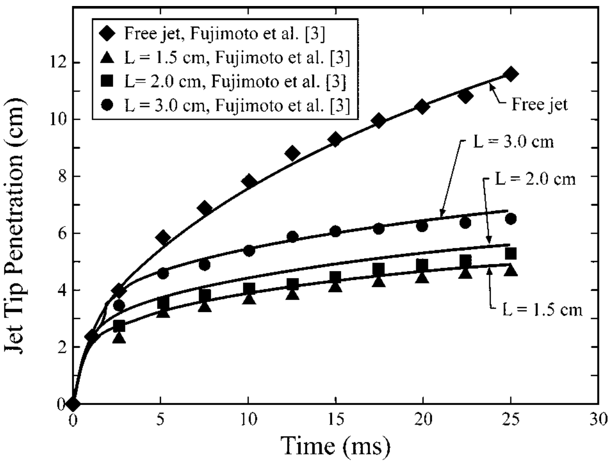

Fig. 5 Measured and computed tip penetrations of free and impinging jets; 0.10 mm(axial)×0.10 mm(radial) minimum grid size

Results and Discussion

Figure 3 shows the measured and computed jet penetrations as a function of time after start of injection (ASI). Results are shown for a free jet and for three impinging jets. The orifice diameter is 0.16 cm. In the case of the computed results, the jet boundary is defined as the locus of points where the fuel mass fraction has reached a value of 0.01. The numerical spatial resolution employed in the computation corresponds to a minimum grid size of 0.025 cm (axial)×0.020 cm (radial). In the case of the free jet, the computed and measured results may be seen to agree within 5%. This is not surprising. It has been shown in prior work that, when adequate resolution is employed, free jet penetration may be reproduced within 5% to 10%, [34]. Closer agreement is not expected because it is well known that the k-ε model has a limitation in reproducing the measured spreading rates of round jets, [37]. The computed spreading rate is typically higher and this results in a slower penetration. In the case of the wall-impinging jets, the differences between computed and measured results are somewhat greater than for free jets. For example, at 20 ms ASI, the measured penetration for the case where the impinging distance is 2.0 cm is 5.0 cm whereas it is 5.7 cm in the computation—a difference of about 14%. Now we will consider effects of numerical resolution on the results for a wall impinging jet.

Figure 4 shows the effect of numerical spatial resolution on the computed results of jet penetration. Results obtained with four resolutions are shown along with the measured results of Fujimoto et al. [3]. The results are shown for the case where the distance from the injector orifice to the wall is 2.0 cm. The resolution of 20 (axial)×50 (radial) corresponds to a minimum grid size of 0.1 cm (axial)×0.02 cm (radial). The 80×50 resolution corresponds to 0.025 cm×0.02 cm. The 200×100 resolution corresponds to 0.01 cm×0.01 cm and the 300×150 corresponds to 0.0067 cm×0.0067 cm. It may be seen that as the resolution is increased the computed jet penetration decreases and approaches the measured value and the numerical results show convergence. For example, at 20 ms ASI, the computed jet penetration is 6.5 cm with the 20×50 grid, 5.7 cm with the 80×50 grid, 5.3 cm with the 200×100 grid, and 5.3 cm with the 300×150 grid where the measured value is 5 cm. These differences correspond to 30%, 14%, 6%, and 6%, respectively. The computed jet penetration with the 300×150 grid is within 3% of that with the 200×100 grid before 5 ms. Figure 5 shows the computed jet penetrations with the 200×100 grid, i.e., 0.01 cm×0.01 cm minimum grid size, for the three impinging jets. The differences between computed and measured results are within 10% for all cases.

It is interesting to explore the effects of wall momentum loss on the computed results. Figure 6 shows computed jet penetrations obtained with the 200×100 grid employed above when free-slip and no-slip boundary conditions are imposed at the walls. It is shown that the computed penetration after impingement with the free-slip boundary condition is higher than that with the no-slip

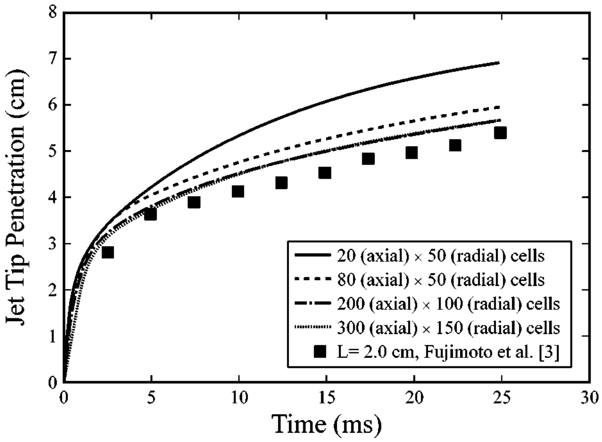

Fig. 4 Effects of resolution on computed tip penetrations

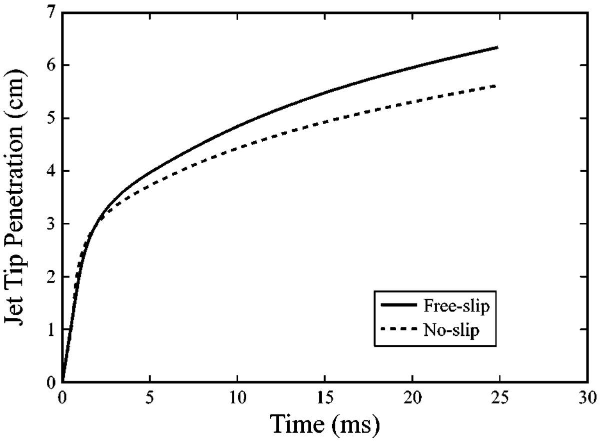

Fig. 6 Computed jet penetrations with no-slip and free-slip boundary conditions

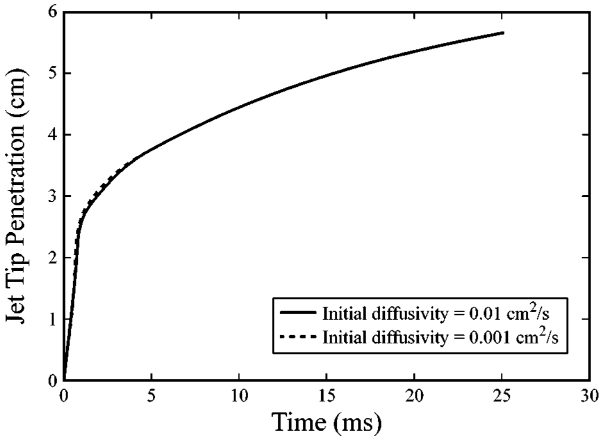

Fig. 7 Effects of initial ambient diffusivity on computed jet penetrations

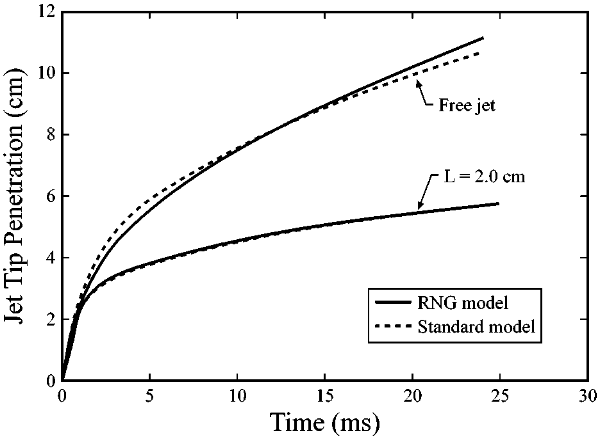

Fig. 9 Computed jet penetrations with standard *k*-*ε* model and RNG *k*-*ε* model

boundary condition. For example, at 20 ms ASI, the momentum loss to the wall reduces the jet penetration by about 12%.

Now we will consider the sensitivity of the computed jet penetration to the initial value of ambient turbulent diffusivity and the manner in which the jet tip is defined. We have employed 0.01 cm^2/s for the initial turbulent diffusivity in the results presented up to this point. Figure 7 shows the computed penetration for the case where the impinging distance is 2 cm. Results are shown on the figure for two cases where different initial values of k and ε are employed which, in turn, result in different initial values of turbulent diffusivity. The diffusivity values are 0.01 cm^2/s and 0.001 cm^2/s. The corresponding values of k and ε are 14.8 $\mathrm{cm}^2/\mathrm{s}^2$, 1.98×10^3 $\mathrm{cm}^2/\mathrm{s}^3$ and 14.8 $\mathrm{cm}^2/\mathrm{s}^2$, 1.98×10^4 $\mathrm{cm}^2/\mathrm{s}^3$, respectively. The understanding is that if the initial value of chamber turbulent diffusivity is small relative to that generated by the jet, the jet diffusivity controls jet penetration and spreading, [34,37]. It may be seen that there are no noticeable difference in the results for the two cases indicating that an initial diffusivity of 0.01 cm^2/s is adequate.

We have defined the boundary of the jet as the locus of points where the fuel mass fraction is 0.01. This is somewhat arbitrary. In fact, defining the boundary of the jet in Reynolds-averaged computations, such as those presented here, in a way that the selected definition would be consistent with that employed in corresponding measurements is challenging, [34]. Our best hope is that the estimated value of jet penetration is not overly sensitive to this definition. Figure 8 shows the computed penetrations where the cutoff values for fuel fraction are 0.001 and 0.01. As expected there is a difference. At 20 ms ASI, the difference is about 5%. We will assume that this difference is rather small and that our conclusions are not affected by it.

Recently, the RNG k-ε model, [26], has been proposed as an alternative to the standard k-ε model, [25]. We have shown in prior work that the computed jet penetration and spreading rates of free jets are not noticeably affected by employing the RNG k-ε model in lieu of the standard k-ε model, [25]. What is the effect on the computed penetration of wall jets? Figure 9 shows the computed jet penetrations as a function of time ASI. Results are shown for the free jet and for the impinging jet where the impinging distance is 2.0 cm. Results are within 5% of each other showing that the differences in computed jet penetrations are rather small.

Now, we will present results in that part of the wall jet which has reached steady state. We will begin by considering the radial velocity distribution in the wall jet in the direction normal to the wall. Figure 10 shows the normalized radial velocity, $U(y)/U_m$, as a function of normalized distance, $y/y_{1/2}$, perpendicular to the wall. The velocity, $U(y)$, in a radial surface is normalized by the maximum radial velocity, U_m, at the surface. The distance, y, is normalized by the jet half-width, $y_{1/2}$. Computed results with the 200×100 grid, i.e., corresponding to 0.01 cm$\times$0.01 cm minimum

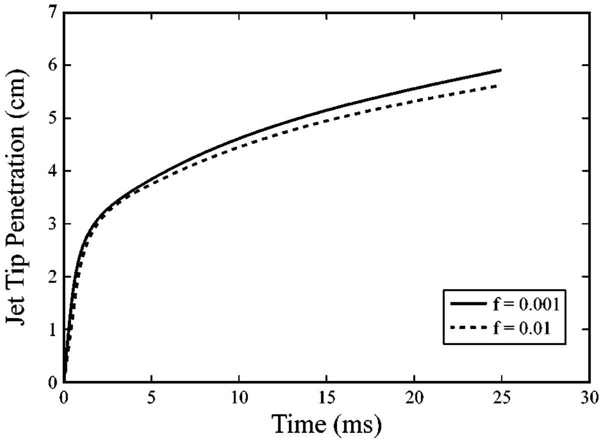

Fig. 8 Computed penetrations with different cutoff values for fuel mass fraction (*f*)

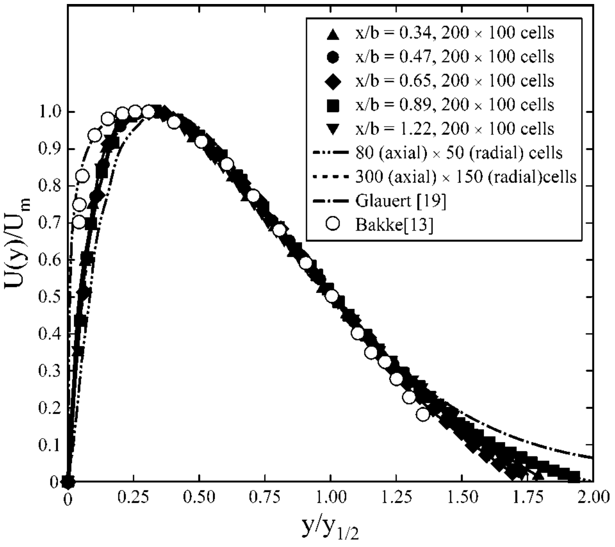

Fig. 10 Similarity velocity profiles in wall jets

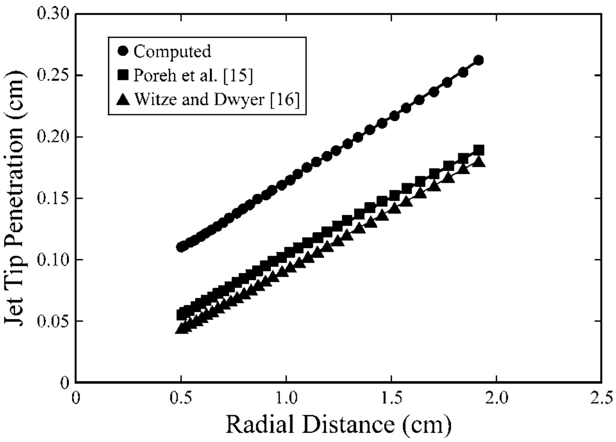

Fig. 11 Variation of the half-width of the jet with distance from the point of impingement

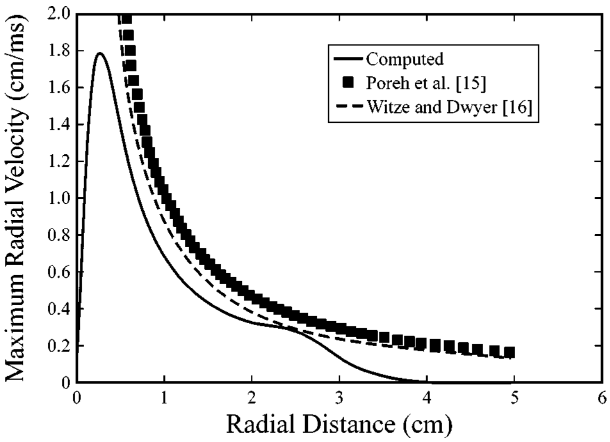

Fig. 12 Variation of the maximum radial velocity with distance from the point of impingement

grid size, are shown at nondimensional distances, x/L, of 0.34, 0.47, 0.65, 0.89, and 1.21. The computed results are compared with the analytical predictions of Glauert [19] and the measured results of Bakke [13]. It may be seen that at these radial locations, the computed velocity profiles are self-similar. The location of the maximum velocities, at a nondimensional distance of 0.25, agrees closely with the measured and analytical results. There is also close agreement between the computed, analytical, and measured results from $y/y_{1/2}$ of 0.25 to about $y/y_{1/2}$ of 1.25. Figure 10 also shows computed velocity profiles with the 300×150 grid, i.e., corresponding to 0.0067 cm×0.0067 cm minimum grid size, and with the 80×50 grid, i.e., corresponding to 0.025 cm×0.02 cm minimum grid size. There is no practical difference between the results with 200×100 cells and those with 300×150 cells. While the numerical results show convergence, even with the highest resolution the computed inner structure, i.e., for $y/y_{1/2}<0.25$, show greater differences than the outer structure when compared to measured and analytical results. A possible explanation is that in the region close to the wall, the laminar diffusivity becomes significant and comparable to the turbulent diffusivity. It appears that in the inner region of the jet, the model may predict the variation of the turbulent diffusivity which affects the corresponding velocity profile with less accuracy than in the outer region.

Figure 11 shows the jet half-width as a function of radial distance. Results are shown for the case where the impinging distance is 2.0 cm. The resolution employed corresponds to the 200×100 grid. In the wall jet region, it is found that a linear relationship

$$y_{1/2}=0.10x+0.06 \quad (\mathrm{cm}) \tag{10}$$

is able to describe the spreading rate obtained from the computation. The spreading rate proportionality constant, 0.10, is about 11% higher than the value of 0.09, given by Launder and Rodi [17] in their review paper. The half-width variation deduced from Eq. (2) with the constants in the equation obtained by Poreh et al. [15] and Witze and Dwyer [16] are also shown. The average measured spreading rate constant is about 0.95, i.e., within 6% of the computed value. The primary difference lies in the virtual origin of the wall jet.

Figure 12 shows the computed maximum radial velocity, U_m, at any radial location as a function of radial distance, x. It may be seen that initially the velocity increases as the free jet that impinges normally on the wall is redirected to form a radial wall jet. The velocity then decays. As implied in Fig. 6, this decay does not result primarily from the loss of momentum to the wall but as a result of entrainment of ambient air by the jet. Shown in Fig. 12 are also results from Eq. (1) with the constants in the equation obtained by Poreh et al. [15] and Witze and Dwyer [16]. While the shapes are relatively close, quantitative agreement of values between the results with different set of constants are only within 25% for the most part. Note that Eq. (1) is not valid in the impinging region (see Fig. 1) but only in the wall jet region.

Having ascertained the limitations of the models and studied the details of the structure of wall jets, we will now employ the model to study the differences in the mixing characteristics of a wall-impinging jet and a free jet. Recall that the measurements of Tomita et al. [18] imply faster entrainment rate in the wall-impinging jet immediately following impingement. We quantify mixing by adopting two approaches. In the first approach, we divide the injected fuel into three parts: rich, flammable and lean, [38,39]. The rich part of the fuel is that which has a local equivalence ratio, $\phi>2.0$. The flammable part is that which has an equivalence ratio in the range $0.5<\phi\leqslant2.0$ and the lean part has $\phi\leqslant0.5$. The equivalence ratio, ϕ, is defined as the stoichiometric air-fuel ratio divided by the local air-fuel ratio. The values of equivalence ratio selected to identify the rich, flammable and lean parts are arbitrary, but as long as they are consistently employed for both free jets and wall-impinging jets, they may indicate useful trends. The idea is that if the entrainment (mixing) rate is faster, then a greater fraction of the injected fuel will be lean. In the second approach, we adopt a procedure similar to the one that Tomita et al. [18] employed in their measurements. We compute the entrained volume by identifying the boundary of the jet with a selected value of fuel mass fraction. The volume and mass of air entrained within the boundary may then be estimated.

We will now present computed results. The computational domain is similar to what is shown in Fig. 2. Results will be presented with two spatial resolutions. The radius of the domain is 10 cm with 120 grids in the radial direction. Stretching of the grid is employed in the radial direction to achieve higher resolution in the jet. As in our previous computations, a uniform grid size is employed in the axial direction. The axial grid size of 0.05 cm. For the higher resolution cases, we employ 120 grids in the radial direction but we increased the resolution in the axial direction. In the case of the free jet, the grid size is halved. In the case of the wall-impinging jet, a stretched grid is employed near the wall such that the minimum grid size normal to the wall is 0.005 cm. C_2H_4 is injected through an orifice of 0.16 cm in diameter with a velocity of 6000 cm/s. The injected fuel has a temperature of 293 K. The ambient air is at a pressure of 101 KPa and temperature of 293 K.

Figures 13 and 14 show computed fuel mass fraction contours in a free jet at 15 ms (Fig. 13(*a*)) and at 20 ms (Fig. 13(*b*)) ASI and in a wall-impinging jet at 15 ms (Fig. 14(*a*)) and 20 ms (Fig. 14(*b*)) ASI, respectively. The results shown in Fig. 14 are for an impinging distance of 5 cm. The contour values selected, 0.1197,

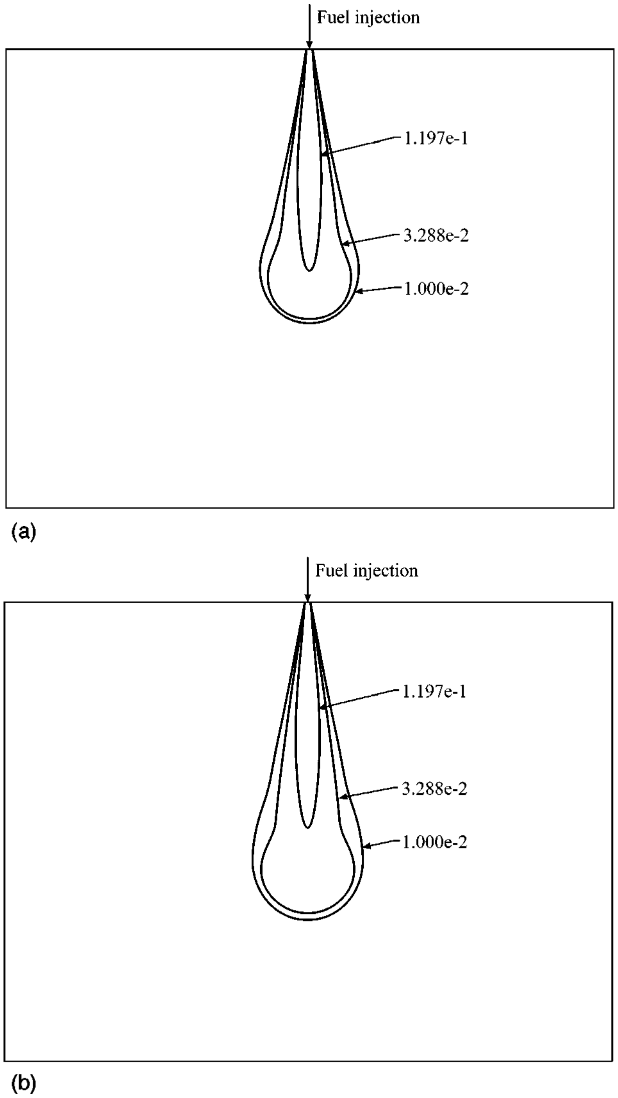

Fig. 13 (***a***) **Fuel mass fraction contours at 15 ms ASI in the free jet,** (***b***) **fuel mass fraction contours at 20 ms ASI in the free jet**

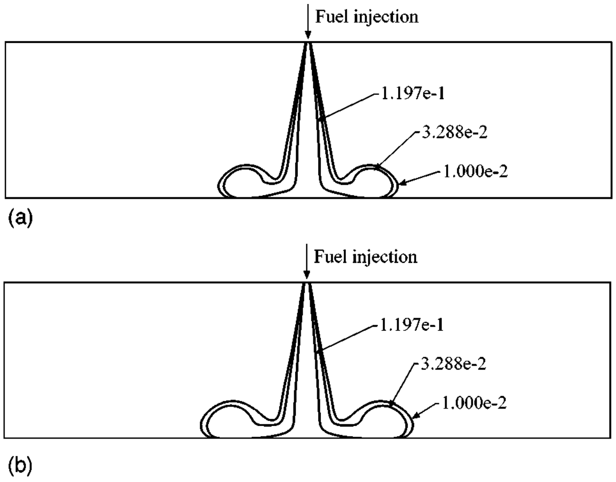

Fig. 14 (***a***) **Fuel mass fraction contours at 15 ms in the wall-impinging jet, $L=5$ cm, i.e., $L/D=31.25$;** (***b***) **fuel mass fraction contours at 20 ms in the wall-impinging jet, $L=5$ cm, i.e., $L/D=31.25$**

0.03288, and 0.01 correspond to equivalence ratios of 2.0, 0.5, and 0.149. It may be seen that at 15 ms ASI, the volume of the fuel-air mixture within the 0.1197 fuel mass fraction contour curve has reached approximately a steady state as it does not appear to increase with time when we compare the contour plots at 15 ms and 20 ms ASI. This implies that when we divide the injected fuel into rich, flammable and lean parts, the rich fraction will decrease beyond 15 ms only because the total quantity of fuel in the domain increases.

Figure 15 shows the rich, flammable and lean fractions plotted as a function of time ASI for the two jets. Results are shown with two impinging distances, L, of 3 cm and 5 cm. We will discuss the results for the case with 5 cm. Impingement occurs at about 5 ms ASI. Till impingement, as expected, the three fractions are practically the same for the two jets. Immediately following impingement, the rich fraction increases and the flammable and lean fractions decrease for the wall-impinging jet relative to the free jet. However, at 10 ms ASI, the rich fraction decreases at about the same rate in the free jet and the wall-impinging jet though the latter shows a greater value. This greater value implies that there is greater mass of "rich" fuel in the jet. At 10 ms ASI, the rate at which the flammable fraction is being formed is greater and the rate at which the lean fraction is being formed is slower in the wall-impinging jet. This gives rise to a difficulty in interpretation. If we relate "mixing" rate to the rate at which the "lean" fraction is formed, it appears that the wall-impinging jet mixes slower. On the other hand, if we relate "mixing" rate to the rate at which the "flammable" fraction is formed, the wall-impinging jet mixes faster. In fact, when we employ different values of fuel mass fraction to identify the jet boundary and estimate the entrained volume, we encounter this difficulty.

Figure 16 shows the computed volume of the free jet and the wall-impinging jet with impinging distances of 3 cm and 5 cm when the jet boundary is defined with a fuel mass fraction value, $f=0.01$. It appears that the free jet has a greater volume than the wall-impinging jet. Figure 17 shows the corresponding results when $f=0.03$ is employed to define the jet boundary. In the case of the wall-impinging jet with an impinging distance of 5 cm, the entrained volume is initially lower but then greater relative to the free jet whereas the volume remains lower for the jet with an impinging distance of 3 cm. Figure 18 shows the computed fuel fractions with relatively higher spatial resolutions for the free jet and for the wall-impinging jet when $L=5$ cm. They are practically the same as the corresponding ones in Figure 15. It appears that the above results are not sensitive to spatial resolution.

In the wall-impinging jet, it appears that the fuel becomes flammable almost as fast as in the free jet, as the rich fractions de-

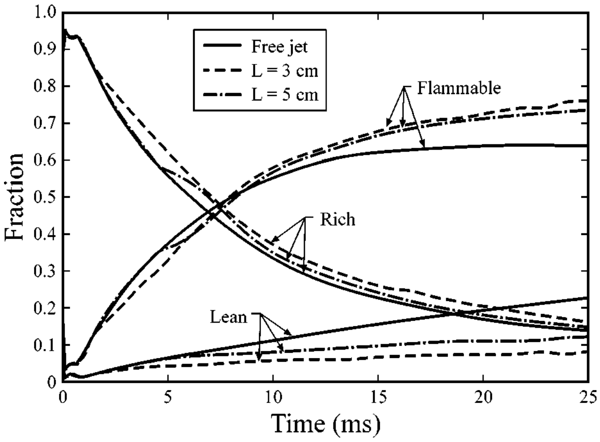

Fig. 15 Rich, flammable, and lean fraction of fuel in the jets

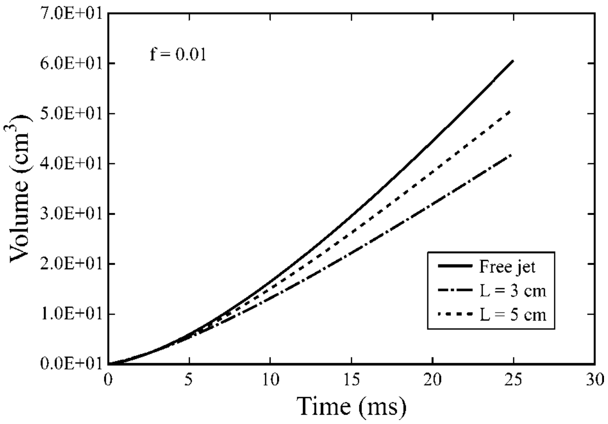

Fig. 16 Entrained volume of the jets

crease at about the same rates, but the additional mixing required to make the fuel even leaner appears to be slower. Hence, the mixing characteristics of the two jets appear to be different and overall mixing in the wall jet appears to be slower. As a final note of caution: The computed results are solutions of Reynolds-averaged equations. Such solutions tend to smear out the boundary of the jet. This smearing represents what would happen when experimental results are ensemble averaged. It is difficult to ascertain the effect of this on the conclusions though we have no reason to believe that this would affect one jet differently from the other. Generally, greater "mixing" results as a result of "smearing."

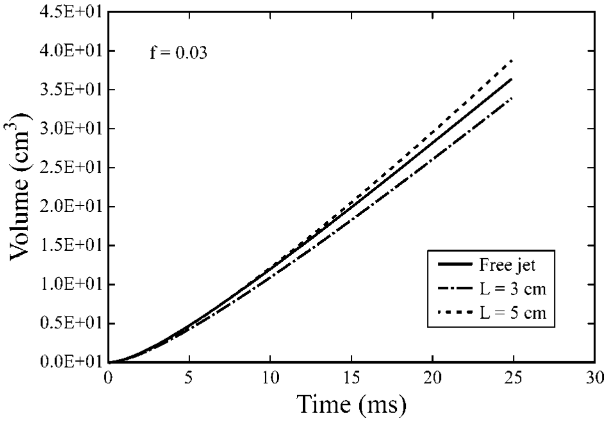

Fig. 17 Entrained volume of the jets

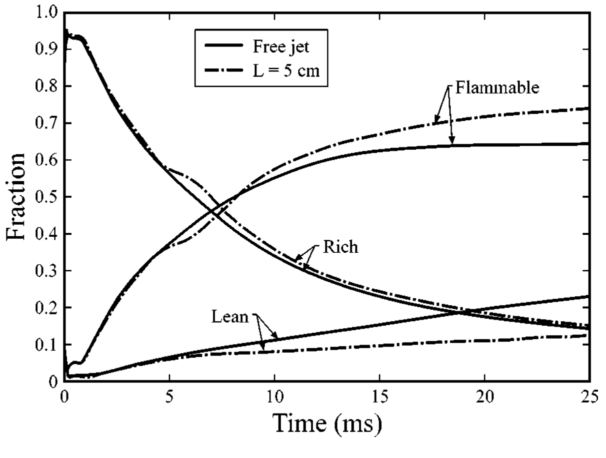

Fig. 18 Rich, flammable, and lean fraction of fuel in the jets; higher resolution

Summary and Conclusions

In this work, the structure of wall-impinging jets is investigated computationally. The k-ε model is employed to represent turbulence, and wall functions are employed to model momentum fluxes at the walls. We present results of tip penetration of the transient part of the jet and velocity distribution, growth rate of the half-width of the jet and decay rate of the maximum velocity of the jet in the steady part of the jet. These computed results for the wall-impinging jet are compared with analytical and measured results in the literature. The computed and measured jet tip penetrations agree within 10%. The loss of momentum to the walls reduces the rate of jet penetration of the wall-impinging jet. The computed, measured, and analytical radial velocities in the wall jet are self-similar when plotted as a function of nondimensional normal distance from the wall and they agree with each other in terms of the location of maximum velocity. Between nondimensional distances of 0.25 and 1.25, the computed velocities are in agreement with the measured and analytical results within 5%. There are greater differences in the near-wall, i.e., at the nondimensional distance that are less than 0.25, and in the outer region, i.e., at nondimensional distances that are greater than 1.25. The computed spreading rate constant of the wall jet is about 0.10 and this value is about 5% greater than the average measured value. Computed mixing characteristics for a free jet that does not impinge on a wall and a wall-impinging jet with the same mass and momentum flow rates show that, in the wall-impinging jet, the fuel becomes "flammable" almost as fast as it does in the free jet but that the additional mixing required to make the fuel even leaner appears to be slower.

Acknowledgments

The authors acknowledge the support of Cummins Engine Company for this work. The authors thank Prof. Vinicio Magi, Basilicata University, Italy, and Dr. Lyle M. Pickett, Sandia National Laboratories, for useful discussions on this paper.

Nomenclature

C_t = model constant
C_μ = model constant, Eqs. (6), (8), and (9)
D = injector orifice diameter
E = model constant, Eq. (8)
f = fuel mass fraction
F_m = constants in this work; in general, functions of Reynolds number, Eq. (1)
F_n = constants in this work; in general, functions of Reynolds number, Eq. (2)
k_p = turbulent kinetic energy in the near wall cell
K = jet kinematic momentum
L = distance from the injector orifice to the wall, Eqs. (1) and (2)
m = constant, Eq. (1)
n = constant, Eq. (2)
p = center of the numerical cell closest to the wall
u^* = friction velocity, Eqs. (5) and (6)
U = radial velocity
U_m = maximum radial velocity
X = radial distance to which the jet has penetrated
x = radial distance
y = perpendicular distance from the wall
$y_{1/2}$ = jet half-width
Y = nondimensional parameter, Eq. (5)
z_p = distance from the wall to the center of the computational cell
ϕ = equivalence ratio

ν = kinematic viscosity
ν_{jet} = jet diffusivity
κ = model constant, Eq. (8)
μ_{lam} = laminar viscosity, Eq. (7)
ρ_g = gas density, Eqs. (5) and (8)
τ_w = momentum flux at the wall, Eqs. (7) and (8)

References

[1] Martin, H., 1977, ''Heat and Mass Transfer between Impinging Gas Jets and Solid Surfaces,'' Adv. Heat Transfer, **13**, pp. 1–60.
[2] Beltaos, S., and Rajaratnam, N., 1972, ''Impinging Circular Turbulent Jets,'' J. Hydraul. Div., Am. Soc. Civ. Eng., **100**, pp. 1313–1328.
[3] Fujimoto, H., Nogami M., Hyun G., Nogami, M., Hirakawa, K., Asai, T., and Senda, J., 1997, ''Characteristics of Free and Impinging Gas Jets by Means of Image Processing,'' SAE Paper 970045.
[4] Jambunathan, K., Lai, E., Moss, M. A., and Button, B. L., 1992, ''A Review of Heat Transfer Data for Single Circular Jet Impingement,'' Int. J. Heat Fluid Flow, **13**, pp. 106–115.
[5] Goldstein, R. J., and Franchett, M. E., 1988, ''Heat Transfer From a Flat Surface to an Oblique Impinging Jet,'' ASME J. Heat Transfer, **110**, pp. 84–90.
[6] Dec, J. E., and Tree, D. R., 2001, ''Diffusion-Flame/Wall Interactions in a Heavy-Duty DI Diesel Engine,'' SAE Paper 2001-01-1295.
[7] Kittelson, D. B., Ambs, J. L., and Hadjkacem, H., 1990, ''Particulate Emissions From Diesel Engines—Influence of In-Cylinder Surface,'' SAE Trans., **99**, pp. 1457–1472.
[8] Song, L., and Abraham, J., 2001, ''Effect of Injector Hole Size, Number and Orientation on Diesel Engine Emissions,'' *Proceedings of the Second Joint Meeting of the US Sections of the Combustion Institute*, Oakland, CA, The Combustion Institute, Pittsburgh, PA.
[9] Iyer, V. A., Post, S., and Abraham J., 2000, ''Is the Liquid Penetration in Diesel Sprays Mixing Controlled?'' *Proceedings of 28th Combustion Institute*, The Combustion Institute, Pittsburgh, PA, pp. 1111–1118.
[10] Iyer, V. A., Abraham, J., and Magi, V., 2002, ''Exploring Injected Droplet Size Effects on Steady Liquid Penetration in a Diesel Spray With a Two-Fluid Model,'' Int. J. Heat Mass Transfer, **45**, pp. 519–531.
[11] Post, S., and Abraham, J., 2001, ''A Computational Study of the Processes That Affect the Steady Liquid Penetration in Full-Cone Diesel Sprays,'' Combust. Sci. Technol., **165**, pp. 1–40.
[12] Siebers, D., 1998, ''Liquid Phase Fuel Penetration in Diesel Sprays,'' SAE Paper 980809.
[13] Bakke, P., 1957, ''An Experimental Investigation of a Wall Jet,'' J. Fluid Mech., **2**, pp. 467–472.
[14] Tanaka, T., and Tanaka, E., 1977, ''Experimental Studies of a Radial Turbulent Jet (2nd Report, Wall Jet on a Flat Smooth Plate),'' Bull. JSME, **20**, pp. 209–215.
[15] Poreh, M., Tsuei, Y. G., and Cermak, J. E., 1967, ''Investigation of a Turbulent Radial Wall Jet,'' ASME J. Appl. Mech., **34**, pp. 457–463.
[16] Witze, P. O., and Dwyer H. A., 1977, ''Impinging Axisymmetric Turbulent Flows: The Wall Jet, the Radial Jet and Opposing Free Jets,'' *Proceedings of the 1st Symposium on Turbulent Shear Flows*, Pennsylvania, pp. 2.33–2.39.
[17] Launder, B. E., and Rodi, W., 1983, ''The Turbulent Wall Jet—Measurements and Modeling,'' Annu. Rev. Fluid Mech., **15**, pp. 429–459.
[18] Tomita, E., Hamamoto, Y., Tsutsumi, H., Takasaki, S., Watanabe, T., and Yoshiyama, S., 1995, ''Visualization of Ambient Air Motion and Entrainment Into a Transient Gas Jet Impinging on a Flat Wall,'' SAE Paper 952513.
[19] Glauert, M. B., 1956, ''The Wall Jet,'' J. Fluid Mech., **1**, Part 6, pp. 625–643.
[20] Patankar, S. V., and Spalding, D. B., 1967, *Heat and Mass Transfer in Boundary Layers*, Morgan-Grampian, London.
[21] Magi, V., 1987, ''A New 3-D Code for Flows, Sprays, and Combustion in Reciprocating and Rotary Engines,'' Mechanical and Aerospace Engineering Report, No. 1793, Princeton University, Princeton, NJ.
[22] Iyer, V., and Abraham, J., 1998, ''The Computed Structure of a Combusting Transient Jet Under Diesel Conditions,'' SAE Trans., **107**, pp. 1669–1693.
[23] Abraham, J., and Magi, V., 1998, ''A Model for Multicomponent Droplet Vaporization in Sprays,'' SAE Trans., **107**, pp. 603–613.
[24] Post, S., Iyer, V., and Abraham, J., 2000, ''A Study of Near-Field Entrainment in Gas Jets and Sprays Under Diesel Conditions,'' ASME J. Fluids Eng., **122**, pp. 385–395.
[25] Launder, B. E., and Spalding, D. B., 1974, ''The Numerical Computation of Turbulent Flows,'' Comput. Methods Appl. Mech. Eng., **3**, pp. 269–289.
[26] Yakhot, V., Orszag, S. A., Thangam, S., Gatski, T. B., and Speziale, C. G., 1992, ''Development of Turbulence Models for Shear Flows by a Double Expansion Technique,'' Phys. Fluids A, **4**, pp. 1510–1520.
[27] Abraham, J., and Magi, V., 1997, ''Computation of Transient Jets: RNG k-ε Model Versus Standard k-ε Model,'' SAE Trans., **106**, pp. 1442–1452.
[28] Chien, K. Y., 1982, ''Predictions of Channel and Boundary-Layer Flows With a Low-Reynolds-Number Turbulent Model,'' AIAA J., **20**, pp. 33–38.
[29] Launder, B. E., and Sharma, B. I., 1974, ''Application of Energy Dissipation Model of Turbulence to the Calculation of Flow Near a Spinning Disc,'' Lett. Heat Mass Transfer, **1**, pp. 131–138.
[30] Jones, W. P., and Launder, B. E., 1972, ''The Prediction of Laminarization With a Two-Equation Model of Turbulence,'' Int. J. Heat Mass Transfer, **15**, pp. 301–314.
[31] Lam, C. K. G., and Bremhorst, K. A., 1981, ''Modified Form of the k-ε Model for Predicting Wall Turbulence,'' ASME J. Fluids Eng., **103**, pp. 456–460.
[32] Patel, V. C., Rodi, W., and Scheuerer, G., 1985, ''Turbulence Models for Near-Wall and Low-Reynolds Number Flows: A Review,'' AIAA J., **23**, pp. 1308–1319.
[33] Wilcox, D. C., 1998, *Turbulence and Modeling for CFD*, 2nd Ed., DCW Industries.
[34] Iyer, V., and Abraham, J., 1997, ''Penetration and Dispersion of Transient Gas Jets and Sprays,'' Combust. Sci. Technol., **130**, pp. 315–334.
[35] Schlichting, H., 1987, *Boundary Layer Theory*, McGraw-Hill, New York.
[36] Abraham, J., 1996, ''Entrainment Characteristics of Transient Gas Jets,'' Numer. Heat Transfer, **30**, pp. 347–364.
[37] Magi, V., Iyer, V., and Abraham, J., 2001, ''The k-ε Model and Computed Spreading Rates in Round and Plane Jets,'' Numer. Heat Transfer, **40**, pp. 317–334.
[38] Abraham, J., and Bracco, F. V., 1989, ''Fuel-Air Mixing and Distribution in a Direct-Injection Stratified Charge Rotary Engine,'' SAE Trans., **98**, pp. 515–526.
[39] Abraham, J., Khan, A., and Magi, V., 1999, ''Jet-Jet and Jet-Wall Interactions of Transient Jets From Multi-Hole Injectors,'' SAE Paper 1999-01-0513.

Development of a Steady Vortex Generator Jet in a Turbulent Boundary Layer

Gregory S. Rixon
Graduate Research Assistant

Hamid Johari[1]
Professor
e-mail: hjohari@wpi.edu

Mechanical Engineering Department,
Worcester Polytechnic Institute,
Worcester, MA 01609

The development of a vortex generator jet within a turbulent boundary layer was studied by the particle image velocimetry method. Jet velocities ranging from one to three times greater than the freestream velocity were examined. The jet was pitched 45 deg and skewed 90 deg with respect to the surface and flow direction, respectively. The velocity field in planes normal to the freestream was measured at four stations downstream of the jet exit. The jet created a pair of streamwise vortices, one of which was stronger and dominated the flow field. The circulation, peak vorticity, and wall-normal position of the primary vortex increased linearly with the jet velocity. The circulation and peak vorticity decreased exponentially with the distance from the jet source for the jet-to-freestream velocity ratios of 2 and 3. The wandering of the streamwise vortex can be as much as ±30% of the local boundary layer thickness at the farthest measurement station.

[DOI: 10.1115/1.1627833]

Introduction

The study of vortex generator jets as a means for flow separation control has grown rapidly over the last ten years. The primary impetus for this growth has been the prospect of implementing active flow control strategies using vortex generator jets (VGJs). These jets are flush-mounted on the flow surface, and the jet velocity vector is pitched and skewed with respect to the freestream. The VGJs, which create streamwise vortices, are favored over solid vane vortex generators since the drag losses associated with the latter vanish when VGJs are not operating. It is anticipated that VGJs will have a notable impact on the future design of active vortex generators used for control of external and internal flows. The present study was undertaken to gain an understanding of the decay of streamwise vorticity created by a VGJ in a flat plate turbulent boundary layer.

A schematic of a single VGJ as well as the coordinate system used is shown in Fig. 1. The key parameters of a VGJ are the jet-to-freestream velocity ratio, $VR = V_j/U_\infty$, the ratio of jet diameter to the local (undisturbed) boundary layer thickness, D/δ, and the orientation of the jet (pitch and skew angles) with respect to the freestream. In Fig. 1, the pitch angle is defined as α and the skew angle as β.

Wallis [1,2] appears to have been the first to suggest an air-jet vortex generator as a method for delaying separation of turbulent boundary layers. More recently, VGJs have been used to control shock-induced separation and separation of low-speed boundary layers under adverse pressure gradients, [3–6]. Effective VGJs have jet velocities close to or greater than the freestream velocity, [5]. The work of Johnston and co-workers, [5,7], has revealed that skew angles between 45 deg and 90 deg produce the strongest streamwise vortex when the jet pitch angle is 45 deg, and the vortex strength increases with the jet exit velocity for $0.7 \leqslant VR \leqslant 1.3$. Pitch angles greater than 60 deg result in streamwise vortices that penetrate quickly through the boundary layer and do not appear to be particularly effective in boundary layer control, [8]. The two pitch angles of 0 deg and 90 deg produce a wall jet and a transverse jet, respectively. It has been shown that VGJs delay or prevent the separation of boundary layers in the same manner as solid vortex generators, [3,5,6]. The issues of spanwise spacing as well as corotating and counterrotating vortices produced by VGJs have been investigated by Johnston and Nishi [5] and by Zhang [9,10].

Pulsing of the vortex generator jets has been pursued by McManus et al. [11–13] in an effort to further enhance the efficiency of vortex generator jets in delaying or preventing the boundary layer separation in low-speed diffuser and airfoil flows. It has been found that pulsed VGJs are able to significantly improve separation control as compared to steady VGJs, with the same mean mass flow rate, and that pressure recovery on significantly larger areas are affected as a result of pulsing the VGJs. In pulsed VGJs, a small duty-cycle coupled with a large velocity ratio has resulted in the best performance in terms of separation control on an airfoil, [12].

Alternative approaches for active boundary layer control have been pursued by Wygnanski and co-workers [14,15] as well as Gad-el-Hak and Blackwelder [16]. Oscillatory, low-momentum, planar wall jets have been implemented on flapped airfoils in [14,15]. On the other hand, a pulsed, two-dimensional jet opposing the freestream was employed to create large-scale spanwise structures in [16]. The forcing of the boundary layer in that study resulted in the modification of both the outer and inner regions of the boundary layer. However, these control methods are different from the vortex generator jets in that the VGJs primarily create streamwise, as opposed to spanwise, vorticity for effective prevention of stalled regions. Additionally, a recent review paper by Joslin et al. [17] provides a comprehensive survey of the many flow control technologies available, and the status of their development.

There has also been a large effort in the past decade to achieve active control of boundary layers through the manipulation of the sublayer streaks, see [18–21], for example. These efforts are primarily aimed at understanding and disrupting the eruption of the streaks in the sublayer, thus reducing the drag of turbulent boundary layers. These efforts and the proposed schemes are not directly related to control of separation in turbulent boundary layers, and would not be applicable to the present study.

The near-field characteristics of VGJs are a crucial element for design and scaling purposes as well as for the optimization of an array of vortex generators. All the past studies of vortices generated by VGJs have been conducted with pointwise velocity probes, which tend to result in smeared vorticity fields when the vortex wanders noticeably (see, for example, Khan and Johnston

---

[1] To whom correspondence should be addressed.

Contributed by the Fluids Engineering Division for publication in the JOURNAL OF FLUIDS ENGINEERING. Manuscript received by the Fluids Engineering Division July 12, 2002; revised manuscript received August 2, 2003. Associate Editor: M. V. Ötügen.

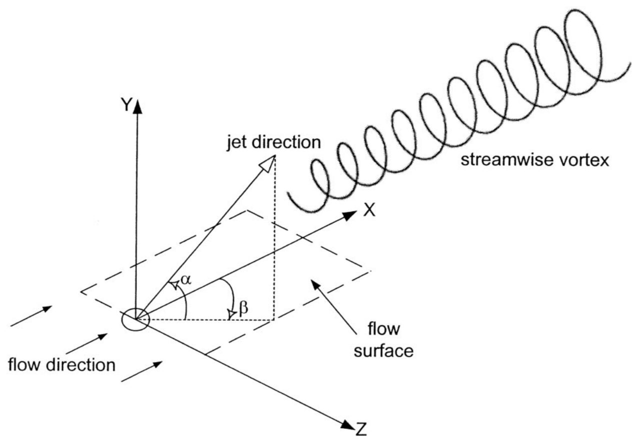

Fig. 1 Schematic of a vortex generator jet and associated coordinate system. The pitch angle is α and the skew angle is β.

[22]). The present paper examines the flow field of a single, steady VGJ embedded in a flat-plate turbulent boundary layer using the particle image velocimetry (PIV) technique for acquiring instantaneous planar velocity data sets. Development of the jet generated vortices and their position within the boundary layer for velocity ratios up to 3 are considered. The data were used to address the following questions:

1. How do the peak vorticity, position, and circulation of the primary streamwise vortex generated by a VGJ vary with velocity ratio, specifically for velocity ratios greater than unity?
2. How do the peak vorticity and circulation decay with downstream distance?
3. Do the instantaneous planar data obtained by PIV differ from the time-averaged data provided by pointwise measurements?

Although the interaction of a single vortex or a vortex pair with a turbulent boundary layer has been examined in the past, [23–25], these vortices were generated external to the boundary layer and their position within the boundary layer was set *a priori*. Moreover, vortices generated by full or half-delta wings tend to have a low-velocity core, unlike the ones generated by VGJs, [7]. Thus, the present set of measurements represents embedded vortices resulting from strong jets emanating from the wall. The experimental setup and the relevant parameters in this study are discussed in the next section. To the extent possible, our data have been compared with those available in the literature.

Table 1 Jet flow parameters

Nominal V_j (cm/s)	Nominal VR	Measured V_j (cm/s)	VR	$\mathrm{Re}_j=V_jD/\nu$
20	1	20.02	0.99	1020
40	2	40.00	1.98	2040
60	3	60.25	2.97	3070

Experimental Approach

The experiments were conducted in a free-surface re-circulating water tunnel at a freestream velocity of 20.3 cm/sec. The freestream turbulence intensity in the test section was measured with an LDV system to be 1.5% at this velocity. The water tunnel test section had a 0.6 m square cross section and was 2.4 m long. Optical access was possible through a window at the end of the tunnel directly downstream of the test section as well as through the test section walls. A schematic of the test section and the setup is shown in Fig. 2.

The boundary layer developed on a clear acrylic flat plate submerged approximately 10 cm below the free surface. The plate spanned the width of the test section and measured 1.40 m in length. The leading edge of the plate was elliptical and the boundary layer was tripped by a staggered set of 60-grit sandpaper strips, placed at 2.5 and 5 cm downstream of the leading edge. The boundary layer profile at the VGJ location (1.15 m from the leading edge) was measured by the LDV system. The turbulent boundary layer was two-dimensional with a 99% thickness of $\delta \approx 3.4$ cm. There was a distinct logarithmic region spanning from $y^+ \approx 30$ to 160; the best-fit line to the data in this range had a slope of 1/0.41. The displacement and momentum thickness were measured to be 4.3 and 3.3 mm, respectively, resulting in a shape factor of 1.3. The Reynolds number based on momentum thickness, Re_θ, was 715.

A single jet was mounted flush in the flat plate 1.15 m downstream of the leading edge using a 5 cm diameter plug. The jet diameter D was 4.76 mm and its orientation was fixed at a 45 deg pitch angle and a 90 deg skew angle. Previous work, [5,7], has shown this orientation to be one of the optimal configurations for producing a strong streamwise vortex. A pressurized diaphragm tank supplied the jet and flow was controlled using a precision valve. The jet orientation with respect to the flat plate is shown in Fig. 2. The origin of the coordinate system used was at the jet exit. The mean jet exit velocity was measured by volumetric flow rate measurements at three nominal velocity ratios of 1, 2, and 3. Table 1 summarizes the resulting flow conditions at the jet exit. The jet inflow tube was sufficiently long to ensure a fully developed profile inside the tube. At the jet exit, however, Johnston et al. [26] have shown that jet velocity profile is distorted due to the inter-

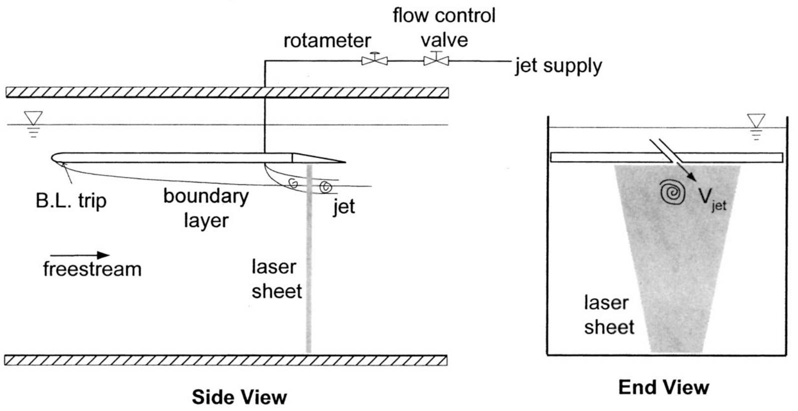

Fig. 2 Schematic of the water tunnel test section and the experimental setup

action with the approaching turbulent boundary layer. They also report that the jet exit profile appears to have little effect on the vortex further downstream. The ratio of jet diameter to the local boundary layer thickness, D/δ, at the jet exit was 0.14.

The velocity measurements were carried out by the PIV technique. For the purposes of these measurements, the entire water tunnel, as well as the jet, was seeded with neutrally buoyant silver-coated glass spheres with an average diameter of 46 μm. The flow was illuminated by a sheet of laser light with a thickness of approximately 3 mm. The light source was a pair of pulsed Nd:YAG lasers, each of which fired at a frequency of 15 Hz. For all of the experiments, the laser pulse separation was set at 5 ms. The laser sheet, which entered from through the bottom of the water tunnel, was placed normal to the freestream (see Fig. 2) so that the secondary velocity components could be measured. The laser sheet was positioned at four stations 5, 10, 20, and 30 D downstream of the jet exit. These locations correspond to data fields at 0.7, 1.4, 2.8, and 4.2 δ.

The cross-correlation technique was used to process the PIV images. A progressive scan CCD camera with a spatial resolution of 768×480 pixels at 30 frames per second was placed outside the tunnel, viewing the laser sheet (y-z plane) through the tunnel's end window. Since a pair of successive images is used for extracting the particle displacements, the resulting velocity field was sampled at 15 Hz. All image pairs were processed with a window size of 32×32 pixels, and a roaming step size of 16×16 (50% window overlap). Allowing for the laser sheet thickness of 3 mm results in an effective spatial resolution of approximately 4 mm. Since particles moving at the freestream velocity traveled only 1 mm during the time between the pulses (5 ms), the majority of the particles remained within the 3-mm light sheet.

At each measurement station, 1000 successive images were recorded for each velocity ratio, yielding 500 instantaneous velocity fields. The streamwise vorticity field was computed from each velocity field. The primary parameters of interest were the peak vorticity in the vortex core and its location within the boundary layer, as well as the vortex circulation. Circulation was computed by integrating the velocity along specific iso-vorticity contours.

The freestream velocity and boundary layer thickness were used for normalizing all parameters. The uncertainty in the boundary layer thickness and freestream velocity were 1.5% and 0.5%, respectively. The jet velocity had an uncertainty of 1%, resulting in an uncertainty of 2.5% for the velocity ratio. The placement of the laser sheet (in the axial direction) had an uncertainty of 1 mm. Based on the subpixel accuracy of the cross-correlation peak and the particle displacements, the measured velocities and computed vorticities are estimated to be accurate to ±1.5% and ±4.5%, respectively.

Results

Vorticity Field. Instantaneous vorticity fields of the VGJ at the first station $x=0.7\ \delta$ are presented in Fig. 3 for $VR=1$ and 3. These specific data fields were chosen because they resemble the average properties of the primary clockwise (CW) vortex, which is indicated by the solid vorticity contours. The minimum vorticity contour level of 2 s^{-1} is the same for the two cases shown in Fig. 3. The primary vortex is significantly stronger in the $VR=3$ case than the one at $VR=1$. Moreover, the vortex core, chosen as the peak vorticity point, has moved further away from the jet source in both the wall-normal and spanwise directions in the $VR=3$ case as compared to $VR=1$ case. The primary vortex core is 1.5 cm away from the wall in the $VR=3$ case in contrast to 0.8 cm for the $VR=1$ case. The counterclockwise (CCW) vortex, marked by the dashed contours, is clearly evident at this station. The instantaneous peak vorticity of the CCW vortex is generally about 40–50% smaller than its stronger counterpart. The CCW vortex position in the y-direction is comparable to that of the primary CW vortex. The primary vortex was always accompanied by the weaker CCW vortex in all of our data fields.

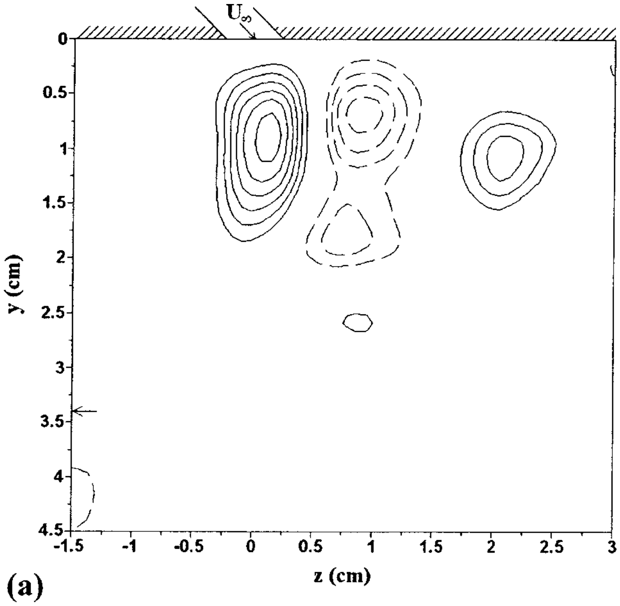

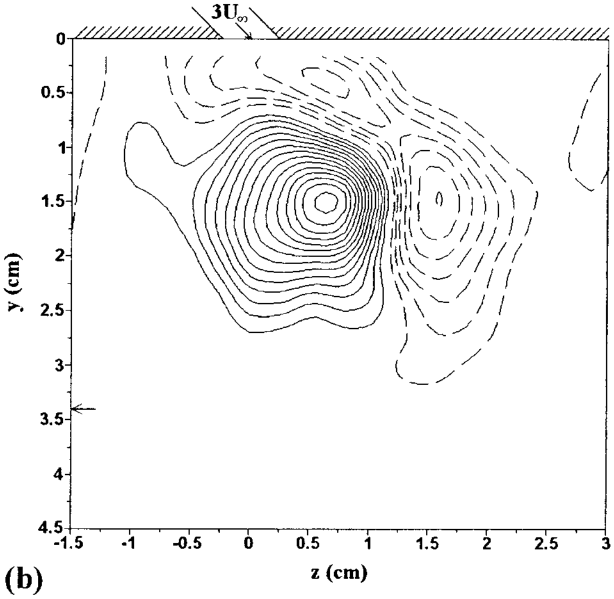

Fig. 3 Instantaneous vorticity fields at $x/\delta=0.7$; (*a*) $VR=1$, minimum $|\omega|$ contour is 2 s^{-1} with an increment of 1 s^{-1}; (*b*) $VR=3$, minimum $|\omega|$ contour is 2 s^{-1} with an increment of 2 s^{-1}. Vorticity in the CW direction is indicated by solid contours. Arrows on the *y*-axes indicate the approximate location of the undisturbed boundary layer edge.

To observe the changes in the vortex structure as it convects downstream, an instantaneous vorticity field for a $VR=3$ jet at $x=4.2\ \delta$ is presented in Fig. 4. This should be contrasted against that in Fig. 3(*b*). Several features stand out when the comparison is carried out: (i) the vortex has stretched and weakened; the first vorticity contour is now approximately at the edge of the undisturbed boundary layer, and (ii) the vortex core has moved further away from the wall to $y=2$ cm. The CCW vortex is still present at this station even though its geometry has changed.

The peak vorticity and its location in the boundary layer were extracted from each instantaneous vorticity field and then averaged. The values obtained in this manner are then free from the smearing effects of vortex wandering (to be discussed later). The variation of the normalized peak vorticity ($\omega_{\max}\delta/U_\infty$) for the $VR=3$ primary vortex at the $x=0.7\ \delta$ station is shown in Fig. 5.

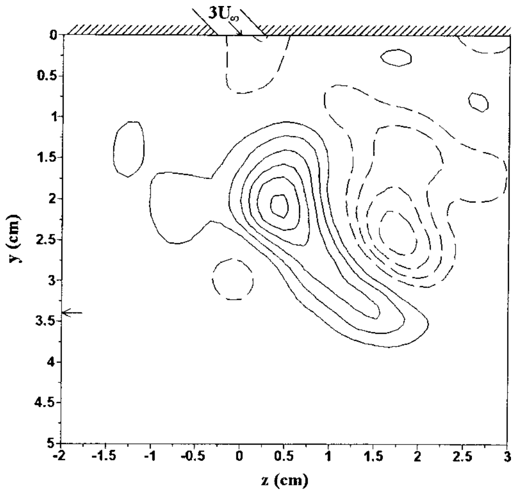

Fig. 4 An instantaneous vorticity field of a $VR=3$ jet at $x/\delta=4.2$, minimum $|\omega|$ contour is 2 s^{-1} with an increment of 2 s^{-1}

The uncertainty of the normalized quantity is estimated to be 7%. The large fluctuations of the peak vorticity, with a standard deviation equal to 20% of the mean, are particularly notable. Such large variations at the $x=5\,D$ (0.7 δ) station are due to the interaction of the primary vortex with the background vorticity in the turbulent boundary layer and possibly the wall-normal vorticity originating from the jet itself. In the absence of the VGJ, the largest streamwise vorticity in the boundary layer was less than $\approx 0.7U_\infty/\delta$ while the average background vorticity was less than 10% of this peak magnitude. These values are considerably smaller than the peak vorticity of $4.74\pm 0.95\ U_\infty/\delta$ in the primary vortex at $x=0.7\ \delta$. Spectral analysis of the peak vorticity fluctuations did not reveal any dominant frequencies.

The dependence of peak vorticity in the primary vortex core on VR and distance from the source is shown in Fig. 6. Each data point has a standard deviation of the mean (SDOM) of less than 2%. The data in Fig. 6(*a*) clearly indicate that the peak vorticity increases linearly with the jet velocity at any location from the jet source in the range of $0.7\leqslant x/\delta\leqslant 4.2$.

Decay of the peak vorticity with downstream distance is presented in a log-linear plot in Fig. 6(*b*). The two higher velocity ratio cases reveal a distinct exponential decay at the same rate. When the exponential decay is combined with the linear increase with VR, the expression

$$\omega_{\max}\cong 1.8\frac{V_j}{\delta}e^{-0.24(x/\delta)} \tag{1}$$

emerges which fits the normalized peak vorticity trends very well for $VR=2$ and 3. The lines representing Eq. (1) for the two higher VR cases are also drawn in Fig. 6(*b*). Although a line could also be fitted to the $VR=1$ case, the exponential decay in this case was not as good and a power law turned out to provide a better fit. Note that the parameter D/δ, which was fixed in our experiments, could be a factor in Eq. (1). It should also be noted that this expression is strictly valid for the range of parameters in the present experiments, and may not apply to positions farther downstream.

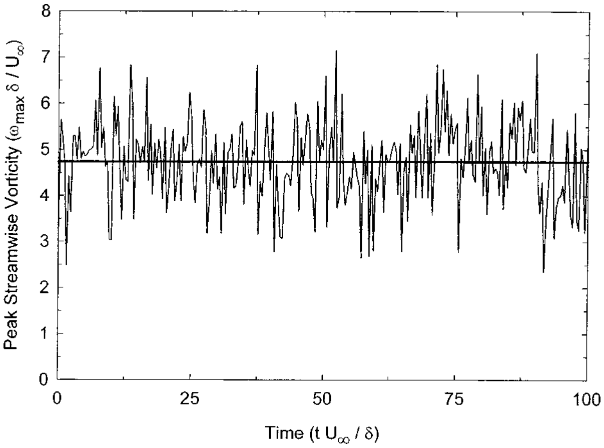

Fig. 5 Temporal variation of peak streamwise vorticity in the primary vortex of a $VR=3$ jet at $x/\delta=0.7$. The straight line denotes the average value.

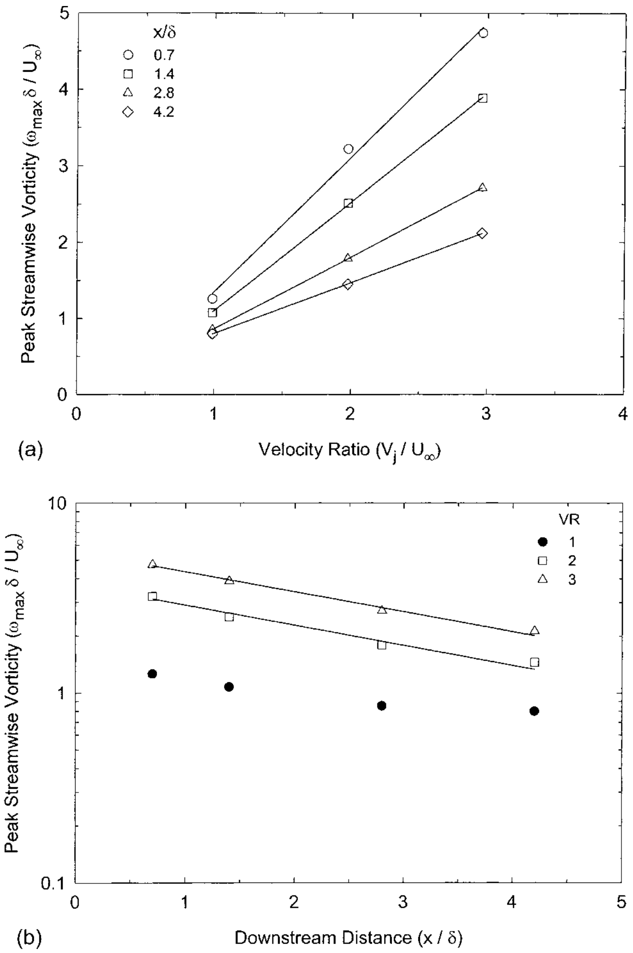

Fig. 6 Dependence of peak streamwise vorticity on velocity ratio (*a*) and downstream location (*b*). The straight lines in (*b*) have the same slope and indicate exponential decay.

Vortex Core Position. The position of the primary vortex within the boundary layer is an important parameter when VGJs are considered. Both the wall-normal, y_c, and spanwise, z_c, position of the primary vortex core were extracted from each instantaneous vorticity field and then averaged. The vortex core position fluctuates significantly within the boundary layer. To illustrate the effect of vortex wandering, instantaneous vortex core positions are mapped in Fig. 7 for $VR=3$ at the farthest measurement station of $x=4.2\ \delta$. The average vortex core position is indicated by the solid square. In this case, the vortex core meandered as much as $\pm 0.3\ \delta$ in both the wall-normal and spanwise directions. Calculation of the peak vorticity in the primary vortex core from the time-averaged field would be 36% lower than the value presented for this case in Fig. 6. It is expected that the wandering increases

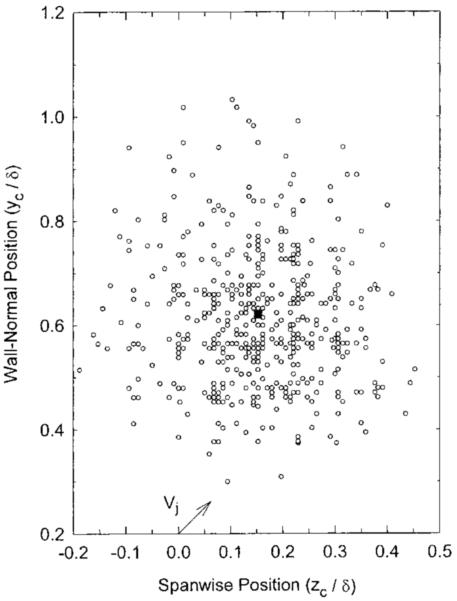

Fig. 7 Instantaneous vortex core locations for a $VR=3$ jet at $x/\delta=4.2$. The average location is represented by the solid square.

to a maximum value and then remains level farther downstream. Our x/δ stations did not extend far enough downstream of the jet source to show this leveling off. The distribution in Fig. 7 is not a Gaussian function of the radial distance from the average core position, and moreover, it is asymmetric in space. The probability of the vortex core being farther away from the wall is greater than being closer to wall (with respect to the average vortex core position).

The meandering of the vortex core is thought to be due to the vortical structures (and the associated turbulent fluctuations) in the boundary layer interacting with the vortex. Meandering of the vortex would result in smearing of the vorticity field and reduced peak vorticities if the flow field were mapped by pointwise anemometry techniques. The smearing effect depends on the distance from the jet source since the vortex meandering worsens as x/δ increases. Another complicating factor due to smearing is the presence of the CCW vortex with an opposite sign in the vicinity of the primary vortex. When our instantaneous data are time-averaged first and then the peak vorticity extracted, the resulting values are reduced by 11% to 58%, depending on the axial distance and jet strength, from the data in Fig. 6.

The average wall-normal position of the primary vortex core as a function of velocity ratio and axial distance is shown in Fig. 8. The uncertainty of y_c/δ measurements is estimated to be 2.5%. As is evident in Fig. 8(*a*), the average wall-normal vortex position increases linearly with the jet strength at each measurement station for the VR in the range of 1 to 3. The slopes of the linear fits, i.e., $d(y_c/\delta)/d(VR)$, are quite close except for the first station at $x=0.7\ \delta$.

The primary vortex moves away from the wall as it convects downstream in the boundary layer. The dependence of y_c/δ on the downstream distance from the jet source is presented in Fig. 8(*b*). The dashed line in the plot indicates the approximate extent of the logarithmic region of the undisturbed boundary layer. All of the $VR=1$ data fall within the log region, whereas the vortex created by the $VR=3$ jet lies mostly outside the log region. The vortex of the $VR=2$ jet breaks through the log region at about $x=2.5\ \delta$. We suspect that the reason for the peak vorticity decay rate of the $VR=1$ jet being different from the two higher VR cases (see Fig. 6(*b*)) is that the $VR=1$ vortex resides completely within the log region. The exponential decay of the peak vorticity, associated with the two higher VR cases, is also consistent with that of solid vane vortex generators that are typically located at the edge of the boundary layer. Also, the smaller slope of the data in Fig. 8(*a*) at $x=0.7\ \delta$ as compared to the other three x/δ stations is due to the fact that the vortex cores for all velocity ratios in our setup lie within the log region for $x/\delta<1$. Hence, the vortex core position with respect to the log region of the boundary layer appears to be an important parameter to assess the characteristics of the primary vortex generated by a VGJ.

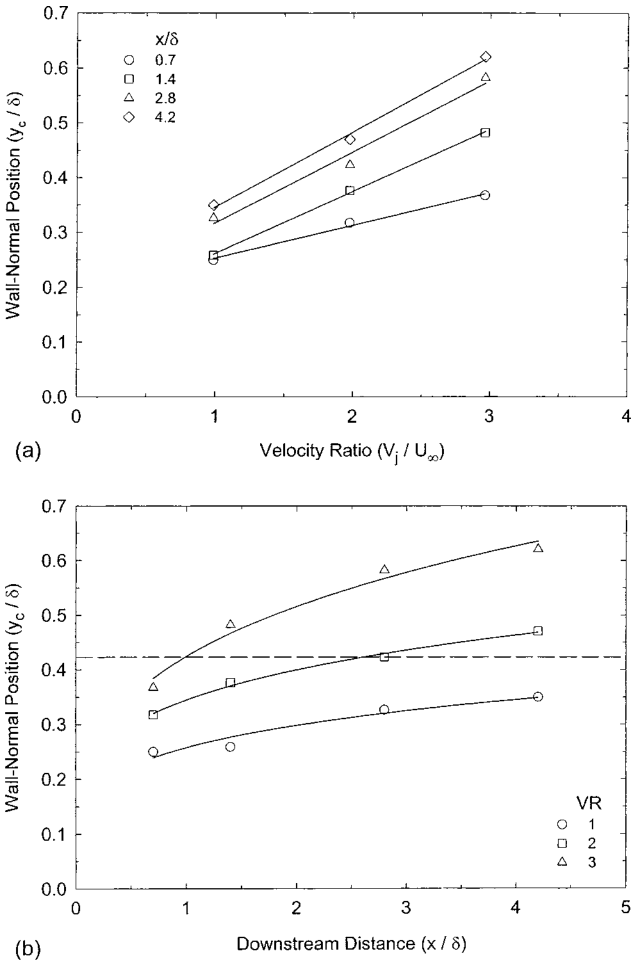

Fig. 8 Wall-normal vortex core location as a function of velocity ratio (*a*) and downstream location (*b*). The solid curves in (*b*) are power-law fits. The dashed line represents the approximate extent of the (undisturbed) boundary layer logarithmic region.

The average vortex core positions in Fig. 8(*b*) were fitted with power laws for the three velocity ratios. The $VR=3$ case resulted in a $(x)^{0.28}$ dependence while the other two velocity ratios had smaller exponents. The penetration of the VGJs can be compared to that of transverse jets, which usually have higher velocity ratios and do not interact significantly with the boundary layer beyond the near field. Pratt and Baines [27] also found an $(x)^{0.28}$ dependence in their transverse jet penetration data. The penetration of the $VR=3$ vortex, which resided mostly outside the boundary layer log region, is similar to that of transverse jets, in contrast to the lower VR jets.

Co-located Velocity Fields. Due to the significant meandering of the primary vortex generated by the VGJ, a conditional averaging scheme, rather than averaging over time, is needed. We ensemble-averaged the data fields after the origin was relocated to the peak vorticity location (of the primary vortex) for each instan-

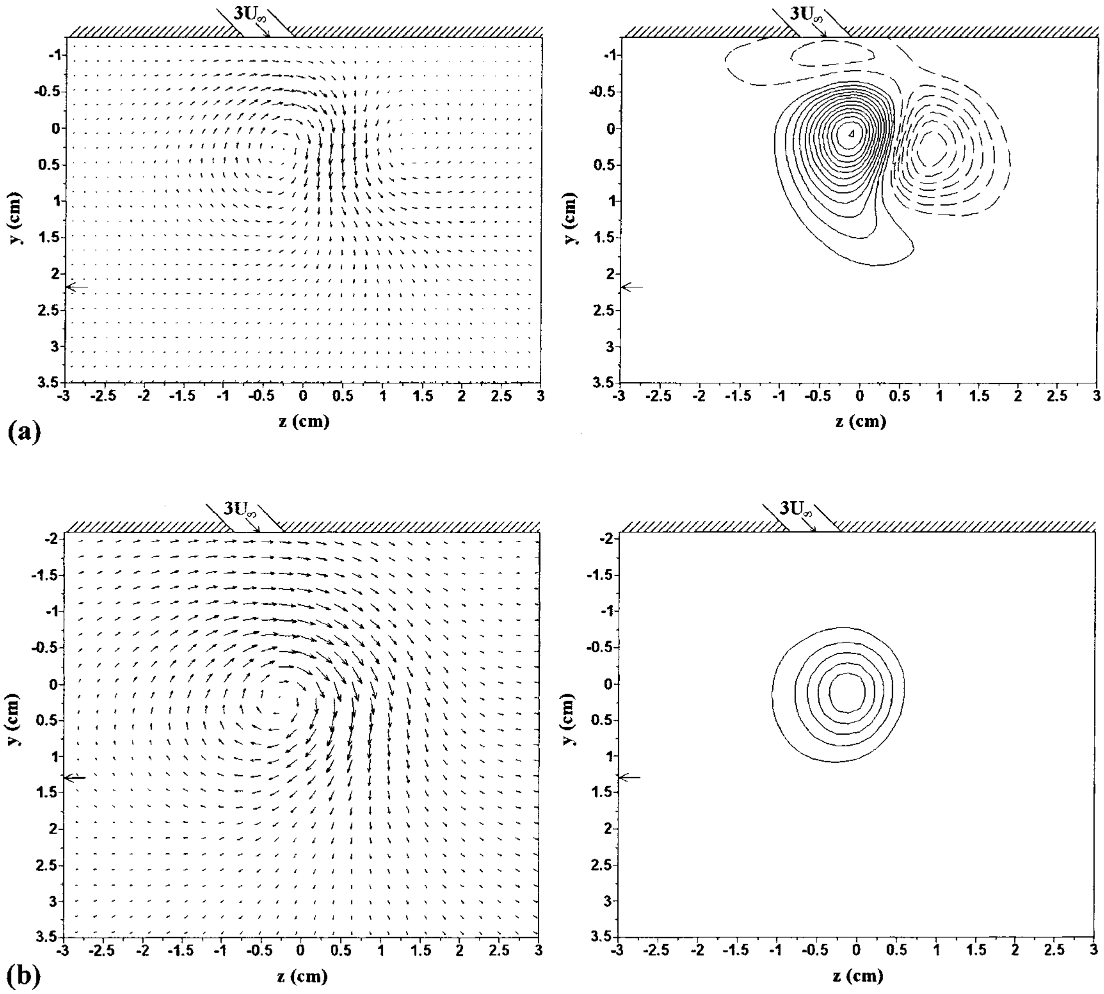

Fig. 9 Co-located velocity and vorticity fields of a *VR*=3 jet at (*a*) *x*/δ=0.7, and (*b*) *x*/δ=4.2; minimum |ω| contour is 2 s^{-1} with a 2 s^{-1} increment. CW Vorticity is indicated by solid contours.

taneous data field. Essentially, the primary vortex for each instantaneous realization was aligned spatially prior to averaging. The resulting average data field is referred to as a "co-located" field. The vorticity field was then computed from the co-located velocity field. The major advantage of this averaging scheme is that the maximum vorticity is very nearly preserved, and the wandering effects of the primary vortex are removed. Of course, the meandering of the CCW vortex is still present to some extent. We believe that the velocity and vorticity fields produced by the co-locating scheme are accurate representatives of the primary vortex field without the fluctuations accompanying the instantaneous data.

The co-located velocity and vorticity fields for the $VR=3$ jet at the $x=0.7\ \delta$ and 4.2 δ are presented in Fig. 9. Note that the origin of the coordinate system is now at the primary vortex core (maximum vorticity location). These fields correspond to the instantaneous ones in Figs. 3(*b*) and 4. The average vortex core positions (in Fig. 8) were used to locate the origin of the co-located fields relative to the surface of the flat plate (in Fig. 9). The smoothness of the co-located fields and the absence of the background vorticity, in comparison with the instantaneous data, are notable. For all co-located cases, the CCW vortex is present and its vorticity extends to the edge of the primary vortex. Though not evident in the figures, examining the data for all conditions shows that the distance between the CCW and primary vortex cores increases with both velocity ratio and downstream distance. This is due to the growth of the primary and secondary vortices. This may indicate a decreasing correlation between the primary and CCW vortices as downstream distance increases. At the $x=0.7\ \delta$ station, the peak vorticity remained the same as the average of the instantaneous data for both the primary and the CCW vortices and the CCW vortex is clearly visible (see Fig. 9(*a*)). This indicates that the wandering of the CCW vortex with respect to the primary vortex is negligibly small at the first station. On the other hand, the CCW vortex at the $x=4.2\ \delta$ station is absent in Fig. 9(*b*) since its vorticity falls below the contour cutoff limit of 2 s^{-1}. The meandering of the CCW vortex relative to the primary vortex is significant enough that its peak vorticity reduces to 1.5 s^{-1}, compared with 9.4 s^{-1} in Fig. 4.

Circulation. To examine the strength of the primary vortex generated by a VGJ, its circulation was computed on an iso-vorticity contour. The difficulty with quantifying circulation is that it may depend on the chosen contour, and there is significant vorticity in the background boundary layer at any instant. Due to the small background vorticity in the co-located fields, circulation values were computed from these fields on iso-vorticity contours of 0.1 s^{-1}. This contour level is sufficiently small so that nearly all the vorticity associated with the primary vortex is accounted for, yet it is greater than the averaged background vorticity in the co-located fields.

Dependence of the computed circulation, Γ_o, on the velocity ratio and downstream distance is shown in Fig. 10. Clearly, circulation increases linearly with the jet velocity at all measurement

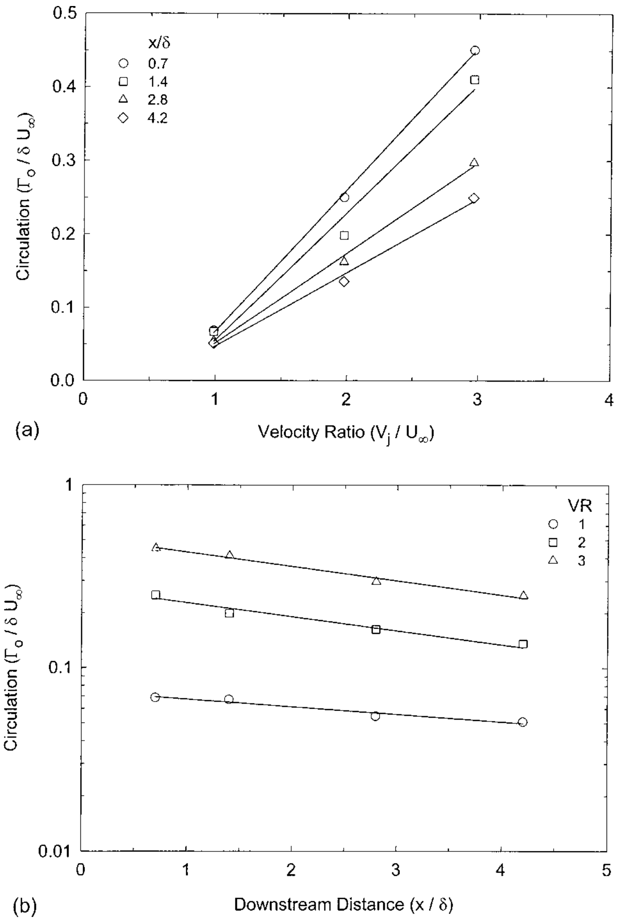

Fig. 10 Dependence of primary vortex circulation on velocity ratio *VR* (*a*) and downstream location (*b*). The straight lines in (*b*) represent exponential fits.

stations. Although the far-field scaling for jets in crossflow reveals a velocity ratio to the power 2/3 for the circulation of the vortex pair, [28], measurements of Fearn and Weston [29] found a linear dependence. Therefore, we expect that circulation of the primary vortex should increase with a power close to unity and our data were fitted with straight lines in Fig. 10(*a*).

Circulation decay with distance from the jet source is presented in Fig. 10(*b*). It is important to point out that circulation decreases with the downstream distance even under ideal conditions (i.e., negligible interaction of the boundary layer with the VGJ vortex). Circulation decays because of the cancellation of opposite-signed vorticity as a result of the close proximity of the CCW vortex as well as the naturally occurring streamwise vorticity in the boundary layer. In the absence of the boundary layer, the circulation of transverse jet vortices decays with $x^{-1/3}$ in the far-field, [28]. Our data indicate that the jets of all three velocity ratios exhibit an exponential decay of circulation with downstream distance, similar to the peak vorticity data. The decay rate is equal for the two higher velocity ratio jets; the $VR=1$ jet has a slower decay rate. Combining the linear increase of circulation with the jet velocity and the exponential decay for the two higher velocity ratio cases, an expression similar to Eq. (1) emerges.

$$\Gamma_o \approx 0.15 \delta V_j e^{-0.18(x/\delta)} \tag{2}$$

This expression is accurate to about ±10% of the measured values of the two higher velocity jets. The above proportionality constants are in between the values that best fitted the $VR=2$ and 3, respectively. Again, it is noteworthy that the parameter D/δ, which was fixed in our experiments, could be a factor in Eq. (2).

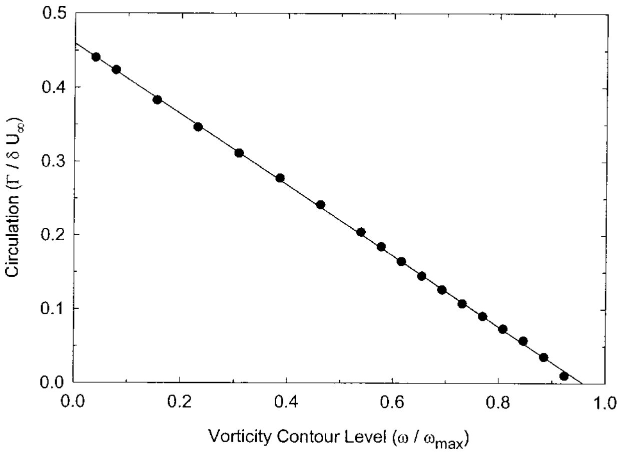

Fig. 11 Circulation as a function of vorticity contour level for a *VR*=3 jet at *x*/*δ*=0.7

The expression in (2) indicates that Γ_o is linearly proportional to V_j, in conformity with the transverse jet data in [29]. If Eq. (2) is extrapolated to the jet source, the initial circulation of the vortices becomes $0.15\ \delta\ V_j = 1.07\ D\ V_j$. Note that the expression in Eq. (2) has been validated only for the range of parameters in the present experiments.

Vorticity Distributions. To further examine the profiles of vorticity and circulation within the primary vortex, we follow the procedure used by Kuzo [30] in his study of transverse jets. Circulation of the primary vortex was computed as a function of the vorticity contour level for the co-located data fields. It turns out that the computed circulation increases linearly as the vorticity contour level decreases. This linear dependence of primary vortex circulation on the vorticity contour level is shown in Fig. 11 for the $VR=3$ jet at the $x=0.7\ \delta$ station. The intercept of the fitted line, which is representative of the circulation as the contour level approaches zero, compares well (generally within 5%) with the circulation values obtained with the 0.1 s^{-1} vorticity contour. This confirms the choice of the 0.1 s^{-1} vorticity contour and the resulting circulation values presented earlier.

One of the implications of the linear dependence of circulation on the chosen contour level is that circulation is proportional to $\omega(=d\Gamma/dA)$, indicating that circulation inside the vortex core is a Gaussian function of the enclosed area *A*. If the vorticity contours are assumed to be circular (see Fig. 9), then the circulation profile within the vortex can be expressed as

$$\Gamma(r) = \Gamma_o(1 - e^{-(r/a)^2}). \tag{3}$$

Here, *r* is the radial distance from the core, and *a* is an effective core radius. At $r=a$ and $2a$, circulation enclosed by the circular contours is 63% and 98% of Γ_o, respectively. If Eq. (3) is differentiated with respect to the enclosed area, $A=\pi r^2$, the vorticity is found to have a Gaussian profile as follows:

$$\omega(r) = \frac{\Gamma_o}{\pi a^2} e^{-(r/a)^2}. \tag{4}$$

We expect the Gaussian profile to be valid primarily at the locations where the vorticity contours are circular, i.e., in the vortex core interior $r \leqslant a$ and at the larger x/δ stations. It is worth reiterating that the position of the vortex in Fig. 7 could not be described by a Gaussian distribution in space. The random motion of a vortex with a top-hat vorticity profile would not result in a Gaussian distribution under the co-located averaging method. The observed Gaussian profile of vorticity is a true characteristic of the primary vortex.

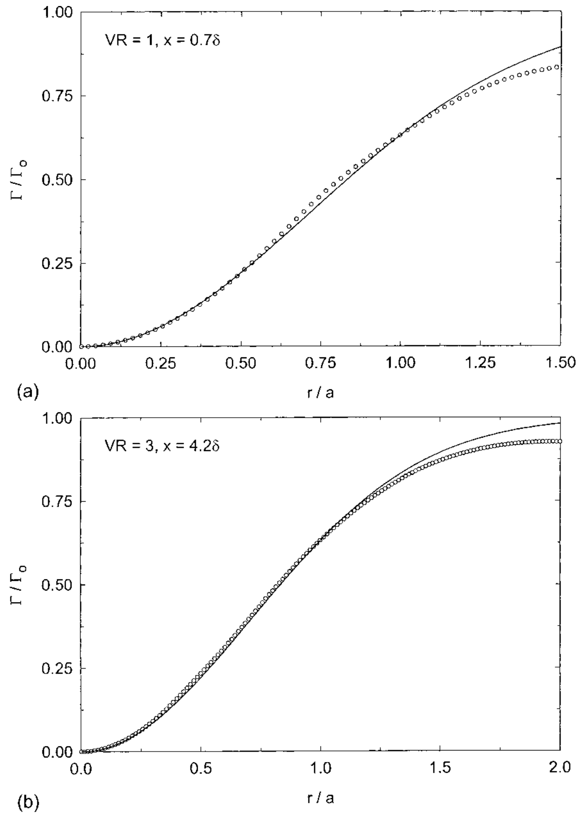

Fig. 12 Circulation distribution on concentric circles for (*a*) a *VR*=1 jet at *x*/*δ*=0.7 and (*b*) a *VR*=3 jet at *x*/*δ*=4.2. The curves represent Eq. (3) fitted to the data.

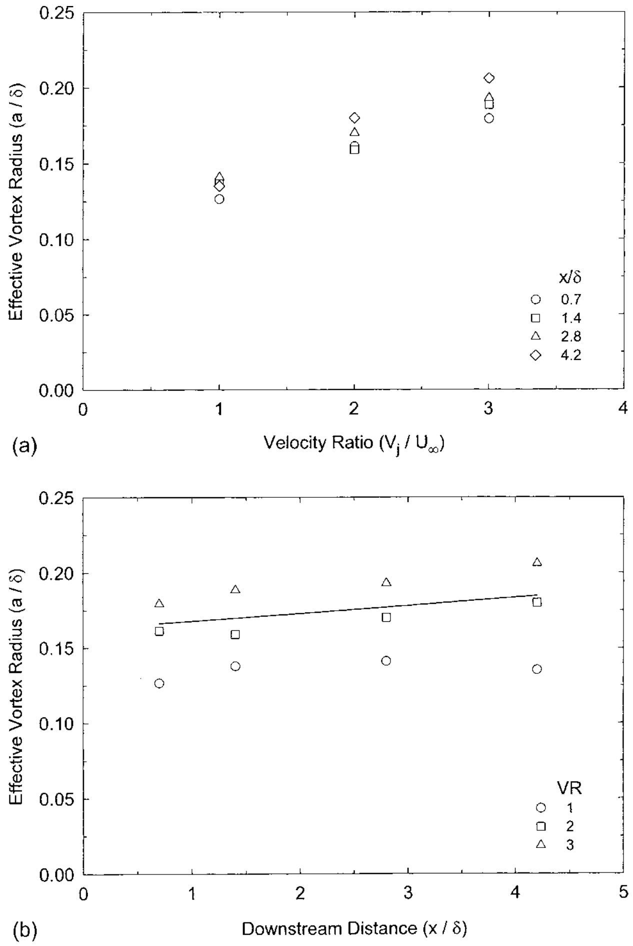

Fig. 13 Dependence of effective vortex radius *a* on velocity ratio *VR* (*a*) and downstream location (*b*). The curve in (*b*) corresponds to Eq. (5).

To check the validity of the Gaussian profile and to obtain the effective vortex radius a, circulation of the primary vortex in co-located fields was calculated on concentric circles originating at the vortex core. Then, the function in Eq. (3) was fitted to the data with a as a fitting parameter. The radial profile of circulation along with the best-fit error function is shown in Fig. 12 for the $VR=1$ and 3 jets at the first and last stations. The agreement between the circulation profiles and the error function is very good for $r \leqslant a$. The deviation of the fitted function from the data at larger radii is due to the vorticity contours not being quite circular, especially at the first measurement station (see Fig. 9(*a*)). Also, the close proximity of the CCW vortex influences the circulation and vorticity profiles. In all cases, the portion of the primary vortex containing 75% of Γ_o is well represented by Eq. (3).

The values of the effective vortex radius a resulting from fitting Eq. (3) to the circular contour circulation data is presented in Fig. 13. The effective radius of the primary vortex ranges from 0.13 to 0.21 δ, corresponding core diameters of 1.8 to 3.0 D. Although the vortex radius increased with velocity ratio, the vortices produced by the two higher velocity jets had radii within 13% of each other. On the other hand, the $VR=1$ jet produced a vortex with a smaller size. The effective vortex radius also increased with the downstream distance from the jet source, albeit at a very slow rate. The rate of increase of a with x was nearly the same for the two higher velocity ratio jets. Again, the different behavior of the vortex produced by the $VR=1$ jet from the higher velocity jets is thought to be due to the placement of the vortex core within the logarithmic region of the boundary layer.

An alternative way of arriving at the effective vortex radius is to evaluate Eq. (4) at the vortex core, i.e., $r=0$. This results in $a=\sqrt{\Gamma_o/\pi\omega_{\max}}$, valid for Gaussian profiles of circulation and vorticity. Since the circulation and peak vorticity of the two higher velocity jets could be represented reasonably by the expressions in Eqs. (2) and (1), respectively, these expressions were used to calculate the following effective vortex radius for $VR=2$ and 3 jets.

$$a \approx 0.163\delta e^{0.03(x/\delta)} \tag{5}$$

The expressions for circulation and peak vorticity both have a linear dependence on V_j, which appears to render a independent of VR. While this is consistent with the relatively small difference between the $VR=2$ and 3 effective radii observed in Fig. 13(*a*), it does belie a weak dependence on VR due to the combination of Eqs. (1) and (2). Moreover, the exponential increase of the effective radius with downstream distance in Eq. (5) can also be interpreted as a linear increase due to the very small exponent. A curve depicting the expression in Eq. (5) is drawn in Fig. 13(*b*) to indicate the close agreement between the values of a obtained from directly fitting the data and the above expression valid for $VR=2$ and 3. Data at stations further downstream are needed to verify whether the slow exponential increase of a with x is valid beyond our range of parameters.

Time-Averaging. To compare our data with past work on vortex generator jets at velocity ratio unity, we averaged the instantaneous fields without any spatial shifting to create velocity and vorticity fields analogous to time-averaged, pointwise data in the literature. Although the wandering of the primary vortex results in reduced peak vorticities due to time-averaging, this averaging allows a direct comparison of our data at $VR=1$ with those of Compton and Johnston [7] and Zhang and Collins [31]. The data in these references were measured in wind tunnels with boundary layer momentum Reynolds numbers of 1500 and 3200,

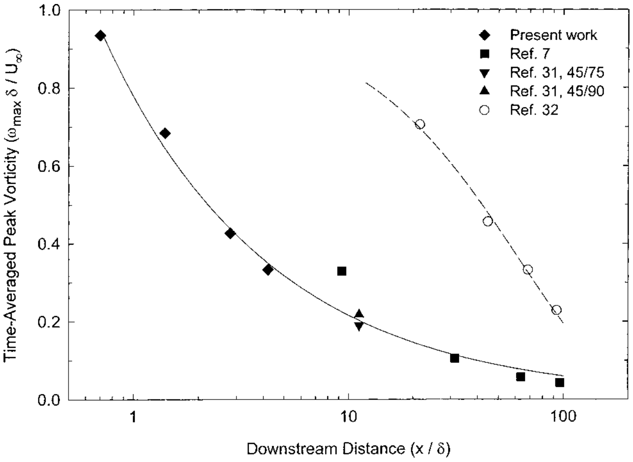

Fig. 14 Comparison of peak vorticity of time-averaged data as a function of downstream location for a $VR=1$ jet. Open circles represent solid vortex generator data. The solid curve is a power-law fit to our data $(0.78(x/\delta)^{-0.56})$. The dashed curve is an exponential fit to the solid vortex generator data. The jet pitch and skew angles for Ref. [31] are shown in the legend. All other jets have a 45 deg pitch and 90 deg skew angle.

respectively. These Re_θ values are considerably greater than the value of 715 in our experiment. The jet diameter to boundary layer thickness ratios in Refs. [7] and [31] are 0.45 and 0.56, respectively, again much larger than 0.14 in our experiment.

The available peak vorticity data are generally at x/δ stations farther downstream than in our experiment. To account for this difference, a power law was used to fit our time-averaged vorticity data. The data and the power law fit are shown in Fig. 14. The power law provides a better fit to the vorticity data than an exponential one for $VR=1$. The jet in [7] had the same pitch and skew angles, whereas that in [31] had a pitch angle of 45 deg and skew angles of 75 deg and 90 deg. The power law fit to our data (solid curve on the plot) appears to match the other data quite well, up to $\approx 100\ \delta$ downstream of the jet source. The close correspondence between the power law and the peak vorticity over an extended range of x/δ for different boundary layers not only verifies our setup and technique, but also reveals that perhaps the primary vortex characteristics do not depend strongly on the boundary layer Re_θ or D/δ. This is a subject of particular interest for future investigations. It appears that the velocity ratio influences the peak vorticity much more than the D/δ ratio or the boundary layer Reynolds number.

Unfortunately, neither of the above mentioned references present the location of the peak vorticity in their data. However, the peak vorticity location of the $VR=1$ jet at a skew angle of 45 deg could be extracted from one of the contour plots in [31]. The wall-normal position of the vortex core at $x=2.8\ \delta$ is at approximately $0.25\ \delta$. This value can be compared to $0.275\ \delta$ at the same axial location in our time-averaged data. The 10% difference can be attributed to the jet skew angles being different by 45 deg.

To assess the strength of the $VR=1$ primary vortex relative to the longitudinal vortex produced by a solid vortex generator, the data of Eibeck and Eaton [32] were utilized. The latter are also plotted in Fig. 14 along with the time-averaged $VR=1$ data. The dashed curve fitted to the solid vortex generator data is an exponential. The exponential fit was chosen because of the past work on solid vortex generators. Moreover, our higher VR jets also decayed exponentially. The comparison between the VGJ and solid vortex generator data confirms the finding of Compton and Johnston [7] that the peak vorticity of VGJs decays much more rapidly at first. However, at larger x/δ stations, roughly from 10 to 100, the decay of peak vorticity for solid vortex generator becomes more rapid.

Discussion

Our data indicate that both the peak vorticity and circulation of the primary streamwise vortex in the range of present setup for the two stronger jets $(VR=2{,}3)$ decay exponentially, analogous to solid vortex generators. The peak vorticity of the weakest jet, in contrast, decays at a lower rate, and appears to have a power law behavior. The faster decay of stronger jets and solid vortex generators is thought to be due to the larger scale motions present in the outer regions of the boundary layer. The linear dependence of vorticity and circulation on the jet velocity reveals that the jet is the main source of vorticity in VGJ vortices. Thus, the mean jet vorticity, which scales with the jet centerline velocity and diameter, determines the vorticity and circulation of the emergent primary vortex.

These arguments imply that the strongest vortices are generated by jets having a larger centerline velocity and a smaller diameter. Then, for a fixed available jet momentum flux, smaller diameter jets have larger velocities and should produce stronger primary vortices. On the other hand, smaller diameters would have a relatively longer distance, in terms of the jet diameter, to penetrate through the boundary layer. Thus, there should be an optimum jet diameter for given jet momentum flux, orientation, and boundary layer structure. An optimum jet diameter was found experimentally by McManus et al. in [12], corroborating our arguments.

The interaction of the naturally occurring vortical structures, and the accompanying turbulence, within the boundary layer and the vortices generated by the VGJs results in the loss of coherence of streamwise vortices and the associated decay of peak vorticity and circulation. The initial values of these parameters are set largely by the jet exit parameters. Vorticity present within a turbulent boundary layer distorts and weakens the coherent vorticity produced by the jet. The decay of vortices also affects their penetration within the boundary layer. Moreover, the boundary layer vortical structures are responsible for the meandering of the primary vortices, as noted earlier.

Conclusions

The evolution of vortices, created by a vortex generator jet, within a turbulent boundary layer was studied experimentally using the particle image velocimetry technique. The jet was pitched 45 deg and skewed 90 deg with respect to the surface and flow direction, respectively, and had a diameter that was 0.14 times the undisturbed boundary layer thickness at the jet source. Jet velocity ratios of 1, 2, and 3 were examined. The instantaneous velocity field in planes normal to the freestream was measured at four stations downstream of the jet exit, $x/D=5$, 10, 20, and 30 corresponding to $x/\delta=0.7$, 1.4, 2.8, and 4.2. The jet created a pair of streamwise vortices, one of which was significantly stronger and dominated the flow field. For the range of parameters in our study, the following conclusions are drawn:

1. The circulation, peak vorticity, and wall-normal and spanwise position of the primary vortex increase linearly with the jet velocity (or VR). All of these parameters fluctuate significantly in time. The circulation and peak vorticity decrease exponentially with the distance from the source for the jet to freestream velocity ratios of 2 and 3.
2. The vortex core of the weakest jet with a velocity equal to the freestream remained within the logarithmic region of the boundary layer, and behaved differently than the two stronger jets that penetrated through the logarithmic region.
3. Due to the significant wandering of the streamwise vortex within the boundary layer, time-averaged data from single-point measurements result in reduced vorticity. The extent of vortex wandering increases with the downstream distance and can be as much as ±30% of the undisturbed boundary layer thickness at $x/\delta=4.2$.
4. Conditional averaging of the velocity and vorticity fields, by co-locating the vortex core among different data sets, indicates

that the circulation and vorticity profiles within the central portion of the primary vortex are nearly Gaussian. The effective vortex radius increased weakly with both the jet velocity and downstream distance.

The consistency of our data with those available in the literature for higher Reynolds number boundary layers indicates that the above findings are perhaps applicable to larger Re_θ boundary layers.

Acknowledgments

This work was supported by a GOALI grant from the National Science Foundation (CTS-9631352). The help of D. Bond and K. J. Desabrais with the experiments is greatly appreciated. Initial discussions with Dr. Keith McManus are also acknowledged.

References

[1] Wallis, R. A., 1952, ''The Use of Air Jets for Boundary Layer Control,'' Aerodynamics Research Laboratories, Aero Note 110, Melbourne, Australia.
[2] Wallis, R. A., 1956, ''A Preliminary Note on a Modified Type of Air-Jet for Boundary Layer Control,'' Current Paper No. 513, Aeronautical Research Council, London, UK.
[3] Pearcey, H. H., Rao, K., and Sykes, D. M., 1993, ''Inclined Air-Jets Used as Vortex Generators to Suppress Shock-Induced Separation,'' AGARD-CP-534, *Computational and Experimental Assessment of Jets in Cross Flow*, pp. 40.1–40.10.
[4] Ball, W. H., 1984, ''Tests of Wall Blowing Concepts for Diffuser Boundary Layer Control,'' AIAA Paper 84-1276.
[5] Johnston, J. P., and Nishi, M., 1990, ''Vortex Generator Jets—Means for Flow Separation Control,'' AIAA J., **28**(6), pp. 989–994.
[6] Selby, G. V., Lin, J. C., and Howard, F. G., 1992, ''Control of Low-Speed Turbulent Separated Flow Using Jet Vortex Generators,'' Exp. Fluids, **12**(6), pp. 394–400.
[7] Compton, D. A., and Johnston, J. P., 1992, ''Streamwise Vortex Production by Pitched and Skewed Jets in a Turbulent Boundary Layer,'' AIAA J., **30**(3), pp. 640–647.
[8] Zhang, X., and Collins, M. W., 1997, ''Measurements of a Longitudinal Vortex Generated by a Rectangular Jet in a Turbulent Boundary Layer,'' Phys. Fluids, **9**(6), pp. 1665–1673.
[9] Zhang, X., 1995, ''Co- and Contra-rotating Streamwise Vortices in a Turbulent Boundary Layer,'' J. Aircr., **32**(5), pp. 1095–1101.
[10] Zhang, X., 1999, ''Counter-rotating Vortices Embedded in a Turbulent Boundary Layer With Inclined Jets,'' AIAA J., **37**(10), pp. 1277–1284.
[11] McManus, K. R., Legner, H. H., and Davis, S. J., 1994, ''Pulsed Vortex Generator Jets for Active Control of Flow Separation,'' AIAA Paper 94-2218.
[12] McManus, K., Ducharme, A., Goldey, C., and Magill, J., 1996, ''Pulsed Jet Actuators for Suppressing Flow Separation,'' AIAA Paper 96-0442.
[13] Magill, J. C., and McManus, K. R., 2001, ''Exploring the Feasibility of Pulsed Jet Separation Control for Aircraft Configurations,'' J. Aircr., **38**(1), pp. 48–56.
[14] Seifert, A., Bachar, T., Koss, D., Sheshelovich, M., and Wygnanski, I., 1993, ''Oscillatory Blowing: A Tool to Delay Boundary-Layer Separation,'' AIAA J., **31**(11), pp. 2052–2060.
[15] Wygnanski, I., 1997, ''Boundary Layer and Flow Control by Periodic Addition of Momentum,'' AIAA Paper 97-2117.
[16] Gad-el-Hak, M., and Blackwelder, R. F., 1987, ''Simulation of Large-Eddy Structures in a Turbulent Boundary Layer,'' AIAA J., **25**(9), pp. 1207–1215.
[17] Joslin, R. D., Kunz, R. F., and Stinebring, D. R., 2000, ''Flow Control Technology Readiness: Aerodynamic Versus Hydrodynamic,'' 18th Applied Aerodynamics Conference & Exhibit, Denver, CO, AIAA Paper 2000-4412.
[18] Landahl, M. T., 1990, ''On Sublayer Streaks,'' J. Fluid Mech., **212**, pp. 593–614.
[19] Johansson, A. V., Alfredsson, P. H., and Kim, J., 1991, ''Evolution and Dynamics of Shear Layer Structure in Near Wall Turbulence,'' J. Fluid Mech., **224**, pp. 579–599.
[20] Rathnasingham, R., and Breuer, K., 1997, ''System Identification and Active Control of a Turbulent Boundary Layer,'' Phys. Fluids, **9**(7), pp. 1867–1869.
[21] Jacobson, S. A., and Reynolds, W. C., 1998, ''Active Control of Streamwise Vortices and Streaks in Boundary Layers,'' J. Fluid Mech., **360**, pp. 179–211.
[22] Khan, Z. U., and Johnston, J. P., 2000, ''On Vortex Generating Jets,'' Int. J. Heat Fluid Flow, **21**, pp. 506–511.
[23] Shabaka, I. M. M. A., Mehta, R. D., and Bradshaw, P., 1985, ''Longitudinal Vortices Imbedded in Turbulent Boundary Layers. Part 1. Single Vortex,'' J. Fluid Mech., **155**, pp. 37–57.
[24] Cutler, A. D., and Bradshaw, P., 1993, ''Strong Vortex/Boundary Layer Interactions. Part I. Vortices High,'' Exp. Fluids, **14**, pp. 321–332.
[25] Cutler, A. D., and Bradshaw, P., 1993, ''Strong vortex/Boundary Layer Interactions. Part II. Vortices Low,'' Exp. Fluids, **14**, pp. 393–401.
[26] Johnston, J. P., Mosier, B. P., and Khan, Z. U., 2002, ''Vortex Generating Jets; Effects of Jet-Hole Inlet Geometry,'' Int. J. Heat Fluid Flow, **23**, pp. 744–749.
[27] Pratt, B. D., and Baines, W. D., 1967, ''Profiles of the Round Turbulent Jet in a Cross Flow,'' J. Hydraul. Div., Am. Soc. Civ. Eng., **92**, pp. 53–64.
[28] Broadwell, J. E., and Breidenthal, R. E., 1984, ''Structure and Mixing of a Transverse Jet in Incompressible Flow,'' J. Fluid Mech., **148**, pp. 405–412.
[29] Fearn, R., and Weston, R. P., 1974, ''Vorticity Associated with a Jet in a Cross Flow,'' AIAA J., **12**(12), pp. 1666–1671.
[30] Kuzo, D. M., 1995, ''An Experimental Study of the Turbulent Transverse Jet,'' Ph.D. dissertation, California Institute of Technology, Pasadena, CA.
[31] Zhang, X., and Collins, M. W., 1997, ''Nearfield Evolution of a Longitudinal Vortex Generated by an Inclined Jet in a Turbulent Boundary Layer,'' ASME J. Fluids Eng., **119**, pp. 934–939.
[32] Eibeck, P. A., and Eaton, J. K., 1987, ''Heat Transfer Effects of a Longitudinal Vortex Embedded in a Turbulent Boundary Layer,'' ASME J. Heat Transfer, **109**, pp. 16–24.

Filling Process in an Open Tank

S. L. Lee
e-mail: sllee@pme.nthu.edu.tw

S. R. Sheu

Department of Power Mechanical Engineering
National Tsing-Hua University,
Hsinchu 30013, Taiwan

A numerical simulation for a filling process in an open tank is performed in this paper. A single set of governing equations is employed for the entire physical domain covering both water and air regions. The great density jump and the surface tension existing at the free surface are properly handled with the extended weighting function scheme and the NAPPLE algorithm. There is no need to smear the free surface. Through the use of a properly defined boundary condition, the method of "extrapolated velocity" is seen to provide accurate migrating velocity for the free surface, especially when the water front hits a corner or a vertical wall. In the present numerical procedure, the unsteady term of the momentum equation is discretized with an implicit scheme. Large time-steps thus are allowed. The numerical results show that when the water impinges upon a corner, a strong pressure gradient forms in the vicinity of the stagnation point. This forces the water to move upward along the vertical wall. The water eventually falls down and generates a gravity wave. The resulting free surface evolution is seen to agree well with existing experimental data. Due to its accuracy and simplicity, the present numerical method is believed to have applicability for viscous free-surface flows in industrial and environmental problems such as die-casting, cutting with water jet, gravity wave on sea surface, and many others. [DOI: 10.1115/1.1624425]

Introduction

Filling process in cavity, mold, and tank is encountered in many scientific and industrial applications. The major difficulties dealing with such problems lie in the treatment of a few particular physical phenomena. First, an accurate tracking of the liquid-air interface (known as free surface) is needed. Second, turnaround of the liquid front should be properly handled when the liquid front impinges upon a corner or a wall. Third, the force balance equation on the free surface including the surface tension, the normal stress, and the shear stresses should be precisely satisfied. Fourth, the dynamic contact angle at the liquid front should be carefully modeled unless the characteristic length of the problem is sufficiently large.

Many numerical methods have been developed for mold-filling. However, the above-mentioned numerical difficulties are still not well resolved. Gilotte et al. [1] determined the stream function inside the liquid region with the potential flow theory, while a liquid jet was divided into branches manually. Instead of tracking the free surface, Advani and co-workers, [2,3], located only the control volumes through which the free surface was passing. Local refinement thus was needed for a more precise free surface profile. Matsuhiro et al. [4] and Zaidi et al. [5] used the marker and cell method (MAC) to track the free-surface advancement. Surface tension and stresses on the free surface were ignored. Sato and Richardson [6] employed fringe elements in addition to fixed Cartesian fundamental elements such that the shape of the free surface could be tracked. Unfortunately, numerical difficulty was encountered when the fringe elements were too small due to a Courant-Friedrich-Lewy stability condition.

In their effort in resolving the free-surface problem, Hirt and Nichols [7] introduced the concept of VOF (volume of fluid). A scalar function $f(x,y,z,t)$ was defined such that f was zero in the air region and jumped to unity in the fluid region. Such a particular function was found to be governed by the hyperbolic differential equation, [7],

$$\frac{\partial f}{\partial t}+u\frac{\partial f}{\partial x}+v\frac{\partial f}{\partial y}+w\frac{\partial f}{\partial z}=0 \tag{1}$$

where (u,v,w) denoted the flow velocity. However, Eq. (1) is a trivial equation either in the liquid region or in the air region, while the VOF function f possesses a discontinuity at the free surface. This gives rise to a great numerical difficulty when Eq. (1) is solved. To circumvent the numerical difficulty, Hirt and Nichols [7] employed the donor-acceptor scheme, [8], to estimate the average f value inside each finite volume instead of solving Eq. (1) directly. However, the numerical procedure was very inefficient especially when applied to three-dimensional mold-filling problems, [9]. Furthermore, the time-step should not be large due to the Courant criterion (advancement of the free surface should be less than one grid mesh in a single time-step).

A few variants of the VOF function f have been proposed for solving Eq. (1) directly. They include at least the indicator function, [10], the marker function, [11], the color function, [12], the level set function, [13,14], and the characteristic function, [15]. All of these variant functions will be simply denoted by f for convenience. Pichelin and Coupez [15] employed an explicit discontinuous Taylor-Galerkin method, [16], to solve Eq. (1) for the characteristic function in a three-dimensional mold-filling problem. However, their method was found to produce an unphysical zigzag free surface.

In the use of the marker function, Pericleous and co-workers, [11,17], employed van Leer's TVD scheme, [18], to solve Eq. (1). This approach yielded free surfaces with acute angles along with substantial numerical smearing. The results do not seem to be physically realistic. The fundamental concept of the level set function is to use a smeared VOF function f instead of the original sharp-step function such that the gradient of f exists across the free surface and thus Eq. (1) is numerically solvable. Very fine grids are generally needed. Otherwise, considerable artificial diffusion might arise. When the level set function was applied on a mold-filling problem, Dhatt et al. [19] found that the choice of the spatial representation of f near the liquid front required experience, insight and personal adjustments. The identification of new fronts from the f-value required as well experience, especially for the corner region and highly curved fronts.

Very recently, Lee and Sheu [20] proposed a new numerical formulation for free-surface flow without smearing the free surface. A force balance equation considering the surface tension was imposed on the free surface through the use of the NAPPLE algorithm, [21]. To achieve a smooth free-surface profile, a particular technique called "extrapolated velocity" was developed. The results showed good agreements with the well-documented dam-breaking experiments from Martin and Moyce [22]. In the present

---

Contributed by the Fluids Engineering Division for publication in the JOURNAL OF FLUIDS ENGINEERING. Manuscript received by the Fluids Engineering Division Nov. 5, 2000; revised manuscript received June 4, 2003. Associate Editor: E. W. Graf.

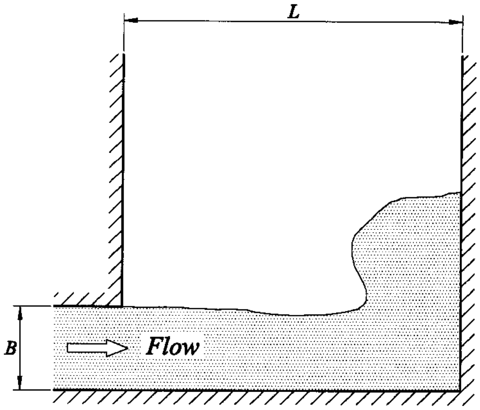

Fig. 1 Configuration of the problem

study, the method by Lee and Sheu [20] is employed to simulate the filling process in an open tank. A modification to the method of "extrapolated velocity" will be performed to properly handle the sharp turnaround of the liquid front after its impingement on a corner of the tank.

Theoretical Analysis

Consider a liquid being forced to fill a two-dimensional open tank of width L. The liquid enters the tank with a uniform velocity $U_{in}(t)$ through a gate of height B on one side of the tank as illustrated in Fig. 1. The flow is assumed laminar and incompressible. All of the physical properties of the liquid are constant. After introducing the dimensionless transformation

$$\begin{gathered} x=X/L, \quad y=Y/L, \quad u=U/U_c, \quad v=V/U_c, \\ p=(P-P_\infty)/(\rho_l U_c^2), \quad \tau=(U_c/L)t, \\ \mathrm{Re}=\rho_l U_c L/\mu_l, \quad \mathrm{Fr}=U_c/\sqrt{gL} \qquad (2) \\ \rho^*=\rho/\rho_l, \quad \mu^*=\mu/\mu_l, \quad b=B/L, \quad u_{in}=U_{in}/U_c \end{gathered}$$

a single set of governing equations covering both the liquid and the surrounding air can be written as

$$\frac{\partial u}{\partial x}+\frac{\partial v}{\partial y}=0 \qquad (3)$$

$$\rho^*\left(\frac{\partial u}{\partial \tau}+u\frac{\partial u}{\partial x}+v\frac{\partial u}{\partial y}\right)=-\frac{\partial p}{\partial x}+\frac{1}{\mathrm{Re}}\left(\frac{\partial}{\partial x}\left(\mu^*\frac{\partial u}{\partial x}\right)+\frac{\partial}{\partial y}\left(\mu^*\frac{\partial u}{\partial y}\right)\right) \qquad (4)$$

$$\rho^*\left(\frac{\partial v}{\partial \tau}+u\frac{\partial v}{\partial x}+v\frac{\partial v}{\partial y}\right)=-\frac{\partial p}{\partial y}-\frac{\rho^*}{\mathrm{Fr}^2}+\frac{1}{\mathrm{Re}}\left(\frac{\partial}{\partial x}\left(\mu^*\frac{\partial v}{\partial x}\right)+\frac{\partial}{\partial y}\left(\mu^*\frac{\partial v}{\partial y}\right)\right). \qquad (5)$$

The associated boundary conditions are

$$\begin{gathered} u(x,y,0)=0, \quad v(x,y,0)=0 \\ u(0,y,\tau)=u_{in}(\tau) \quad \text{for } 0\leqslant y<b, \\ u(0,y,\tau)=0 \quad \text{for } y\geqslant b, \quad v(0,y,\tau)=0 \qquad (6) \\ u(x,0,\tau)=0, \quad v(x,0,\tau)=0, \quad u(1,y,\tau)=0, \quad v(1,y,\tau)=0. \end{gathered}$$

Physically speaking, the boundary conditions for the surrounding air do not have a significant influence on the liquid flow, [20]. In addition, the filling process considered in the present study will terminate before the liquid reaches the height $y=1$. Hence, the computational domain is truncated at $y=1$ with the simplest artificial boundary condition

$$u(x,1,\tau)=0, \quad \partial v(x,1,\tau)/\partial y=0. \qquad (7)$$

Mathematically, the dimensionless density ρ^* and viscosity μ^* appearing in Eqs. (4) and (5) are step functions across the liquid-air interface. They have the value of unity in the liquid region and jump to another constant in the air region, i.e.,

$$\rho^*=\begin{cases} 1 & \text{in liquid} \\ \rho_a/\rho_l & \text{in air} \end{cases} \qquad (8a)$$

$$\mu^*=\begin{cases} 1 & \text{in liquid} \\ \mu_a/\mu_l & \text{in air} \end{cases} \qquad (8b)$$

where the subscripts a and l denote, respectively, the properties of the air and the liquid. Note also that in the governing Eqs. (3)–(5), the liquid-air interface is treated as an internal boundary such that no additional treatment is needed for the shear stresses there. In this connection, effect of surface tension is taken into account by considering the force balance equation on the liquid-air interface, [20,23,24],

$$p_l=p_a+\frac{\kappa}{\mathrm{We}}+\frac{1}{\mathrm{Re}}\left((\sigma_{nn})_l-\left(\frac{\mu_a}{\mu_l}\right)(\sigma_{nn})_a\right) \qquad (9)$$

$$\mathrm{We}=\frac{\rho_l U_c^2 L}{\gamma}, \quad \sigma_{nn}=2\frac{\partial v_n}{\partial n} \qquad (10)$$

where p_l and p_a stand for the dimensionless pressures on the liquid side and the air side, respectively. The symbols γ and κ are, respectively, the coefficient of surface tension and the dimensionless curvature of a convex free-surface profile. The notation σ_{nn} denotes the normal stress, while $\partial v_n/\partial n$ represents the normal strain rate. For convenience, the liquid-air interface will be referred to as "free surface" in the present study, although it is not really "free of stresses."

Solution Method

In the present study, the momentum Eqs. (4) and (5) are solved with the extended weighting function scheme, [20], on a fixed and nonstaggered Cartesian grid system. Due to the integration form of this particular scheme, the great discontinuity of the density ρ^* across the free surface can be effectively handled. It is noteworthy that both liquid and air are considered incompressible even though their densities are significantly different. Thus, the law of "volume conservation," (3), is valid for the entire computational domain including the free surface itself and both regions of liquid and air. Through the use of the NAPPLE algorithm, [20,21], the continuity Eq. (3) is converted into a pressure-linked equation. The pressure solution then is solved with the SIS solver, [25], while the force balance Eq. (9) is imposed on the free surface. The numerical procedure has been clearly described in Ref. [20].

As mentioned earlier, one of the major difficulties in solving a moving free-surface problem is the prediction of the free-surface advancement. For two nonimmersed fluids of similar viscosities, the migrating velocity of their interface can be easily interpolated from the velocity solution. However, this is not the case when the viscosity ratio is large. A large viscosity ratio gives rise to a large discontinuity in the velocity gradient across the free surface. Thus, when the solution (u,v,p) for a given time is obtained, the migrating velocity of the free surface cannot be precisely interpolated from the velocity solution at the grid points on both sides of the free surface. In view of the fact that the velocity gradient on the liquid side is very small as compared to the air side, Lee and Sheu [20] proposed the method of "extrapolated velocity from the liquid region" to estimate the migrating velocity of the free surface.

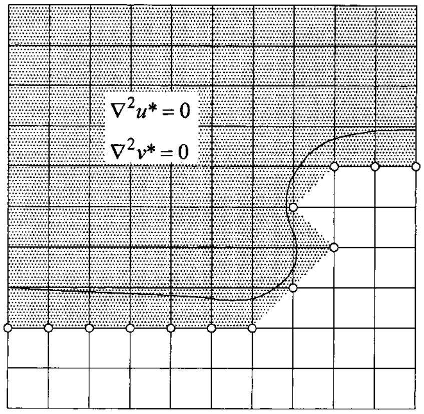

Fig. 2 Computational domain for the artificial velocity (u^*, v^*)

Figure 2 shows a schematic free surface (the solid curve) in a computational domain on a fixed Cartesian grid system. The grid points (the white nodes) adjacent to the free surface on the liquid side separate the computational domain into two regions. One of the two regions contains only liquid, while the other (the gray region) includes the whole air region, the free surface itself and a narrow liquid layer between the white nodes and the free surface. Based on the concept of the "extrapolated velocity," [20], one solves the Laplace equations

$$\frac{\partial^2 u^*}{\partial x^2} + \frac{\partial^2 u^*}{\partial y^2} = 0, \quad \frac{\partial^2 v^*}{\partial x^2} + \frac{\partial^2 v^*}{\partial y^2} = 0 \tag{11}$$

on the gray region (see Fig. 2) with known velocities at the white nodes to yield an artificial velocity (u^*, v^*). The migrating velocity of the free surface is then interpolated from this artificial velocity.

As remarked by Lee and Sheu [20], the Laplace Eq. (11) are used only to extrapolate the liquid velocity in a narrow region between the white nodes (see Fig. 2) and the free surface. Influence of the boundary conditions imposed on the other boundaries of the computational domain (the gray region) would not be significant. Hence, the following artificial boundary conditions are assigned for the boundaries when they are exposed to air

$$\begin{gathered} \partial v^*(0,y)/\partial x = 0, \quad \partial v^*(1,y)/\partial x = 0, \\ \partial u^*(x,0)/\partial y = 0, \quad v^*(x,0) = 0, \quad u^*(x,1) = 0, \\ \partial v^*(x,1)/\partial y = 0. \end{gathered} \tag{12}$$

Definition of the boundary conditions for u^* on the vertical walls $x = 0$ and $x = 1$ will be discussed later. After the artificial velocity (u^*, v^*) is known and the migration velocity of the free surface is obtained, the free-surface advancement for the next time-step can be easily estimated with a numerical procedure proposed by Lee and Sheu [20].

Results and Discussion

Hwang and Stoehr [26] performed an experiment on filling process of water flow inside a mold of a vertical square plate "casting" similar to the open tank shown in Fig. 1 on the xy-plane. The width of the tank and the height of the gate were $L = 15.2$ cm and $B = 3.8$ cm, respectively. The free surface was found to be essentially two-dimensional due to the fact that the third dimension (thickness) of the tank is rather small as compared to the width of the tank L. A sequence of photographs was taken to record the evolution of the free surface profile. However, the inlet condition at the gate was not known. Fortunately, the volume of water inside the tank can be evaluated from the photographs. The result is approximately

$$Q(t) = 0.005t(6 - t) \tag{13}$$

which implies

$$U_{in}(t) = 0.7896(1 - t/3) \tag{14}$$

if the velocity profile is assumed to be uniform, where Q, U_{in}, and t are measured in m^2/s, m/s and s, respectively.

In the present computation, the physical properties of water and air at 25°C are employed, i.e.,

$$\begin{gathered} \rho_w = 998 \ \text{kg/m}^3, \quad \mu_w = 0.99 \times 10^{-3} \ \text{kg/m s} \\ \rho_a = 1.205 \ \text{kg/m}^3, \quad \mu_a = 1.81 \times 10^{-5} \ \text{kg/m s} \\ \rho_a/\rho_w = 0.001207, \quad \mu_a/\mu_w = 0.01828 \\ \gamma = 0.0720 \ \text{N/m} \end{gathered} \tag{15}$$

while the gravity is $g = 9.806$ m/s^2. The characteristic velocity is assigned as

$$U_c = U_{in}(0) = 0.7896 \ \text{m/s}. \tag{16}$$

The corresponding Reynolds number, Froude number, and Weber number are, respectively, $\text{Re} = 1.210 \times 10^5$, $\text{Fr} = 0.6468$, and $\text{We} = 1314$. The dimensionless gate height and inlet velocity are $b = 0.25$ and $u_{in}(\tau) = 1 - 0.06417\tau$, respectively. The maximum air velocity (occurring at $\tau = 0$) has a Mach number of only 0.002282. Thus, the compressibility effect of the air is negligible. The dimensionless curvature κ is evaluated from every three successive makers on the free surface, [20], i.e., three points define a circle.

Numerical results including the evolution of the free-surface profile, velocity, and pressure were obtained on various combinations of grid meshes and time steps. Among them, the finest grid is $\Delta x = \Delta y = 0.0125$ and $\Delta\tau = 0.006494$ which corresponds to 0.19 cm and 0.00125 s, respectively. The results obtained on the finest grid are shown in Figs. 3 and 4. Influence of the grid meshes and the time steps on the numerical solution will be discussed later.

Figure 3 shows the isobars (with increment $\Delta p = 0.1$) and the velocity at four representative times, i.e., $t = 0.1$ s, 0.3 s, 0.45 s, and 0.65 s. The conversion factor between t and τ is $t = t_c \tau$ and $t_c = L/U_c = 0.1925$ s. As expected, the pressure jump across the free surface is not significant in the present case. This can be attributed to the large Weber and Reynolds numbers (9). By contrast, the pressure gradient has a large discontinuity across the free surface due to the large density ratio of the water and the air (15). As a result, the pressure in the air region is essentially zero. This leads to a difficulty in plotting the isobar $p = 0$. In Fig. 3, $p = 0.001$ was employed instead of $p = 0$ when the isobar $p = 0$ was plotted.

The evolution of the free surface profile at every 0.05 s is plotted in Fig. 4(a). To clearly observe the sharp advancement of the free surface in the period $0.2 \text{ s} \leq t \leq 0.3 \text{ s}$, the free surface is presented in Fig. 4(b) at every 0.01 s in that period. The results reveal that the water enters the tank as a wall jet along the tank bottom on $y = 0$. After the water front hits the opposite wall on $x = 1$, a large pressure gradient forms in the vicinity of the stagnation point. This forces the water flow to jump up along the vertical wall on $x = 1$. It is quite interesting to note that after reaching the highest point ($y = 0.84$) at $t = 0.25$ s, the water falls down and forms a gravity wave traveling in the $-x$ direction. It flows up the vertical wall on $x = 0$ after the wave reaches this wall. The computation was terminated at $t = 0.65$ s in view of the boundary condition (7).

It should be pointed out here that using a nonpermeable condition

$$u^*(1,y) = 0 \tag{17}$$

for the extrapolated velocity (u^*, v^*) will give rise to a physically unrealistic situation that the water front will never reach the opposite wall on $x = 1$. By contrast, the use of the freely permeable boundary condition

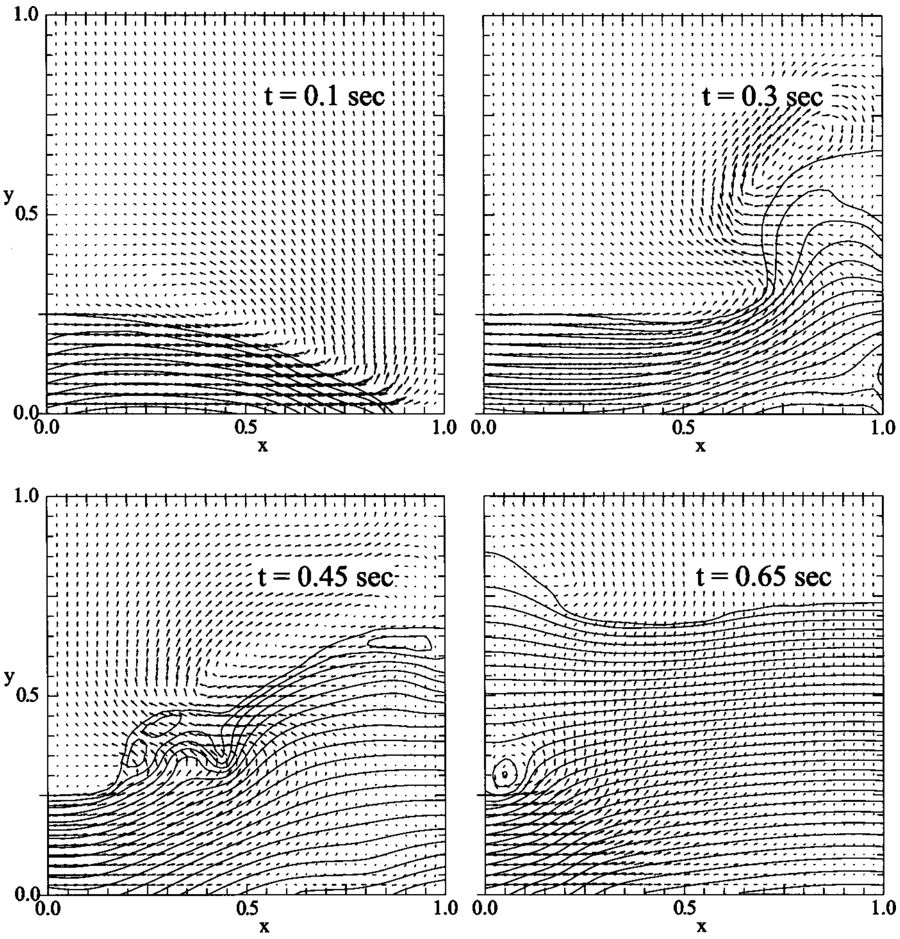

Fig. 3 The isobars (with increment $\Delta p = 0.1$) and the velocity vectors at four representative times

$$\partial u^*(1,y)/\partial x = 0 \tag{18}$$

could produce a water front that penetrates the solid wall $x = 1$, i.e., $u(1,0) > 0$. This is physically unrealistic either. Physically, the water does not "sense" the existence of the vertical wall $x = 1$ before it reaches there. Once the water front hits the wall $x = 1$, the boundary condition on the water front would suddenly transit from the "free surface" situation to a nonpermeable condition. This instantly decelerates the water flow ($\partial u/\partial \tau \leq 0$) and thus induces a strong pressure increase in a region covering the stagnation point. In the present study, the freely permeable boundary condition (18) is employed before the water reaches the wall $x = 1$, and thereafter, the nonpermeable condition (17) is assumed. Suppose the water front just touches the wall at time τ^* during a time-step elapsing in the period $\tau_{n-1} \leq \tau \leq \tau_n$. This particular time-step is divided into two substeps ($\tau_{n-1} \leq \tau \leq \tau^*$ and $\tau^* \leq \tau \leq \tau_n$) such that the freely permeable condition (18) can be applied

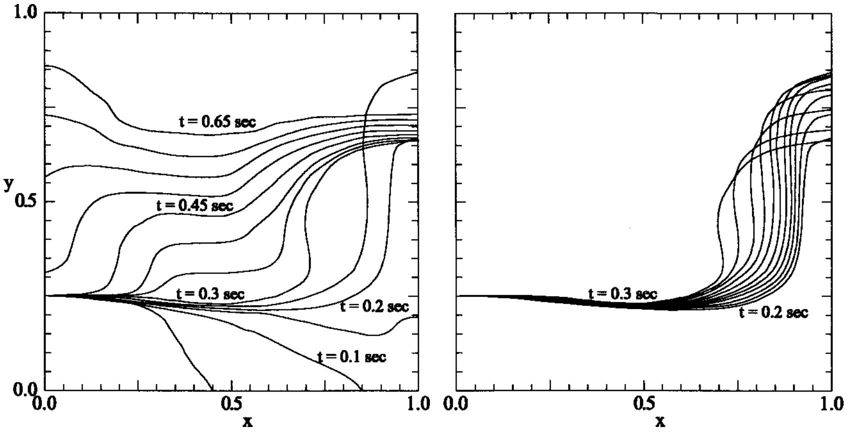

Fig. 4 Evolution of the free surface profile (*a*) at every 0.05 s, and (*b*) at every 0.01 s in the period 0.2 s$\leq t \leq$0.3 s

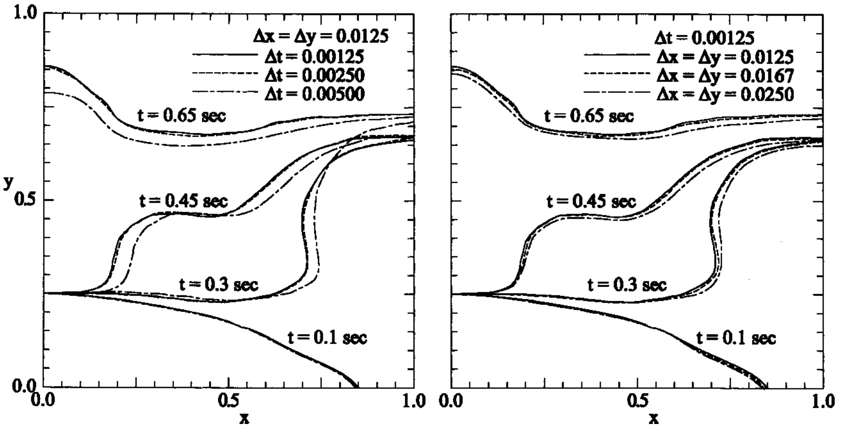

Fig. 5 Influence of (*a*) time steps, and (*b*) spatial grid meshes on the free-surface profiles

exactly up to the time τ^*. Similar treatment is performed when the gravity wave hits the wall $x=0$.

Figure 5(*a*) shows the influence of various time-steps on the free-surface profiles at four representative times. Similar grid testing is performed to investigate the influence of the spatial grid meshes as shown in Fig. 5(*b*). Furthermore, to examine the reliability of the present numerical method, the computational result of free-surface advancement is compared with the experimental observation from Hwang and Storhr [26] in Fig. 6. From Fig. 5, the grid mesh $\Delta x=\Delta y=0.0125$ along with the time-step $\Delta t=0.00125\,\mathrm{s}$ as adopted in Figs. 3 and 4 is found adequate for the present problem. Excellent agreement between the present prediction and the experimental data is observable from Fig. 6.

The water volume inside the tank is examined in Fig. 7. The white dots in Fig. 7 are the water volume estimated from the experimental observation of Hwang and Steohr [26]. The dashed curve, a least-square approximation of the white dots, stands for the inlet conditions (13) and (14) on which the present computation is based. The solid curve is the water volume directly evaluated from Fig. 4. From Fig. 7, one sees a satisfactory agreement between the present computation and the experimental data (the solid curve and the dashed curve). This demonstrates the accuracy of the present numerical method on the mass conservation. As a final note it is mentioned that, the two-dimensional assumption taken in the present computation neglects the viscous friction on the *z*-surfaces of the tank. Thus, the computed pressure gradient would be slightly underpredicted. Nevertheless, the mass flow is not influenced due to the use of a known velocity (14) for the inlet boundary condition (6).

Conclusion

This paper presents a numerical simulation for a filling process in an open tank. A single set of governing equations is employed for the entire physical domain covering both water and air regions. The large density jump across the water-air interface (free surface) is handled with the extended weighting function scheme such that there is no need to smear the free surface. A force balance equation (including surface tension) is imposed on the free surface through the use of the NAPPLE algorithm. In this connection, a modified "extrapolated velocity" is developed to track the sharp turnaround of the water front when it impinges upon a corner. Excellent agreement between the present numerical results and an existing experiment is found. The numerical method employed in this work is very simple and accurate. It applies to industrial and environmental problems such as die-casting, cutting with water jet, gravity waves on sea surface, and many others as well.

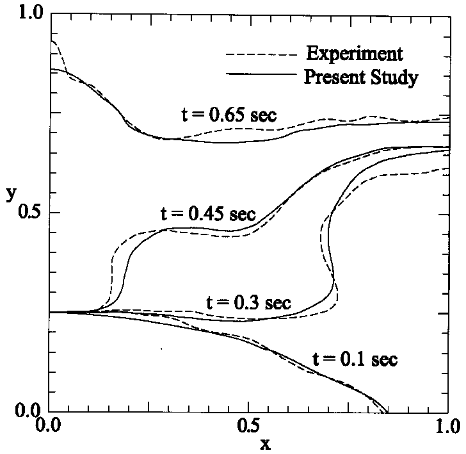

Fig. 6 Comparison of free-surface advancement between the present prediction and the experimental observation (Hwang and Stoerhr [26])

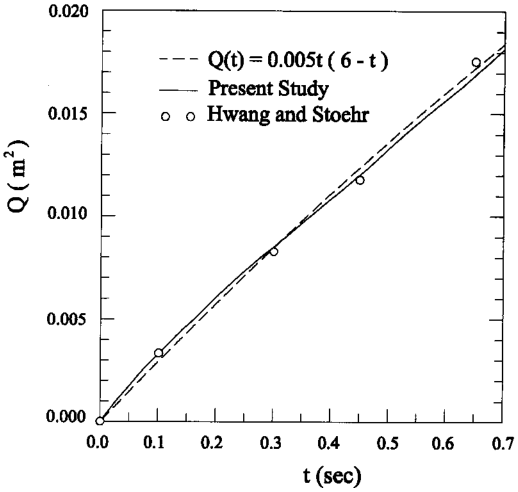

Fig. 7 An examination of the computed mass conservation inside the tank

Acknowledgments

The authors wish to express their appreciation to the National Science Council of Taiwan for the financial support of this work through the contract NSC 89-2212-E007-032.

Nomenclature

b, B = height of the gate, $b=B/L$
f = VOF function, $f=1$ in liquid and $f=0$ in air
g = gravity acceleration
Fr = Froude number, $U_c/\sqrt{gL}$
L = width of the tank (characteristic length of the problem)
p = dimensionless pressure, Eq. (2)
Q = water volume inside the tank
Re = Reynolds number, $\rho_l U_c L/\mu_l$
t = time
(u,v) = dimensionless velocity, Eq. (2)
(u^*,v^*) = artificial velocity, Eq. (11)
U_c = characteristic velocity, Eq. (16)
U_{in} = inlet velocity
We = Weber number, $\rho_l U_c^2 L/\gamma$
(x,y,z) = dimensionless coordinate system

Greek Letters

γ = coefficient of surface tension
κ = dimensionless curvature (based on the characteristic length L) of a convex free-surface profile
μ, μ^* = viscosity and dimensionless viscosity, $\mu^*=\mu/\mu_l$
ρ, ρ^* = density and dimensionless density, $\rho^*=\rho/\rho_l$
σ_{nn} = normal stress
τ = dimensionless time, Eq. (2)

Subscripts

a = air
l = liquid
n = normal direction
w = water

References

[1] Gilotte, P., Huynh, L. V., Etay, J., and Hamar, R., 1995, ''Shape of the Free Surfaces of the Jet in Mold Casting Numerical Modeling and Experiments,'' ASME J. Eng. Mater. Technol., **17**, pp. 82–85.
[2] Bruschke, M. V., and Advani, S. G., 1994, ''A Numerical Approach to Model Non-Isothermal Viscous Flow Through Fibrous Media With Free Surfaces,'' Int. J. Numer. Methods Fluids, **19**, pp. 575–603.
[3] Maier, R. S., Rohaly, T. F., Advani, S. G., and Fickie, K. D., 1996, ''A Fast Numerical Method for Isothermal Resin Transfer Mold Filling,'' Int. J. Numer. Methods Eng., **39**, pp. 1405–1417.
[4] Matsuhiro, I., Shiojima, T., Shimazaki, Y., and Daiguji, H., 1990, ''Numerical Analysis of Polymer Injection Moulding Process Using Finite Element Method With Marker Particles,'' Int. J. Numer. Methods Eng., **30**, pp. 1569–1576.
[5] Zaidi, K., Abbes, B., and Teodosiu, C., 1996, ''Finite Element Simulation of Mold Filling Using Marker Particles and k-ε Model of Turbulence,'' Comput. Methods Appl. Mech. Eng., **134**, pp. 241–247.
[6] Sato, T., and Richardson, S. M., 1994, ''Numerical Simulation Method for Viscoelastic Flows With Free Surfaces—Fringe Element Generation Method,'' Int. J. Numer. Methods Fluids, **19**, pp. 555–574.
[7] Hirt, C. W., and Nichols, B. D., 1981, ''Volume of Fluid (VOF) Method for the Dynamics of Free Boundaries,'' J. Comput. Phys., **39**, pp. 201–225.
[8] Ramshaw, J., and Trapp, J., 1976, ''A Numerical Technique for Low Speed Homogeneous Two-Phase Flow With Sharp Interface,'' J. Comput. Phys., **21**, pp. 438–453.
[9] Chen, C. W., Li, C. R., Han, T. H., Shei, C. T., Hwang, W. S., and Houng, C. M., 1994, ''Numerical Simulation of Filling Pattern for an Industrial Die Casting and Its Comparison With the Defects Distribution of an Actual Casting,'' Trans. Am. Found. Soc., **104**, pp. 139–146.
[10] Unverdi, S. O., and Tryggvason, G., 1992, ''A Front-Tracking Method for Viscous, Incompressible, Multi-Fluid Flows,'' J. Comput. Phys., **100**, pp. 25–37.
[11] Pericleous, K. A., Chan, K. S., and Cross, M., 1995, ''Free Surface Flow and Heat Transfer in Cavities: The SEA Algorithm,'' Numer. Heat Transfer, **27B**, pp. 487–507.
[12] Wu, J., Yu, S. T., and Jiang, B. N., 1996, ''Simulation of Two-Fluid Flows by the Least-Square Finite Element Methods Using a Continuum Surface Tension Model,'' NASA CR-202314, Lewis Research Center, Cleveland, OH.
[13] Sussman, M., Fatemi, E., Smereka, P., and Osher, S., 1998, ''An Improved Level Set Method for Incompressible Two-Phase Flows,'' Comput. Fluids, **27**, pp. 663–680.
[14] Hetu, J.-F., and Ilinca, F., 1999, ''A Finite Element Method for Casting Simulations,'' Numer. Heat Transfer, Part A, **36A**, pp. 657–679.
[15] Pichelin, E., and Coupez, T., 1999, ''A Taylor Discontinuous Galerkin Method for the Thermal Solution in 3D Mold Filling,'' Comput. Methods Appl. Mech. Eng., **178**, pp. 153–169.
[16] Pichelin, E., and Coupez, T., 1998, ''Finite Element Solution of the 3D Mold Filling Problem for Viscous Incompressible Fluid,'' Comput. Methods Appl. Mech. Eng., **163**, pp. 359–371.
[17] Chan, K. S., Pericleous, K., and Cross, M., 1991, ''Numerical Simulation of Flows Encountered During Mold-Filling,'' Appl. Math. Model., **15**, pp. 624–631.
[18] van Leer, B., 1977, ''Towards the Ultimate Conservative Difference Scheme. IV. A New Approach to Numerical Convection,'' J. Comput. Phys., **23**, pp. 276–299.
[19] Dhatt, G., Gao, D. M., and Cheikh, A. B., 1990, ''A Finite Element Simulation of Metal Flow in Moulds,'' Int. J. Numer. Methods Eng., **30**, pp. 821–831.
[20] Lee, S. L., and Sheu, S. R., 2001, ''A New Numerical Formulation for Incompressible Viscous Free Surface Flow Without Smearing the Free Surface,'' Int. J. Heat Mass Transfer, **44**, pp. 1837–1848.
[21] Lee, S. L., and Tzong, R. Y., 1992, ''Artificial Pressure for Pressure-Linked Equation,'' Int. J. Heat Mass Transfer, **35**, pp. 2705–2716.
[22] Martin, J. C., and Moyce, W. J., 1952, ''An Experimental Study of the Collapse of Liquid Columns on a Rigid Horizontal Plane,'' Philos. Trans. R. Soc. London, Ser. A, **244A**, pp. 312–324.
[23] Sarpkaya, T., 1996, ''Vorticity, Free Surface, and Surfactants,'' Annu. Rev. Fluid Mech., **28**, pp. 83–128.
[24] Tsai, W. T., and Yue, D. K. P., 1996, ''Computation of Nonlinear Free-Surface Flows,'' Annu. Rev. Fluid Mech., **28**, pp. 249–278.
[25] Lee, S. L., 1989, ''A Strongly-Implicit Solver for Two-Dimensional Elliptic Differential Equations,'' Numer. Heat Transfer, Part B, **16B**, pp. 161–178.
[26] Hwang, W.-S., and Stoehr, R. A., 1988, ''Modeling of Fluid Flow,'' *Metal Handbook*, 9th Ed., ASM International, Metals Park, OH, **15**, pp. 867–876.

K. S. Sujatha
M. F. Webster[1]

Department of Computer Science,
Institute of Non-Newtonian Fluid Mechanics,
University of Wales,
Swansea, SA2 8PP, UK

Modeling Free-Surface Flow in Part-Filled Rotating Vessels: Vertical and Horizontal Orientations

This paper reports on the numerical simulation of rotating flows with free surfaces, typically that arise in dough-kneading situations found within the food processing industry. Free-surface flow in a rotating cylinder is investigated when a fluid is stirred in a cylindrical-shaped vessel with a stirrer attached to its lid. The problem is posed in a three-dimensional cylindrical polar frame of reference. Numerical predictions are based on a Taylor-Galerkin/pressure-correction finite element formulation, with particle tracking to accommodate free-surface movement. Peeling and wetting conditions are incorporated to predict fluid-surface movement in contact with solid boundaries. Free-surface profiles are presented for different speeds of rotation and predictions compare closely to equivalent experimental results. The algorithmic implementation is validated against Newtonian analytical solutions. Typical results are presented to demonstrate the difference between Newtonian and inelastic model fluids. [DOI: 10.1115/1.1625685]

1 Introduction

This paper addresses the numerical simulation of free-surface flows in rotating cylindrical-shaped vessels that arise in the food processing industry. The motivation for this work is to develop an advanced technology to model dough kneading. The ultimate objective is to provide a predictive capability from which optimal designs for dough mixer-vessels may emerge, based upon rheological considerations and influence upon the kneading process itself. Free-surface flows are common in everyday experience and many industrial processes. There are several approaches commonly proposed in treating moving free surfaces, a comprehensive review of which is provided in Wang and Lee [1]. The first category comprises methods that move the mesh system itself in a Lagrangian sense, following the movement of the fluid (e.g., marker and cell (MAC) method (Harlow and Welch [2] and Welch et al. [3]). This method introduces complications within the discrete representation of the problem, as in the course of time, the moving mesh system often suffers gross distortion, which necessitates remeshing to rebalance mesh aspect ratios.

With Eulerian-based methods, the actual position of free boundary points are localized in a fixed mesh. The governing equations are solved in a larger domain than that is actually occupied by the fluid, distinguishing between wet and dry regions (e.g., as achieved in the volume of fluid method (VOF) of Hirt and Nichols [4]). The original VOF method employed a finite difference scheme and was not straightforward to implement for problems involving complicated boundaries. This method was later extended by various investigators to solve a variety of problems, such as mold filling and metal casting. A VOF variant, based on finite element techniques, has also been developed and applied to solve relatively simple problems (Gethin et al. [5]). Later, an Eulerian finite element method for free-surface problems was developed, [6], although its ability to treat complex geometries was the only significant advantage over more basic methods, such as MAC. See, for example, Rudman [7,8] who employed a MAC-type momentum advection technique for the simulation of multi-fluid flows with large density variations on staggered grids. Subsequently, an improved version of the VOF method has been developed, in which the flow field is treated as a two-phase system. In this method, the regions filled with fluid are assumed to be within a single phase. The dry region, separated by the free-surface boundary is considered as a second phase, consisting of a virtual fluid of artificial physical properties. Such a formulation is termed a pseudo-density method, [9]. To avoid the use of artificial physical properties, Nassehi and Ghoreishy [10] proposed the strategy to treat the dry section as a compressible fluid.

An alternative approach was proposed by Sato and Richardson [11], appealing to a fringe element generation method based upon a hybrid finite element/finite volume scheme. No remeshing was required as the fluid was assumed to flow over a fixed mesh, wetting fresh regions. New fringe elements were created in the surface neighborhood, conforming to the original mesh structure and avoiding excessive mesh distortion. A similar strategy was adopted by Ding et al. [12] and Manogg et al. [13] for the computation of moving boundaries encountered in injection molding situations. Medale and Jaeger [14] developed a simulation technique for free-surface flows in two-dimensional geometries, based on a finite element analysis with an Eulerian approach and an unstructured fixed mesh. These authors presented several numerical examples to demonstrate the accuracy of their procedures.

Artificial Lagrangian-Eulerian methods combine the respective advantages of both Lagrangian and Eulerian methods, [15–17]. In the Lagrangian phase, the mesh velocity equates to the fluid velocity, that removes the convective fluxes from the momentum transport equation. In this manner, nodal point location may be computed via a velocity-correction scheme. Subsequently, the mesh velocity is updated using these nodal point locations. In the Eulerian phase, convective fluxes are evaluated. Finally, an updated position of the free surface is computed, using both fluid and mesh velocities. A mixed Lagrangian-Eulerian method was developed by Ramaswamy [16] for calculating the transient dynamics of incompressible, viscous fluids with free surfaces. This mixed method mitigates excessive mesh distortion that may arise during the Lagrangian phase.

In the present work, interest is centred around unsteady free-surface flows encountered in dough kneading. Two different dough mixer designs are investigated, with single and double stir-

---

[1] To whom correspondence should be addressed.

Contributed by the Fluids Engineering Division for publication in the JOURNAL OF FLUIDS ENGINEERING. Manuscript received by the Fluids Engineering Division January 14, 2002; revised manuscript received June 6, 2003. Associate Editor: A. K. Prasad.

rers. Stirrers are located either in a concentric or eccentric arrangement, with respect to the axis of the vessel. As an alternative to conventional mixer operation, the motion is assumed to be driven by the rotation of the vessel, for convenience within the modeling. Aspects of this study, dealing with numerical and experimental comparisons for filled vessels, have been published elsewhere, [18–19]. Here, the mixer is considered to be partially filled, and in both a vertical and horizontal standing orientation. This leaves the surface of the fluid to move freely. The free surface is described by a number of particles, the evolution of which is tracked. In addition, novel strategies are proposed to accommodate wetting and peeling phenomena, which arise at the interface between fluid and solid surfaces.

The simulation procedure employs a Taylor-Galerkin/pressure-correction finite element formulation for the generalized momentum/continuity equation system. This formulation applies a temporal discretization in a Taylor series, prior to a Galerkin spatial discretization. A semi-implicit treatment for diffusion is used to address linear stability constraints. The flow is modeled as incompressible via a pressure-correction procedure. A fixed finite element mesh covers the whole domain, that is divided dynamically into two different sections: one wet and another dry. The position of the free-surface interface defines the wet fluid region, upon which solution for field variables is activated. The equivalent experimental results presented in this paper involve laser scatter technology and contemporary imaging techniques, [19,20]. Similar procedures have been used by Prakash and Kokini [21–23] to determine velocity vectors associated with flows in model mixers, to ultimately discern shear-rate distributions. In the kneading process, the quality of the final product (where internal material structure is developed through kneading), depends upon the distribution and type of mechanical work put into the dough. In this regard and within the present study, it has proved instructive to construct secondary field data of velocity gradients, local shear rates and local rate of work done. These quantities may be estimated from primary finite element solution field data. Hence, torque and power may be computed, which provide a torque-time trace. Such data are gleaned out to aid ultimately in the overall appreciation of effective dough kneading, by associating localized deformation with its influence on buildup of material structure (via shear and extension).

2 Basic Equations and Numerical Scheme

For incompressible isothermal flow, the generalized momentum and continuity equations may be expressed as

$$\rho \mathbf{U}_t = \nabla.(\mu \nabla \mathbf{U}) - \rho \mathbf{U}.\nabla \mathbf{U} - \nabla P + \rho \mathbf{g}, \tag{1}$$

$$\nabla.\mathbf{U} = 0, \tag{2}$$

where dependent variables ($\mathbf{U}$) and pressure (P) are defined over independent variables of space and time. $\mathbf{U}_t$ represents a time derivative, and spatial gradient and divergence operators follow standard conventional notation. Fluid material properties are given via density (ρ) and viscosity (μ), and $\mathbf{g}$ is the gravitational constant vector. A Carreau-Yasuda (C-Y) model is employed to describe the shear-thinning rheology, providing the functional variation for viscosity μ, viz,

$$\mu = \frac{\mu_o - \mu_\infty}{1 + (\lambda \dot{\gamma})^m} + \mu_\infty, \tag{3}$$

where μ_o is a reference viscosity at low shear rates and μ_∞ is an asymptotic value of viscosity at large shear rates; $\dot{\gamma} = 2\sqrt{I_2}$ with the second invariant I_2 ($I_2 = \frac{1}{2}\mathrm{trace}(D^2)$) the rate-of-strain tensor, ''D'' is the rate-of-deformation tensor, m is a power-law index and λ is a material constant. To be specific, we take $m = 0.6$ and $\lambda = 0.083$ s.

To facilitate experimental flow visualization, a viable model fluid must be translucent. Hence, dilute polymer solutions were employed as model fluids in the equivalent experimental program of work, against which comparison and validation is based. The corresponding experimental model fluids employed were 1% CMC, 2% CMC, 3% CMC, and 4% CMC. As the concentration of CMC increases, the elastic properties of the fluid increases. The Carreau-Yasuda model has been selected based on the rheological characterization of actual dough samples and these particular model fluids quoted, [19]. Such materials are observed to be shear thinning and may be fitted to the above model. So, for example in this respect, the rheology of 4% CMC corresponds to the shear behavior of dough, with 1.3 times the normal levels of water.

For convenience of representation, we adopt nondimensional variables and the following scales: L, V, and μ_c (where $\mu_c = \mu_0 = 1.05$ Pa.s) are characteristic length, velocity, and viscosity, respectively.

$$X^* = \frac{X}{L}, \quad \mathbf{U}^* = \frac{\mathbf{U}}{V}, \quad \mu^* = \frac{\mu}{\mu_c}, \quad t^* = \frac{V}{L}t, \quad P^* = \frac{L}{\mu_c V}P. \tag{4}$$

We adopt L as the diameter of the stirrer (18 mm) and V, the speed of rotation of the vessel. The body force term involving gravity, ''F,'' equates to the ratio between Reynolds and Froude number, defined as

$$F = \frac{\mathrm{Re}}{\mathrm{Fr}} = \frac{\rho L^2 g}{\mu_c V}, \quad \text{where} \quad \mathrm{Re} = \frac{\rho L V}{\mu_c} \quad \text{and} \quad \mathrm{Fr} = \frac{V^2}{Lg}. \tag{5}$$

Henceforth, we discard the * notation for ease of presentation. Substitution of the above dimensionless variables into Eq. (1) yields the nondimensional equivalent generalized system of equations

$$\mathrm{Re}\,\mathbf{U}_t = \nabla.(\mu^* \nabla \mathbf{U}) - \mathrm{Re}\,\mathbf{U}.\nabla \mathbf{U} - \nabla P + F, \tag{6}$$

$$\nabla.\mathbf{U} = 0. \tag{7}$$

The algorithm invoked in this study follows references [24–26] where greater detail is provided. Briefly, a semi-implicit time-stepping procedure, namely, a Taylor-Galerkin/pressure-correction finite element scheme is employed to solve the governing equations relating to the conservation of mass and momentum. The time-stepping scheme is derived through Taylor series expansions up to second-order in time-step and a two-step predictor-corrector scheme is assumed. This, in conjunction with a second-order pressure-correction method, to accommodate the incompressibility constraint, produces a fractional-staged equation system. The whole system is solved over three distinct phases within a single time-step. A semi-implicit Crank-Nicolson treatment is adopted in time to discretize the diffusion terms. A Galerkin finite element spatial discretization renders a fully discrete system. The choice is made of piecewise continuous quadratics for velocity, and linears for pressure based upon tetrahedral elements in three dimensions (and triangles in two dimensions). The viscosity of the fluid is represented through the Carreau-Yasuda model, and the nonlinear viscosity representation enters the formulation within the momentum equation. The three fractional stages per time-step may be identified as follows:

Stage 1: From initial velocity and pressure fields, nondivergence-free $\mathbf{U}^{n+\frac{1}{2}}$ and $\mathbf{U}^*$ fields are calculated via a two-step predictor-corrector procedure. The corresponding equations are solved iteratively by a Jacobi scheme in an element-by-element fashion.

Stage 2: Adopting the auxiliary variable $\mathbf{U}^*$, calculate the pressure difference ($P^{n+1} - P^n$) via a Poisson equation, applying a direct Choleski method of solution.

Stage 3: Based on the pressure difference ($P^{n+1} - P^n$), determine the divergence-free velocity field $\mathbf{U}^{n+1}$ by Jacobi iteration.

Adopting quadratic and linear interpolation functions, $\mathbf{U}(x,t)$ and $P(x,t)$ may be expressed as

$$\mathbf{U}(x,t) = \mathbf{U}_j(t)\phi_j(x), \quad P(x,t) = P_j(t)\psi_j(x).$$

The equation stages in fully discrete form[2] may be concisely summarized, viz:

Stage 1a:

$$\left[\frac{2\,\mathrm{Re}}{\Delta t}M+\frac{1}{2}S_u\right](\mathbf{U}^{n+1/2}-\mathbf{U}^n)=\{-[S_u\mathbf{U}+\mathrm{Re}\,N(U)\mathbf{U}]+L^TP+F\phi_i\}^n \tag{8}$$

Stage 1b:

$$\left[\frac{\mathrm{Re}}{\Delta t}M+\frac{1}{2}S_u\right](\mathbf{U}^*-\mathbf{U}^n)=[-S_u\mathbf{U}+L^TP+F\phi_i]^n-\mathrm{Re}[N(U)\mathbf{U}]^{n+1/2} \tag{9}$$

Stage 2:

$$K(P^{n+1}-P^n)=-\frac{2}{\Delta t}L\mathbf{U}^* \tag{10}$$

Stage 3:

$$\frac{\mathrm{Re}}{\Delta t}M(\mathbf{U}^{n+1}-\mathbf{U}^*)=\frac{1}{2}L^T(P^{n+1}-P^n) \tag{11}$$

where $\mathbf{U}^n$, $\mathbf{U}^{n+1}$, P^n, and P^{n+1} are nodal vectors of velocity and pressure at time t^n and t^{n+1}, respectively; $\mathbf{U}^*$ is an auxiliary nodal vector introduced at Step 1b; M, S_u, $N(U)$, K, and L are mass matrix, momentum diffusion matrix, convection matrix, pressure stiffness matrix, and divergence pressure gradient matrix, respectively. In a cylindrical three-dimensional coordinate frame of reference, (r,θ,z), the above matrices may be defined as

$$M=\begin{bmatrix} M_{11} & 0 & 0\\ 0 & M_{22} & 0\\ 0 & 0 & M_{33}\end{bmatrix}\quad \text{where}(M_{ll})_{ij}=\int_\Omega \phi_i\phi_j d\Omega \tag{12}$$

$$S_u=\begin{bmatrix} S_{11} & S_{12} & S_{13}\\ S_{21} & S_{22} & S_{23}\\ S_{31} & S_{32} & S_{33}\end{bmatrix} \tag{13}$$

$$(S_{11})_{ij}=\int_\Omega \mu^*\left\{2\frac{d\phi_i}{dr}\frac{d\phi_j}{dr}+\frac{1}{r^2}\frac{d\phi_i}{d\theta}\frac{d\phi_j}{d\theta}+\frac{2}{r^2}\phi_i\phi_j+\frac{d\phi_i}{dz}\frac{d\phi_j}{dz}\right\}d\Omega \tag{14}$$

$$(S_{12})_{ij}=(S_{21})^T=\int_\Omega \mu^*\left\{\frac{2}{r^2}\phi_i\frac{d\phi_j}{d\theta}-\frac{1}{r^2}\frac{d\phi_i}{d\theta}\phi_j+\frac{1}{r}\frac{d\phi_i}{d\theta}\frac{d\phi_j}{dr}\right\}d\Omega \tag{15}$$

$$(S_{13})_{ij}=(S_{31})^T=\int_\Omega \mu^*\left\{\frac{d\phi_i}{dz}\frac{d\phi_j}{dr}\right\}d\Omega \tag{16}$$

$$(S_{22})_{ij}=\int_\Omega \mu^*\left\{\frac{2}{r^2}\frac{d\phi_i}{d\theta}\frac{d\phi_j}{d\theta}-\frac{1}{r}\frac{d\phi_i}{dr}\phi_j+\frac{d\phi_i}{dr}\frac{d\phi_j}{dr}+\frac{1}{r^2}\phi_i\phi_j-\frac{1}{r}\frac{d\phi_j}{dr}\phi_i+\frac{d\phi_i}{dz}\frac{d\phi_j}{dz}\right\}d\Omega \tag{17}$$

$$(S_{23})_{ij}=(S_{32})^T=\int_\Omega \mu^*\left\{\frac{1}{r}\frac{d\phi_i}{dz}\frac{d\phi_j}{d\theta}\right\}d\Omega \tag{18}$$

$$(S_{33})_{ij}=\int_\Omega \mu^*\left\{\frac{d\phi_i}{dr}\frac{d\phi_j}{dr}+\frac{1}{r^2}\frac{d\phi_i}{d\theta}\frac{d\phi_j}{d\theta}+2\frac{d\phi_i}{dz}\frac{d\phi_j}{dz}\right\}d\Omega \tag{19}$$

$$L=(L_r,L_\vartheta,L_z) \tag{20}$$

$$L_r=\int_\Omega \psi_m\left(\frac{\phi_i}{r}+\frac{d\phi_i}{dr}\right)d\Omega,\quad L_\theta=\int_\Omega \psi_m\left(\frac{d\phi_i}{d\theta}\right)d\Omega,\quad L_z=\int_\Omega \psi_m\left(\frac{d\phi_i}{dz}\right)d\Omega \tag{21}$$

$$N(U)_{ij}=\int_\Omega \phi_i\phi_k\mathbf{U}_k\nabla\phi_j d\Omega \tag{22}$$

$$(K)_{lm}=\int_\Omega \nabla\psi_l\,.\nabla\psi_m d\Omega \tag{23}$$

where $d\Omega=rdrd\theta dz$; and $\{i,j,k\}_1^r,\{l,m\}_1^s$, where in three dimensions $\{r,s\}=\{10,4\}$, while in two dimensions $\{r,s\}=\{6,3\}$.

After solving for velocities and pressure in the flow field, rate of work done $(\dot{w})$, and torque (T_q) are computed, using the following relations:

$$\dot{w}(t)=\int_\Omega (\tau:\nabla\mathbf{U})d\Omega=P_w \tag{24}$$

$$(\tau:\nabla\mathbf{U})=\frac{1}{2}\mu\left(\frac{dU_i}{dX_j}+\frac{dUj}{dX_i}\right)^2=\dot{w}(t,X) \tag{25}$$

$$P_w=T_q\omega \tag{26}$$

where ''P_w'' represents the power, "τ" stress tensor, "$\mathbf{U}$" velocity vector (components (V_r,V_θ,V_z)), "ω" rotational rate of the vessel, "Ω" fluid volume, and ''t'' time. Localized rate of work, $\dot{w}(t,X)$, may be interpreted as the integrand of Eq. (24).

For mesh convergence studies, we have chosen three distinct meshes, adopting a hierarchial mesh refinement approach, where each parent element at the coarser mesh level is divided into four subcells, connecting midside nodes. Between solutions and any variable component on two consecutive refined meshes, a discrepancy of order 1% is tolerated. The meshes used within these convergence studies are illustrated in Fig. 1. In addition, simulations are conducted using different numbers of particles for the free surface, to quantify and calibrate the precision of determination. This has led to the position where 1,000 particles are chosen for tracking free surface in the three-dimensional vertical-vessel case, whereas 3,600 particles are employed in the two-dimensional horizontal vessel-orientation instance.

Apropos flow problem specification, the three and two-dimensional flow domains are represented in Figs. 2(*a*,*b*), with corresponding meshes in Figs. 2(*c*–*f*). For the three-dimensional vertical-standing vessel-orientation instance, a cylindrical vessel with a stirrer (or stirrers) is considered, placed in concentric or eccentric orientation with respect to the axis of the vessel. The fluid is driven by the outer vessel-wall and the stirrers are fixed at the top of the vessel to a lid, as shown in Fig. 2(*a*). To create a three-dimensional tetrahedral finite element mesh, first each brick element is constructed, which is subdivided into six tetrahedra. For a single stirrer vessel, Fig. 2(*e*), this leads to 6000 tetrahedral elements, 9240 velocity nodes and 1320 pressure (vertex) nodes; for the double stirrer, Fig. 2(*f*), there are equivalently 8400 tetrahedral elements, 13,145 velocity nodes and 1902 pressure nodes. At initiation of the flow, the vessel stands some 60% filled with fluid at rest. The outer vessel-wall attached to the bottom plate (bottom of vessel), rotates at different rotational speeds and the top lid is held stationary (along with the stirrers). For the two-dimensional horizontal vessel-orientation instance, the flow geometry is discretized into a triangular mesh, as in Figs. 2(*c*), (*d*). So

---

[2] Note in Eqs. (8), (9), the use of Crank-Nicolson discretization in time on diffusion *S*-matrix terms, so that averages over two time levels are recognized to reflect difference quotients.

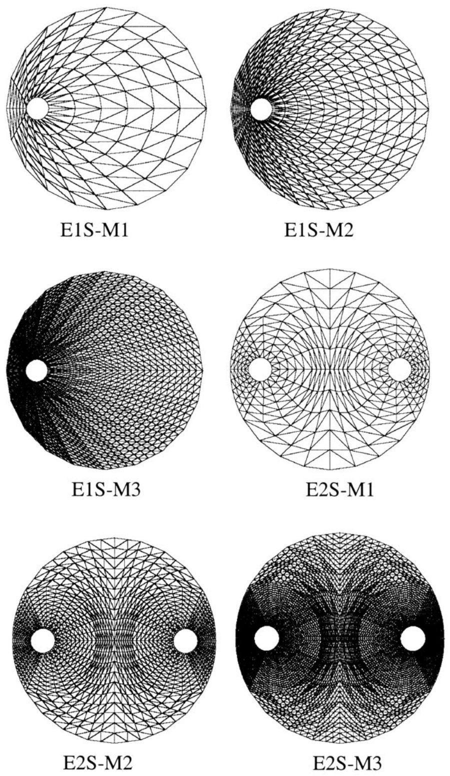

Fig. 1 Meshes: M1, M2, M3; one (E1S) and two-stirrer (E2S) cases

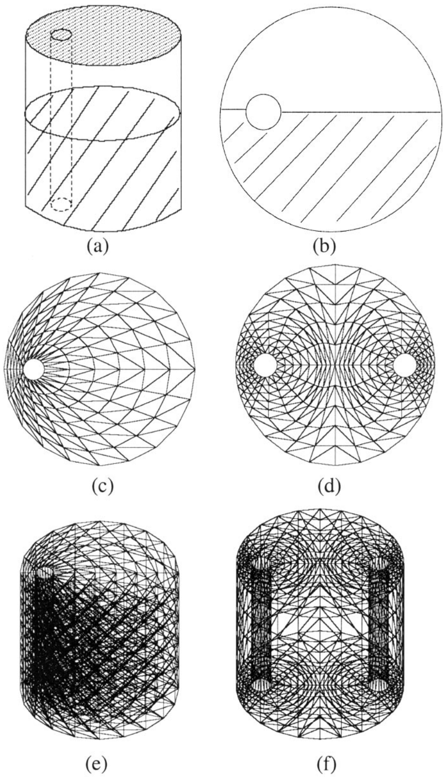

Fig. 2 Meshes: vertical (three-dimensional) and horizontal (two-dimensional) views; flow domain and surface; (*a*)–(*c*), (*e*) 1 stirrer; (*d*), (*f*) 2 stirrers

typically, the flow domain is discretized in Fig. 2(*c*) into 240 triangular elements, 520 velocity nodes and 140 pressure nodes; likewise, for the two-stirrer instance of Fig. 2(*d*), discretization leads to 560 triangular elements, 1195 velocity nodes, and 317 pressure nodes. We comment that mesh density may not be so fine, due to recourse to quadratic interpolation on velocity fields.

To provide a well-posed specification for each flow problem, it is necessary to prescribe appropriate initial and boundary conditions. Simulations commence from a quiescent initial state. Boundary conditions are taken assuming that the fluid sticks to the solid surfaces, so that the components of velocity vanish on the solid walls of the inner stirrer boundary (no-slip). On the outer rotating cylindrical vessel, a fixed constant velocity boundary condition is applied ($V_r=0$, $V_\theta=1$ and $V_z=0$), and a constant ambient pressure level is specified on the free surface (taken to vanish).

3 Free-Surface Tracking

An Euler time-stepping scheme is employed to deal with free surfaces. A fixed finite element mesh applies to the flow domain, which is divided dynamically into the two distinct wet and dry sections. The position of the free surface defines the interface between wet and dry zones, and hence, the fluid region itself, the effective domain of solution. The solution of field variables, in velocity, pressure and stress, are computed within the wet fluid zone alone.

3.1 Particle Tracking Scheme. Free-surface profiles are obtained by tracking particle histories, assuming that the fluid surface is delineated by a series of particles. In this manner, the wet-dry interface is identified. Particles are placed in regular patterns initially, distributed uniformly in radial and azimuthal directions, but translate according to the evolution of local kinematics. For tracking free-surface positions, we follow reference Ding et al. [25], which suggested a well-established predictor-corrector Runge-Kutta scheme. Here, it is found to be pragmatic and adequate to consider the one-step version, an explicit Euler step:

$$X_p^{n+1}=X_p^n+\Delta t\mathbf{U}(X_p,t^n) \tag{27}$$

where, for particle p, X_p^n is a position at time t^n, $\mathbf{U}(X_p,t^n)$ is a velocity at X_p^n at time t^n, X_p^{n+1} is a position at time t^{n+1}. This scheme is performed after stage 3 of each time-step of the Taylor-Galerkin algorithm, that is, at the end of each time-step cycle. For practical convenience, a miniscule virtual gap is introduced between the first surface particle and the cylinder wall to circumvent the indeterminacy of conditions at the free surface-solid wall interface. Essentially, this creates two nodal points to represent the contact point, one on the free surface and a second on the solid boundary.

Particles are introduced on the top of the fluid surface at the start of each simulation run. The Taylor-Galerkin finite element calculations are performed for the complete domain (wet and dry) to obtain velocities and pressures at all field nodes. The dry and wet regions are distinguished on the basis of material properties (viscosity). If a node is dry, the viscosity vanishes, and hence the solution is null. For moving particles, velocities $\mathbf{U}(X_p,t^n)$ are calculated by interpolating nodal velocities,

$$\mathbf{U}(X_p,t^n)=\sum_i \phi_i(X_p^n)\mathbf{U}_i^n, \tag{28}$$

where Σ_i implies a sum over nodes of elements containing X_p^n.

Surface particles are moved by the particle-tracking scheme to obtain their temporal update locations. At the end of each time-step, the most up to date wet and dry regions are identified and the status of all nodes reassigned accordingly, as to whether wet or dry. For elements which are part wet, the material properties are allowed to adjust over a single element. We impose a weak natural

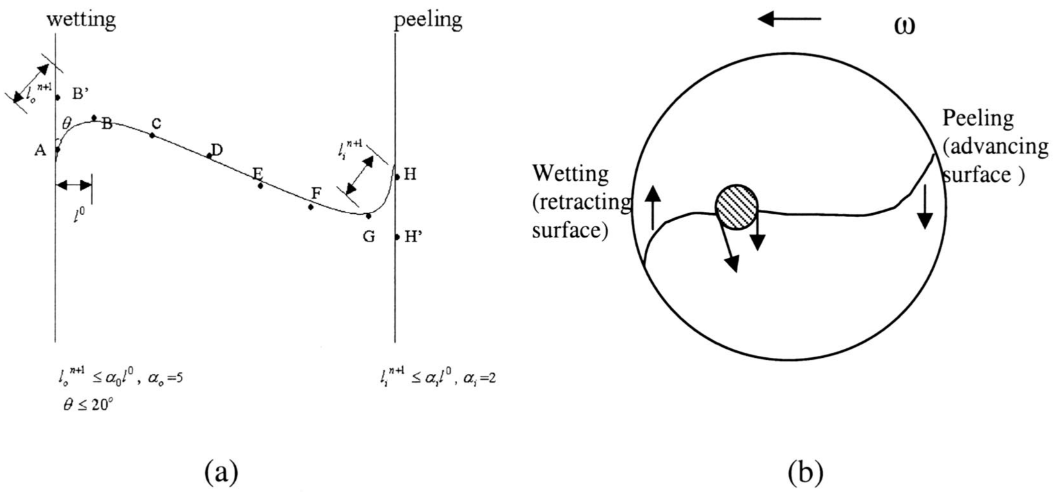

Fig. 3 Schematic representation of wetting and peeling: (*a*) vertical and (*b*) horizontal (r,θ) orientation

boundary condition on the free surface. This change is incorporated directly into the finite element formulation, since appropriate material properties are assigned to each Gauss quadrature sample point,[3] within the associated representation of the integrands in question. Therefore, no local remeshing is required close to the interface. Having assigned nodal status and reassigned material properties, velocity and pressure fields for the new domain are computed at the next time-step t^{n+1}. The velocity, $\mathbf{U}(X_p^{n+1})$, at free-surface particles with subsequent movement, is calculated via

$$\mathbf{U}(X_p)^{n+1} = \mathbf{U}(X_p)^n + \sum_i (\mathbf{U}_i^{n+1} - \mathbf{U}_i^n)\phi_i(X_p^{n+1}), \qquad (29)$$

where Σ_i represents the sum over the nodes of an element containing X_p^{n+1}. In this manner, particles are shifted to updated positions for the next time-step. This procedure is repeated until a stable steady-state is reached.

3.2 Wetting/Peeling on Free Surfaces. Specific considerations have been applied to the free surface, that is itself delineated by a series of particles. In vertical mixer orientation, Fig. 3(*a*), with a concentric/eccentric stirrer arrangement and outer vessel moving, surface wetting (''folding-on of fluid'') occurs at the outer vessel and ''peeling off'' occurs at the inner stirrer. For the concentric-stirrer instance, symmetric patterns arise as the flow is a pure shear flow and wetting/peeling apply uniformly about vessel/stirrer. In a horizontal orientation and at the vessel wall, peeling may be observed at the advancing surface in contact with the vessel wall; wetting occurs at the retracting surface side (dragging surface). On the stirrer, peeling occurs at both advancing and retarding surfaces fronts, as illustrated in Fig. 3(*b*).

The stretch (or strain rate) of free-surface segments (segments connecting the surface particles) is employed as a criterion to monitor the extent of wetting and peeling. Stretch is assessed via the ratio of the newly obtained segment length against its initial length for a two-dimensional case. As such, wetting or peeling is detected if a free-surface segment in contact with a solid boundary is stretched/contracted beyond some specified limiting criteria. This is equivalent to a balance between strain energy and stress. When this situation arises, the free surface is retarded iteratively, relaxing the newly calculated position, at which the velocity is adjusted accordingly. This automatically relieves the level of stressing. At the same time, governed by restrictions on minimal distance spacing, particle coalescence and vanishing/buckling of free-surface line segments may be guarded against. If two particles come too close together, we consider them as having merged into a single-particle collapsing line-segment reference and individual particle reference.

In the present work, novel algorithms have been devised to deal with wetting and peeling conditions, between fluid and solid surfaces, represented diagrammatically in Fig.3(*a,b*). This provides a schematic illustration for the treatment of fluid-solid body contact points, arising at both outer and inner boundaries in the three-dimensional concentric scenario. In our modeling assumptions, particles lying close to the inner and outer boundaries, would move little in the vertical direction, being heavily influenced by the prevailing imposition of no-slip. For example in Fig. 3(*a*), consider particle A located at the contact point between the free surface and the outer vessel-wall. This particle is stationary due to no-slip. In contrast, due to centrifugal forces, a neighbor particle B will strive to migrate towards the vessel wall and adhere there. When the angle between the line segment AB and the wall becomes less than θ (say, 20 deg), particle B is presumed to have attached onto the wall (at B′ in Fig. 3(*a*)). This is recognized as the new contact point for the next time step. In practice, particles A and B are taken to have coalesced at B′. Wetting (or peeling) is also controlled by assessing surface-segment stretch ratio at fluid-boundary contact points (e.g., at A). Both criteria (stretch/angle) are employed when monitoring wetting and peeling. The physical nature of wetting, being a folding phenomena, means that the angle of contact is important. In contrast, peeling may occur more as a result of an energy constraint, where stretch is more important. Stretch adjustment is handled in such a manner as to impact upon control of local stress experienced (relating extent of wetting/peeling to degree and assessment of stretch rate). For example, at and near the inner stirrer, particles migrate away from the stirrer (peel) due to centrifugal forces. Hence, the flow in this region is of a stretching nature. Let us consider two particles close to the inner stirrer-boundary, namely G and H. When the stretch of GH reaches ''α'' times its original length (say, twice), the stationary particle H is relocated at H′. In this manner, the free-surface rolls off (peels from) solid surfaces. Thus, peeling (or wetting) is detected if a limiting stretch factor (α) of a line surface segment nearest the solid boundary is exceeded, according to

$$\frac{\Delta l_i^{n+1}}{\Delta l_i^o} \geqslant \alpha. \qquad (30)$$

The factor (α) is taken from empirical estimation and guided by

---

[3] Comparisons were made for accuracy in employing 1, 3, 7, 15 Gauss quadrature sample points within an element. The seven-point option was found to be sufficiently accurate for present purposes, noting the increased spatial coverage that larger numbers of quadrature points provide.

experimental visualization. Here, Δl_i^o and Δl_i^{n+1} represent the length of a segment i adjacent to a solid boundary at initial time, $t=0$, and new time, t^{n+1}, respectively.

For both horizontal and vertical orientations with one stirrer, it is found expedient to adopt a limiting value α of 5.0 at the outer vessel, and 2.0 at the inner stirrer. Further improvements have been made in the horizontal vessel-orientation instance (of greater complexity, with advancing/retarding fluid fronts), which demands variation with respect to particular (stirrer) boundary location. Then, dynamic selection of α is more appropriate to differentiate between inner and outer stirrer-fluid contact points, dependent upon resultant local stressing. Once peeling (or wetting) criteria are satisfied, the position of the free surface is reassessed, as discussed above, to the relief of stress (or strain) levels. Subtime-steps are introduced to improve field consistency after free-surface movement. Separate time-step control is enforced on surface movement from that for the full wet-domain computation, to reflect the physical problem more closely. Typically, upon each Taylor-Galerkin time-step, this would necessitate around 100 subtime-steps to be performed on the field.

4 Results

Numerical simulations for the above-mentioned problems have been conducted at various speeds. The materials represented within the simulation studies are model fluids with shear thinning properties, results for which reflect close agreement against their equivalent experimental counterparts, [19,20], of syrup (Newtonian) and 1% CMC (inelastic fluids). There is no apparent change noted in the free-surface profiles between inelastic (C-Y) and Newtonian flows at this level of concentration of CMC. Nevertheless, field quantities, such as power, rate of work done and torque, do manifest some differences, [18]. Typical results for both one and two-stirrer situations are provided in Figs. 4 and 5, to quantify such differences.

The numerical results presented are analyzed through the following separate phases:

a. influence of increasing inertia (Re), by increasing the rotational speed of the vessel;
b. material influence from Newtonian to inelastic fluids;
c. comparison of concentric-stirrer symmetric flow to eccentric-stirrer asymmetric flow.

The concentric-stirrer rotating-cylinder flow for a Newtonian fluid admits the following analytical solution, [27]:

$$V_\theta = \Omega_o R_o \frac{\left(\dfrac{R_i}{r} - \dfrac{r}{R_i}\right)}{\left(\dfrac{R_i}{R_o} - \dfrac{R_o}{R_i}\right)}, \tag{31}$$

where R_i and R_o are the radii of the inner and outer concentric cylinders, respectively; r is the radial coordinate and $R_o\Omega_o$ is the rotational speed of the outer cylinder. Employing the semi-implicit Taylor-Galerkin/pressure-correction scheme above, the departure from the analytical solution in velocity and pressure is found to be within an order of 1%. For this problem, the flow is circular symmetric and of pure shearing form. Analytic and numerical representations are contrasted in Table 1 at radial locations (any angle θ) between the vessel (point 1) and the stirrer (point 11). The free-surface configuration for a Newtonian fluid in a rotating cylinder adopts a parabolic shape, [27]. To validate the accuracy of the current particle tracking scheme, one may look to the shape of the free surface obtained for a Newtonian fluid in a rotating cylindrical vessel with a concentric stirrer, and compare this against analytical solutions. Once more, any differences detected are found to lie within an order of 1%.

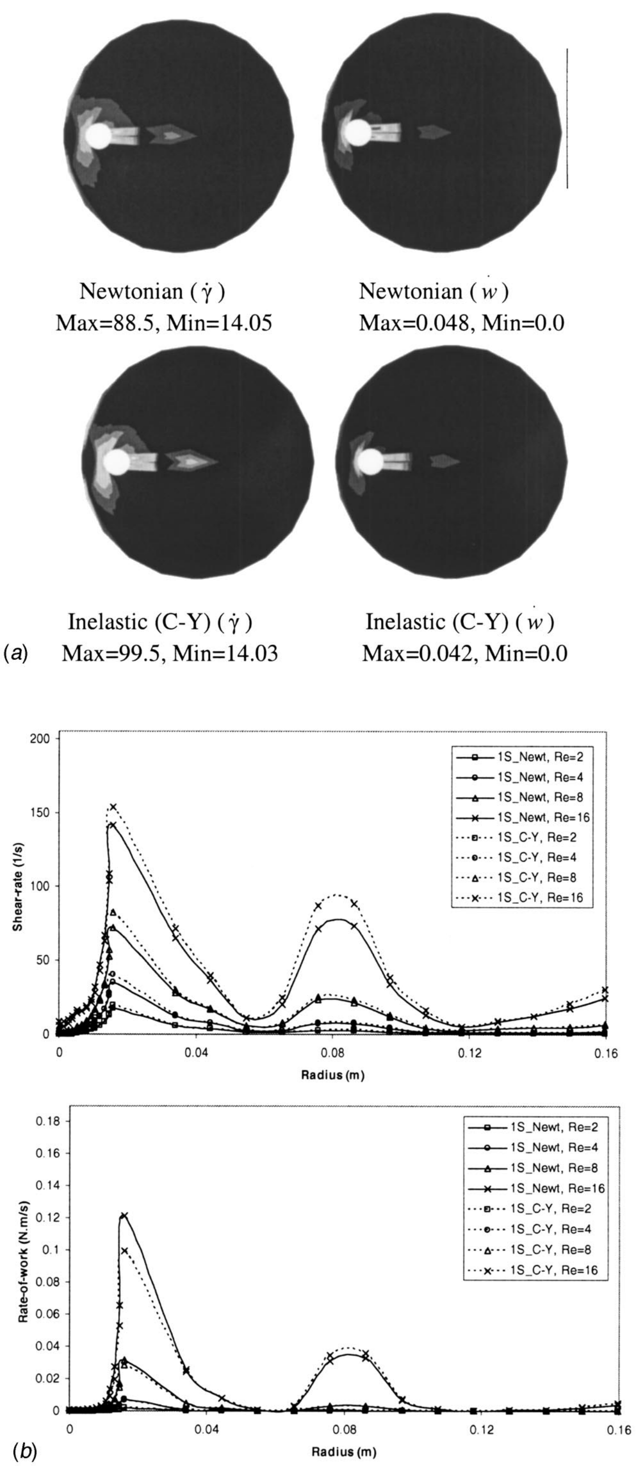

Fig. 4 (*a*) **Field plots: Newtonian and inelastic fluids for one-stirrer case, shear rate and rate of work, Re=8.** (*b*) **Radial line plots: Newtonian and inelastic fluids for one-stirrer case, shear rate, and rate of work, different Re.**

A mesh convergence study has been conducted for both one-stirrer (E-1S) and two-stirrer (E-2S) scenarios to verify solution mesh independence. The meshes used for this study, M1, M2, and M3, for both one-stirrer and two-stirrer situations are depicted in Fig. 1. Simulations are conducted at a speed of 50 rpm (Re=8), and a discrepancy of order 1% is tolerated between solutions of any variable on two consecutive refined meshes. Solutions generated confirm the mesh quality, even with the more coarse mesh (M1). Table 2 records the detailed mesh characteristics, and the shear-rate maxima obtained on meshes M1, M2, and M3, with E-1S and E-2S mixer vessel designs.

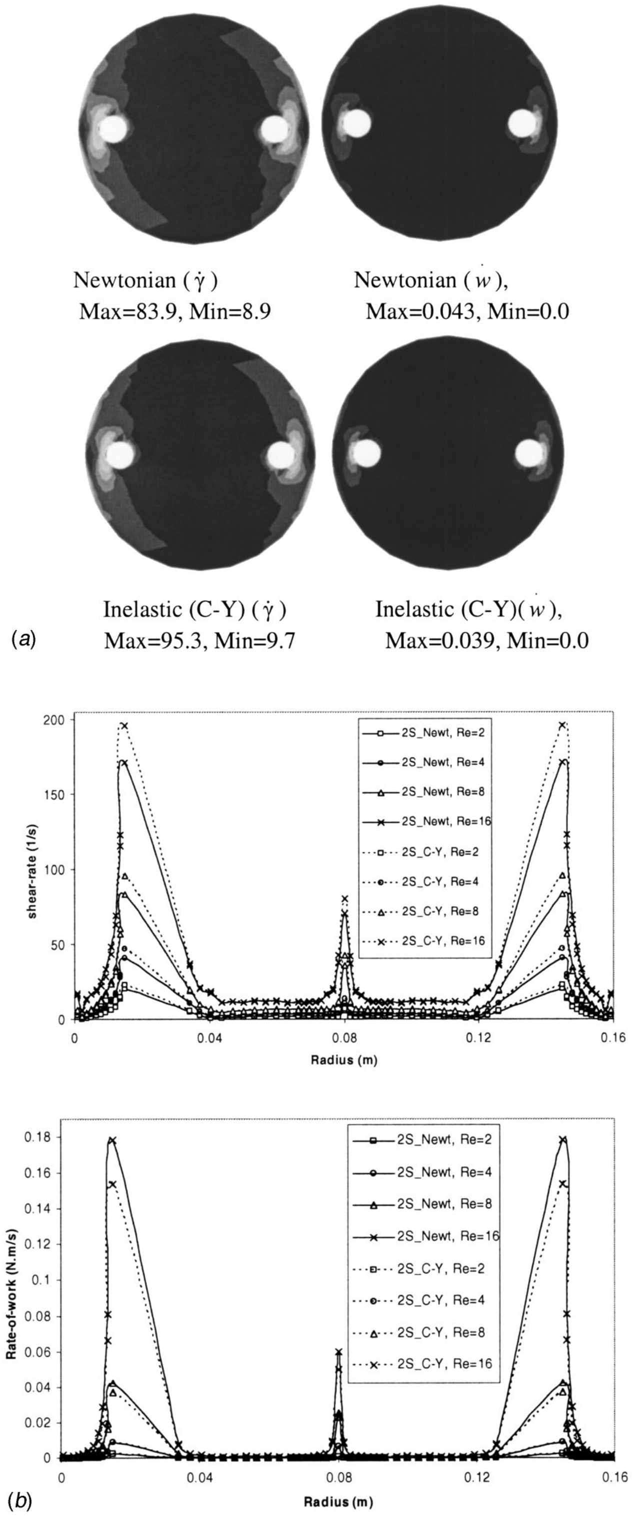

Fig. 5 (*a*) **Field plots: Newtonian and inelastic fluids for two-stirrer case, shear rate, and rate of work, Re=8.** (*b*) **Radial line plots: Newtonian and inelastic fluids for two-stirrer case, shear rate, and rate of work, different Re.**

Table 1 Numerical and analytical solutions for Newtonian flow

Points	Radical Loc.	$(V_\theta)_{\mathrm{anal}}$	$(V_\theta)_{\mathrm{num}}$	P_{anal}	P_{num}
1	4.440	1.0000	1.0000	0.2165	0.2286
2	4.046	0.9088	0.9162	0.1799	0.1858
3	3.652	0.8174	0.8249	0.1400	0.1477
4	3.258	0.7257	0.7325	0.1120	0.1137
5	2.864	0.6334	0.6394	0.0800	0.0838
6	2.470	0.5403	0.5455	0.0533	0.0585
7	2.076	0.4461	0.4504	0.0370	0.0374
8	1.682	0.3497	0.3533	0.0207	0.0208
9	1.288	0.2495	0.2522	0.0080	0.0087
10	0.894	0.1402	0.1421	0.0018	0.0018
11	0.500	0.0000	0.0000	0.0000	0.0000

With one and two-stirrer designs, Table 3 draws out the comparison in localized maxima of shear rate and rate of work, and global torque measurement, between Newtonian and inelastic materials. Quantities are reported for a typical trial run at a speed of 50 rpm (Re=8). For an equivalent speed, shear-rate maxima are about 12% higher for the inelastic (C-Y) fluid due to the effects of shear thinning. Torque also declines as inelastic rheology is introduced. Local rate-of-work maxima and power reduce for inelastic above Newtonian fluids, being dominated by the decrease in viscosity.

Figures 4(*a*) and 5(*a*) illustrate the corresponding field distributions of shear rate and rate of work done for single-stirrer and two-stirrer scenarios. Results for Newtonian and inelastic (C-Y) fluids are included. These are three-dimensional results represented in a horizontal slice at the midplane of the vessel. Furthermore and equivalently to field plots, we extract diagnostic line profiles in Figs. 4(*b*) and 5(*b*). These quantify variation in shear rate and rate of work done at different levels of inertia along the horizontal radial axis (central through origin) at the vessel midplane, for one and two-stirrer situation, respectively. The maximum values of shear rate and rate of work done are observed to lie particularly within the narrow-gap section, between the stirrer and the vessel wall. Hence, more shearing and stretching of the fluid occurs in this region and the rate of work done peaks to a maximum there. For the two-stirrer case, localized maxima in shear rate and rate of work may decline from the one-stirrer state.[4] Nevertheless, there is an increased resistance arising from the presence of the second stirrer. The torque reflects the complete field contributions of the rate of work done, the magnitude for which is greater for the two-stirrer than the single-stirrer flow. In Fig. 4(*b*), the first shear-rate peak corresponds to the vicinity of

Table 2 Mesh convergence study for E-1S, E-2S, on shear-rate maxima, Re=8

Meshes	Elements	Nodes	Shear-rate Maxima (s^{-1})
E-1S			
Mesh-M1	240	520	88.54
Mesh-M2	960	2000	87.42
Mesh-M3	3840	7840	87.37
E-2S			
Mesh-M1	560	1195	83.90
Mesh-M2	2240	4631	82.10
Mesh-M3	8960	18223	82.00

Table 3 Comparison between Newtonian and inelastic (C-Y) fluids, Re=8

	One Stirrer		Two Stirrers	
Field Variables	Newtonian	Inelastic (C-Y)	Newtonian	Inelastic (C-Y)
Shear rate (s^{-1})	88.5	99.5	83.9	95.3
Rate of work (N.m/s)	0.048	0.042	0.043	0.039
Torque (N.m)	4.32	4.06	5.61	5.38

---

[4] E1-S maxima are shifted further away from the central axis through the narrow gap as speed increases, extenuating greater asymmetry.

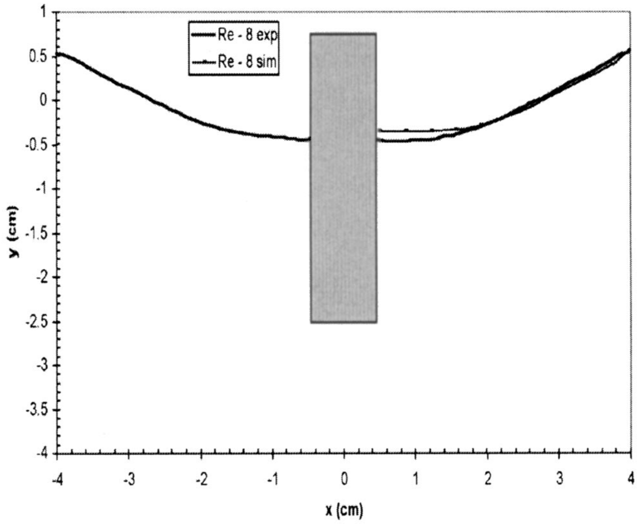

Fig. 6 Steady-state surface positions, Re=8 (50 rpm); simulation versus experiment

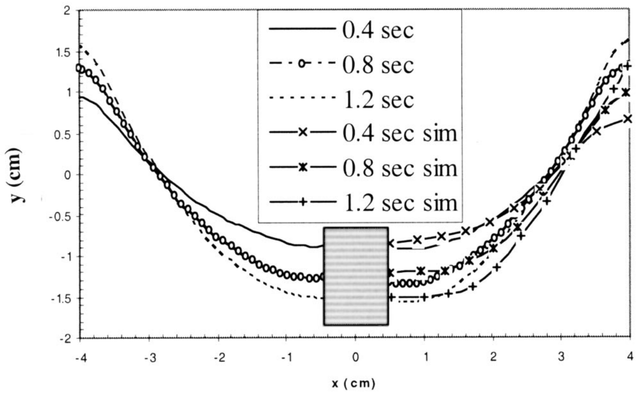

Fig. 7 Surface positions with time, Re=16, (100 rpm); simulation versus experiment

the stationary stirrer. In a single stirrer scenario, a central vortex appears located horizontally opposite to the stirrer (see [19]). This gives rise to a secondary lower peak in shear rate. In the two-stirrer design, a pair of vortices emerges, generated by the separating flow about each stirrer. The flow pattern is one of a figure-of-eight structure as reported by Binding et al. [19]. In the corresponding profile plot of Fig. 5(*b*), the secondary shear-rate peak is at the vessel center (origin), where the bifurcation point lies between the pair of vortices (heart of the figure-of-eight pattern within stagnant flow). The other two lateral peaks on both sides of the origin reflect the symmetry of the two-stirrer flow and the respective positions of the two stirrers themselves. From these figures, it is apparent that localized shear rates rise while rate of work decreases as inelastic shear thinning (C-Y) rheology is introduced, consistent with earlier arguments. For field maxima in shear rate, Figs. 4(*a*) and 5(*a*), and Table 3. These trends are replicated, but scaled down correspondingly, as speeds of rotation decline and greater flow symmetry is recovered (see Figs. 4(*b*) and 5(*b*)). Hence, the slowest rotation rates barely reflect any differences between Newtonian and inelastic (C-Y) fluids.

4.1 Vertical Vessel Orientation. For three-dimensional simulations and vertical vessel-orientation, a cylindrical vessel with stirrer positions, concentric and eccentric to the axis of the vessel, have been considered. For the concentric stirrer instance, free-surface profiles are computed to steady-state for different speeds, namely, 25, 50, and 100 rpm (Re=4, 8, 16), and compared against equivalent experimental data. Figure 6 demonstrates a typical comparison set for 50 rpm (Re=8). Since the surface is symmetric, a sample slice in depth is taken through the vessel-center along a diameter and surface positions are plotted in two dimensions. The fluid motion is instigated from rest with a level fluid surface. As time progresses, the fluid wets onto the outer vessel-wall and peels away from the stirrer, due to the prevailing centrifugal forces. As expected physically, final steady-state surface profiles are noted to take up a parabolic shape away from boundary contact.

In both experimental and simulation modes, the transient rise of the free surface for a typical vessel-rotation speed of 100 rpm (Re=16) is demonstrated in Fig. 7. In this case, the surface position reaches a steady-state after 1.2 sec. Comparison between steady-states in Figs. 6 and 7 disclose a slight deviation at the higher speed (100 rpm, Re=16) between the experimental and simulation data. This discrepancy may be attributed to the difference in initial fluid-fill states and the uniform setting of the wetting-peeling criteria adopted in the simulations, here applied equally across all speeds. We point out that, to date, most attention has been paid to predicting results at the standard speed of 50 rpm (Re=8) of Fig. 6. Free-surface representations in a three-dimensional mode are presented in Fig. 8. These are created by imposing particle positions obtained from simulation onto a three-dimensional frame. As speed increases, the depth of the surface rise is observed to increase (difference between maximum and minimum height levels). Hence, the extent of wetting and peeling increases with increased vessel rotation speed. In addition, simulations have been conducted for the standard mixing mode with the stirrer rotating and outer vessel stationary, to validate the numerical algorithm and associated predictive software. In this case, a dip in the free surface arises in the vicinity of the stirrer, as illustrated in Fig. 9. Once more, this reflects the physical situation for viscous fluids accordingly.

Figure 10 demonstrates local stress and stretch plotted against time, for a surface line-segment in contact with the stirrer (where peeling occurs). Local stretch is measured as the change in length of a line segment connecting two particles in a radial line within the vicinity of and making contact with the solid wall (bar the miniscule virtual gap imposed to overcome no-slip conditions there, see above). The local stress is the peeling/pulling stress experienced along this same surface. The stress is calculated from

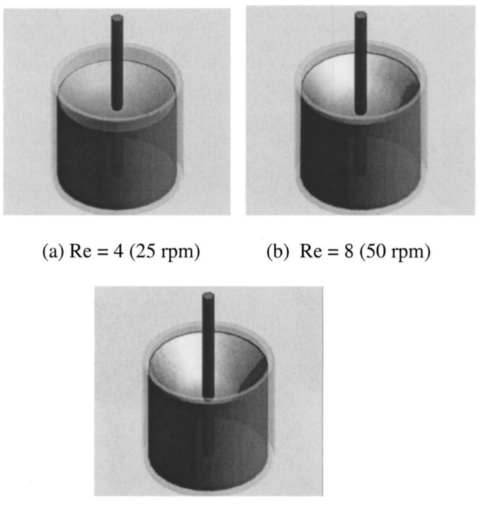
(a) Re = 4 (25 rpm) (b) Re = 8 (50 rpm)

(c) Re = 16 (100 rpm)

Fig. 8 Surface patterns: vessel rotating, increasing speed, three-dimensional mode

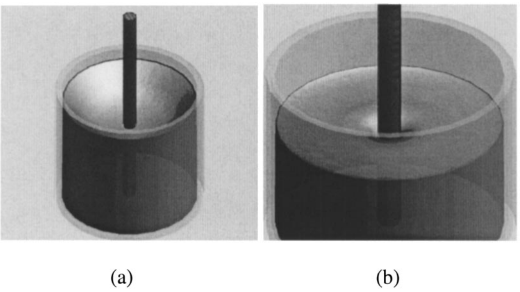

Fig. 9 Surface patterns: (*a*) outer and (*b*) inner vessel rotation; three-dimensional mode, Re=8 (50 rpm)

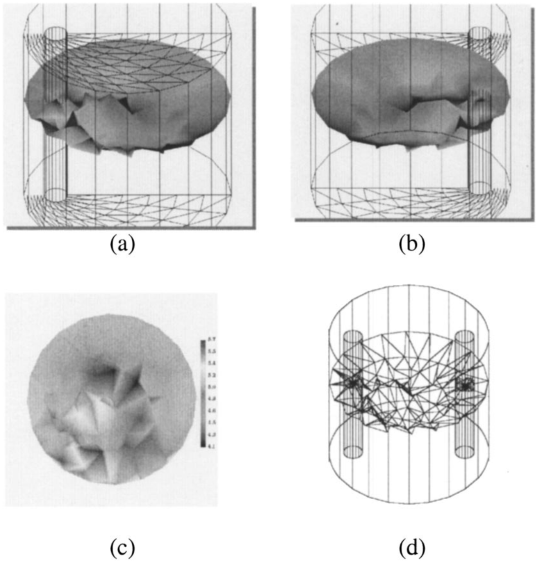

Fig. 11 Steady-state free-surface representations (simulation): eccentric, one stirrer, a-c; two stirrers, d; Re=8 (50 rpm)

the gradients of the tangential component of velocity along the line surface-segment. This is accomplished by resolving particle velocities into components along the line segment. As the distance between particles increases, the stretch increases, until a critical level is attained. At this stage, the stress experienced on the surface reaches the critical peeling stress. Beyond this phase the fluid peels from the boundary, stress levels are relieved and the surface stretch decreases. This state of affairs and corresponding procedure equate to satisfaction of a form of energy balance. The local stress follows the same sort of pattern as that associated with the stretch. The match in pattern of stretch and peeling-stress time-trace indicates that either would be equally as valid as monitoring criteria within the algorithmic implementation. One only needs to relate to different absolute levels of the parameter chosen to recognize the onset of such critical conditions. The flexibility of the techniques employed, in their ability to deal with these most complex boundary interaction phenomena, highly commends this transient approach. One may comment that the same ideas would extend equally to model slip-scenarios, where hysteresis and transient influences apply.

With eccentric stirrer location, the surface patterns are somewhat more complex than their concentric counterparts. There is rise and fall of the surface position about the stirrer, varying continuously around the stirrer. For comparison between free-surface profiles obtained from simulation and experiment, we focus largely upon the eccentric one-stirrer geometry. Since the surface shape is highly complex, exact comparison is difficult and, only qualitative comparison is possible. Clearly, any method employed here will suffer limitation and these results may be interpreted as a guidance only. Here, the surface particles are connected by triangles using Delauney triangulation to aid visualization. Plots of surface shape (height) from simulation (speed of 50 rpm, Re=8) are illustrated in Fig. 11. Equivalent plots from experimental visualizations performed are presented in Fig. 12. Figures 11(*a*) and (*b*) illustrate two different orientation views with respect to the vessel, that provide some feel for the surface characteristics, and Fig. 11(*c*) depicts height contours (perspective view). The maximum and minimum values of height are represented by red and blue colors, respectively. Stirrer position in Fig. 11(*c*) corresponds to that shown in Fig. 11(*a*). In the vicinity of the stirrer and taking a radial view, there is a dip at the backside of the stirrer (away from the narrow gap), whereas the fluid attempts to climb up the stirrer at its front, front orientation being taken with respect to the

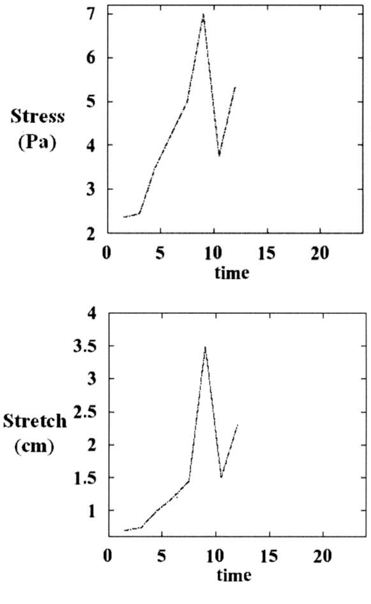

Fig. 10 Variation of stress and stretch with time; peeling from stirrer; three-dimensional, Re=8 (50 rpm)

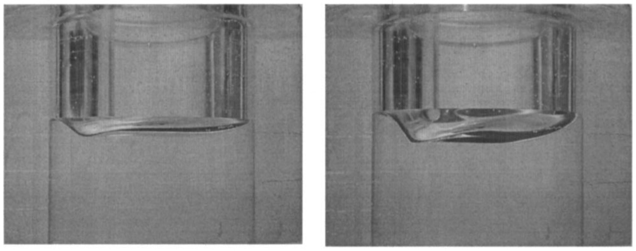

(a) 25 rpm (b) 50 rpm

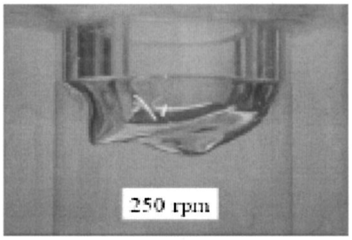

(c) 250 rpm

Fig. 12 Steady-state free-surface profiles (experiment): one stirrer, three speeds

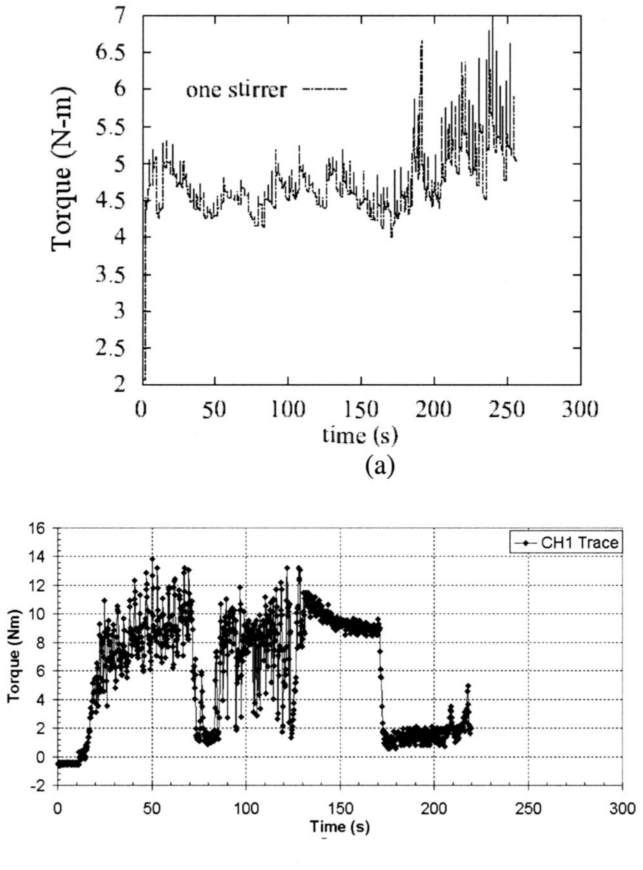

(a)

(b)

Fig. 13 Torque-time trace: (*a*) simulation, (*b*) experiment; three-dimensional, Re=8 (50 rpm)

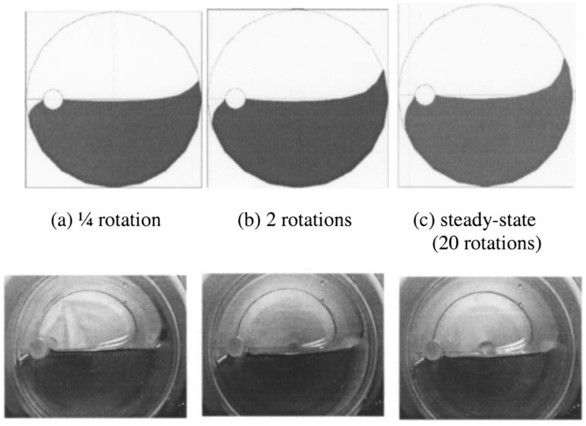
(a) ¼ rotation (b) 2 rotations (c) steady-state (20 rotations)

(d) ¼ rotation (e) 2 rotations (f) steady-state (20 rotations)

Fig. 14 Temporal development, surface deformation patterns, horizontal orientation, Re=8 (50 rpm)

narrow gap between stirrer and vessel. Considering the gap flow itself taken upon the outer vessel-wall, there is rise in fluid level before entering the gap (viewed from the backside of stirrer) and a dip in level departing the gap (viewed from forefront of stirrer). This resembles a sloshing wave motion against an obstruction. These features can be discerned between Figs. 11(*a*) and 11(*b*), being confirmed through the perspective plot of Fig. 11(*c*). This complexity is actual, as observed in reality (see Fig. 12(*c*)). Furthermore, simulations were performed for the two-stirrer option in likewise mode, reproducing a similar pattern about the second stirrer (see Fig. 11(*d*)).

Figure 13(*a*) demonstrates a typical torque-time trace for inelastic (C-Y) fluids from simulation runs for the eccentric one-stirrer geometry, where torque is an integrated quantity of the rate of work done in the whole field. A similar curve is presented in Fig. 13(*b*) for actual dough from experimental measurements. These curves cannot be compared directly, acknowledging the differences in torque levels and rheology of the fluids. Nevertheless, some similarities over restricted time-periods can be extracted. In the simulations with model fluids, torque levels are halved from the experiments, as apparent in Fig. 13(*b*). In the actual dough mixing process, different mixing modes are identified, where the dough comes into contact with and departs the stirrer in a cyclic manner. This is reflected in the periodic nature of the curve of Fig. 13(*b*), which oscillates about some mean level. When the dough comes into contact with the stirrer, torque levels are high. Low values of torque represent periods when the dough departs from the stirrer. Within the simulations for inelastic (C-Y) fluids, predictions only cover the state when the fluid is in contact with the stirrer. As such, we have identified different periods in the mixing process which may be compared. Simulations commence from rest, therefore the start-up period can be ignored (0–180 seconds). If we consider the time when the dough is in contact with the stirrers in Fig 13(*b*), that is, between 20–70 seconds and 90–130 seconds, this trend can be contrasted to the response depicted in Fig. 13(*a*), between 180–260 seconds. Some correspondence in overall pattern and trend is borne out here. At this stage of the modeling, only these periods may be characterized, and qualitatively, this is held to be a reasonable physical reflection of such process phases.

4.2 Horizontal Vessel Orientation. In this section, we discuss the corresponding scenario, when the vessel is held in a horizontal orientation and the free-surface patterns are obtained by simulation for the two-dimensional (r-θ) orientation of the mixer. Figures 14(*a–f*) illustrate the computational predictions in deformation patterns for viscous fluids at 50 rpm (Re=8), at a quarter of a rotation, two rotations and after 20 rotations of the vessel. Figures 14(*a*), (*b*), and (*c*) represent simulated predictions; Figs. 14(*d–f*) depict still images extracted from video sequences of the equivalent experiments. Free surfaces are observed to move smoothly and approach a steady-state after some twenty rotations of the vessel. Both wetting and peeling phenomena are detected at advancing (forward) and retreating (backward) surface fluid-vessel contact points. The effect of wetting is to push more retreating surface segments onto the vessel-wall. Peeling is also identified at the contact point, between the dragging surface and the stirrer. One notes at this stage when utilizing a constant α-factor setting on the stirrer, peeling goes relatively undetected on contact between the forward advancing surface on the stirrer (towards vessel center). This is apparent in Figs. 14(*a–c*) and is due to the relatively low levels of kinematic activity in this particular zone, exacerbated by the asymmetry of the geometry. In contrast and according to the experimental images (true three-dimensional flow with end effects), the fluid is observed to undergo some peeling in this region, for which its development is illustrated in Figs. 14(*d–f*). This is a highly localized feature near the inner section of the stirrer towards vessel center, and as such, is difficult to capture accurately in the modeling. In this regard, we are able to adaptively adjust the control factor α. With both horizontal and vertical orientation and a single stirrer, a limiting value α of five for outer vessel-wall surface conditions is found suitable. For the stirrer, different values of α (line surface segment-solid boundary factor) are applied according to local dictates and sections of the stirrer. For vertical vessel orientation, a static α_{stir}-value of two on the stirrer is reasonably acceptable. The

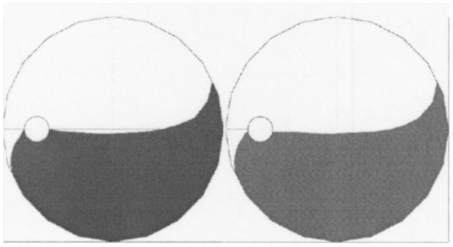

Fig. 15 Steady-state surface patterns, 20 rotations (in time), simulations, Re=8 (50 rpm): left, $\alpha_{\text{stir}}=2$; right, $\alpha_{\text{stir-outer}}=1.3$, $\alpha_{\text{stir-inner}}=0.8$

horizontal setting has demanded a more dynamic approach, with the α_{stir}-value varying from 1.3 for the outer stirrer section (narrow gap) to 0.8 for the inner stirrer section (wide gap). The contrast between results in the horizontal mode for static and dynamic setting of α_{stir} is demonstrated clearly in Fig. 15. Particular note should be taken of the center vessel surface profile generated in the image to the right of Fig. 15, generated as a consequence of the dynamic allocation of α_{stir}. Here, this adjustment is found absolutely necessary to match closely with the equivalent experimental observations. Again, this complements the flexibility and power of the techniques commended, to identify such fine flow features.

5 Conclusions

We have successfully demonstrated the use of a numerical flow solver for inelastic non-Newtonian fluids, along with an arbitrary Lagrangian-Eulerian scheme to track free surfaces in flows within part-filled rotating vessels. Such scenarios are representative of industrial dough kneading processes, against which we have been able to furnish physically realistic predictions. Suitable conditions for wetting and peeling are incorporated within the modelling, that provide a close match with the free-surface profiles obtained from counterpart experiments.

In vertical vessel orientation, parabolic surface deformation patterns have been obtained for a concentric rotating vessel with a fixed stirrer. Results confirm the wetting of fluid and rising level at the vessel wall, and peeling (falling away) of fluid at the stirrer. Localized surface-segment peeling-stress and stretch values, estimated from local stretch rate, are found to be of the same order as the critical peeling stress measured experimentally. There is correspondence extracted between simulated and experimentally calibrated results, inclusive of three-dimensional steady-state and transient surface profiles, and torque-time traces. This extends to scenarios of vessel or stirrer-driven motion.

In the present context, horizontal vessel orientation has presented the more complex wetting and peeling setting. Here, even the fine detail of wetting and peeling on different boundary sections are faithfully reflected through the flexibility of the procedures proposed. This study goes some way in practically casting insight upon such complicated physical processes and in establishing numerical predictive tools to accommodate the same.

Acknowledgments

Financial support for this work, from BBSRC (grant no: 58/D08174), RHM Research, United Biscuits, Pilsbury Co., Mono Equipment and Sasib Bakeries, is acknowledged. The support work of Dr. D. Ding, especially within the two-dimensional free-surface modeling, is also gratefully acknowledged.

References

[1] Wang, H. P., and Lee, H. S., 1989, ''Free and Moving Boundary Problems,'' *Fundamentals of Computer Modeling for Polymer Processing*, C. L. Tucker, III, ed., Hanser, Munich.

[2] Harlow, F. H., and Welch, J. E., 1965, ''Numerical Calculation of Time-Dependent Viscous Incompressible Flow of Fluid With Free-Surface,'' Phys. Fluids A, **8**, pp. 2182–2189.

[3] Welch, J. E., Harlow, F. H., Shannon, J. P., and Daly, B. J., 1965, ''The MAC Method: A Computing Technique for Solving Viscous, Incompressible, Transient Fluid-Flow Problems Involving Free Surfaces,'' LASL Report LA-3425, Los Alamos, NM.

[4] Hirt, C. W., and Nichols, B. D., 1981, ''Volume of Fluid Method for the Dynamics of Free Boundaries,'' J. Comput. Phys., **39**, pp. 201–225.

[5] Gethin, D. T., Lewis, R. W., and Tadayon, M. R., 1992, ''A Finite Element Approach for Modeling Metal Flow and Pressurized Solidification in the Squeeze Casting Process,'' Int. J. Numer. Methods Eng., **35**, pp. 939–950.

[6] Wang, S. P., and Wang, K. K., 1994, ''A Net Inflow Method for Incompressible Viscous Flow With Moving Free Surfaces,'' Int. J. Numer. Methods Fluids, **18**, pp. 669–694.

[7] Rudman, M., 1997, ''Volume Tracking Methods for Interfacial Flow Calculations,'' Int. J. Numer. Methods Fluids, **24**, pp. 671–691.

[8] Rudman, M., 1998, ''A Volume Tracking Method for Incompressible Multifluid Flows With Large Density Variations,'' Int. J. Numer. Methods Fluids, **28**, pp. 357–378.

[9] Thompson, E., 1986, ''Use of Pseudo-Concentration to Follow Creeping Viscous Flows During Transient Analysis,'' Int. J. Numer. Methods Fluids, **6**, pp. 749–761.

[10] Nassehi, V., and Ghoreishy, M. H. R., 1997, ''Simulation of Free Surface Flow in Partially Filled Internal Mixers,'' Int. Polym. Process., **4**, pp. 346–353.

[11] Sato, T., and Richardson, S. M., 1994, ''Numerical Simulation Method for Viscoelastic Flows With Free Surfaces-Fringe Element Generation Method,'' Int. J. Numer. Methods Fluids, **19**, pp. 555–574.

[12] Ding, D., Townsend, P., and Webster, M. F., 1997, ''Finite Element Simulation of an Injection Moulding Process,'' Int. J. Numer. Methods Heat Fluid Flow, **7**, pp. 751–766.

[13] Manogg, G. J., Townsend, P., and Webster, M. F., 1997, ''Numerical Simulation of Multilayer Injection Moulding,'' J. Non-Newtonian Fluid Mech., **68**, pp. 153–167.

[14] Medale, M., and Jaeger, M., 1997, ''Numerical Simulation of Incompressible Flows With Moving Interfaces,'' Int. J. Numer. Methods Fluids, **24**, pp. 615–638.

[15] Hirt, C. W., Amsden, A. A., and Cook, J. L., 1974, ''An Arbitrary Lagrangian-Eulerian Computing Method of All Speeds,'' J. Comput. Phys., **14**, pp. 227–253.

[16] Ramaswamy, B., 1990, ''Numerical Simulation of Unsteady Viscous Free Surface Flow,'' J. Comput. Phys., **90**, pp. 396–430.

[17] Hughes, T. J. R., and Kiu, W. K., 1981, ''Lagrangian-Eulerian Finite Element Formulation for Incompressible Viscous,'' Comput. Methods Appl. Mech. Eng., **29**, pp. 329–349.

[18] Sujatha, K. S., and Webster, M. F., 2003, ''Modelling Three-Dimensional Rotating Flows in Cylindrical-Shaped Vessels,'' Int. J. Numer. Methods Fluids, (in press).

[19] Binding, D. M., Couch, M. A., Sujatha, K. S., and Webster, M. F., 2003, ''Experimental and Numerical Simulation of Dough Kneading in Filled Geometries,'' J. Food. Eng., **58**, pp. 111–123.

[20] Couch, M. A., and Binding, D. M., 2002, ''An Experimental Study of the Peeling of Dough From Solid Surfaces,'' J. Food. Eng., (in press).

[21] Prakash, S., and Kokini, J. L., 2000, ''Estimation and Prediction of Shear-Rate Distribution as a Model Mixer,'' J. Food. Eng., **44**, pp. 135–148.

[22] Prakash, S., and Kokini, J. L., 1999, ''Determination of Mixing Efficiency in a Model Food Mixer,'' Adv. Polym. Technol., **18**, p. 3.

[23] Prakash, S., Karwe, M. V., and Kokini, J. L., 1999, ''Measurement of Velocity Distribution in the Brabender Farinograph as a Model Mixer, Using Laser-Doppler Anemometry,'' J. Food. Eng., **44**, pp. 435–454.

[24] Hawken, D. M., Tamaddon-Jahromi, H. R., Townsend, P., and Webster, M. F., 1990, ''A Taylor-Galerkin-Based Algorithm for Viscous Incompressible Flow,'' Int. J. Numer. Methods Fluids, **10**, pp. 327–351.

[25] Ding, D., Townsend, P., and Webster, M. F., 1995, ''On Computations of Two and Three-Dimensional Unsteady Thermal Non-Newtonian Flows,'' Int. J. Numer. Methods Heat Fluid Flow, **5**, pp. 495–510.

[26] Matallah, H., Townsend, P., and Webster, M. F., 1998, ''Recovery and Stress-Splitting Schemes for Viscoelastic Flows,'' J. Non-Newtonian Fluid Mech., **75**, pp. 139–166.

[27] Bird, R. B., Stewart, W. E., and Lightfoot, E. N., 1960, *Transport Phenomena*, John Wiley and Sons, New York.

Numerical Simulations of Flows Inside a Partially Filled Centrifuge

Fang Yan

Bakhtier Farouk[1]
e-mail: bfarouk@coe.Drexel.edu

Department of Mechanical Engineering,
Drexel University,
Philadelphia, PA 19104

A numerical study was conducted to predict the dynamics of gas/liquid flows in a partially filled cylinder undergoing moderate to rapid rotation. Two specific problems were considered: spinup from rest of a partially filled circular container and the steady flow field in a partially filled rotating circular cylinder with an overrotating lid. Numerical solutions of the time-dependent axisymmetric Navier-Stokes equations were obtained by using a homogeneous multiphase model. The evolution of the free surface along with the flow fields in both the gas and liquid phases are predicted. The computed results were compared with available experimental data. Details of flow field structures are examined by studying the numerical solutions. Radial profiles of axial and azimuthal velocities for both the liquid and gas phases are also presented. The model developed can be used for analyzing flows and mixing problems in complex-geometry centrifuges.
[DOI: 10.1115/1.1627832]

Introduction

The internal flow of viscous fluids in a partially filled closed container, induced either by spinup or the independent overrotation of an end lid have been studied in the past in rotating fluid dynamics research. Consider a closed container that is partially filled with liquid that begins to rotate rapidly about its axis (at a rotational speed Ω). The term, ''spinup'' refers to the transient process of fluid motion when the rotation rate of the container is suddenly increased. Studies of such kind of rotating flows were initiated by Greenspan and Howard [1], who considered the effect of small changes of rotation rate (Rossby number $\varepsilon=\Delta\Omega/\Omega \ll 1$) of a completely filled container on the flow field. The linearized mathematical analysis of Greenspan and Howard is based on the additional assumption that the Ekman number $E=\nu/\Omega H^2$ is very small, where ν is the fluid kinematic viscosity and H the characteristic dimension of the container. They demonstrated that the essential dynamic ingredients were the suction mechanism of the Ekman layers formed on the endwalls and the subsequent radially inward meridional circulations in the interior core. Consequently, the major phase of transient motions is substantially accomplished over a convection time scale $E^{-1/2}\Omega^{-1}$. This physical picture has since been verified by several numerical and experimental investigations (see, e.g., Warn-Varnas et al. [2]). The essential elements of spinup dynamics in a completely filled container were outlined in the review papers by Benton and Clark [3] and Duck and Foster [4]. A model was proposed by Wedemeyer [5], building upon the ideas of Greenspan and Howard, which captured the principal characteristics of the transient process in such flows. The vital role of the Ekman layer pumping mechanism was recognized. With several assumptions, Wedemeyer's model yielded a simplified partial differential equation for the axisymmetric interior core region. The qualitative correctness of this model has been verified by numerical simulations, [6–8], as well as by experimental results, [9].

The above-referenced works on spinup, relating to the Wedemeyer model, were concerned with the case when the liquid completely fills the enclosed cylinder. A natural extension of the model is the process of spinup from rest in a *partially* filled cylinder—which is one of the topics addressed in this paper. The transient dynamics of this problem are of relevance to technological applications, such as centrifugal separation of biological and chemical substances. The early study of Goller and Ranov [10] developed a simplified computing scheme based on the Wedemeyer model to tackle the spinup with a free surface. Utilizing the extended Wedemeyer-Goller-Ranov model, Homicz and Gerber [11,12] further refined the model in order to predict the free-surface shape as well as the dominant azimuthal velocity structure with modest amount of computing efforts. Extensive experimental verifications on the deformation of the free surface were performed by Choi et al. [13,14]. However, their semi-analytical model (based upon the work of Goller and Ranov) is only applicable to axisymmetric cylinders and simplified equations were solved for the liquid phase only with several assumptions. Based on the columnar flow approximation, a simplified version of the momentum equation having angular velocity v as the main unknown variable was obtained. A functional relationship $u=f(v,r)$ was also derived to close the system where u and v are the radial and azimuthal velocity components, respectively.

The other type of flow in partially filled centrifuges that we address in this paper is the steady flow induced by an ''overrotating'' lid. Shadday et al. [15] investigated the overrotating lid flow problem experimentally and implemented the Navier-Stokes simulation for the liquid region only. The rotation speed of the centrifuge was large enough to create a vertical liquid/gas interface. For the numerical simulation, the time-evolution of free surface and the effect of gas flow field were neglected by Shadday et al.

For a more complete study of rotating flows with free surface in complex geometry centrifuges, a general numerical model accounting for both gas and liquid flow fields is necessary. The present paper reports on results from a comprehensive and systematic investigation to simulate the free-surface shape and flow fields in partially filled centrifuges for the spinup and the ''overrotating'' lid flow problems by solving the Navier-Stokes equations with a homogeneous multiphase model. A control-volume based finite difference numerical procedure is used to obtain the time-dependent solutions of the evolution of the free surface as well as the flows induced in the liquid and the gas phases. Mesh refinements were done for the spatial grids to achieve grid-independent solutions. Small time steps (much smaller than the spinup time $(L^2/\Omega\nu)^{1/2}$, Greenspan et al. [1]) were used to properly capture the transient developments in the flow fields. Com-

---

[1] To whom correspondence should be addressed.

Contributed by the Fluids Engineering Division for publication in the JOURNAL OF FLUIDS ENGINEERING. Manuscript received by the Fluids Engineering Division Mar. 20, 2002; revised manuscript received July 3, 2003. Associate Editor: Y. Tsujimoto.

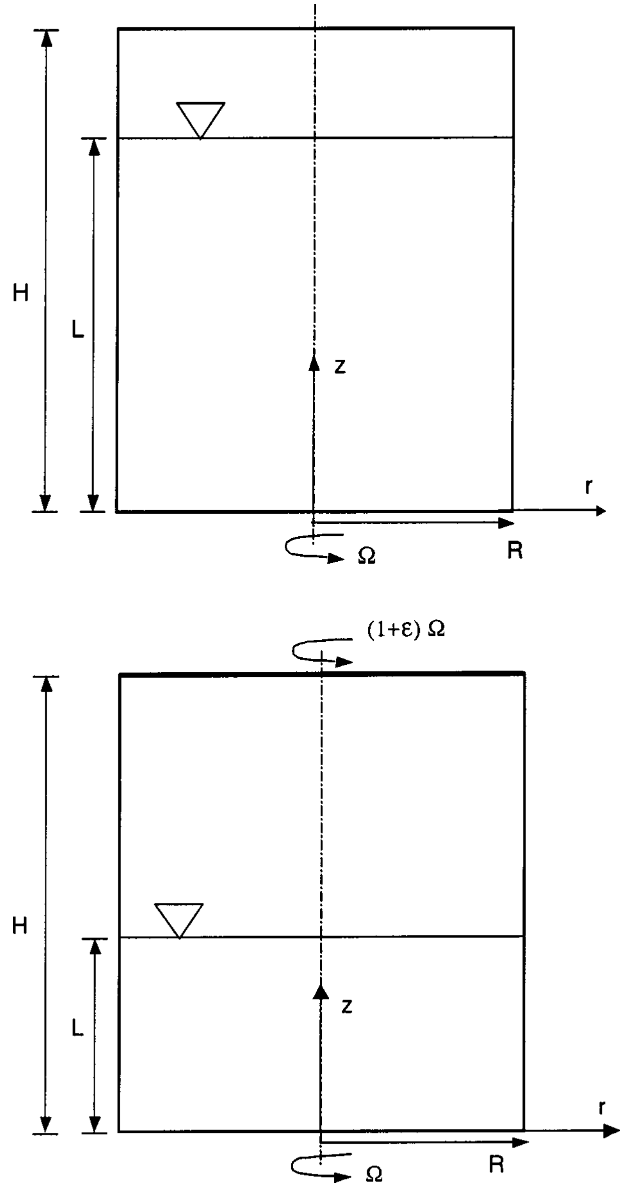

Fig. 1 (*a*) Schematic diagram of the spinup problem, (*b*) schematic diagram of the "overrotating" lid problem

parisons are made between the calculated results and available measurement data of the "partially filled cylinder spinup" and "overrotating lid" problems. The presented results demonstrate that the numerical model is suitable for accurately predicting the time evolution of the free-surface problem with rotation. The numerical model is appropriate for predicting the gas-liquid transport in complex centrifuges used for the separation or mixing of biological and chemical specimens.

Problem Geometries

The schematics of the two problems, which form the basis of our discussion, are illustrated in Fig. 1(*a*) and 1(*b*), respectively. As shown in these figures, both cylindrical containers are partially filled with liquid and rotate. The dimensions for the case shown in Fig. 1(*a*) are from the spinup experiments conducted by Choi et al. [13]. The cylinder (inside diameter 94 mm and height 141 mm with an aspect ratio $H/R=3.0$) is partially filled with water by volume up to 80%. Initially, the whole system is at rest. At $t \geqslant 0$, the cylinder begins to rotate with a constant rotating speed of 400 rpm about its axis. The free surface shape and flow field evolutions during the process are investigated numerically. Transient flow fields develop both in the liquid and the gas-phase during the spinup process. Solid-body rotation is achieved by the liquid at steady state.

The dimensions used for the over-rotating lid problem shown in Fig. 1(*b*) are the same as those reported in Shadday et al. [15]. The cylinder, 194 mm in length, 189 mm in diameter is filled to 30% by volume with glycerin-water solution having a viscosity 10 times that of pure water. The cylinder rotation rate (1000 rpm) is sufficiently high that the steady free surface is essentially vertical. In addition, the upper lid is overrotated by 5%, that is 50 rpm ($\Delta\Omega$), to provide for an additional driven velocity component. For this case the flow fields at the steady state are predicted by numerical simulation via the time-marching procedure as before.

Numerical Model

In this section, the mathematical formulation and the numerical scheme used in this study are described. The flow is incompressible and axisymmetric. It is also assumed that the gas and liquid phases are separated by a distinct interface and interphase diffusion is negligible. The velocity components in the r, θ, and z coordinates are u, v, and w, respectively. Using the relative velocity $u^*=u/\Omega R$, $v^*=v/\Omega R$, $w^*=w/\Omega R$, the nondimensional pressure $p^*=p/\rho\Omega^2R^2$, and the space and time variables $r^*=r/R$, $z^*=z/H$, $t^*=t/T$, the continuity equation for the liquid phase is

$$\frac{1}{\Omega T}\frac{\partial \gamma_1}{\partial t^*}+\frac{\partial}{\partial r^*}(\gamma_1 r^* u^*)+\frac{R}{H}\frac{\partial}{\partial z^*}(\gamma_1 w^*)=0. \tag{1}$$

The volume fractions are distinct with the restriction that they sum to unity:

$$\gamma_1+\gamma_2=1. \tag{2}$$

The overall continuity equation is given by

$$\frac{1}{\Omega T}\frac{\partial \rho^*}{\partial t^*}+\frac{\partial}{\partial r^*}(\rho^* r^* u^*)+\frac{R}{H}\frac{\partial}{\partial z^*}(\rho^* w^*)=0 \tag{3}$$

where ρ_1 and ρ_2 are the liquid and gas densities, respectively, and $\rho^*=\gamma_1\rho_1+\gamma_2\rho_2/\rho_1$. The momentum equations are given in nondimensional form:

$$\frac{1}{\Omega T}\frac{\partial u^*}{\partial t^*}+u^*\frac{\partial u^*}{\partial r^*}-\frac{v^{*2}}{r^*}+\sqrt{E}\,\mathrm{Re}w^*\frac{\partial u^*}{\partial z^*}$$

$$=-\frac{\partial p^*}{\partial r^*}+\frac{1}{\mathrm{Re}}\left[\frac{\partial^2 u^*}{\partial r^{*2}}+\frac{1}{r^*}\frac{\partial u^*}{\partial r^*}-\frac{u^*}{r^{*2}}+E\,\mathrm{Re}\frac{\partial^2 u^*}{\partial z^{*2}}\right] \tag{4a}$$

$$\frac{1}{\Omega T}\frac{\partial v^*}{\partial t^*}+u^*\frac{\partial v^*}{\partial r^*}+\frac{u^* v^*}{r^*}+\sqrt{E}\,\mathrm{Re}w^*\frac{\partial v^*}{\partial z^*}$$

$$=\frac{1}{\mathrm{Re}}\left[\frac{\partial^2 v^*}{\partial r^{*2}}+\frac{1}{r^*}\frac{\partial v^*}{\partial r^*}-\frac{v^*}{r^{*2}}+E\,\mathrm{Re}\frac{\partial^2 v^*}{\partial z^{*2}}\right] \tag{4b}$$

$$\frac{1}{\Omega T}\frac{\partial w^*}{\partial t^*}+u^*\frac{\partial w^*}{\partial r^*}+\sqrt{E}\,\mathrm{Re}w^*\frac{\partial w^*}{\partial z^*}$$

$$=-\frac{\sqrt{E}\,\mathrm{Re}}{Fr}-\sqrt{E}\,\mathrm{Re}\frac{\partial p^*}{\partial z^*}$$

$$+\frac{1}{\mathrm{Re}}\left[\frac{\partial^2 w^*}{\partial r^{*2}}+\frac{1}{r^*}\frac{\partial w^*}{\partial r^*}+E\,\mathrm{Re}\frac{\partial^2 w^*}{\partial z^{*2}}\right] \tag{4c}$$

where the nondimensional numbers are given as $\mathrm{Re}=\Omega R^2/\nu$, $E=\nu/\Omega H^2$, $\mathrm{Fr}=(\Omega R)^2/gH$ and the effective kinematic viscosity is given by

$$\nu=\nu_1\gamma_1+\nu_2\gamma_2.$$

The homogeneous model is a simplification of the multifluid multiphase flow models, [16]. Here the phases are assumed to move at the same velocity. Compared to the volume-of-fluid (VOF) method, [17], one major advantage of the homogeneous multiphase model is that it is less expensive in computation. Unlike VOF in which a distinct interface is reconstructed all the time, the interface is smeared out in the homogeneous multiphase model. The volume fraction in each cell can be any value between zero and one, depending on the space occupied by liquid phase and gas phase. The interface is specified where the volume fraction is 0.5 for both phases. In the homogeneous model, the boundary conditions at the interface are not implemented explicitly.

While VOF can predict a complicated free surface (e.g., a submerged bubble in a liquid), the homogenous model is particularly suitable for flows under gravity where the phases are completely stratified, for example free-surface flows. In this case, the volume fractions of the phases are equal to one or zero everywhere except at the phase boundaries, and it makes sense to use a single velocity field. The homogeneous multiphase model is applied to solve the continuity Eq. (1) and momentum Eqs. (4*a*)–(4*c*). The volume fraction of the gas phase is computed by using Eq. (2). The SIMPLE algorithm is implemented to achieve the pressure-correction. The overall continuity equation (given by Eq. (3)) is used to determine the pressure filed in the SIMPLE algorithm.

The liquid phase continuity equation is solved to determine the volume fraction and the momentum equations are solved over both phases for the entire flow field. Due to symmetry, only one-half of the centrifuge geometry is considered for the simulations. The finite volume model used to approximate the above equations uses a variable-sized mesh so that nodes may be concentrated on areas having large velocity and volume fraction gradients. No-slip boundary conditions are applied at both ends and the sidewall. For the spinup problem (Fig. 1(*a*)) at $t>0$:

$$u=w=0, \quad v=R\Omega \quad \text{at } r=R$$

$$u=0, \quad \frac{\partial v}{\partial r}=\frac{\partial w}{\partial r}=0 \quad \text{at } r=0$$

$$u=w=0, \quad v=r\Omega \quad \text{at } z=0 \quad \text{and} \quad z=H.$$

For the ‘‘overrotating’’ lid problem (Fig. 1(*b*)) at $t>0$:

$$u=w=0, \quad v=R\Omega \quad \text{at } r=R$$

$$u=0, \quad \frac{\partial v}{\partial r}=\frac{\partial w}{\partial r}=0 \quad \text{at } r=0$$

$$u=w=0, \quad v=r\Omega \quad \text{at } z=0$$

$$\text{and} \quad u=w=0, \quad v=r(\Omega+\Delta\Omega) \quad \text{at } z=H.$$

At the initial state of rest, the conditions are

$$\text{at } t\leqslant 0, \quad u=v=w=0.$$

The flows in the boundary layer and inner flow region are considered to be laminar. Schlichting [18] reports that the flow in the neighborhood of a rotating disk remains laminar at Reynolds number, $\mathrm{Re}=\Omega R^2/\nu<3\times 10^5$, and all the simulations in this paper consider flow with Reynolds number below this value. Experimental measurement by Choi et al. [13] and Shadday et al. [15] also verifies our laminar flow assumption for the cases studied here.

For the numerical scheme, the diffusion terms are modeled using second central differences, and the third-order accurate QUICK differencing scheme, [19], is used for the advection terms. It is noted that the nonlinear term is dominant in the boundary layer and not negligible. The third-order scheme possesses the stability of the first-order upwind formula and is free from substantial numerical diffusion experienced with the usual first-order methods. An implicit differencing scheme was chosen for the time derivative. A grid independence study was carried out for both problems considered in this paper. Further details of these studies are given in the next section. Care was taken to distribute several grid points inside the thin boundary (Ekman and Stewartson) layers that form along the walls of the centrifuge. Denser grids were also used at the locations of the gas/liquid interfaces.

To prevent unphysical solutions where the volume fraction of one phase is larger than one or attains negative values, time steps as small as 0.01 s are used for the computations. For both problems, time to reach steady state was in the order of tens of seconds. No oscillations in the flow field or the liquid-gas interface were observed and any ‘‘phase’’ error of the time-marching scheme is believed to be insignificant. At each time level, convergence was assumed when the following criterion was satisfied:

$$\frac{|\varphi_n-\varphi_{n-1}|}{|\varphi_n|}\leqslant 10^{-4} \quad \text{for all } \varphi$$

where φ denotes any dependent variable and n denotes the iteration number. If φ_n is close to zero ($<10^{-3}$, then $|\varphi_{n+1}-\varphi_n| \leqslant 10^{-7}$ is used as the criterion. These convergence criteria are enforced for all points.

For the problems studied in this paper, we neglect the effects of surface tension at the free surface due to the relatively large sizes of the containers (see earlier discussion) and the fluids considered (air and water). The curvature of the free surface is of the order $1/R$. The resulting pressure jump due to surface tension is therefore very small compared to pressure drop due to gravity. All computations were performed on an IBM-RISC-6000 (Model 7044) workstation. Typical computation time ranged from 70 to 80 hours for a case.

Results and Discussion

Spin-up Problem in a Partially Filled Centrifuge. The dimensions of the cylindrical system and the rotational speed have been discussed earlier. The values for the five characteristic parameters (the Reynolds number, Re, the Froude number, Fr, the Ekman number, E, the aspect ratio H/R and the filling ratio L/H) in the simulations are the following: $\mathrm{Re}=\Omega R^2/\nu=1.172\times 10^5$; $\mathrm{Fr}=(\Omega R)^2/gH=3.0$, where g is the gravity; $E=\nu/\Omega H^2=9.48\times 10^{-7}$; $H/R=3.0$; and $L/H=0.8$. Here ν is the kinematic viscosity of the liquid. The computed time evolution of free-surface shape for the spinup problem is shown in Fig. 2. Only one-half of the cylindrical area is shown in Fig. 2 where the left-hand boundary is the cylinder centerline. The free surface is identified where the volume fraction $\gamma_1=\gamma_2=0.5$. The measured profiles at different times, [13], are also shown in Fig. 2. The maximum uncertainty for the experimental measurement is ± 0.02 in z/R and ± 0.007 in r/R. The present predictions of free-surface evolution and the shapes are in good agreement with the measurements. The maximum deviation of the present numerical results from the experimental data $\Delta s/R$ is less than 1.5% where Δs is the distance between two free-surface shapes. It is noted that the current numerical simulation is better than the semi-analytical solution provided by Choi [13] (with maximum discrepancy $\Delta s/R$ about 3.5%). By the instant $\Omega t=2000$ (Fig. 2), the steady-state limit is achieved, which is consistent with the steady configuration given by Gerber [20]. The fluid attains the rigid-body rotation at a convection time scale $E^{-1/2}\Omega^{-1}$ which is an order of magnitude smaller than the diffusion time scale $\mathrm{Re}\,\Omega^{-1}$. The analytical model of Homicz and Gerber [11] underpredicts the degree of spinup, [13], because of simplified forms assumed in the model. The encouraging comparison illustrated in Fig. 2 verifies the appropriateness of the numerical simulations of the Navier-Stokes equations using the homogeneous multiphase model in predicting the evolution of the free surface. Another verification of this computer code was done by comparing the numerical simulation with analytical solution as shown in Fig. 3. For the same geometry, at relatively low rotating rate, $\Omega=150$ rpm, the free surface does not interact with the top end. The free-surface shape at the steady state

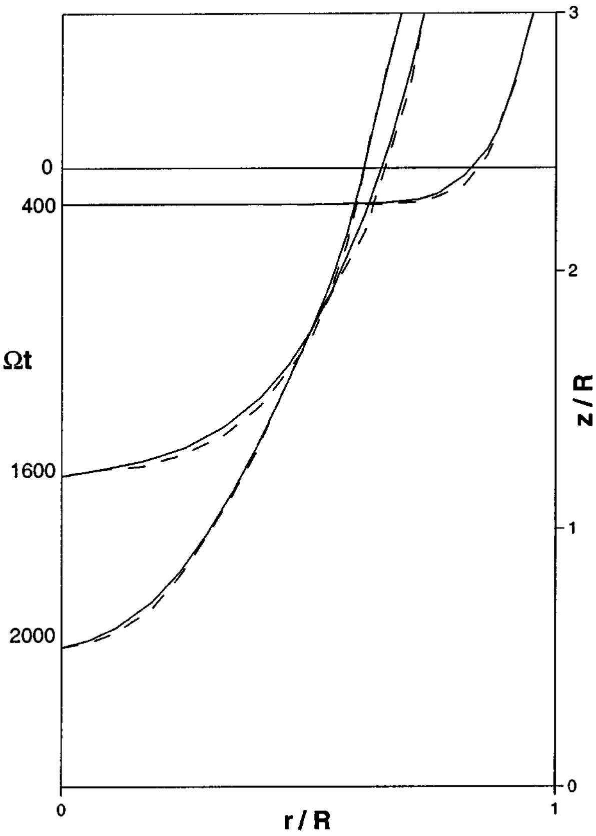

Fig. 2 Comparison of the transient free-surface shapes for the spinup case, ——, experimental data; — — —, numerical results

is the well-known parabolic profile. It can be seen from Fig. 3 that the agreement between numerical predictions with the analytical solution is very good.

In the numerical simulation, there must be sufficient number of nodes in the top and bottom Ekman layers to get the accurate solution of the spinup time evolution. If coarse grids are used, the development of the free surface (with time) will be greatly underpredicted. It means that the predicted time to reach the final steady state will be much larger than the measured values. Because the bottom Ekman layer is mainly responsible for the transport in the spinup process, it is critical that the Ekman layer is properly resolved in the simulations. Here nonuniform grids, which are constructed by 88 nodal points in axial direction and 48 nodal points in radial direction, are used. The minimum mesh size is 3×10^{-5} m near the bottom wall so that approximately five grid points are arrange within the Ekman layer.

The effect of mesh size on the development of the free surface is depicted in Fig. 4(*a*). When 60×32 grids are used, the development of free surface after $\Omega t = 400$ is well below the prediction by 88×48 grids. Computations were then carried out with 100×60 mesh size. There was no significant change in the free surface shape for the mesh sizes 100×60 and 88×48 with the maximum difference $\Delta s/R$ less than 0.4%. Similarly, the effect of mesh size on the velocity component is also illustrated in Fig. 4(*b*). The radial velocity profiles at the instant $\Omega t = 400$ along the radial direction predicted with different mesh sizes are displayed at the section $z = 0.25$ mm which is inside the Ekman boundary layer near the bottom wall. The axial velocity profiles are not presented here due to their small magnitudes compared to the values of the radial velocity component. It can be seen that the numerical results obtained with 88×48 and 100×60 grids are slightly different (maximum changes within 1%). When 60×32 grids are used, the maximum radial velocity component is also underpredicted. Compared to the difference between numerical simulation and experimental data, the mesh size 88×48 was considered adequate for the spinup simulation. The time-step influence on numerical simulation is presented in Fig. 5. There is little change in free-surface development when the step size decreased from 0.01 s to 0.005 s.

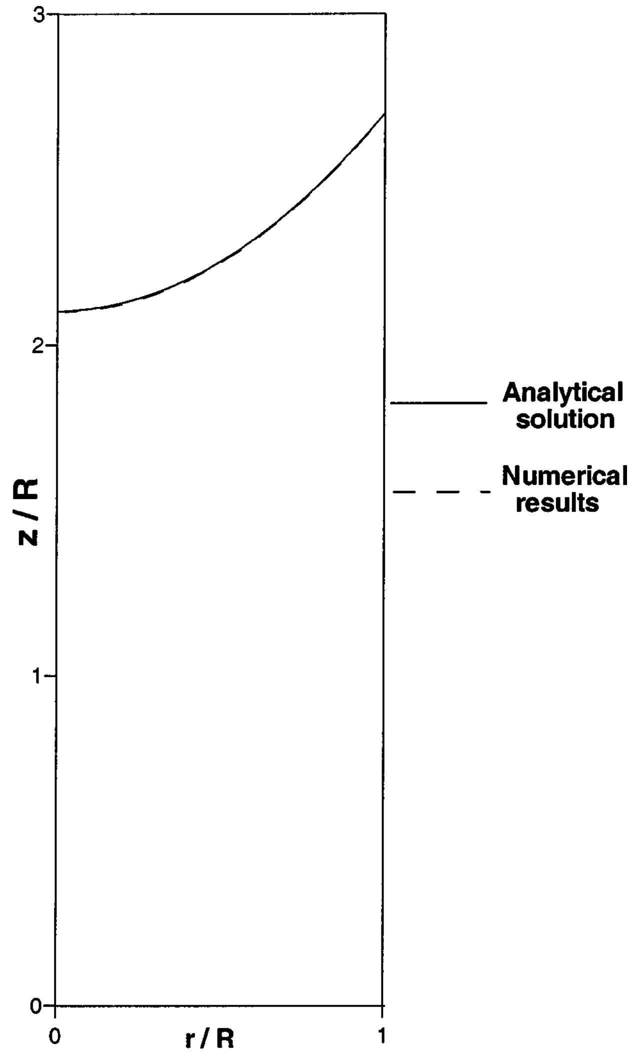

Fig. 3 Comparison of the predicted steady free-surface shape with analytic solution

Figures 6(*a*) and 6(*b*) display the streamlines in both the gas and liquid phases at the instant $\Omega t = 200$ for the spinup problem. For axisymmetric incompressible flows, the stream function in cylindrical coordinates is defined as

$$u = -\frac{1}{r}\frac{\partial \psi}{\partial z}, \quad w = \frac{1}{r}\frac{\partial \psi}{\partial r}.$$

The stream function ψ was set to be zero at $r = 0$, $r = R$, $z = 0$, $z = H$ as the boundary conditions. The secondary flows induced during the transient process are illustrated in these plots. Evidently, the Ekman layer near the bottom wall is extremely thin. We show a magnified view of the streamlines near the bottom wall in Fig. 6(*b*). It can be seen from Fig. 6(*a*) that the sidewall Stewartson [21] layer is much thicker compared to the bottom Ekman layer. Since both boundary layers transport almost the same amount of mass, the velocity in the Stewartson layer must be much smaller (by one order of magnitude) than the u velocity in the bottom Ekman layer. Greenspan et al. [1] stated that in a completely filled container the Ekman layer plays the significant role

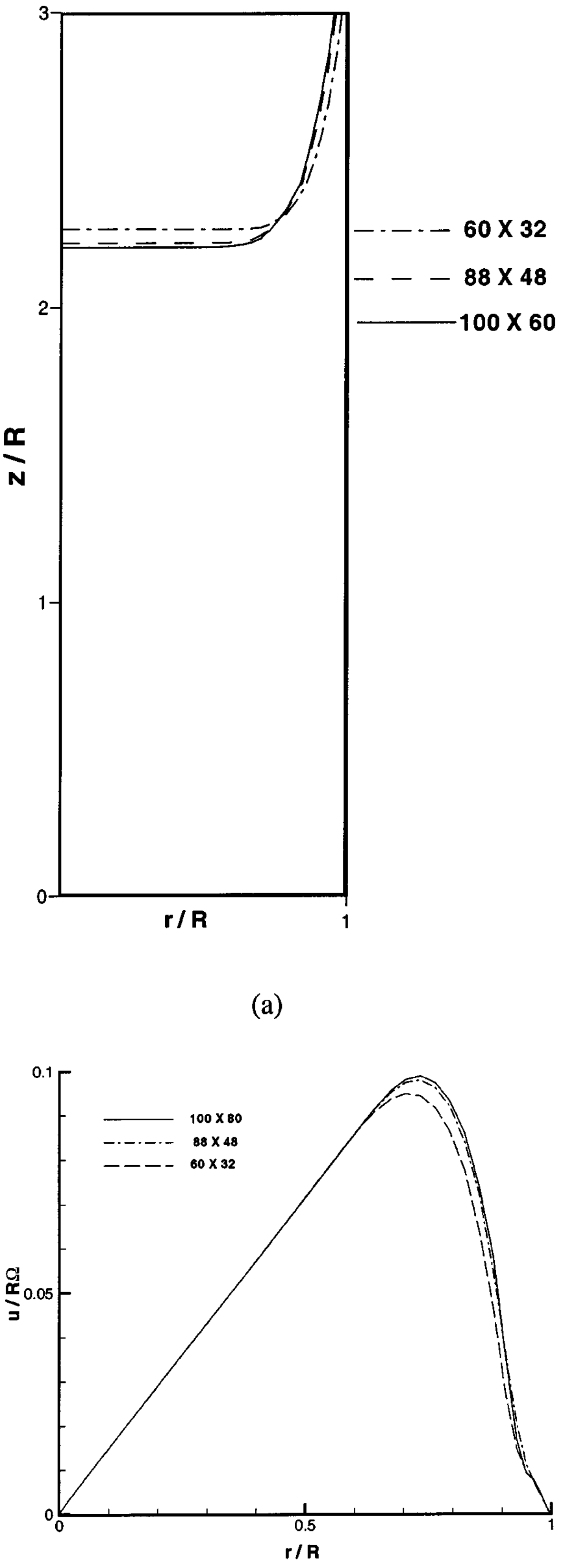

(a)

(b)

Fig. 4 The effect of mesh sizes on the numerical results at nondimensional time, $\Omega t=400$; (*a*) development of free surface, (*b*) radial velocity along the *r* direction at section $z=0.25$ mm

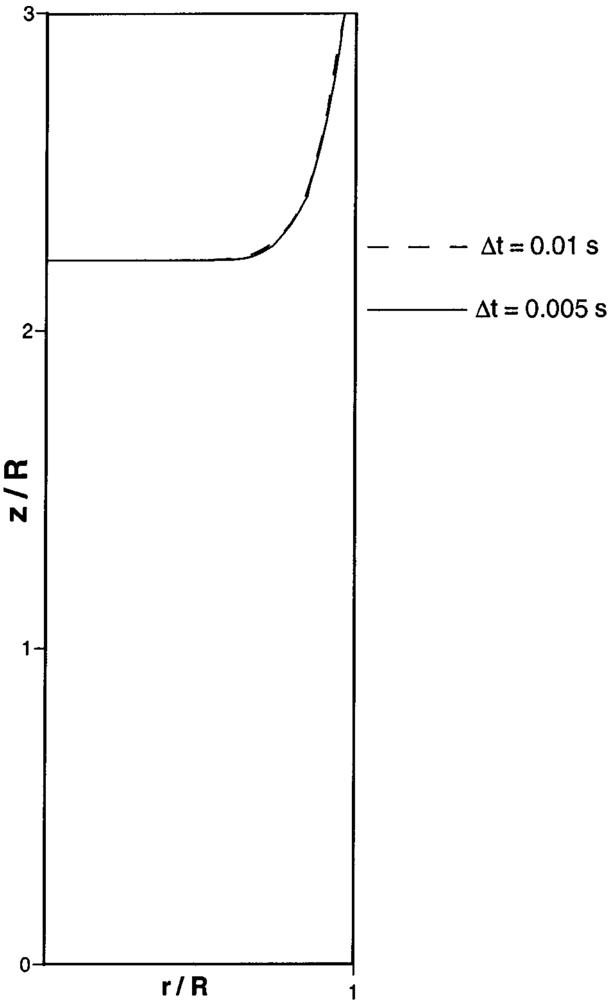

Fig. 5 The effect of time-step sizes on the numerical results at instant $\Omega t=400$

in the transient process by inducing a small circulatory secondary flow. Similar mechanism is also found (in our simulations) for the free-surface development in a partially filled centrifuge. Within a few revolutions after the abrupt spinup from rest, under the effect of viscous diffusion, a quasi-steady Ekman boundary layer forms in the vicinity of the bottom wall. Because of the no-slip boundary condition, the liquid adjacent to the bottom end must rotate with a velocity of the same order of magnitude as the cylinder's speed. Therefore, subject to a radial centrifugal force, the Ekman layer is characterized by a radial flow moving outward. This outward flow induces a secondary flow in the interior core region and its transport is balanced by a small flux into the boundary layer from the essentially inner flow. Low angular momentum fluid entering the layer from the interior core region is replaced by fluid with high angular momentum convected inward to conserve mass. Similar secondary flows are also observed (in our simulations) in the air region.

Streamlines in both the gas and the liquid phases at the instants $\Omega t=400$ are shown in Fig. 7 for the spinup problem. Near the free surface (close to the top wall), there is another circulation in the airflow with an opposite direction to the main secondary flow. This additional circulation is induced by the change of the shape of the free surface. Since the free surface is gradually transforming to a paraboloid, air particles near the corner of the intersection between the free surface and the top wall are driven radially inward by the liquid interface, moving downward and then upward back to the top wall. However, the counterpart of this additional

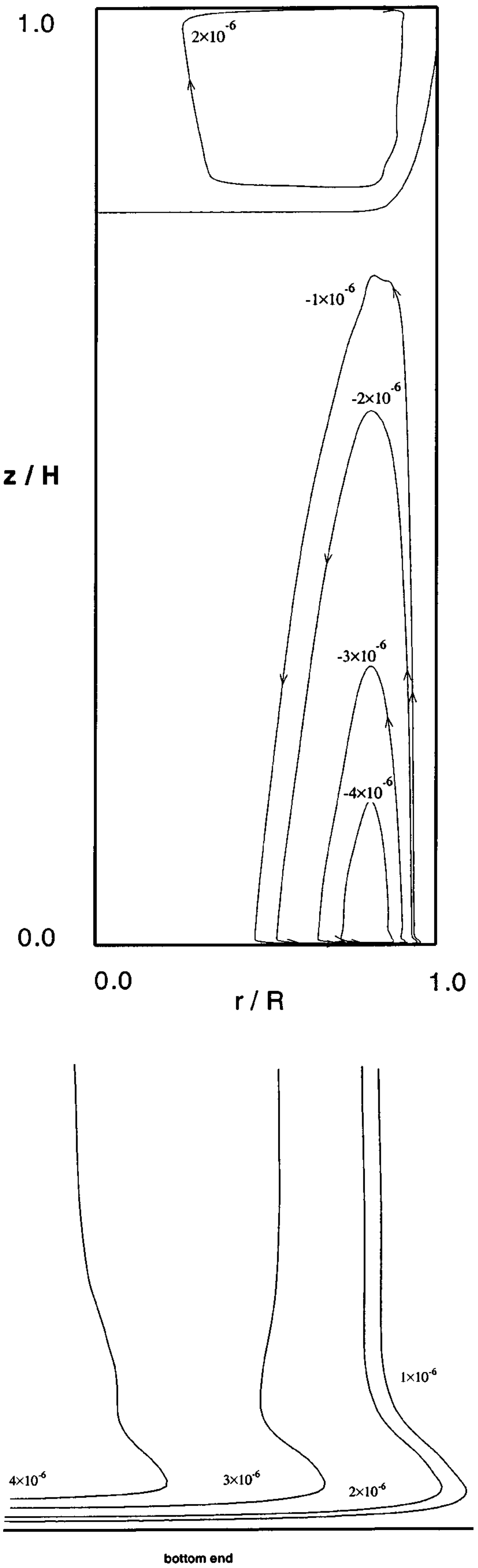

Fig. 6 (*a*) Streamlines at time $\Omega t = 200$ for the spinup case; (*b*) details of streamlines near the bottom end at time $\Omega t = 200$ for the spinup case

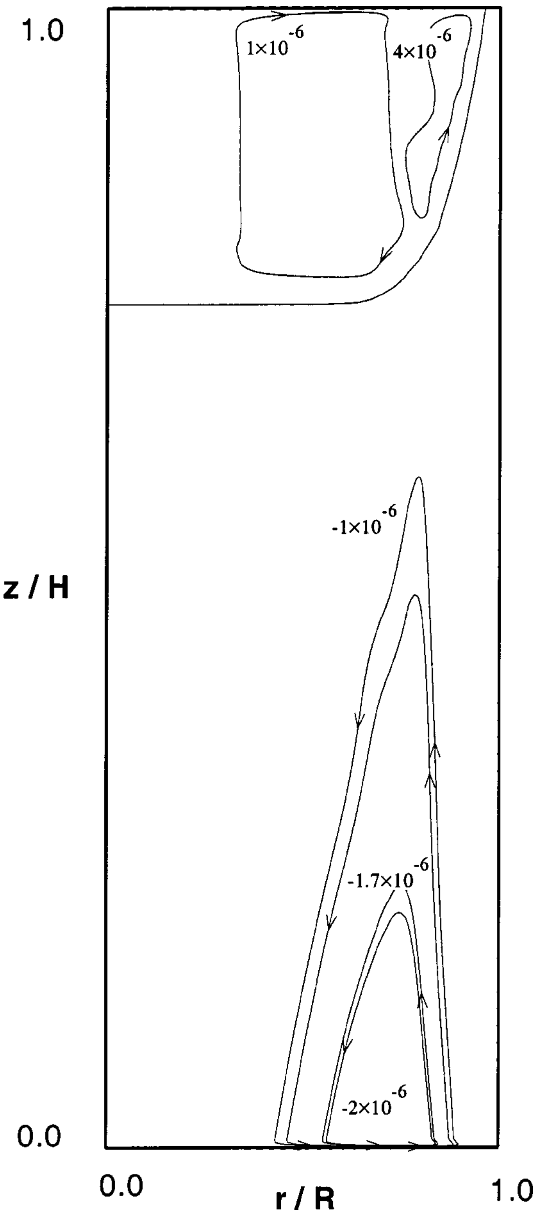

Fig. 7 Streamlines at time $\Omega t = 400$ for the spinup case

secondary flow in the liquid zone is insignificant. Due to huge density difference, the additional secondary flow induced by the interaction between the liquid and air has almost no effect on the liquid core flow. As the steady state approaches ($\Omega t \geqslant 2000$), all predicted secondary flows decay and solid-body rotation is attained for the gas and liquid phases.

Steady Flow in a Partially Filled Centrifuge With an "Overrotating" Lid. Interesting steady flows exist in a centrifuge where the free surface attains a vertical orientation and the upper lid overrotates. For the geometry shown in the Fig. 1(*b*), we investigate the steady fluid flow problem in a partially filled centrifuge. We use the same parameters in our time-dependent numerical simulations, as used by Shadday et al. [15] in his experiments. These include the centrifuge rotation speed (1000 rpm), the upper lid speed (1050 rpm), the cylinder length (194 mm), the inside diameter (189 mm) and the fluid (glycerin-water mixture, $\nu = 10^{-5}\,\mathrm{m}^2/\mathrm{s}$). Essentially, the steady flow is characterized by three dimensionless parameters here: the Rossby number

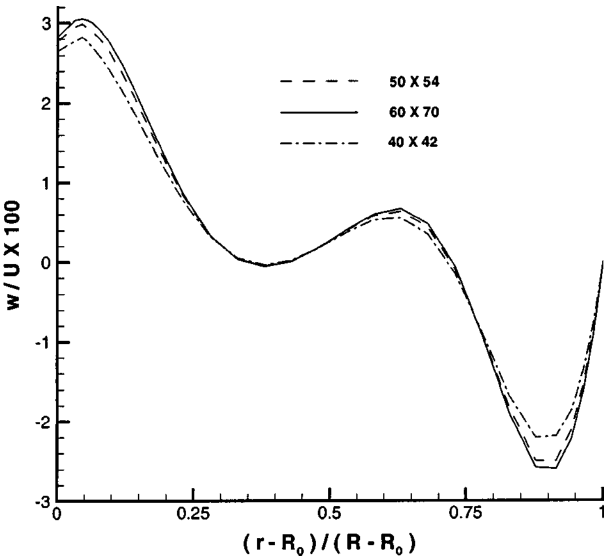

Fig. 8 The effect of mesh size on axial velocity profile at $z/H = 0.438$ in the liquid region for the "overrotating" lid case (the origin of the horizontal axis indicates the free surface)

$\varepsilon = \Delta\Omega/\Omega$, the Ekman number $E = \nu/\Omega H^2$ and the filling ratio L/H. For the given conditions, $\varepsilon = 0.05$, $E = 2.5 \times 10^{-6}$ and $L/H = 0.3$.

For the time-dependent simulations, the effects of grid size and time steps were carefully evaluated for this problem also. The spinup time scale $(L^2/\Omega\nu)^{1/2}$ in this case (without overrotation of the upper lid) is about 6 seconds and our simulations (with a time step of 0.01 s) predict the free surface to be approximately vertical at this time. The radius of the air core R_0 is 75.5 mm. This result (not shown) is in good agreement with experiment by Shadday et al. [15].

The computations were carried out for another 6 seconds (with overrotation of the upper lid) to attain the steady flow fields in the gas and liquid regions (separated by an almost vertical interface). Figure 8 presents the effects of mesh size on the results of prediction where the radial profile of the axial velocity at the liquid layer is plotted at $z/H = 0.438$. The axial velocity here is normalized by the overrotating lid relative peripheral velocity $\Delta V = \varepsilon R \Omega$. At this section, the liquid flows upward near the vertical interface, then undergoes flow reversal near the middle of the liquid layer. Computations were done with the following grid sizes: 40×42, 50×54 and 60×70. As the grid size increased, the density of the grids near the interface also increased. Since the difference in the solutions obtained by the 50×54 and 60×70 grid sizes was of the order of 1–2%, compared to the uncertainty in the experimental measurement ±0.03 U, [15], the 50×54 grid size was considered adequate for the simulations. The 50 axial grids are set with variable spacing to resolve the boundary layers at the top and the bottom walls. In the radial direction also, 54 grids are arranged with variable spacing with high densities of grids near the vertical wall and the vertical interface. The radial and axial resolutions are sufficient to give more than five nodes near the free surface and in the boundary layers along walls. Also, since the single velocity formulation (gas and liquid have the same velocity in partially filled cells) is used, the grid size near the free surface is fine enough so that the variation of velocities from the partially filled cells to the neighbor fully filled cells is small. The nonuniform meshes used in the simulation is displayed in Fig. 9 to illustrate the grid size at the interface.

Figure 10 shows the streamlines obtained from our numerical

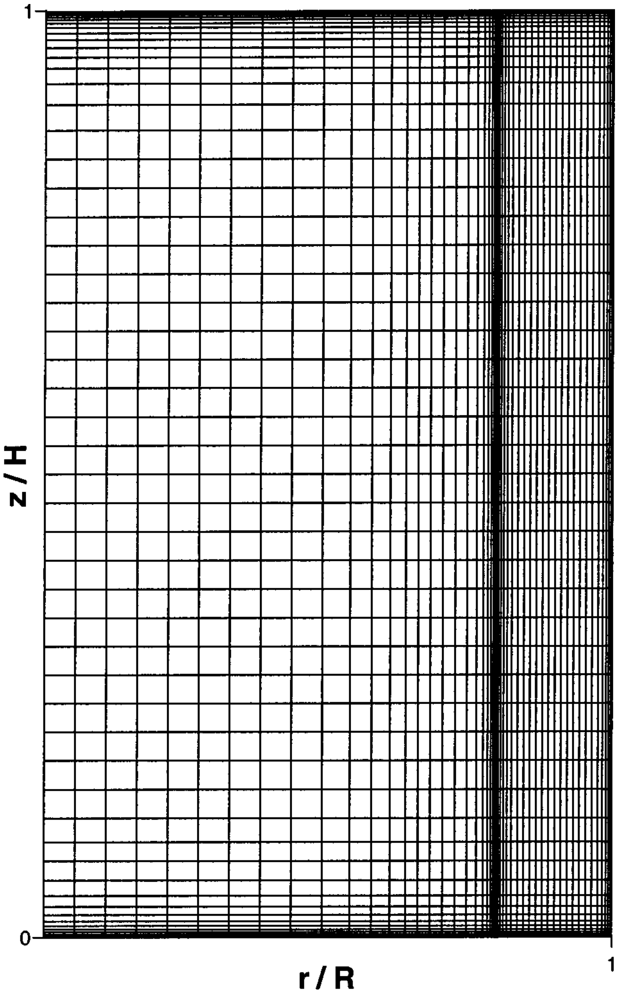

Fig. 9 Nonuniform grid generated for the overrotating case

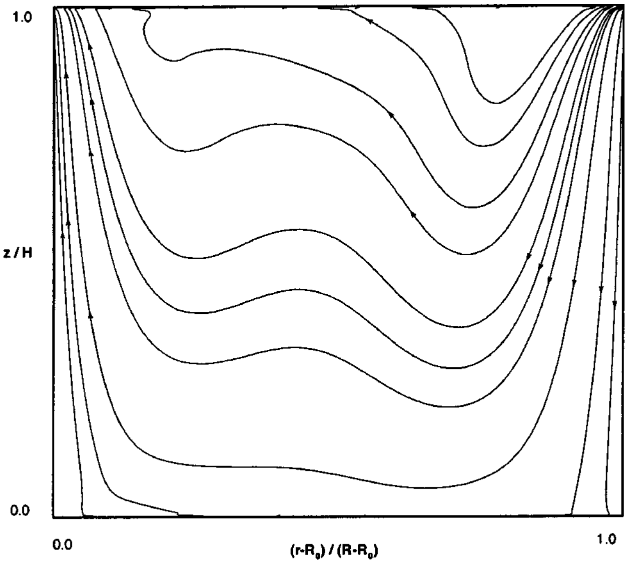

Fig. 10 Streamlines in the liquid region for the overrotating case (the vertical left side indicates the free surface) (the stream function values along each stream lines in the figure are equally distributed between 1×10^{-6} and 6×10^{-6})

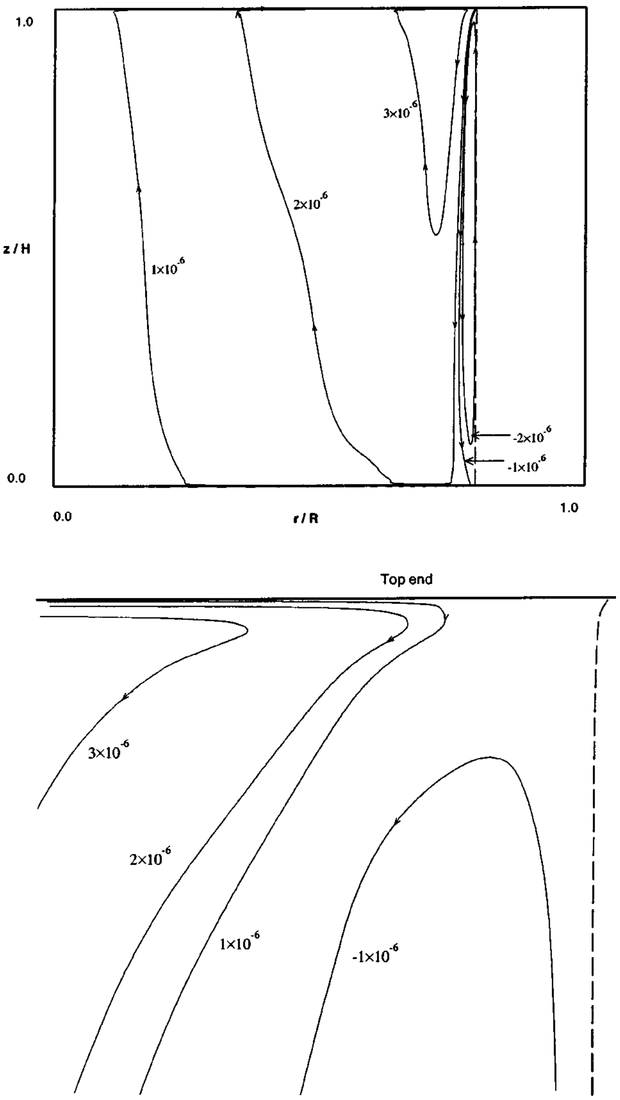

Fig. 11 (*a*) Streamlines in the gas region for the overrotating case (the dashed line on the right indicates the free surface); (*b*) details of streamlines near the top end in the air flow region for the overrotating case (the dashed line on the right indicates the free surface)

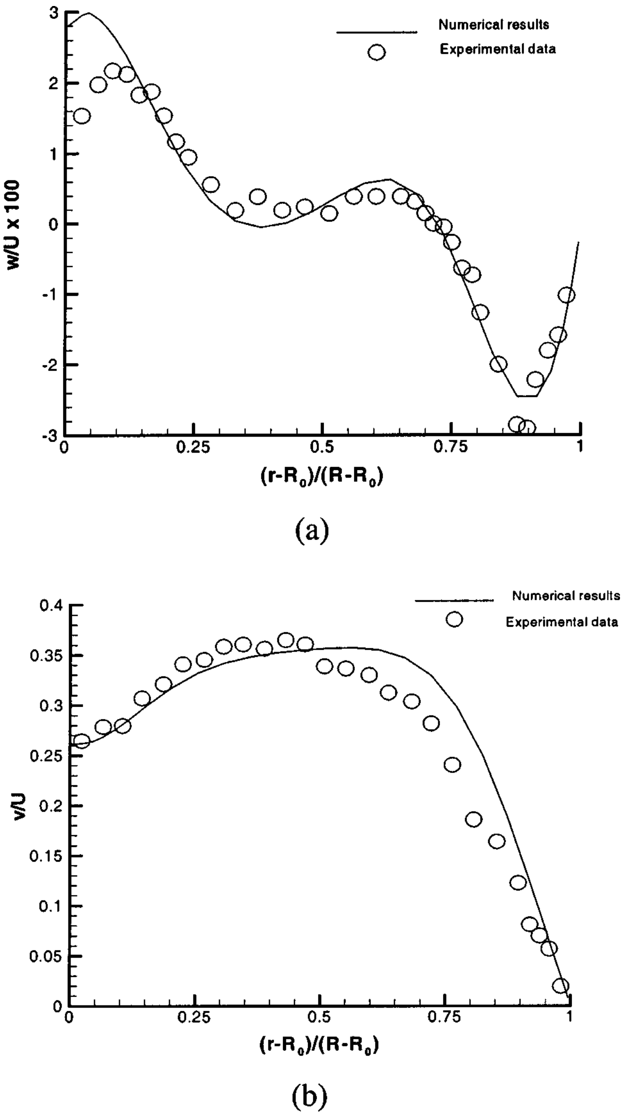

Fig. 12 Computed radial profiles of (*a*) axial (*b*) and relative azimuthal velocity at $z/H=0.438$ in the liquid region for the overrotating case

predictions, in the liquid region. Normalized axial and radial coordinates are used in the figure. The radial axis has been expanded so that the details of the flow may be better seen. A complicated flow field exists in the liquid region with very thin boundary layers near the overrotating upper lid. The predictions agree well the predictions by Shadday et al. [15] and Ribando and Shadday [22].

Figures 11(*a*) and 11(*b*) show the steady streamlines induced in the gas region. Figure 11(*b*) shows the details of the gas flowfield near the top "overrotating" lid. Two circulations are shown in Fig. 11(*a*). Air in the upper horizontal Ekman layer is accelerated radially by the centrifugal force and expelled downward into the air core. The flow proceeds continuously into the bottom Ekman layer where fluid is transported radially inward, feeding as it goes, the local, vertical upward flux near the wall required by the top plate. This is the main circulation induced by the overrotating lid. At the interface, liquid is moving upward, unaware of the air core, to close the mass transport of that amount of fluid from top surface to the bottom. It follows that air particles in the boundary layer near the interface are also driven in the same direction. Evidently, it is in the opposite direction of the main secondary flow. Therefore, an additional circulation is formed in the gas region but confined to a very thin region along the free surface.

Axial and relative azimuthal velocity profiles in the liquid region at two sections ($z/H=0.438$ and 0.83) are shown in Figs. 12 and 13, respectively. The azimuthal component plotted is the relative velocity with respect to the rotational velocity of the centrifuge. Again, both components of velocity have been normalized by the overrotating lid relative peripheral velocity $\Delta V=\varepsilon R\Omega$. In Figs. 12 and 13 we compare experimental measurements by Shadday et al. in the liquid region with our numerical predictions. Good agreement is obtained and the trends of the velocity profiles within the liquid layer are well predicted. Near the interface, however, the predicted amplitude of the axial velocity is higher than the measured values reported by Shadday et al. The numerical predictions by Shadday et al. (considered only the liquid layer flow, neglecting the flows in the gas layer) also show the same trend. This discrepancy is perhaps due in part to limitations in the radial resolution of the LDV system, [15]. It is also noted that the present predictions agree with the measurements near the wall, compared to the numerical predictions of Shadday et al. (not reported here). Although the shear stress at the surface does not change the essential flow pattern in the liquid, however, it affects the velocity components near the surface quantitatively. In our simulations, this mismatch near the free surface is greatly im-

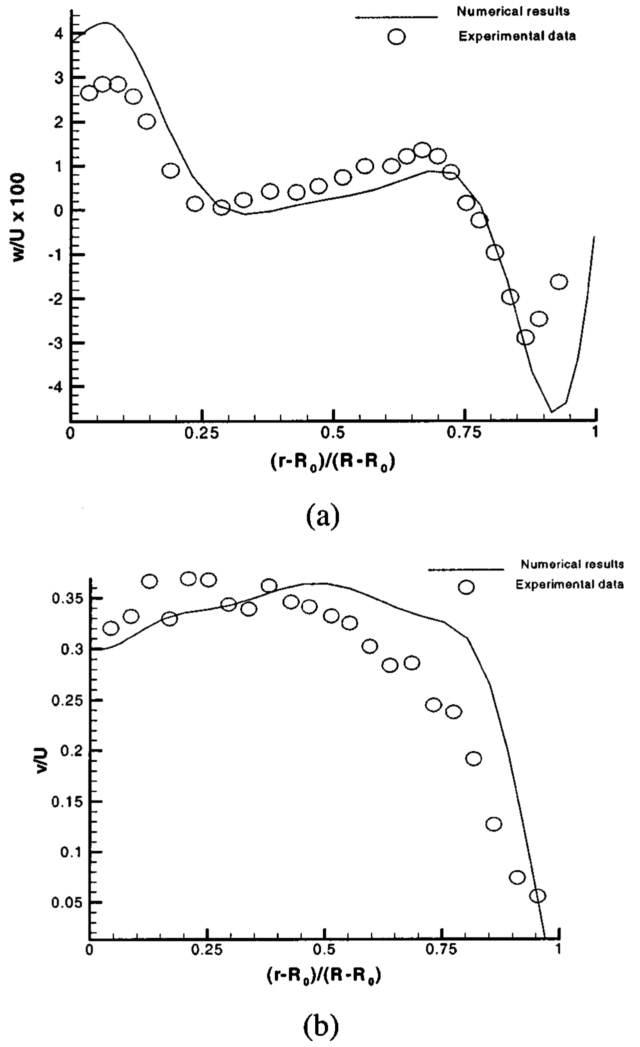

Fig. 13 Computed radial profiles of (*a*) axial and relative azimuthal velocity at $z/H=0.83$ in the liquid region for the overrotating case

proved by implementing the homogenous multiphase flow model for the whole centrifuge. As shown in Figs. 12(*a*) and 13(*a*), the experimentally observed trends for the axial velocity near the interface are predicted numerically.

Figures 14(*a*), 14(*b*) and 15(*a*), 15(*b*) show the radial distributions of axial and relative azimuthal velocity components in both the gas and the liquid layers at two axial positions. The liquid region (right side of the dashed line) is comparatively thin, dominated by vertical boundary layers. The thickness of sidewall and free-surface boundary layer are proportional to $E^{1/3}$ that agrees with the predictions of Shadday et al. [15]. In this case, there is no interior inviscid region in the liquid film. For the gas layer, an interior region of inviscid flow is demonstrated in Figs. 14(*a*) and 15(*a*). In addition to the weak axial flow in the interior, an axial boundary layer exists along the free surface for the gas. As depicted in Figs. 14(*b*) and 15(*b*), the relative azimuthal velocity at each section attains a peak value in the gas and the liquid layers, respectively. The relative azimuthal velocity is induced by the high angular momentum fluid transported from the top Ekman layer.

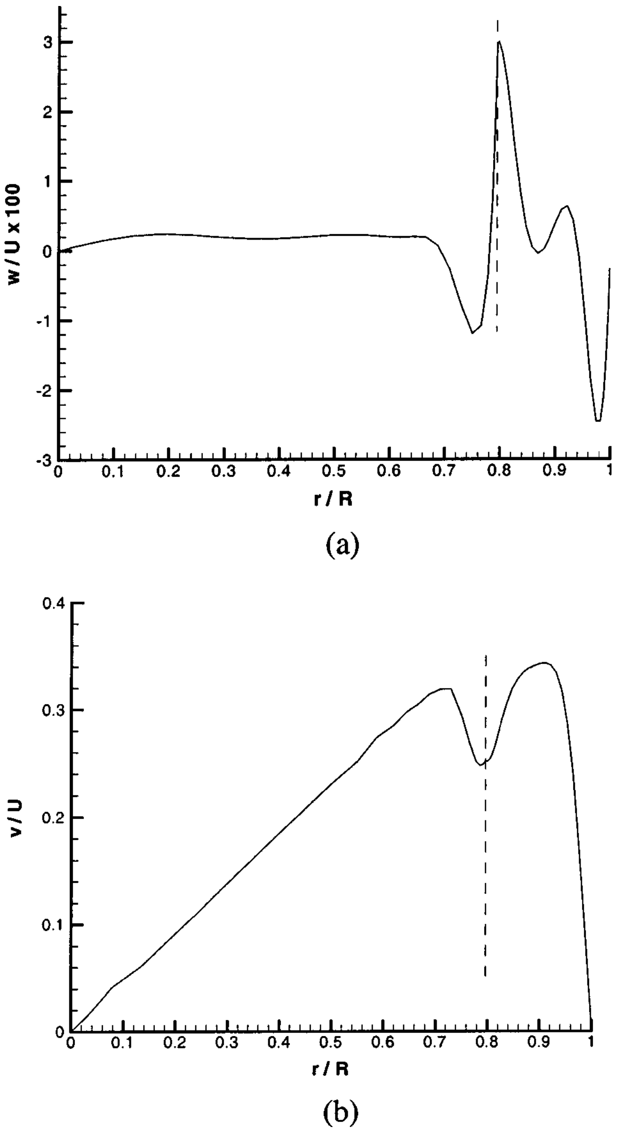

Fig. 14 Computed radial profiles of (*a*) axial and (*b*) relative azimuthal velocity at $z/H=0.438$ in gas and liquid phases for the overrotating case (the dashed line indicates the free surface)

Conclusions

A comprehensive numerical investigation was carried out for predicting the liquid/gas interface and flow fields in both the liquid and gas regions in partially filled centrifuges. The axisymmetric Navier-Stokes equations with a homogeneous multiphase model are solved for both gas and liquid phases. Flow pattern details inside the boundary layers of the transient flow fields in both the gas and liquid regions are revealed for the spinup problem. For the steady flow in the partially filled centrifuge with an overrotating lead, similar interesting flow fields are found in both the gas and the liquid regions. Comparison of the numerical results with experimental measurements indicate that the developed model provides better understanding of the characteristic of spinup from rest of a partially filled centrifuge and the steady flows induced in a partially filled centrifuge with an overrotating lid. The model is general in nature and can be easily extended to full three-dimensional flow fields. The model can also be applied to investigate mixing and separation problems in centrifuges where the assumptions of axisymmetry and laminar flows can be satisfied.

Nomenclature

E = Ekman number$=\nu/\Omega H^2$
Fr = Froude number$=(\Omega R)^2/gH$

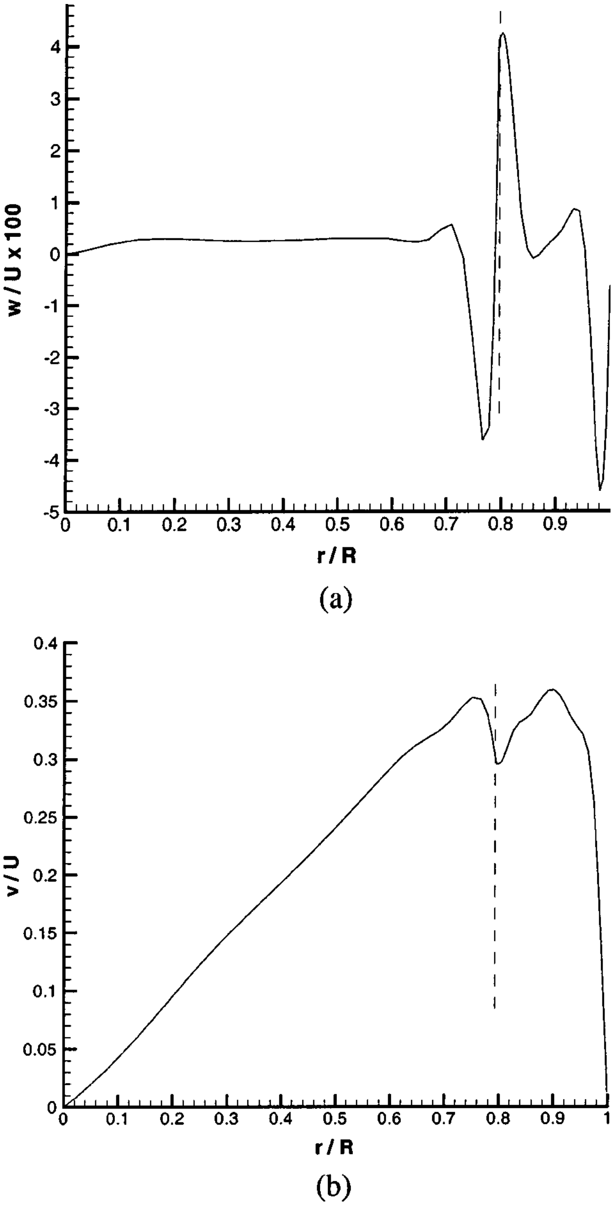

Fig. 15 Computed radial profiles of axial (*a*) and azimuthal (*b*) velocity at $z/H=0.83$ in gas and liquid phases for the overrotating case (the dashed line indicates the free surface)

g = gravity
H = height of the cylinder
L = initial depth of liquid in the cylinder
P = pressure of fluid
r = radial coordinate
R = radius of the cylinder
R_o = radius of air core
Re = Reynolds number$=\Omega R^2/\nu$
u, v, w = velocity components in r, θ, and z directions
v_{rel} = relative azimuthal velocity $(v-r\Omega)$
ΔV = overrotating lid relative peripheral velocity$=\varepsilon R\Delta\Omega$
z = axial coordinate

Greek Symbols

θ = azimuthal coordinate
Ω = angular speed of rotation
$\Delta\Omega$ = overrotating speed
ε = Rossby number$=\Delta\Omega/\Omega$
γ = volume fraction of fluid
μ = molecular viscosity
ν = kinematic viscosity
ρ = fluid density
ψ = stream function

Superscript

$*$ = nondimensional value

Subscript

1 = liquid phase
2 = gas phase

References

[1] Greenspan, H. P., and Howard, L. N., 1963, "On Time-Dependent Motion of a Rotating Fluid," J. Fluid Mech., **17**, pp. 385–404.
[2] Warn-Varnas, A., Fowlis, W. W., Piacsek, S., and Lee, S. M., 1978, "Numerical Solutions and Laser-Doppler Measurements of Spin-up," J. Fluid Mech., **85**, pp. 609–639.
[3] Benton, E. R., and Clark, Jr., A., 1974, "Spin-up," Annu. Rev. Fluid Mech., **6**, pp. 259–280.
[4] Duck, P., and Foster, M., 2001, "Spin-up of Homogeneous and Stratified Fluids," Annu. Rev. Fluid Mech., **33**, pp. 231–263.
[5] Wedemeyer, E. H., 1964, "The Unsteady Flow Within a Spinning Cylinder," J. Fluid Mech., **20**, pp. 383–399.
[6] Kitchens, Jr., C. W., 1980, "Ekman Compatibility Conditions in Wedemeyer Spin-up Model," Phys. Fluids, **23**, pp. 1062–1064.
[7] Kitchens, Jr., C. W., 1980, "Navier-Stokes Equations for Spin-up in a Filled Cylinder," AIAA J., **18**, pp. 929–934.
[8] Hyun, J. M., Leslie, F., Fowlis, W. W., and Warn-Varnas, A., 1983, "Numerical Solutions for Spin-up From Rest in a Cylinder," J. Fluid Mech., **127**, pp. 263–281.
[9] Watkins, W. B., and Hussey, R. G., 1977, "Spin-up From Rest in a Cylinder," Phys. Fluids, **20**, pp. 1596–1604.
[10] Goller, H., and Ranov, T., 1968, "Unsteady Rotating Flow in a Cylinder With a Free Surface," ASME J. Basic Eng., **90**, pp. 445–454.
[11] Homicz, G. F., and Gerber, N., 1986, "Numerical Model for Fluid Spin-up From Rest in a Partially Filled Cylinder," AIAA Paper 86-1121, pp. 1–9.
[12] Homicz, G. F., and Gerber, N., 1987, "Numerical Model for Fluid Spin-up From Rest in a Partially Filled Cylinder," ASME J. Fluids Eng., **109**, pp. 194–197.
[13] Choi, S., Kim, J. W., and Hyun, J. M., 1989, "Transient Free Surface Shape in an Abruptly Rotating, Partially Filled Cylinder," ASME J. Fluids Eng., **111**, pp. 439–443.
[14] Choi, S., Kim, J. W., and Hyun, J. M., 1991, "Experimental Investigation of the Flow With a Free Surface in an Impulsively Rotating Cylinder," ASME J. Fluids Eng., **113**, pp. 245–249.
[15] Shadday, M. A., Ribando, R. J., and Kauzlarich, J. J., 1983, "Flow of an Incompressible Fluid in a Partially Filled, Rapidly Rotating Cylinder With a Differentially Rotating Endcap," J. Fluid Mech., **130**, pp. 203–218.
[16] Wang, C. Y., and Cheng, P., 1996, "A Multiphase Mixture Model for Multiphase, Multicomponent Transport in Capillary Porous Media—I. Model Development," Int. J. Heat Mass Transfer, **39**, pp. 3607–3618.
[17] Hirt, C. W., and Nichols, B. D., 1981, "Volume of Fluid (VOF) Method for the Dynamics of Free Boundaries," J. Comput. Phys., **39**, pp. 201–225.
[18] Schlichting, H., 1962, *Boundary Layer Theory*, 4th Ed., McGraw-Hill, New York (translated by J. Kestir).
[19] Freitas, C. J., Street, R. L., Findikakis, A. N., and Koseff, J. R., 1985, "Numerical Simulations of Three-Dimensional Flows in a Cavity," Int. J. Numer. Methods Fluids, **5**, pp. 561–575.
[20] Gerber, N., 1975, "Properties of Rigidly Rotating Liquids in Closed Partially Filled Cylinders," ASME J. Appl. Mech., **97**, pp. 734–735.
[21] Stewartson, K., 1957, "On Almost Rigid Rotations," J. Fluid Mech., **3**, pp. 17–26.
[22] Ribando, R. J., and Shadday, M. A., 1984, "The Ekman Matching Condition in a Partially Filled, Rapidly Rotating Cylinder," J. Comput. Phys., **53**, pp. 266–288.

Guohua Li
Graduate Student

Jim C. P. Liou
Professor

Department of Civil Engineering,
University of Idaho,
Moscow, ID 83844-1022

Swing Check Valve Characterization and Modeling During Transients

The hydraulic torque on the disk of a swing check valve strongly influences the dynamic valve-fluid interaction. This torque is difficult to quantify. In this study, the hydraulic torque is separated into a torque due to flow around a stationary disk and a torque due to disk rotation. Laboratory tests have been conducted to characterize these components. Numerical simulations of a check valve slam are made and the results compared with measured disk angle and pressure traces. The validity of the hydraulic torque characterization is demonstrated by the close agreement between the simulation results and the measurements. [DOI: 10.1115/1.1625689]

Introduction

A swing check valve is commonly used where sustained reverse flow in a pipeline is not allowed. This type of check valves closes under reverse flow and valve slam is common. Water hammer upon valve slam can create overpressure. In pump stations where several pumps and check valves co-exist, startup of one pump can trigger multiple check valve slams.

Ideally, the hydraulic torque should be calculated from the pressure distribution around the valve disk. However, it is nearly impossible to determine the pressure distribution analytically or experimentally due to complicated flow patterns. The hydraulic torque has been estimated a number of different ways. Uram [1], Safwat et al. [2], and Arastu et al. [3] estimated the hydraulic torque by the difference of pressures measured at two locations across the check valve where steady one-dimensional flow assumption prevails. As shown later, such an approach does not capture the effects of the unsteady nonuniform flow around the disk.

Kane and Cho [4] and Koch [5] regarded the hydraulic torque as a product of the relative velocity between the flow and the disk and an experimentally determined torque coefficient. This coefficient varied with disk angle and flow velocity if the pipeline Reynolds number was less than 10^6 but varied with disk angle for higher Reynolds numbers (Kane and Cho [4]). This approach did not satisfactorily predict the experimental results of Ball and Tullis outlined in Kane and Cho [4]. In addition, the torque coefficient becomes infinite when the relative motion is zero, which is not physical.

Some other researchers considered the hydraulic torque to be made up of two components that are additive. Rahmeyer [6] assumed that the hydraulic torque is composed of two terms: flow velocity and pressure differential across the valve. Botros et al. [7,8] adopted this approach to a check valve in gas flow. In theory, since the flow velocity and pressure differential are related, their effects should not be treated separately. Esleek et al. [9] represented the hydraulic torque as two separate moments: a flow moment and a damping moment. The flow moment is a function of the square of the flow velocity multiplied by a flow coefficient that varies with the disk angle. The damping moment is a function of the square of the angular velocity of the disk multiplied by a constant damping coefficient. Pool et al. [10] modified the work of Esleek et al. [9] by making the damping coefficient a function of the disk angle. Ellis and Mualla [11,12] used a similar approach described by Pool et al. [10] to determine both the flow coefficient and the damping coefficient. The flow coefficient was determined experimentally from a steady-state flow test and the damping coefficient by free movement of the disk in initially still water. The effects of the relative motion between the through flow and the disk rotation were not considered. The damping coefficient was assumed to be independent of the angular velocity of the disk.

Kruisbrink [13] outlined a concept framework where many terms are used to describe the hydraulic torque in a dimensionless manner. These are: flow velocity, flow acceleration, disk angle, disk velocity, disk acceleration, the product of disk velocity and flow velocity, three drag coefficients, and two added mass coefficients.

Provoost [14,15] regarded the dynamic characteristic of a check valve as a curve that relates the magnitude of the maximum reversed flow just prior to closure to a characteristic deceleration of the water column. In estimating the pressure rise due to valve slam, one first simulates the system transients without the presence of the check valve to obtain the deceleration of the fluid at the location of the check valve. Knowing the deceleration, the maximum reversed flow is determined from the dynamic characteristic curve. Assuming the valve is pushed to close fully by the reverse flow, a pressure rise is then calculated according to the Joukowsky formula. This approach was later expanded by Koetzier et al. [16], Thorley [17,18], and Kruisbrink et al. [19]. The Provoost's approach cannot be used in a general setting where the check valve may or may not close fully during transients, nor can it be used where multiple check valves may interact with one another.

Experimentally, Rahmeyer [6] used clear plastic view ports to observe disk motion. Au-Yang [20] used ultrasonic signals to determine the disk angle. Kruisbrink [13] used a potentiometer for disk angle measurement. No direct measurements of disk angular velocity and acceleration were found in the literature.

This paper takes a fundamental approach using the moment of momentum equation where the net torque acting on the disk is equated to the time rate of change of the angular momentum of the rotating mass. The torques acting on the check valve disk are: the torque due to the submerged weight of the disk assembly, the torque due to the friction of the valve shaft, any external torque such as that caused by a spring or counter weight, and the torque due to the flow around the valve disk. The weight torque and the external torque are functions of the disk angle and can be accurately determined from the material and the geometry of the valve. The shaft friction torque is usually small and negligible. However, in laboratory testing of instrumented small check valves, the shaft friction torque can be significant. Characterizing the shaft torque is addressed in this study. For the hydraulic torque, we adopt the

---

Contributed by the Fluids Engineering Division for publication in the JOURNAL OF FLUIDS ENGINEERING. Manuscript received by the Fluids Engineering Division January 15, 2003; revised manuscript received June 23, 2003. Associate Editor: Y. Tsujimoto.

approach that the hydraulic torque is separable into two components: the torque created by the flow around a stationary disk and the torque created by the rotation of the disk. Laboratory tests to quantify these torque components are described and discussed for a two-inch swing check valve. Validation of the proposed approach to check valve characterization is demonstrated by the excellent match between the measured disk angle and pressure traces of valve slam transients with numerical simulations based on a dynamic balance of all torques in volved.

Hydraulic Torque and Its Presentation

The dynamic behavior of a swing check valve is described by the moment of momentum equation of the disk. Considering all the torques involved and regarding the opening torque (counterclockwise) as positive, (see Fig. 1), the moment of momentum equation can be written as

$$T_W+T_{FK}+T_E+T_H=(I+I_E+I_f)\ddot{\theta}. \tag{1}$$

In this equation, T_W is the torque due to the submerged weight of the valve disk assembly:

$$T_W=-W_sL\sin(\theta+\theta_s), \tag{2}$$

where W_S=submerged weight of the of the disk assembly, L=length between the mass center of the disk assembly and the shaft axis, θ=disk angle positive counterclockwise, and θ_s=angle of the valve when seated (see Fig. 1). T_{FK} is the kinetic frictional torque due to the valve shaft and the associated instrumentation. T_{FK} is a function of the angular speed of the disk. T_E is a known external torque applied by attaching a weighted frame to the valve shaft. It can be clockwise or counterclockwise. For a given applied weight, T_E varies with the disk angle. T_H is a hydraulic torque due to the pressure distribution on the surface of the disk. It is a complex function of the through flow velocity, disk angle, and disk angular velocity. I is the moment of inertia of the disk assembly with respect to the valve shaft axis. I_E is the moment of inertia of the device through which T_E is applied. I_f is the moment of inertia of the added mass due to disk acceleration. The moment of inertia of the disk assembly can be accurately calculated. The moment of inertia of the added mass is based on an added mass equaling to that of a fluid sphere at the same diameter of the disk (Thorley et al. [21] and Worster [22,23]).

We also regard the hydraulic torque as made of two additive components. The first component is a torque acting on a fixed disk herein called stationary component of the hydraulic torque T_{HS}. As the disk swings, the changing pressure distribution on the disk surface creates an additional torque. We call this additional torque the rotational component of the hydraulic torque T_{HR}. These two torques are independent of each other and can be either clockwise or counterclockwise. The hydraulic torque is the sum of these two:

$$T_H=T_{HS}+T_{HR}. \tag{3}$$

The magnitude of the stationary torque, expressed in terms of a torque coefficient, is written as

$$|T_{HS}|=C_{HS}\rho A_v\frac{V^2}{2}L \tag{4}$$

where C_{HS}=the stationary hydraulic torque coefficient, ρ=the fluid density, V=the velocity of through flow which equals the volumetric flow rate divided by cross-sectional area of the pipe, and A_v=the valve disk area. The magnitude of the rotational hydraulic torque is represented as

$$|T_{HR}|=C_{HR}\rho A_v\frac{(L\dot{\theta})^2}{2}L \tag{5}$$

where C_{HR}=the rotational hydraulic torque coefficient. Both C_{HS} and C_{HR} are quantifiable by laboratory tests.

Experimental Setup

The schematic of the test rig is shown in Fig. 2. At the initial steady state, water is pumped through inlet valve 1 toward upper tank 5 that overflows at a constant head. The inlet valve is a quarter-turn ball valve that can be shut off very quickly. Downstream of the inlet valve is a 50 mm schedule 40 steel pipe with an internal diameter of 52.5 mm. It runs horizontally for 19.67 m and then turns vertically upwards for another 4.72 m to the bottom of the upper tank. The tank depth is 0.86 m. Water overflows at a constant head of 5.58 m above the centerline of the test section. Lower tank 4 and bypass valve 2 are for reverse flow tests. The flow into the lower tank can be diverted to a weighting tank for flow rate measurements. For some tests, control valves 10 and 11 replace the vertical pipe leading to the upper tank. Pressure taps P1, P2, P3, and P4 are located at 0.23, 12.38, 13.83, and 19.57 m

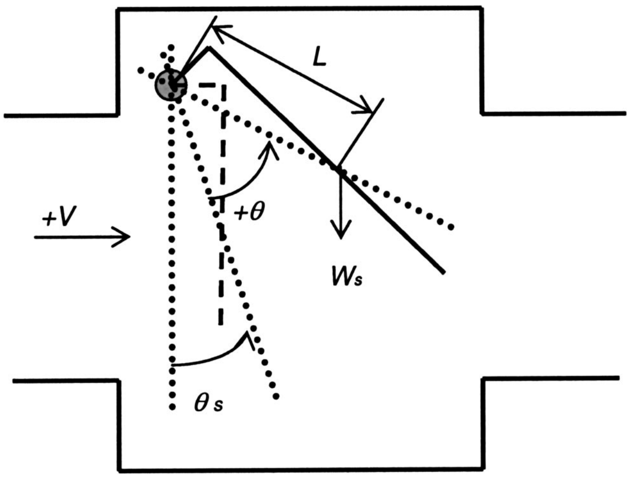

Fig. 1 Definition of variables associated with a swing check valve

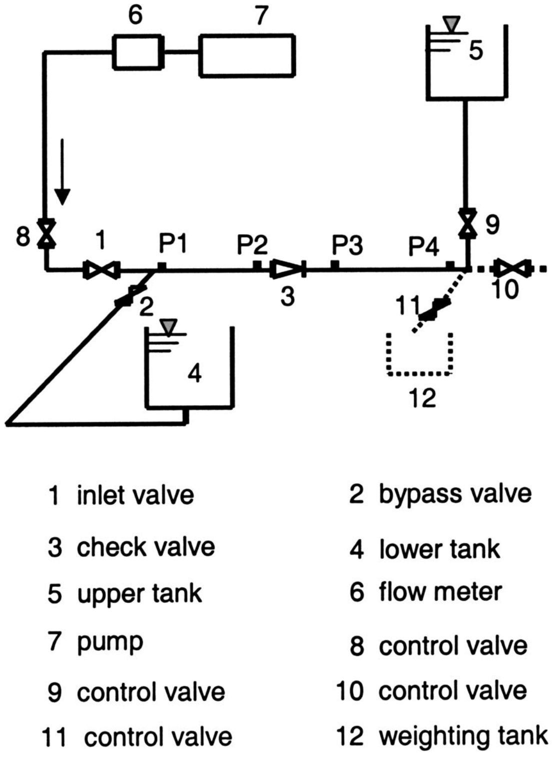

Fig. 2 The schematic of the test rig

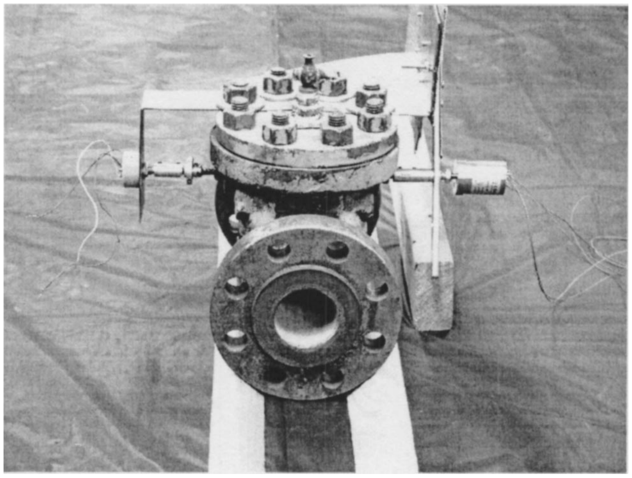

Fig. 3 Replacement shaft and measuring devices (left: potentiometer, right: accelerometer)

from the discharge flange of the inlet valve 1, respectively. The acoustic wave speed of the water pipe system is 1353 m/s, determined by measuring the travel time of a disturbance between P1 and p4 and, separately, by extracting the dominate frequency of pressure traces at P3. Details are given in Li [24]. The shaft of the check valve is 13.06 m downstream from the outlet flange of the inlet valve.

The check valve is a 50 mm Wheatley swing check valve (model No. 910-0251). Its disk seat is slanted 14.8° from the vertical. The disk angle varies from 0° (closed) to 70° (full open). A synthetic rubber ''O'' ring is inlaid in the disk to provide water tightness when the disk is closed. Prior to testing, the valve was disassembled so that the weight, the moment arm, and the moment of inertia of the disk assembly could be determined from direct measurements. The results are:

valve disk diameter	74.93 mm
submerged weight in water:	3.65 N
moment arm:	0.055 m
moment of inertia of rotational parts:	0.0018 N-m-s^2
moment of inertia of added mass:	0.0007 N-m-s^2

Modifications were made to the disk-axis assembly to enable measurement of angular position, velocity and acceleration of the disk. The disk is keyed to a replacement shaft that protrudes outside the valve body (see Fig. 3). The space between the shaft and the valve body is filled with silicon grease for lubrication and water tightness.

In order to investigate the effect of angular velocity of the disk on the torque coefficients, a frame attachable to the valve shaft is used to exert external torque of different magnitude and direction.

A single-turn wire-wound potentiometer (Spectral model 132-0-0-1 02) was connected to one end of the protruding shaft to measure the disk angle. The potentiometer has a tolerance of 3% and a nonlinearity of less than 1%. Its moment of inertia is less than 1% of that of the disk. The frictional torque associated with the wiper movement against the wound wire is significant and is addressed later.

The measured disk angle versus time traces were numerically smoothened by the ''supersmooth'' function of MathCad before differentiation to obtain angular velocity and acceleration. Supersmooth smoothens data by a symmetric *k*-nearest neighbor linear least-square fitting procedure in which *k* is adaptively chosen. The angular velocity so obtained is compared with angular velocity measurement using a pulse encoder (Encoder Products Co., 260-N-T-01-S-2500-R-HV-1-S-1-N). The angular acceleration obtained by numerical differentiations is compared with the angular acceleration measurements using a force-balance angular accelerometer (Columbia Research Laboratory, Inc. SR-220 RNP). The details of the treatment of the disk angle data and its numerical differentiations can be found in Li [24].

The pressures were measured by Validyne variable reluctance differential pressure transducer DP15-52's, each in conjunction with a Validyne carrier demodulator CD15. A deadweight tester (Ametek M&G model 10-1525) was used to calibrate all the transducer and demodulator sets prior to each test. Each pressure transducer is connected to the pipe through a short connector tube. The tube has a significant effect on the measured pressures when the rise time of the pressure is short. This effect has been quantified and corrected by Liou and Li [25].

Steady-state flow rates are measured by an ultrasonic flow meter (Controlotron Corp., System 990P). A weighing tank was used to calibrate the flow meter and to measure flow rate for some of the tests with very low flow rates.

A PC and a 12-bit resolution MetraByte DAS-16 analog & digital I/O board are used for data acquisition.

Frictional Torques of the Valve Shaft and the Potentiometer

The frictional torque was generated by the friction between the valve shaft and its housing and by the potentiometer. The potentiometer torque is approximately of the same a magnitude as the shaft torque. In this study they are considered together as frictional torque. It is necessary to consider the static frictional torque when disk rotation is pending and the kinetic frictional torque when the disk is rotating.

The static frictional torque is determined by equilibrium tests of the check valve in air (i.e., valve removed from the test rig). An external torque is applied against the dry valve assembly weight torque (designated as T_C and T_W, respectively) to keep the valve stationary at a given disk angle. The external torque is then gradually increased until the disk started to swing upwards. The external torque at the moment of impending disk upswing is recorded. From the known disk angle, the weight torque of the disk assembly is calculated. The frictional torque is then obtained by subtracting the assembly weight torque from the external torque. This process is repeated at different disk angles to obtain the ''impending'' upswing static frictional torque (T_{FS}^u) versus disk angle curve.

Similar tests were carried out in which the external torque was gradually reduced to produce a downswing of the valve disk. The ''impending'' downswing static frictional torque (T_{FS}^d) is obtained by subtracting the external torque from the assembly weight torque. Figure 4 shows the data from such tests and the resulting frictional torques as a function of disk angle. We note that the applied external torque and the weight torque are of similar magnitude. The difference between the two has a greater uncertainty than the individual weight torques. This uncertainty is estimated at about 30%. Consequently, the difference between the upswing and downswing frictional torques is not significant, nor is the variation of the frictional torque with respect to the disk angle. The average magnitude for the static frictional torque is estimated to be 0.018 N-m.

The kinetic frictional torque is determined by tests. We assume that the magnitude of the kinetic frictional torque of the shaft is the sum of its static torque plus an increment that is proportional to the angular speed of the disk. The valve disk is held at the full open position (70 deg) and then let go. The disk's angular position and acceleration are recorded as it falls clockwise. The moment of momentum equation for the disk is

$$-C\dot{\theta}+T_{FS}-WL\sin(\theta+\theta_s)=I\ddot{\theta} \tag{6}$$

in which T_{FS} is the static frictional torque (0.018 N-m), W is the

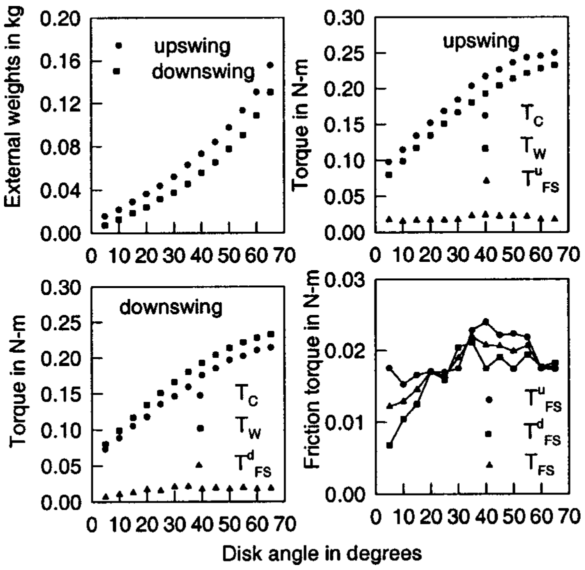

Fig. 4 Estimated static frictional torque

dry weight of the disk assembly and C is a damping coefficient. In this group of tests, both the damping torque (the first term on the left side of Eq. (6)) and the static torque oppose the weight torque of the disk assembly. The negative sign preceding the damping torque signifies that this torque is counterclockwise (positive) since the angular velocity of the disk $\dot{\theta}$ is clockwise (negative). From the known initial disk angle and the initial disk angular velocity, trial values for C are used to solve Eq. (6) until the calculated θ best matches the measured trace. The C value so determined is 0.003 N-m-s. Thus, for our instrumented check valve, the kinetic frictional torque in N-m is

$$T_{FK}=T_{FS}-C\dot{\theta}=\pm 0.018-0.003\dot{\theta}. \tag{7}$$

In the above, the sign preceding 0.018 is positive when $\dot{\theta}$ is negative and negative when $\dot{\theta}$ is positive.

Stationary Hydraulic Torque Coefficient

The stationary hydraulic torque coefficient C_{HS} is regarded as a function of disk angle and the direction of through velocity, and is established by tests for both forward and backward through flows. In the forward flow tests, the valve disk is maintained at a certain angle by the through flow. The through flow is then very gradually increased (so as to minimize disk acceleration) to produce a disk upswing. The flow rate and the disk angle at the instant of impending rotation are recorded. At the instant

$$C_{HS}\rho\frac{V_u^2}{2}A_vL-|T_W|-|T_{FS}|-|T_E|=0 \tag{8}$$

in which V_u=the through flow velocity at the moment of impending upswing of the valve disk. The purpose of applying T_E is to investigate the effect of through flow velocity on C_{HS}. This test is repeated for a range of disk angles. Next, the through flow is very gradually decreased to produce a disk downswing. The flow rate and the disk angle at the instant of impending rotation are recorded. At this instant,

$$C_{HS}\rho\frac{V_d^2}{2}A_vL-|T_W|+|T_{FS}|-|T_E|=0 \tag{9}$$

in which V_d=the through flow velocity at the moment of impending downswing of the disk. Based on the frictional torque measurements, we assume that, at a given disk angle, the static frictional torques at the moment of impending disk upswing and downswing are equal in magnitude, therefore, we eliminate the frictional torques in Eqs. (8) and (9) to obtain

$$C_{HS}=\frac{2(|T_W|+|T_E|)}{\rho A_vLV^2} \tag{10}$$

where

$$V^2=\frac{1}{2}(V_u^2+V_d^2).$$

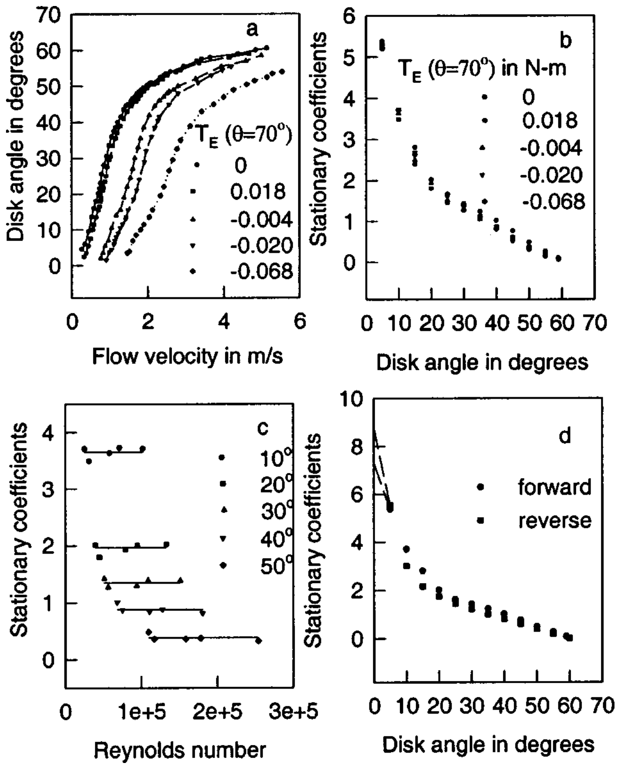

Fig. 5 Stationary hydraulic torque coefficients; (*a*) disk angle versus through flow velocity, (*b*) stationary coefficient versus disk angle, (*c*) stationary coefficient versus Reynolds number, (*d*) stationary coefficient for forward and reverse flows

In determining C_{HS} for backward through flow, the weight torque and the stationary hydraulic torque are both in the direction of closing the valve (i.e., clockwise). A counterclockwise external torque is applied to balance these two torques and maintain a certain disk angle at a set flow. The external torque is then gradually increased (decreased) to generate an upswing (downswing) of the disk. The disk angle, the flow velocity, and the external torque at the instant of impending disk rotation are recorded to compute C_{HS}

$$C_{HS}=\frac{|T_E^u|+|T_E^d|-2|T_W|}{\rho A_vLV^2} \tag{11}$$

in which the superscripts ^{u} and ^{d} denote disk upswing and downswing.

Figure 5(*a*) shows a set of five curves of disk angle versus velocity V for forward through flow. Each curve is associated with a clockwise external torque as indicated. The C_{HS}, computed from Eq. (10), is plotted as a function of disk angle in Fig. 5(*b*). Figure 5(*c*) demonstrates the insensitivity of C_{HS} with respect to the through flow velocity at a fixed disk angle. Figure 5(d) shows C_{HS} as a function of disk angle for both forward and backward through flows. The uncertainty bound in terms of relative error for C_{HS} is estimated to be 15% for θ between 5 and 15 deg and 5% for θ greater than 15%.

Rotational Hydraulic Torque Coefficient

The rotational hydraulic torque coefficient C_{HR} is regarded as a function of the disk angle, the disk angular velocity, and the direction and the magnitude of the through flow. C_{HR} is discussed in terms of the disk angular velocity versus the through flow plane. This plane is divided into four quadrants by the through flow axis (horizontal) and the disk angular velocity axis (vertical). In quadrant 1, the valve is opening with forward flow. Since the valve disk is essentially rotating with the flow, the rotational hydraulic torque coefficient C_{HR} in this quadrant is assumed to be the same as the C_{HR} obtained when there is no through flow. In quadrant 2, the valve is opening in reversed through flow. Since this condition is not likely to occur, the rotational torque coefficient in this quadrant was not investigated. In quadrant 3, the valve is closing in reversed flow. This quadrant belongs to the late stage of a check valve slam. In quadrant 4, the valve is closing in forward flow. This quadrant belongs to the early stage of a check valve closure during a system shutdown. Quantification of C_{HR} in quadrants 3 and 4 is described below.

From Eqs. (1), (3), (5), and (7), the rotational hydraulic torque coefficient in quadrants 3 and 4 can be expressed as

$$C_{HR}=\frac{|T_W|\pm|T_E|-(C\dot{\theta}+|T_{FS}|)\pm|T_{HS}|+(I+I_E+I_F)\ddot{\theta}}{0.5\rho A_v L(L\dot{\theta})^2}. \tag{12}$$

In the above equation, the positive sign before T_{HS} should be used in quadrant 3 and the negative sign in quadrant 4. The external torque T_E is used to generate disk falls with different disk velocity so that the effect of disk velocity on C_{HR} can be evaluated.

For quadrant 3 tests, the vertical pipe leading to the upper tank is replaced by valve 10 and the lower tank is valved off. The check valve is turned around so it opens clockwise. The flow is

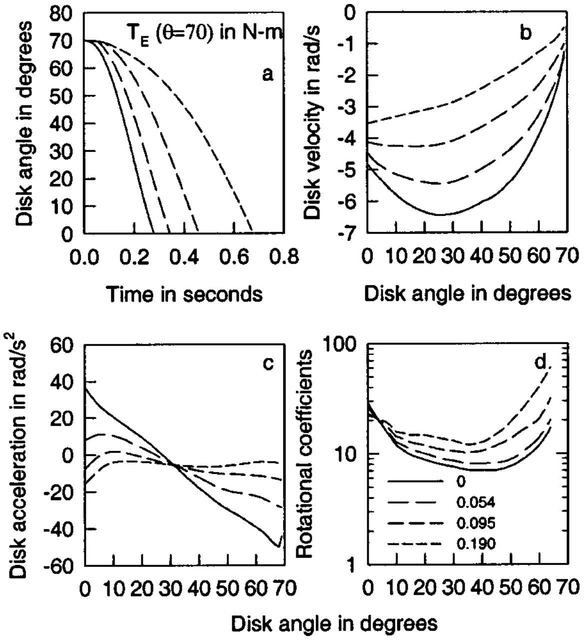

Fig. 6 Results in quadrant 3 ($V=-0.41$ m/s); (*a*) disk angle versus time, (*b*) disk velocity versus disk angle, (*c*) disk acceleration versus disk angle, (*d*) rotational coefficient versus disk angle

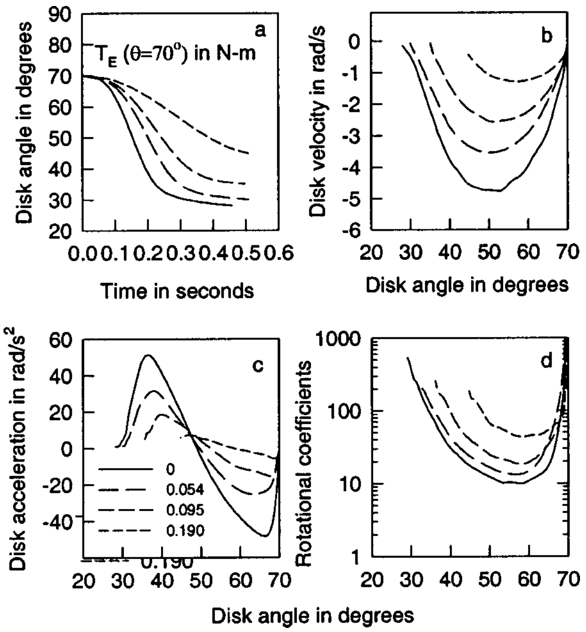

Fig. 7 Results in quadrant 4 ($V=0.76$ m/s); (*a*) disk angle versus time, (*b*) disk velocity versus disk angle, (*c*) disk acceleration versus disk angle, (*d*) rotational coefficient versus disk angle

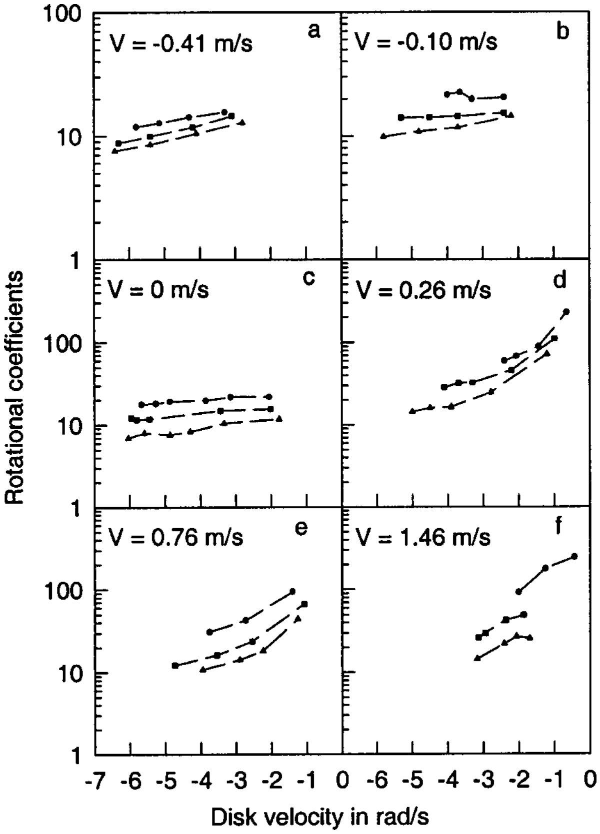

Fig. 8 Rotational coefficients in quadrants 3 and 4. The disk angles are 10, 20, and 30 deg for the top, middle, and bottom traces in panels (*a*) and (*b*) 20, 30, and 40 deg for panels (*c*) and (*d*) 40, 50, and 60 deg for panels (*e*) and (*f*).

directed from the inlet valve 1 to valve 10. The flow rate is measured by the ultrasonic flow meter. When the flow rate is small, valve 10 is closed and the flow is diverted through valve 11 to a weighting tank for accurate flow measurement. The through flow velocity was essentially constant during the disk-falling period since the head drop across the check valve is small relative to the system head loss. For each test, the desired reverse flow rate is controlled by valve 10 or 11. The check valve disk is held wide open against the reversed flow and then let go. We record disk angle and disk acceleration over time. We then numerically differentiate the smoothened disk angle versus time trace to obtain the disk velocity trace. Knowing the disk angle, velocity, and acceleration, all the terms on the right side of Eq. (12) can be evaluated and C_{HR} computed. The results for a through flow velocity of -0.41 m/s are shown in Fig. 6.

For quadrant 4 tests, the flow arrangement is the same as for quadrant 3 tests except that the check valve is returned to its normal direction (i.e., opens counterclockwise). The test procedure, measurements, and data reduction are the same as those in quadrant 3. The results for a through flow velocity of 0.76 m/s are shown in Fig. 7.

We note that in the fall tests, the disk angular velocity is not directly controllable. Nonetheless, the angular velocity is "independently" varied by using different T_E's at each through flow. For example, Fig. 7 shows that at a through flow velocity of 0.76 m/s, the C_{HR} is 23.9 for a disk angle of 50 deg and a disk velocity of 2.54 rad/s. Linear interpolation is used to estimate a desired disk velocity when the latter does not fall on tested curve. The information contained in Figs. 6 and 7 is condensed in Fig. 8, which shows C_{HR} as a function of disk angle and disk velocity for six out of ten through velocities tested with a range from -0.82 m/s to 1.81 m/s. Upon specifying a through flow, a disk angle, and a disk velocity, the corresponding rotational hydraulic torque coefficient can be obtained by interpolation. The uncertainty bound for the rotational hydraulic torque coefficient is estimated at 12%.

Inherent Hydraulic Characteristic of the Check Valve

Valve manufacturers use the flow coefficient C_v to characterize a valve. The flow coefficient at a specified valve opening is defined as the volumetric rate of flow of 60°F water in gpm when the pressure drop across the valve is one psig. The dimensionless flow coefficient of the 50 mm Wheatley check valve as a function of the disk angle for both forward and reverse flows were determined in the laboratory (C_{v0} is the flow coefficient at fully valve opening). The results are shown in Fig. 9. The uncertainty bounds for the C_v and the disk angle are 2% and 0.5%, respectively.

Modeling the Interaction Between the Liquid and the Check Valve

The interaction between the check valve and the liquid is modeled numerically by the method of characteristics using the discrete free-gas cavity model of Wylie [26] for possible column separation. There are eight unknowns: the head, the flow, and the free gas volume immediately upstream of the valve, the head, the flow, and the free gas volume immediately downstream of the valve, the disk angle, and the flow through the valve. Eight equations are available. They are: the continuity equation immediately upstream of the check valve, the continuity equation immediately downstream of the check valve, the equation of state for the lumped gas-vapor mass immediately upstream of the check valve, the equation of state for the lumped gas-vapor mass immediately downstream of the check valve, the C+ compatibility equation for the pipe reach upstream of the check valve, the C− compatibility equation for the pipe reach downstream of the check valve, the orifice equation that relates the head drop across the check valve to the disk angle, and the moment of momentum equation of the check valve disk.

The modeling of dynamic check valves is incorporated into a computer code (Kellum [27]) for simulating detailed transients inside typical booster pump stations for oil pipelines. This code is used to simulate check valve slam transients described next.

Check Valve Slam Tests and Numerical Modeling

In check valve slam tests, a desired initial steady flow is established through the test rig and discharges out of the upper tank by overflowing. The disk angle is in equilibrium with the net torque applied. The lower tank is valved off. Transients are initiated by suddenly shutting off the inlet valve. The disk angle, the pressures at P1, P2, and the P3 are measured over time at a sample rate of 1250 samples per second for 1.6 seconds.

The nature of the transients is as follows. Upon the closure of the inlet valve, the local pressure drops to vapor pressure and a vapor cavity forms at the discharge side of the closed valve. The water column continues to move toward the upper tank at a reduced velocity and the check valve starts to close. Eventually, the head at the upper tank stops the water column and turns it around. The check valve, now being acted upon by the hydraulic torque of the reversed flow, slams shut. At the instant of valve closure, a water hammer pressure rise occurs at the closed check valve. At about 0.018 seconds later, the wave reflected from the upper tank draws away the water at the check valve. Consequently, the local pressure drops to vapor pressure and the check valve starts to open. Some time later, the head at the upper tank drives the water column back and slam close the check valve again. Depending on the timing, the peak pressure of the second slam can be greater than the first. The closure of the check valve prevents the returning water column from reaching the inlet valve. The pressure at the inlet valve stays at vapor pressure during the sampling period.

Four models for the interaction between the liquid and the check valves are compared with the measurements.

1 The C_v model. The hydraulic torque is computed from the pressure differential across the check valve.

$$T_{HC_v}=A_vL\gamma\Delta H=A_vL\gamma\frac{D^4}{0.001123C_v^2}\frac{Q_v|Q_v|}{2gA^2} \qquad (13)$$

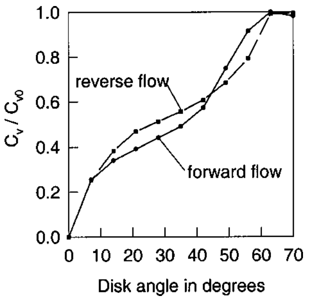

Fig. 9 Inherent hydraulic characteristic of the check valve

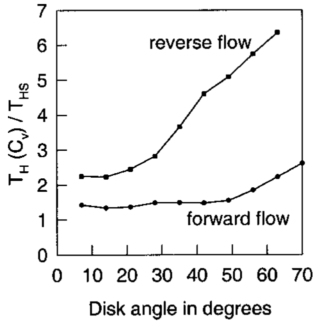

Fig. 10 Ratio hydraulic torque in the C_v model over stationary hydraulic torque

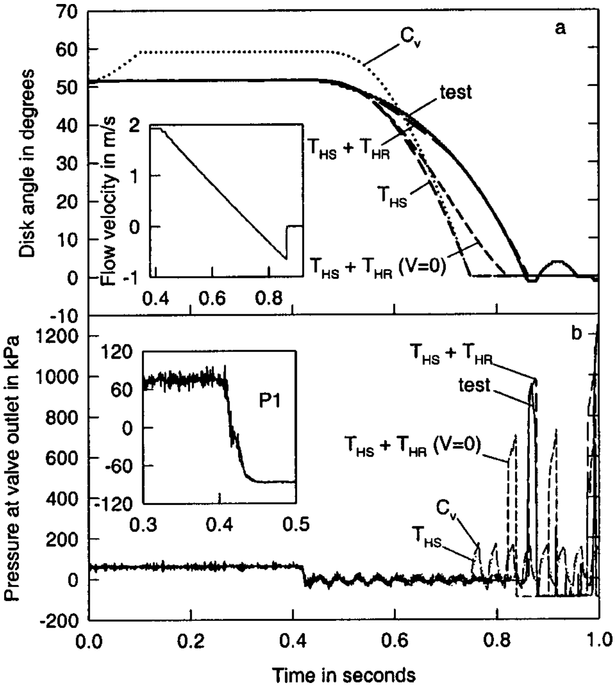

Fig. 11 Comparisons between simulation results and test data (steady state through flow velocity=1.93 m/s)

where γ is the specific weight of fluid and the diameter D is in inches. This model was used by Uram [1], Safwat et al. [2], and Wylie and Streeter [28]. Some commercial software packages for pipeline transients such as LIQT® and RELAP5® use this approach also. Many packages simply do not have the capability to model the dynamics of check valves. To put this torque in perspective, we form the following ratio:

$$\frac{T_{HC_y}}{T_{HS}} = \frac{D^4}{0.001123 C_v^2 C_{HS}} \tag{14}$$

in which D is the pipe diameter in inches. The ratio is a function of the angular position and is plotted in Fig. 10. It is seen that the hydraulic torque from this C_v model over estimates the stationary hydraulic torque.

2 The T_{HS} model. The hydraulic torque comes from the stationary hydraulic torque only. The rotational hydraulic torque is ignored. This model is used to interpret the results of the C_v model and to underline the importance of the rotational hydraulic torque.

3 The $T_{HS}+T_{HR}(V=0)$ model. The hydraulic torque is the sum of the stationary hydraulic torque and the rotational torque at zero through flow. The relative motion between the through flow and the disk rotation is ignored. This is the model proposed by Pool et al. [10] and Ellis and Mualla [11,12].

4 The $T_{HS}+T_{HR}$ model. This is our approach to quantify the hydraulic torque.

In simulating the transients, the inlet boundary condition is the measured pressure at P1. This pressure is shown in the inset in Fig. 11(*b*). The purpose of using this inlet boundary condition is to avoid modeling uncertainties upstream of P1. The outlet boundary condition is the constant head 5.58 m at the upper tank.

The results of these four models are compared with the measured disk angle and the pressure at the P3 of a representative test. The initial through flow velocity is 1.93 m/s. The initial disk angle is at 51.59 deg. The steady-state average pressure at P3 is about 61.02 kPa. The inlet valve is shut off suddenly at about 0.42 seconds, creating the check valve slam transients described above. A void fraction of 4×10^{-6} at the initial steady state is used. This void fraction is determined by trial and error so that the simulated pressure at P3 during low pressure period (about 0.42 to 0.83 s in Fig. 11(*b*) best matches the measured trace. Forty computational reaches are used in the numerical simulations. Numerical uncertainties are negligible.

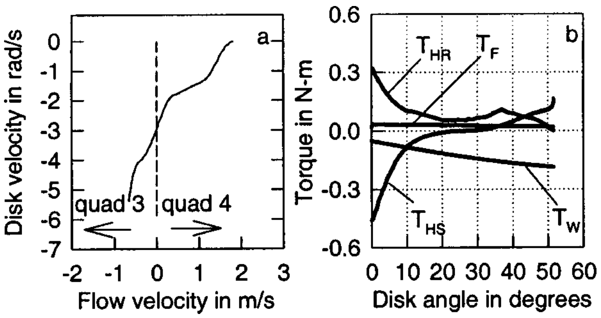

Fig. 12 Simulated disk velocity and torque components (steady-state through flow velocity=1.93 m/s)

The calculated disk angles as a function of time from the four models are compared with the measured trace in Fig. 11(*a*). Since the C_v model overestimates the hydraulic torque, it could not maintain the initial disk angle at the steady-state prior to 0.42 seconds. The simulated disk angle drifts up to reach an equilibrium that is higher than the measured value. The other three models are able to hold the initial disk angle prior to closing the inlet valve. During closure, the C_v model and the T_{HS} model behaved similarly and the simulated valve closure is premature. The $T_{HS}+T_{HR}(V=0)$ model shows that the inclusion of the rotational hydraulic torque, even though the effect of the relative motion between the through flow and the disk on C_{HR} was ignored, improves the valve closure time. However, the simulated disk angle trace failed to track the measured one. The $T_{HS}+T_{HR}$ model, on the other hand, tracks the measured disk angle trace closely during the entire closure time period. This dramatic improvement indicates that the relative motion between the through flow and the disk has to be properly accounted for.

The recorded negative disk angle, visible in Fig. 11(*a*) is due to the fact that as the disk slams close, it compresses the rubber "O" ring inlaid (described in Experimental Setup) and moves past the zero reference point. The rebounds of the disk shown there are not addressed in this paper and are not modeled.

The calculated and measured pressures at P3 are shown in Fig. 11(*b*). Since the simulated valve closure is premature for the C_v model and the T_{HS} model, the reverse flow stopped by the valve closure was too small. As a result, the simulated pressure rise in these two models occurred too early and the magnitude too low. The $T_{HS}+T_{HR}(V=0)$ model yielded better result but the pressure rise was still too early and too low. The $T_{HS}+T_{HR}$ model matched the measured water hammer pressure change both in timing and in magnitude.

The inset in Fig. 11(*a*) shows the simulated flow through the check valve. The flow reversal is clearly shown. Although the transient through flow cannot be measured to check the simulated values, the magnitude of the reverse flow just prior to the valve slam matches well with the measured pressure rise at the moment of valve slam through the Joukowsky relationship. Thus we are confident that the simulated flow trace is valid.

Some additional simulation results from the $T_{HS}+T_{HR}$ model are worth noting. Figure 12(*a*) shows the check valves transitioning from quadrant 3 to quadrant 4 on the disk velocity versus through flow plane. The disk velocity is already appreciable when entering quadrant 3. Figure 12(*b*) shows how each torque varies with the disk angle. The stationary hydraulic torque changes sign when quadrant 3 is entered. This torque causes the valve to slam. The rotational hydraulic torque is positive at all times. This torque opposes the closing of the check valve. Its increased magnitude at small angles prevents the premature closure seen in the other three models.

Conclusions

1 The hydraulic torque can be separated into two components: the stationary hydraulic torque and the rotational hydraulic torque. These torques are expressed in terms of a stationary and rotational torque coefficients.

2 Both torque coefficients have been quantified for a two-inch swing check valve by laboratory tests. The stationary torque coefficient depends on the valve disk angle and the direction (but not the magnitude) of through flow. The rotational torque coefficient varies with the disk angle, the disk angular velocity, and the direction and the magnitude of the through flow.

3 Using the stationary and rotational torque coefficients, a moment-of-momentum equation has been incorporated into a numerical model for transients based on the discrete free-gas cavity model of Wylie [26].

4 Check valve slam tests were conducted and produced laboratory data for time histories of valve disk angle and pressures at multiple locations.

5 The close match between the numerical simulation results and the laboratory data demonstrate the validity of the proposed approach to swing check valve characterization.

Acknowledgments

The Colonial Pipeline Company of Atlanta, Georgia, funded this work. The authors are thankful to Prof. E. B. Wylie for his input throughout this study, and to Mr. H. M. Gibson who constructed and maintained the test loop.

Nomenclature

A = pipe cross-sectional area
A_v = check valve disk area
C = damping coefficient in establishing kinetic friction torque
C_{HR} = rotational coefficient
C_{HS} = stationary coefficient
C_v = flow coefficient as a function of angular position
D = valve diameter
G = gravitational acceleration
I = moment of inertia of the disk
I_f = moment of inertia of the added mass
I_E = moment of inertia of the counterweight device
L = arm length
T_C = external torque in determining static shaft friction
T_E = external torque
T_F = friction torque
T_{FK} = kinetic friction torque
T_{FS} = static friction torque
T_H = hydraulic torque
T_{HR} = rotational hydraulic torque
T_{HS} = stationary hydraulic torque
T_W = torque due to submerged weight of the disk assembly
V = through flow velocity
W = dry weight of the disk assembly
W_s = submerged weight of the disk
θ = disk angle
θ_s = inclination angle of the valve disk when closed (see Fig. 1)
ρ = fluid mass density
γ = fluid specific weight

References

[1] Uram, E. M., 1977, "A Method for Estimating Steam Hammer Effects on Swing-Check Valves During Closure," ASME J. Eng. Gas Turbines Power, Paper No. 76-JPGC-PWR-6.
[2] Safwat, H. H., Arastu, A. H., and Noman, A., 1985, "Study of Check Valve Slamming in a BWR Feedwater System Following a Postulated Pipe Break," *Forum on Unsteady Flow*, ASME, New York, pp. 13–15.
[3] Arastu, A. H., and Husaini, S. M., 1995, "A Comprehensive Check Valve Dynamic Model for Water Hammer Applications," *Proceedings of the ASME Fluids Engineering Division*, ASME, New York, FED-Vol. 234, pp. 45–50.
[4] Kane, R. S., and Cho, S. M., 1976, "Hydraulic Performance of Tilting-Disk Check Valves," J. Hydraul. Div., Am. Soc. Civ. Eng., **HY1**, pp. 57–72.
[5] Koch, B., 1981, "Computer Simulation of Water Hammer Applied to Check Valves and Valve Stroking in Pipe Networks," paper presented at the *Conference on Computer Simulation*, Harrogate, May 13–15.
[6] Rahmeyer, W. J., 1993, "Sizing Swing Check Valves for Stability and Minimum Velocity Limits," ASME J. Pressure Vessel Technol., **115**, pp. 406–410.
[7] Botros, K. K., Jones, B. J., and Roorda, O., 1997, "Effects of Compressibility on Flow Characteristics and Dynamics of Swing Check Valves—Part 1," ASME J. Pressure Vessel Technol., **119**, pp. 192–198.
[8] Botros, K. K., and Roorda, O., 1997, "Effects of Compressibility on Flow Characteristics and Dynamics of Swing Check Valves—Part II," ASME J. Pressure Vessel Technol., **119**, pp. 199–206.
[9] Esleek, S. H., and Rosser, R. M., 1959, "Check Valve Water Hammer Characteristics," paper presented at the *American Nuclear Society Meeting*, Nov.
[10] Pool, E. B., Porwit, A. J., and Carlton, J. L., 1962, "Prediction of Surge Pressure From Check Valve for Nuclear Loops," Paper No. 62-WA-219.
[11] Ellis, J., and Mualla, W., 1983, "Wave Induced Transients by a Pumping Station Storm Overflow," *Proceedings of the 4th International Conference on Pressure Surges*, BHRA, Bath, England, pp. 243–262.
[12] Ellis, J., and Mualla, W., 1986, "Numerical Modeling of Reflux Valve Closure," ASME J. Pressure Vessel Technol., **108**(1), pp. 92–97.
[13] Kruisbrink, A. C. H., 1996, The Dynamic Behavior of Check Valves in Pipeline Systems, Ph.D. dissertation, City University of London.
[14] Provoost, G. A., 1980, "The Dynamic Behavior of Non-Return Valves," *Proceedings of the 3rd International Conference on Pressure Surges*, BHRA, Canterbury, England, pp. 415–428.
[15] Provoost, G. A., 1982, "The Dynamic Characteristics of Non-Return Valves," paper presented at the *11th Symposium of the Section of Hydraulic Machinery, Equipment and Cavitation: "Operating Problems of Pump Stations and Power Plants*," IAHR, Amsterdam, the Netherlands, Sept. 13–17.
[16] Koetzier, H., Kruisbrink, A. C. H., and Lavooij, C. S. W., 1986, "Dynamic Behavior of Large Non-Return Valves," *Proceedings of the 5th International Conference on Pressure Surges*, BHRA, Hannover, Germany, pp. 237–244.
[17] Thorley, A. R. D., 1983, "Dynamic Response of Check Valves," *Proceedings of the 4th International Conference on Pressure Surges*, BHRA, Bath, England, pp. 231–242.
[18] Thorley, A. R. D., 1989, "Check Valve Behavior Under Transient Flow Conditions, a State-of-the-Art Review," ASME J. Fluids Eng., **111**, pp. 178–183.
[19] Kruisbrink, A. C. H., and Thorley, A. R. D., 1994, "Dynamic Characteristics for Damped Check Valves," *Proceedings of the 2nd International Conference on Water Pipeline Systems*, BHR Group Limited, Edinburgh, pp. 459–476.
[20] Au-Yang, M. K., 1993, "Acoustic and Ultrasonic Signals as Diagnostic Tools for Check Valves," ASME J. Pressure Vessel Technol., **115**, pp. 135–141.
[21] Thorley, A. R. D., and Oei, J. H., 1981, "Dynamic Behavior of a Swing Check Valve," *Proceedings of the 5th International Symposium on Water Column Separation*, IAHR, Obernach, Germany, Sept. 26–28.
[22] Worster, R. C., 1959, "The Closing of Reflux Valves," Paper presented at the *6th Conference on Hydromechanics*, BHRA, Troon, Scotland, May 5–10.
[23] Worster, R. C., 1960, "The Use of Linearized Equations in Calculating the Motion of Reflux Valves," Report RR 676, British Hydromechanics Research Association, Cranfield, England.
[24] Li, G., 2002, Characterization and Modeling of Swing Check Valves During Transients, Ph.D. dissertation, University of Idaho, Moscow, ID.
[25] Liou, C. P., and Li, G., 2003, "Transient Pressure Measurements by Recess-Mounted Transducers," *Proceedings of FEDSM'03, 4th ASME/JSME Joint Fluids Engineering Conference*, FEDSM2003-45252, Honolulu, HI, July.
[26] Wylie, E. B., 1984, "Simulation of Vaporous and Gaseous Cavitation," ASME J. Fluids Eng., **106**, pp. 307–311.
[27] Kellum, B. G., 1995, Booster Pump Station Modeling With Neural Network Applications, MS thesis, University of Idaho, ID.
[28] Wylie, E. B., and Streeter, V. L., 1993, *Fluid Transients in Systems*, Prentice-Hall, Englewood Cliffs, NJ, pp. 134–135.

Ali Y. Alharbi
Assistant Instructor,
Department of Mechanical Power and Refrigeration,
PAAET College of Technological Studies,
P.O. Box 42325,
Shuwaikh 70654, Kuwait
e-mail: aalharbi@paaetms.paaet.edu.kw

Deborah V. Pence[1]
Assistant Professor
e-mail: pence@engr.orst.edu

Rebecca N. Cullion
Research Assistant
e-mail: cullion@engr.orst.edu

Department of Mechanical Engineering,
Oregon State University,
204 Rogers Hall,
Corvallis, OR 97331-6001

Fluid Flow Through Microscale Fractal-Like Branching Channel Networks

Flow through fractal-like branching networks is investigated using a three-dimensional computational fluid dynamics approach. Results are used to assess the validity of, and provide insight for improving, assumptions imposed in a previously developed one-dimensional model. Assumptions in the one-dimensional model include (1) reinitiating boundary layers following each bifurcation, (2) constant thermophysical fluid properties, and (3) negligible minor losses at the bifurcations. No changes to the redevelopment of hydrodynamic boundary layers following a bifurcation are recommended. It is concluded that temperature varying fluid properties should be incorporated in the one-dimensional model to improve its predictive capabilities, especially at higher imposed heat fluxes. Finally, a local pressure recovery at each bifurcation results from an increase in flow area. Ultimately, this results in a lower total pressure drop and should be incorporated in the one-dimensional model. [DOI: 10.1115/1.1625684]

1 Introduction

Societal demands have resulted in extremely compact yet powerful electronic devices, which require high watt-density cooling techniques. Heat sinks incorporating microscale channels are very effective in this endeavor by increasing both the convective heat transfer coefficient as well as the convective surface area per unit volume in the heat sink.

However, the improved heat transfer provided by a series of parallel microchannels is not without drawbacks. The small diameter of the channels produces large pressure drops and nonuniform temperature distributions along the wall of the channel often occur. If used to cool an electronic component, a non-uniform temperature distribution, if significant enough, could result in uneven thermal expansion of the electronic device, possibly damaging it or affecting the electrical properties.

Tuckerman and Pease [1] first introduced the idea of microchannel heat sinks for cooling integrated circuits. Since that time, numerous investigations of single, straight microchannels and microchannel arrays in a heat sink have been conducted. Much of the experimental data prior to 2000, as noted in the review article by Sobhan and Garimella [2], are conflicting. Conclusions made by several of the original authors suggest that fluid and thermal transport phenomena through microchannels with characteristic flow diameters between 50 μm and 1 mm are different than macroscale phenomena. However, Obot [3] also reviewed numerous papers dealing with friction and heat and mass transfer in microchannels. Through careful reexamination of several works, he concluded that there is no supporting evidence to suggest that transport phenomena of liquids through microchannels is different from macrochannels. He further recommends use of conventional macroscale correlations for predicting pressure drop and heat transfer through such networks.

Bau [4] demonstrated, using a mathematical model, that a microchannel with a variable cross-sectional area can be optimized to reduce temperature gradients along the channel length. Reduction in the maximum heated surface temperature can be achieved by tapering a channel in the direction of the flow. However, a decrease in axial channel diameter can be accompanied by an increase in velocity and, hence, an increase in pumping power.

To improve the temperature uniformity while decreasing the pressure drop, Pence [5] proposed a fractal-like bifurcating flow network in a two-dimensional heat sink. The fractal-like flow network was designed using fixed diameter and length scale ratios between consecutive branching levels, as were proposed by West et al. [6] for natural transport systems. Using an optimization approach to minimize pumping power while adhering to a minimal volume constraint, Bejan [7] identified, on average, the same branching level ratios reported by West et al. [6]. The relation between engineered flow networks and those of natural systems is the subject of a book by Bejan [8].

Pence [9] developed a one-dimensional model, using macroscopic correlations, for predicting both the pressure distribution in, and wall surface temperature along, a fractal-like branching channel network. Results were compared to an array of straight channels having the same channel length and same convective surface area as the branching network. A lower maximum wall temperature along the fractal flow network was consistently noted for identical pressure drop, flow rate, and total pumping power through both flow networks. Chen and Chang [10], assuming fully developed conditions and negligible minor losses, assessed the pressure drop and heat transfer capacity of fractal-like channel networks for several levels of branching and various branching diameter ratios.

Wechsatol et al. [11] recently investigated, in a disk-shaped geometry similar to that proposed by Pence [5,9], the optimal channel length distribution, assuming fully developed, laminar flow with negligible minor losses. Length-scale ratios that vary at each bifurcating level were deemed optimal in terms of minimizing flow resistance.

2 Method of Analysis

Pence [5] developed a preliminary, non-optimized branching channel network in a disk-shaped heat sink using the following branching ratios:

$$\frac{d_{k+1}}{d_k}=n^{-1/3} \tag{1}$$

---

[1] To whom correspondence should be addressed.

Contributed by the Fluids Engineering Division for publication in the JOURNAL OF FLUIDS ENGINEERING. Manuscript received by the Fluids Engineering Division Jan. 22, 2003; revised manuscript received June 6, 2003. Associate Editor: K. D. Squires.

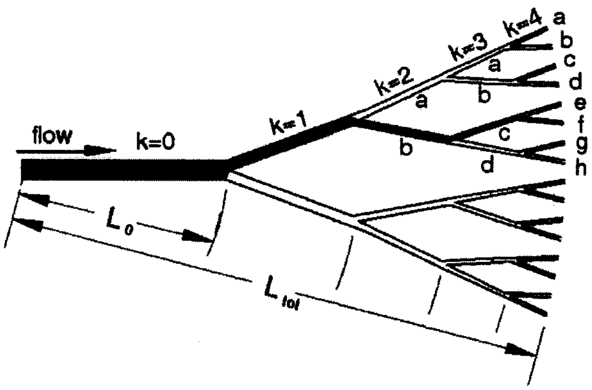

Fig. 1 Fractal-like branching channel network (shaded path includes branches $k=0$, $k=1$, $k=2b$, $k=3c$, $k=4f$)

$$\frac{L_{k+1}}{L_k}=n^{-1/2} \tag{2}$$

where d is the hydraulic diameter, L is the length of a channel segment, and n is the number of branches into which each channel splits. For the present analysis, $n=2$. Subscript k represents the lower-order branching level and subscript $k+1$ represents the higher-order branching level at a bifurcation. In reference to Fig. 1, the first branch emanating from the inlet flow plenum is the zeroth-order branch, i.e., $k=0$. The shaded region and the letters denoted in the figure are discussed later.

It is the objective of the present work to analyze the pressure distribution in microscale fractal-like branching channel networks using a three-dimensional computational fluid dynamics (CFD) analysis. The commercially available CFD package, STAR-CD, was employed. Results of these analyses are used to assess the validity of assumptions imposed in the one-dimensional model of Pence [9]. The initial flow network proposed by Pence [5] is employed for this purpose, as heat sinks with this flow network are available for experimental testing. Dimensions of the flow network are provided in Table 1. Note that the total channel length reported for the fractal-like flow network is the radial distance from the entrance of the $k=0$ branch to the exit of the $k=4$ branch level. The length of each branch is defined by radial distances in Fig. 1. Also note from Fig. 1 that the two new branches bifurcate asymmetrically from a lower level branch segment for $k \geqslant 1$.

2.1 One-Dimensional Predictive Model. In the one-dimensional model developed by Pence [9], the pressure distribution and wall temperature distribution along rectangular cross-section ducts in a fractal-like branching flow network are predicted using hydrodynamic theory and empirical correlations for heat transfer. The one-dimensional model is restricted to laminar flow with the assumptions that (1) both the thermal and hydrodynamic boundary layers redevelop following each channel bifurcation, (2) minor losses are negligible, and (3) thermophysical properties of the working fluid are held constant. It is the purpose of the present investigation to assess the validity of these three assumptions.

Table 1 Channel dimensions for fractal-like flow network ($\Sigma_{k=0}^{4} L_k = L_{\mathrm{tot}}=16.3$ mm)

k	H_k (mm)	w_k (mm)	d_k (mm)	L_k (mm)	α_k
0	0.250	0.539	0.342	5.80	0.389
1	0.250	0.296	0.271	4.10	0.750
2	0.250	0.189	0.215	2.90	0.830
3	0.250	0.130	0.171	2.05	0.562
4	0.250	0.093	0.136	1.45	0.400

The pressure drop correlation in White [12], which includes increased pressure due to developing flow conditions, and the Nusselt number data for simultaneously developing thermal and hydrodynamic boundary layers from Wibulswas [13], and referred to in Shah and London [14], are employed in the one-dimensional model. Water is used as the working fluid, and a constant heat flux is applied to the walls of the ducts composing the flow network.

2.2 Three-Dimensional Computational Model. Numerical simulations were performed using the finite-volume based, commercially available computational fluid dynamics (CFD) software STAR-CD (version 3.0B) from Computational Dynamics Limited. Three-dimensional CFD simulations were performed with water as the working fluid for a fractal-like flow network and a parallel flow network. Held identical between these flow networks are the total channel length, the terminal branch hydraulic diameter, the convective surface area, the heat flux applied to the convective surface area, and the total pumping power. Note that a representative path length for the fractal network is shown as a shaded region in Fig. 1. The steady, incompressible form of the three-dimensional continuity, momentum and energy equations governing the transport in this investigation are as follows:

Continuity:

$$\frac{\partial V_i}{\partial x_i}=0 \tag{3}$$

Momentum:

$$\rho\left(\frac{\partial(V_iV_j)}{\partial x_i}\right)=\frac{\partial}{\partial x_i}\left(\mu\frac{\partial V_j}{\partial x_i}\right)-\frac{\partial p}{\partial x_i} \tag{4}$$

Energy Equation:

$$\rho\left(\frac{\partial(V_ic_pT)}{\partial x_i}\right)=\frac{\partial}{\partial x_i}\left(\lambda\frac{\partial T}{\partial x_i}\right) \tag{5}$$

Consistent boundary conditions between the two flow networks are the inlet and exit flow boundary conditions and no slip, impermeable conditions at all walls. At the inlet, the bulk fluid temperature is fixed, as is the velocity profile, which is assumed uniform. The flow discharges to a water-filled reservoir assumed to be at atmospheric pressure at the point of discharge. A uniform heat flux is applied at the wall of the flow network.

The steady, incompressible, three-dimensional continuity, energy and momentum equations are solved using a central differencing scheme for the diffusion terms and the STAR-CD MARS scheme for the advection terms. MARS stands for monotone advection and reconstruction scheme. It is a two-step scheme of second-order accuracy which, of the available discretization schemes, is least sensitive to errors resulting from mesh structure and skewness. Pressure-velocity coupling was accomplished using the SIMPLE method. Under-relaxation parameters of 0.2, 0.7, and 0.95 were employed for pressure, velocity, and temperature, respectively, in this study.

3 Results and Discussion

Three-dimensional computational results are sought that provide a means for assessing the assumptions imposed in the one-dimensional model by Pence [9] for predicting pressure distributions through fractal-like flow networks. Again, these assumptions include (1) reinitiation of hydrodynamic and thermal boundary layers following each channel bifurcation, (2) negligible minor losses, and (3) constant thermophysical properties of the working fluid.

Of particular interest from the three-dimensional investigation is the axial pressure distribution. Fluid properties of the water are held constant initially, and then allowed to vary with temperature.

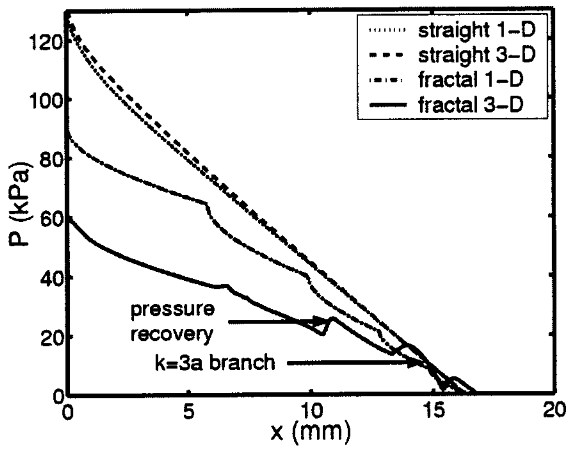

Fig. 2 Constant property pressure distribution through fractal-like and straight channel networks

The three-dimensional model results assuming constant properties are compared to the one-dimensional model results to assess the validity of assumptions 1 and 2. To assess the validity of assumption 3, results from the three-dimensional model with fluid properties allowed to vary with temperature are compared to three-dimensional results assuming constant thermophysical properties.

The three-dimensional CFD simulated pressure distribution along a fractal-like network is also compared to that through a single straight channel. The straight channel exists within a series of parallel channels having an identical hydraulic diameter as the terminal channel in the fractal-like flow network. Also identical between the fractal-like and straight channel networks are channel length, convective surface area, heat flux, and pumping power. Three-dimensional simulated pressure drop through a fractal-like network with an inlet flow plenum is compared with that obtained experimentally. In previous investigations, Pence [5,9] provided one-dimensional comparisons of fractal-like heat sinks to parallel channel heat sinks with different heat sink surface areas, with differing total channel lengths, and under various flow rate conditions.

3.1 Constant Property Analysis. As was done in Pence [9], results through a fractal-like flow network are compared to a network of parallel, straight channels with the same hydraulic diameter as the terminal branch of the fractal channel network, 136 μm, but with a square cross-section. The radial distance from the edge of the inlet plenum to the exit plenum is 16.3 mm and assumed to be the total length, regardless of path taken, through a fractal network. The total channel length and the convective wall surface area for the straight channel network are the same as for the fractal-like network. Two fractal-like and thirteen parallel flow networks are investigated, yielding total convective surface areas, defined by the walls of the flow networks, of 115 mm^2 and 114 mm^2, respectively.

To achieve identical pumping power between the straight and fractal-like flow networks, the total fluid flow through the thirteen straight channels is 1.2 ml/s and 1.8 ml/s through the two fractal-like flow networks. These flow rates ensure laminar flow through each channel in each flow network, with the largest Reynolds number, on the order of 2000, occurring in the largest diameter branch of the fractal network. A constant heat flux of 45 W/cm^2 is applied to the periphery of each channel in both networks. Properties of the coolant fluid are held constant in this part of the analysis, and are assessed at the average temperature of the inlet and exit bulk fluid temperatures.

Centerline pressure distributions for both flow networks are shown in Fig. 2. The pressure distribution presented from the three-dimensional model simulation is that along the path defined in Fig. 1 by the following branches: $k=0$, $k=1$, $k=2a$, $k=3a$, and $k=4a$. Note that each branching level is identified by a number, i.e., $k=0$ is the original branch, and each branch segment of each level beyond $k=1$ is identified by the branch level as well as by a letter, *a*, *b*, *c*, etc. Due to asymmetry in the fractal-like flow network shown in Fig. 1, the three-dimensional pressure distribution might be slightly different from path to path. Based on the three-dimensional CFD simulations, the pressure drop through the straight channel network is about 70 kPa higher than that through the fractal-like network. The one-dimensional model and the three-dimensional CFD results for the straight channel are within 4%, suggesting that the one-dimensional model provides very good predictions for flow through a straight, constant hydraulic diameter microscale channel. However, for the fractal-like network, the one-dimensional model over-predicts the pressure drop by nearly 50%. Note that the total length of the fractal network in the three-dimensional CFD model, which was designed by dividing 16.3 mm into radial lengths adhering to Eq. (2), is slightly longer than the path length in the one-dimensional model.

Three possible reasons why the one-dimensional model over-predicts the three-dimensional simulations are considered. First, for the fractal-like network in the one-dimensional model, the velocity profile was assumed uniform at the inlet of each successive branching channel, resulting in the redevelopment of the hydrodynamic boundary layer at the entrance of each fractal segment. This is assumed at each wall, even though it is not truly anticipated at the top or bottom channel walls between branching levels due to a constant channel depth. Hence, it is anticipated that this may result in a greater pressure drop predicted from the one-dimensional model. Despite the difference in total pressure drop predicted from the one-dimensional model and the three-dimensional CFD model, the distributions follow a similar trend in the developing flow region, suggesting that the assumption of hydrodynamic boundary layer redevelopment at every wall following a bifurcation should be retained.

Second, noted in the three-dimensional pressure distribution is an instantaneous pressure recovery at each bifurcation, which tends to lower the total pressure drop. A pressure recovery is absent from the one-dimensional distribution. The observed pressure recovery in the three-dimensional simulations may result from the tapered increase in cross-sectional area, which acts similarly to a 'diffuser' following each bifurcation. Note that the pressure recovery is largest for the higher order branches, which have smaller branching angles. In the direction of increasing branching level, branching angles are 40, 36, 29, and 22 deg, respectively. The magnitude of the pressure recovery also depends upon the flow path taken due to the asymmetry of each bifurcation.

Third, an additional trend not noticed in the one-dimensional model is the three-dimensional pressure distribution through the $k=3a$ branch. The distribution in this branch is similar to that through the $k=3d$ branch, but qualitatively different from all other branch distributions. To explain the observed pressure recovery and the anomalous $k=3a$ pressure distribution, details of the flow characteristics are further investigated.

Details of the flow field just upstream and immediately following each bifurcation are investigated to gain better insight into the flow phenomena responsible for the observed pressure recovery. The flow path investigated is that shaded in Fig. 1. Because the axial flow direction changes through each branch, a separate coordinate system is established for each branch segment in each level. The origin of the coordinate system is the apex of the inner wall, as noted in Fig. 3. Variable *x* represents the axial flow direction, *y* represents the spanwise direction from the origin at the inner wall to the outer wall, and *z* is measured from the bottom of the channel to the top of the channel. Because *z* is always measured from the bottom of the channel, the right-hand rule is violated for the following branches: $k=2b$, $k=3b$, $k=3d$, $k=4b$, $k=4d$, $k=4f$, and $k=4h$. It is also relevant to note that the beginning of the outer wall of the $k=3c$ branch is not aligned

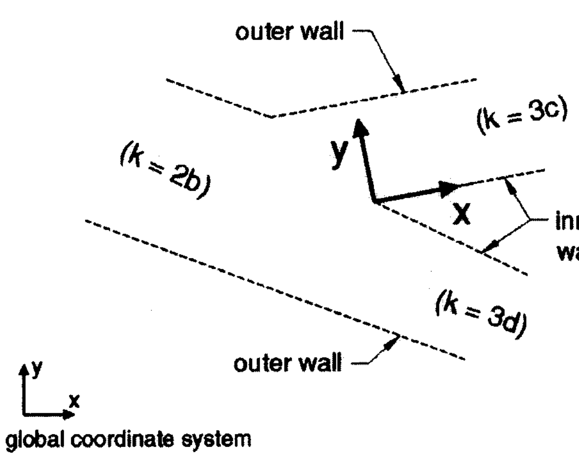

Fig. 3 Local coordinate system for $k=3c$ branch. Note that z is always out of the page and that the channel $k=3d$ is tapered.

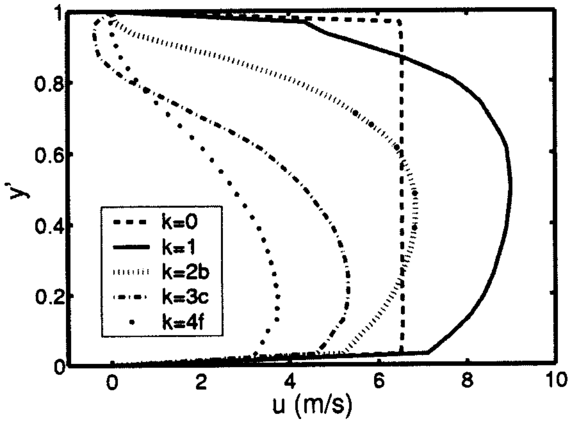

Fig. 5 Axial velocity profiles at $x'=0$ and $z'=0.5$ for all branches along shaded path in Fig. 1

with the origin, but rather corresponds to a negative value of x relative to the local coordinated system shown in Fig. 3.

In Fig. 4 are shown three-dimensional velocity magnitude contours at mid-depth in the x-y plane ($z'=0.5$) between the $k=0$ and $k=1$ branches. Note that $z'=z/H$, where H is the depth of the channel and equal to 250 μm. As the cross-sectional flow area is increased following the bifurcation, the total volume flow is decelerated. This is most noticeable along the outer channel walls. It is also clear from Fig. 4 that the boundary layer at the outer wall does not reinitiate as is assumed in the one-dimensional model. However, development of a new laminar boundary layer is clearly noted at the inner wall with a pronounced influence of the inner wall felt upstream. The two first-level branches ($k=1$) have mirrored image profiles due to symmetry in the angle at which they bifurcate from the $k=0$ branch.

In Fig. 5, axial (x-component) velocity profiles at the inlet, $x'=0$, of each branch taken at the x-y midplane, $z'=0.5$, along the shaded path in Fig. 1 are provided. Data are normalized by the width, w, of each branching level, i.e., $y'=y/w$, which decreases for increasing values of k. Values of y' equal to 0 and 1, respectively, represent the inner and outer walls, while values of z' equal to 0 and 1, respectively, represent the bottom and top walls of the channel network. The variable x' represents the axial distance along the inner wall normalized by the inner wall length. Of particular interest in Fig. 5 are (1) the reduction in maximum velocity with each branching level, which is anticipated due to the increase in total flow area following each bifurcation, (2) the initiation of a boundary layer at the inner wall which originates following a bifurcation, (3) the asymmetry in the velocity profiles due to asymmetry in the bifurcating angle, and (4) the flow reversal near the outer wall observed for the $k=3c$ branch.

Shown in Fig. 6 are the axial velocity profiles at the inlet, $x'=0$, of each branching level along the shaded path in Fig. 1, taken from the x-z midplane at $y'=0.5$. Unlike the velocity profiles in Fig. 5, which are asymmetric due to asymmetric branching angles, the velocity profiles in Fig. 6 are symmetric. This is attributed to a constant channel depth. Note the absence of a redeveloping boundary layer at the top and bottom walls.

In Fig. 7 and Fig. 8 are plotted the axial velocity profiles at the exit of each channel along the flow path shaded in Fig. 1. Figure 7 shows the axial velocity profiles at $x'=1$ for the x-y midplane ($z'=0.5$), whereas Fig. 8 shows the axial velocity profiles at $x'=1$ for the x-z midplane ($y'=0.5$). In comparing the profiles in Fig. 7 with those in Fig. 5, the development of boundary layers from channel inlet to exit at the inner wall ($y'=0$) for the $k=2b$ and $k=3c$ branches is evident. The profile for the $k=1$ branch in Fig. 7 shows an accelerating flow near the inner wall at the channel exit, but shows clearly the boundary layer development at the outer wall ($y'=1$). The $k=0$ branch in Fig. 7 shows a symmetric profile with flow deceleration near the centerline. The $k=4f$ branch, which discharges to the exit plenum, is also sym-

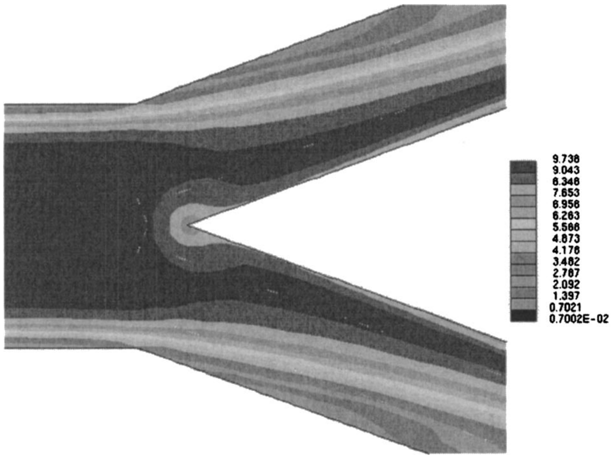

Fig. 4 Mid-depth, $z'=0.5$, velocity magnitudes at the junction between branching level 0 and level 1

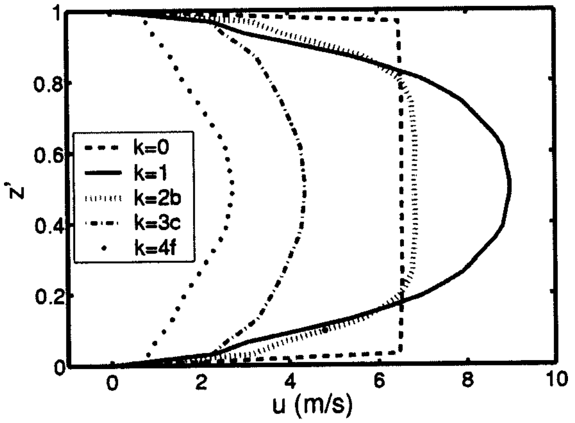

Fig. 6 Axial velocity profiles at $x'=0$ and $y'=0.5$ for all branches along shaded path in Fig. 1

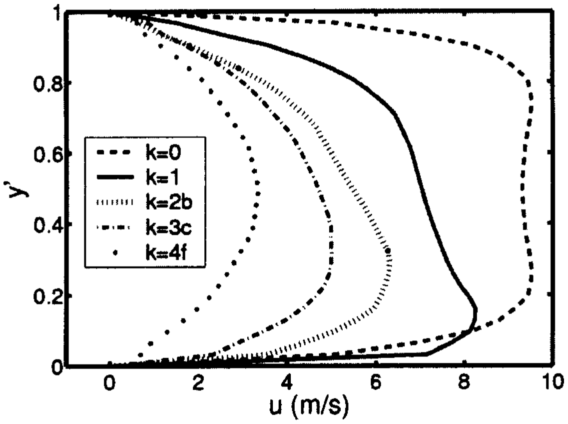

Fig. 7 Axial velocity profiles at $x'=1$ and $z'=0.5$ for all branches along shaded path in Fig. 1

metric. The $k=3c$ profile in Fig. 7 shows that the negative flow near the outer wall at the branch inlet, shown in Fig. 5, is positive at the branch exit.

Figure 8 shows the x-z midplane ($y'=0.5$) axial velocity profiles at the exit, $x'=1$, of each branch in the path in Fig. 1. Notice that the $k=0$ branch, the only branch which symmetrically bifurcates, and the $k=4f$ branch which discharges into the plenum, do not exhibit flow deceleration at the centerline. However, the branches anticipating an asymmetric bifurcation show noticeable deceleration at the centerline in the $y'=0.5$ midplane. The shape of the decelerated profiles in Fig. 8 and the asymmetric profiles in Fig. 7 may be a consequence of a secondary flow.

Figures 9 and 10 show the y-z component velocity vectors at $x'=1$ for branch $k=0$ and $k=1$, respectively. The largest magnitude of the nonaxial flow vectors in Fig. 9 is 1.2 m/s, approximately 10% of the axial velocity at the centerline. This secondary flow is symmetric about both the $y'=0.5$ and $z'=0.5$ axes, in agreement with the symmetric bifurcation following the exit of this channel. The regions along $z'=0.5$ in Fig. 9 where the secondary flow magnitude, denoted by the length of the velocity vector arrows, is highest coincide with the maximum velocity locations observed in Fig. 7 for the $k=0$ branch.

Figure 10 shows the y-z component velocity vectors at the exit of the $k=1$ branch. The largest magnitude of the non-axial flow vectors is 2 m/s, approximately 20% of the axial velocity at the centerline. There is an asymmetry noted in this figure, which shows a strong secondary flow toward branch level $k=2b$ (the right hand side of the figure). The flow toward branch $k=2a$ (the left hand side of the figure) appears to be primarily in the axial direction, with little secondary flow. Again, the secondary flow along $z'=0.5$ is strongest nearer $y'=0$, in agreement with the largest axial flow observed for branch $k=1$ in Fig. 7. The velocity profiles in Figs. 7 and 8 demonstrate a tendency for flow diverted or accelerated in one direction, i.e., in the x-y plane, to decelerate flow in the orthogonal direction, i.e., the x-z plane.

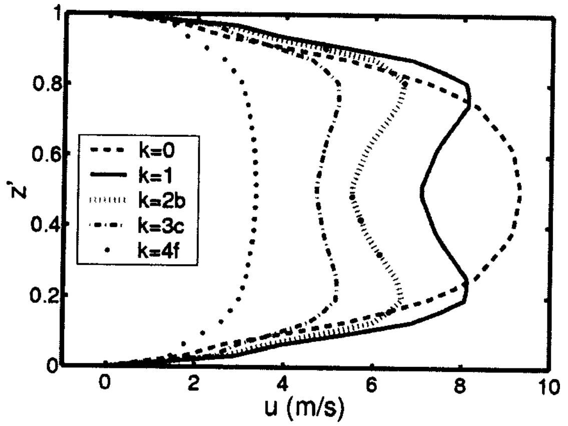

Fig. 8 Axial velocity profiles at $x'=1$ and $y'=0.5$ for all branches along shaded path in Fig. 1

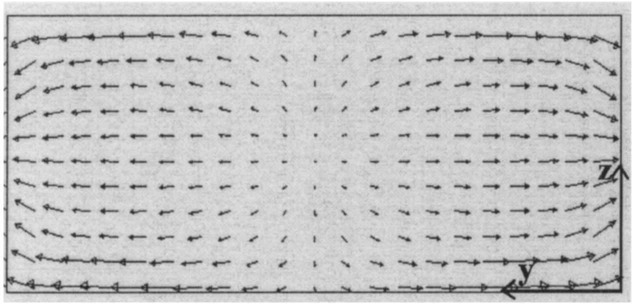

Fig. 9 Nonaxial velocity vectors at $x'=1$ for branch $k=0$

Figure 11 shows how a particle with no mass, placed in the flow field near $y'=0.9$ and $z'=0.65$ near the inlet to branch segment $k=3d$, follows a circulatory flow pattern. The particle trace in Fig. 11, shown from an x-y projection, is actually three-dimensional in nature and is a consequence of a strong secondary flow. In summary, it appears that flow deceleration and recirculation resulting from an increase in flow area and a distinct bifurcation angle may be responsible for the pressure recovery observed

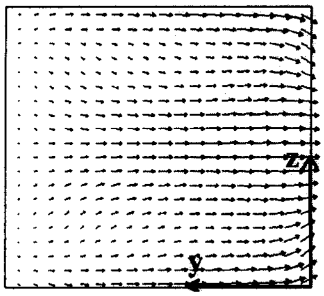

Fig. 10 Nonaxial velocity vectors at $x'=1$ for branch $k=1$

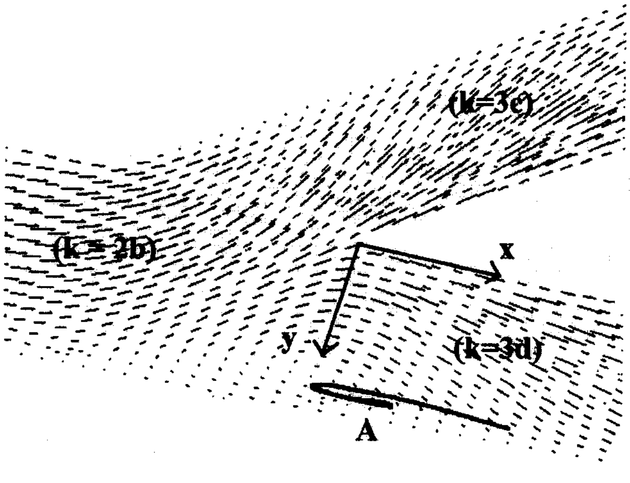

Fig. 11 Particle trace of massless particle introduced near $(x',y',z')=(0,0.9,0.65)$ of $k=3d$ branch

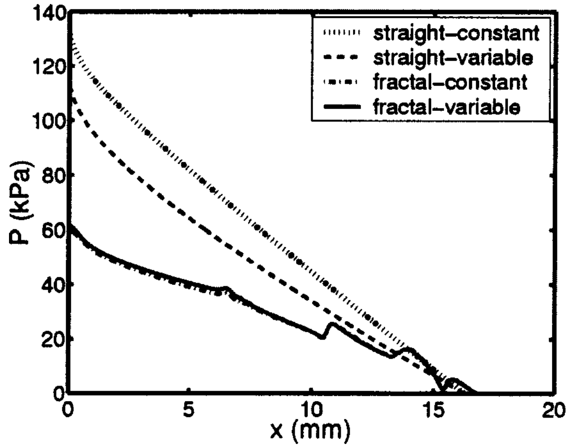

Fig. 12 Three-dimensional CFD pressure distributions for fractal-like and straight channel networks with constant and variable fluid properties

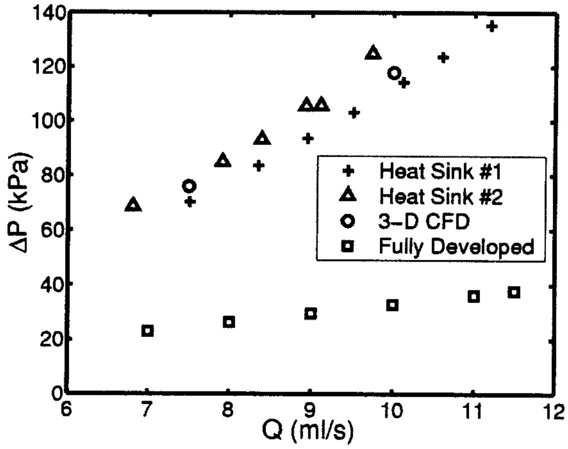

Fig. 13 Experimental pressure drop from two prototypes compared with pressure drop from three-dimensional CFD model with an inlet plenum. Fully developed assessments are based on theory with no inlet plenum.

at each bifurcation in Fig. 2. The degree of recirculation appears to be heavily dependent on the angle at which bifurcation occurs.

Finally, recall that the pressure distribution through the $k=3a$ branch in Fig. 2 is qualitatively different than that through all other branches, except for the $k=3d$ branch. Because all four $k=3$ branches exhibit a negative flow near the outer wall at $x'=0$, but only $k=3a$ and $k=3d$ branches are tapered, the shape of the pressure distribution through the $k=3a$ branch in Fig. 2 is attributed to the tapered channel geometry.

In summary, the general shapes of the one-dimensional and three-dimensional pressure distributions simulated assuming constant properties are qualitatively similar, with the exception of the pressure recovery and the distribution through the tapered channel. For this reason, incorporation of minor losses, or more appropriately the increased area, at the bifurcations in the one-dimensional model appears necessary. It also appears that the assumption of a redeveloping hydrodynamic boundary layer at all walls, although it is physically only occurring at the inner walls, provides a good prediction of the pressure distribution in the entrance region of each branch. Further assessment of this assumption can be made once minor losses due to the bifurcation are incorporated.

3.2 Variable Property Analysis. Specific heat, thermal conductivity and molecular viscosity of water change by 1.6%, 20% and 84%, respectively, over the range of temperatures from 20°C to 100°C. Although the temperature dependence of specific heat can be neglected, it appears the same is not so for thermal conductivity and viscosity. In this section, the validity of assuming constant properties in the one-dimensional model is investigated. Results from the three-dimensional CFD model run with constant, and then run with temperature-dependent thermophysical properties are compared. Thermal conductivity and molecular viscosity are determined, for the constant temperature case, using the average temperature between the inlet and exit bulk fluid temperatures.

Figure 12 shows the three-dimensional CFD pressure distributions in the straight channel network and the fractal-like branching channel network with temperature-dependent properties and with constant, fluid properties. The pressure distribution in the fractal-like network is along the path defined by the following branches in Fig. 1: $k=0$, $k=1$, $k=2a$, $k=3a$, and $k=4a$. The total pressure drop simulated using constant fluid properties for the straight channel network is noticeably higher, approximately 17%, than for temperature dependent fluid properties. In contrast, for the fractal-like flow network the variable property effects are negligible. The reason for this is that the straight channel case has a higher velocity for the same power input; therefore, the shear stress for the straight channel is much higher than that through the fractal-like flow network. Hence, the viscosity has a more significant influence on the pressure drop through the straight channel array.

For water, molecular viscosity decreases with increases in temperature. For a fixed mass flow rate, the decreased viscosity results in a reduced wall stress; hence, a lower pressure drop. On the other hand, the Reynolds number, by definition, tends to increase with a decrease in molecular viscosity. The increased Reynolds number would tend to contribute to an increase in the hydraulic entrance length, which would in turn result in an increase in pressure drop. Therefore, of these two competing factors, the lower shear stress has a more significant effect on the pressure drop. The differences in pressure drop between the constant and variable fluid properties cases suggest that the one-dimensional model should be modified to account for temperature dependent fluid properties in order to be a more dependable predictive tool. This will be of more importance at higher heat fluxes.

3.3 Numerical Uncertainty. Numerical errors reported from the three-dimensional CFD analysis include those caused by mesh spacing, irregularity and nonorthogonality, and the choice of the differencing scheme used for the convective term. These are typically less than 0.1% and 0.2%, respectively, for pressure in the straight channel and fractal-like channel networks, with localized errors on the order of ±0.5% and ±1.5%. Anticipated errors in the one-dimensional model include discretization errors that, based on a spatial grid twice the resolution as that employed, are computed to be less than 0.1 Pa. Both three-dimensional CFD and one-dimensional model results exhibit errors due to imposed assumptions, which are expected to be large when fluid properties are held constant and when minor losses in the one-dimensional model for the fractal flow network are neglected.

3.4 Experimental Analysis. Doerr [15] provided pressure drop data for two prototypes of the fractal-like heat sink. Because the experimental test devices had an inlet plenum, this plenum was modeled in a three-dimensional CFD analysis assuming a uniform inlet velocity to the plenum. Fluid properties were assumed constant in the CFD analysis because all experiments were conducted with water at atmospheric conditions. Pressure drop through both heat sink test fixtures for several flow rates are provided in Fig. 13. Three-dimensional CFD simulated pressure drop for two flow rates within the flow rate range of experimental data are also shown in Fig. 13. Pressure drop through a fractal flow network was also estimated as a function of flow rate assuming no inlet plenum and fully developed flow conditions. These results are added to Fig. 13 as a means to assess the anticipated error in pressure drop due to assuming negligible losses through the plenum and at the bifurcations, and by assuming fully developed flow conditions.

Experimental errors in pressure drop and flow rate are on the order of ±3 kPa and ±0.05 ml/s, respectively, as determined from the standard error of the fit to calibration data and the accuracy of the standards employed in the calibration process. Calibration standards were dead weight testers for the pressure transducers and a catch-and-weigh method for the flowmeters. The aforementioned errors do not take into account uncertainties in wall surface characteristics or actual channel dimensions following the bonding process. Based on a sensitivity analysis using measured discrepancies in channel dimensions, these are anticipated to result in another ±15% uncertainty in the experimental pressure drop. Figure 13 suggests that the three-dimensional CFD is adequately validated by experiments for flow with an inlet plenum. Because flow without an inlet plenum cannot be tested experimentally, experimental validation of CFD pressure results is assumed by extrapolation.

4 Conclusions and Recommendations

In the present research, flow through straight and fractal-like branching networks was investigated using a three-dimensional CFD approach. Results of the pressure distribution through a three-dimensional flow network were compared to that predicted using a one-dimensional model. The one-dimensional model incorporates macroscale correlations. A three-dimensional model was used to assess the validity of, and provide insight for improving, assumptions imposed in the one-dimensional model. Assumptions include (1) redeveloping flow conditions following each bifurcation, (2) negligible minor losses, and (3) constant thermophysical fluid properties.

Pressure distributions for a straight channel network and for a fractal-like branching channel network assuming both constant and temperature dependent fluid properties were considered. Constant between the two configurations are length of a single flow path from inlet to exit, the convective surface area, the terminal hydraulic diameter, the applied heat flux and the supplied pumping power required to move the fluid through the flow network.

The three-dimensional CFD results show that the pressure drop through the fractal-like network is 50% less than that through the straight channel network. Results from the one-dimensional and three-dimensional models, both assuming constant properties, are compared to assess the validity of the developing flow and negligible minor losses assumptions. Although the one-dimensional model well predicts, within 4%, the three-dimensional CFD pressure drop for a straight channel network, a noticeable difference in pressure drop, approximately 30%, for the fractal-like network was observed between the two models. This difference in pressure drop is primarily the result of a local pressure recovery at each bifurcation. Axial velocity profiles along the flow network demonstrate asymmetric flow development as well as a region of negative flow. Nonaxial velocity vectors in the cross-section plane at a channel exit, immediately preceding a bifurcation, show a strong secondary flow. The pressure recovery is believed to be a consequence of these secondary flow conditions resulting from an increased cross-sectional flow area and the presence of a bifurcating channel.

Comparison of the three-dimensional CFD pressure drop for both networks with and without variable fluid properties provides a means of assessing the assumption of constant thermophysical properties. Pressure drop results are slightly higher with constant properties versus variable properties, on the order of 17% for the straight channel design. This was attributed to the decrease in wall shear stress resulting from a decrease in viscosity with an increase in fluid temperature. Finally, a three-dimensional CFD model with an inlet plenum and assuming constant properties was validated with experimental data from two prototypes.

It is concluded that temperature varying fluid properties and minor loss effects following a bifurcation should be incorporated in the one-dimensional model to improve its predictive capabilities. Assuming redevelopment of the hydrodynamic boundary layer following each bifurcation seems to provide plausible trends in the pressure distribution near the inlet of each channel branch.

Nomenclature

H = channel height, mm
L = channel length, mm
T = temperature, K
V = total velocity, m/s
c_p = specific heat, J/kg K
d = hydraulic diameter, mm
k = branch level
n = number of bifurcating channels per segment
p = pressure, Pa
u = axial velocity component, m/s
w = channel width, mm
x = axial direction
y = spanwise direction
z = transverse direction
x' = dimensionless axial direction (x/L)
y' = dimensionless spanwise direction (y/w)
z' = dimensionless transverse direction (z/H)
α = aspect ratio $(\min[w,H]/\max[w,H])$
λ = thermal conductivity, W/m K
μ = molecular viscosity, N s/m^2
ρ = density, kg/m^3

Subscripts

i, j = coordinate indices

References

[1] Tuckerman, D. B., and Pease, R. F. W., 1981, ''High-Performance Heat Sinking for VLSI,'' IEEE Electron Device Lett., **EDl-2**(5), pp. 126–277.
[2] Sohban, B. S., and Garimella, S. V., 2001, ''A Comparative Analysis of Studies on Heat Transfer and Fluid Flow in Microchannels,'' Microscale Thermophys. Eng., **5**, pp. 293–311.
[3] Obot, N. T., 2000, ''Toward a Better Understanding of Friction and Heat/Mass Transfer in Microchannels—A Literature Review,'' *Proc. International Conference on Heat Transfer and Transport Phenomena in Microscale*, Banff, Canada, Begell House, New York, pp. 72–79.
[4] Bau, H. H., 1998, ''Optimization of Conduits' Shape in Micro Heat Exchangers,'' Int. J. Heat Mass Transfer, **41**, pp. 2717–2723.
[5] Pence, D. V., 2000, ''Improved Thermal Efficiency and Temperature Uniformity Using Fractal-Like Branching Channel Networks,'' *Proc. International Conference on Heat Transfer and Transport Phenomena in Microscale*, Banff, Canada, Begell House, New York, pp. 142–148.
[6] West, G. B., Brown, J. H., and Enquist, B. J., 1997, ''A General Model for the Origin of Allometric Scaling Laws in Biology,'' Science, **276**, pp. 122–126.
[7] Bejan, A., 1997, ''Constructal Tree Network for Fluid Flow Between a Finite-Size Volume and One Source or Sink,'' Rev. Gen. Therm., **36**, pp. 592–604.
[8] Bejan, A., 2000, *Shape and Structure, from Engineering to Nature*, Cambridge University Press, Cambridge, UK.
[9] Pence, D. V., 2002, ''Reduced Pumping Power and Wall Temperature in Microchannel Heat Sinks With Fractal-Like Branching Channel Networks,'' Microscale Thermophys. Eng., **6**(4), pp. 319–330.
[10] Chen, Y., and Cheng, P., 2002, ''Heat Transfer and Pressure Drop in Fractal Tree-Like Microchannel Nets,'' Int. J. Heat Mass Transfer, **45**, pp. 2643–2648.
[11] Wechsatol, W., Lorente, S., and Bejan, A., 2002, ''Optimal Tree-Shaped Networks for Fluid Flow in a Disc-Shaped Body,'' Int. J. Heat Mass Transfer, **45**, pp. 4911–4294.
[12] White, F. M., 1991, *Viscous Fluid Flow*, McGraw-Hill, New York.
[13] Wibulswas, P., 1966, ''Laminar Flow Heat Transfer in Non-Circular Ducts,'' Ph.D. dissertation, University of London, London, UK.
[14] Shah, R. K., and London, A. L., 1978, ''Laminar Flow Forced Convection in Ducts,'' *Advances in Heat Transfer*, Supplement 1, Academic Press, New York.
[15] Doerr, A., 2000, ''Bifurcating Fractal Microchannel Heat Exchanger,'' Senior Project Report, Oregon State University, Corvallis, OR.

John D. Wright
Project Leader,
Fluid Flow Group,
e-mail: john.wright@nist.gov Mem. ASME

Michael R. Moldover
Group Leader,
Fluid Science Group

Aaron N. Johnson
Fluid Flow Group

Process Measurements Division,
Chemical Science and Technology Laboratory,
National Institute of Standards and Technology,
100 Bureau Drive,
Gaithersburg, MD 20877

Akisato Mizuno
Professor,
Department of Mechanical Engineering,
Kogakuin University,
Nakano-Machi 2665,
Hachioji-shi, Tokyo 192-0015, Japan

Volumetric Gas Flow Standard With Uncertainty of 0.02% to 0.05%

A new pressure, volume, temperature, and time (PVTt) primary gas flow standard for calibrating flowmeters has an expanded uncertainty $(k=2)$ *of between 0.02% and 0.05%. The standard diverts a steady flow into a collection tank of known volume during a measured time interval. The standard spans the flow range of 1 slm*[1] *to 2000 slm using two collection tanks (34 L and 677 L) and two flow diversion systems. We describe the novel features of the standard and analyze its uncertainty. The thermostatted collection tank allows determination of the average gas temperature to 7 mK (0.0023%) within an equilibration time of 20 min. We developed a mass cancellation procedure that reduced the uncertainty contributions from the inventory volume to 0.017% at the highest flow rate. Flows were independently measured throughout the overlapping flow range of the two systems and they agreed within 0.015 %. The larger collection system was evaluated at high flows by comparing single and double diversions; the maximum difference was 0.0075%.* [DOI: 10.1115/1.1624428]

Introduction

Accurate gas flow measurements are needed for quality, economy, and safety in the chemical process, manufacturing, and medical industries. Manufacturers of electronic components participating in a NIST organized workshop on mass flow controllers asked for primary flow standards with uncertainty of 0.025% to meet the needs of their industry, [1]. The most commonly used primary gas flow standards (piston provers and bell provers) have uncertainty of about 0.2%, [2]. Meanwhile, several generic flowmeter types show reproducibility of less than 0.05%. Therefore, the uncertainty of many gas flowmeters used in manufacturing processes is limited by the flow standards used to calibrate them. For these reasons, and to facilitate research into further improvements in gas flowmeters, NIST undertook a project to reduce the uncertainty of our primary gas flow standards by nearly an order of magnitude. Several novel features in the design and operation of the new PVT*t* system documented here were necessary to achieve our uncertainty goal.

PVT*t* systems have been used as primary gas flow standards for more than 30 years, [3–7]. The PVT*t* systems at NIST consist of a flow source, valves for diverting the flow, a collection tank, a vacuum pump, pressure and temperature sensors, and a critical flow venturi (CFV) (see Fig. 1).

The PVT*t* system measures flow using a volumetric timed-collection technique, whereby a steady flow is diverted into a nearly evacuated collection vessel of known volume for a measured time interval. The average gas temperature and pressure in the tank are measured before and after the filling process. These measurements are used to determine the density change and thereby the mass change in the collection volume. It is also necessary to consider the mass change in the inventory volume, a volume about 1/500th the size of the tank, bounded by the sonic line of the CFV and the two diverter valves (the gray region in Fig. 1). By writing a mass balance for the control volume composed of the inventory and tank volumes (see the dashed line in Fig. 1), one can derive an equation for the average mass flow during the collection time:

$$\dot{m}=\frac{\Delta m_T+\Delta m_I}{\Delta t}=\frac{V_T(\rho_T^f-\rho_T^i)+V_I(\rho_I^f-\rho_I^i)}{t^f-t^i}, \qquad (1)$$

where V_T and V_I are the tank and inventory volumes, ρ is the gas density determined via a real gas equation of state, t is time, and the superscripts i and f indicate initial and final values.

Features of the New PVT*t* Standard

In order to achieve the uncertainty goal of 0.05% or better, we reviewed previous PVT*t* flow standards. We concluded that the new flow standard required (1) improved measurement of the average temperature of the collected gas and (2) reduced uncertainty of the mass change in the inventory volume. We met these requirements by designing a novel, well-thermostated collection tank and by adopting an inventory mass-cancellation procedure. These innovations are fully described in the following sections. Then, we describe the remaining important contributors

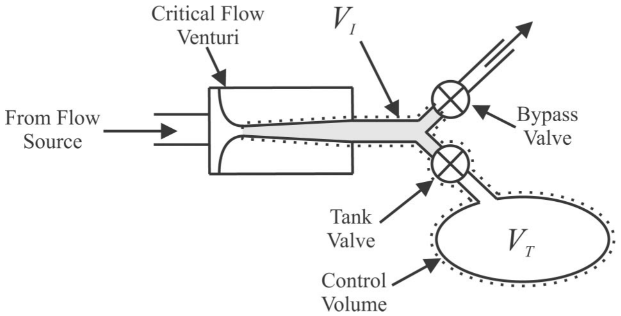

Fig. 1 Arrangement of equipment in the PVT*t* system

Contributed by the Fluids Engineering Division for publication in the JOURNAL OF FLUIDS ENGINEERING. Manuscript received by the Fluids Engineering Division Nov. 15, 2002; revised manuscript received June 4, 2003. Associate Editor: S. Ceccio.

[1] slm=standard liters per minute, reference conditions are 293.15 K and 101.325 kPa.

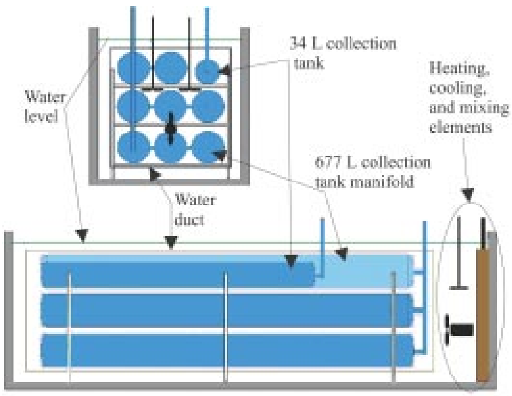

Fig. 2 Schematic diagram of the PVT*t* collection tanks, water bath, duct, and temperature control elements

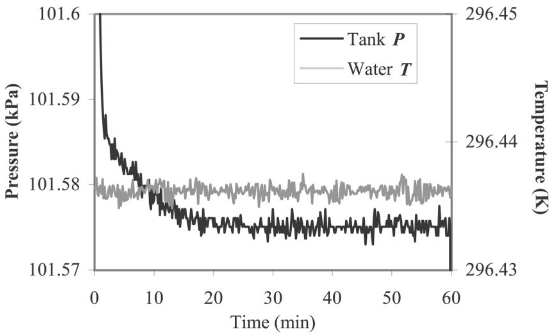

Fig. 3 The collection tank pressure and the water bath temperature immediately following a tank filling, 25 slm in the 34 L tank

to the uncertainty of the new flow standard, namely, the determination of the tank volume and the determination of the density of the collected gas.

Average Temperature of the Collected Gas. One of the most important sources of uncertainty in a PVT*t* flow standard is the measurement of the average temperature of the gas in the collection tank, particularly after filling. The evacuation and filling processes lead to cooling and heating of the gas within the volume due to flow work and kinetic energy phenomena, [8]. The magnitude of the effect depends on the flow, however, the temperature rise in an adiabatic tank can be 10 K or more. Hence, immediately after filling and evacuation, significant thermal gradients exist within the collected gas. For a large tank, the equilibration time for the gas temperature can be many hours. If the exterior of the tank has non-isothermal or time varying temperature conditions, stratification and nonuniform gas temperatures will persist even after many hours.

In this flow standard, we avoided long equilibration times and the difficult problem of measuring the average temperature of a nonuniform gas by designing the collection tanks for rapid equilibration of the collected gas and by immersing the tanks in a well-mixed, thermostatted, water bath (see Fig. 2). Because the equilibration of the 677 L tank is slower, we consider it here. The 677 L tank is composed of eight 2.5 m long, stainless steel cylinders connected in parallel by a manifold. Each cylinder has a wall thickness of $l = 0.6\,\mathrm{cm}$ and an internal radius of $a = 10\,\mathrm{cm}$. Because all of the collected gas is within 10 cm of a nearly isothermal cylinder, the gas temperature quickly equilibrates with that of the bath. After the collected gas equilibrates with the bath, the gas temperature is determined by comparatively simple measurements of the temperature of the recirculating water. In the following sections we describe the bath and the equilibration of the collected gas.

The Water Bath. The water bath is a rectangular trough 3.3 m long, 1 m wide, and 1 m high. Metal frames immersed in the bath support all the cylinders and a long duct formed by four polycarbonate sheets. The duct surrounds the top, bottom, and sides of the cylinders: however, both ends of the duct are unobstructed. At the upstream end of the bath, the water is vigorously stirred and its temperature is controlled near the temperature of the room (296.5 K) using controlled electrical heaters and tubing cooled by externally refrigerated, circulated water. A propeller pushes the stirred water through the duct along the cylinders. When the flowing water reaches the downstream (unstirred) end of the trough, it flows to the outsides of the duct and returns to the stirred volume through the unobstructed, 10 cm thick, water-filled spaces between the duct and the sides, the top, and the bottom of the rectangular tank.

The uniformity and stability of the water temperature was studied using 14 thermistors. The thermistors were bundled together and zeroed at one location in the water bath. Then, they were distributed throughout the water bath. Data recorded at 5 s intervals from these 14 thermistors over a typical 20 min long equilibration interval is generally within ±1 mK of their mean and the standard deviation of the data from their mean is only 0.4 mK. The largest temperature transients occur where the mixed water enters the duct, indicating incomplete mixing. The tank walls attenuate these thermal transients before reaching the collected gas. Thus, after equilibration, the nonuniformity of the water bath and the fluctuations of the average gas temperature are less than ±1 mK, which is equivalent to $3\times10^{-6}\,T$.

Equilibration of the Collected Gas. For design purposes, we estimated the time constant (τ_g) that characterizes the equilibration of the gas within the collection tank after the filling process. The estimate considers heat conduction in an infinitely long, isotropic, ''solid'' cylinder of radius *a*, [9]. For the slowest, radially symmetric heat mode, $\tau_g = (a/2.405)^2/D_T$, where D_T is the thermal diffusivity of the gas. This estimate gives $\tau_g = 80\,\mathrm{s}$ for nitrogen in the 677 L tank. This estimate for τ_g is too large insofar as it neglects convection, conduction through the ends of the tanks, and the faster thermal modes, all of which hasten equilibration. The time constants for heat to flow from the gas through the tank walls and the time constant for a hot or cold spot within a wall to decay have been calculated and found to be less than a second. Therefore, we expect the collected gas to equilibrate with a time constant of less than 80 s.

The equilibration of the collected gas was observed experimentally by using the tank as a constant-volume gas thermometer. After the tank valve was closed, the pressure of the collected gas was monitored, as shown in Fig. 3. Our analysis of data such as those in Fig. 3 leads to the experimental values τ_g of less than 60 s for both the 677 L and 34 L tanks, in reasonable agreement with the estimates. The measured time constant and Fig. 3 show that a wait of 20 min guarantees that the collected gas is in equilibrium with the bath, within the resolution of the measurements.

The manifold linking the eight cylindrical shells is completely immersed in the water bath. Thus, the gas in the manifold quickly equilibrates to the bath temperature as well. However, each collection system has small, unthermostatted, gas-filled volumes in the tubes that lead from the collection tanks to the diverter valves, the pressure transducers, etc. A temperature uncertainty from this source was calculated from the room temperature variations and the size of the volume outside the bath and it is, at most, $4\times10^{-6}\,T$. The combined uncertainty of the average gas temperature is 7 mK, and the largest contributor is, by far, the drift in the sensors between periodic calibrations. The relative standard uncertainty of the density of nitrogen gas in the full collection tank is

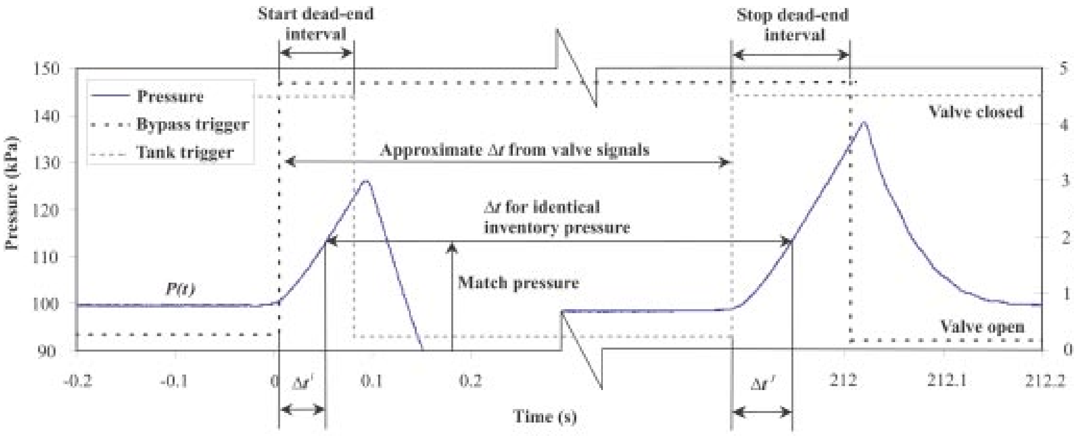

Fig. 4 Data from the pressure sensor in the inventory volume during a PVT*t* flow measurement, showing the transients that occur during the dead-end intervals

68×10^{-6}, and the largest contributor is the pressure measurement due to sensor calibration drift over time, [7] (see below).

Mass Cancellation in the Inventory Volume

Figure 4 illustrates the changes in pressure within the inventory volume during the course of a single PVT*t* flow measurement. Initially, flow moves through the open bypass valve to the room while the collection tank is evacuated (tank valve closed) and the inventory pressure is nominally 100 kPa. When flow is diverted into the tank, there is a short period ($<$100 ms) during which both the bypass and tank valves are closed to ensure clear accountability of the flow during diversion (the start dead-end time interval). During the dead-end time, steady-state flow continues to pass through the critical flow venturi (since the critical pressure ratio is maintained) and mass accumulates in the inventory volume. Hence a rapid rise in pressure and temperature (not shown) results. Once the valve to the evacuated tank opens, the inventory pressure drops to low values. The tank valve is left open until the tank fills to the initial inventory pressure (approximately 100 kPa) and then the flow is diverted back through the bypass valve, causing the stop dead-end time interval. Trigger voltages generated from the bypass and tank valve closed positions give approximate collection times. We will explain other elements of Fig. 4 later in this paper.

The start and stop times can be chosen at any point during the dead-end time intervals as long as the inventory conditions are measured coincidentally. Why is this true? Implicit in the PVT*t* mass balance (Eq. (1)) are two requirements: (1) the measurement of ρ_I^i and ρ_I^f (the initial and final densities) must be coincident with the measurement of t_i and t_f (the start and stop times) and (2) the only source or sink of mass to the control volume is the critical flow venturi. The second condition is met for the entire time that the bypass valve is fully closed, including the start and stop dead-end times. It is not necessary to determine m_T^i and m_T^f (the initial and final mass in the collection tank) coincidentally with t_i and t_f because m_T^i and m_T^f do not change while the tank valve is closed. Indeed, it is advantageous to measure m_T^i and m_T^f when the tank conditions have reached equilibrium.

It is difficult to determine either m_I^f or m_I^i within the inventory volume accurately (especially at high flows) because both the pressure and temperature in the inventory volume rise rapidly as the flow through the critical venturi accumulates in the inventory volume (see Fig. 5). However, it is possible to select m_T^i and m_T^f such that the difference $m_I^f-m_I^i$ is nearly zero. We call our strategy for arranging this "mass cancellation." Our strategy for dealing with the inventory mass change has two elements. First, by design, the inventory volume V_I is much smaller than the collection tank volume V_T. ($V_T/V_I=500$ and 700 for the 34 L and 677 L systems, respectively.) Thus, the uncertainty of mass flow is relatively insensitive to uncertainty in m_I^f and m_I^i because both are small compared with the total mass of collected gas. Second, we choose t^i late in the dead-end time and we chose t^f such that $P(t^f)=P(t^i)$. With these choices, the initial and final inventory densities are essentially equal. In fact, we will assume that Δm_I is zero and consider the quantity only in terms of flow measurement uncertainty, not as part of the flow calculation.

In the remainder of this section, we describe conditions within the inventory volume during the dead-end times using both a model and measurements. The measurements show that $T(t)$ and $P(t)$ are nearly the same during the start and stop dead-end times. Finally, we show that Δm_I is insensitive to the exact choice of t^i, provided that the condition $P(t^i)=P(t^f)$ is applied during the latter portion of the dead-end interval.

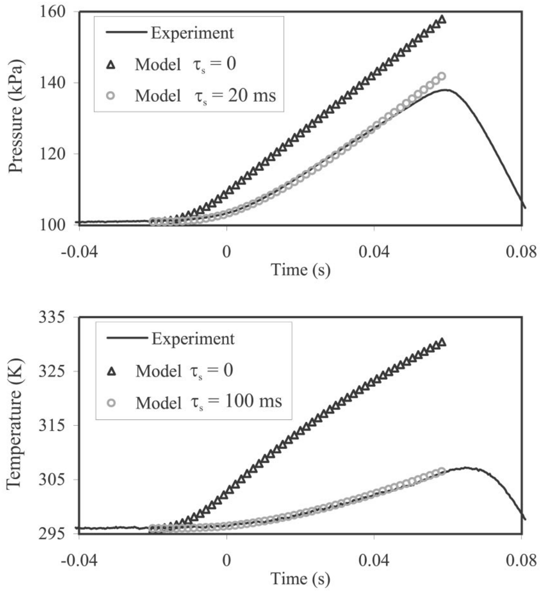

Fig. 5 Experimentally measured data (25 slm, 34 L collection system) and predictions for zero and nonzero sensor time constants. The predictions demonstrate that neglect of the sensors' response times would cause significant error in the measurement of inventory conditions.

Conditions Within the Inventory Volume. Figure 5 displays the time dependent temperature $T(t)$ and pressure $P(t)$ in the inventory volume during the dead-end interval of the smaller collection system at a typical collection rate ($\dot{m}=25\,\mathrm{slm}$; collection time=82 s). The triangles in Fig. 5 were calculated from the lumped-parameter, thermodynamic model developed by Wright and Johnson [8], in this case for perfectly fast pressure and temperature sensors ($\tau_s=0$). The model assumes a constant mass flow $\dot{m}$ at the entrance to the inventory volume. The model neglects heat transport from the gas to the surrounding structure and non-uniform conditions, such as the jet entering the volume from the CFV outlet. For Fig. 5, $T(t)$ and $P(t)$ were calculated on the assumption that the diverter valve reduced the flow linearly (in time) to zero during the interval $-0.02\,\mathrm{s}<t<0$. Experimentally measured values of $T(t)$ and $P(t)$ recorded at 3000 Hz (smooth curves) are also shown in Fig. 5. Most of the differences between the measured curve and the calculated triangles ($\tau_s=0$) result from the time constants of the sensors used to measure $T(t)$ and $P(t)$. This is demonstrated by the agreement between the experimental curve and the model results when time constants are incorporated (circles).

In Fig. 5, the calculated curves do not display features that mark either the onset or the completion of the diverter valve closing. Thus, even $T(t)$ and $P(t)$ data from perfect sensors cannot be used to detect these events. For this reason, t^i and t^f were chosen such that they were clearly within the dead-end time intervals. We relied on the pressure sensor to choose t^i because the pressure responds more quickly than the temperature sensor and also because the pressure sensor responds to the average conditions throughout the inventory volume. In contrast, the temperature sensor responds primarily to the conditions at only one location. We choose t^i near the end of the dead-end time, where the $P(t)$ measurements have nearly the same slope as the $\tau_s=0$ model. In this regime, the dependence of $P(t)$ on precisely how the valve closed has decayed. Therefore, we expect that $P(t)$ will be the same during the start and the stop dead-end times, improving the mass cancellation as well as the correlation of initial and final inventory density uncertainties.

Near Symmetry of Start and Stop Behavior of $P(t)$. Figure 6 shows records of $T(t)$ and $P(t)$ taken during the dead-end time intervals at the start and stop of a single flow measurement. The data were recorded at 3000 Hz for 500 ms and the plots were displaced along the horizontal axis until they nearly overlapped. The pressure and the temperature at the beginning of the start dead-end time were slightly lower than those at the stop dead-end time (the "trigger pressure difference"); however, the two records match closely during the dead-end time. This implies that the time-dependent densities $\rho(t)$ also nearly match.

At both diversions shown in Fig. 6, valve trigger signals were gathered along with the temperature and pressure measurements using a commercially manufactured data acquisition card (see Fig. 4). The trigger signals originate from an LED/photodiode pair and a flag on the valve actuator positioned so that the circuit output rises to a positive voltage when the valve is closed. These valve signals are used to trigger timers that give the approximate collection time.

As represented in Fig. 4, the inventory record is post-processed to obtain both the initial and final measurements of pressure and temperature in the inventory volume as well as the final collection time. An arbitrary "match pressure," $P(t^i)$, that was measured late within the start dead-end time is selected. The same value of the pressure is found in the stop data series and the time differences between the match pressure measurements and the start and stop trigger signals are determined from the data record (Δt^i and Δt^f). These time corrections are used to correct the approximate times from the trigger signals and calculate the time interval between matching inventory pressures. As shown in Fig. 6, the temperatures are also nearly matched; thus, the initial and final inventory densities nearly match and inventory mass cancellation occurs.

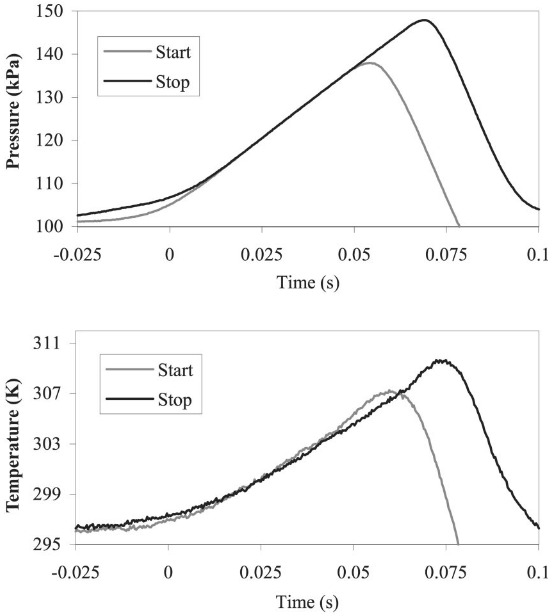

Fig. 6 Superimposed inventory data traces for a start diversion and a stop diversion in the 34 L tank at 25 slm demonstrating "symmetric" diverter valve behavior. The start dead-end time was approximately 50 ms; the stop dead-end time was approximately 15 ms longer.

Uncertainty of Δm_I. Imperfections of the mass cancellation procedure contribute to the uncertainty of Δm_I. The most significant of these uncertainty components (due to sensor time constants) are correlated between the start and stop diversions. Other correlated inventory volume uncertainties include the pressure and temperature sensor calibrations and the differences between sensed and stagnation values of pressure and temperature. The uncertainty of the mass change within the inventory volume caused by the *correlated* pressure and temperature uncertainties can be expressed as

$$u(\Delta m_I)=\frac{V_I M}{ZR}\left[\left(\frac{1}{T_I^f}u(P_I^f)-\frac{1}{T_I^i}u(P_I^i)\right)^2+\left(\frac{P_I^f}{(T_I^f)^2}u(T_I^f)-\frac{P_I^i}{(T_I^i)^2}u(T_I^i)\right)^2\right]^{1/2} \tag{2}$$

where in this equation, $u(P_I)$, $u(T_I)$, and $u(\Delta m_I)$ are the uncertainties of the inventory pressure, inventory temperature, and inventory mass change during the collection, respectively. Note that if the uncertainties and the initial and final conditions are equal (i.e., $u(T_I^i)=u(T_I^f)$, $u(P_I^i)=u(P_I^f)$, $T_I^i=T_I^f$, and $P_I^i=P_I^f$), then the terms within parentheses cancel, and the flow uncertainty related to the inventory volume is zero. Equation (2) demonstrates the benefit of matching the initial and final inventory conditions to optimize the cancellation of correlated uncertainties.

Not all of the measurement uncertainties of the inventory volume are correlated. Inconsistencies in the pressure and temperature fields may originate from a change in the inventory wall temperature or from differences in the flow paths between the start and stop diversions. In our uncertainty analysis, we assumed that the spatial inconsistencies are uncorrelated and that their magnitude is proportional to the mass flow. Hence, the inventory uncertainties are negligible at the lowest flows for each system, but account for about half the mass flow uncertainty under high flow

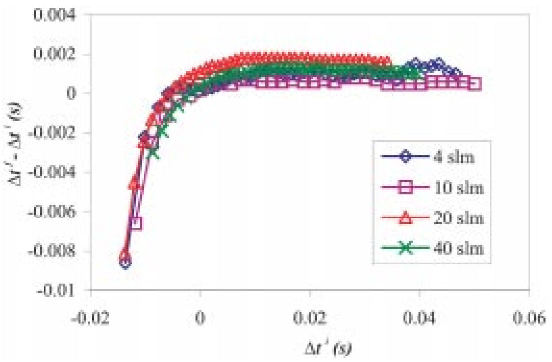

Fig. 7 The time correction for the 34 L tank versus the time relative to the trigger signal indicating bypass valve closure

conditions. Maximum values for the uncorrelated inventory uncertainties of 3 kPa and 9 K were assumed and their magnitude was verified by the flow comparison and double-diversion experiments described later.

Insensitivity of Δm_I to the Match Pressure. For a perfectly symmetric diverter system (identical tank and bypass valves and identical "start-diversion" and "stop-diversion" pressures), and with a perfectly fast pressure sensor ($\tau_s = 0$), the correction time ($\Delta t^f - \Delta t^i$) would be a constant for any point in the dead-end time interval. For the real system, the best correction times are calculated during the latter portion of the dead-end time, after the effects of trigger pressure differences and the flow differences during valve closure have decayed from the pressure sensor measurements.

Figure 7 shows the total correction time ($\Delta t^f - \Delta t^i$) versus the initial time correction (Δt^i) for several flows in the 34 L system. For values of Δt^i less than zero (i.e., the bypass valve is in the process of closing), the time corrections are as large as 10 ms. Later in the dead end time ($\Delta t^i > 10\,\mathrm{ms}$) the time corrections are near zero and constant to within 0.5 ms (for a given flow). The time corrections are nearly constant after the differences in the mass flow between the two valve closures and the trigger pressure differences have decayed from the $\tau_s = 20\,\mathrm{ms}$ pressure sensor. The experimental results given in Fig. 7 and the Wright-Johnson model show that matching the conditions late in the dead-end interval (i.e., at times $> 2\tau_s$) result in nearly constant correction times, while low match pressures (early in the dead-end time) give much larger corrections.

Figure 7 also illustrates the concept that uncertainties related to the inventory volume can be treated not only as mass measurement uncertainties, but as time measurement uncertainties as well. One can consider the uncertainty in the measurement of time between conditions of perfect mass cancellation, or one can consider the uncertainty in the measurement of inventory mass differences between the start and stop times. Both perspectives offer insight and verification of the uncertainties of the inventory volume and flow diversion process.

Measurement of the Tank and Inventory Volumes

Gas Gravimetric Method. The volume of the 677 L tank was determined by a gas gravimetric method. In this method, the mass of an aluminum high pressure cylinder was measured before and after discharging its gas into the evacuated collection tank. The change in mass of the high pressure cylinder and the change in density of the gas in the collection tank were used to calculate the collection tank volume, V_m. Nominally,

$$V_m = \frac{m_c^i - m_c^f}{\rho_T^f - \rho_T^i} - V_e, \tag{3}$$

where the m_c indicates the mass of the high pressure cylinder and V_e is the small volume within the tubing and the valve body that temporarily connected the collection tank to the high pressure weighing cylinder. The extra volume is calculated from dimensional measurements or measured by liquid volume transfer methods. The density of the gas in the collection tank (ρ_T^f and ρ_T^i) was measured with a relative standard uncertainty of 68×10^{-6}, as discussed below.

In practice, a more complex formula than Eq. (3) was used to account for a small amount of gas that enters the control volume from the room when the cylinder is disconnected from the collection tank because the final tank pressure was less than atmospheric. For the volume determinations performed for the 677 L tank, the effect amounts to only $5 \times 10^{-6}\,V$.

Independent volume determinations were conducted with both nitrogen and argon gas. In all cases, high purity gas was used (99.999 % mol fraction) and care was taken to evacuate and purge the system. When nitrogen was used, the aluminum cylinder weighed approximately 4200 g when filled at 12.5 MPa, and approximately 3800 g after it was emptied to 55 kPa. When argon was used, the initial and final masses were 4440 g and 3820 g, respectively. The standard deviation of the six volume measurements (4 with nitrogen, 2 with argon) was $16 \times 10^{-6}\,V$.

The initial and final masses of the gas cylinder were measured using a substitution process with reference masses and a mass comparator enclosed in a wind screening box. The comparator has a full scale of 10 kg and resolution of 1 mg. The cylinder and a set of reference masses of nearly the same weight were alternated on the scale five times. The zero corrected scale readings were then calibrated to the reference masses and buoyancy corrected via the following formula:

$$m_c = \frac{S_c}{S_r} m_r \left(1 - \frac{\rho_a}{\rho_r}\right) + \rho_a V_o, \tag{4}$$

where S represents the scale reading, the subscripts r and c indicate the reference masses and the cylinder respectively, ρ_a is the ambient air density where the measurements were conducted, and V_o is the external volume of the high pressure cylinder and its valve and fittings. The density of the ambient air was calculated from the barometric pressure, the temperature and humidity inside the wind screen, and an air density formula that includes humidity, [10]. The cylinder mass was measured with a relative standard uncertainty of 1×10^{-6}.

The external volume of the high pressure cylinder appears in Eq. (4) due to air buoyancy corrections. The external volume of the cylinder was measured by Archimedes principle, i.e., by measuring the change in apparent mass of the object in air and in distilled water. The thermal expansion corrections to the external volume were less than $0.5\,\mathrm{mL}$ ($100 \times 10^{-6}\,V_o$) and were not significant since the external volume has a small sensitivity coefficient in the collection tank volume determination process. The expansion of the external cylinder volume as a function of its internal pressure was not negligible. The Archimedes principle measurements showed a volume increase from 4697.5 mL to 4709 mL between the 100 kPa and 12.5 MPa pressures. This change agreed well with predictions based on material properties, and the appropriate experimental values for external volume were used in the cylinder mass calculations (Eq. (4)), depending on whether the cylinder was empty or full. If this issue were neglected, it would lead to errors in the mass change measurements of about $35 \times 10^{-6}\,\Delta m_c$.

In summary, the gravimetric determinations of the 677 L collection tank volume made with nitrogen and with argon agreed with each other; the mean of the six measurements had a standard deviation of $16 \times 10^{-6}\,V_T$. Because the volume was measured at essentially the same pressure and temperature at which it is used for flow measurements, changes in V_T due to pressure dilation and thermal expansion are negligible. The gas density of the full collection tank contributed 92 % of the uncertainty of V_T. This is discussed below.

Volume Expansion Method. The 34 L collection tank volume, the inventory volume for the large collection tank, and the small inventory volume were all determined via a volume expansion method. In this method, a known volume is pressurized, the unknown volume is evacuated, a valve is opened between the two volumes, and the resulting density changes within the two volumes are used to calculate the unknown volume. Applying conservation of mass to the system of the two tanks yields

$$V_2=\frac{(\rho_1^f-\rho_1^i)V_1}{(\rho_2^i-\rho_2^f)}-V_e, \tag{5}$$

where the subscripts 1 and 2 refer to the known and unknown volumes, respectively. As before, the density values are based on pressure and temperature measurements of the gas within the volumes and gas purity issues must be considered. Note that in many cases the final densities can be considered the same in both volumes 1 and 2, but for the determination of the 34 L tank volume, elevation differences between the two tanks required a head correction to the pressure measurements and therefore the two densities were not strictly equal. The difference in elevation resulted in a relative difference in gas density of 20×10^{-6} even though the two tanks were connected. The relative standard uncertainty of the 34 L tank volume was 116×10^{-6}, and the largest contributors were the known 677 L volume and the density change in the 34 L tank (traceable to the measurement of pressure change).

Density in the Collection Tank

The density of the nitrogen (or argon) in the collection tank was determined from measurements of the gas pressure, temperature of the water bath, and the equation of state, as correlated in the NIST database Refprop 23, [11]. Of these, the pressure measurement contributed most to the uncertainty. The pressure was measured with a 200 kPa full-scale absolute pressure transducer. For the 100 kPa and 296 K conditions present in the full collection tank, the pressure measurement uncertainty is $64\times10^{-6}\,P$ and the temperature uncertainty is $17\times10^{-6}\,T$. For both pressure and temperature measurements, the largest source of uncertainty is sensor drift between periodic calibrations. The equation of state contributes a relative uncertainty of 10×10^{-6} to the density determinations and more detail about all of these uncertainty sources can be found in Ref. [7].

Mass Flow Uncertainty

The uncertainty of a mass flow measurement made with the PVT*t* standard was calculated following the propagation of uncertainties techniques described in the ISO Guide to the Expression of Uncertainty in Measurement, [12]. The uncertainty of each of the inputs to a flow measurement is determined, weighted by its sensitivity, and combined with the other uncertainty components by root-sum-square (RSS) to arrive at a combined uncertainty. Figure 8 schematically lists the components that have been considered in the uncertainty analysis and their relationship to the mass flow measurement. The uncertainties of the components have been quantified in detail in a prior publication, [7].

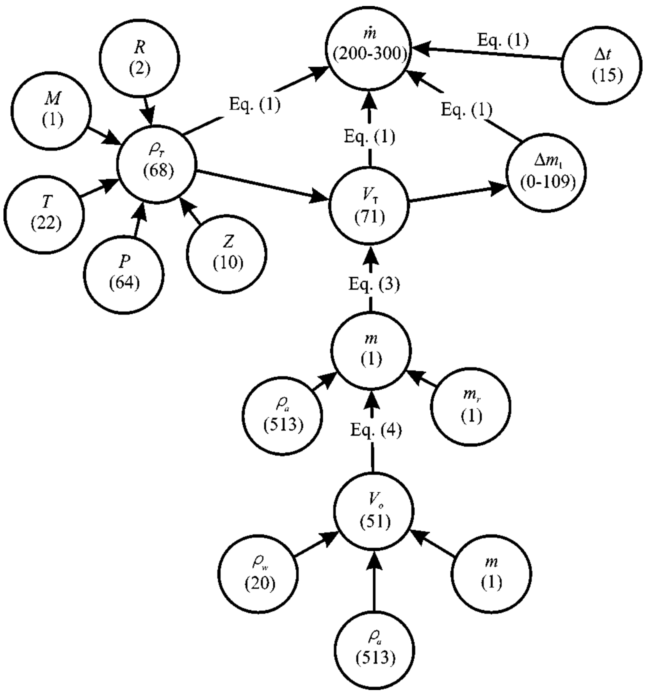

Fig. 8 The chain of measurements and equations used for the PVT*t* flow standard. The subcomponents are labeled with their relative standard uncertainty $\times10^6$ ($k=1$) for the 677 L system. The mass flow uncertainty is a $k=2$ or approximately 95% confidence value.

The uncertainty for flows between 20 slm and 2000 slm of nitrogen in the 677 L tank is given in Table 1 and in Fig. 8. The standard uncertainty of each subcomponent is given in both relative ($\times10^6$) and dimensional forms. The units of the dimensional values are given. The relative contribution of each subcomponent to the combined uncertainty is listed in the fourth column. This contribution is the %age of the squared individual component relative to the sum of the squares of all subcomponents. The uncertainty from the inventory volume, the combined uncertainty, the expanded uncertainty, and the uncertainty contributions are given as a range covering the minimum to maximum flow.

At the highest flow, uncertainty contributions are principally divided between the tank volume, the final gas density, and the inventory uncertainty. The relative expanded uncertainty falls to 200×10^{-6} for the smallest flows as the uncertainty contributions of the inventory volume become negligible. For an air flow mea-

Table 1 Uncertainty of measuring nitrogen flows from 20 slm to 2000 slm with the 677 L standard

Uncertainty Category Flow (677 L, N_2)	**Standard Uncertainty ($k=1$)**		**Contribution (%)**
	Relative ($\times10^6$)	**Dimensional**	
Tank volume	71	48.5 cm^3	50 to 23
Tank initial density	10	1.14×10^{-8} g/cm^3	1 to 0
Tank final density	68	7.77×10^{-8} g/cm^3	45 to 21
Inventory mass change	0 to 109	(0 to 0.084) g	0 to 53
Collection time	15	0.287 ms	0 to 1
Std deviation of repeated meas.	20	0.001 g/s	4 to 2
RSS (combined uncertainty)	102 to 150		
Expanded uncertainty (k=2)	204 to 300		

Table 2 Uncertainty of measuring nitrogen flows from 1 slm to 100 slm with the 34 L standard

Uncertainty Category Flow (34 L, N_2)	Standard Uncertainty ($k=1$) Relative ($\times 10^6$)	Standard Uncertainty ($k=1$) Dimensional	Contribution (%)
Tank volume	116	4.0 cm^3	72 to 28
Tank initial density	10	1.14E−08 g/cm^3	1 to 0
Tank final density	68	7.77E-08 g/cm^3	25 to 10
Inventory mass change	0 to 170	(0 to 0.007) g	0 to 61
Collection time	15	0.287 ms	0 to 0
Std deviation of repeated meas.	20	4.0E−05 g/s	2 to 1
RSS (combined uncertainty)	**137 to 219**		
Expanded uncertainty ($k=2$)	**274 to 438**		

surement, the relative expanded uncertainty of the 677 L system must be increased to approximately 500×10^{-6} over the entire flow range because the moisture content of the compressed air is not well controlled. Then, the largest uncertainty is the density of the air in the collection tank (80% contributor).

The standard uncertainty of the tank final density ($68 \times 10^{-6}\,\rho_T$) is a large contributor to both the tank volume determination as well as the mass flow measurement. The most significant contributions to the density uncertainty are pressure (88%) and temperature (10%). The largest uncertainty contributions to the pressure and temperature measurements are calibration drift between calibrations (88% and 77%, respectively). Therefore sensors with more stable calibrations, particularly for pressure, would dramatically improve the uncertainty of mass flow measurements.

Table 2 presents the uncertainty of flow measurements from the 34 L system for flows between 1 slm and 100 slm. The relative expanded uncertainty varies between 270×10^{-6} and 440×10^{-6}. At high flows, the significant uncertainty sources are the tank volume, the tank final density, and the uncorrelated inventory uncertainties. For low flows, the major contributors are tank volume and final gas density. For air flow measurements, the 34 L system has a nearly constant relative expanded uncertainty over its entire flow range of approximately 500×10^{-6}. The largest contribution to this is the uncertainty of the density of the humid air in the collection tank.

Experimental Validation of the Uncertainty Analysis

Comparison of the 34 L and 677 L Flow Standards. We conducted flow comparisons between the 34 L and the 677 L flow standards to test the mass cancellation strategy and the validity of the uncertainty analyses. To test the 34 L system, we conducted calibrations of critical flow venturis at identical flows spanning the range $3\,\text{slm} < \dot{m} < 100\,\text{slm}$ (0.06 g/s to 2.3 g/s) in both the small and the large systems. The large system can be used as a reference for the small system because its inventory (and total) uncertainties are quite small in this flow range. The collections ranged from as short as 18 s to more than 4 hours.

Figure 9 shows the difference in the discharge coefficients of several critical flow venturis as measured by the 34 L and 677 L systems, plotted versus flow. The maximum disagreement between the two flow standards is less than $150\times 10^{-6}\,\dot{m}$ over the entire range tested. The throat diameters of the venturis used for the comparisons ranged between 0.3 mm and 1.7 mm. The comparisons were done with the same pressure and temperature sensors associated with the CFV during the testing on both flow standards in order to reduce some possible sources of discharge coefficient differences. Numerous collections were made for each tank at each flow to confirm stability of the conditions at the critical flow venturi.

How well should the two systems agree? The difference between the discharge coefficients measured by the two PVTt systems should be less than the RSS of the uncertainties of the two standards, especially when one considers that the uncertainties due to pressure and temperature measurements are correlated between the two standards. For the lowest flows of the comparison range, the uncertainties originating from the inventory volume are quite small for both systems and the observed differences between them are dominated by tank volume uncertainties. From Fig. 9 it can be seen that the two systems differ by about $100\times 10^{-6}\,\dot{m}$ for flows less than 20 slm. The RSS of the two relative volume uncertainties from Tables 1 and 2 is 137×10^{-6} ($k=1$).

At the higher flows of the comparison range, the uncertainties associated with the transient conditions in the inventory volume should be negligible in the 677 L system; however, they will increase with flow for the 34 L system. Because the collection times were 1/20th as long when using the smaller tank, any timing error (or, equivalently any imperfection of the mass cancellation technique) was 20 times more important for the smaller tank. Figure 9 suggests that the transient conditions cause a bias such that the 34 L flow standard reads too high as the flow is increased. The bias is approximately $200\times 10^{-6}\,\dot{m}$ at the largest flow compared. This bias is comparable to the 170×10^{-6} ($k=1$) of relative uncertainty contributed by the inventory volume at the highest flows in the 34 L system according to our uncertainty analysis (see Table 2). Therefore, the bias observed in the comparison is consistent with the uncertainty analysis.

Figure 9 also examines the tank comparison results from the perspective of time measurement uncertainty rather than the mass. We interpreted the comparison results using the simplified model $\dot{m} = m/t$, where m is the mass collected and t is the collection time using the 34 L tank. If we assume that a constant bias δm is present in all of the mass measurements for all flows (for example, from an error in the volume of the 34 L tank) and that a constant bias δt is present in all the time measurements (for example from differing responses of the pressure sensor to closing the tank valve

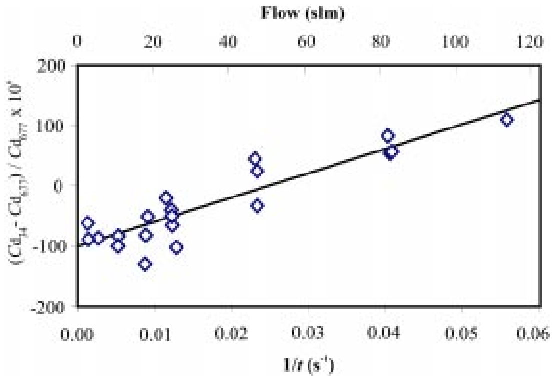

Fig. 9 Relative difference in the discharge coefficient of critical flow venturis calibrated on both the 34 L (C_{d34}) and 677 L (C_{d677}) flow standards versus flow and the inverse of the collection time for the 34 L tank. Also plotted is a linear best fit of the data.

and the bypass valve) we expect that the bias of the mass flow measurement will be a linear function of the inverse collection time, i.e.,

$$\frac{\delta \dot{m}}{\dot{m}} = \frac{\delta m}{m} - \frac{\delta t}{t}. \tag{7}$$

The measurements in Fig. 9 are consistent with such a linear function. The slope implies a constant timing error of 4 ms. A timing error of this order is not surprising because the timing is based on a pressure sensor with a time constant of approximately 20 ms. The relative standard deviation of the flow measurements from the best fit line is 24×10^{-6}.

The intercept of the line in Fig. 9 could be used to "correct" the volume of the 34 L tank, thereby improving the agreement between the two systems at low flows. The slope of the line in Fig. 9 could be used to improve agreement at higher flows. If this were done, the comparison differences would be zero with a standard deviation of $24\times10^{-6}\,\dot{m}$. These corrections have not been made at the present time for four reasons. (1) The comparison results are consistent with the present uncertainty analysis. (2) We plan to improve the measurements of the pressure in the inventory volume; this may reduce the slope in the comparison data. (3) We plan to refine the volume expansion process used to determine the 34 L tank size; this may reduce the apparent volume difference. (4) By refraining from making a correction, we adhere to the definition of a primary standard for both collection systems because both have been calibrated with reference to SI units, not with reference to another flow standard.

During some of the comparison flows, we noticed that the pressure downstream of the critical flow venturi was significantly higher in the 34 L system than in the 677 L system (108 kPa versus 100 kPa) due to the smaller tube size and resultant higher pressure drop. For some of our venturis (with relatively short diffusers) this pressure difference caused slight changes in the upstream pressure (and the discharge coefficient), even at conditions well above the critical pressure ratio. Therefore, our assumption that for the same throat Reynolds number, the discharge coefficient of the venturi is independent of the downstream pressure may not be completely valid. We suspect that some of the differences observed between the tanks in Fig. 9 are due to the venturis (even though long diffusers were used).

In one series of experiments, the trigger pressure difference was intentionally varied over the range from −2 kPa to 27 kPa at the constant flow of 82 slm in the 34 L system. The purpose of the test was to measure the dependence of the venturi discharge coefficient on the trigger pressure difference and hence to assess its influence on the inventory uncertainties. The tests showed a relative change of 10×10^{-6} in discharge coefficient for each 1 kPa change in the trigger pressure difference. Because the largest trigger pressure difference is less than 3 kPa in the present system, this effect is expected to contribute only 30×10^{-6} to the flow uncertainty. If further measurements confirm this, we must admit that the major contributor to the slope in Fig. 9 is unknown. Perhaps it is an inconsistency of the pressure and temperature fields between the start and stop diversions.

Multiple Diversions in the 677 L Flow Standard. To independently test the uncertainty analysis for the inventory volume of the 677 L collection system, we performed CFV calibrations at identical flows following two different protocols. In the first protocol, the inventory volume was dead-ended at the beginning and end of the collection interval, in the usual manner. In the second protocol, the collection interval was divided into two subintervals, i.e., each flow measurement had two start and stop diversions. If the mass cancellation procedure introduced a bias Δm_I, the second protocol would double this bias and allow assessment of its uncertainty contribution. The CFV discharge coefficients from the two protocols were compared to assess the magnitude of the uncertainties introduced by the inventory volume and the flow diversion process. Three flows between 300 slm and 1600 slm were tested. The two protocols produced relative differences in discharge coefficient that were all less than 75×10^{-6} (see Table 3), which is within the relative standard uncertainty assumed in the analysis (109×10^{-6} in Table 1).

Table 3 Differences in CFV discharge coefficients (C_d) for two and one diversion in the 677 L flow standard

Flow (slm)	$[C_d\ (2\ \text{Diversions}) - C_d]/C_d\times10^6$
300	53± 25
700	−27± 31
1600	75±122

Conclusions

The design of a new gas flow standard composed of two PVT*t* collection tanks (34 L and 677 L) has been presented. The system is designed to calibrate critical flow venturis for flows from 1 slm to 2000 slm. The flow standard has several novel features. The collection tanks are immersed in a water bath that matches the nominal room temperature and is stable and uniform to better than 1 mK. The collection tanks are divided into sections of small enough diameter that the gas inside them achieves thermal equilibrium with the surrounding water bath in 20 min or less. This reduces the contribution of temperature to the flow measurement uncertainty to a very low level.

Uncertainties related to the inventory volume and the diversion of gas into the collection tank at the start and stop of a flow measurement have been studied in great detail. A thermodynamic model of the inventory volume during diversion was utilized to understand the importance of large pressure and temperature transients and of sensor time constants on the flow measurement uncertainty. The flow standard is operated to achieve "mass cancellation" in the inventory volume, thereby taking advantage of correlated sensor uncertainties to minimize uncertainty contributions from the inventory volume.

An uncertainty analysis for the mass flow measurements from the two systems has been presented. The analysis used the PVT*t* basis equation and followed the propagation of uncertainties method suggested by international standards. The uncertainty analysis shows that the 677 L system measures mass flow with a relative expanded uncertainty between 200×10^{-6} and 300×10^{-6} for a pure gas like nitrogen or argon, where the higher uncertainty applies to higher flows. For the 34 L tank and pure gases, the relative expanded uncertainties range from 270×10^{-6} to 440×10^{-6}. The uncertainties are larger for the 34 L tank because the tank volume uncertainty is greater and the ratio of collection tank volume to inventory volume is smaller for the small system. For pure gas measurements, the largest sources of uncertainty can be traced to pressure measurement ($64\times10^{-6}\,P$) which is the major contributor to both gas density and tank volume uncertainties. For air flow measurements using gas from a compressor and drier, mass flow relative expanded uncertainties are about 500×10^{-6} for both standards and the major contribution is the uncertainty in the moisture content of the air.

Comparisons between the 34 L and 677 L standards from 3 slm to 100 slm show agreement within $150\times10^{-6}\,\dot{m}$ or better. Experiments using single diversions (normal operation) and double diversions to the collection tank were used to validate the uncertainty estimates of the 677 L inventory volume and the differences between these two methods were less than $75\times10^{-6}\,\dot{m}$. The evaluation results along with comparisons to previously existing gas flow standards support the uncertainty statements for the new standards.

Nomenclature

a = radius of gas collection tank
C_d = discharge coefficient for a critical flow venturi
D_T = thermal diffusivity
k = uncertainty coverage factor
m = mass
M = molecular weight
P = pressure
R = universal gas constant
T = temperature
t = time
$u(x)$ = uncertainty of quantity x
V = volume
Z = compressibility
ρ = density
τ = time constant

Subscripts

a = ambient air
c = cylinder
e = extra
g = gas
I = inventory
m = gravimetric
o = external
r = reference
s = sensor
T = tank
w = water
1 = known
2 = unknown

Superscripts

i = initial
f = final

Acronyms

CFV = critical flow venturi
PVTt = pressure, volume, temperature, and time
RSS = root sum square

References

[1] Berg, R., Green, D., and Mattingly, G., 2000, *Semiconductor Measurement Technology: Workshop on Mass Flow Measurement and Control for the Semiconductor Industry*, NIST Special Publication 400-101, National Institute of Standards and Technology, Gasunie, Gaithersburg, MD, p. 17.
[2] Wright, J., 2003, ‘‘What is the ‘Best’ Transfer Standard for Gas Flow?’’ *Proceedings of FLOMEKO*, Groningen, The Netherlands.
[3] Olsen, L., and Baumgarten, G., 1971, ‘‘Gas Flow Measurement by Collection Time and Density in a Constant Volume,’’ *Flow: Its Measurement and Control in Science and Industry*, The Instrumentation, Systems, and Automation Society, Research Triangle Park, NC, pp. 1287–1295.
[4] Kegel, T., 1995, ‘‘Uncertainty Analysis of a Volumetric Primary Standard for Compressible Flow Measurement,’’ *Proceedings of Flow Measurement 3rd International Symposium*, San Antonio, TX, Colorado Engineering Experiment Station, Nunn, Co.
[5] Ishibashi, M., Takamoto, M., and Watanabe, N., 1985, ‘‘New System for the Pressurized Gas Flow Standard in Japan,’’ *Proceedings of International Symposium on Fluid Flow Measurements*, American Gas Association.
[6] Wright, J., 2001, ‘‘Laboratory Primary Standards in Flow Measurement,’’ *Flow Measurement: Practical Guides for Measurement and Control*, 2nd Ed., D. W. Spitzer ed., The Instrumentation, Systems, and Automation Society, Research Triangle Park, NC, pp. 731–760.
[7] Wright, J., Johnson, A., and Moldover, M., 2003, ‘‘Design and Uncertainty Analysis for a PVTt Gas Flow Standard,’’ J. Res. Natl. Inst. Stand. Technol., **108**, pp. 21–47.
[8] Wright, J., and Johnson, A., 2000, ‘‘Uncertainty in Primary Gas Flow Standards Due to Flow Work Phenomena,’’ *Proceedings of FLOMEKO*, Salvador, Brazil, Institute for Technological Research, Sao Paulo, Brazil.
[9] Carslaw, H., and Jaeger, J., 1946, *Conduction of Heat in Solids*, 2nd Ed., Clarendon Press, Oxford, pp. 198–201.
[10] Jaeger, J., and Davis, R., 1984, *A Primer for Mass Metrology*, NBS Special Publication 700-1, National Bureau of Standards, Gaithersburg, MD, p. 22.
[11] Lemmon, E., McLinden, M., and Huber, M., 2002, *Refprop 23: Reference Fluid Thermodynamic and Transport Properties*, NIST Standard Reference Database 23, Version 7.0, 7/30/02, National Institute of Standards and Technology, Boulder, CO.
[12] International Organization for Standardization, 1996, *Guide to the Expression of Uncertainty in Measurement*, Switzerland.

Journal of Fluids Engineering

Technical Briefs

Phase-Averaged Velocity Field Measurements of Flow Around an Isolated Axial-Fan Model

Sang-Joon Lee[1]
Professor, Department of Mechanical Engineering,
Pohang University of Science and Technology,
Pohang 790-784, Korea
e-mail: sjlee@postech.ac.kr

Jayho Choi
Research Engineer, Digital Applicance Research
Laboratory, LG Electronics, Seoul 153-802, Korea
e-mail: jayho@LGE.com

Jong-Hwan Yoon
Research Engineer, Power Plant Technology
Research Team, Doosan Heavy Industry, Changwon
641-742, Korea
e-mail: jhyoon@doosanheavy.com

The phase-averaged flow characteristics around a forward-swept axial fan model were investigated using a two-frame PTV method. The velocity fields in the sagittal and axial planes show clearly the periodic variations of flow structure and periodic shedding of the tip and trailing vortices according to the fan blade phase.

[DOI: 10.1115/1.1624422]

Introduction

In order to improve the fan efficiency and reduce the acoustic noise, accurate measurements of the flow field around the fan is not only essential, but also indispensable for future developments of different kinds of turbomachinery.

Ravindranath and Lakshminarayana [1] measured the flow velocity in the wake of a compressor rotor blade using a tri-axial hot-wire probe rotating with the rotor. They revealed that large velocity decay occurs at the trailing edge of the blade and that the wake width in the trailing edge region varies rapidly. Morris et al. [2] investigated the wake of an automotive cooling fan using a hot-wire anemometry.

The accurate measurements of the flow around an axial turbomachinery, however, are difficult using pointwise measurement techniques due to the three-dimensional turbulent structure. Recently, the particle image velocimetry (PIV) and particle tracking velocimetry (PTV) methods have been also employed for measuring flow field around turbines and pumps, etc.

Shepherd et al. [3] measured the flow around a centrifugal fan and an axial-fan using the optical PIV method. The double-exposed particle images recorded on 35-mm films were processed by optical means using Fourier transform lens and traverse system.

Sinha and Katz [4] used an autocorrelation PIV technique with a high-resolution CCD camera to measure the velocity fields inside a centrifugal pump. Wernet [5] developed a digital PIV system to measure flows in the blade passage region of a transonic axial compressor and the diffuser region of a high-speed centrifugal compressor.

The objective of this study is to investigate of the flow structure of an isolated forward-swept axial-fan model. A high-speed CCD camera was used along with the two-frame PTV velocity field measurement system, [6]. Phase-averaged mean velocity fields, vorticity fields, and turbulence intensity distributions were obtained by ensemble averaging 500 velocity fields.

Experimental Apparatus and Method

The isolated axial-fan model used in the present study has five forward-swept blades. The tip-to-tip diameter and the hub diameter of the fan are 50 mm and 14.3 mm, respectively. The fan tested in this experiment is a 1/10 scale scale-down model of the outdoor cooling fan used for commercial air conditioners (LG Electronics Inc.). The axial fan was installed inside a rectangular basin. Tap water was used as the working fluid in which small particles (Vestosint) with an average diameter of 37 μm and a specific gravity of 1.016 were seeded. The rotation speed of the axial fan was set at a constant 240 rpm throughout the experiments.

The schematic diagrams of the axial fan and velocity field measurement planes are shown in Fig. 1. The four measurement phases are placed at angular intervals of 18° from the trailing edge of a blade tip and labeled as phases 1, 2, 3, and 4. The coordinate axes and the field of view for axial plane measurements are shown in Fig. 1(*b*).

For the derivation of velocity field data, a two-frame PTV system consisting of a Nd:YAG laser, a high-speed CCD camera (Speedcam+) of 512×512 pixels resolution, a synchronization circuit and a PC was employed. The two-frame PTV algorithm is based on the iterative estimation of match probability, [6]. For updating the match probability, match probabilities of neighboring particles satisfying heuristics of small velocity change and common motion are used.

When small vortices with large velocity gradients exist across a small interrogation region, the PTV method can resolve the corresponding velocity vectors as long as the particle centroids are discernible. However, conventional PIV method can yield a zone-averaged velocity vector at reduced accuracy due to broadening of

---

[1] To whom correspondence should be addressed.

Contributed by the Fluids Engineering Division for publication in the JOURNAL OF FLUIDS ENGINEERING. Manuscript received by the Fluids Engineering Division April 21, 2000; revised manuscript received June 25, 2003. Associate Editor: J. Katz.

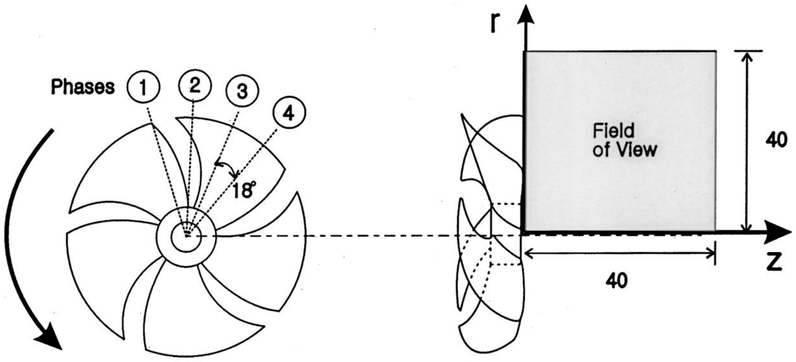

(a) Sagittal plane measurements

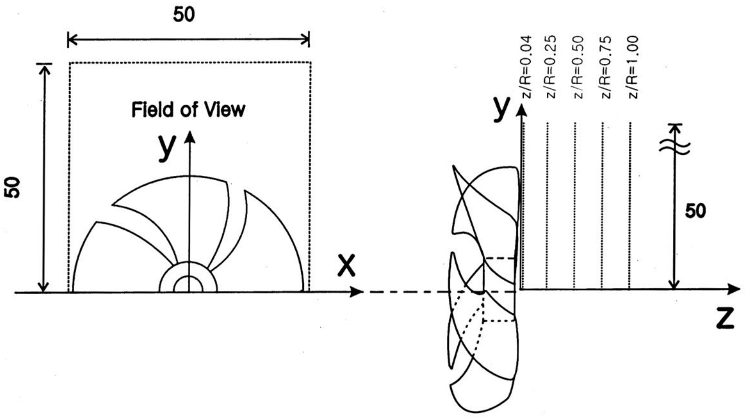

(b) Axial plane measurements

Fig. 1 Field of views and coordinate system for sagittal and axial plane measurements (units: mm)

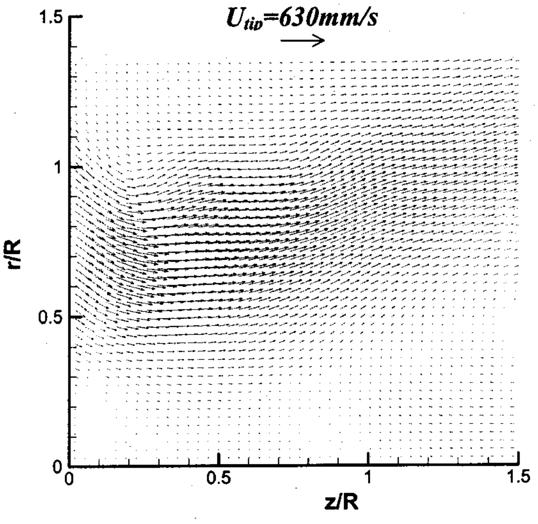

Fig. 2 Mean velocity vector field in the sagittal plane at phase 1

the displacement peak and produce erroneous vectors inside the interrogation window in which a solid boundary is located.

The high-speed CCD camera captured sequential particle images with the frame straddling technique. Since the consecutive velocity fields enable us to see the temporal evolution of flow structures such as velocity fields and vorticity contours, this type of measurements is very useful for investigating internal flow of turbomachineries.

A comparison study was carried out for a backward facing step flow to evaluate the measurement error of the two-frame PTV system. The mean velocity and turbulence intensity profiles obtained with a laser Doppler velocimetry (LDV) were compared with the two-frame PTV results measured under the same flow condition, [7]. The mean velocity was found to have measurement error less than 2% and the uncertainty of turbulence intensity measurements was estimated to be smaller than 5%.

Results and Discussion

Sagittal Planes. Figure 2 shows the mean velocity vector field in the sagittal plane at phase 1. A relatively high-momentum flow toward the hub is observed in the region just behind the fan ($z/R \approx 0.1$). The maximum axial velocity is located in the mid section of $0.6 < r/R < 0.7$. This result is in agreement with the results of Morris et al. (Fig. 9(*a*) of [2]) in which the maximum velocity occurs at the mid section ($0.7 < r/R < 0.8$) at $z/R = 0.172$.

Figure 3 shows the vorticity contours derived from the phase-averaged velocity field data. In phase 1, a positive tip vortex is located behind the blade tip region. A region of negative vorticity

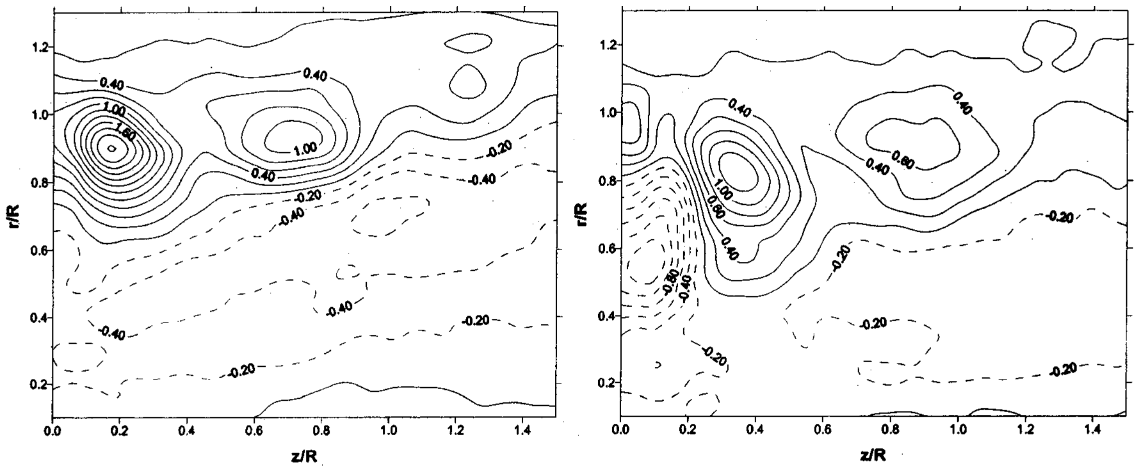

(a) Phase 1

(b) Phase 2

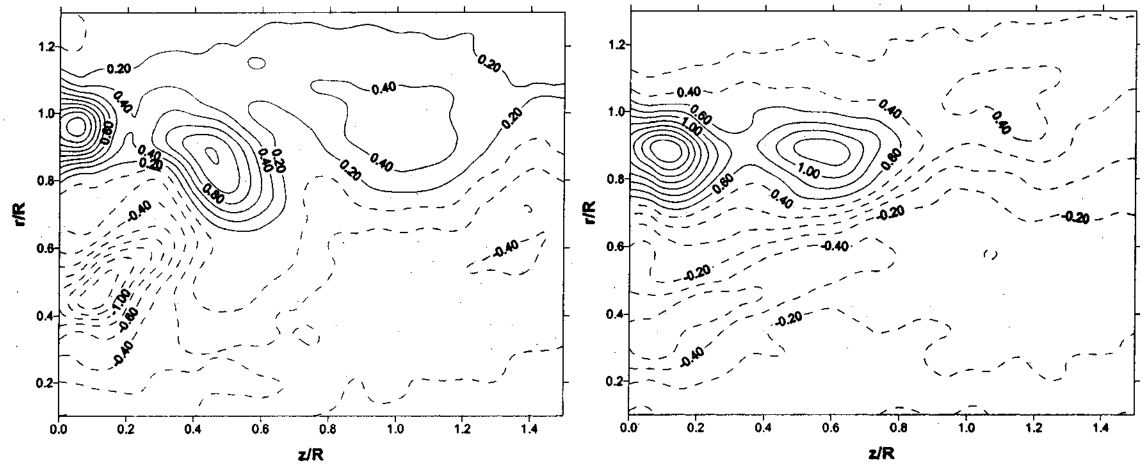

(c) Phase 3

(d) Phase 4

Fig. 3 Vorticity contours in the sagittal plane

exists between the hub and the midsection of the fan blade. In this region, vortices of circular shape are difficult to find. In phase 2, a large-scale negative vortex is shed from the blade in the region $0<z/R<0.2$, $0.4<r/R<0.8$. The positive tip vortex in phase 1 is moved downstream and its center is shifted from $z/R=0.17$ to $z/R=0.25$. For the case of phase 3, the negative trailing vortex near the hub is increased in size and is transferred downstream. The center location of the vortex is moved toward the axis of rotation from $r/R=0.55$ in phase 2 to $r/R=0.45$ in phase 3, while a new positive vortex is shed from the blade tip region. When the positive vortex moves downstream, the vorticity value is decreased. In phase 4, the tip vortex shedding from the previous phase is moved downstream and the trailing vortex located in the lower half region in phase 3 is elongated. The vorticity contours measured at consequent blade phases clearly showed the periodic change of flow structure behind the axial fan.

Figure 4 shows the axial turbulence intensity distributions with respect to the blade phase. The local minimum turbulence intensity is located near $r/R=0.8$ in the immediate wake region behind of the fan blade in phase 3. However, the axial turbulence intensities have relatively high values in phase 2. This may be attributed to the unblocked space between the fan blades.

In the wake region behind the fan blade where $r/R<1$, the axial turbulence intensity has large values in the far field ($z/R>0.5$). However, the radial turbulence intensity, not shown in here due to the page limitation, has large values in the near field ($z/R<0.5$). It can be noted that local maximum values exist in an alternating manner, which is due to the periodic flow structure and the tip and trailing vortices alternatively occurring in the axial direction.

Axial Planes. Figure 5 shows the phase-averaged velocity fields measured in the axial plane at $z/R=0.04$, perpendicular to the axis of rotation. The velocity field shows azimuthally repeated flow structure at the same intervals as the fan blades. In the region just behind the blade spacing between two adjacent blades, the flow direction is drastically changed.

The vorticity contour plots calculated from the phase-averaged velocity fields are shown in Fig. 6. At the axial plane $z/R=0.04$, the negative vortices located around the blade tips represent the tip vortex shedding from the blade tip. The elongation along the blade tips is due to the forward-swept geometry of the fan blades. The trailing vortices having positive vorticity are also elongated along the fan blade. This elongation is mainly due to the roll up of the flow at the lower surface of the blades on the suction side of the fan. The vorticity contour at the $z/R=0.25$ plane (Fig. 6(*b*)), the angular distance between the trailing vortex and the tip vortex is changed and the strength of the two vortices is de-

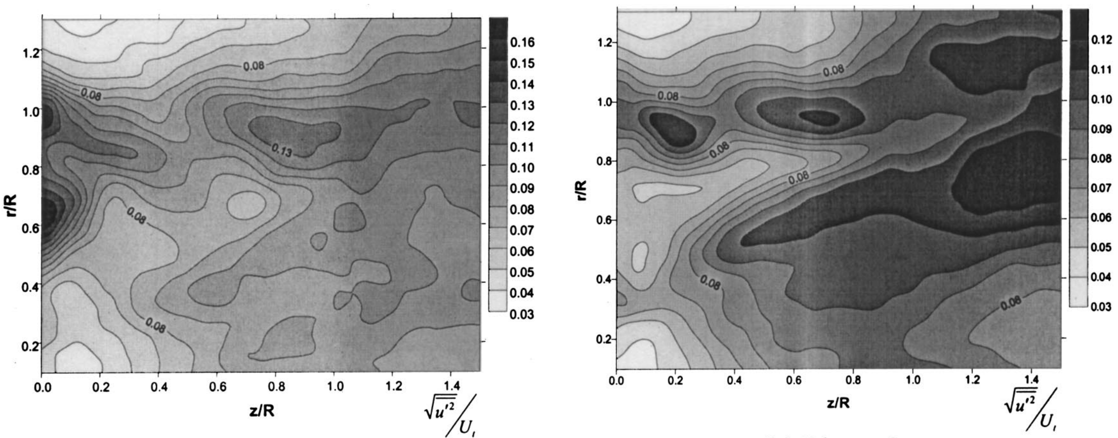

(a) Phase 1

(b) Phase 2

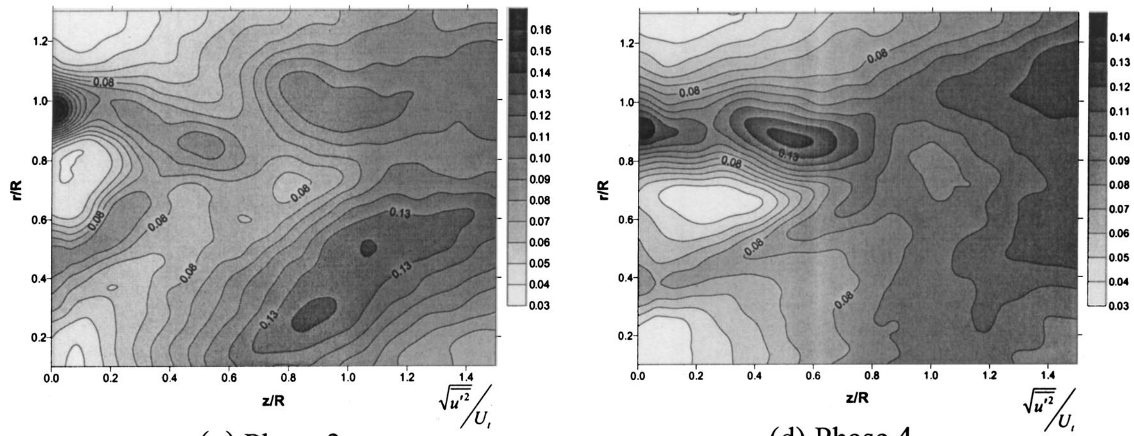

(c) Phase 3

(d) Phase 4

Fig. 4 Contour plots of the axial turbulence intensity distribution

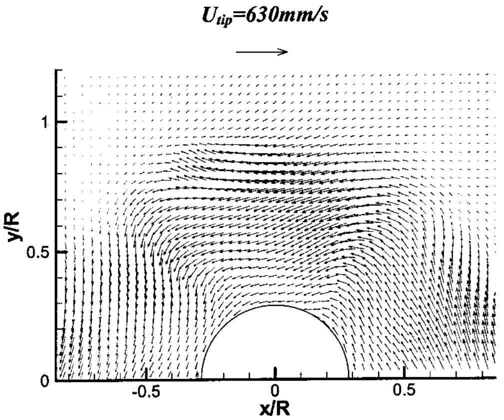

Fig. 5 Mean velocity vector field in the axial plane at $z/R = 0.04$

creased. As the flow goes downstream from the fan, the strength of the trailing vortices and tip vortices is decayed and their relative angular positions are changed continuously. From these contour plots, the spiral flow motion can be conjectured. In addition, the angular convection velocities of the two vortices are different and the tip vortex is dissipated earlier than the trailing vortex.

In the $z/R = 1.0$ plane (Fig. 7), it is difficult to find the tip vortex, and only five weak trailing vortices generated from the five fan blades are observed. Five decaying trailing vortices were found evenly distributed at constant intervals around the hub. The complete experimental data set and specifications of the axial-fan model tested are available on the website (http://efcl.postech.ac.kr/data/data.asp).

Conclusion

The turbulent wake behind an axial-fan model was investigated experimentally using a phase-average two-frame PTV technique. The wake flow has a periodic flow structure according to the blade phase. Strong vortices rotating in the counterclockwise direction are shed from the trailing edges of the blade and local maximum values of axial and radial turbulence intensities appear in an alternating manner.

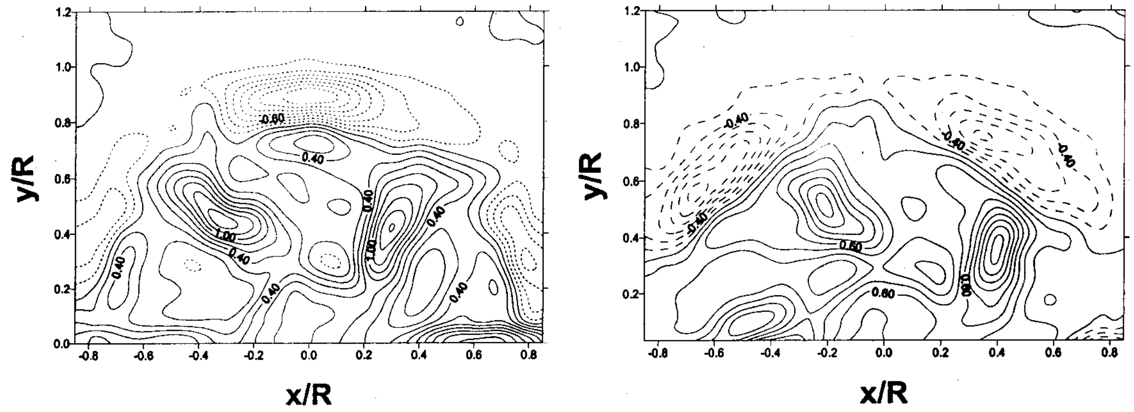

(a) z/R=0.04 (b) z/R=0.25

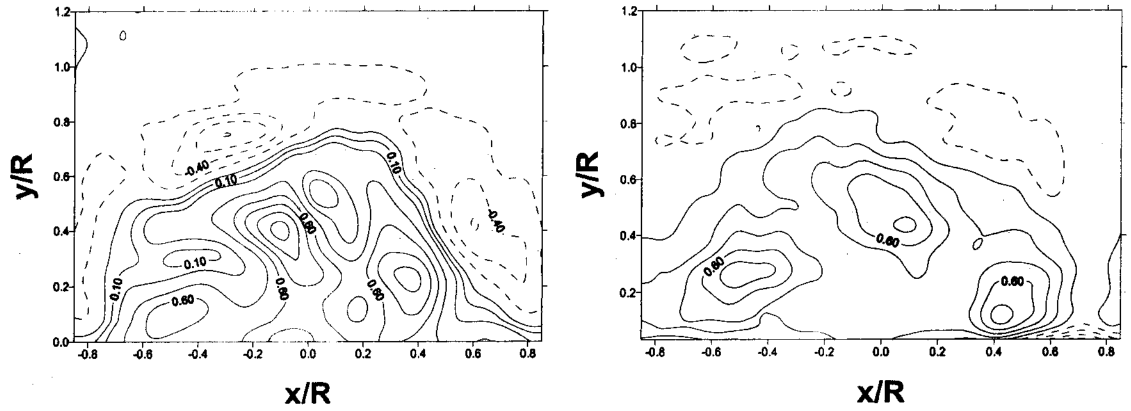

(c) z/R=0.5 (d) z/R=0.75

Fig. 6 Contour plots of mean vorticity in the axial planes

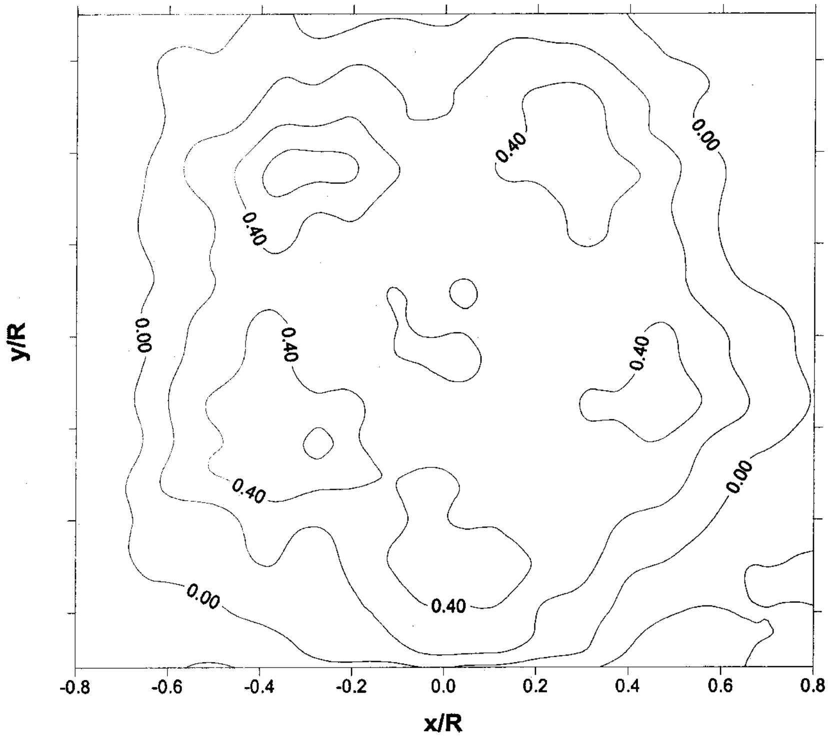

Fig. 7 Contour plot of mean vorticity in the axial plane $z/R=1.0$

References

[1] Ravindranath, A., and Lakshminarayana, B., 1980, ‘‘Mean Velocity and Decay Characteristics of the Near and Far-Wake of a Compressor Rotor Blade of Moderate Loading,’’ ASME J. Eng. Power, **102**, pp. 535–548.

[2] Morris, S. C., Good, J. J., and Foss, J. F., 1998, ‘‘Velocity Measurements in the Wake of an Automotive Cooling Fan,’’ Exp. Therm. Fluid Sci., **17**, pp. 100–106.

[3] Shepherd, I. C., Fotaine, R. F. L., Welch, L. W., and Downie, R. J., 1994, ‘‘Velocity Measurement in Fan Rotors Using Particle Image Velocimetry,’’ *Laser Anemometry–1994: Advances and Applications*, ASME, New York, ASME FED-Vol. 191, pp. 179–183.

[4] Sinha, M., and Katz, J., 1998, ‘‘Flow Structure and Turbulence in a Centrifugal Pump With a Vaned Diffuser,’’ *Proc. 1998 ASME Fluids Engineering Division*, ASME, New York, FEDSM98-5129.

[5] Wernet, M. P., 2000, ‘‘Development of Digital Particle Velocimetry for Use in Turbomachinery,’’ Exp. Fluids, **28**, pp. 97–115.

[6] Baek, S. J., and Lee, S. J., 1996, ‘‘A New Two-Frame Particle Tracking Algorithm Using Match Probability,’’ Exp. Fluids, **22**, pp. 23–32.

[7] Baek, S. J., 1997, ‘‘Development of Two-Frame Particle Tracking Velocimetry System and Its Applications to Turbulent Shear Flows,’’ Ph.D. thesis, POSTECH, Korea.

Rapid Transition to Turbulence in Pipe Flows Accelerated From Rest

David Greenblatt[1] and Edward A. Moss

University of the Witwatersrand, PO WITS 2050, South Africa

Rapid transition to turbulence in a pipe flow, initially at rest, was achieved by temporally accelerating the flow and then sharply decelerating it to its final Reynolds number. The acceleration phase was characterized by the growth of a laminar boundary layer close to the wall. The subsequent rapid deceleration resulted in inflectional velocity profiles near the wall, followed immediately by transition to turbulence. The time taken to transition was significantly less than the time to transition in a pipe flow monotonically accelerated to the same Reynolds number. Transition is intrinsically different to that observed in oscillatory pipe flows, but is qualitatively similar to pipe flows decelerated to rest. [DOI: 10.1115/1.1624423]

1 Introduction

Transition to turbulence in pipe flows is one of the classic problems of fluid mechanics, and is still the subject of active research. Transition occurs when the Reynolds number (Re) exceeds a critical value Re_c, that is strongly influenced by disturbances at the pipe inlet (e.g., Wygnanski and Champagne [1]) or within the unstable developing entrance flow (e.g., Morkovin and Reshotko [2]). Thus Re_c is facility dependent with values as low as about 2000 provided that disturbances at the inlet are large enough. The precise mechanisms by which turbulence develops far downstream of an inlet are even now not fully understood, mainly due to the fact that pipe-Poiseuille flows are known to be stable to infinitesimal disturbances (e.g., Davey and Drazin [3]), while their response to finite amplitude disturbances is unresolved and still the subject of ongoing research (e.g., Patera and Orszag [4], Shan et al. [5], Ma et al. [6], Eliahou et al. [7], and Han et al. [8]). The addition of unsteadiness, superimposed on the base flow, further complicates the analysis of experimental data as well as theoretical investigations. For example, when the flow is oscillated periodically, four different transition regimes have been identified (e.g., Hino et al. [9]). Transition is seen to occur at the end of the acceleration phase and is ‘‘violent’’ (Hino et al. [9]) or appears ‘‘explosively’’ (Akhavan et al. [10]) throughout the entire pipe (e.g., Merkli and Thomann [11]). This is believed to be due to inflectional instability of the velocity profiles (Das and Arakeri [12]). Nevertheless, quasi-steady stability analyses based on ‘‘frozen’’ profiles predict that the most unstable inflectional profiles occur at the start of the acceleration phase, which is nearly 180° out of phase with observations of sudden transition (Akhavan et al. [10]).

In some applications, it is desirable to attain as high a Re_c as possible, because laminar flows are associated with reduced frictional losses. However, in many instances, it is desirable to reduce the critical Reynolds number, for example, in order to promote turbulent momentum and heat transfer and to enhance mixing or combustion. In steady flows this generally involves the introduction of disturbances at the pipe inlet (e.g., Wygnanski and Champagne [1]). For pipe flows started from rest, however, disturbances are usually washed down or intermittent (e.g., Moss and Abbot [13]) thereby delaying the time taken for turbulent flow to be fully established with the entire pipe. This transition mechanism can be a problem in pipes of high aspect ratio and may result, for example, in transient ‘‘hot spots’’ in heat exchanger systems due to the different flow regimes existing simultaneously in the pipe. However, in pipe flows accelerated to high Reynolds numbers ($\mathrm{Re} \geqslant 240{,}000$), transition is seen to occur globally within the pipe and can be delayed to $\mathrm{Re} > 500{,}000$ providing the acceleration is severe enough (Lefebvre and White [14]). A different approach was adopted by Das and Arakeri [12], who studied pipe flows accelerated from rest, maintained at a constant velocity, and then subsequently decelerated to rest. On the basis of calculated velocity profiles, they concluded that the time taken to transition (t_{tr}) following the deceleration was approximately $39/\Delta u/\delta$ (Δu and δ are the difference between maximum and minimum velocity and boundary layer thickness, averaged over the deceleration, respectively).

The present investigation employs a similar technique for inducing rapid transition in pipe flows accelerated from rest. The method involves initially accelerating the pipe flow to a Re in excess of that desired, but then rapidly decelerating it to a nonzero Re, unlike Das and Arakeri [12] whose final Reynolds number was zero. Presently, velocity profiles are measured and details of the ensemble averaged flow development and subsequent transition are presented. These are compared with the mechanism and time scales required to achieve transition by the conventional method of directly establishing the final Re. Furthermore, the present results are contrasted with observations in oscillatory pipe flows and examined in light of the observations and analysis of Das and Arakeri [12].

2 Experimental Setup

Experiments were performed on a pipe flow facility comprising eight 1.5 m long sections of high-accuracy glass piping, of internal diameter $d = 48$ mm, joined together smoothly by means of Teflon sleeves. A large pressurized vessel supplied water to the piping via a standard bell-mouth entrance contraction, i.e., the pipe inlet. Single-component laser Doppler velocimeter (LDV) measurements were made along the horizontal radial axis of the piping, from the near pipe wall ($y = 0$) to the pipe centerline ($y = a = d/2$). The piping section furthest downstream was connected to PVC tubing, that incorporated a magnetic flowmeter for monitoring the instantaneous cross-sectional velocity $U_m(t)$. The PVC tubing further incorporated a pneumatically operated valve that was located further downstream. Water exited the valve and flowed through additional tubing, to a reservoir, from where it was pumped back to the supply vessel. For this facility, $\mathrm{Re}_c \approx 13{,}000$ and disturbance levels immediately downstream of the inlet were $1\% < u'/U_m < 1.4\%$ irrespective of Reynolds number.

Flow acceleration from rest was achieved by opening the pneumatically operated valve at constant speed to its maximum setting over two seconds, and then partially closing it at constant speed over 0.5 s to its final setting, while maintaining a 1 atm supply vessel pressure. For purposes of comparison, direct acceleration

---

[1] Present address: NASA Langley Research Center, Mail Stop 170, 1 East Reid Street, Hampton, VA 23681-2199. E-mail: fn.d.greenblatt@larc.nasa.gov

Contributed by the Fluids Engineering Division for publication in the JOURNAL OF FLUIDS ENGINEERING. Manuscript received by the Fluids Engineering Division January 13, 2003, revised manuscript received June 23, 2003. Associate Editor: T. B. Gatski.

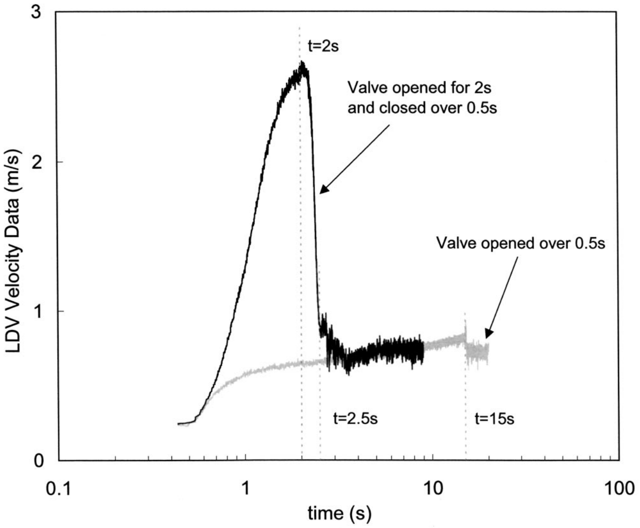

Fig. 1 LDV data acquired at $y/a\approx1.0$ for (1) a simple acceleration from rest; and (2) acceleration from rest, followed by deceleration

from rest was achieved by opening the valve at constant speed to its final setting, with the same supply vessel pressure. For both cases, the final Reynolds number ($\mathrm{Re}\equiv U_m d/\nu$) was 31,000 ($\nu$ is the kinematic viscosity). Velocity data were acquired at 25 radial locations, 9.12 meters (190 diameters) downstream of the pipe inlet. Time-dependent velocity profiles $U(y,t)$ were obtained by averaging repeated experimental runs within 50 ms time windows. Repeated runs indicated pre-transition U differences of less than 0.5%. Uncertainty associated with determination of the wall location was $y/a=\pm0.005$.

3 Discussion of Results

The problem associated with attaining rapid transition is illustrated in Fig. 1, which compares LDV data at $y/a\approx1.0$ for two cases. In the first case, the valve is opened over 0.5 seconds to produce a final Reynolds number of 31,000; in the second case the valve is opened to its maximum and then partially closed at $t=2$ s, over 0.5 s, to produce the same final Reynolds number. The continuously increasing velocity for $t<15$ s in the first case is indicative of the velocity profile gradually developing towards a parabaloid shape. In fact, laminar flow is maintained at this downstream location despite the fact that the Reynolds number is supercritical for this pipe system. At $t=15$ s, transition to turbulence can clearly be seen, where the mechanism was believed to be wash down from the inlet, since $\int U_m dt=9.01$ m from $t=0$ s to 15 s, which is close to the measurement location 9.12 meters (190 diameters) downstream of the pipe inlet. In the second case, the flow is accelerated to a much higher velocity (corresponding to $\mathrm{Re}\approx120{,}000$) where it nevertheless remains laminar due to the stabilizing effect of the acceleration. The abrupt deceleration causes rapid transition approximately 0.5 s later, resulting in a 12 s difference in time taken to attain transition. Transition is clearly not due to wash down of the entrance flow since $\int U_m dt=2.99$ m from $t=0$ to 2.5 s, and this is discussed further below.

Figures 2(*a*) and 2(*b*) show the velocity profile development (U versus y/a) over the entire radius and close to the wall ($y/a<0.25$), respectively, during the acceleration for $t<2$ s (legend on Fig. 2(*b*)). For the first recorded velocity profile, at $t=0.475$ s, the flow across the pipe has an almost constant velocity, with viscous effects evident only very near to the wall ($y/a<0.05$). As the cross-sectional velocity increases, these viscous effects are evident progressively further from the wall, indicating a temporal growth of the boundary layer. Simultaneously, the velocity outside the boundary layer remains approximately constant. Comparing data close to the wall ($y/a<0.08$) at $t=1.275$ s and $t=1.975$ s, shows a local velocity reduction even though the cross-sectional velocity increases during this time interval. The reduction is due to the diffusion of viscous shear away from the wall with time—leading to boundary layer growth and a reduction of wall shear, despite the fact that the cross-sectional velocity has increased. This results in a relatively steep velocity gradient associated with the boundary layer just prior to the termination of the acceleration phase ($t=2$ s).

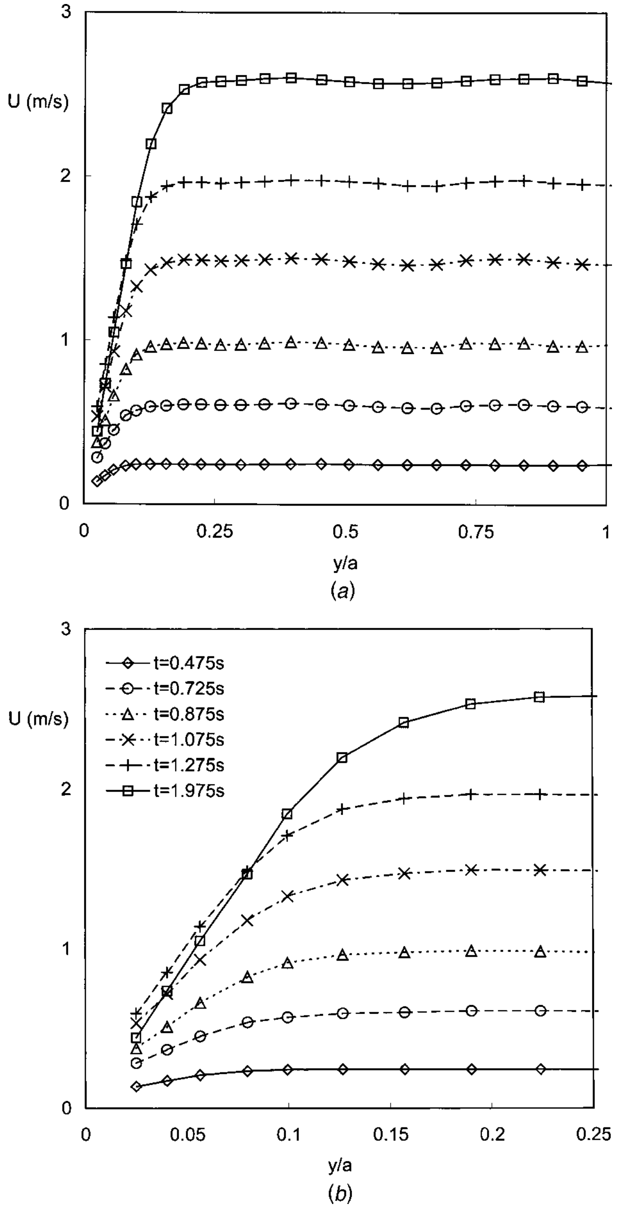

(*a*)

(*b*)

Fig. 2 Velocity profiles during the acceleration phase ($t<2$ s), showing (*a*) flow development across the pipe radius, and (*b*) near-wall details of the boundary layer (caption on Fig. 2(*b*)).

For the time interval $2\text{ s}<t<2.5$ s, the flow is decelerated from its maximum value ($\mathrm{Re}\approx120{,}000$) to its final value ($\mathrm{Re}=31{,}000$). Velocity profiles close to the wall ($y/a<0.3$) for this interval are shown in Fig. 3, while the velocity remains effectively constant for $y/a\geqslant0.3$ (not shown). Shortly after commencement of the deceleration ($t=2.025$ s), the velocity profile is seen to develop an "inflection region" (at $y/a\approx0.07$), which is present throughout the deceleration. The shaded area on the figure approximately identifies this region, which was determined by a third-order polynomial least-squares curve fit to the developing

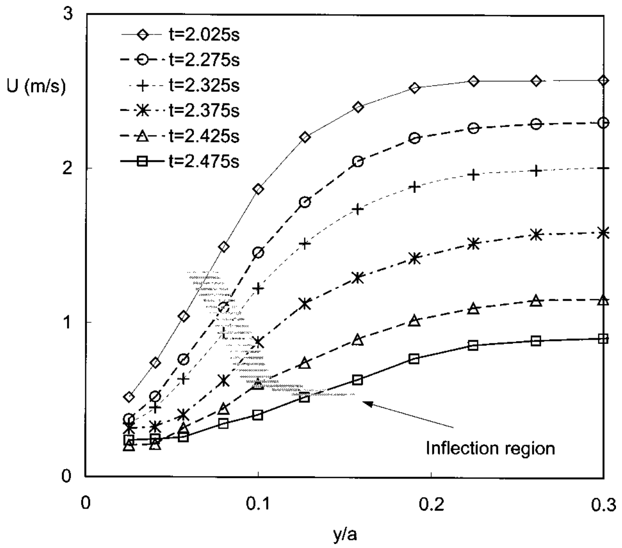

Fig. 3 Near-wall velocity profiles during the deceleration phase (2 s$<t<$2.5 s)

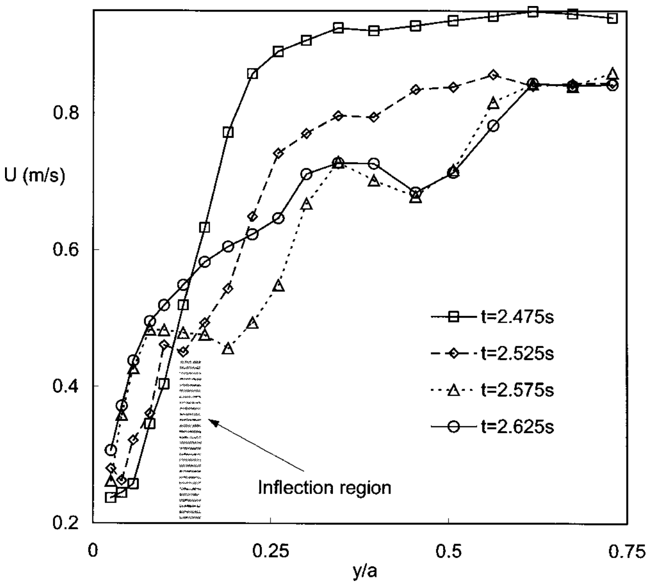

Fig. 4 Velocity profiles subsequent to the deceleration phase ($t>$2.5 s)

velocity profile. The uncertainty associated with determination of the inflection, is based on curve fits to successive profiles. Data, presented at 50 ms intervals, shows that this region moves away from the wall, from $y/a \approx 0.07$ to $y/a \approx 0.10$ over the time interval 2.025 s$<t<$2.425 s, consistent with the temporally increasing boundary layer thickness. The final stages of the acceleration (2.425 s$<t<$2.475 s) are accompanied by significantly more movement of the inflection from $y/a \approx 0.10$ to $y/a \approx 0.14$. Over this latter period the velocity close to the wall ($y/a<0.05$) increases, despite the overall mean flow deceleration. Thus, the final stages of the acceleration are characterized by a relatively large change in the nature of the inflectional profile. For the purpose of analyzing the subsequent development of the flow we shall refer to $y/a \approx 0.14$ as the final inflection location.

Subsequent to the deceleration phase, the velocity profiles undergo substantial distortion, consistent with abrupt transition to turbulence during the interval 2.475 s$<t<$2.625 s, as illustrated in Fig. 4. The first evidence of transition in the context of the ensemble-averaged data is a kink in the velocity profile at $t=2.525$ s, which occurs in the vicinity of the inflection location (shown on Fig. 4). This is followed at $t=2.575$ s by a dramatic increase in flow velocity between this location and the wall, together with a decrease and distortion of the profile for values of y/a greater than the final inflection location. Finally, velocities in the vicinity of the final inflection location ($0.09 \lesssim y/a \lesssim 0.3$) increase abruptly, while the remainder of the profile remains virtually unchanged. The net effect is to render the profile more turbulent-like, with relatively large velocities near the wall, although the profile is still somewhat distorted.

The present experiment, namely an acceleration followed immediately by a deceleration, can be considered similar to the half-cycle of an oscillatory flow. However, in oscillatory flows, transition is seen to occur explosively at the end of the acceleration phase (e.g., Hino et al. [9], and Akhavan et al. [10]). Presently, the flow is seen to remain laminar throughout the deceleration, despite the fact that a velocity profile inflection is discernable from the commencement of the deceleration ($t>2$ s). The only obviously common feature is the relatively abrupt nature of transition, which is presently less than 0.2 seconds. In the absence of fluctuating velocity data the role of the inflection towards the end of the deceleration cannot be clearly discerned, but given the time-varying nature of the averaged velocity profiles an inflectional instability mechanism emerges as a leading candidate for further scrutiny.

This investigation has more in common with that of Das and Arakeri [12], where the flow is accelerated from rest, maintained at constant velocity and subsequently decelerated to rest. In both investigations, transition occurred at the end of the deceleration, which is intrinsically different to oscillatory flows where transition occurs towards the end of the acceleration cycle (e.g., Hino et al. [9] and Akhavan et al. [10]). Presently, however, velocity profiles were measured and not inferred from calculation as in the case of [12]. Unlike oscillatory flows, the observations in these two investigations are consistent with quasi-steady stability theory, [10,12]. A possible explanation is that transition in oscillatory flows is affected by the *temporal* flow history in much the same way as transition in *steady* flows is affected by inlet or entrance flow history. In this context, temporally decaying residual turbulence, generated during previously intermittent turbulent events but present in the relaminarized flow, may act as a bypass trigger. The problem could be further exacerbated by lack of homogeneity within a developing flow. This investigation, as well as that of [12], differs from oscillatory flow investigations in that turbulence was not generated at an earlier time. The lack of

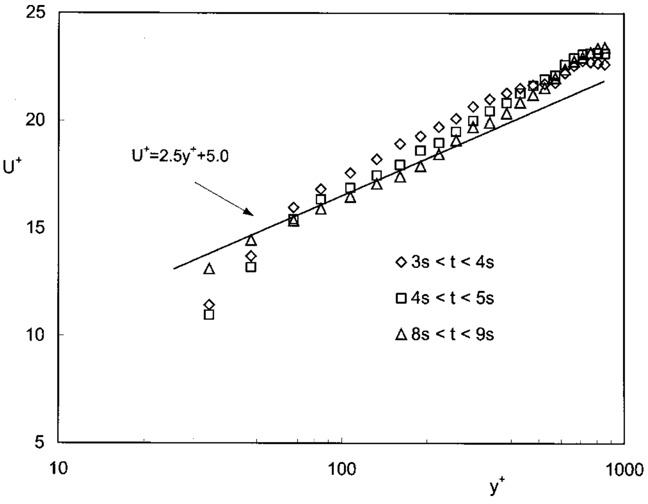

Fig. 5 Velocity profiles averaged over 1 s time intervals subsequent to transition

residual turbulence may be a factor in determining the transition mechanism and explaining its consistency with quasi-steady stability theory.

An important difference between this investigation and that of [12], was the time taken to transition following the deceleration, which was long relative to the deceleration time in [12] but short presently. One possible reason for this discrepancy may be the difference in the maximum Reynolds numbers employed, namely 8500 in [12] versus 120,000 presently. In addition, the current flow is not decelerated to rest, but rather to a final nonzero Reynolds number and even though the present velocity profiles are inflectional, there is no evidence of the near-wall reverse-flow of the type computed by Das and Arakeri [12]. This may be because our flow is developing both spatially and temporally with relatively large velocity gradients near the wall—not only temporally as in the analysis and assumptions of Das and Arakeri [12], and this may further limit the applicability of their analysis to the present work.

The time taken to transition referenced to the time at which the deceleration commences (t_{tr}), used by Das and Arakeri [12] is approximately 0.55 s for the present experiment. However, the time scale based on the analysis of Das and Arakeri [12] using the velocity profiles measured presently, indicates that $t_{tr}\approx 39/\Delta u/\delta = 0.15$ s, which suggests that this scaling is inappropriate in the current context.

For data acquired at $t > 2.65$ s, repeated runs showed variations in averaged velocity from individual runs to be greater than 5%, thus precluding a meaningful assessment of the final stages of transition. However, because of the relatively slow evolution of the velocity profiles, it was appropriate to compute time averaged velocities for the intervals $3\,\mathrm{s} < t < 4$ s, $4\,\mathrm{s} < t < 5$ s and $8\,\mathrm{s} < t < 9$ s. The data are presented in Fig. 5, where all quantities are presented in wall coordinates $U^+ = U/U_\tau$ and $y^+ = yU_\tau/\nu$ (where $U_\tau \equiv (\tau/\rho)^{1/2}$ and τ was calculated from Blasius' turbulent pipe flow correlation based on the final Reynolds number (see Schlichting [15]) and compared to the log-law. Although the flow immediately following transition is a nonequilibrium flow, the data are plotted in this manner to illustrate its turbulent nature. Steady state is effectively achieved during the interval $8\,\mathrm{s} < t < 9$ s, while at the intermediate state defined by $4\,\mathrm{s} < t < 5$ s, the log and wake regions are almost fully constituted. A comparison of the three velocity profiles shows that the largest changes with time occur in the vicinity of $y^+ \approx 30$. For $t > 9$ s, changes in the velocity profile are negligible and the entire pipe flow can be considered to be fully turbulent.

4 Concluding Remark

The method of accelerating and then rapidly decelerating a pipe flow was shown to be an effective method for achieving rapid transition to turbulence that does not rely on wash down from the entrance. The rapid deceleration generates an inflectional velocity profile with subsequent transition to turbulence and thus an inflectional instability mechanism may play a role in the transition process. This transition mechanism is intrinsically different from those observed in oscillatory pipe flows, but is believed to be qualitatively similar to that in pipe flows decelerated to rest. Nevertheless, time scales characterizing transition during the deceleration are presently much more rapid than those in pipe flows decelerated to rest. Future work will involve a parametric study considering initial and final Reynolds numbers as well as the relevant acceleration and deceleration time scales.

References

[1] Wygnanski, I. J., and Champagne, F. H., 1973, ''On Transition in a Pipe. Part 1. The Origin of Puffs and Slugs and the Flow in a Turbulent Slug,'' J. Fluid Mech., **59**, pp. 281–335.

[2] Morkovin, M. V., and Reshotko, E., 1990, ''Dialogue on Progress and Issues in Stability and Transition Research,'' *Laminar-Turbulent Transition*, IUTAM Symposium, Toulouse, D. Arnal and R. Michel, eds., Springer, Berlin, pp. 1–29.

[3] Davey, A., and Drazin, P. G., 1969, ''The Stability of Poiseuille Flow in a Pipe,'' J. Fluid Mech., **221**, pp. 209–218.

[4] Patera, A. T., and Orszag, S. A., 1981, ''Finite Amplitude Stability of Axisymmetric Pipe Flow,'' J. Fluid Mech., **112**, pp. 467–474.

[5] Shan, H., Zhang, Z., and Nieuwstadt, F. T. M., 1999, ''Direct Numerical Simulation of a Puff and a Slug in Transitional Cylindrical Pipe Flow,'' J. Fluid Mech., **387**, pp. 39–60.

[6] Ma, B., van Doorne, C. W. H., Zhang, Z., and Nieuwstadt, F. T. M., 1999, ''On the Spatial Evolution of a Wall-Imposed Periodic Disturbance in Pipe Poiseuille Flow at Re=3000. Part 1. Subcritical Disturbance,'' J. Fluid Mech., **398**, pp. 181–224.

[7] Eliahou, S., Tumin, A., and Wygnanski, I., 1998, ''Laminar-Turbulent Transition in Poiseuille Pipe Flow Subjected to Periodic Perturbation Emanating From the Wall,'' J. Fluid Mech., **361**, pp. 333–349.

[8] Han, G., Tumin, A., and Wygnanski, I., 2000, ''Laminar-Turbulent Transition in Poiseuille Pipe Flow Subjected to Periodic Perturbation Emanating From the Wall, Part II: Late Stage of Transition,'' J. Fluid Mech., **419**, pp. 1–27.

[9] Hino, M., Sawamoto, M., and Takasu, S., 1976, ''Experiments on Transition to Turbulence in an Oscillating Pipe Flow,'' J. Fluid Mech., **75**, pp. 193–207.

[10] Akhavan, R., Kamm, R. D., and Shapiro, A. H., 1991, ''An Investigation of Transition to Turbulence in Bounded Oscillatory Stokes Flows. Part 1. Experiments,'' J. Fluid Mech., **225**, pp. 395–422.

[11] Merkli, P., and Thomann, H., 1975, ''Transition to Turbulence in Oscillating Pipe Flow,'' J. Fluid Mech., **68**, pp. 567–575.

[12] Das, D., and Arakeri, J. H., 1998, ''Transition of Unsteady Velocity Profiles With Reverse Flow,'' J. Fluid Mech., **374**, pp. 251–283.

[13] Moss, E. A., and Abbot, A. H., 2002, ''The Effect of Finite Amplitude Disturbance Magnitude on Departures From Laminar Conditions in Impulsively Started and Steady Pipe Entrance Flows,'' ASME J. Fluids Eng., **124**, pp. 236–240.

[14] Lefebvre, P. J., and White, F. M., 1989, ''Experiments on Transition to Turbulence in a Constant-Acceleration Pipe Flow,'' ASME J. Fluids Eng., **124**, pp. 236–240.

[15] Schlichting, H., 1979, *Boundary Layer Theory*, McGraw-Hill, New York, Chap. XVI, pp. 448–452.

Use of Large-Eddy Simulation to Characterize Roughness Effect of Turbulent Flow Over a Wavy Wall

Jie Cui

Ching-Long Lin

Virenda C. Patel

IIHR-Hydroscience and Engineering and Department of
Mechanical and Industrial Engineering,
The University of Iowa, Iowa City, IA 52242-1585

Large-eddy simulation is used to study turbulent flow over a sinusoidal wavy wall from the perspective of surface roughness effects. Simulation results are averaged in time and space to obtain the so-called roughness function (shift in the logarithmic law), the equivalent sand-grain roughness and the virtual origin, and the dependence of these quantities on the amplitude-to-wavelength ratio. The results demonstrate the usefulness of LES to quantify roughness effects that have hitherto fore been the purview of laboratory experiments. [DOI: 10.1115/1.1624424]

1 Introduction

Turbulent flow over a sinusoidal wavy boundary has generated much interest during the past several decades because it contributes to understanding of fundamental mechanisms that control distorted flows and helps answer practical environmental and engineering questions. One of these questions relates to the effect of a

---

Contributed by the Fluids Engineering Division for publication in the JOURNAL OF FLUIDS ENGINEERING. Manuscript received by the Fluids Engineering Division Mar. 25, 2003; revised manuscript received June 30, 2003. Associate Editor: F. F. Grindstein.

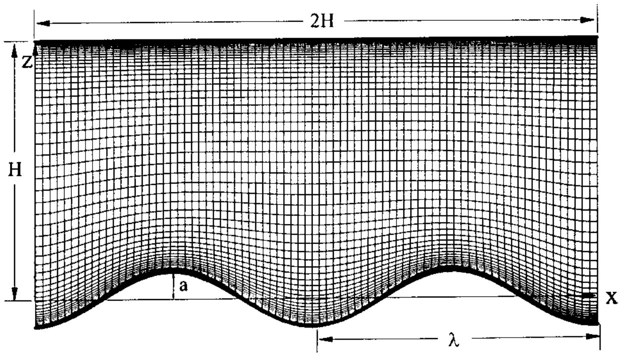

Fig. 1 Computational grid in the wavy channel

wavy boundary when it is regarded as surface roughness. Recent experimental and numerical investigations have yielded quite detailed information about the flow over sinusoidal wavy walls. In particular, large-eddy simulations (LES), [1,2,3], have provided information about flow separation and reattachment, mean and fluctuating pressure and friction distributions, the turbulence structure, and the complex eddy motions close to the wavy surface.

In this technical brief we analyze the LES data of Cui et al. [3] in the framework of roughness effects. Using a consistent method of analysis, it is shown that these data provide information about the effect of the wavy wall on the external flow when averaged in time and space, and lead to insights into the traditional concepts of a roughness function, namely, the downward shift in the logarithmic law from its smooth-wall position, equivalent sand-grain roughness, and location of the virtual origin. Although the sinusoidal wavy surface is used as an example, the underlying concepts can be extended to other boundary shapes and roughness geometry.

Figure 1 shows the channel geometry with a sinusoidal wavy wall. The steepness of the wavy boundary is defined as $2a/\lambda$, where $2a$ is the height from trough to crest, and $\lambda(=H)$ is the wavelength. There is no variation in the spanwise direction, i.e., the wavy wall is two-dimensional. In the LES of Cui et al. [3], the three-dimensional, unsteady, incompressible, filtered continuity and Navier-Stokes equations were solved with a dynamic subgrid-scale model using a finite volume method. Surface-fitted grids with 82×42×66 points in the streamwise, spanwise, and wall-normal directions, respectively, were generated for three values of wave steepness: 0.05, 0.1, and 0.2. The imposed mean pressure gradient was adjusted to keep the Reynolds number (Re), based on the bulk velocity (U_b) and half-channel height ($H/2$), constant at 10,000. Periodic boundary conditions were imposed in both the streamwise (x) and spanwise (y) directions. No-slip boundary conditions were applied at the top and bottom channel boundaries. Detailed descriptions of the LES method, code validation and flow features are given in Cui et al. [3].

2 Analysis of Wavy Wall as Surface Roughness

2.1 Resistance Components. Resistance to the flow in the channel with a wavy wall comprises pressure and friction components. These components of resistance (drag force) calculated from the LES results are summarized in Table 1 (Note: Forces are per unit width of channel, and are normalized by $\rho U_b^2 H$).

For the wall with the smallest amplitude waves, $2a/\lambda = 0.05$, the pressure drag is almost twice the friction drag. Total resistance of the channel with the smallest amplitude waves is only slightly higher than that of the flat channel (0.0105 versus 0.010). Therefore, in the terminology of roughness, this channel may be regarded as *hydrodynamically smooth.*

Table 1 Resistance components

	Drag Force (Resistance)				
	Lower Wall				
$2a/\lambda$	Pressure Drag	Friction Drag	Upper Wall	Total	Imposed Force
0.05	0.00395	0.00205	0.00446	0.0105	0.0106
0.10	0.0153	0.00207	0.00515	0.0225	0.0220
0.20	0.0415	0.00076	0.0067	0.0489	0.0490

For the case $2a/\lambda = 0.1$, the friction drag on the wavy boundary remains almost unchanged while the pressure drag is nearly four times larger than the case $2a/\lambda = 0.05$. For the case with the highest wave amplitude, $2a/\lambda = 0.2$, the friction drag from the lower wall is almost negligible due to the large separation zone and there is a large pressure drag. The contribution from the top wall increases but is much less significant in comparison with the pressure drag.

The results in Table 1 show that the waves are very effective in generating drag. The last column of Table 1 is the mean pressure force imposed in the streamwise direction to drive the mean flow. As noted above, the mean pressure gradient was adjusted to maintain a constant Reynolds number of 10,000 in the three cases. In all cases, the imposed pressure force balances the total drag from lower and upper surfaces, validating the numerical method and verifying that sufficient sampling times are used to process the LES results.

2.2 The Law of the Wall and Roughness Function. The principal result obtained from experiments in pipes, closed and open channels, and boundary layers on rough walls over diverse types of roughness is that the velocity distribution near a rough wall, when plotted in the semi-logarithmic form of the law of the wall, has the same slope as on a smooth wall, but different intercept:

$$U^+ = \frac{1}{\kappa}\ln(z^+) + B - \Delta B. \tag{1}$$

In this equation U^+ is the velocity, normalized by the *friction velocity* u_τ, z is distance from the wall measured from some *virtual origin* and normalized by ν/u_τ, ν is kinematic viscosity of the fluid, κ=0.418, $B = 5.45$, [4], and the shift ΔB is called the *roughness function*. For sandgrain roughness, ΔB is a function of $k_s^+(=k_s u_\tau/\nu)$, where k_s is the sandgrain height. For roughness other than sandgrain, ΔB depends on the type and size of roughness. Currently, there is no theoretical way to predict ΔB for any roughness configuration.

The LES results were processed to calculate the wave-averaged velocity and the virtual origin as follows. The time-and-spanwise-averaged velocity field was first mapped onto a Cartesian grid by interpolation to facilitate the wave averaging. The mapping was of second-order accuracy, same as the original LES. These velocities were then averaged along constant z surfaces over a wavelength. The location of zero wave-averaged streamwise velocity is taken as the virtual origin. This virtual origin is located at a distance z_0 *from the top of the wavy surface* and is listed in Table 2 for the three wave amplitudes. It is found that the virtual origin is close to

Table 2 Roughness parameters

$2a/\lambda$	$z_0/2a$	ΔB	k_s^+	$k_s/2a$
0.05	0.90	1.05	5.6	0.10
0.1	0.74	10.00	234	1.255
0.2	0.505	14.65	1,630	2.81

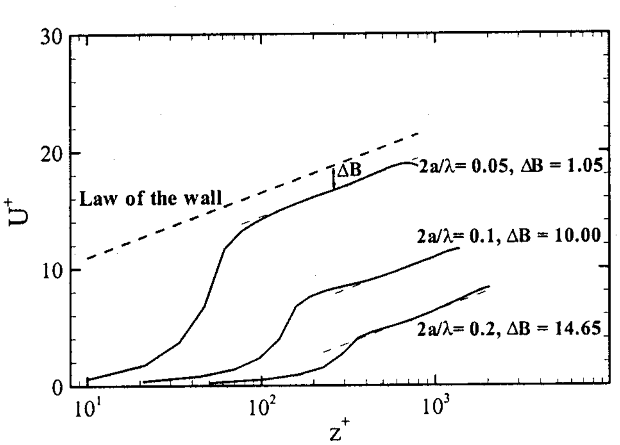

Fig. 2 Wave-averaged velocity profiles

the bottom of the wave for the smallest amplitude and moves toward the wave center for the largest amplitude. This is consistent with the increasing volume of reverse flow with increasing wave amplitude.

The distributions of the wave-averaged velocity normalized by the wave-averaged friction velocity (u_τ) derived from the total resistance on the wavy surface (including the pressure and friction components) are plotted in the traditional format in Fig. 2. Compared with the law of the wall on a smooth wall, these velocity profiles have the same slope (i.e., the same Karman constant κ) in the logarithmic region but a roughness function ΔB that increases with increasing wave amplitude. This result shows that a wavy wall can indeed be regarded as a roughness in the classical way. It is also noted that the logarithmic region begins at a higher z^+ position from the virtual origin with increasing wave amplitude, further indicating stronger roughness effects generated by waves with higher amplitude.

For sufficiently large sandgrain roughness, in the so-called *fully rough regime*, Schlichting [5] gives the following correlation between the roughness function and roughness height:

$$B-\Delta B=8.5-\frac{1}{\kappa}\ln k_s^+ . \tag{2}$$

Cebeci and Bradshaw [6] give the following correlation to extend Eq. (2) to transitional roughness:

$$\Delta B=\left[B-8.5+\frac{1}{\kappa}\ln k_s^+\right]\sin\{0.4285(\ln k_s^+-0.811)\} \tag{3}$$

for $2.25<k_s^+<90$, with $B=5.2$ and $\kappa=0.42$. For $k_s^+>90$, this formula reduces to Eq. (2). The values of the roughness function obtained from Fig. 2 and the corresponding k_s^+ from Eqs. (2) and (3) for the three wavy walls are listed in Table 2. Also shown is the ratio $k_s/2a$. For the case $2a/\lambda=0.2$, the equivalent sandgrain roughness height is $5.62a$, i.e., sandgrains almost three times larger than the wave amplitude would be required to generate the same roughness effect.

3 Conclusions

Data from large-eddy simulation (LES) of turbulent flow in a channel with a sinusoidal wavy wall are analyzed to examine the wave-averaged velocity profile in the framework of surface roughness effects. The wave-averaged velocity profiles, when normalized by the wave-averaged friction velocity that includes both the friction and pressure components, show all of the well-known characteristics of turbulent flow over a rough wall. This analysis gives the so-called roughness function, the virtual origin and the equivalent sandgrain roughness. This study shows that LES may be used to provide information that is normally established by recourse to experiment, and raises the interesting possibility of exploring other types of roughness used in fluids engineering.

References

[1] Calhoun, R. J., 1998, "Numerical Investigations of Turbulent Flow Over Complex Terrain," Ph.D. thesis, Stanford University, Stanford, CA.
[2] Henn, D. S., and Sykes, R. I., 1999, "Large-Eddy Simulation of Flow Over Wavy Surfaces," J. Fluid Mech., **383**, pp. 75–112.
[3] Cui, J., Patel, V. C., and Lin, C. L., 2003, "Prediction of Turbulent Flow Over Rough Surfaces Using a Force Field in Large Eddy Simulation," ASME J. Fluids Eng., **125**, pp. 2–9.
[4] Patel, V. C., 1965, "Calibration of the Preston Tube and Limitations on Its Use in Pressure Gradient," J. Fluid Mech., **23**, pp. 185–208.
[5] Schlichting, H., 1979, *Boundary-Layer Theory*, 7th Ed., McGraw-Hill, New York.
[6] Cebeci, T., and Bradshaw, P., 1977, *Momentum Transfer in Boundary Layers*, Hemisphere, Washington, DC.